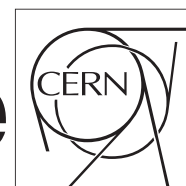


The Compact Muon Solenoid Experiment

CMS Draft Note

Mailing address: CMS CERN, CH-1211 GENEVA 23, Switzerland



2013/01/18

Head Id: 162782

Archive Id: 165458M

Archive Date: 2012/12/28

Archive Tag: trunk

Updated results on the new boson discovered in the search for the standard model Higgs boson in the $H \rightarrow ZZ \rightarrow 4\ell$ channel in pp collisions at $\sqrt{s} = 7$ and 8 TeV

N. Amapane¹, I. Anderson², P. Avery³, M. Bachtis⁴, S. Baffioni⁵, F. Beauvette⁵, A. Belknap¹¹, D. Benedetti⁶, C. Bernet⁴, P. Bhat⁷, J. Bochenek⁸, S. Bolognesi², A. Bonato⁴, D. Bortoletto⁶, C. Botta⁴, S. Braibant⁹, N. Cartiglia¹, S. Cassaso¹, F.R. Cavallo⁹, C. Charlot⁵, M. Chen³, Y. Chen¹⁵, T. Cheng³, R. Covarelli²⁰, M. Dalchenko⁵, S. Dasu¹¹, A. Drozdetskiy³, N. De Filippis¹⁰, Y. Gao⁷, P. Giacomelli⁹, A. Gritsan², M. Gomez-Ceballos¹², K. Hahn¹⁹, P. Janot⁴, K. Johnson⁸, M. Klute¹², R. Khurana¹³, A. Korytov³, M. Kovac^{5,18}, A. Levin¹², J. Lykken⁷, B. Mangano¹⁴, M. Mannelli⁴, E. Di Marco¹⁵, C. Mariotti^{1,4}, C. Martin², K. Matchev³, E. Migliore¹, P. Milenovic³, G. Miniello¹⁰, G. Mitselmakher³, M. Masciovecchio⁹, M. Meneghelli⁹, A. Mohammadi¹⁶, M. Mozer⁴, C. Ochando⁵, G. Ortona¹, C. Paus¹², M. Pelliccioni¹, E. Perez⁴, G. Petrucciani¹⁴, R. Plestina^{5,18}, H. Prosper⁸, I. Puljak¹⁸, D. Ralph¹², A. Rinkevicius³, I. Ross¹¹, D. Sabes⁵, R. Salerno⁵, A. Savin¹¹, V. Sharma¹⁴, G. Singh¹⁰, Y. Sirois⁵, J. Smith¹⁷, M. Snowball³, K. Sung¹², M. Spiropulu¹⁵, A. Takeda¹⁵, S. Tentido⁸, N. Tran⁷, A. Vartak¹⁴, P. Verwilligen¹⁰, A. Whitbeck², S. Xie¹⁵, and C. You²

¹ Torino University² John Hopkins University³ University of Florida⁴ CERN⁵ Laboratoire Leprince-Ringuet⁶ Purdue University⁷ FNAL⁸ Florida State University⁹ Bologna University¹⁰ Bari University¹¹ University of Wisconsin¹² Massachusetts Institute of Technology¹³ Saha Institute of Nuclear Physics and Visva-Bharati University¹⁴ University of California, San Diego¹⁵ California Institute of Technology¹⁶ Universit libre de Bruxelles¹⁷ University of California, Davis¹⁸ University of Split

Abstract

Measurements of the properties of the new boson recently observed at a mass near 125 GeV in the CMS experiment are reported. The results are obtained from a comprehensive search for the standard model Higgs boson in the $H \rightarrow ZZ$ decay channel, where both Z's decay to electron, muon, or tau lepton pairs. The search covers Higgs boson mass hypotheses in the range $110 < m_H < 1000$ GeV. The analysis uses pp collision data recorded by the CMS detector at the LHC, corresponding to integrated luminosities of 5.1 fb^{-1} at $\sqrt{s} = 7 \text{ TeV}$ and 12.2 fb^{-1} at $\sqrt{s} = 8 \text{ TeV}$. The new boson is observed with a local significance above the expected background of 4.5 standard deviations. The signal strength μ , relative to the expectation for the standard model Higgs boson, is measured to be $\mu = 0.80^{+0.35}_{-0.28}$ at 126 GeV. A measurement of its mass gives $126.2 \pm 0.6 \text{ (stat)} \pm 0.2 \text{ (syst)} \text{ GeV}$. The hypothesis 0^+ of the standard model for the spin $J = 0$ and parity $P = +1$ quantum numbers is found to be consistent with the observation. The data disfavor the pseudoscalar hypothesis 0^- with a CL_s value of 2.4%. No other significant excess is found, and upper limits at 95% confidence level exclude the ranges 113–116 GeV and 129–720 GeV while the expected exclusion range for the standard model Higgs boson is 118–670 GeV.

This box is only visible in draft mode. Please make sure the values below make sense.

PDFAuthor:

The HZZ4l team

PDFTitle:

Search for the standard model Higgs boson in the decay channel H to ZZ to 4l in pp collisions

PDFSubject:

CMS

PDFKeywords:

CMS, physics, Higgs

Please also verify that the abstract does not use any user defined symbols

1 Contents

1	1	Introduction	2
2	1.1	Overview of the ICHEP and HCP Analysis	4
3	1.2	ICHEP General Analysis Strategy	4
4	1.3	Main Changes Since ICHEP Analysis	7
5	1.4	Blinding policy	7
6	2	Datasets and Triggers	8
7	2.1	Experimental Data	8
8	2.2	Simulated Samples	9
9	3	Leptons Observables	12
10	3.1	Electron Reconstruction and Identification	12
11	3.2	Muon Reconstruction and Identification	25
12	3.3	Primary and Secondary Leptons	26
13	3.4	Lepton Isolation	26
14	4	Leptons Measurements	29
15	4.1	T&P methodology	29
16	4.2	Electrons	29
17	4.3	Muons	40
18	5	Photon Observables and FSR recovery	45
19	5.1	Photon Reconstruction and Identification	45
20	5.2	Photon Isolation	46
21	5.3	Building Z's with FSR Photon Recovery	46
22	5.4	Studies on $H \rightarrow ZZ$, SM ZZ MC	47
23	5.5	Studies on data	48
24	6	Event Selection	50
25	6.1	Selection Performance and Control	51
26	7	Signal Model and uncertainties	56
27	7.1	Signal model	56
28	7.2	High Mass model	62
29	7.3	Signal model uncertainties	68
30	7.4	Four-lepton mass: scale and resolution	72
31	8	Irreducible ZZ Background Model and uncertainties	114
32	8.1	$ZZ^{(*)}$ yields	114
33	8.2	$ZZ^{(*)}$ Background Model	114
34	8.3	$ZZ^{(*)}$ model uncertainties	116
35	9	Reducible Background Model and Systematic Uncertainties	119
36	9.1	Reducible background prediction	119
37	9.2	Reducible Backgrounds Uncertainties	131
38	9.3	Summary	133
39	10	Kinematic Discriminant (MELA)	136
40	10.1	Introduction of the methodology	136
41	10.2	Construction of the MELA discriminant	138
42	10.3	Parameterization of the MELA discriminant	144

44	11	Summary of Selection and Systematic Uncertainties	149
45	11.1	Event yields and errors	149
46	11.2	Distributions of events	149
47	11.3	Anatomy of the signal	155
48	11.4	FSR performances	158
49	11.5	Summary of systematic uncertainties	160
50	12	Statistical Analysis	162
51	12.1	Methodology using 2D distributions ($m_{4\ell}$, KD)	162
52	12.2	Limits	162
53	12.3	Significance of excesses	162
54	12.4	Cross section/signal strength	162
55	12.5	Statistical analysis with per-event mass error as observable	167
56	12.6	Approach to Higgs Boson Spin and Parity Measurements	179
57	13	Summary and Conclusions	193
58	A	Appendix #1 Approach to VBF/VH Production Mechanism Measurement	198
59	A.1	Selection of tagged VBF events	199
60	A.2	Systematic sources on the VBF tag	203
61	A.3	$p_{T,4\ell}/m_{4\ell}$ description for untagged VBF events - 126 GeV	207
62	A.4	$p_{T,4\ell}/m_{4\ell}$ description for untagged VBF events - full mass range	207
63	A.5	Systematic sources on $p_{T,4\ell}/m_{4\ell}$ description	208
64	A.6	Results	209
65	B	Appendix #2 Control of lepton efficiencies from data, tables	224
66	C	Appendix #3 Control of lepton efficiencies from data, tables	225
67	D	Appendix #4 Analysis using MEKD Kinematic Discriminant	226
68	D.1	Matrix Element Kinematic Discriminant (MEKD)	226
69	D.2	Kinematic Discriminant distributions and parameterization	230
70	D.3	Results and comparison with MELA	234
71	E	Appendix #5 Matrix Element with Vector Algebra Method for $H \rightarrow ZZ \rightarrow 4\ell$ Studies	235
72	E.1	ME evaluated with MCFM	235
73	E.2	ME evaluated with JHUGen for signal hypothesis separations	236
74	E.3	Correction for lepton interference and parameterization of KD templates	237
75	E.4	Performance with the KD	242
76	E.5	Spin-parity analysis	242

78 1 Introduction

79 TO BE UPDATED (talk about discovery paper, etc...)

80 The standard model (SM) of electroweak interactions [1–3] relies on the existence of the Higgs
 81 boson, a scalar particle of mass m_H associated with the field responsible for the spontaneous
 82 electroweak symmetry breaking [4–9]. The mass m_H is not fixed by the theory and the existence
 83 of the scalar boson has not yet been established experimentally. The Higgs boson production
 84 followed by the decay $H \rightarrow ZZ$ is expected to be one of the main discovery channels at the

85 CERN proton-proton (pp) Large Hadron Collider (LHC) for a wide range of m_H values.

86 Direct searches for the SM Higgs bosons have been performed by the ATLAS and CMS experiments using each about 4.7 fb^{-1} of pp data from the LHC collected in 2010 and 2011 at $\sqrt{s} = 7 \text{ TeV}$. Searches for the SM Higgs boson in the $H \rightarrow ZZ \rightarrow 4\ell$ channel ($\ell = e, \mu$), have been carried by ATLAS [10] and CMS [11]. Search results combining these with various production and decay channels were obtained by both collaborations [12, 13]. The results from CMS exclude the SM Higgs boson in the mass range 127–600 GeV at 95% confidence level (CL). Direct searches for the SM Higgs boson at the LEP e^+e^- collider and the Tevatron $p\bar{p}$ collider have led, respectively, to a lower mass bound of $m_H > 114.4 \text{ GeV}$ [14], and to an exclusion in the range 162–166 GeV [15], at 95% CL. Indirect constraints from precision measurements favour the mass range $m_H < 158 \text{ GeV}$ [16, 17] at 95% CL.

96 In this paper, a search in the four-lepton decay channels $H \rightarrow 4\ell$ and $H \rightarrow 2\ell 2\tau$, with $\ell = e$ or μ , is presented. The analysis is designed for a Higgs boson in the mass range $110 < m_H < 600 \text{ GeV}$. It re-uses the data collected by CMS in 2011, combined with the new data collected in 99 2012 at $\sqrt{s} = 8 \text{ TeV}$ which corresponds to an additional integrated luminosity of $X.X \text{ fb}^{-1}$.

100 The search essentially relies on the reconstruction, identification and isolation of leptons. Compared to previous CMS analyses [11, 18], it profits from improved lepton reconstruction and 102 isolation efficiencies, combined with the usage of a discriminant exploiting the production and 103 decay kinematics expected for the signal events. The analysis achieves high lepton reconstruction 104 efficiencies for a ZZ system composed of two pairs of same-flavour and opposite-charge 105 isolated leptons, e^+e^- , $\mu^+\mu^-$, or $\tau^+\tau^-$, in the measurement range $m_{4\ell}, m_{2\ell 2\tau} > 110 \text{ GeV}$. One 106 or both of the Z bosons can be off-shell. The single-resonant four-lepton production ($Z \rightarrow 4\ell$) 107 is used as a standard candle in the mass range $70 < m_{4\ell} < 110 \text{ GeV}$. The background sources 108 include an irreducible four-lepton contribution from direct ZZ (or $Z\gamma^*$) production via $q\bar{q}$ anni- 109 hilation and gg fusion. Reducible contributions arise from Zbb and $t\bar{t}$ where the final states contain 110 two isolated leptons and two b jets producing secondary leptons. Additional background 111 of instrumental nature arises from $Z + \text{jets}$ events where jets are misidentified as leptons.

112 The analysis and results described in this note represent an extension of a similar analysis 113 previously published by the CMS Collaboration with collected data in 2010 and 2011. It accom- 114 panies the paper HIG-12-016 in preparation. A comparable note (AN-11-123, version 7) 115 accompanied the HIG-11-004 PAS released for the EPS HEP 2011 conference, then (AN-11-123, 116 version 9) accompanied the HIG-11-015 PAS released for the Lepton-Photon 2011 conference 117 and finally AN-11-386 accompanied the HIG-11-025 and PRL paper. A full independent cross- 118 check analysis as also been performed and is documented in the note.

119 The reader being familiar with the CMS detector, we give here only a short summary for com- 120 pleteness. A detailed description of the can be found elsewhere [19]. The detector comprises a 121 superconducting solenoid providing a uniform magnetic field of 3.8 T. The bore of the solenoid 122 is instrumented with various particle detection systems. The inner tracking system is com- 123 posed of a pixel detector with three barrel layers and a silicon strip tracker with 10 barrel 124 detection layers. Each system is completed by two end caps, extending the acceptance up 125 to $|\eta| < 2.5$. The pseudorapidity η is defined as $\eta = -\ln \tan(\theta/2)$ where θ is the polar angle 126 with respect to the direction of the proton beam. A lead tungstate crystal electromagnetic 127 calorimeter (ECAL) with fine transverse ($\Delta\eta, \Delta\phi$) granularity and a brass-scintillator hadronic 128 calorimeter (HCAL) surround the tracking volume and cover the region $|\eta| < 3$. The steel 129 return yoke outside the solenoid is in turn instrumented with gas detectors which are used to 130 identify muons in the range $|\eta| < 2.4$. The barrel region is covered by drift tube chambers and 131 the end cap region by cathode strip chambers, each complemented by resistive plate chambers.

1.1 Overview of the ICHEP and HCP Analysis

1.2 ICHEP General Analysis Strategy

In this analysis reported in [20, 21], we use data collected with the di-electron and di-muon triggers and select events with well-reconstructed four leptons: $e^+e^-e^+e^-$, $\mu^+\mu^-\mu^+\mu^-$, $e^+e^-\mu^+\mu^-$. An optimal analysis in the 4ℓ channel must preserve the highest possible reconstruction efficiency for the Higgs boson signal.

The sample of events with reconstructed 4ℓ receives an irreducible contribution from $ZZ^{(*)}$ production via $q\bar{q}$ and gluon-induced processes. It further receives the main reducible background contributions from $Zb\bar{b}$ and $t\bar{t} \rightarrow W^+bW^-\bar{b}$, with W undergoing leptonic decays, where the final states contain two isolated leptons and two b jets possibly giving rise to secondary leptons. Reconstructed 4ℓ events can also arise from instrumental background such as $Z+jets$ or $WZ + jet(s)$ where jets are misidentified as leptons.

It has been shown in previous studies that an optimal working point can be found where the contribution from the reducible and instrumental backgrounds are quasi-eliminated. This is achieved by applying cuts on the maximum allowed energy flow in the isolation cones around leptons and on the maximum impact parameter of lepton tracks with respect to the primary interaction vertex. The analysis aims at the highest possible lepton reconstruction, identification and isolation efficiencies, that are compatible with a quasi-negligible reducible and instrumental background, in the acceptance range used for this analysis, i.e. with transverse momentum and pseudorapidity for electrons of $p_T^e > 7$ GeV/c, $|\eta^e| < 2.5$, and for muons of $p_T^\mu > 5$ GeV/c, $|\eta^\mu| < 2.4$.

Electron identification relies on a multivariate Boosted Decision Tree and Muons are asked to fulfill the Particle Flow Muons criteria. Lepton isolation is computed with the Particle Flow approach and is corrected from pile-up contributions attaching charged particles to the primary vertex and correcting neutral component with the so-called "effective area" methodology.

The $pp \rightarrow ZZ \rightarrow 4\ell$ background prediction relies fully on the theory. All instrumental uncertainties associated with selecting four prompt leptons (trigger, reconstruction, isolation and impact parameter cuts) are derived directly from data.

The remaining contribution of reducible backgrounds is evaluated using data driven techniques. This includes the overall rates of 4ℓ events, passing all selection cuts, and their mass distributions. Two different technics are used. Comparable background counts in the signal region are found within uncertainties from both methods. An envelope comprising these results is used as the final estimate.

A Kinematic Discriminant (KD) is built using variables fully describing the kinematics of the $H \rightarrow ZZ \rightarrow 4\ell$ (five angles and two masses). It is constructed based on the probability ratio of the signal and background hypotheses, $KD = Psig/(Psig + Pbkg)$. The signal and $q\bar{q} \rightarrow ZZ$ background (when $m4\ell$ is above the $2 m_Z$ threshold) pdf's are coming from fully analytical parametrisations. When $m4\ell$ is below the $2 m_Z$ threshold, background has significant contribution from the $q\bar{q} \rightarrow ZZ^{(*)}/Zg^{(*)}$ processes and instead of analytical parametrisation it is tabulated in a correlated template distribution using POWHEG simulation at generator level.

The statistical analysis of selected events is based on their four-lepton mass ($m_{4\ell}$) distribution. The presence of the Higgs boson is expected to manifest itself as a resonance over the continuum $m_{4\ell}$ distribution of the $pp \rightarrow ZZ \rightarrow 4\ell$ origin. The width of the peak for a SM Higgs boson with a low mass ($m_H < 250$ GeV) is expected to be defined by the detector resolution. For higher masses, SM Higgs boson's intrinsic width quickly overtakes the detector resolution.

¹⁷⁷ Final results (limits, p-values,...) are extracted via simultaneous likelihood fit of the six two-dimensional ($m_{4\ell}$, KD) distributions, for each mass hypothesis, using the standard statistical
¹⁷⁸ approaches adopted by CMS.

¹⁸⁰ The ICHEP analysis was conducted with data corresponding to integrated luminosities of 5.05fb^{-1}
¹⁸¹ at \sqrt{s} TeV and 5.26fb^{-1} at \sqrt{s} TeV. The table 1 summarizes the number of selected events, com-
¹⁸² pared to the expected background yields and expected number of signal events for various m_H .
¹⁸³ The four-lepton invariant mass distributions for $m_{4\ell}$ was found to be consistent with the stan-
¹⁸⁴ dard model expectations for ZZ production for invariant masses above 180 GeV (see figure 1,
¹⁸⁵ a).

¹⁸⁶ Upper limits at 95% confidence level exclude the standard model Higgs boson in the range 131–
¹⁸⁷ 162 and 172–525 GeV, while the expected exclusion range is 121–570 GeV (see figure 1, b). An
¹⁸⁸ excess of events is observed in the low $m_{4\ell}$ mass range (see figure 1, e), making the observed
¹⁸⁹ limits weaker than expected in the absence of a signal. These events cluster around a mass $m_{4\ell}$
¹⁹⁰ 125.5 GeV with a high score of the kinematic discriminant, as expected from signal events (see
¹⁹¹ figure 1, c and d). This clustering gives rise to a local excess with respect to the background
¹⁹² expectation, with a significance of 3.2 sigma (see figure 1, f) for an expected significance of 3.8
¹⁹³ sigma. This result constitutes evidence for a new massive state.

Table 1: The number of event candidates observed, compared to the mean expected back-
ground and signal rates for each final state. For the Z +X background, the estimations are
based on data. The results are given integrated over the full mass measurement range for the
Higgs boson search from 100 to 800 GeV and for 2011 and 2012 data combined.

Channel	4e	4 μ	2e2 μ
ZZ background	29.27 ± 3.43	49.01 ± 5.08	75.45 ± 8.02
Z+ X	$3.0^{+2.7}_{-1.94}$	$2.2^{+1.56}_{-1.32}$	$5.0^{+3.96}_{-2.98}$
All background expected	$32.27^{+4.37}_{-3.94}$	$51.21^{+5.31}_{-5.25}$	$80.45^{+8.96}_{-8.56}$
$m_H = 120$ GeV	0.77 ± 0.12	1.64 ± 0.19	1.94 ± 0.25
$m_H = 125$ GeV	1.36 ± 0.22	2.74 ± 0.32	3.44 ± 0.44
$m_H = 126$ GeV	1.51 ± 0.24	2.99 ± 0.35	3.81 ± 0.49
$m_H = 130$ GeV	2.14 ± 0.34	4.08 ± 0.47	5.39 ± 0.69
$m_H = 200$ GeV	8.34 ± 1.06	13.25 ± 1.47	21.63 ± 2.48
$m_H = 350$ GeV	4.79 ± 0.7	7.46 ± 0.99	12.65 ± 1.72
$m_H = 500$ GeV	1.68 ± 0.39	2.58 ± 0.57	4.39 ± 0.98
Observed	32	47	93

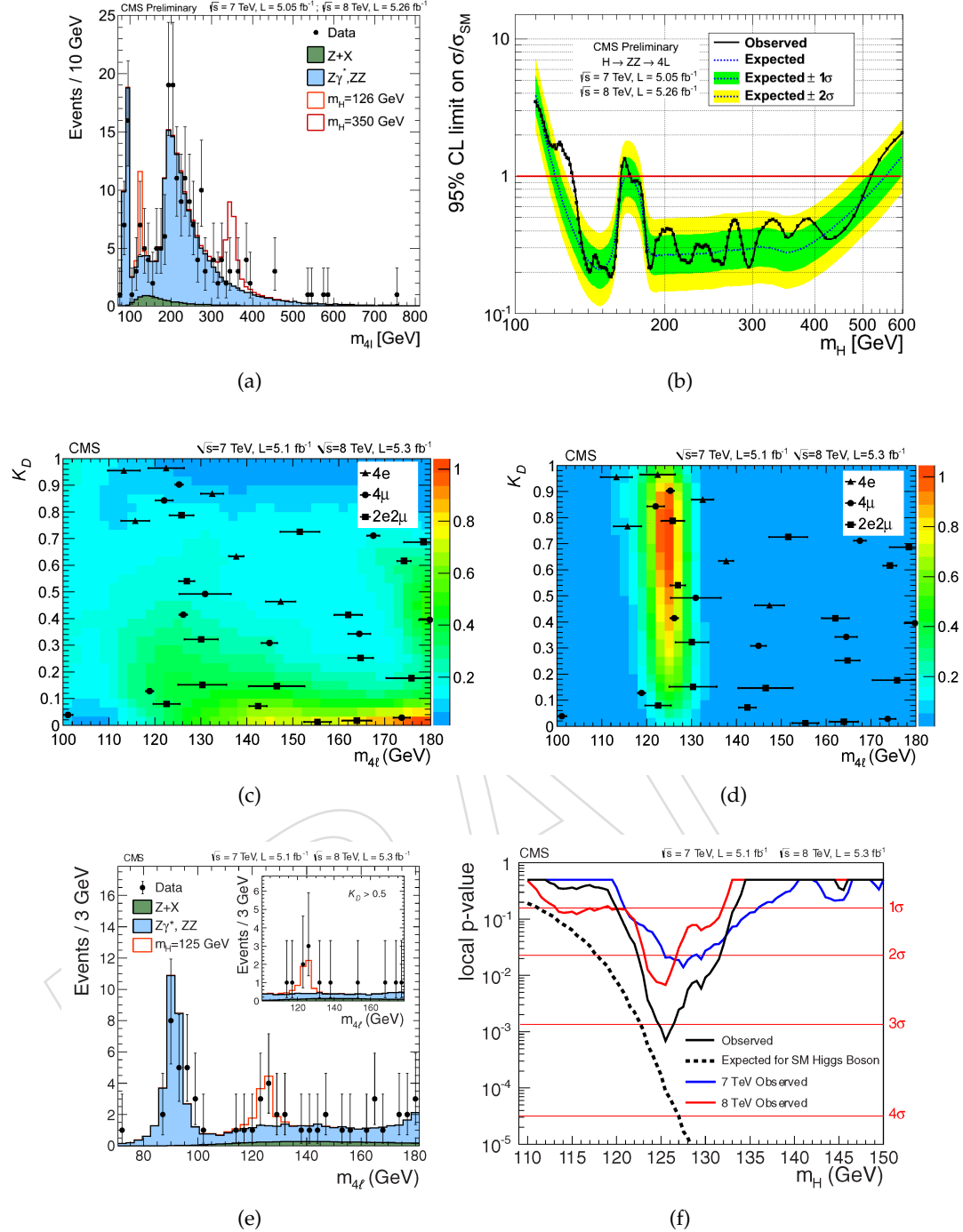


Figure 1: Distribution of the four-lepton invariant mass in the full mass range (a) and the in low mass range (e). The inset in (e) shows the m_{4l} distribution after selection of events with $K_D > 0.5$. Distribution of the MELA K_D versus the four-lepton reconstructed mass m_{4l} in the low-mass range [100-180] GeV ((c) and (d)). The points representing the individual events are shown together with their reconstructed mass uncertainties. The contours represent the background (c) or the signal ($m_H = 125$ GeV) expectations. Observed p-values (f) for a standard model Higgs boson decaying via ZZ to 4e, 4 μ , or 2e2 μ in the range [110-180] GeV. Dashed line represents the expected p-value for a standard model Higgs boson at the corresponding mass. The blue (resp. red) lines represent the 7 (resp. 8) TeV results, whereas black line is the combined result.

194 1.3 Main Changes Since ICHEP Analysis

195 For this analysis, while the general strategy remains almost un-changed with respect to the 2012
 196 ICHEP analysis [20, 21], we brought some improvements in various areas. This section briefly
 197 summarized the main changes. They were mainly focused on improving and cross-checking
 198 the Kinematic Discriminant as well as extending the measurements of properties (cross-section,
 199 mass, spin, production mode) of the new discovered boson:

- 200 • use of 53X reconstruction for both 2012 and MC. 2012 ICHEP dataset (A and B pe-
 201 riods) profits from a ReReco, improving in particular our knowledge and perfor-
 202 mances of the ECAL sub-detector.
- 203 • use of Tri-Electron triggers in OR with Double Electrons for both 2011 and 2012 anal-
 204 ysis to recover some efficiency at low mass in the 4e channel (see Sections 2.1, 4.2.4).
- 205 • small fix of the PF-electron isolation (see Section 3.4).
- 206 • use of Energy Regression for the ECAL energy measurement, similar to what is used
 207 for the $H \rightarrow \gamma\gamma$ analysis (see Section 3.1.3).
- 208 • additional criteria based on "shared segments" to reject "ghost muons" (see Sec-
 209 tion 3.2.3).
- 210 • muon momentum now profits from scale and smearing corrections approved by
 211 Muon POG (see Section 3.2.2).
- 212 • the analysis is extended to 1 TeV, taking into account the necessary re-weighting of
 213 the signal line shape(see Section 7.2) and thus removing the huge uncertainty put
 214 so far above $m_H=400$ GeV. A better modeling of the signal shape at low mass is
 215 achieved (see Section 7).
- 216 • the Kinematic Discriminant (MELA) now profits from full analytical parameteriza-
 217 tion below ZZ* instead of a POWHEG template (see Section 10).
- 218 • extensive studies of Alternative KD's are reported: cross-checks with Matrix Ele-
 219 ment approach from MCFM, Madgraph or CalcHEP (see appendix ??, D).
- 220 • limits, significance of excess, signal strength are updated (see Section 12).
- 221 • mass measurement includes event-by-event errors (see Section 12.5).
- 222 • measurement of different spin/parity hypothesis of the new discovered boson are
 223 reported (see Section 12.6).
- 224 • studies of pT(H) are reported and its usage to separate gluon-gluon fusion and VBF
 225 production mode, together with a specific dijet-tagged category, is described (see
 226 sections A). **However, this is not intended to go for HCP.**

227 In addition, the Tag and Probe measurements are updated with the full dataset (see Section 4).
 228 The method to estimate irreducible and reducible backgrounds are unchanged and updated
 229 numbers will therefore be reported (see Sections 8, 9).

230 The documentation will mainly focus of the changes and will invite the reader to report to [20]
 231 if he needs some more details.

232 1.4 Blinding policy

233 The blinding strategy remains un-changed with respect to [20, 21]. It is repeated here for
 234 completeness.

235 In the channel with low background and high resolution, $H \rightarrow ZZ \rightarrow 4l$, do not look (either

236 make no plots with such events or exclude events at ntuple level) at m_{4l} between 110 and 140,
 237 and above 300 GeV. The m_{4l} distribution can be checked in the full mass range either in the
 238 control regions (with no signal expected) or with significantly relaxed cuts (when signal cannot
 239 be seen under about 100 larger background).

240 The blinding procedure applies both to the analysis of 2011 (if any change with respect to
 241 published analysis is done) and 2012 data.

242 2 Datasets and Triggers

243 2.1 Experimental Data

244 The data sample used in this analysis was recorded by the CMS experiment during 2011 for the
 245 run range from 160431 to 180252 and during 2012 for the run range from 190645 to 203002. The
 246 CMS standard selection of runs and luminosity sections is applied which requires high quality
 247 data with a good functioning of the different sub-detectors. Thus, similar detector operation
 248 conditions are imposed for the validation of the data to be used for the analysis of the $4e$, 4μ
 249 and $2e2\mu$ channels.

250 Of the total integrated luminosity \mathcal{L} of $XXX \text{ pb}^{-1}$, a sample corresponding to $\mathcal{L} = 5.1 \text{ fb}^{-1}$ in
 251 2011 at 7 TeV and $\mathcal{L} = 12.2 \text{ fb}^{-1}$ in 2012 at 8 TeV. The absolute pp luminosity is known with a
 252 precision of 2.2% [22] in 2011 and 4.4% in 2012 (ref).

253 The analysis relies on primary datasets (PDs) produced centrally and which combine various
 254 collections of High Level Triggers (HLT). The detailed content of the PDs evolves in phase
 255 with the evolution of the trigger menu to cope with ever increasing instantaneous luminosity.
 256 For the 2011 data, the analysis relies on the so-called "DoubleElectron" and "DoubleMuon"
 257 PDs [23]. These latter PDs are formed by a "OR" between various triggers with symmetric
 258 or asymmetric trigger thresholds for the two leptons, with or without additional identification
 259 and isolation requirements. They also include triggers requiring three leptons above a low p_T
 260 threshold. In 2012 cross-triggers are added to recover few percent of inefficiency in the $2e2\mu$
 261 channel at low Higgs boson masses, forming the so-called "MuEG" PD. One novelty of this
 262 analysis with respect to the previous iteration [20, 21] is the usage of tri-electron triggers for
 263 both 2011 and 2012 data (see details in Section 4.2.4).

264 The PDs and trigger paths used for this analysis are summarized in Table 2.

265 Some comments:

- 266 • In 2011, when applying double muon triggers other than `HLT_Mu17_Mu8` one
 267 has to require 2 offline recoMuons to be matched with L3Muons $p_T > 8 \text{ GeV}$ and
 268 $p_T > 17 \text{ GeV}$.
- 269 • When running on data we get: 4μ channel from DoubleMu datasets, $4e$ channel
 270 from DoubleElectron datasets and $2e2\mu$ channel from DoubleElectron and from Dou-
 271 bleMu vetoing DoubleElectrons triggers for 2011 data, while for 2012 we use in ad-
 272 dition MuEG dataset vetoing DoubleElectrons and DoubleMuons triggers.
- 273 • Only a subset of runs from 06Aug re-reco are used. These are runs where the ecal
 274 laser corrections were recovered and not present in PromptReco.
- 275 • In 2012, a small quantity of data were taken with low pile-up special conditions. As
 276 the triggers we are using were turned off, we rejected these runs.

277 In Table 3 we list all the triggers used with 2012 data.

Datasets	
2011	2012
/DoubleElectron/Run2011A-16Jan2012-v1	/DoubleElectron/Run2012A-13Jul2012-v1
/DoubleMu/Run2011A-16Jan2012-v1	/DoubleMu/Run2012A-13Jul2012-v1
/DoubleElectron/Run2011B-16Jan2012-v1	/MuEG/Run2012A-13Jul2012-v1/
/DoubleMu/Run2011B-16Jan2012-v1	/DoubleElectron/Run2012A-recover-06Aug2012-v1
	/DoubleMu/Run2012A-recover-06Aug2012-v1
	/MuEG/Run2012A-recover-06Aug2012-v1
	/DoubleElectron/Run2012B-13Jul2012-v1
	/DoubleMu/Run2012B-13Jul2012-v4
	/MuEG/Run2012B-13Jul2012-v1
	/DoubleElectron/Run2012C-24Aug2012-v1
	/DoubleElectron/Run2012C-PromptReco-v2
	/DoubleMu/Run2012C-24Aug2012-v1
	/DoubleMu/Run2012C-PromptReco-v2
	/MuEG/Run2012C-24Aug2012-v1
	/MuEG/Run2012C-PromptReco-v2
Muon triggers	
HLT_DoubleMu7 OR HLT_Mu13_Mu8 OR HLT_Mu17_Mu8	HLT_Mu17_Mu8
Electron triggers	
HLT_Ele17_CaloTrk_Ele8_CaloTrk OR HLT_Ele17_CaloTrk_Ele8_CaloTrk OR HLT_TripleEle10_CaloIdL_TrkIdVL	HLT_Ele17_CaloTrk_Ele8_CaloTrk HLT_Ele15_Ele8_Ele5_CaloIdL_TrkIdVL
Cross triggers	
	HLT_Mu17_TkMu8 OR HLT_Mu8_Ele17_CaloTrk OR HLT_Mu17_Ele8_CaloTrk
Integrated luminosity	
5.1 fb ⁻¹	12.2 fb ⁻¹

Table 2: Datasets and triggers used in the analysis. CaloTrk = CaloIdT_CaloIsoVL_TrkIdVL_TrkIsoVL

2.2 Simulated Samples

SM Higgs boson signal samples, as well as samples for a large variety of electroweak and QCD-induced SM background processes, have been obtained using detailed Monte Carlo (MC) simulations. All datasets were subject to full reconstruction and skimming. The signal and background samples have been used for the optimization of the event selection strategy prior to the analysis of the experimental data. They are further used in this analysis for the comparisons with the measurements, the evaluation of acceptance corrections and systematics, and for the background evaluation procedure where measurements in a "background control" region are extrapolated to the "signal" region.

The backgrounds include indistinguishable 4ℓ contributions from di-boson production, via $q\bar{q} \rightarrow ZZ^{(*)}$ and $gg \rightarrow ZZ^{(*)}$, as well as instrumental backgrounds in which hadronic jets or secondary leptons from heavy meson decays are misidentified as primary leptons. Here and henceforward, Z stands for Z, Z^* , and γ^* (where possible). For the event generation, ℓ is to be understood as being any charged lepton, e , μ or τ . The analysis will focus on reconstructed final states with electrons or muons. The main possible sources of instrumental background contributions, are the Z + jets production with $Z \rightarrow \ell^+\ell^-$ decays, the $Zb\bar{b}$ (and $Zc\bar{c}$) associated production with $Z \rightarrow \ell^+\ell^-$ decays, and the production of top quark pairs in the decay mode $t\bar{t} \rightarrow WbW\bar{b} \rightarrow \ell^+\ell^-\nu\bar{\nu}b\bar{b}$. Multiple jet production from QCD hard interactions can also contribute in early stages of the analysis, as well as other di-boson (WW, WZ, Z γ) and single top backgrounds.

Table 4 summarizes the Monte Carlo simulation datasets used for this analysis.

All the signal and background processes cross sections are re-weighted to NLO. In the case of

# Channel	Purpose	HLT path	L1 seed	prescale
4e	main	HLT_Ele17_CaloTrk_Ele8_CaloTrk OR HLT_Ele15_Ele8_Ele5_CaloIdL_TrkIdVL	L1_DoubleEG_13_7 L1_TripleEG_12_7_5	1 1
4 μ	main	HLT_Mu17_Mu8 OR HLT_Mu17_TkMu8	L1_Mu10_MuOpen L1_Mu10_MuOpen	1 1
2e2 μ	main	HLT_Ele17_CaloTrk_Ele8_CaloTrk OR HLT_Mu17_Mu8 OR HLT_Mu17_TkMu8 OR HLT_Mu8_Ele17_CaloTrk OR HLT_Mu17_Ele8_CaloTrk	L1_DoubleEG_13_7 L1_Mu10_MuOpen L1_Mu10_MuOpen L1_MuOpen_EG12 L1_Mu12_EG6	1 1 1 1
4 μ	backup	HLT_TripleMu5	L1_TripleMu0	1
4e and 2e2 μ 4e and 2e2 μ 4 μ and 2e2 μ 4 μ and 2e2 μ	Z T&P Z T&P low pT Z T&P J/psi T&P	HLT_Ele17_CaloTrkVT_Ele8_Mass50 HLT_Ele20_CaloTrkVT_SC4_Mass50_v1 HLT_IsoMu24_eta2p1 HLT_Mu7_Track7_Jpsi HLT_Mu5_Track3p5_Jpsi HLT_Mu5_Track2_Jpsi	L1_DoubleEG_13_7 L1_SingleIsoEG18er L1_SingleMu16er	5 10

Table 3: Triggers in 2012 data analysis. CaloTrk = CaloIdT_CaloIsoVL_TrkIdVL_TrkIsoVL, CaloTrkVT = CaloIdVT_CaloIsoVT_TrkIdT_TrkIsoVT

300 Higgs production via the gluon fusion mechanism, the most recent NNLO+NNLL calculations
301 of the cross sections are included [24].

302 The general multi-purpose Monte Carlo event generator PYTHIA [25] is used for several pro-
303 cesses including QCD multijet production. It serves either to generate a given hard process at
304 leading order (LO), or, in cases where the hard processes are generated at higher orders, only
305 for the showering, hadronization, decays, and for adding the underlying event. This is the case
306 for the MadGraph (MadEvent) Monte Carlo [26] event generators which are used to generate
307 multi-parton amplitudes and events for some important background processes. This is also
308 the case for POWHEG NLO generator [27] which is used for the Higgs boson signal and for the
309 ZZ and $t\bar{t}$ background. For the latter the $t\bar{t}$ decays are handled, exceptionally, within POWHEG.
310 Finally, this is also the case for the dedicated tool GG2ZZ [28] used to generate the $gg \rightarrow ZZ$
311 contribution to the ZZ cross section. For the underlying event, the so-called “PYTHIA tune Z2”
312 in 2011 and “PYTHIA tune Z2 star” in 2012, which relies on p_T -ordered showers is used. For
313 the parton density functions in the colliding protons, the CTEQ6M set is used except for the
314 POWHEG samples from the “Fall11 and Summer12” which makes use of CT10.

315 More details on the event generators and the background samples used in this analysis are
316 given in [20].

Process	MC generator	$\sigma_{(N)NLO}$ 7 TeV	$\sigma_{(N)NLO}$ 8 TeV	Comments and sample name
Higgs boson $H \rightarrow ZZ \rightarrow 4\ell$				
$gg \rightarrow H$	POWHEG	[1-20] fb	[1.2-25] fb	$m_H = 110-1000 \text{ GeV}/c^2$
$VV \rightarrow H$	POWHEG	[0.2-2] fb	[0.3-25] fb	$m_H = 110-1000 \text{ GeV}/c^2$
ZZ continuum				
$q\bar{q} \rightarrow ZZ \rightarrow 4e(4\mu, 4\tau)$	POWHEG	66.09 fb	76.91 fb	ZZTo4e(4mu,4tau)
$q\bar{q} \rightarrow ZZ \rightarrow 2e2\mu$	POWHEG	152 fb	176.7 fb	ZZTo2e2mu
$q\bar{q} \rightarrow ZZ \rightarrow 2e(2\mu)2\tau$	POWHEG	152 fb	176.7 fb	ZZTo2e(2mu)2tau
$gg \rightarrow ZZ \rightarrow 2\ell 2\ell'$	gg2ZZ	3.48 fb	12.03 fb	GluGluToZZTo2L2L
$gg \rightarrow ZZ \rightarrow 4\ell$	gg2ZZ	1.74 fb	4.8 fb	GluGluToZZTo4L
Other di-bosons				
$WW \rightarrow 2\ell 2\nu$	Madgraph	4.88 pb	5.995 pb	WWJetsTo2L2Nu
$WZ \rightarrow 3\ell\nu$	Madgraph	0.868 pb	1.057 pb	WZJetsTo3LNu
$t\bar{t}$ and single t				
$t\bar{t} \rightarrow \ell^+\ell^-\nu\bar{\nu} b\bar{b}$	POWHEG	17.32 pb	23.64 pb	TTTo2L2Nu2B
t (s-channel)	POWHEG	3.19 pb	3.89 pb	T_TuneXX_s-channel
\bar{t} (s-channel)	POWHEG	1.44 pb	1.76 pb	Tbar_TuneXX_s-channel
t (t-channel)	POWHEG	41.92 pb	55.53 pb	T_TuneXX_t-channel
\bar{t} (t-channel)	POWHEG	22.65 pb	30.00 pb	Tbar_TuneXX_t-channel
t (tW -channel)	POWHEG	7.87 pb	11.77 pb	T_TuneXX_tW-channel-DR
\bar{t} (tW -channel)	POWHEG	7.87 pb	11.77 pb	Tbar_TuneXX_tW-channel-DR
Z/W + jets ($q = d, u, s, c, b$)				
$W + \text{jets}$	MadGraph	31314 pb	36257.2 pb	WJetsToLNu
$Z + \text{jets}, m_{\ell\ell} > 50$	MadGraph	3048 pb	3503.7 pb	DYJetsToLL*M-50
$Z + \text{jets}, 10 < m_{\ell\ell} < 50$	MadGraph	12782.63 pb	915 pb	DYJetsToLL*M-10To50

Table 4: Monte Carlo simulation datasets used for the signal and background processes; Z stands for Z, Z^*, γ^* ; ℓ means e, μ or τ ; V stands for W and Z; \hat{p}_T is the transverse momentum for $2 \rightarrow 2$ hard processes in the rest frame of the hard interaction. Comment: $q\bar{q} \rightarrow ZZ$ samples at 8 TeV have lower cut in m_{ll} , 4 GeV instead of 12 GeV at 7 TeV. TuneZ2 is used for 7 TeV, while TuneZ2star is used for 8 TeV analysis. The low mass Drell-Yann was produced with a filter for the 8 TeV analysis.

317 3 Leptons Observables

- 318 The reconstruction of the SM Higgs boson in the decay chain $H \rightarrow ZZ^{(*)} \rightarrow 4\ell$ imposes
 319 high-performance lepton reconstruction, identification and isolation as well as excellent lep-
 320 ton energy-momentum measurements. The identification of isolated leptons emerging from
 321 the event primary vertex allows for a drastic reduction of QCD-induced sources of misidenti-
 322 fied (“fake”) leptons. The precision energy-momentum measurements translates in a precision
 323 Higgs boson mass measurement $m_{4\ell}$, the most discriminating observable for the Higgs boson
 324 search.
- 325 The leptons used in this analysis are almost un-changed with respect to the ICHEP analy-
 326 sis [20, 21]. The following sections will therefore just remind the definitions of leptons used,
 327 the working points for the different algorithms and focus on the small changes made. The
 328 reader interested to have more details is invited to look at [20, 21].

329 3.1 Electron Reconstruction and Identification

330 3.1.1 Reconstruction

331 The electron reconstruction [29] combines ECAL and tracker information. Electron candidates
 332 are reconstructed from clusters of energy deposits in the ECAL, which are then matched to hits
 333 in the silicon tracker. The standard CMS electron reconstruction algorithm is used [30–32] for
 334 this analysis.

335 The energy deposited in the electromagnetic calorimeter (ECAL) is measured in clusters of
 336 clusters (superclusters) which collect Bremsstrahlung photons emitted in the tracker volume.
 337 Superclusters are used to search for hits in the innermost tracker layers which are used to seed
 338 electron tracks. This procedure is complemented by a tracker-driven approach allowing to
 339 improve the reconstruction efficiency at low p_T . Trajectories in the tracker volume are recon-
 340 structed using a dedicated modeling of the electron energy loss and fitted with a Gaussian
 341 Sum Filter. A cleaning is performed to resolve ambiguous cases where several tracks are recon-
 342 structed due to the conversion of radiated photons in the tracker material. Electron candidates
 343 are preselected using loose cuts on track-cluster matching observables so to preserve the high-
 344 est possible efficiency while removing part of the QCD background.

345 For the physics analysis, the electron candidates are required to have transverse momentum p_T^e
 346 larger than 7 GeV/c and a reconstructed $|\eta^e| < 2.5$.

347 The reconstruction efficiency for isolated electron is expected to be above $\approx 90\%$ over the full
 348 ECAL acceptance, apart from some narrow “crack” regions. It will be discussed in details in 4.

349 Electron charge mis-identification has been measured on 2010 data using Z events and a charge
 350 mis-ID of 0.004 ± 0.001 (0.028 ± 0.003) was measured in the ECAL barrel (ECAL endcaps) in
 351 very good agreement with the simulation [33]. No significant p_T dependency was observed in
 352 the range of on-shell Z boson decays, also in agreement with the expectation.

353 3.1.2 Momentum Estimation

354 The four-momenta for an electron is obtained by taking angles from the associated Gaussian
 355 Sum Filter (GSF) track, and the energy from a combination of tracker and ECAL informa-
 356 tion [30]. The information from the track is measured at the distance-of-closest approach to
 357 the beam spot position in the transverse plane. Electron tracks are not re-fitted to the common
 358 primary vertex.

359 In this analysis, the ECAL information is obtained via a Regression technic, described in the
 360 next section.

361 The electron momentum scale and resolution can be controlled using Z boson (and J/Ψ) decays
 362 to electrons.

363 Some discrepancies with respect to simulation are still present, especially in the low p_T part of
 364 the electron spectrum and in the endcaps. Based on $Z \rightarrow ee$ data and simulated events, these
 365 discrepancies are dealt with by correcting the energy scale in data and by then determining the
 366 smearing needed to apply to the simulated samples so as to have the best match between data
 367 and simulation. The procedure described in [34] ($H \rightarrow \gamma\gamma$ analysis) has been extended within
 368 e/g to also provide scale corrections for electrons and for the particular energy regression used
 369 in this analysis.

370 The procedure consists of two steps:

- **absolute scale corrections for data.** The supercluster energy scale is tuned and corrected varying the scale in the data to match the Monte Carlo in $Z \rightarrow ee$ events. The data-MC difference is time dependent; moreover the time dependence is not the same in different pseudorapidity regions while it is very similar for showering and non showering electrons. This is done in two R_9 bins, since this variable categorizes two different kinds of clusters. The final energy scale correction is then derived as the product of the two corrections in $n(\text{run range}) \times 4(\text{pseudorapidity region}) \times 2(R_9)$ categories. The values as provided by e/g for electrons using the above described method [35] are shown in Table 5 to Table 12 for the 7 TeV and the 8 TeV periods.

- **MC energy smearing.** The method developed in [34] which applies direct smearing to the MC energies is used to estimate more efficiently the effective resolution of the electromagnetic calorimeter. The electron supercluster energy is modified by applying a Gaussian multiplicative factor centered in $1 + \Delta E/E$ and with a $\Delta\sigma$ resolution, where $\Delta E/E$ is the relative energy scale difference $\Delta E/E = (\Delta m_{\text{data}} - \Delta m_{\text{MC}})/m_Z$ and $\Delta\sigma$ is the additional constant term in the energy resolution. The extra smearings are shown in Table 13 and Table 14 ([35]).

387 Both the data scale corrections and the smearings have been obtained by fits to the high statistics
 388 $Z \rightarrow ee$ control sample. The spectrum for electrons from Z is typically peaking at $p_T \approx 45$
 389 GeV, while the electrons from $H \rightarrow ZZ \rightarrow 4\ell$ typically span from 7 to 50 GeV (higher for he
 390 high m_H hypotheses).

391 Detailed comparisons between data and MC, after e-scale corrections on DATA and smearing
 392 on MC, will be shown in Section 7.4.12.

393 3.1.3 ECAL Energy Measurement using a Multivariate Regression

394 It has been demonstrated [36] that a multivariate regression approach for determining the en-
 395 ergy of an electron can significantly improve the resolution of the measurement. We employ
 396 such a technique for the analysis to improve the mass resolution for final states involving
 397 electrons. Details of the method and performance can be found in reference [37].

398 We use the GBRForest implementation of the regression algorithm using boosted decision trees.
 399 We train the boosted decision tree on the Drell-Yan Monte Carlo sample using the exact same
 400 variables that have been used for the analysis [36]. Different sets of input variables are used
 401 depending on whether the electron is detected in the barrel or the endcap of the electromagnetic
 402 calorimeter. The variables that are used for both the barrel and the endcap are the following:

Table 5: Barrel ($|\eta| < 1$) scale factor E_{corr}/E applied to the reconstructed energy in the data, and the corresponding relative energy scale difference $\Delta E/E = (\Delta m_{data} - \Delta m_{MC})/m_Z$ between data and MC as the result of the two step procedure described in the text for the 7 TeV data. The error given is statistical.

category	RunStart - RunEnd	E_{corr}/E	$\Delta E/E$	error
EB 0 $\leq \eta < 1 R9 < 0.94$	160431 - 167913	1.0014	-0.0014	0.0002
EB 0 $\leq \eta < 1 R9 < 0.94$	170000 - 172619	1.0016	-0.0016	0.0002
EB 0 $\leq \eta < 1 R9 < 0.94$	172620 - 173692	1.0017	-0.0017	0.0002
EB 0 $\leq \eta < 1 R9 < 0.94$	175830 - 177139	1.0021	-0.0021	0.0002
EB 0 $\leq \eta < 1 R9 < 0.94$	177140 - 178421	1.0025	-0.0025	0.0002
EB 0 $\leq \eta < 1 R9 < 0.94$	178424 - 180252	1.0024	-0.0024	0.0002
EB 0 $\leq \eta < 1 R9 > 0.94$	160431 - 167913	0.9941	0.0059	0.0002
EB 0 $\leq \eta < 1 R9 > 0.94$	170000 - 172619	0.9954	0.0046	0.0002
EB 0 $\leq \eta < 1 R9 > 0.94$	172620 - 173692	0.9955	0.0045	0.0002
EB 0 $\leq \eta < 1 R9 > 0.94$	175830 - 177139	0.9958	0.0042	0.0002
EB 0 $\leq \eta < 1 R9 > 0.94$	177140 - 178421	0.9962	0.0038	0.0002
EB 0 $\leq \eta < 1 R9 > 0.94$	178424 - 180252	0.9961	0.0039	0.0002

Table 6: Barrel ($|\eta| > 1$) scale factor E_{corr}/E applied to the reconstructed energy in the data, and the corresponding relative energy scale difference $\Delta E/E = (\Delta m_{data} - \Delta m_{MC})/m_Z$ between data and MC as the result of the two step procedure described in the text for the 7 TeV data. The error given is statistical.

category	RunStart - RunEnd	E_{corr}/E	$\Delta E/E$	error
EB 1 $\leq \eta < 1.4442 R9 < 0.94$	160431 - 167913	1.0045	-0.0045	0.0006
EB 1 $\leq \eta < 1.4442 R9 < 0.94$	170000 - 172619	1.0066	-0.0066	0.0008
EB 1 $\leq \eta < 1.4442 R9 < 0.94$	172620 - 173692	1.0058	-0.0058	0.0007
EB 1 $\leq \eta < 1.4442 R9 < 0.94$	175830 - 177139	1.0074	-0.0073	0.0006
EB 1 $\leq \eta < 1.4442 R9 < 0.94$	177140 - 178421	1.0076	-0.0075	0.0006
EB 1 $\leq \eta < 1.4442 R9 < 0.94$	178424 - 180252	1.0072	-0.0071	0.0006
EB 1 $\leq \eta < 1.4442 R9 > 0.94$	160431 - 167913	0.9917	0.0084	0.0013
EB 1 $\leq \eta < 1.4442 R9 > 0.94$	170000 - 172619	0.9937	0.0063	0.0014
EB 1 $\leq \eta < 1.4442 R9 > 0.94$	172620 - 173692	0.9930	0.0071	0.0013
EB 1 $\leq \eta < 1.4442 R9 > 0.94$	175830 - 177139	0.9944	0.0056	0.0013
EB 1 $\leq \eta < 1.4442 R9 > 0.94$	177140 - 178421	0.9946	0.0054	0.0013
EB 1 $\leq \eta < 1.4442 R9 > 0.94$	178424 - 180252	0.9942	0.0058	0.0013

Table 7: Endcap ($|\eta| < 2$) scale factor E_{corr}/E applied to the reconstructed energy in the data, and the corresponding relative energy scale difference $\Delta E/E = (\Delta m_{data} - \Delta m_{MC})/m_Z$ between data and MC as the result of the two step procedure described in the text for the 7 TeV data. The error given is statistical.

category	RunStart - RunEnd	E_{corr}/E	$\Delta E/E$	error
EE $1.566 \leq \eta < 2 R9 < 0.94$	160431 - 167913	1.0083	-0.0082	0.0008
EE $1.566 \leq \eta < 2 R9 < 0.94$	170000 - 172619	1.0025	-0.0025	0.0011
EE $1.566 \leq \eta < 2 R9 < 0.94$	172620 - 173692	1.0035	-0.0035	0.0010
EE $1.566 \leq \eta < 2 R9 < 0.94$	175830 - 177139	1.0017	-0.0017	0.0009
EE $1.566 \leq \eta < 2 R9 < 0.94$	177140 - 178421	1.0010	-0.0010	0.0009
EE $1.566 \leq \eta < 2 R9 < 0.94$	178424 - 180252	0.9970	0.0030	0.0009
EE $1.566 \leq \eta < 2 R9 > 0.94$	160431 - 167913	1.0033	-0.0033	0.0010
EE $1.566 \leq \eta < 2 R9 > 0.94$	170000 - 172619	0.9976	0.0024	0.0012
EE $1.566 \leq \eta < 2 R9 > 0.94$	172620 - 173692	0.9986	0.0014	0.0011
EE $1.566 \leq \eta < 2 R9 > 0.94$	175830 - 177139	0.9968	0.0032	0.0010
EE $1.566 \leq \eta < 2 R9 > 0.94$	177140 - 178421	0.9960	0.0040	0.0010
EE $1.566 \leq \eta < 2 R9 > 0.94$	178424 - 180252	0.9922	0.0079	0.0010

Table 8: Endcap ($|\eta| > 2$) scale factor E_{corr}/E applied to the reconstructed energy in the data, and the corresponding relative energy scale difference $\Delta E/E = (\Delta m_{data} - \Delta m_{MC})/m_Z$ between data and MC as the result of the two step procedure described in the text for the 7 TeV data. The error given is statistical.

category	RunStart - RunEnd	E_{corr}/E	$\Delta E/E$	error
EE $2 \leq \eta < 2.5 R9 < 0.94$	160431 - 167913	1.0064	-0.0064	0.0008
EE $2 \leq \eta < 2.5 R9 < 0.94$	170000 - 172619	1.0046	-0.0046	0.0009
EE $2 \leq \eta < 2.5 R9 < 0.94$	172620 - 173692	1.0029	-0.0029	0.0009
EE $2 \leq \eta < 2.5 R9 < 0.94$	175830 - 177139	1.0040	-0.0040	0.0009
EE $2 \leq \eta < 2.5 R9 < 0.94$	177140 - 178421	1.0050	-0.0050	0.0008
EE $2 \leq \eta < 2.5 R9 < 0.94$	178424 - 180252	1.0059	-0.0059	0.0009
EE $2 \leq \eta < 2.5 R9 > 0.94$	160431 - 167913	0.9958	0.0042	0.0006
EE $2 \leq \eta < 2.5 R9 > 0.94$	170000 - 172619	0.9940	0.0060	0.0008
EE $2 \leq \eta < 2.5 R9 > 0.94$	172620 - 173692	0.9924	0.0077	0.0007
EE $2 \leq \eta < 2.5 R9 > 0.94$	175830 - 177139	0.9933	0.0067	0.0007
EE $2 \leq \eta < 2.5 R9 > 0.94$	177140 - 178421	0.9944	0.0056	0.0007
EE $2 \leq \eta < 2.5 R9 > 0.94$	178424 - 180252	0.9953	0.0047	0.0007

Table 9: Barrel ($|\eta| < 1$) scale factor E_{corr}/E applied to the reconstructed energy in the data, and the corresponding relative energy scale difference $\Delta E/E = (\Delta m_{data} - \Delta m_{MC})/m_Z$ between data and MC as the result of the two step procedure described in the text for the 8 TeV data. The error given is statistical.

category	RunStart - RunEnd	E_{corr}/E	$\Delta E/E$	error
EB $0 \leq \eta < 1 R9 < 0.94$	190645 - 190781	1.0020	-0.0020	0.0004
EB $0 \leq \eta < 1 R9 < 0.94$	190782 - 191042	1.0079	-0.0079	0.0004
EB $0 \leq \eta < 1 R9 < 0.94$	191043 - 193555	0.9989	0.0011	0.0002
EB $0 \leq \eta < 1 R9 < 0.94$	193556 - 194150	0.9974	0.0026	0.0002
EB $0 \leq \eta < 1 R9 < 0.94$	194151 - 194532	0.9980	0.0020	0.0002
EB $0 \leq \eta < 1 R9 < 0.94$	194533 - 195113	0.9983	0.0017	0.0002
EB $0 \leq \eta < 1 R9 < 0.94$	195114 - 195915	0.9984	0.0016	0.0002
EB $0 \leq \eta < 1 R9 < 0.94$	195916 - 198115	0.9975	0.0025	0.0002
EB $0 \leq \eta < 1 R9 < 0.94$	198116 - 199803	1.0010	-0.0010	0.0001
EB $0 \leq \eta < 1 R9 < 0.94$	199804 - 200048	1.0021	-0.0021	0.0002
EB $0 \leq \eta < 1 R9 < 0.94$	200049 - 200151	1.0035	-0.0035	0.0003
EB $0 \leq \eta < 1 R9 < 0.94$	200152 - 200490	1.0013	-0.0013	0.0002
EB $0 \leq \eta < 1 R9 < 0.94$	200491 - 200531	1.0035	-0.0035	0.0003
EB $0 \leq \eta < 1 R9 < 0.94$	200532 - 201656	1.0017	-0.0017	0.0002
EB $0 \leq \eta < 1 R9 < 0.94$	201657 - 202305	1.0026	-0.0026	0.0002
EB $0 \leq \eta < 1 R9 < 0.94$	202305 - 203002	1.0037	-0.0037	0.0002
EB $0 \leq \eta < 1 R9 > 0.94$	190645 - 190781	0.9980	0.0020	0.0004
EB $0 \leq \eta < 1 R9 > 0.94$	190782 - 191042	1.0039	-0.0039	0.0004
EB $0 \leq \eta < 1 R9 > 0.94$	191043 - 193555	0.9949	0.0051	0.0002
EB $0 \leq \eta < 1 R9 > 0.94$	193556 - 194150	0.9934	0.0066	0.0002
EB $0 \leq \eta < 1 R9 > 0.94$	194151 - 194532	0.9940	0.0060	0.0002
EB $0 \leq \eta < 1 R9 > 0.94$	194533 - 195113	0.9943	0.0057	0.0002
EB $0 \leq \eta < 1 R9 > 0.94$	195114 - 195915	0.9944	0.0056	0.0002
EB $0 \leq \eta < 1 R9 > 0.94$	195916 - 198115	0.9936	0.0064	0.0002
EB $0 \leq \eta < 1 R9 > 0.94$	198116 - 199803	0.9970	0.0030	0.0002
EB $0 \leq \eta < 1 R9 > 0.94$	199804 - 200048	0.9982	0.0018	0.0002
EB $0 \leq \eta < 1 R9 > 0.94$	200049 - 200151	0.9996	0.0004	0.0003
EB $0 \leq \eta < 1 R9 > 0.94$	200152 - 200490	0.9973	0.0027	0.0002
EB $0 \leq \eta < 1 R9 > 0.94$	200491 - 200531	0.9995	0.0005	0.0003
EB $0 \leq \eta < 1 R9 > 0.94$	200532 - 201656	0.9978	0.0022	0.0002
EB $0 \leq \eta < 1 R9 > 0.94$	201657 - 202305	0.9986	0.0014	0.0002
EB $0 \leq \eta < 1 R9 > 0.94$	202305 - 203002	0.9998	0.0002	0.0002

Table 10: Barrel ($|\eta| > 1$) scale factor E_{corr}/E applied to the reconstructed energy in the data, and the corresponding relative energy scale difference $\Delta E/E = (\Delta m_{data} - \Delta m_{MC})/m_Z$ between data and MC as the result of the two step procedure described in the text for the 8 TeV data. The error given is statistical.

category	RunStart - RunEnd	E_{corr}/E	$\Delta E/E$	error
EB 1 $\leq \eta < 1.4442 R9 < 0.94$	190645 - 190781	1.0032	-0.0032	0.0017
EB 1 $\leq \eta < 1.4442 R9 < 0.94$	190782 - 191042	1.0063	-0.0063	0.0017
EB 1 $\leq \eta < 1.4442 R9 < 0.94$	191043 - 193555	0.9998	0.0002	0.0007
EB 1 $\leq \eta < 1.4442 R9 < 0.94$	193556 - 194150	0.9954	0.0046	0.0007
EB 1 $\leq \eta < 1.4442 R9 < 0.94$	194151 - 194532	0.9965	0.0035	0.0007
EB 1 $\leq \eta < 1.4442 R9 < 0.94$	194533 - 195113	0.9984	0.0016	0.0006
EB 1 $\leq \eta < 1.4442 R9 < 0.94$	195114 - 195915	0.9977	0.0023	0.0005
EB 1 $\leq \eta < 1.4442 R9 < 0.94$	195916 - 198115	0.9965	0.0035	0.0006
EB 1 $\leq \eta < 1.4442 R9 < 0.94$	198116 - 199803	0.9999	0.00010	0.0005
EB 1 $\leq \eta < 1.4442 R9 < 0.94$	199804 - 200048	1.0008	-0.0008	0.0007
EB 1 $\leq \eta < 1.4442 R9 < 0.94$	200049 - 200151	1.0017	-0.0017	0.0011
EB 1 $\leq \eta < 1.4442 R9 < 0.94$	200152 - 200490	1.0003	-0.0003	0.0008
EB 1 $\leq \eta < 1.4442 R9 < 0.94$	200491 - 200531	1.0017	-0.0017	0.0011
EB 1 $\leq \eta < 1.4442 R9 < 0.94$	200532 - 201656	0.9999	0.00010	0.0006
EB 1 $\leq \eta < 1.4442 R9 < 0.94$	201657 - 202305	1.0003	-0.0003	0.0005
EB 1 $\leq \eta < 1.4442 R9 < 0.94$	202305 - 203002	1.0010	-0.0010	0.0007
EB 1 $\leq \eta < 1.4442 R9 > 0.94$	190645 - 190781	0.9919	0.0082	0.0021
EB 1 $\leq \eta < 1.4442 R9 > 0.94$	190782 - 191042	0.9951	0.0049	0.0021
EB 1 $\leq \eta < 1.4442 R9 > 0.94$	191043 - 193555	0.9885	0.0116	0.0014
EB 1 $\leq \eta < 1.4442 R9 > 0.94$	193556 - 194150	0.9841	0.0162	0.0014
EB 1 $\leq \eta < 1.4442 R9 > 0.94$	194151 - 194532	0.9852	0.0150	0.0014
EB 1 $\leq \eta < 1.4442 R9 > 0.94$	194533 - 195113	0.9872	0.0130	0.0014
EB 1 $\leq \eta < 1.4442 R9 > 0.94$	195114 - 195915	0.9864	0.0138	0.0013
EB 1 $\leq \eta < 1.4442 R9 > 0.94$	195916 - 198115	0.9852	0.0150	0.0013
EB 1 $\leq \eta < 1.4442 R9 > 0.94$	198116 - 199803	0.9886	0.0115	0.0013
EB 1 $\leq \eta < 1.4442 R9 > 0.94$	199804 - 200048	0.9895	0.0106	0.0014
EB 1 $\leq \eta < 1.4442 R9 > 0.94$	200049 - 200151	0.9905	0.0096	0.0017
EB 1 $\leq \eta < 1.4442 R9 > 0.94$	200152 - 200490	0.9890	0.0111	0.0015
EB 1 $\leq \eta < 1.4442 R9 > 0.94$	200491 - 200531	0.9905	0.0096	0.0017
EB 1 $\leq \eta < 1.4442 R9 > 0.94$	200532 - 201656	0.9887	0.0114	0.0013
EB 1 $\leq \eta < 1.4442 R9 > 0.94$	201657 - 202305	0.9891	0.0110	0.0013
EB 1 $\leq \eta < 1.4442 R9 > 0.94$	202305 - 203002	0.9897	0.0104	0.0014

Table 11: Endcap ($|\eta| < 2$) scale factor E_{corr}/E applied to the reconstructed energy in the data, and the corresponding relative energy scale difference $\Delta E/E = (\Delta m_{data} - \Delta m_{MC})/m_Z$ between data and MC as the result of the two step procedure described in the text for the 8 TeV data. The error given is statistical.

category	RunStart - RunEnd	E_{corr}/E	$\Delta E/E$	error
EE $1.566 \leq \eta < 2 R9 < 0.94$	190645 - 190781	0.9945	0.0055	0.0026
EE $1.566 \leq \eta < 2 R9 < 0.94$	190782 - 191042	0.9996	0.0004	0.0029
EE $1.566 \leq \eta < 2 R9 < 0.94$	191043 - 193555	0.9968	0.0032	0.0011
EE $1.566 \leq \eta < 2 R9 < 0.94$	193556 - 194150	0.9969	0.0031	0.0011
EE $1.566 \leq \eta < 2 R9 < 0.94$	194151 - 194532	0.9986	0.0014	0.0011
EE $1.566 \leq \eta < 2 R9 < 0.94$	194533 - 195113	1.0006	-0.0006	0.0010
EE $1.566 \leq \eta < 2 R9 < 0.94$	195114 - 195915	1.0010	-0.0010	0.0009
EE $1.566 \leq \eta < 2 R9 < 0.94$	195916 - 198115	1.0020	-0.0020	0.0009
EE $1.566 \leq \eta < 2 R9 < 0.94$	198116 - 199803	0.9963	0.0037	0.0008
EE $1.566 \leq \eta < 2 R9 < 0.94$	199804 - 200048	0.9965	0.0035	0.0011
EE $1.566 \leq \eta < 2 R9 < 0.94$	200049 - 200151	0.9992	0.0008	0.0018
EE $1.566 \leq \eta < 2 R9 < 0.94$	200152 - 200490	0.9991	0.0009	0.0013
EE $1.566 \leq \eta < 2 R9 < 0.94$	200491 - 200531	0.9995	0.0005	0.0018
EE $1.566 \leq \eta < 2 R9 < 0.94$	200532 - 201656	0.9978	0.0022	0.0010
EE $1.566 \leq \eta < 2 R9 < 0.94$	201657 - 202305	0.9987	0.0013	0.0009
EE $1.566 \leq \eta < 2 R9 < 0.94$	202305 - 203002	1.0003	-0.0003	0.0011
EE $1.566 \leq \eta < 2 R9 > 0.94$	190645 - 190781	0.9881	0.0120	0.0027
EE $1.566 \leq \eta < 2 R9 > 0.94$	190782 - 191042	0.9932	0.0068	0.0030
EE $1.566 \leq \eta < 2 R9 > 0.94$	191043 - 193555	0.9904	0.0097	0.0014
EE $1.566 \leq \eta < 2 R9 > 0.94$	193556 - 194150	0.9905	0.0096	0.0014
EE $1.566 \leq \eta < 2 R9 > 0.94$	194151 - 194532	0.9922	0.0079	0.0014
EE $1.566 \leq \eta < 2 R9 > 0.94$	194533 - 195113	0.9943	0.0057	0.0013
EE $1.566 \leq \eta < 2 R9 > 0.94$	195114 - 195915	0.9946	0.0054	0.0012
EE $1.566 \leq \eta < 2 R9 > 0.94$	195916 - 198115	0.9956	0.0044	0.0012
EE $1.566 \leq \eta < 2 R9 > 0.94$	198116 - 199803	0.9899	0.0102	0.0011
EE $1.566 \leq \eta < 2 R9 > 0.94$	199804 - 200048	0.9901	0.0100	0.0014
EE $1.566 \leq \eta < 2 R9 > 0.94$	200049 - 200151	0.9928	0.0073	0.0020
EE $1.566 \leq \eta < 2 R9 > 0.94$	200152 - 200490	0.9927	0.0074	0.0015
EE $1.566 \leq \eta < 2 R9 > 0.94$	200491 - 200531	0.9931	0.0069	0.0020
EE $1.566 \leq \eta < 2 R9 > 0.94$	200532 - 201656	0.9914	0.0087	0.0012
EE $1.566 \leq \eta < 2 R9 > 0.94$	201657 - 202305	0.9923	0.0078	0.0012
EE $1.566 \leq \eta < 2 R9 > 0.94$	202305 - 203002	0.9940	0.0060	0.0014

Table 12: Endcap ($|\eta| > 2$) scale factor E_{corr}/E applied to the reconstructed energy in the data, and the corresponding relative energy scale difference $\Delta E/E = (\Delta m_{data} - \Delta m_{MC})/m_Z$ between data and MC as the result of the two step procedure described in the text for the 8 TeV data. The error given is statistical.

category	RunStart - RunEnd	E_{corr}/E	$\Delta E/E$	error
EE $2 \leq \eta < 2.5$ $R9 < 0.94$	190645 - 190781	0.9965	0.0035	0.0024
EE $2 \leq \eta < 2.5$ $R9 < 0.94$	190782 - 191042	1.0010	-0.0010	0.0024
EE $2 \leq \eta < 2.5$ $R9 < 0.94$	191043 - 193555	0.9987	0.0013	0.0011
EE $2 \leq \eta < 2.5$ $R9 < 0.94$	193556 - 194150	0.9988	0.0012	0.0011
EE $2 \leq \eta < 2.5$ $R9 < 0.94$	194151 - 194532	0.9994	0.0006	0.0011
EE $2 \leq \eta < 2.5$ $R9 < 0.94$	194533 - 195113	0.9999	0.0001	0.0010
EE $2 \leq \eta < 2.5$ $R9 < 0.94$	195114 - 195915	1.0004	-0.0004	0.0009
EE $2 \leq \eta < 2.5$ $R9 < 0.94$	195916 - 198115	0.9992	0.0008	0.0009
EE $2 \leq \eta < 2.5$ $R9 < 0.94$	198116 - 199803	1.0044	-0.0044	0.0008
EE $2 \leq \eta < 2.5$ $R9 < 0.94$	199804 - 200048	1.0060	-0.0060	0.0011
EE $2 \leq \eta < 2.5$ $R9 < 0.94$	200049 - 200151	1.0101	-0.0100	0.0019
EE $2 \leq \eta < 2.5$ $R9 < 0.94$	200152 - 200490	1.0073	-0.0072	0.0013
EE $2 \leq \eta < 2.5$ $R9 < 0.94$	200491 - 200531	1.0106	-0.0105	0.0019
EE $2 \leq \eta < 2.5$ $R9 < 0.94$	200532 - 201656	1.0069	-0.0069	0.0010
EE $2 \leq \eta < 2.5$ $R9 < 0.94$	201657 - 202305	1.0121	-0.0120	0.0009
EE $2 \leq \eta < 2.5$ $R9 < 0.94$	202305 - 203002	1.0144	-0.0142	0.0012
EE $2 \leq \eta < 2.5$ $R9 > 0.94$	190645 - 190781	0.9862	0.0140	0.0024
EE $2 \leq \eta < 2.5$ $R9 > 0.94$	190782 - 191042	0.9907	0.0094	0.0024
EE $2 \leq \eta < 2.5$ $R9 > 0.94$	191043 - 193555	0.9884	0.0117	0.0010
EE $2 \leq \eta < 2.5$ $R9 > 0.94$	193556 - 194150	0.9885	0.0116	0.0010
EE $2 \leq \eta < 2.5$ $R9 > 0.94$	194151 - 194532	0.9891	0.0110	0.0010
EE $2 \leq \eta < 2.5$ $R9 > 0.94$	194533 - 195113	0.9896	0.0105	0.0009
EE $2 \leq \eta < 2.5$ $R9 > 0.94$	195114 - 195915	0.9900	0.0101	0.0008
EE $2 \leq \eta < 2.5$ $R9 > 0.94$	195916 - 198115	0.9889	0.0112	0.0008
EE $2 \leq \eta < 2.5$ $R9 > 0.94$	198116 - 199803	0.9941	0.0059	0.0007
EE $2 \leq \eta < 2.5$ $R9 > 0.94$	199804 - 200048	0.9957	0.0043	0.0011
EE $2 \leq \eta < 2.5$ $R9 > 0.94$	200049 - 200151	0.9999	0.0001	0.0018
EE $2 \leq \eta < 2.5$ $R9 > 0.94$	200152 - 200490	0.9970	0.0030	0.0012
EE $2 \leq \eta < 2.5$ $R9 > 0.94$	200491 - 200531	1.0004	-0.0004	0.0018
EE $2 \leq \eta < 2.5$ $R9 > 0.94$	200532 - 201656	0.9967	0.0033	0.0009
EE $2 \leq \eta < 2.5$ $R9 > 0.94$	201657 - 202305	1.0018	-0.0018	0.0008
EE $2 \leq \eta < 2.5$ $R9 > 0.94$	202305 - 203002	1.0042	-0.0042	0.0011

Table 13: The additional energy resolution component determined from the comparison of data to Monte Carlo for $Z \rightarrow ee$ events for the 7 TeV MC.

Category	σ_E/E (%)
EB, $ \eta < 1, R9 > 0.94$	$0.74 \pm 0.14 \pm 0.22$
EB, $ \eta < 1, R9 < 0.94$	$0.96 \pm 0.14 \pm 0.24$
EB, $ \eta > 1, R9 > 0.94$	$1.41 \pm 0.55 \pm 0.60$
EB, $ \eta > 1, R9 < 0.94$	$1.96 \pm 0.08 \pm 0.59$
EE, $ \eta < 2, R9 > 0.94$	$2.68 \pm 0.26 \pm 0.90$
EE, $ \eta < 2, R9 < 0.94$	$2.79 \pm 0.11 \pm 0.30$
EE, $ \eta > 2, R9 > 0.94$	$2.93 \pm 0.10 \pm 0.34$
EE, $ \eta > 2, R9 < 0.94$	$3.01 \pm 0.12 \pm 0.52$

Table 14: The additional energy resolution component determined from the comparison of data to Monte Carlo for $Z \rightarrow ee$ events for the 8 TeV MC.

Category	$\sigma_E / E (\%)$
EB, $ \eta < 1, R_9 > 0.94$	0.90 ± 0.06
EB, $ \eta < 1, R_9 < 0.94$	1.03 ± 0.05
EB, $ \eta > 1, R_9 > 0.94$	1.56 ± 0.64
EB, $ \eta > 1, R_9 < 0.94$	1.90 ± 0.09
EE, $ \eta < 2, R_9 > 0.94$	2.87 ± 0.30
EE, $ \eta < 2, R_9 < 0.94$	2.69 ± 0.14
EE, $ \eta > 2, R_9 > 0.94$	3.21 ± 0.09
EE, $ \eta > 2, R_9 < 0.94$	3.64 ± 0.14

- 403 • SCRawEnergy: the uncorrected energy of the supercluster,
- 404 • scEta: η coordinate of the supercluster
- 405 • scPhi: ϕ coordinate of the supercluster
- 406 • R9: ratio of the energy in the 3-by-3 grid of crystals around the seed crystal to the
407 uncorrected energy of the supercluster,
- 408 • etawidth: width of the supercluster in the η direction,
- 409 • phiwidth: width of the supercluster in the ϕ direction,
- 410 • NClusters: the number of clusters forming the supercluster,
- 411 • HoE: ratio of hadronic energy to electromagnetic energy,
- 412 • rho: measure of the energy density of the pileup in the event,
- 413 • vertices: number of reconstructed primary vertices,
- 414 • EtaSeed: η coordinate of the seed cluster,
- 415 • PhiSeed: ϕ coordinate of the seed cluster,
- 416 • ESeed: energy of the seed cluster,
- 417 • E3x3Seed: energy in the 3-by-3 grid of crystals around the seed crystal,
- 418 • E5x5Seed: energy in the 5-by-5 grid of crystals around the seed crystal,
- 419 • $\sigma_{i\eta i\eta}$
- 420 • $\sigma_{i\phi i\phi}$
- 421 • $\sigma_{i\eta i\phi}$
- 422 • EMaxSeed: energy of the highest energy crystal,
- 423 • E2ndSeed: energy of the second highest energy crystal,
- 424 • ETopSeed: energy of the adjacent crystal above the highest energy crystal,
- 425 • EBottomSeed: energy of the adjacent crystal below the highest energy crystal,
- 426 • ELeftSeed: energy of the adjacent crystal to the left of the highest energy crystal,
- 427 • ERightSeed: energy of the adjacent crystal to the right of the highest energy crystal,
- 428 • E2x5MaxSeed,
- 429 • E2x5TopSeed,
- 430 • E2x5BottomSeed,
- 431 • E2x5LeftSeed,
- 432 • E2x5RightSeed,

- 433 • pt: transverse momentum of the electron computed using the standard combination
434 of the ECAL energy measurement and the track momentum measurement.

435 In addition, the following variables which indicate the proximity of the electron to gaps be-
436 tween modules and supermodules are used for electrons in the barrel:

- 437 • IEtaSeed: the index of the seed crystal in the η coordinate,
438 • IPhiSeed: the index of the seed crystal in the ϕ coordinate,
439 • IEtaSeed mod 5,
440 • IPhiSeed mod 2,
441 • $(|IEtaSeed| \leq 25) \times (IEtaSeed \text{ mod } 25) +$
442 $(|IEtaSeed| > 25) \times ((IEtaSeed - 25 \times |IEtaSeed| / IEtaSeed) \text{ mod } 20)$,
443 • IPhiSeed mod 20,
444 • EtaCrySeed: the η of the seed crystal in local coordinates,
445 • PhiCrySeed: the η of the seed crystal in local coordinates.

446 For endcap electrons, we additionally include the ratio of the energy measured in the preshower
447 to the energy of the supercluster.

448 We train each regression separately for barrel and endcap electrons. In order to test against
449 over-training, these samples were explicitly divided in two. Only one half is used for training,
450 while the remaining half is used to test the performance of the regression. The training was
451 restricted to non-radiative electrons, with radiated energy fraction < 0.01 as determined from
452 the Monte Carlo truth information. This is done in order to factorize the effect of final state
453 radiation recovery, for which there is a separate algorithm in this analysis. The target of the
454 regression is chosen to be the ratio of the generated energy to the raw energy of the supercluster
455 for barrel electrons, and the ratio of the generated energy to the sum of the supercluster raw
456 energy and the preshower energy for endcap electrons.

457 This energy measurement is then combined with the momentum measurement from the GSF
458 track to form the combined electron momentum measurement using the standard combination
459 algorithm [30]. The performance is evaluated using the resonance, where we compare the
460 resolution for the dielectron mass computed using the regression energy measurement and the
461 mass computed using the supercluster corrected energy. This is shown in Figures 2, where
462 we observe an increase in performances. In Figure 3, we also show the comparison of the
463 reconstructed Higgs boson mass for the four electrons and two electrons two muons final state,
464 where we observe an improvement in the resolution of more than 10%, in agreement with what
465 is observed with Z's events.

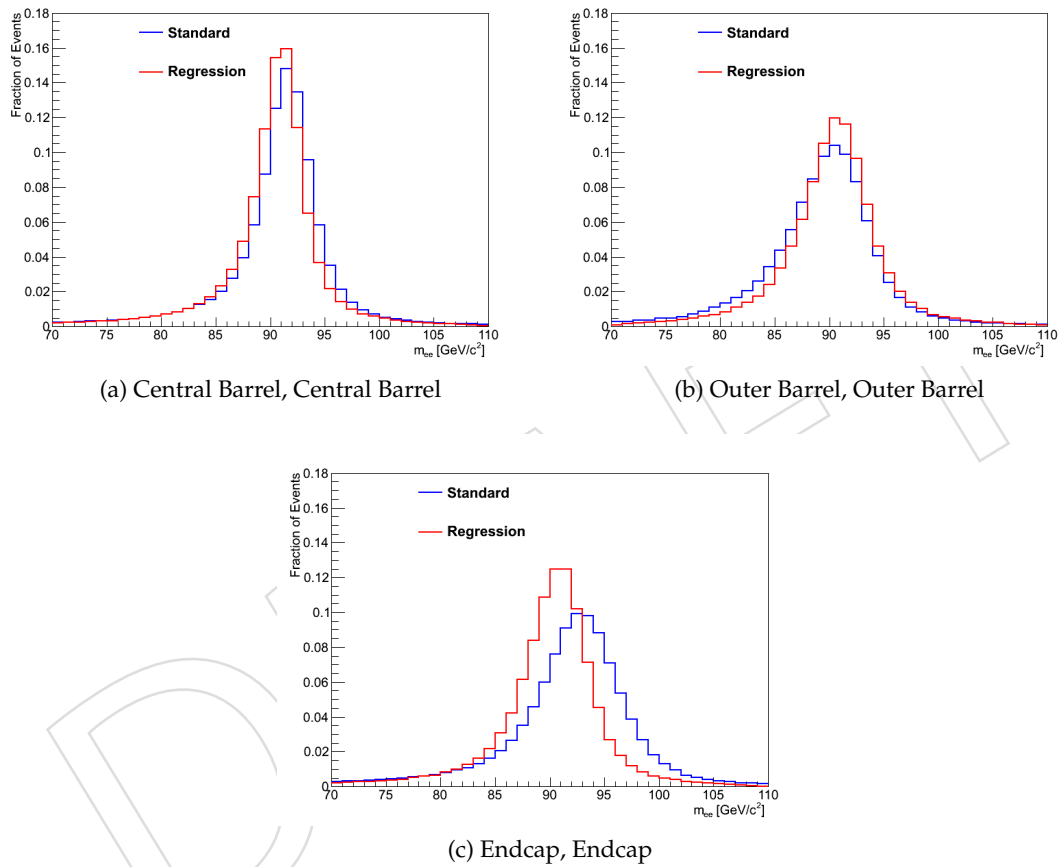


Figure 2: A comparison of the reconstructed $Z \rightarrow ee$ mass using the standard electron momentum assignment and the regression assignment are shown for the Monte Carlo simulation separately in events where both electrons are in the central barrel ($|\eta| < 0.8$), both are in the outer barrel ($0.8 \leq |\eta| < 1.479$), and both are in the endcap ($|\eta| > 1.479$).

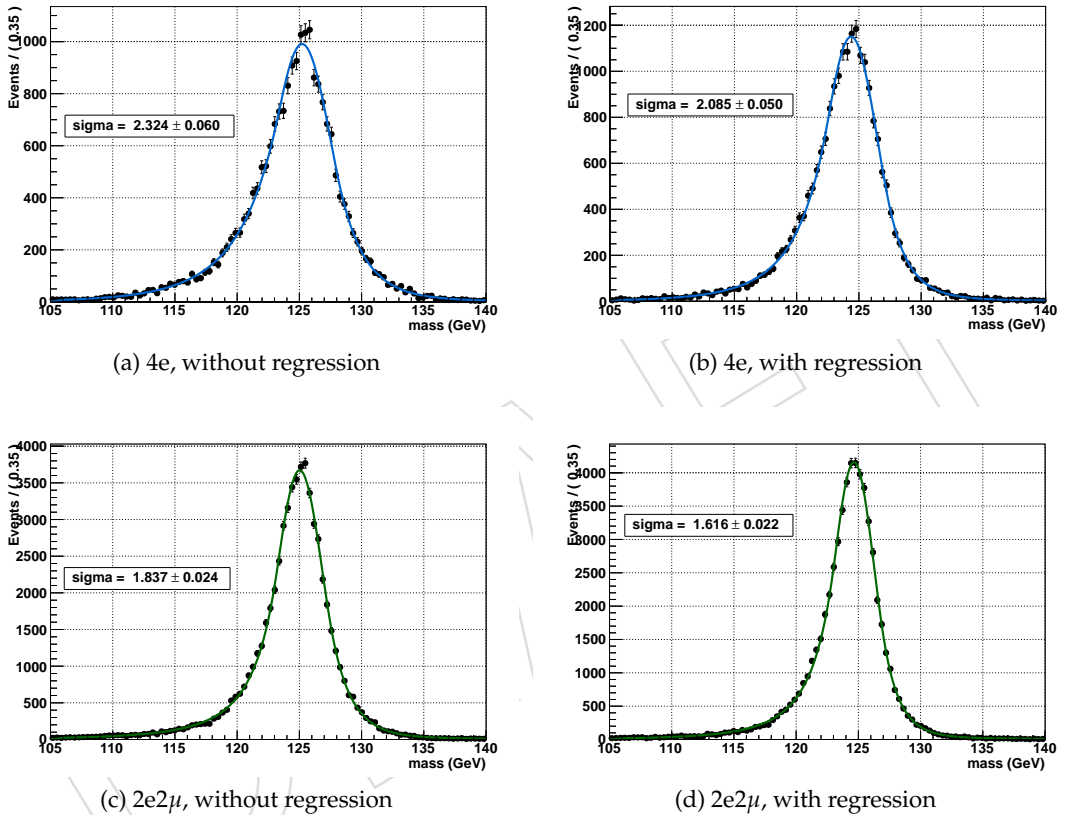


Figure 3: A comparison of the reconstructed Higgs boson mass distributions after applying Monte Carlo to data corrections for the standard electron momentum assignment (left) and the regression assignment (right), for the 4e (top) and 2e2μ (bottom) channel. A fit is superimposed and the parameter linked to resolution shown.

466 3.1.4 Identification

467 The identification of electrons relies on a Boosted Decision Tree (BDT) multivariate technique [38]
 468 that combines observables sensitive to the amount of bremsstrahlung along the electron trajec-
 469 tory, the geometrical and momentum matching between the electron trajectory and associated
 470 clusters, as well as shower-shape observables. The multivariate identification was trained us-
 471 ing a Higgs boson Monte Carlo (MC) sample for the signal and a $W + 1$ -fake electron data
 472 sample for background. The working point was optimized using a $Z + 1$ -fake electron data
 473 sample.

474 The cut values on the BDT output resulting from the optimization procedure are summarized
 475 below:

- 476 • $5 < p_T < 10 \text{ GeV}$:
 - 477 • $|\eta| < 0.8 : BDT > 0.47$
 - 478 • $0.8 < |\eta| < 1.479 : BDT > 0.004$
 - 479 • $|\eta| > 1.479 : BDT > 0.295$
- 480 • $p_T > 10 \text{ GeV}$
 - 481 • $|\eta| < 0.8 : BDT > 0.5$
 - 482 • $0.8 < |\eta| < 1.479 : BDT > 0.12$
 - 483 • $|\eta| > 1.479 : BDT > 0.6$

DRAFT

484 3.2 Muon Reconstruction and Identification

485 3.2.1 Reconstruction

486 In the standard CMS reconstruction for pp collisions, muon tracks are first reconstructed inde-
 487 pendently in the inner tracker (*tracker track*) and in the muon system (*standalone-muon track*).
 488 Based on these objects, two reconstruction approaches are used [39]: *Global Muon (outside-in)*.
 489 and *Tracker Muon (inside-out)*.

490 Tracker Muon reconstruction is more efficient than the Global Muon reconstruction at low mo-
 491 menta, $p \lesssim 5\text{ GeV}/c$, because it requires only a single muon segment in the muon system,
 492 whereas Global Muon reconstruction is designed to have high efficiency for muons penetrat-
 493 ing through more than one muon station and typically requires segments in at least two muon
 494 stations.

495 Thanks to the high tracker-track efficiency [40] and a very high efficiency of reconstructing
 496 segments in the muon system, about 99% of muons produced in pp collisions and having suffi-
 497 ciently high momentum are reconstructed either as a Global Muon or a Tracker Muon, and very
 498 often as both. Candidates found both by the Global Muon and the Tracker Muon approaches
 499 that share the same tracker track are merged into a single candidate. Muons reconstructed
 500 only as standalone-muon tracks have worse momentum resolution and less favourable colli-
 501 sion muon to cosmic-ray muon ratio than the Global and Tracker Muons and are usually not
 502 used in physics analyses.

504 3.2.2 Momentum Estimation and corrections

505 In this analysis, momentum scale calibrations are applied to muons both in data and in simu-
 506 lations, derived from the $1/p_T$ distributions of muons from Z decays [41]. The corrections are
 507 designed to calibrate the overall momentum scale and to remove any dependency of the scale
 508 on the p_T , η , ϕ and charge of the muon, thereby improving also the momentum resolution. In
 509 addition, on simulation a smearing of the momentum measurement is applied to better match
 510 the momentum resolution in data.

511 Detailed comparisons between data and MC, after mu-scale corrections on DATA and smearing
 512 on MC, will be shown in Section 7.4.12.

513 3.2.3 Ghost Muon Removal

514 Due to a change in the tracking in 5XX releases, a class of "bad" muons (called as well "ghost
 515 muons) appeared, for which there are two flavors:

- 516 • *split tracks*: the tracker track of a muon is broken in two, both are identified as muons.
 517 The signature is as follows: shared muon segments, small ΔR , same sign.
- 518 • *Mismatch tracks*: the track of another particle in the event is also found to be compati-
 519 ble with the same muon hits. The signature is shared segments.

520 These "bad muons" have almost no influence in the signal region thanks to the application of
 521 Particle Flow Muon Identification criteria (see next section) that reject most of them. However,
 522 in the background control region (see Section 9) where these criteria are relaxed, thus allowing
 523 "ghost muons" to enter in this phase space, they could perturb the estimation of reducible
 524 background. At the time of ICHEP analysis [20, 21], simple criteria were applied to reject
 525 "ghost muons":

- 526 • Require a $\Delta R > 0.02$ between the muons. It rejects split tracks (and some low mass

527 resonances).

- 528 • Require the non-Global Tracker Muon to be arbitrated. It removes a large fraction of
 529 the mismatch tracks.

530 After these cuts, the residual contamination of "ghost muons" in the background control region
 531 was estimated to be from 4 to 9% of the total events. It was decided to stay with this contamina-
 532 tion, knowing that the overall background is low in μ -channels and that a large uncertainty is
 533 assigned. For this analysis, we added an additional requirement, targeted to kill the remaining
 534 "mismatch tracks" events:

- 535 • a muon is tagged as "ghost" if it has more than 50% of shared segments.
- 536 • preference is always given to the muons passing the PF Muon Identification criteria.
- 537 • for same-sign muons with $\Delta R < 0.03$, we pick the best according to $\sigma(p_T)/p_T$. For
 538 other cases, we pick the muon with the largest number of segments. Final ambigu-
 539 ties, if any, are resolved by choosing the muon with highest p_T .
- 540 • a Global Muon or Tracker Muon with two arbitrated matches is never cleaned.

541 It has been checked that the impact of all these "ghost muons" cleaning requirements have an
 542 impact on $H \rightarrow ZZ \rightarrow 4\mu$ of the order of 0.03%, thus negligible.

543 3.2.4 Identification

544 The combination of different algorithms provides a robust and efficient muon reconstruction.
 545 A given physics analysis can achieve the desired balance between identification efficiency and
 546 purity by applying a selection based on various muon identification variables. For this analysis
 547 we choose the *Particle Flow Muon selection*.

548 The PF Muons are selected among the reconstructed muon track candidates by applying min-
 549 imal requirements on the track components in the muon system and taking into account a
 550 matching with small energy deposits in the calorimeters.

551 More details of the Particle-Flow Muon selection are described in Ref. [42].

553 3.3 Primary and Secondary Leptons

554 The notion of leptons originating from a "common primary vertex" is taken throughout the
 555 analysis a meaning that each individual lepton as an associated track with a small impact
 556 parameter with respect to the event primary vertex. In practice for the event selection (see
 557 section 6), the significance of the impact parameter to the event vertex, $|SIP_{3D}| = \frac{|IP|}{\sigma_{IP}}$ is used
 558 where IP is the lepton impact parameter in three dimensions at the point of closest approach
 559 with respect to the primary interaction vertex, and σ_{IP} the associated uncertainty. Hereafter, a
 560 "primary lepton" is a lepton satisfying $|SIP_{3D}| < 4$.

561 3.4 Lepton Isolation

562 We applied (almost) no changes to our way to compute the lepton isolation with respect to
 563 FIXME ICHEP AN. We therefore summarized the overall methodology.

564 Standard tools provided by CMS are used in the following manner. The isolation is defined
 565 by performing the scalar sum of the transverse momentum of the particle flow candidates
 566 reconstructed in a ΔR cone of 0.4, defined as:

$$\text{RelPFiso} = \frac{\sum_{\text{lepton}}^{\text{chargedhadron}} p_T + \sum_{\text{lepton}}^{\text{neutralhadron}} p_T + \sum_{\text{lepton}}^{\text{photon}} p_T}{p_T} \quad (1)$$

567 In case of electrons, the particle-based isolation of a GSF electron requires some vetoes on the
 568 candidates in the cone. We follow the e/g recommandations:

569 • barrel and endcap:

- 570 1. veto all the reconstructed particle flow electrons (in the most of the cases, this
 571 requirement removes the pf-electron correspondent to the GSF electron, with
 572 all its brem clusters)
- 573 2. veto all the charged hadrons that share the same GSF track or the closest CTF
 574 track with the electron

575 • endcap:

- 576 1. veto all the charged hadrons in a cone $\Delta R=0.015$ around the electron
- 577 2. veto all the photons in a cone $\Delta R=0.08$ around the electron

578 With these vetoes the footprint of the electron in both barrel and endcap is reduced to less than
 579 1% (see [38]).

580 One novelty of this analysis is to use the latest recommendations from the e/g POG¹. Due to
 581 a change in the tracking (between 51X and 52X releases), it was noticed that the number of
 582 electrons with missing expected inner hits (mhits) greater than 0 has increased by 1%. In this
 583 analysis, we ask electrons to have mhits ≥ 2 . The inefficiency of the cut therefore transfer into
 584 the isolation. Indeed, if mhits ≥ 0 the Particle Flow algorithm is building a photon instead of an
 585 electron and this PF-photon will enters the isolation sum. Since this PF-photon has the same
 586 SuperCluster as the GSF electron, it can be easily identified and removed from the isolation
 587 sum.

588 With this fix, we expect to gain about 1% more efficiency per electron for signal events. We
 589 expect also a small increase in the fake rate used to estimate reducible background.

590 3.4.1 Pile-up corrections

591 Isolation variables are among the most pile-up sensitive variables in this analysis. Pile-up
 592 causes the mean energy deposited in the detector to increase, leading to the rise of the mean
 593 isolation values. Thus, the efficiency of a cut on isolation variables strongly depends on pile-up
 594 conditions. In order to have a pile-up robust analysis, the isolation variable has to be corrected.

595 The degradation of isolation performances due to pile-up can be partly mitigated associating
 596 the charged particle flow candidates to the primary vertices. We do this through this association
 597 with pfNoPileup association, which consists in filtering the sample of charged particle flow
 598 candidates associated with the other primary vertices excluding the one with the highest $\sum p_T^2$
 599 of the associated tracks.

However, the neutral component (neutral hadron and photons), for which this association cannot be trivially done, need a special treatment. Among several correction methods, the one using FastJet [43, 44] energy density (ρ) in the event has been chosen to estimate the mean pile-up contribution within the isolation cone of a lepton. A ρ variable is defined for each jet in

¹https://twiki.cern.ch/twiki/bin/view/CMS/EgammaPFBasedIsolation#The_25th_May_update

a given event and the median of the ρ distribution for each event is taken. The correction to the neutral component of the isolation variable is then applied according to the formula :

$$\sum_{neutral}^{corr} p_T = \max\left(\sum_{neutral}^{uncorr} p_T - \rho \cdot A_{eff}, 0 \text{ GeV}\right) \quad (2)$$

600 where the *effective area* (A_{eff}) of a given component is defined as the ratio between the slope of
 601 the average isolation *iso* and ρ as a function of number of vertices.

602 We are currently using the ICHEP and HCP recommendations from the e/g and muon POGs
 603 regarding ρ computation and A_{eff} . However, while work is in progress to align the slightly
 604 different approaches followed for electrons and muons, we take as a reference for ICHEP what
 605 has been proposed by POGs and describe them in what follows. More details can be found about
 606 effective areas and ρ computation in [20].

607 3.4.2 Working Point

608 In [20, 21], we found that the best working point was, for both electrons and muons and over
 609 the whole η range:

$$\text{RelPFiso} < 0.4 \quad (3)$$

DRAFT

610 4 Leptons Measurements

611 4.1 T&P methodology

612 The efficiencies for reconstruction, identification and trigger for electrons and muons is mea-
 613 sured with data based on a selection of events of inclusive single Z production. The well-known
 614 tag-and-probe technique [39, 45] combines the requirements of a mass constraint from a pair of
 615 basic objects (e.g. tracks for muons, or clusters of calorimetry cells for electrons) with a tight
 616 lepton selection applied on one leg (the "tag"), so to ensure sufficient purity. The other leg (the
 617 "probe") is used to measure the efficiency of a given reconstruction algorithm or identification
 618 criterium. The efficiency is defined as the ratio of the number of passing probes to the total
 619 number of probes before the cut.

620 The rate of background is significantly reduced due to the presence of the additional tight
 621 photon and through the constraint on the three-body mass.

622 It is important to perform such a measurement with the exact electron and muon objects as
 623 used in this analysis. By using appropriate definitions for probes, the overall efficiency per
 624 lepton can be factorized in a series of terms, that can be measured independently:

$$\epsilon = \epsilon_{\text{RECO}|\text{trackorclustering}} \times \epsilon_{\text{ID}|\text{RECO}} \times \epsilon_{\text{ISO}|\text{ID}} \times \epsilon_{\text{SIP}|\text{ISO}} \quad (4)$$

625 where each term represents the efficiency for the probe to pass a given selection or reconstruc-
 626 tion step, given that it passes the criteria for the previous one. The clustering efficiency for
 627 electrons is assumed to be 100% efficient which is checked by MC to be the case within few per
 628 mille in the p_T range of interest for this analysis. The efficiency to reconstruct a muon in the in-
 629 ner tracker has been measured separately and is included as an extra term in the factorization.
 630 By applying the method to both data and simulation we derive data to simulation scale factors.
 631 These scale factors are later used to either correct the signal efficiency in the simulation (us-
 632 ing in this case their uncertainty as systematic error) or to provide systematic uncertainties (cf.
 633 section 7.3.2). Statistical uncertainties on the efficiencies are estimated using Clopper-Pearson
 634 confidence intervals [46, 47]. In the computation of the final systematics on the signal efficiency
 635 the systematics on the tag-and-probe method are also considered; they are evaluated varying
 636 the signal and background modeling.

637 The tables with all numbers for the efficiencies measured with the Tag and Probe technique on
 638 data, MC and the data/MC ratio are collected in Appendix C.

639 4.2 Electrons

640 For electrons, we define three group of tag requirements — one for reconstruction and identifi-
 641 cation efficiency measurements, another for isolation and impact parameter and a last one only
 642 used for some trigger efficiency measurement. The two definitions are as follows:

643 1. Reconstruction and identification tags:

- 644 • $p_T > 20 \text{ GeV}$, $|\eta| < 2.5$ and $E_T^{\text{miss}} < 25 \text{ GeV}$
- 645 • pass a set of VBF cuts, Working Point 60% (WP60) which involves cuts on
 646 pure identification variables ($|\Delta\eta_{\text{in}}|$, $|\Delta\phi_{\text{in}}|$, H/E and $\sigma_{i\eta i\eta}$), track and calori-
 647 meter isolation as well as conversion removal [48].
- 648 • matched geometrically to the leg of the double object trigger used for the study
 649 that has requirement on the electron ID at trigger level,

650 2. Isolation and impact parameter tags:

- 651 • $p_T > 20 \text{ GeV}$, $|\eta| < 2.5$ and $E_T^{\text{miss}} < 25 \text{ GeV}$
- 652 • pass a set of VBF cuts, WP80 (80% efficient) which is looser than previously
- 653 defined WP60,
- 654 • particle-based isolation is used instead of detector-based.

655 3. Trigger tags:

- 656 • $p_T > 20 \text{ GeV}$, passing "Tight Trigger Working Point 2012" (tighter than trigger
- 657 requirements), and spatially matched ($\Delta R < 0.1$) with an online HLT electron
- 658 passing the HLTFILTER `hltEle20CaloIdVTCaloIsoVTTrkIdTTrkIsoVTSC4TrackIsoFilter`.

659 In the later case, the purity of the tag-and-probe sample is higher, justifying the looser selection
 660 choice, since reconstruction and identification criteria already removes a lot of background
 661 from fake electrons.

662 The reconstruction, identification, isolation and impact parameter efficiencies are measured in
 663 several p_T and η bins by performing a simultaneous extended likelihood fit of the passing and
 664 failing sample invariant mass distribution in each bin. A Breit-Wigner (BW) convoluted with a
 665 Crystall-Ball function (CB) is used to model the signal peak. Breit-Wigner shape is fixed to the
 666 Z-pole mass (91.2 GeV) and width (2.5 GeV) to describe the natural shape of the Z. Crystall-Ball
 667 function is suited for describing the detector resolution effects as well as the low-mass radiative
 668 tail. By careful study of the shape from MC Drell-Yan sample requiring the matching between
 669 the generated and reconstructed electrons, two additional effects were noted:

- 670 • exponential tail of Drell-Yan spectrum for low p_T bins
- 671 • threshold effect for the bin around 20 GeV

672 For this reason an $\text{erf}(m_{TP})$ or an $\text{erf}(m_{TP}) \times \exp(m_{TP})$ is added to the signal model, where
 673 $\text{erf}(m_{TP})$ is error function and $\exp(m_{TP})$ exponential. Purely exponential function is added to
 674 the signal model when fitting the tail of Drell-Yan spectrum in low p_T bins and exponential
 675 times error function is used to model the threshold effect for the bin around 20 GeV. A few
 676 example MC fits are shown on Fig. 6. This method minimizes dependance on simulation and
 677 uses a minimum set of parameter values obtained from fits in simulation are to constrain the
 678 data fit. The ratio between the integral under the exponential tail and the $BW \otimes CB$ core and
 679 the CB tail parameters are fixed for the fit to data while other parameters are left floating with
 680 initial values taken from the MC fit. This turned out to give the best fit stability and tail control
 681 with minimum number of parameters fixed from the fit to simulation.

682 The functional forms to describe the remaining background is again an error function times an
 683 exponential. In some cases where the charge miss-identification permitted, to avoid the inter-
 684 ference with signal tail description, parameters for the background were constrained from the
 685 signal-free phase space asking for the same sign leptons.

686 The fit method was crosschecked with the template method where invariant mass histogram
 687 from the simulation is used to "fit" the data with normalization as a free parameter. As in
 688 the fit method, simultaneous "fit" to dielectron invariant mass distribution in tag+passing and
 689 tag+failing samples is done. Efficiency is a fit parameter so that fit uncertainties are automati-
 690 cally propagated through the likelihood contours.

691 Very good agreement between two methods in the high $p_T > 20 \text{ GeV}$ region is observed. In the
 692 low $7 < p_T < 20 \text{ GeV}$ region some discrepancies between two methods were observed mainly
 693 due to the background contamination of the invariant mass distribution which makes fitting

694 very challenging. For the final results, the two methods are therefore combined, as explained
 695 later.

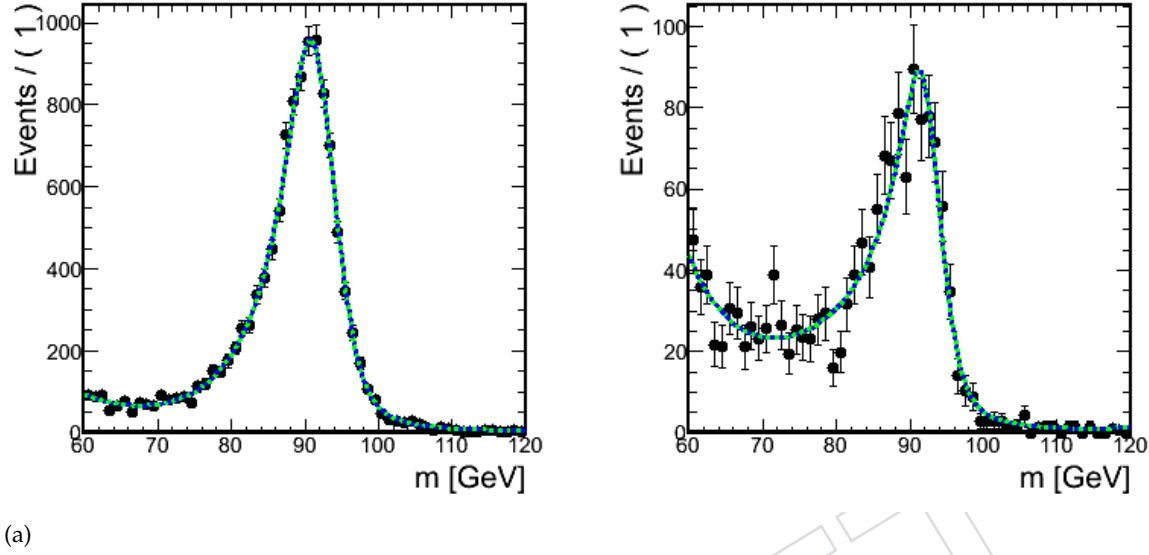


Figure 4: $|\eta| < 1.442, 10 < p_T < 15 \text{ GeV}$

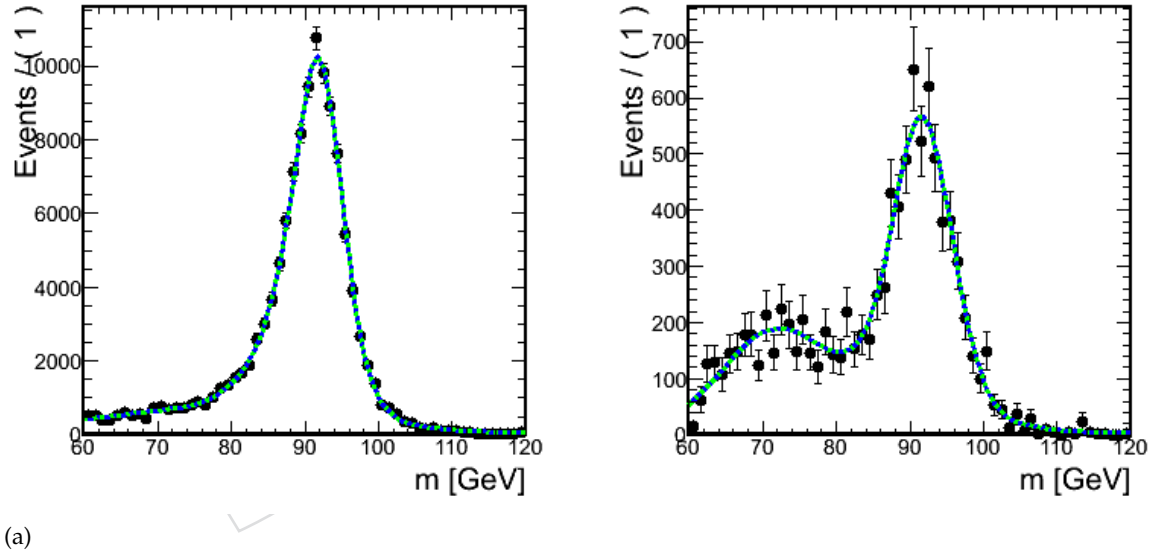


Figure 5: $|\eta| < 1.442, 20 < p_T < 30 \text{ GeV}$

Figure 6: Fits for simulated invariant mass of two electrons matched with generated electrons with an error times exponential or pure exponential part added to the signal model. (a) The exponential tail covers the residual Drell-Yan falling spectrum. (b) The error times exponential accounts for the threshold effect.

696 4.2.1 Electron Reconstruction and Identification

697 Electron reconstruction efficiency has been measured on 2011 data following the methodology
 698 described in [46] and the results reported in [49] are used in this analysis for the 7 TeV Analysis.

- 699 Special tag-and-probe triggers present in “SingleElectron” dataset are used in 2012 8 TeV data,
700 and a matching of a tag with the triggered electron is required to avoid bias. Then, if a probe
701 supercluster is geometrically matched to a GsfElectron in the event, it is considered passing.
702 No additional cuts were applied on the probe supercluster.
- 703 The measured reconstruction efficiencies for single electrons as a function of the SuperCluster
704 probe E_T (with $E_T > 10 \text{ GeV}/c$) are shown in Figure 7 for 8 TeV data, for electrons in ECAL
705 barrel and in ECAL endcaps.

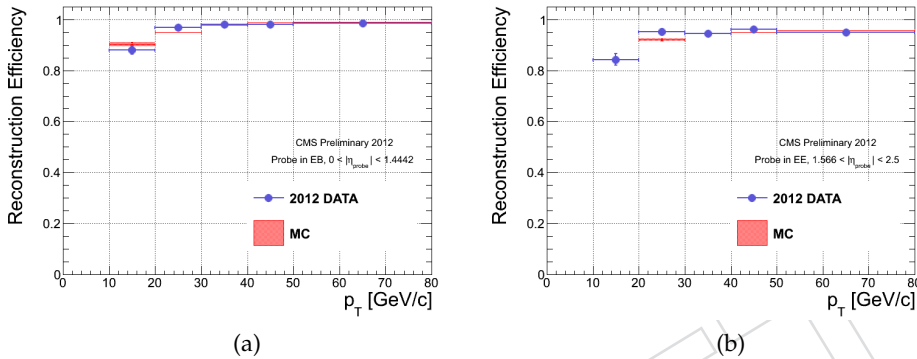


Figure 7: Electron reconstruction efficiencies computed with the tag-and-probe method as a function of the SuperCluster probe E_T in two different η bins: (a) $|\eta| < 1.442$, (b) $1.442 < |\eta| < 2.5$. Results are for 8 TeV data.

706 The measured identification efficiencies for single electrons as a function of the electron probe
707 p_T (with $p_T > 7 \text{ GeV}/c$) are shown in Figure 8 for 7 TeV data and in Figure 9 for 8 TeV data,
708 together with MC efficiencies. The latter were obtained fitting signal simulation, where the
709 probe electron is matched with a generated electron. In addition, the tail in data is constrained
710 by what is obtained from MC. The efficiencies are computed in bins of η coverage and all data
711 taking periods are considered together. Given the limited statistics available for 8 TeV, only two
712 η bins are currently shown. All numerical values are tabulated in Appendix C.

713 There is an overall good data/MC agreement in the barrel and the endcaps. Only statistical er-
714 rors are reported on the plots. The differences observed at low p_T and in the endcaps between
715 data and MC are mostly due to the background estimation (with higher background in the low
716 p_T and high η regions) and the known discrepancies between data and MC of some of the vari-
717 ables used in the electron ID.

718 As an example, the $m_{\ell\ell}$ distributions for passing and failing probes used for the measurement of the electron identification efficiency in the $(10 - 15) \text{ GeV}/c$ p_T bin and for $1.566 \leq |\eta| < 2$ in 2011 data is shown in Figure 10.

721 4.2.2 Electron Isolation and $|SIP3D|$

722 For electron isolation and $|SIP3D|$ efficiencies measurement are done simultaneously. The
723 probes are identified electrons satisfying the BDT requirements described above. The passing
724 criterium for probes is $R_{iso} < 0.4$ and $|SIP3D| < 4$. The isolation+ $|SIP3D|$ efficiency relative to
725 the identified electrons is measured by requiring the probe electron to fulfil the identification
726 criteria, thus reducing significantly the amount of background events in the sample. In addi-
727 tion, for the low p_T bins (below 20 GeV), the identification criteria has been tightened on the probe
728 in order to reject more background, under the assumption that the small correlation between

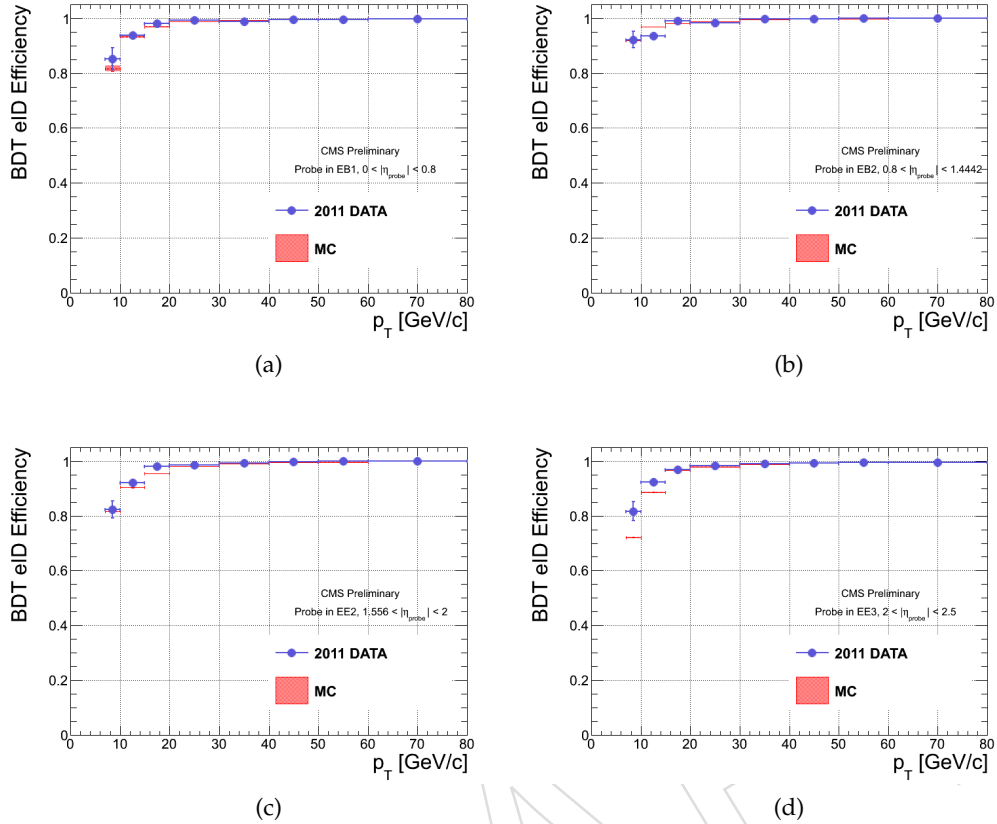


Figure 8: Electron identification efficiencies computed with the tag-and-probe method as a function of the probe p_T in four different η bins: (a) $|\eta| < 0.78$, (b) $0.78 \leq |\eta| \leq 1.442$, (c) $1.566 \leq |\eta| < 2$ and (d) $2 \leq |\eta| < 2.5$. Results are for 7 TeV data.

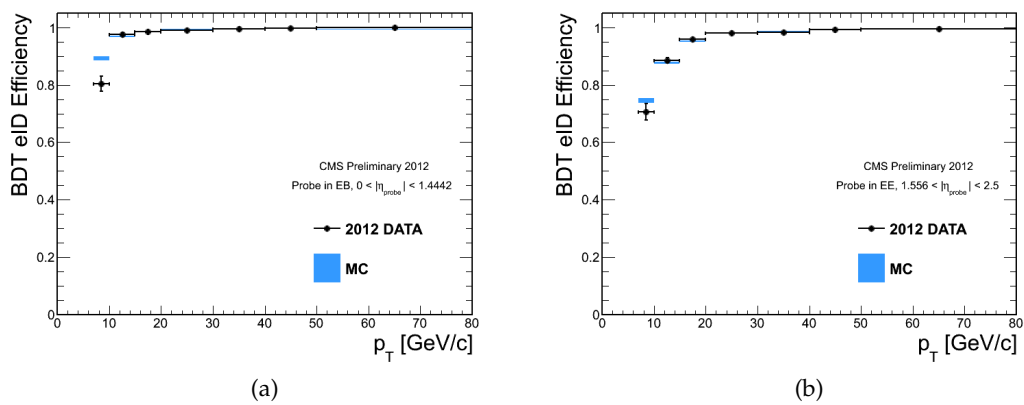


Figure 9: Electron identification efficiencies computed with the tag-and-probe method as a function of the probe p_T in two different η bins: (a) $|\eta| < 1.442$, (b) $1.442 < |\eta| < 2.5$. Results are for 8 TeV data.

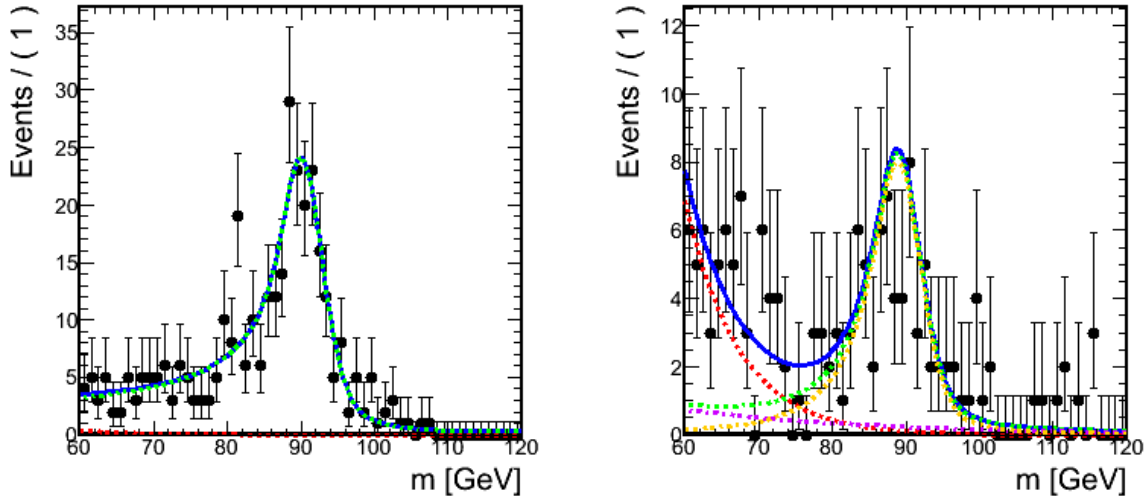


Figure 10: The $m_{\ell\ell}$ distributions and fits for passing and failing probes used for the electron identification efficiency measurement in the $(7 - 10)$ GeV p_T bin and for $0 \leq |\eta| < 1.479$. Black points are 2012 data, green dashed line is signal model, yellow dashed line is $BW \otimes CB$ part of the signal function, purple dashed line is exponential part of the signal function, red line is background model and blue line is signal+background.

729 the identification and the isolation and impact parameter is either fully negligible or correctly
730 reproduced by the simulation so that the data/MC scale factors remain unchanged.

731 Some examples of $m_{\ell\ell}$ distributions for passing and failing probes used for the the measurement
732 of the electron isolation+ $|SIP3D|$ efficiency in the $(10 - 15)$ GeV/c p_T bin and for $1.566 \leq$
733 $|\eta| < 2$ in 2011 data is shown in Figure 11.

734 The measured identification+isolation+ $|SIP3D|$ efficiencies for single electrons as a function of
735 the probe p_T , together with MC efficiencies, are shown in Figure 12 for 2011 data and Figure 13
736 for 2012 data. In 2011, the measurement in the ECAL Barrel-Endcap transition region has been
737 performed in a single bin, integrated over the whole p_T range. The agreement overall is very
738 good. Only statistical errors are reported on the plots.

739 4.2.3 Scale factors

740 Efficiencies measured in data and simulation using the tag-and-probe method in a grid of
741 (p_T, η) -bins are presented in preceding sections. They will be used in final statistical analysis
742 either to correct MC yields or as a source of systematic uncertainties. In this section, we briefly
743 discuss and bring data-to-MC scale factors as obtained by tag-and-probe method on electrons
744 as well as adjacent systematic uncertainties.

745 Systematic uncertainties due to background modeling and Drell-Yan tail miss-modeling have
746 to be accounted for. In order to be conservative, we varied the number of events in the tails by
747 a factor of two up and down recomputing the efficiency and taking the difference to the value
748 assessed from fit as a systematic uncertainty. The uncertainties arising from the background
749 normalization is not accounted for. An additional systematic from the Z pole modeling as sug-
750 gested by Ref. [46] (1%) is used and combined in quadrature with other sources to obtain a final
751 scale factor.

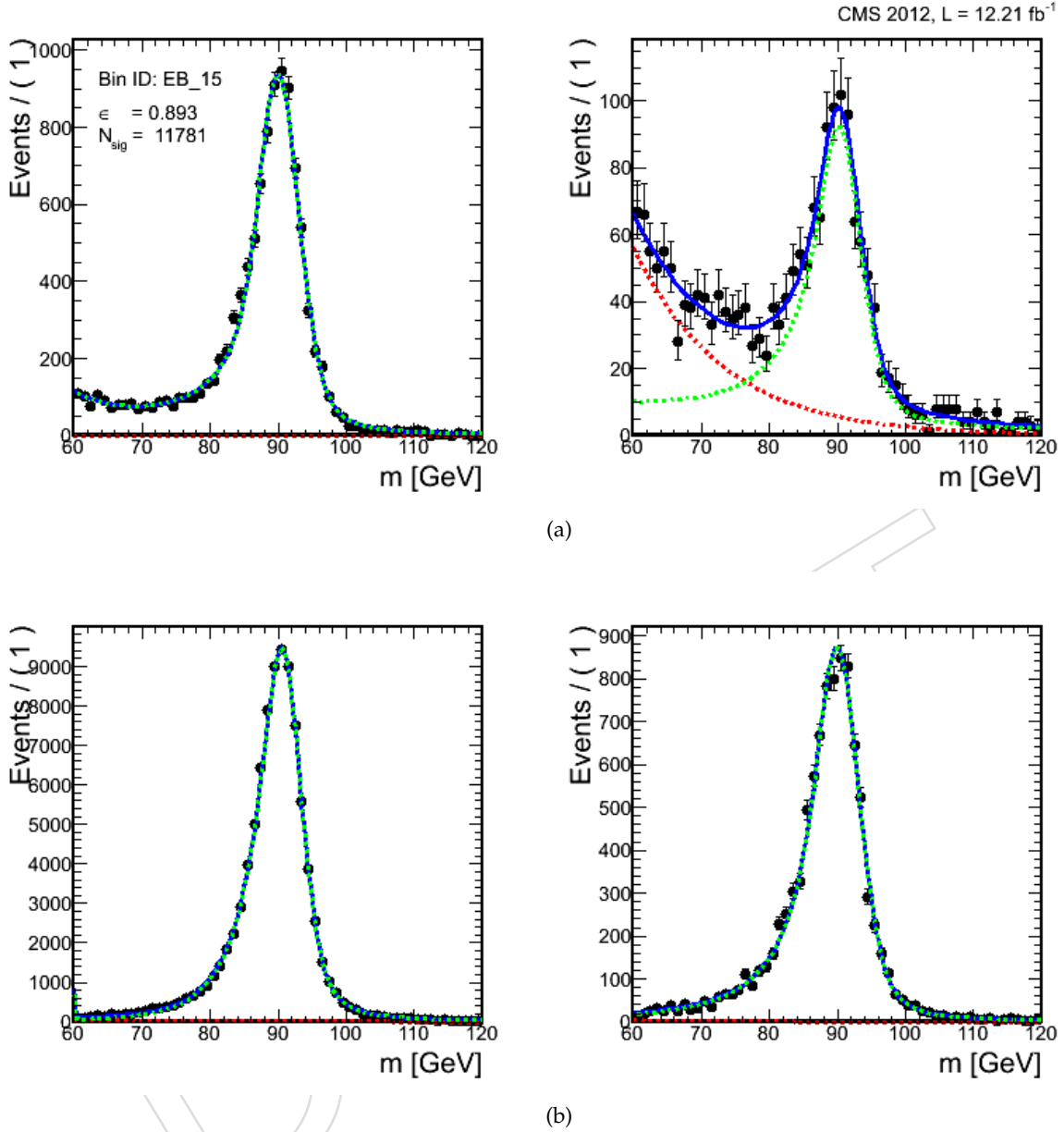


Figure 11: The m_{ee} distributions and fits for passing and failing probes used for the electron isolation and $|SIP3D|$ efficiency measurement in a) the $(15 - 20)$ GeV/c p_T bin in the barrel and b) the $(30-40)$ p_T bin for $2 \leq |\eta| < 2.5$. Black points are 2012 data, green dashed line is signal model, red line is background model and blue line is signal+background.

752 Additionally, for 8 TeV data two different methods had to be taken into account. As a final
 753 result for 8 TeV data the mean value of scale factors obtained with fit and template methods
 754 was taken. As a systematic error the envelope between two methods was taken.

755 The scale factors together for the combination of reconstruction, identification, isolation and
 756 impact parameter are shown on the Fig. 14 and on Fig. ???. The errors quoted are a combination
 757 of statistical and systematic uncertainties. They are all propagated as systematic errors in the
 758 final analysis.

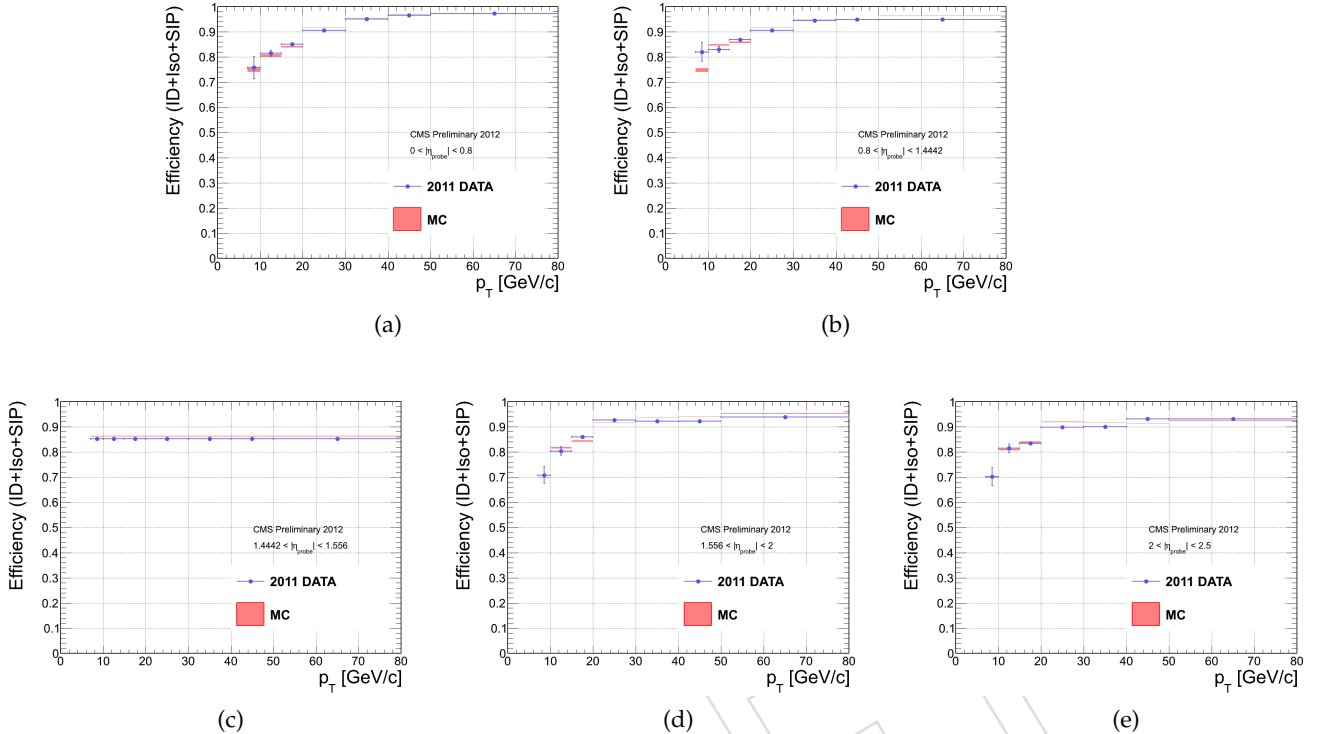


Figure 12: Electron identification+isolation+ $|SIP3D|$ efficiencies computed with the tag-and-probe method as a function of the probe p_T in five different η bins: (a) $0 \geq \eta < 0.78$, (b) $0.78 \geq \eta \leq 1.442$, (c) $1.442 \geq \eta \leq 1.566$, (d) $1.566 \geq \eta < 2$ and (e) $2 \geq \eta < 2.5$. The measurement in (c) has been performed in a single bin, integrated over the whole p_T range. Results are shown for 7 TeV data.

759 4.2.4 Electron trigger

760 The Tag & Probe technic was used on 2012 data to measure the trigger efficiency for the Double
 761 Electron trigger used in the analysis:

762 HLT_Ele17_CaloIdT_CaloIsoVL_TrkIdVL_TrkIsoVL_Ele8_CaloIdT_CaloIsoVL_TrkIdVL_TrkIsoVL
 763

764 This HLT path is composed by three HLT filters:

- 765 • hltEle17TightIdLooseIsoEle8TightIdLooseIsoTrackIsoFilter (*Ele17* in the following),
- 766 • hltEle17TightIdLooseIsoEle8TightIdLooseIsoTrackIsoDoubleFilter (*Ele17Ele8* in the follow-
 767 ing),
- 768 • hltEle17TightIdLooseIsoEle8TightIdLooseIsoTrackIsoDZ (*Ele17Ele8dZ* in the following).

769 An event fired the trigger if the three filters are satisfied. To measure the trigger efficiency, events should
 770 satisfy the following selection:

- 771 • T&P trigger: HLT_Ele20_CaloIdVT_CaloIsoVT_TrkIdT_TrkIsoVT_SC4_Mass50_v1
- 772 • Tag: electron with $p_T > 20$ GeV, passing "Tight Trigger Working Point 2012" (tighter than
 773 trigger requirements), and spatially matched ($\Delta R < 0.1$) with an online HLT electron passing
 774 the HLTFilter hltEle20CaloIdVTCaloIsoVTTTrkIdTTrkIsoVTSC4TrackIsoFilter.
- 775 • Probe: electron passing the analysis selection (BDT eID, PF Iso and SIP) and spatially matched
 776 ($\Delta R < 0.1$) with an online HLT electron passing the HLTFilter hltEle20CaloIdVTCaloIsoVTTTrkIdTTrkIsoVTSC4PMMassFilter.

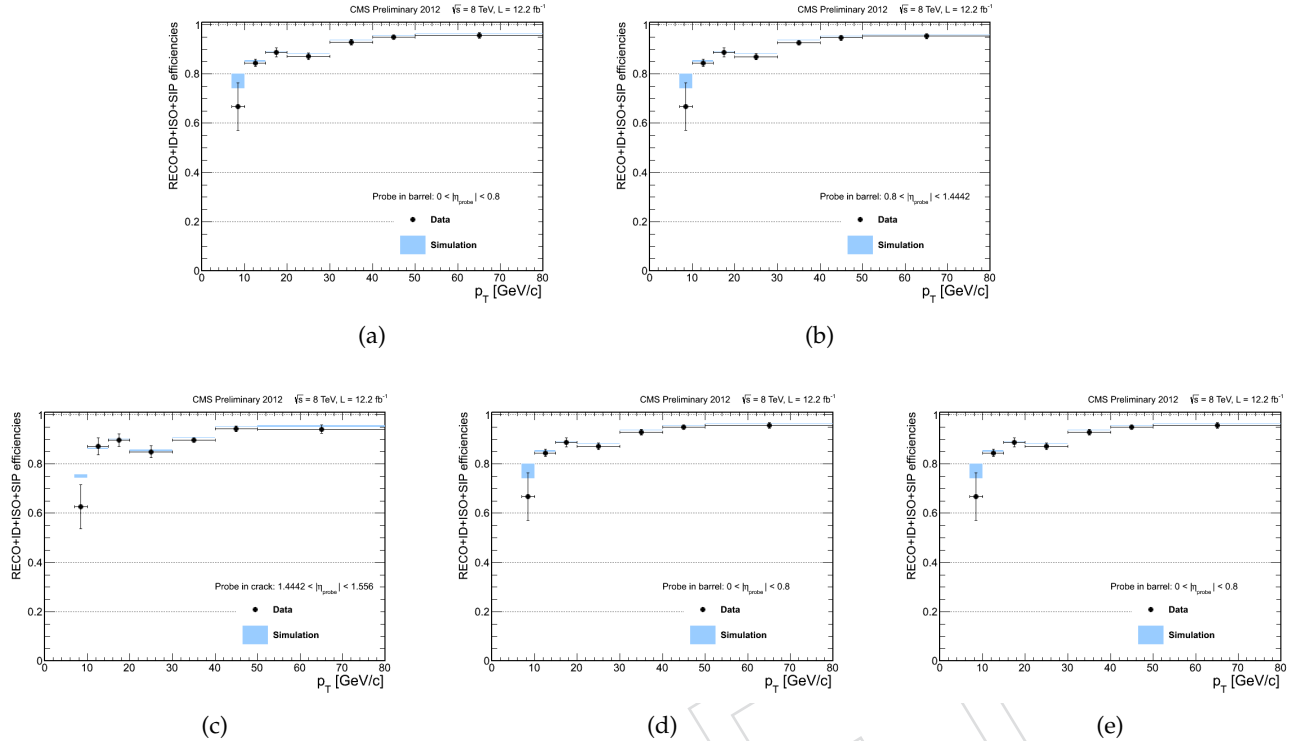


Figure 13: Electron identification+isolation+ $|SIP3D|$ efficiencies computed with the tag-and-probe method as a function of the probe p_T in five different η bins: (a) $0 < |\eta| < 0.8$, (b) $0.8 < |\eta| < 1.4442$, (c) $1.4442 < |\eta| < 1.556$, (d) $1.556 < |\eta| < 2$ and (e) $2 < |\eta| < 2.5$. Results are for 8 TeV data.

777 • Tag and Probe electrons must have opposite sign and their invariant mass must be recon-
778 structed between 60 and 120 GeV.

779 It's not possible to directly measure the efficiency to pass the Ele8 leg. Indeed, the second (and third)
780 filter are requiring two electrons: one with $E_T > 17$ GeV and one with $E_T > 8$ GeV. In the following,
781 we make the assumption that all electrons passing 17 GeV threshold are passing the 8 GeV one. The
782 efficiency to pass the Ele8 leg is therefore computed from electrons passing these filters.
783

784 The efficiency to pass Ele17 is calculated as the number of probes passing Ele17 and Ele17Ele8dZ over the
785 total number of probes. The efficiency to pass Ele17Ele8dZ is calculated as the number of probes passing
786 Ele17Ele8dZ over the total number of probes.
787

788 The Figure 15 is showing the comparison between data and MC of the trigger efficiency for the filters
789 Ele17 and Ele17Ele8dZ for electrons in ECAL barrel and endcaps.

790 Data and MC are in fair agreement for the Ele17 leg. The differences are less than 0.3% for the plateau
791 and 0.5% for the turn-on. Discrepancies are slightly higher for the Ele17Ele8dZ leg with a difference of
792 about 1 GeV in the plateau for electrons in the ECAL barrel (0.5 GeV in the endcaps) and a difference of
793 1-2 GeV in the turn-on.

794 These turn-ons have been used to compute the efficiency of signal events to pass the trigger require-
795 ments. The following prescription was used for each of the four electron candidates on an event-by-
796 event basis. For each electron, with a given p_T and η , the probability to pass a given filter is computed
797 from the turnon-ons. A random number is thrown between 0 and 1. If the number is below the proba-

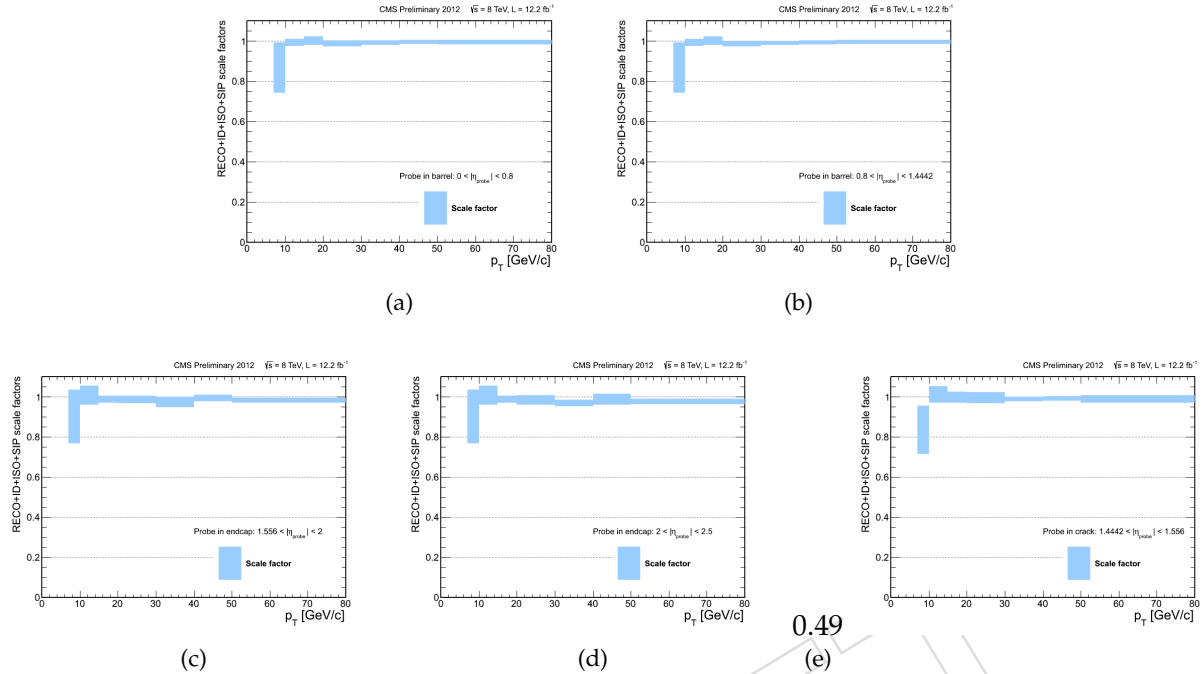


Figure 14: Electron total scale factors obtained from tag-and-probe method for 8 TeV data in barrel and endcap. (a) $0 < |\eta| < 0.8$, (b) $0.8 < |\eta| < 1.4442$, (c) $1.556 < |\eta| < 2$, (d) $2 < |\eta| < 2.5$ and (e) $1.4442 < |\eta| < 1.556$.

798 bility, the electron is passing the filter considered. If at least 2 electrons are passing *Ele17Ele8dZ* and at
 799 least one electron is passing *Ele17*, the event fired the trigger. The trigger efficiency has been computed
 800 after all other analysis cuts and has been compared to the direct measurement, requiring the trigger bit.

As can be seen from the Figure 16 (left), the efficiency computed with turn-ons (red or blue curves) are higher than the ones computed requiring the trigger bit. This is understood as being an effect due to the different algorithms used at HLT and offline levels for the electron isolation. Particle-based isolation is indeed used at offline level, vetoing other leptons in the isolation cone, while detector-based isolation is used at HLT level, without any veto on additional leptons. Events with nearby electrons therefore tend to fail the trigger requirements.

807 The turn-ons computed on single electrons don't allow to compute the "real" trigger efficiency. How-
 808 ever, comparing the trigger efficiency obtained this way with turn-ons measured on data and MC allows
 809 to estimate a possible correction to apply to the direct measurement with the trigger bit. It can be ap-
 810 preciated on Figure 16 (left) that there are little differences between data (blue) and MC (red). As a
 811 consequence, we don't apply any correction on the MC related to trigger.

812 The trigger efficiency is not 100%, especially at low mass. It has been shown that the usage of a OR
 813 between the Double Electron and a Tri-Electrons trigger permits to recover 3.3% efficiency for $m_H = 125$
 814 GeV (see Figure 16, right). This is one of the novelty of this analysis, for both 2011 and 2012 analysis.

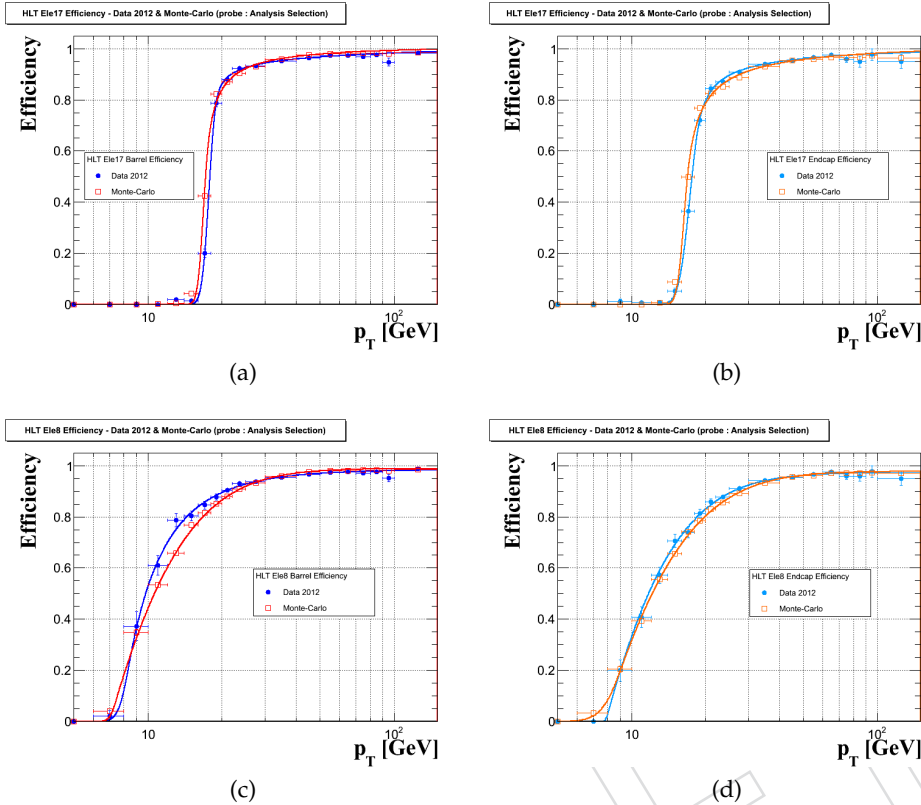


Figure 15: Electron HLT Trigger efficiency for the *Ele17* (resp. *Ele17Ele8dZ*) filter as a function of the probe p_T for electrons in ECAL barrel (a) and endcaps (b) (resp. (c) and (d)). Results are shown for 8 TeV data (blue) and Summer12 MC (red), with parameterizations superimposed. Probes are asked to pass ID, Isolation and SIP requirements of the analysis.

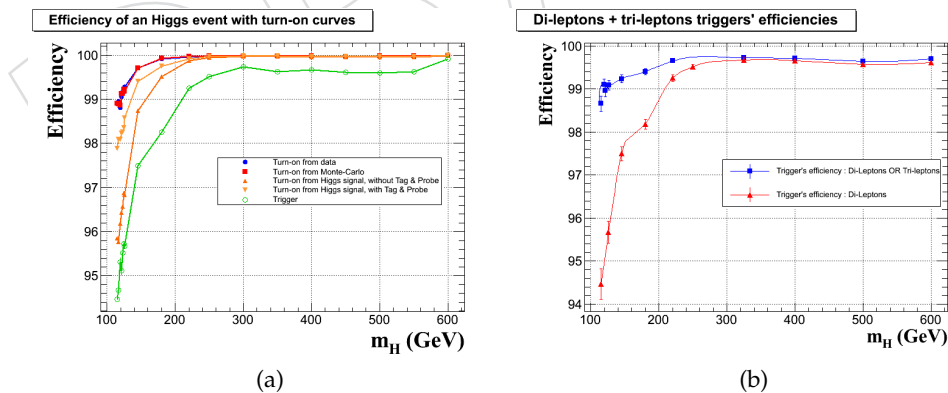


Figure 16: As a function of the Higgs mass (a), Electron HLT Trigger efficiency of the Double Electron Trigger computed with turn-ons measured on $Z \rightarrow ee$ data (red), $Z \rightarrow ee$ MC (blue), Higgs events with (orange), without (dark orange) Tag & Probe techniques and with the trigger bit (green). As a function of the Higgs mass (b), Electron HLT trigger efficiency of the Double Electron trigger (red) and of a OR between the Double and Tri-Electrons triggers, computed with the trigger bit. The trigger efficiencies are computed after all other analysis cuts.

815 4.3 Muons

816 The overall offline selection efficiency for muons is factorized as the product of:

- 817 • the efficiency to reconstruct a track in the inner detector (ϵ_{trk}),
- 818 • the efficiency of the Particle Flow muon reconstruction and identification for muons that have
- 819 been successfully reconstructed in the inner tracker ($\epsilon_{\text{id}|\text{tk}}$),
- 820 • the efficiency of the impact parameter requirement, for muons passing the identification
- 821 ($\epsilon_{\text{sip}_{3d}|\text{id}}$),
- 822 • the muon tracking efficiency.
- 823 • the efficiency of the isolation requirement, for muons passing all other selection criteria ($\epsilon_{\text{iso}|\text{sip}_{3d}}$).

824 4.3.1 Tracking

825 The tracking efficiency in the silicon tracker was measured using as a Tag a "tight" muon (without
 826 dz cut), satisfying an isolation requirement $\text{RelPFIso} < 0.2$ (computed from charged particles only),
 827 and matched to the HLT object corresponding to SingleMuon triggers; the probe is required to be any
 828 standalone muon with valid hits in the muon system. The efficiency is computed matching the probe to
 829 a track with $\Delta R < 0.3$ (directions defined at the PCA to the beam line). In addition, the Δz between the
 830 tag and the matched track should be smaller than 1 cm to suppress Pile-Up. A correction is applied to
 831 the measured efficiency to account for the possibility of spurious matches between the standalone muon
 832 and another track from a charged hadron, as described in [50]; the size of this correction is about 5% of
 833 the measured inefficiency, and thus below 0.1% in absolute.

834 For the 2010 and 2011 running periods, the efficiency from data is found to be very close to 100% and
 835 in agreement with the predictions from simulation to better than 0.2%[51]. A slight loss in efficiency is
 836 instead observed in the 2012 running period, where the tolerances used in the tracking algorithm have
 837 been reduced to cope with the increase in pile-up. The comparisons between 2012 data and MC are
 838 shown in Figure 17. It can be seen that the data presents an inefficiency with respect to the MC, growing
 839 as $|\eta|$ increase and reaching 2% for $|\eta| = 2.4$.

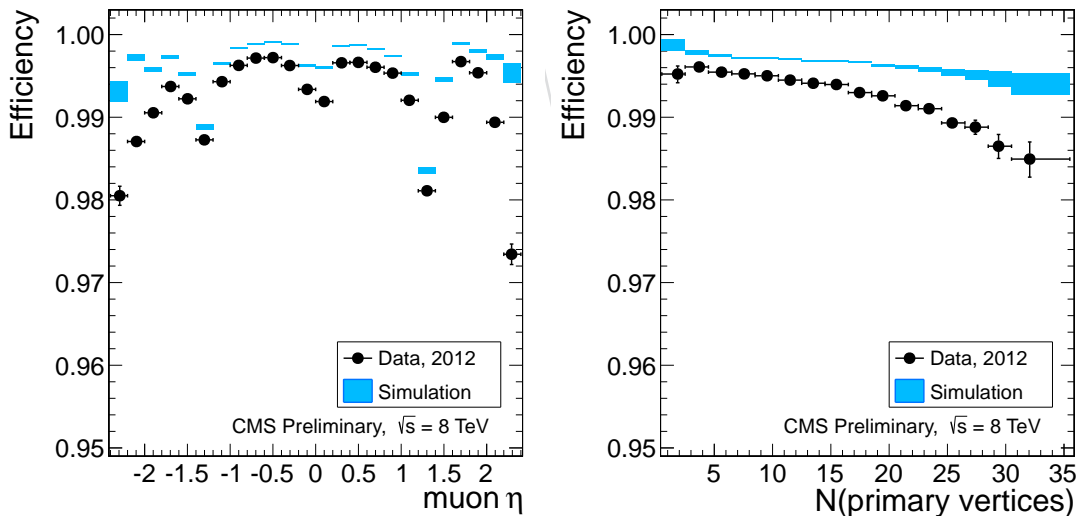


Figure 17: Muon tracking efficiency as a function of the muon η for 2012 data and MC, as function of η (left) and the multiplicity of primary vertices (right).

840 4.3.2 Reconstruction and identification

841 For muons that are successfully reconstructed as a track in the inner tracker, the performance of the
 842 reconstruction in the muon system and the identification criteria for Particle Flow muons has been mea-
 843 sured in 2011 and 2012 data using the tag-and-probe method using dimuons from Z (for $p_T > 15 \text{ GeV}$)

and J/Ψ decays (for $p_T < 15 \text{ GeV}$). A detailed description of the method, and results on 2010 data, can be found elsewhere[39]. The efficiencies measured from data, and the corresponding values obtained applying the same procedure on simulated Z and J/Ψ events are shown in Fig. 18. The simulated events used for comparisons in the two data taking periods have been reconstructed with the same software algorithms as the data, and are weighted as function of the number of reconstructed primary vertices to match the multiplicity observed in data.

For the 2011 data taking period, in the barrel region ($|\eta| < 1.2$) the results of the measurement on data are in very good agreement with the predictions from simulations for all p_T values above 5 GeV relevant for the analysis, and the plateau value of the efficiency is reproduced within 0.3% or better. In the endcaps, the plateau value of the efficiency is about 0.8% lower in data than in the simulation, due to some issues in the CSC readout system during the second part of the data taking. An even better agreement is observed in 2012 data, where the CSC readout problem was fixed.

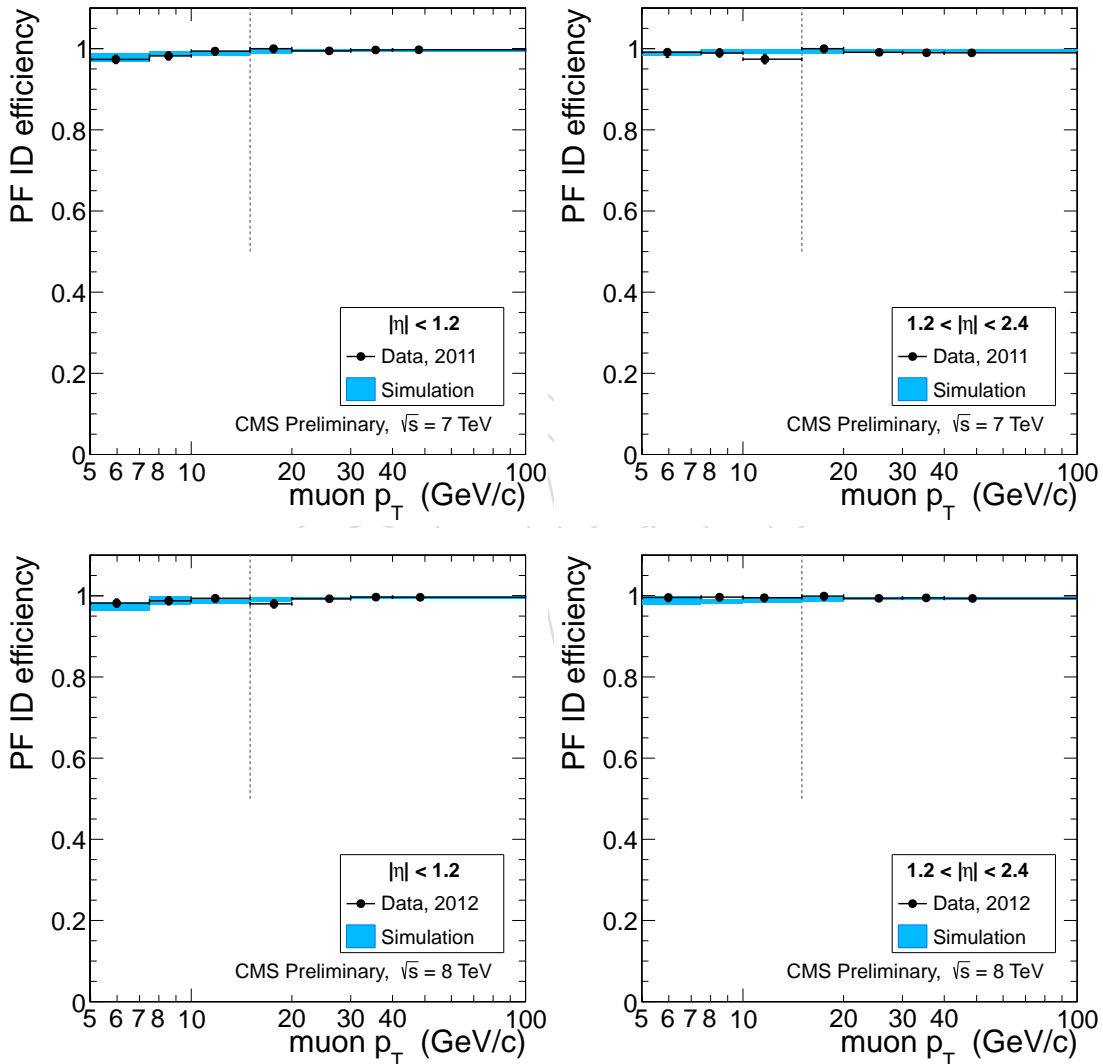


Figure 18: Muon reconstruction and identification efficiency for Particle Flow muons, measured with the tag-and-probe method on 2011 data (top) and 2012 data (bottom) as function of muon p_T , in the barrel (left) and endcaps (right).

4.3.3 SIP3D

The same tag-and-probe method has been used also to measure the efficiency of the requirement on the significance of the 3D impact parameter, for muons passing the Particle Flow identification requirements. In this context, only muons from Z decays can be used, as the J/ Ψ decays contain a significant contamination of non-prompt J/ Ψ 's from B hadron decays.

The efficiency of the $|SIP3D| < 4$ criteria is found to be above 99.5% in the barrel, and decreasing slightly down to about 99% in the forward part of the detector (Fig. 19). In the latter region, the efficiency in data about 0.4% lower than in simulations. No differences is seen between the 2012 A, B and C data taking periods. Moreover, the efficiency does not show a significant dependance to pile-up as it is flat as a function of the number of vertices. Moreover,

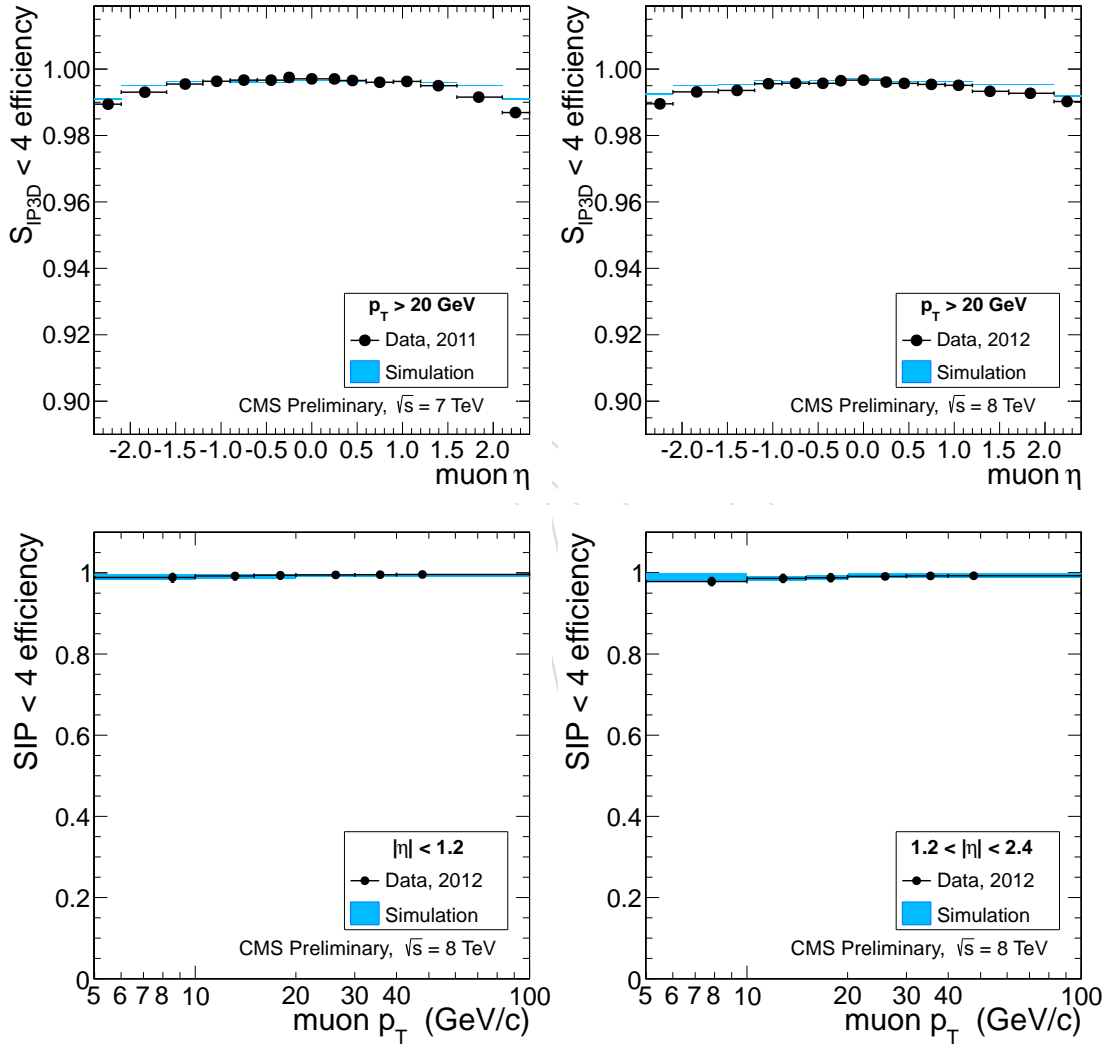


Figure 19: Efficiency for the requirement on the 3D impact parameter significance $|SIP3D| < 4$. Top row: efficiency as as function of the muon pseudorapidity, for 2011 data (left), and 2012 data (right), for muons with $p_T > 20$ GeV; bottom row: efficiency in 2012 data as function of the muon p_T in the barrel (left) and endcaps (right). Muons satisfying the Particle Flow identification requirements are used.

866 **4.3.4 Isolation**

867 The isolation efficiency, the last component of the offline selection efficiency, has been measured on data
 868 using the tag-and-probe method for muons passing the Particle Flow identification and the $|SIP3D| < 4$
 869 criteria. Similarly to the efficiency measurement of impact parameter requirements, only muons from Z
 870 decays can be used, since muons from J/Ψ 's are not expected to be isolated, especially for non-prompt
 871 J/Ψ mesons. The measurement is statistically limited in the 5–10 GeV p_T region, but otherwise an excel-
 872 lent agreement is observed between data and expectations from simulation (Fig. 20).

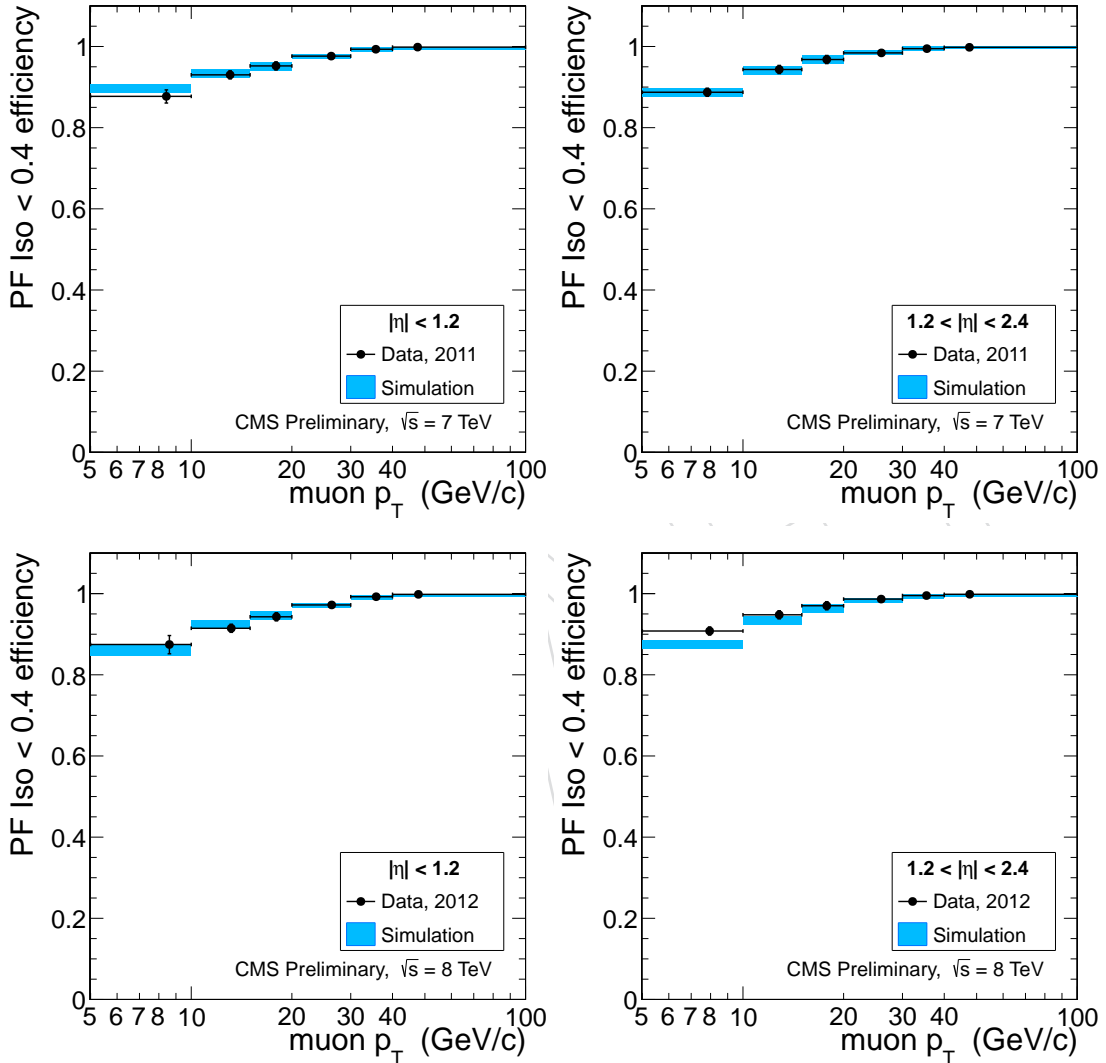


Figure 20: Muon isolation efficiency for Particle Flow muons passing the impact parameter requirements, measured with the tag-and-probe method on 2011 data (top) and 2012 data (bottom) as function of muon p_T , in the barrel (left) and endcaps (right).

873 **4.3.5 Trigger**

874 The tag-and-probe method has also been used to measure the per-muon efficiency for double muon
 875 triggers: as the requirements for either leg of the double muon trigger are always looser than the sin-
 876 gle muon trigger used to select the tags, the tag+probe pair will satisfy a given double muon trigger
 877 requirement whenever the probe satisfies the requirements of a leg of that muon trigger. The double
 878 muon trigger requirements are not symmetric for the two legs, but the information about the HLT ob-
 879 jects can be used to determine if the probe leg satisfies the requirements only of the loose leg or also of
 880 the tight one.

881 The measurement has been performed in 2011, both inclusively and separately for the “Run2011A” and
 882 “Run2011B” periods, for the dimuon trigger with p_T thresholds of 17 and 8 GeV (HLT_Mu17_Mu8); as in
 883 the rest of the analysis, for the earlier part of the data taking this trigger is emulated by requiring the
 884 events to fire a dimuon trigger with lower thresholds but whose associated HLT objects have p_T above
 885 the 17 and 8 GeV. For the 2012 running period, measurements have been performed both for the dimuon
 886 triggers with only L3 muons as in 2011 (HLT_Mu17_Mu8) and for the one exploiting also tracker muon
 887 reconstruction (HLT_Mu17_TkMu8), and for the logical OR of the two.

888 The position and sharpness of the turn-on curve of the trigger efficiency as function of p_T measured on
 889 data is in very good agreement with the expectations from simulation for all the triggers considered; two
 890 representative results are shown in the top panels of Fig. 21. A measurement of the trigger efficiency on
 891 the plateau as function of pseudorapidity η reveals a lower efficiency in data compared to simulation in
 892 the endcaps and in the narrow transition between the two wheels of the barrel (Fig. 21, lower panels).
 893 The effect of this inefficiency is however mitigated by the fact that multiple leptons in the event can fire
 894 the trigger, and so no correction factor is applied at present in the analysis.

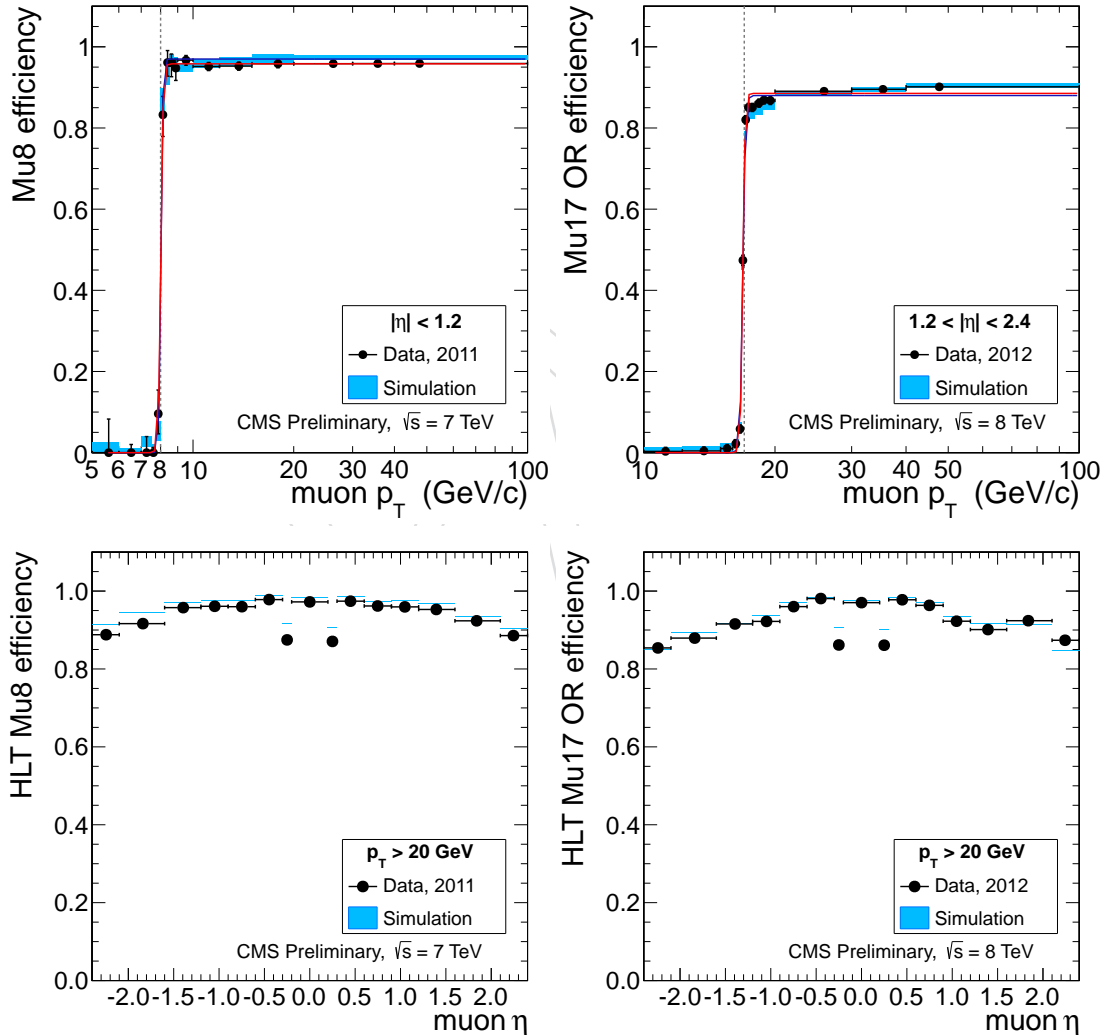


Figure 21: Muon HLT Trigger efficiency for the Mu8 leg (on the left), the Mu17 leg (right), as a function of the muon p_T (top), of the muon η (bottom). Muons are asked to pass ID, Isolation and SIP requirements of the analysis.

895 5 Photon Observables and FSR recovery

896 The photons used in this analysis and the FSR recovery algorithm is the same as in [20, 21]. It is repro-
 897 duced in the following for completeness.

898 A Z decay into a lepton pair can be accompanied by final state radiation (FSR), $Z \rightarrow \ell^+ \ell^- \gamma$. If the
 899 photon transverse momentum, p_T^γ , is required to exceed 2 GeV/c, about 8% (15%) of the decays into
 900 muons (electrons) are affected. As the photon emission is most often collinear with one of the leptons,
 901 electron measured energies automatically include the energy of a large fraction of the emitted photons
 902 in the associated electromagnetic super-cluster. On the other hand, muon measured momenta do not
 903 include the emitted photons. Final state radiation is therefore expected to degrade the Z mass resolution
 904 when measured with the sole muon pairs, and in turn degrade the Higgs boson mass resolution when
 905 measured with the four leptons momenta, especially in the 4μ and in the $2e2\mu$ final states and, to a lesser
 906 extent, in the $4e$ final state. It is also expected to reduce the efficiency of the lepton isolation cut when
 907 the emitted photon is in the lepton isolation cone

908 Both an excellent Higgs boson mass resolution and a large selection efficiency are essential ingredients
 909 in view of the small production cross section in the 4ℓ channels, in particular to discriminate the Higgs
 910 boson signal with the background continuum. It is the purpose of this analysis to recover the FSR
 911 photons with large efficiency and purity, to remove the energy of the recovered photons from the lepton
 912 isolation cones, and to measure the mass of the Higgs boson candidate from the momenta of the leptons
 913 and the recovered photons.

914 In addition to being collinear with the leptons, final state radiation also tends to favour low energy
 915 photon emission collinear to the lepton. An efficient recovery thus requires photon identification and
 916 reconstruction in the vicinity of other particles, down to photon transverse momenta of the order of
 917 the Higgs mass core resolution, *i.e.*, down to a couple GeV/c. Less energetic photons are expected to
 918 degrade the mass resolution in an insignificant manner, and are increasingly difficult to reconstruct and
 919 separate from the background.

920 5.1 Photon Reconstruction and Identification

921 Identifying low energy photons overlapping with other particles is included in the particle-flow concept
 922 developed in CMS [?].

923 Photons (type 1) are identified and reconstructed with the particle-flow reconstruction with a specific
 924 clustering algorithm, efficient down to an energy of 230 MeV in the ECAL barrel and 600 MeV in the
 925 ECAL end-caps. The determination of the photon energies and directions is monitored in the data with
 926 $\pi^0 \rightarrow \gamma\gamma$ decays, and is shown to be accurate, reliable, and in agreement with the predictions from
 927 simulation [? ?].

928 The particle-flow reconstruction includes an identification of showering muons, tuned for energetic
 929 muons. In the rare cases in which such a showering muon is identified, the energies of the particle-
 930 flow clusters linked to the muon do not give rise to separate particles. For the transverse momenta of
 931 interest in the low-mass Higgs boson search, however, the showering probability is vanishingly small,
 932 which leads to the loss of a not entirely negligible fraction of collinear FSR photons. Particle-Flow ECAL
 933 clusters linked to identified showering muons are therefore identified as photons (type 2) in this analysis.
 934 Specifically, the energy of these photons is set to `pfmuon.ecalEnergy()`, and its direction is chosen
 935 to be that of the muon.

936 In rare occurrences, the particle-flow reconstruction may identify a photon although it is already included
 937 in the electron super-cluster, due to imperfect cross cleaning. It is therefore required that photons be
 938 further away from the direction of any electron by 0.05 in pseudo-rapidity, and by 2.0 rad in azimuth.

939 The last two points are clear area of improvement in the particle-flow reconstruction algorithm logic,
 940 improvements that are beyond the scope of this note.

941 In the four-muon final state, the total efficiency of the photon reconstruction for $p_T^\gamma > 2$ GeV/c and

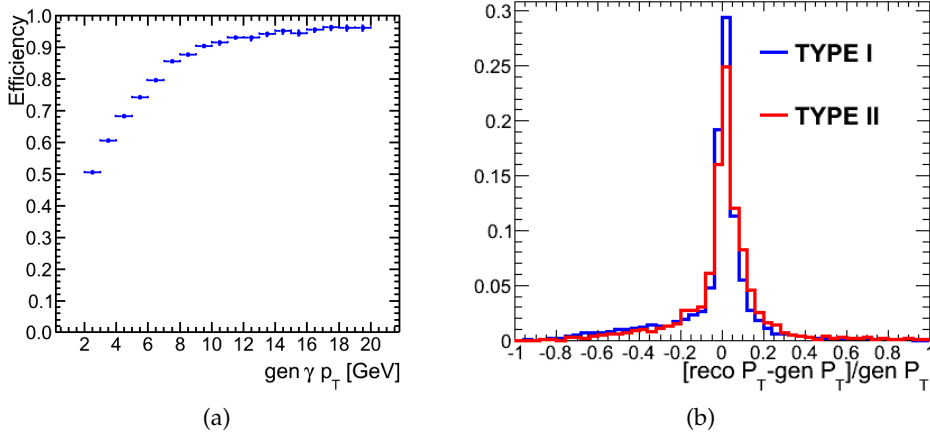


Figure 22: Reconstruction efficiency (a) and transverse energy resolution (b) for photons produced by final state radiation in $H \rightarrow ZZ \rightarrow 4\mu$ events

942 $|\eta_\gamma| < 2.4$, determined by matching reconstructed photons to generated photons from FSR with a match-
 943 ing cut $\Delta R < 0.10$, is shown in Fig. 22a as a function of p_T^γ . The expected energy resolution for the two
 944 types of photons is displayed in Fig. 22b. In the four-muon final state, about 20% of the FSR photons are
 945 of type 2.

946 5.2 Photon Isolation

947 The photon isolation is determined from the charged hadrons, photons and neutral hadrons identified
 948 by the particle-flow reconstruction in a cone of size $\Delta R = 0.30$ around the photon direction. In this cone,
 949 all charged hadrons compatible with originating from the signal primary vertex (in the `pfPileUp.cc`
 950 meaning) and with a p_T larger than 200 MeV/ c , all photons and neutral hadrons with a p_T larger than
 951 500 MeV/ c are included in the iso-deposits.
 952 The absolute photon isolation is defined as the sum of the transverse momenta of all these iso-deposits.
 953 To discriminate against photons that are produced in pileup interactions, an additional isolation deposit
 954 is defined that corresponds to the charged particle sum from the vertices other than the primary vertex.
 955 Finally, the pileup-corrected relative isolation is obtained by dividing the absolute isolation by the pho-
 956 ton transverse momentum, p_T^γ , and is given by:

$$I_\gamma = \frac{I_{ch} + I_\gamma + I_{neut} + I_{PU}}{p_T} \quad (5)$$

957 5.3 Building Z's with FSR Photon Recovery

958 The way to build Z candidates is defined in section 6. It uses leptons passing all selection criteria,
 959 including isolation. In case a FSR photon candidate is selected in the event, the isolation sum may have
 960 to be modified. This section describes how the building of Z candidates is made in presence of an FSR
 961 photon. In the present analysis, only photons with p_T^γ in excess of 2 GeV/ c and well in the tracker
 962 acceptance ($|\eta| < 2.4$) are considered, and tentatively assigned to a lepton and to a Z from the candidate
 963 Higgs boson decay. The association to a lepton goes as follows.

- 964 (i) Photons are considered only if the minimum ΔR distance wrt any of the Z leptons is smaller
 965 than $\Delta R < 0.5$.
- 966 (ii) If the distance of the photon to the closest lepton is between 0.07 and .50, the probability that

967 this photon arise from pile-up or, to a lesser extent, from the underlying event, becomes ap-
 968 preciable, because of the large annulus area. To enrich the photon sample in genuine FSR
 969 photons, the p_T^γ cut is tightened to 4 GeV/c and the photon is required to be somewhat iso-
 970 lated from other particles: the relative PF isolation including pileup contribution is required
 971 to be smaller than 1.0.

972 (iii) For both Z candidates, only the photons that make a mass with a lepton pair closer to the
 973 nominal Z mass (taken here to be 91.2 GeV/ c^2) but with a maximum $m_{\ell\ell\gamma} < 100$ GeV are
 974 kept.

975 (iv) After the photons have been selected with the above criteria the best photon is selected as
 976 following:

- 977 • If there is at least one photon with $p_T > 4$ GeV the one with the highest transverse
 978 momentum is associated to the Z boson
- 979 • If there is no photon with $p_T > 4$ GeV the closest photon to any of the leptons is
 980 associated to the Z

981 The invariant mass criteria defined in section 6 are applied using the four-vector defined by the sum of
 982 the four-vectors of the two leptons and the photon.

983 An event can therefore have zero, one or two selected FSR photon candidates. If no candidate is se-
 984 lected, the default four lepton analysis applies. Otherwise, the selected photons are removed from the
 985 corresponding lepton isolation cones (if in the isolation cones), and the default four lepton analysis flow
 986 proceeds with the modified lepton isolations, and with the Z candidate masses determined with the
 987 corresponding lepton pair and the associated photon.

988 Finally, the Higgs boson candidate mass is determined from the momenta of the four leptons and those
 989 of all FSR photon candidates. The performance of the FSR identification algorithm is quantified using
 990 samples from simulation and data. The gain of the FSR algorithm is two fold

- 991 • Events with associated photons move to the nominal reconstructed mass improving the res-
 992 olution.
- 993 • New events migrate into the sample by the higher isolation efficiency and the improved def-
 994 inition of the mass of the Z.

995 The following performance metrics are used to quantify the performance of FSR reconstruction:

- 996 • **Efficiency:** Number of Identified FSR photons matched to generated FSR photons with $p_T >$
 997 2 GeV and $|\eta| < 2.4$ divided by the number of generated FSR photons with $p_T > 2$ GeV and
 998 $|\eta| < 2.4$
- 999 • **Rate:** Number of Events with Identified FSR photons divided by the total number of events
 1000 after all selection requirements
- 1001 • **Purity:** Number of Events with Identified FSR photons where the mass of the system consist-
 1002 ing of the leptons and the photons is nearer to the nominal mass of the studied resonance wrt
 1003 the mass of the leptons alone.
- 1004 • **Yield Gain:** Number of events after all selection requirements after applying the FSR recovery
 1005 algorithm divided by the number of events after all selection requirements without applying
 1006 the FSR recover algorithm.

1007 The performance of the algorithm in the signal and irreducible background has been quantified using
 1008 simulated $H \rightarrow ZZ$ and SM ZZ samples with an average PU of 20 interactions. Additonal studies have
 1009 been performed in data exploiting decays of $Z \rightarrow \ell\ell, Z \rightarrow 4\ell$. In addition, studies of the shapes and
 1010 rates of the reducible backgrounds have been performed in signal free control regions.

1011 5.4 Studies on $H \rightarrow ZZ$, SM ZZ MC

1012 The FSR identification algorithm is tested on simulated Higgs signal events with a mass of 125 GeV with
 1013 an average PU of 20 interactions. The total efficiency is compared by running the full selection with and
 1014 without the FSR algorithm applied. Figure 23 shows the comparison of the invariant mass distribution

before and after FSR recovery for events with an identified FSR photon and overall events. The FSR algorithm recovers performance by moving the events from the FSR tail back to the Higgs peak bulk distribution. In addition, due to the isolation requirements and the new definition of the masses of the Z

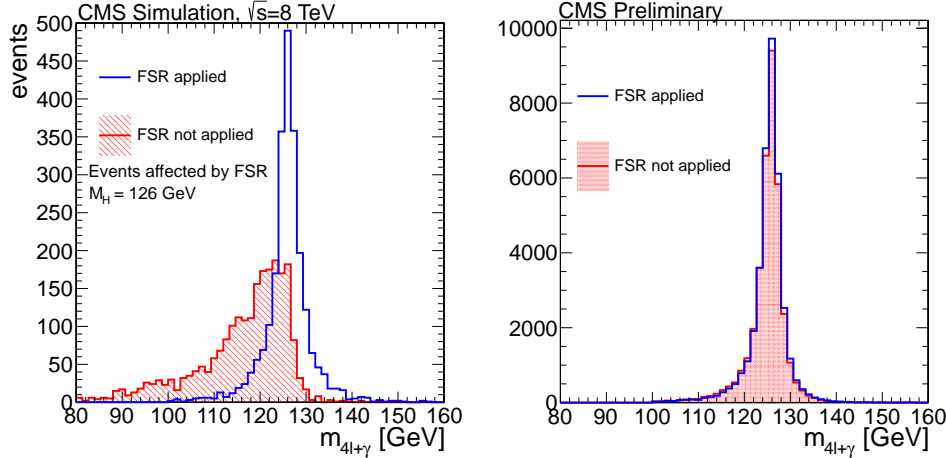


Figure 23: Invariant mass reconstruction of the Higgs candidate of the events with an identified FSR photon (left) and all events (right) for Higgs signal with $m_H = 126 \text{ GeV}$

bosons more events are introduced in the final selection after FSR recovery. In the case of Higgs signal, the tails are reduced and the arithmetic RMS is improved from 7.1% to 6.9% while the Gaussian RMS is not modified showing that the effect on the width distribution due to the impurity is negligible. In the case of the ZZ continuum the performance is expected to be similar. The rate , efficiency and purity for Higgs signal and SM ZZ is presented in table 15

final state	rate (%)	purity (%)	gain (%)
$H \rightarrow ZZ(\text{all})$	6.0	80	2.0
$H \rightarrow ZZ \rightarrow 4\mu$	9.1	82	3.0
$H \rightarrow ZZ \rightarrow 2e2\mu$	5.0	78	0.6
$H \rightarrow ZZ \rightarrow 4e$	1.4	72	1.8
SM ZZ(all)	6.7	81	2.1
SM ZZ $\rightarrow 4\mu$	10.1	83	3.0
SM ZZ $\rightarrow 2e2\mu$	6.5	77	0.6
SM ZZ $\rightarrow 4e$	1.8	72	1.8

Table 15: Rate, purity and efficiency gain for signal and ZZ background

The effect of FSR on electrons is much smaller due to the absorption of nearby FSR photons in the electromagnetic super-cluster, therefore the four muon final state is affected the most. An increase in the total efficiency of 2% is expected and this is mainly attributed to the subtraction of the photon from the isolation annulus of the leptons and to the increased efficiency of the di-lepton mass requirements after including the photon.

5.5 Studies on data

The FSR algorithm is studied in detail in Z decays in two or four leptons and in topologies compatible with the $Z + X$ reducible background hypothesis. The performance of the FSR recovery algorithm in Z decays is presented in figure 24. Excellent performance is observed in Z data as the Z peak becomes steeper. The observed rate on $Z \rightarrow ll$ events is 1.9% while the efficiency gain is 0.9%. The $Z \rightarrow 4l$ final state is reconstructed with loose criteria to increase the event yield and demonstrate the performance of the algorithm. Significant improvement is observed in the reconstruction of the Z peak.

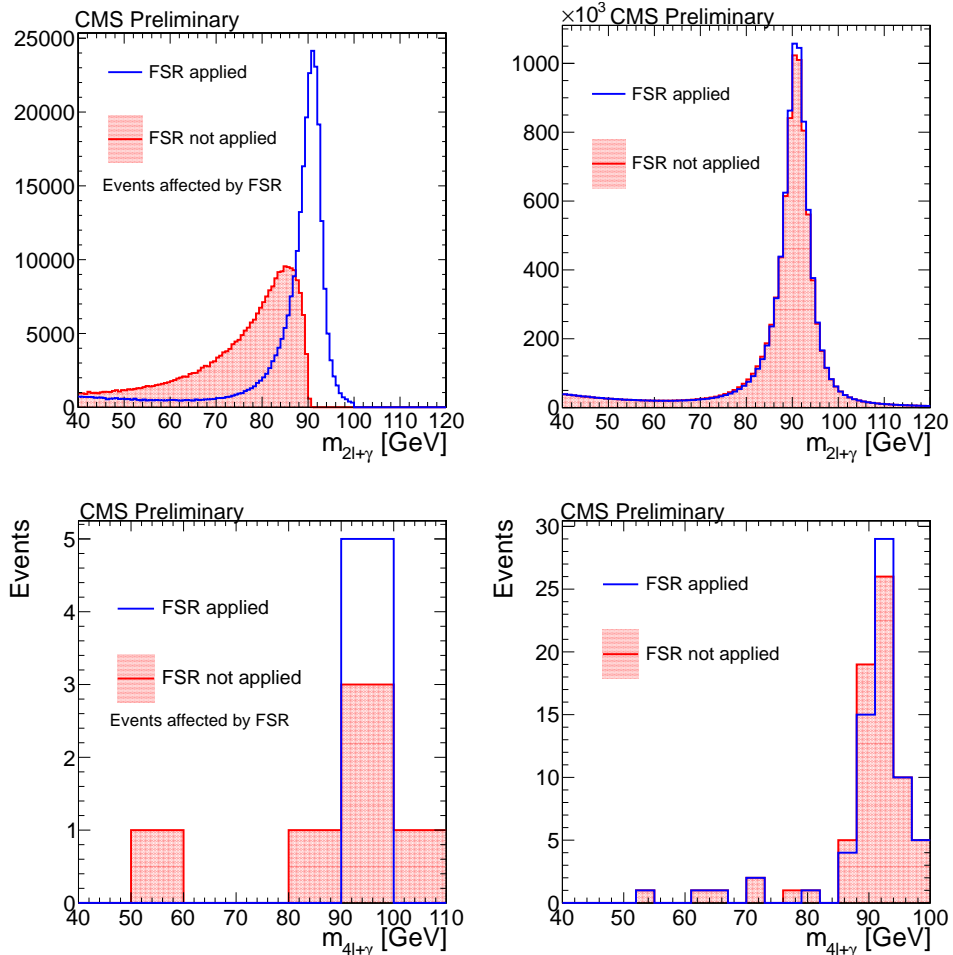


Figure 24: Invariant mass of the Z before and after FSR recovery for events with an identified FSR photon(left) and overall number of events for $Z \rightarrow \ell\ell$ decays (top) and $Z \rightarrow 4\ell$ decays (bottom)

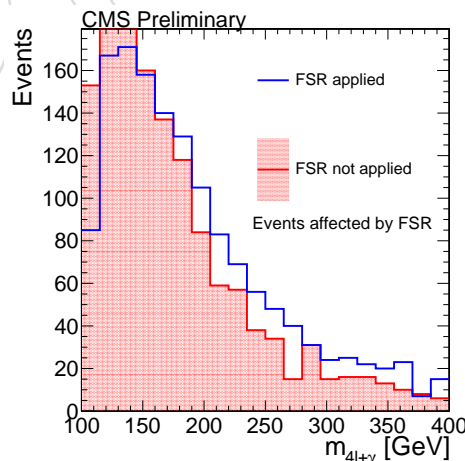


Figure 25: Invariant mass of the four lepton system for the background enriched region for events affected by FSR(left) and all events(right)

1035 To study the effect of FSR in the reducible background shape a background enriched region is selected by
 1036 requiring that the Z_2 leptons have same sign, and by dropping ID and isolation requirements. Figure 25
 1037 shows the FSR effect on this control region. The effect on the background shape is explained by the result
 1038 of the FSR algorithm in jets. If a lepton is inside a jet, a possible π^0 can be attributed to FSR therefore
 1039 the rate is much higher than in the case of isolated leptons and corresponds to a total of 60%. The
 1040 fake photons associated as FSR result into a flattening of the background shape that results to reduced
 1041 background in the region of interest.

6 Event Selection

1043 The selection is essentially un-changed (apart from the new muon ghost cleaning, see Section 3.2.4) with
 1044 respect to the analysis described in [20, 21]. It is reproduced here for completeness.

1045 The selection starts by the requirement of at least one good primary vertex (PV) fulfilling the following
 1046 criteria: high number of degree of freedom ($N_{PV} > 4$), collisions restricted along the z -axis ($z_{PV} < 24$
 1047 cm) and small radius of the PV ($r_{PV} < 2$ cm).

1048 Two flavors of leptons on which the selection steps act on are defined:

- 1049 1. *loose leptons*: electrons within the geometrical acceptance of $|\eta^e| < 2.5$, with $p_T^e > 7$ GeV/c and
 1050 having 0 or 1 expected missing inner hits, muons (global or tracker) satisfying $|\eta^\mu| < 2.4$, $p_T^\mu >$
 1051 5 GeV/c. Both electrons and muons should satisfy loose requirements on the transverse ($d_{xy} < 0.5$
 1052 cm) and longitudinal ($d_z < 1$ cm) impact parameter with respect to the primary vertex. Non-
 1053 global tracker muons must be arbitrated and a requirement on the shared segments is asked (see
 1054 Section 3.2.4). In addition, it is required that $\Delta R > 0.02$ between the leptons. The *loose leptons* are
 1055 used in the estimation of reducible background (see section 9).

- 1056 2. *good leptons*: these are *loose leptons* on which additional criteria are imposed. Namely:

- 1057 • electrons should pass the electron identification criteria as described in section 3.1.4,
 1058 muons should meet the Particle Flow Muons requirements (see section 3.2.4);
- 1059 • Relative PFIso < 0.4 (see section 3.4);
- 1060 • the significance of the impact parameter to the event vertex, SIP_{3D} , is required to satisfy
 1061 $|SIP_{3D}| = \frac{|IP|}{\sigma_{IP}} < 4$ for each lepton, where IP is the lepton impact parameter in three
 1062 dimensions at the point of closest approach with respect to the primary interaction
 1063 vertex, and σ_{IP} the associated uncertainty.

1064 Before building *good leptons* candidates, an e/μ cross cleaning procedure is applied. *Loose electrons* are
 1065 discarded if they satisfy: $\Delta R(e, \mu) < 0.05$, where the muons considered are *loose muons* passing Particle
 1066 Flow or Global muons criteria.

1067 The events are then requested to have fired the relevant electron and muon triggers, consistently in data
 1068 and MC (see section 2.1).

1069 We therefore impose the following sequence of selection requirements:

- 1070 1. *First Z*: a pair of *good lepton* candidates of opposite charge and matching flavour (e^+e^- , $\mu^+\mu^-$)
 1071 with reconstructed mass $m_{1,2}$ closest to the nominal Z boson mass is retained and denoted Z_1 . The
 1072 selected pair should satisfy $40 < m_{Z_1} < 120$ GeV/c².
- 1073 2. *Three or more leptons*: at least another *good lepton* candidate of any flavour or charge.
- 1074 3. *Four or more leptons and a matching pair*: a fourth *good lepton* candidate with the flavour of the third
 1075 lepton candidate from the previous step, and with opposite charge.
- 1076 4. *Choice of the “best 4ℓ” and Z_1, Z_2 assignments*: retain a second lepton pair, denoted Z_2 , among all the
 1077 remaining $\ell^+\ell^-$ combinations. If more than one Z_2 combination satisfies all the criteria, the one
 1078 built from leptons of highest p_T is chosen. The selected pair should satisfy $4 < m_{Z_2} < 120$ GeV/c²
 1079 . At this stage, it is required that any two leptons from the four selected have $p_{T,i} > 20$ GeV/c and
 1080 $p_{T,j} > 10$ GeV/c.

1081 5. *QCD suppression*: the reconstruction mass of opposite-sign and same-flavor lepton pair must sati-
 1082 fisfy $m_{\ell\ell} > 4 \text{ GeV}/c^2$.

1083 6. $m_{4\ell}, Z$ and $Z^{(*)}$ kinematics: with $m_{4\ell} > m_{4\ell}^{\min}$, $m_{Z1}^{\min} < m_{Z_1} < 120 \text{ GeV}/c^2$ and $m_{Z2}^{\min} < m_{Z_2} <$
 1084 $120 \text{ GeV}/c^2$, where m_{Z2}^{\min} and m_{Z2}^{\max} are defined below.

1085 Three sets of kinematic cuts are therefore introduced to allow studies of the s -channel contribution or to
 1086 maximize the sensitivity in different ranges of Higgs boson mass hypothesis:

1087 • **$Z \rightarrow 4\ell$ phase space** analysis defined by requiring $m_{Z2}^{\min} \equiv 4 \text{ GeV}/c^2$ and $m_{Z1}^{\min} \equiv 40 \text{ GeV}/c^2$
 1088 $m_{4\ell}^{\min} \equiv 70 \text{ GeV}/c^2$ and $m_{4\ell}^{\max} \equiv 110 \text{ GeV}/c^2$.

1089 • **baseline Higgs phase space** analysis defined by requiring $m_{Z2}^{\min} \equiv 12 \text{ GeV}/c^2$ and $m_{Z1}^{\min} \equiv$
 1090 $40 \text{ GeV}/c^2$ and $m_{4\ell}^{\min} \equiv 100 \text{ GeV}/c^2$. This provides a best sensitivity for masses $m_H <$
 1091 $130 \text{ GeV}/cc$

1092 • **High-mass phase space** analysis is defined by requiring $m_{Z2}^{\min} \equiv 60 \text{ GeV}/c^2$ and $m_{Z1}^{\min} \equiv$
 1093 $60 \text{ GeV}/c^2$. It is used to measure the ZZ cross-section.

1094 The events satisfying the high-mass selection are a subset of those satisfying the baseline selection. The
 1095 enlarge phase space of the baseline selection for the Higgs boson signal is needed at very low masses
 1096 given the very small cross section \times branching ratio, at the price of a larger background. The increased
 1097 acceptance for the signal becomes small for mass (< 10% in relative compared to the baseline selection)
 1098 above $\approx 130 \text{ GeV}/cc$ where reducing the phase space to better suppress the background become ad-
 1099 vantageous. For Higgs boson masses above $\approx 2 \times m_Z$, further restricting the phase space of the pair of
 1100 Z boson can be made without significant loss of acceptance for the signal, with the benefit of a slight
 1101 reduction of the ZZ* background.

1102 6.1 Selection Performance and Control

1103 The signal detection efficiencies from MC for a 4ℓ system within the geometrical acceptance² as a func-
 1104 tion of Higgs boson mass hypothesis are shown in Fig. 26 for the baseline selection. It rises from
 1105 about 30% / 58% / 42% at $m_H = 125 \text{ GeV}/c^2$ to about 62% / 85% / 74% at $m_H = 400 \text{ GeV}/c^2$ for the
 1106 $4e / 4\mu / 2e2\mu$ channels. With respect to the ICHEP analysis, we managed to gain between 2 and 4% in
 1107 absolute efficiencies in channels involving electrons.

1108 The invariant mass of two good leptons (Z_1) as built in the first step of the selection is shown in Fig. 27 for
 1109 both electron and muon channels and for both 7 and 8 TeV data. A good agreement can be appreciated
 1110 between data and Monte Carlo expectations.

1111 The events yields as a function of the selection steps are shown in Fig. 28 and Fig. 29 for the baseline
 1112 selection in the $4e, 4\mu$ and $2e2\mu$ channels and for 7 and 8 TeV analysis. We observe an overall good
 1113 agreement between Data and MC expectations only (and no additional scale factors are applied). In the
 1114 analysis, the reducible background is ultimately taken from DATA; Monte Carlo is only used to check
 1115 the background composition.

²In this case the geometrical acceptance is defined having the generated electrons satisfying $|\eta^e| < 2.5$ and generated muons satisfying $|\eta^\mu| < 2.4$, no p_T cut is requested.

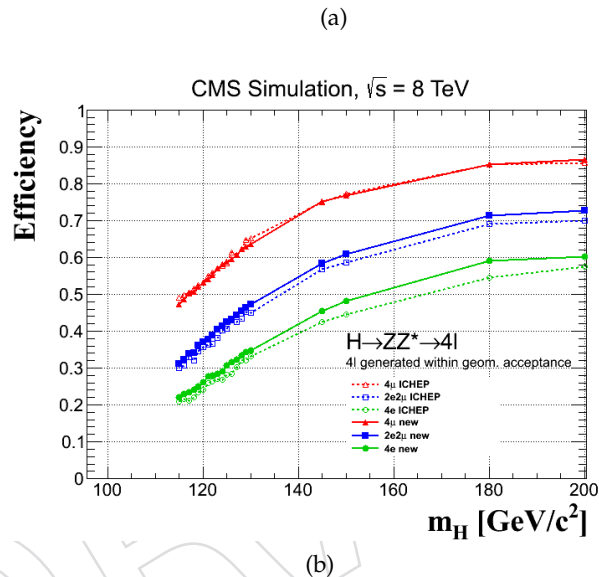


Figure 26: Signal detection efficiencies from MC for a 4ℓ system within the geometrical acceptance in the $4e$ (green), 4μ (red) and $2e2\mu$ (blue) channels as a function of Higgs boson mass hypothesis, for the full range (a) and a zoom on the low mass range (b).

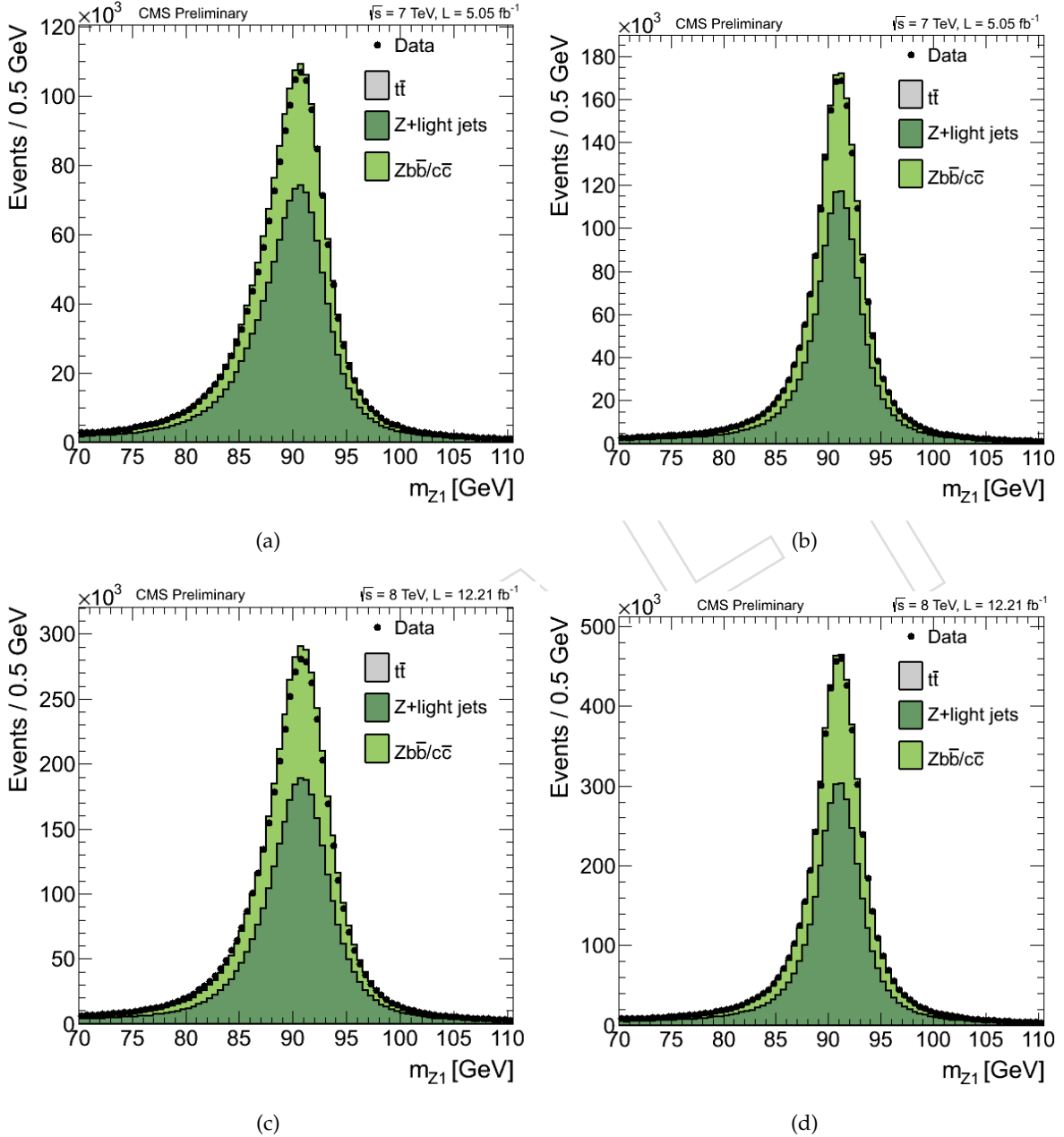


Figure 27: Comparison of Z_1 invariant mass in (a) ee 7TeV, (b) $\mu\mu$, 7TeV (c) ee 8TeV, (d) $\mu\mu$, 8 TeV, between data and MonteCarlo expectations. The samples correspond to an integrated luminosity of $\mathcal{L} = 5.1 \text{ fb}^{-1}$ for the 7 TeV data, and 12.2 fb^{-1} for the 8 TeV data.

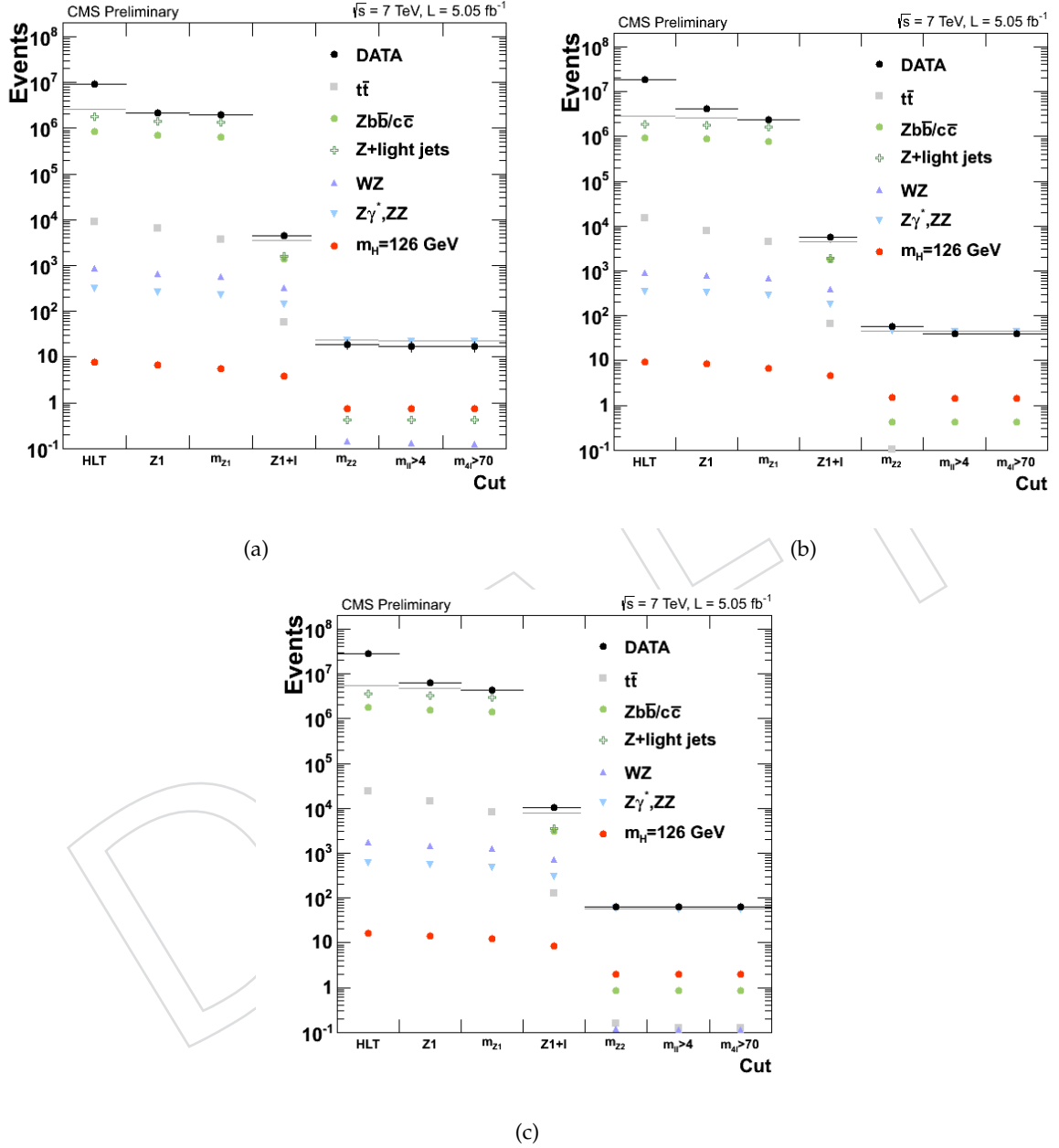


Figure 28: Event yields in the (a) $4e$, (b) 4μ and (c) $2e2\mu$ channels as a function of the event selection steps. The MC yields are not corrected for background expectation. The samples correspond to an integrated luminosity of $\mathcal{L} = 5.1 \text{ fb}^{-1}$ of 7 TeV data.

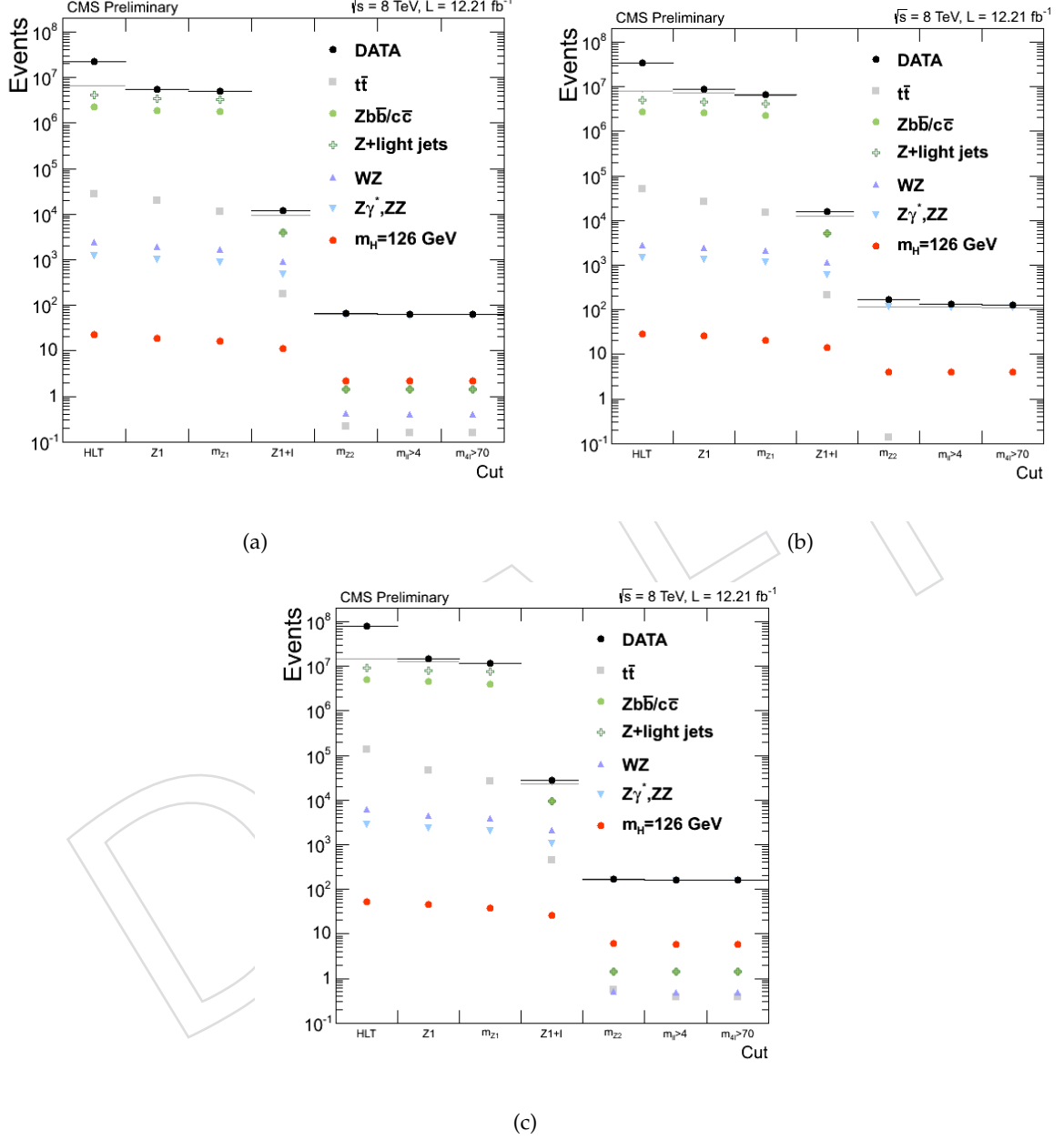


Figure 29: Event yields in the (a) $4e$, (b) 4μ and (c) $2e2\mu$ channels as a function of the event selection steps. The MC yields are not corrected for background expectation. The samples correspond to an integrated luminosity of $\mathcal{L} = 12.2 \text{ fb}^{-1}$ of 8 TeV data.

1116 7 Signal Model and uncertainties

1117 The modeling of the signal changed with respect to [20, 21]. We define two ranges:

- 1118 • $m_H=115 \text{ GeV} - m_H=400 \text{ GeV}$ (low and intermediate mass range): instead of convoluting the
1119 relativistic Breit-Wigner pdf with a single CrystalBall function, we use now a double Crystal-
1120 Ball function.
- 1121 • $m_H=400 \text{ GeV} - m_H=1000 \text{ GeV}$ (high mass range): one novelty of this analysis is to use the best
1122 theoretically known lineshape. The re-weighting procedure and its uncertainties are therefore
1123 described in this section.

1124 This section also document the effort to understand the scale and the resolution of the 4 leptons invariant
1125 mass, using standard candles, as well as the event-by-event error. All these are key ingredients for a
1126 precise mass measurement of the new discovered boson.

1127 7.1 Signal model

For the low mass range we model the signal $f(m_{4l}|m_H)$ pdf as the convolution function of the relativistic Breit-Wigner $pdf_1(m_{H^*}|m_H)$:

$$f(m_{4l}|m_H) = \frac{\Gamma_{gg}(m_{4l}) \cdot \Gamma_{ZZ}(m_{4l}) \cdot m_{4l}}{(m_{4l}^2 - m_H^2)^2 + m_{4l}^2 \cdot \Gamma^2(m_{4l})} \quad (6)$$

1128 and the a Double Crystal-ball function $dCB(m_{4\ell}|m_{H^*})$. This function has six independent parameters,
1129 and is intended to capture the Gaussian core (σ_m) of the four-lepton mass resolution function, system-
1130 atic mass shift Δm_{H^*} of the peak, and the left- and right-hand tail originating from leptons emitting
1131 brem in the tracker material, present for both electrons and muons, and from the non-Gaussian mis-
1132 measurements specific to interactions of electrons with the detector material (two parameters, n and α ,
1133 for each side of the mean):

$$dCB(\xi) = N \cdot \begin{cases} A \cdot (B + |\xi|)^{-n_L}, & \text{for } \xi < \alpha_L \\ A \cdot (B + |\xi|)^{-n_R}, & \text{for } \xi > \alpha_R \\ \exp(-\xi^2/2), & \text{for } \alpha_L \leq \xi \leq \alpha_R \end{cases} \quad (7)$$

1134 where $\xi = (m_{4\ell} - m_{H^*} - \Delta m_{H^*})/\sigma_m$. The prominence of the left-right-hand tail is defined the power
1135 n_L, n_R , respectively. The parameters α_L, α_R define where the splicing of the tails and the core are made,
1136 in units of σ_m . Parameters A and B are not independent; they are defined by requiring the continuity of
1137 the function itself and its first derivatives. N is the normalizing constant.

1138 The actual signal PDF is build by the convolution:

$$f(m_{4\ell}|m_H) = DCB(m_{4\ell}|m_{H^*}) \otimes pdf_1(m_{H^*}|m_H) \quad (8)$$

1139 The Breit-Wigner pdf is described in [52] and it is fully determined by the Higgs boson mass. The Double
1140 Crystal-ball function is described by two parameters *sigma* and *mean* for its Gaussian component and
1141 by the two parameters α and n for each exponential tail (left and right). This is different from the signal
1142 model used for ICHEP12 analysis (single Crystal Ball was used [20, 21]), because it has been found that
1143 a tail on higher $m(4l)$ values with respect the mean value has to be modeled as well, to get a reasonable
1144 fit.

1145 The six parameters of the double Crystal-ball are obtained from the fit of simulated signal events, after
1146 the full lepton and event selections are applied. Figures 30 (7 TeV) and 31 (8 TeV) show the fits for 4μ
1147 (μ left), $4e$ (center) and $2\mu 2e$ (right) events simulated with $\sqrt{s} = 7 \text{ TeV}$ and 8 TeV .

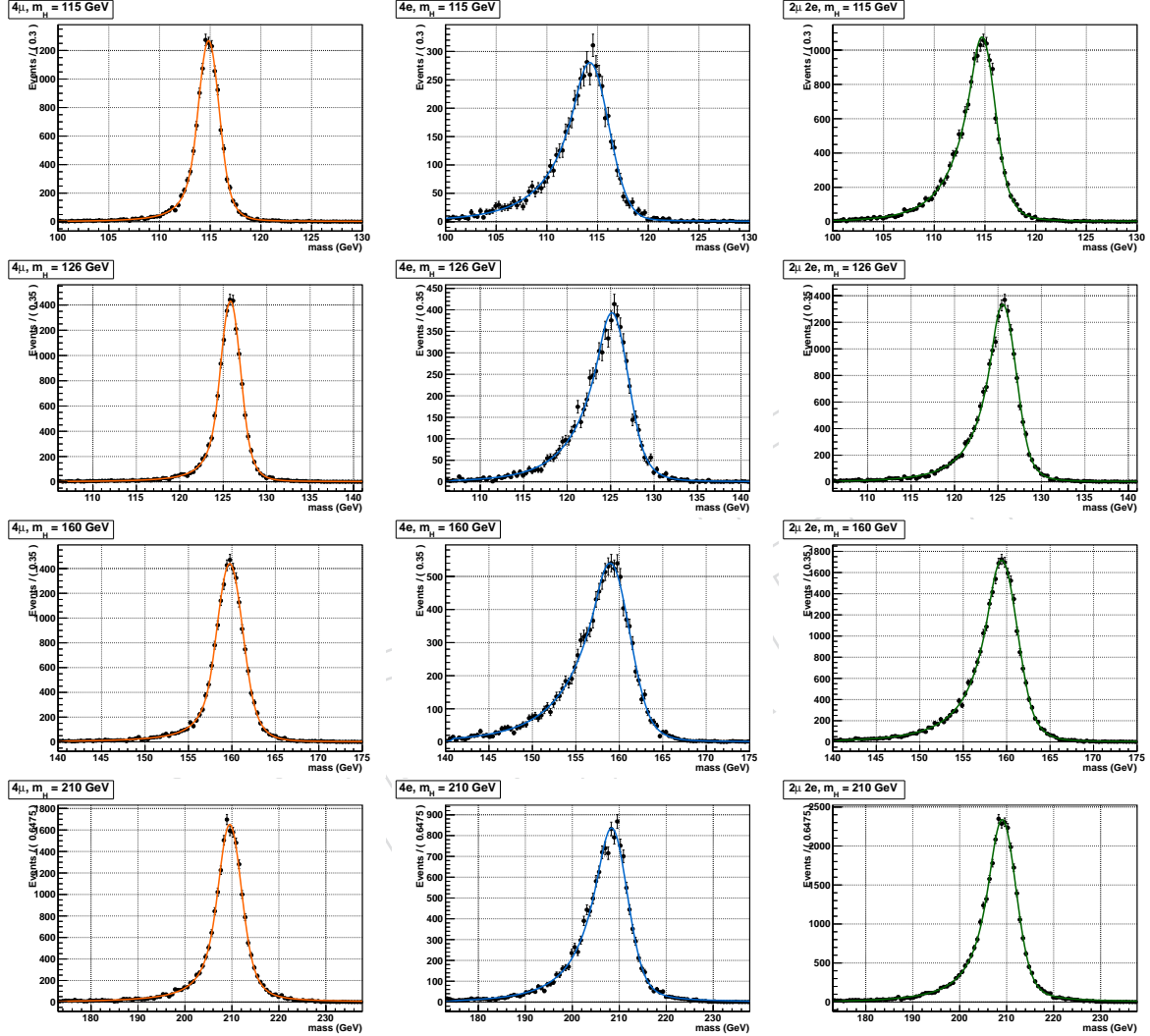


Figure 30: Probability density functions $f(m_{4l}|m_H)$ for the Higgs boson mass at the reconstruction level after the full lepton and event selections are applied. The distributions obtained from 7 TeV MC samples are fitted with the model described in the text for 4μ (left), $4e$ (center) and $2\mu 2e$ (right) events.

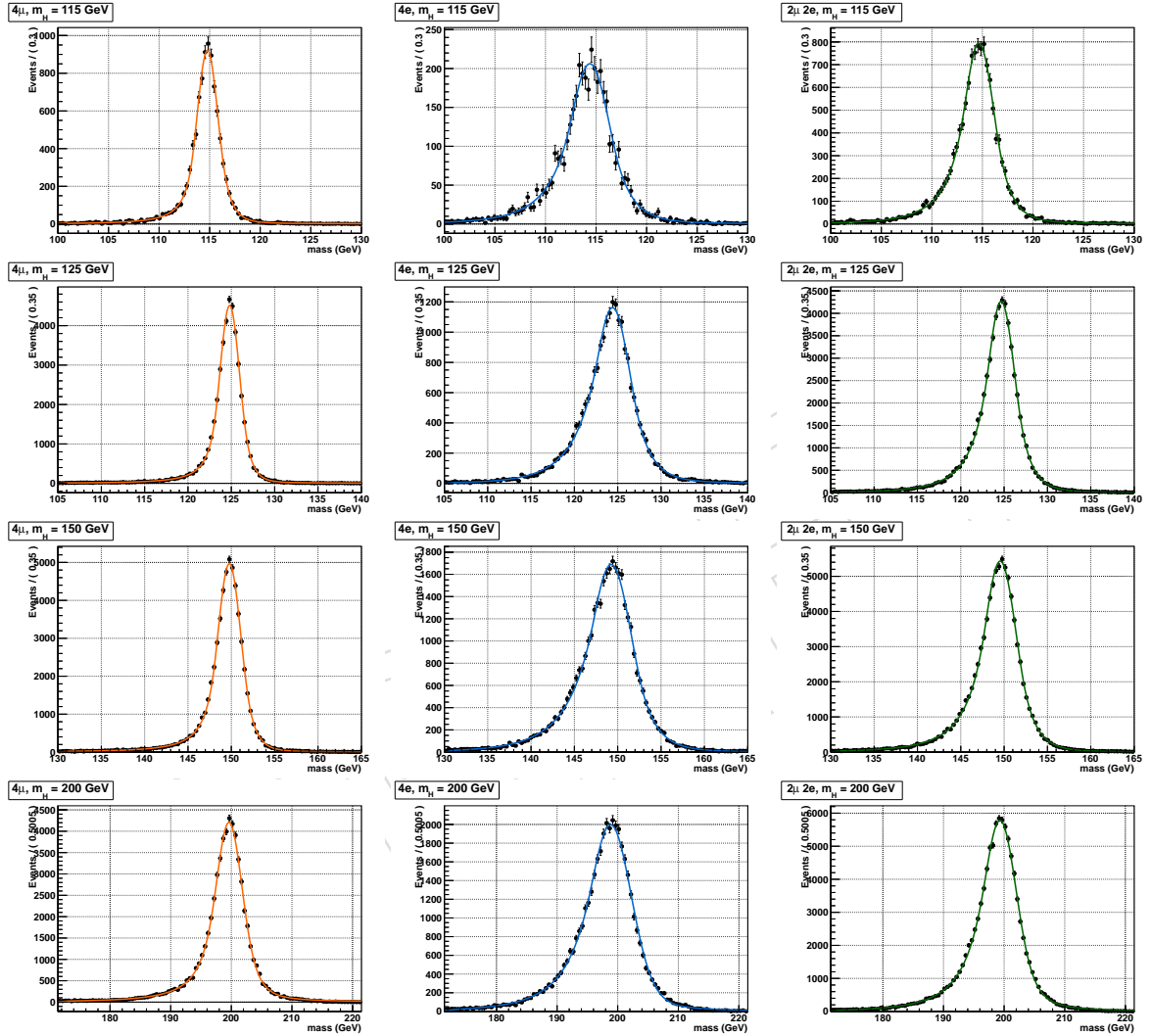


Figure 31: Probability density functions $f(m_{4l}|m_H)$ for the Higgs boson mass at the reconstruction level after the full lepton and event selections are applied. The distributions obtained from 8 TeV MC samples are fitted with the model described in the text for 4μ (left), $4e$ (center) and $2\mu 2e$ (right) events.

- 1148 After the parameters of the signal model are obtained for all the simulated samples, the parameters are
1149 fitted to obtain the signal model parameterization also for the intermediary mass values. Figures 32 (7
1150 TeV) and 33 (8 TeV) show the six double crystal-ball parameters for all the simulated mass bins at 7 TeV
1151 and 8 TeV, respectively. The same figures also show the result of the subsequent fit of the parameters as
1152 a function of the Higgs boson mass.
- 1153 The values from this last parametrization are used for all the mass bins, regardless whether they have
1154 the corresponding samples simulated or not.

DRAFT

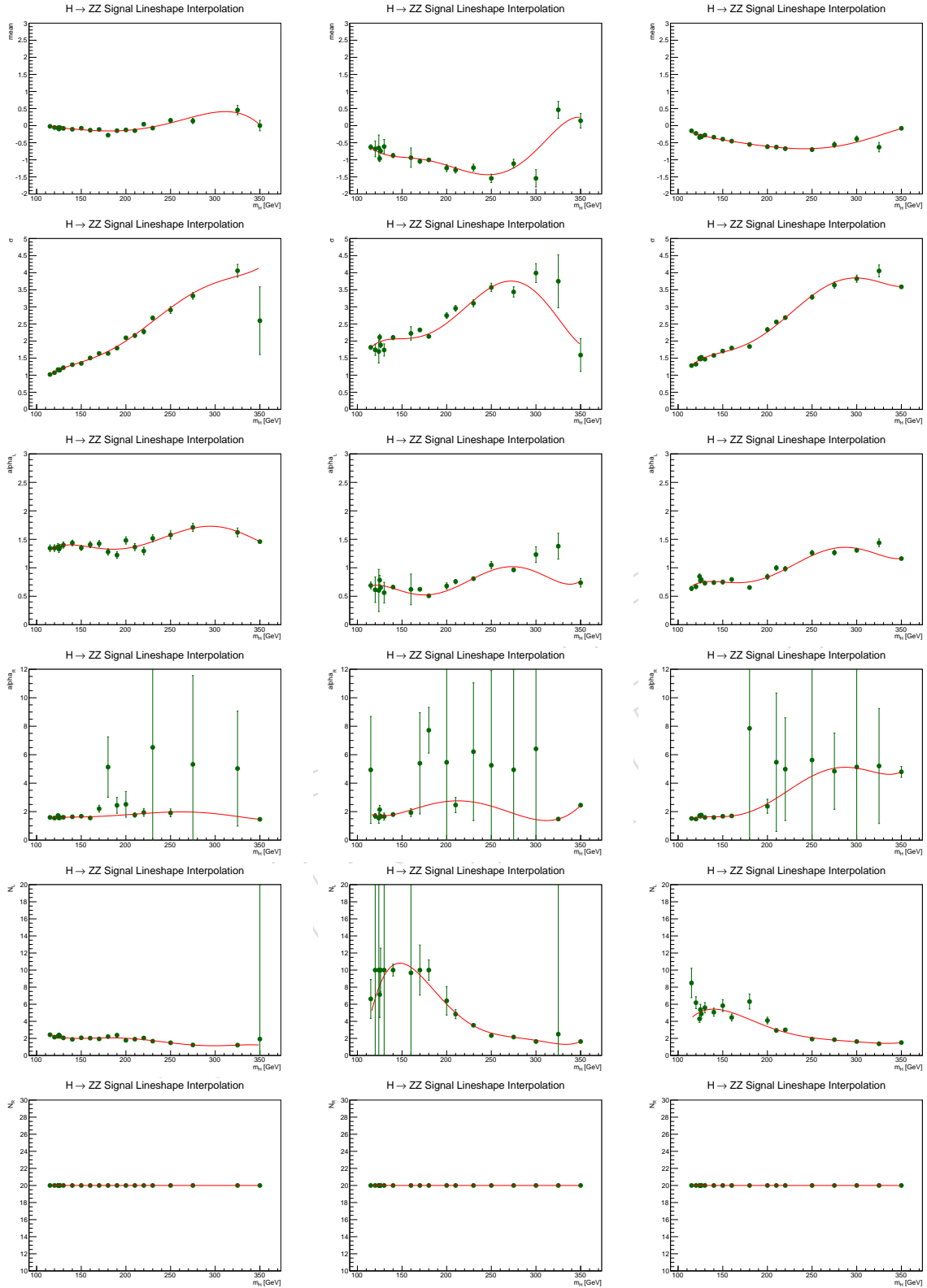


Figure 32: Linear and constant fits of the 4 parameters describing the signal $f(m_{4l}|m_H)$ pdf as a function of m_H . The pdf is modeled as a double crystal-ball function convoluted with the relativistic Breit-Wigner function described in the text. From the first row to the last one, the crystal-ball's mean, σ , α_1 , α_2 , n_1 and n_2 parameters are shown respectively for 4μ (left), $4e$ (center) and $2\mu 2e$ (right) events simulated for $\sqrt{s} = 7$ TeV.

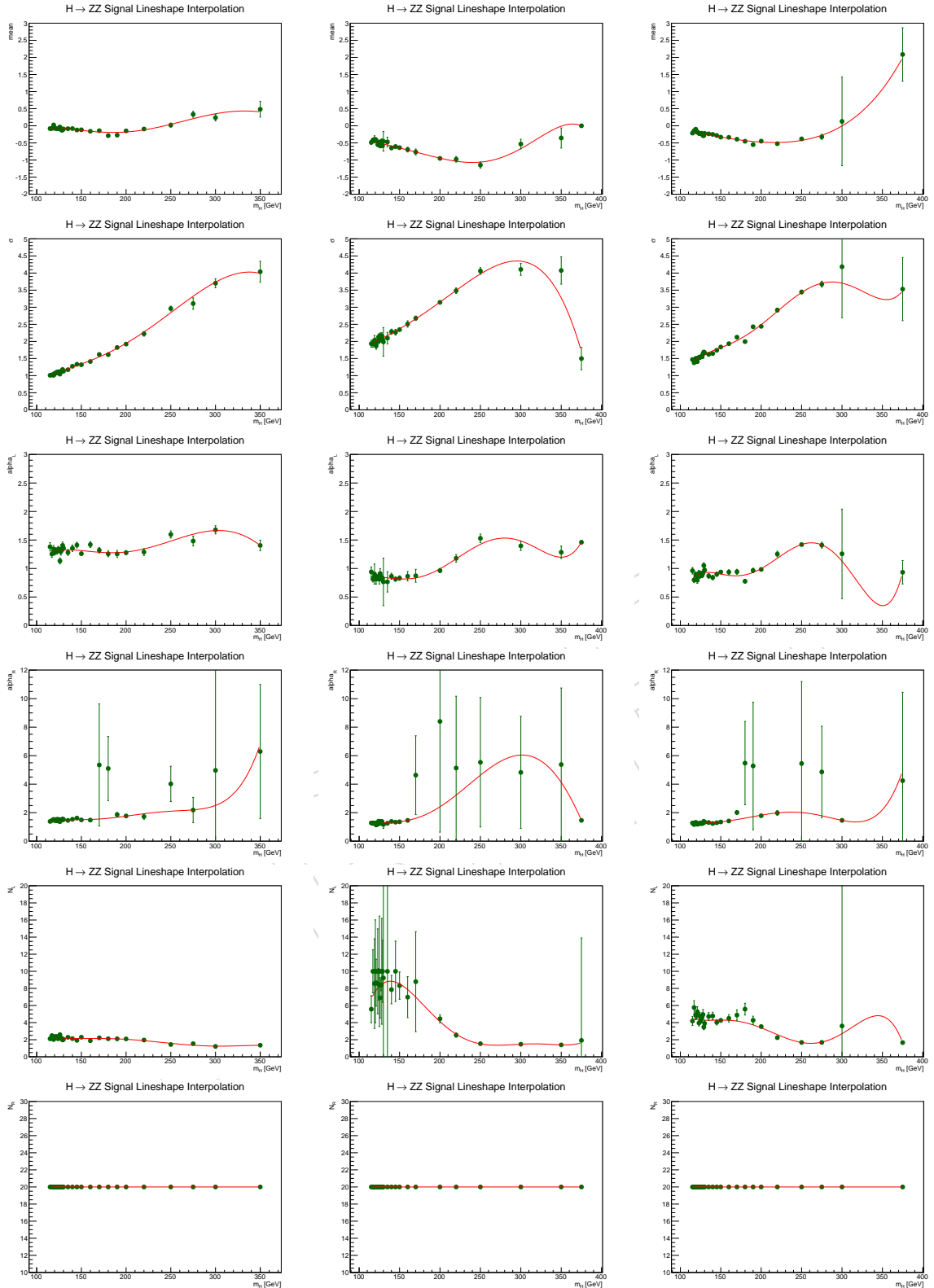


Figure 33: Linear and constant fits of the 4 parameters describing the signal $f(m_{4l}|m_H)$ pdf as a function of m_H . The pdf is modeled as a double crystal-ball function convoluted with the relativistic Breit-Wigner function described in the text. From the first row to the last one, the crystal-ball's mean, σ , α_1 , α_2 , n_1 and n_2 parameters are shown respectively for 4μ (left), $4e$ (center) and $2\mu 2e$ (right) events simulated for $\sqrt{s} = 8$ TeV.

1155 7.2 High Mass model

1156 7.2.1 Lineshape with Complex Pole Scheme

1157 The Higgs search at low mass is carried out in the framework of narrow-width approximation, describing
 1158 the Higgs lineshape with a Breit-Wigner distribution. This approximation breaks down at high
 1159 Higgs mass (typically > 400 GeV) due to the very large Higgs width (> 70 GeV). The problem has
 1160 been discussed in details in Ref. [53] and a more correct approach to describe the Higgs invariant-mass
 1161 distribution has been proposed, known as Complex Pole Scheme (CPS). The total Higgs production
 1162 cross-section has been recomputed by the Higgs Cross-Section Working Group to include corrections
 1163 due to CPS at high Higgs mass [54]. In the present work we rely on those updated values for the to-
 1164 tal cross-section and we exploit a new functionality developed in POWHEG [27] in order to reweight
 1165 Higgs-signal samples to match the Higgs lineshape predicted in the CPS approach.

1166 At high Higgs mass the interference between the Higgs signal and the $gg \rightarrow ZZ$ background becomes
 1167 very large, as recently discussed in Ref. [55]. The effect of interference has been shown to be constructive
 1168 below the Higgs mass peak and destructive above. It has therefore a negligible effect on the total cross-
 1169 section (1-2%) but it strongly biases the ZZ invariant-mass distribution. Moreover the interference
 1170 has been computed only at LO while the signal is known at NNLO. In this analysis we follow the
 1171 approach proposed in Ref. [55] to estimate the uncertainty due to missing higher perturbative order on
 1172 the interference. Given the signal at NNLO ($S_{NNLO} = S_{LO} \times K$) and the interference at LO (I), three
 1173 alternative estimation of signal + interference can be considered:

$$S_{LO} \times K + I \quad (9)$$

$$S_{LO} \times K + I \times K' \quad (10)$$

$$(S_{LO} + I) \times K \quad (11)$$

1174 respectively called additive, intermediate and multiplicative recipes. The intermediate recipe is built
 1175 considering the ratio (K') between NNLO Higgs-diagrams with only gg initial state and LO Higgs-
 1176 diagrams:

$$K = \frac{S_{NNLO}(gg \rightarrow Hg + qg \rightarrow Hq + qq \rightarrow Hg)}{S_{LO}(gg \rightarrow H)} = K' + K^{rest} \quad (12)$$

$$K' = \frac{S_{NNLO}(gg \rightarrow Hg)}{S_{LO}(gg \rightarrow H)} \quad (13)$$

1177 In the present analysis the Higgs lineshape has been reweighted to include the effect of the interference
 1178 as described by the intermediate recipe. Alternative lineshapes are also built with the additive and
 1179 multiplicative recipes to set the uncertainty on the missing higher perturbative orders on the interference
 1180 calculation.

1181 The effect of the CPS and interference corrections on the $H \rightarrow ZZ$ invariant-mass distribution and the
 1182 related uncertainties are shown in Fig. 34.

1183 Beyond the uncertainties due to missing terms in the perturbative QCD expansion and imprecise knowl-
 1184 edge of parton distribution functions, the following electroweak (EW) corrections also gain large impor-
 1185 tance at high Higgs mass:

- 1186 • EW corrections in the Higgs production, included in the total cross-section, (< 10% up to 1
 1187 TeV Higgs mass) while the effect on the Higgs lineshape is negligible in the present analysis.
- 1188 • EW corrections for complex pole, included in lineshape uncertainty
- 1189 • EW uncertainty for the decay, included in lineshape uncertainty

1190 For Higgs masses larger than the top mass (m_t). an additional uncertainty should be considered: the
 1191 computation of the NNLO Higgs cross-section as well as the generation of the NLO Monte Carlo sam-
 1192 ples used in this analysis are done in the approximation of an effective theory with $m_t \rightarrow \infty$ (HQ ap-
 1193 proximation). This approximation breaks down at large Higgs mass but it is expected to have negligible
 1194 effect on the total cross-section and on the Higgs lineshape. The effect of the HQ approximation and

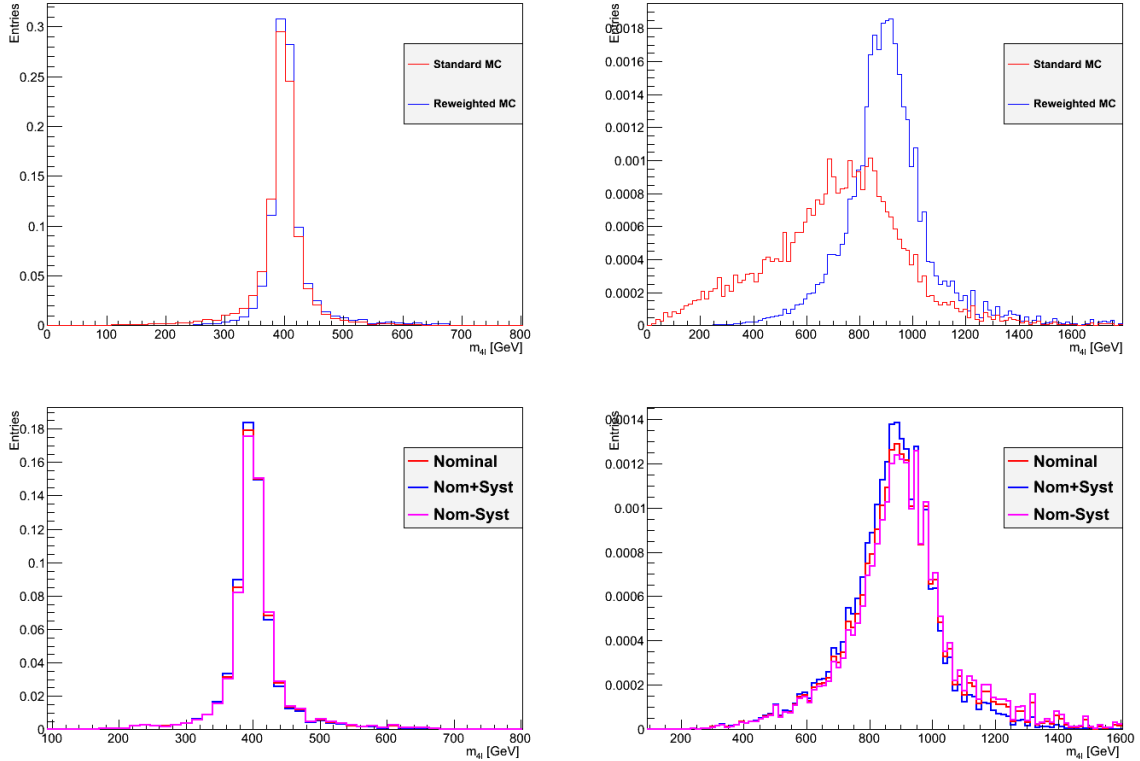


Figure 34: Top: four leptons invariant mass distribution at generator level before and after the CPS + interference corrections for an Higgs mass of 400 GeV (left) and 900 GeV (right). Bottom: reconstructed invariant mass for a 400 (900) GeV invariant mass Higgs boson after the CPS + interference corrections. The alternative shapes to describe the lineshape uncertainty are also shown.

of the EW corrections in the Higgs production, previously mentioned, are studied at NLO with a new version of POWHEG which implements CPS, EW production and HQ corrections.

While the effect of the EW corrections and of the interference on the Higgs lineshape may be different in gluon-gluon production and Vector Boson Fusion (VBF), in the present inclusive analysis we use the $gg \rightarrow H$ lineshape to describe both the cases since the gluon-gluon contribution dominates in most of the Higgs mass spectrum. The effect of the signal-background interference in the VBF case is under study.

Evaluation of the high-mass corrections systematic uncertainties

Figure 34 (bottom) shows the size of the uncertainties on the shape given by the high mass corrections. In order to propagate this systematic effect on the UL and p-value calculations, we refit the signal shape function with the two alternative hypotheses. In this fit, all the parameters describing the signal PDF are fixed to the values obtained from the nominal fit, but for the Γ of the Breit-Wigner function. In this way we propagate the uncertainty on the high-mass corrected shapes to the parameter representing the width of our theoretical PDF. Once the fits to the two alternative hypotheses are performed, we calculate the difference between the nominal value of Γ and the value determined by the alternative fits, and consider as a systematic uncertainty on Γ the largest variation between the two. We perform this procedure for all the mass points and measure a systematic effect on Γ between 3% and 5% among the whole spectrum. We choose to put a systematic of 5% for any Higgs mass hypothesis.

7.2.2 High Higgs Mass Signal Model

For the high mass range, after the re-weighting described above, instead of using the typical form used for low mass in 6 we use a modified version of the Breit-Wigner with the following form:

$$f(m_{4l}|m_H) = \frac{m_{4l}}{(m_{4l}^2 - m_H^2)^2 + m_{4l}^2 \cdot \Gamma^2(m_{4l})} \quad (14)$$

letting the Γ parameter to float in the fit. With this approach will loose the correlation of the Γ parameter with the physical Higgs width, but allows to get a good fit. Systematics on the lineshape will be established by varying of $\pm 1\sigma$ the weights used to reweight the signal events.

We then use a convolution of this high mass Breit-Wigner with the double Crystall-Ball.

In order to get a smoothly (and monotonically) varying function of the Γ of the Breit Wigner and σ_{DCB} , we perform a constrained likelihood fit to the signal Monte Carlo events assuming that the physical width of the Higgs for $m_H > 400$ GeV is larger than the experimental resolution, which is regulated by σ_{DCB} . We show the fits for some of the high Higgs mass points in Fig. 35 (7 TeV) and in Fig. 36 (8 TeV).

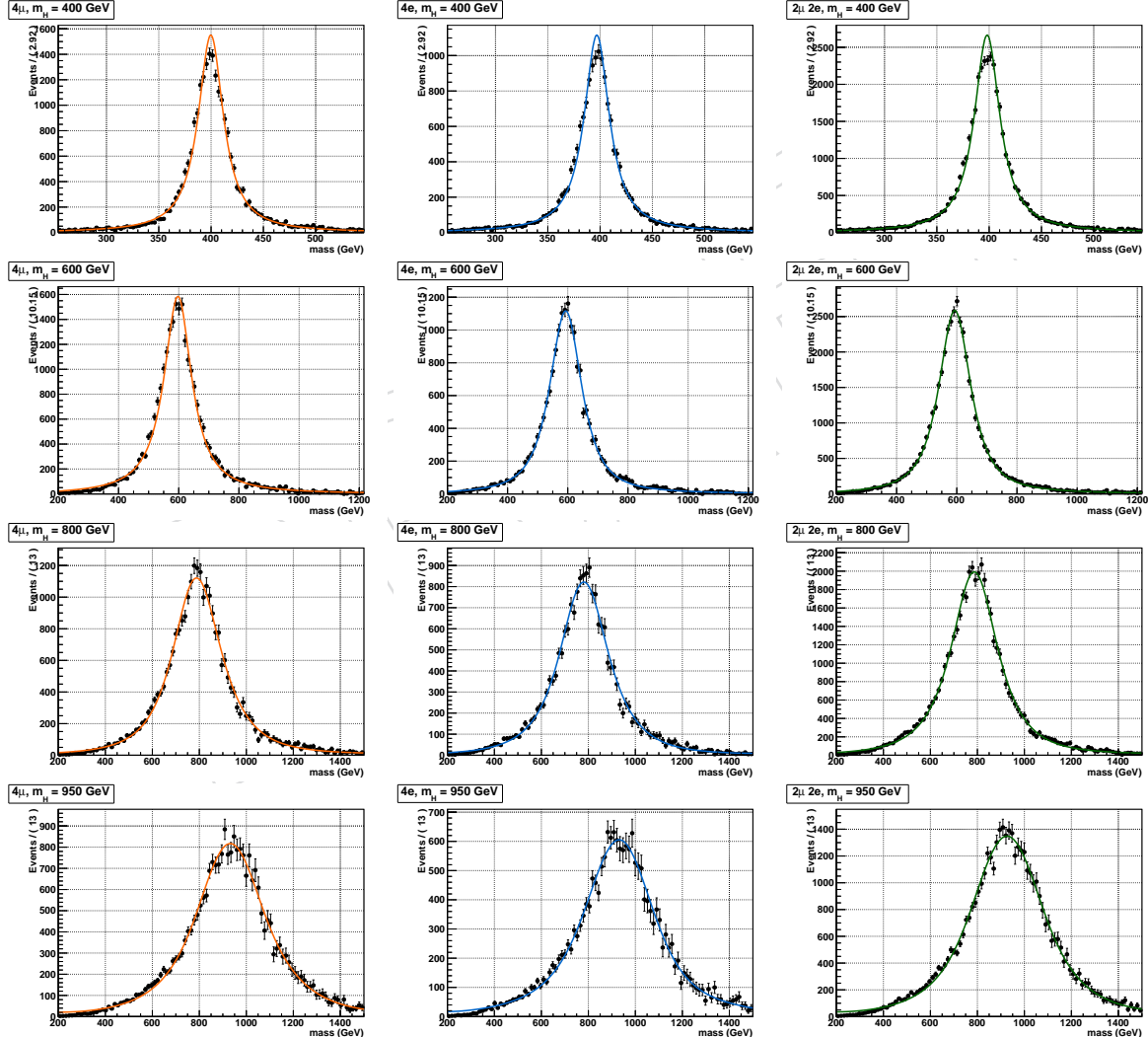


Figure 35: Probability density functions $f(m_{4l}|m_H)$ for the Higgs boson mass at the reconstruction level after the full lepton and event selections are applied. The distributions obtained from 7 TeV MC samples are fitted with the model described in the text for 4μ (left), $4e$ (center) and $2\mu 2e$ (right) events.

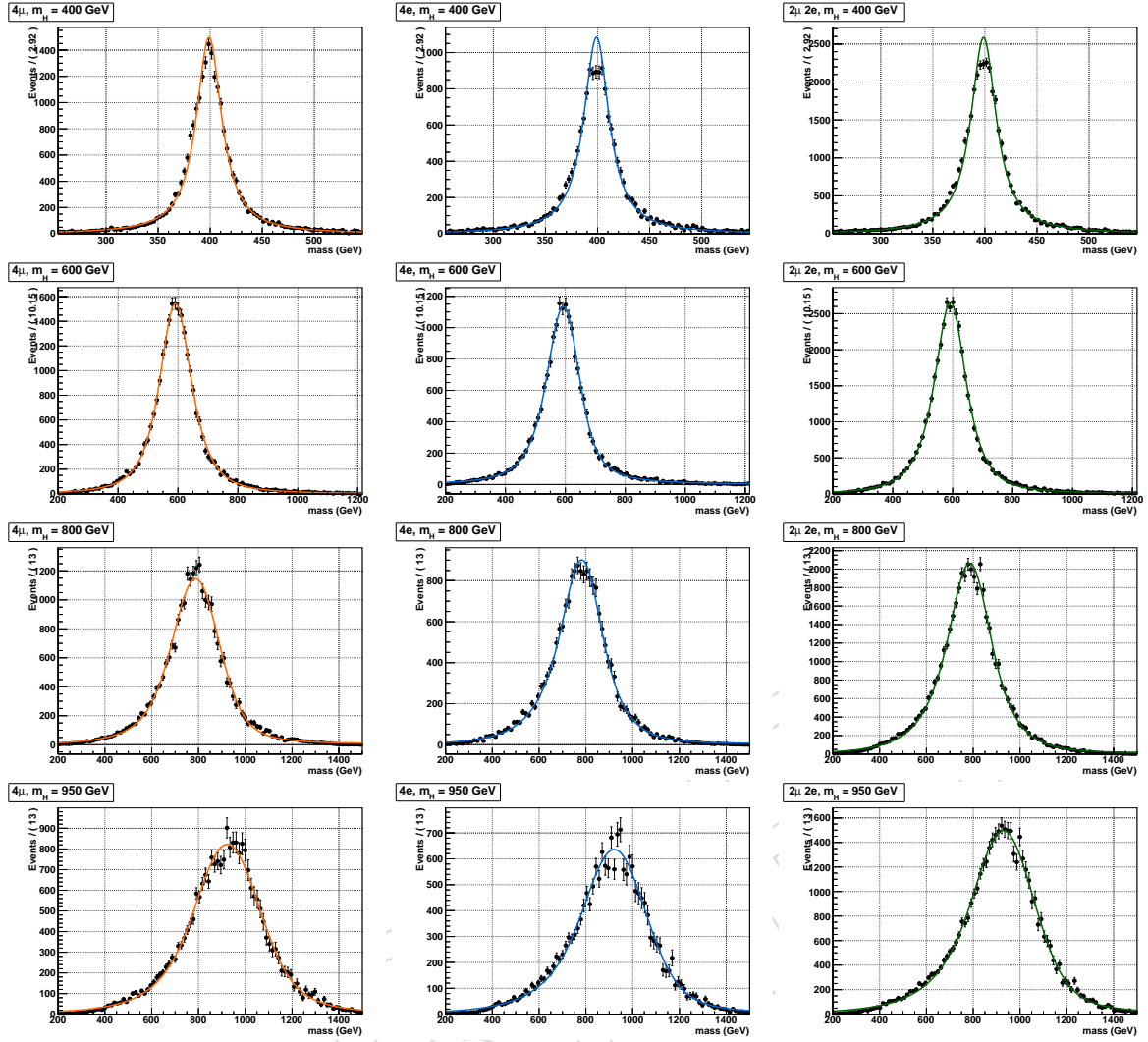


Figure 36: Probability density functions $f(m_{4l}|m_H)$ for the Higgs boson mass at the reconstruction level after the full lepton and event selections are applied. The distributions obtained from 8 TeV MC samples are fitted with the model described in the text for 4μ (left), $4e$ (center) and $2\mu 2e$ (right) events.

In this way we get a parameterisation of the signal that can be interpolated with a polynomial. The interpolation of the parameters is shown in Fig. 38. We show the validation of the interpolated PDFs in the appendix in Fig. ??, where we superimpose the interpolated PDF to the distribution of the actual simulation points.

For the systematic evaluation on this parameterization, we simplified the approach verifying that the variations of the lineshape are completely covered by variations in the Γ of the high mass BW. So we evaluate a unique systematics fixing the double Crystal Ball to the nominal value and fitting the alternative shape obtaining by reweighting the events with the lineshape weights varied between $\pm 1\sigma$. We obtain a systematics which is almost flat in m_H and it is about 5%.

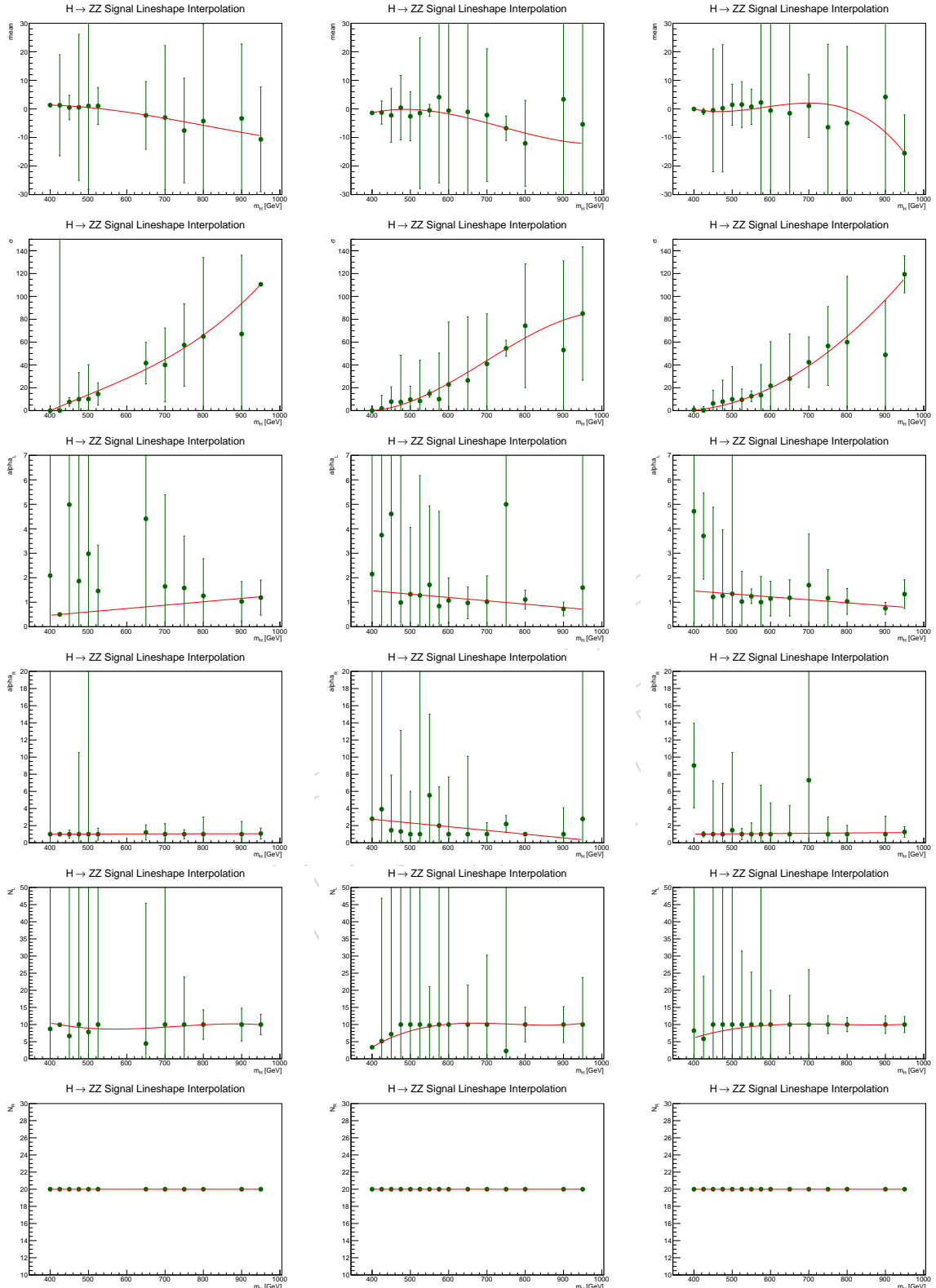


Figure 37: Linear and constant fits of the 4 parameters describing the signal $f(m_{4l}|m_H)$ pdf as a function of m_H . The pdf is modeled as a double crystal-ball function convoluted with the relativistic Breit-Wigner function described in the text. From the first row to the last one, the crystal-ball's mean, σ , α_1 , α_2 , n_1 and n_2 parameters are shown respectively for 4μ (left), $4e$ (center) and $2\mu 2e$ (right) events simulated for $\sqrt{s} = 7$ TeV.

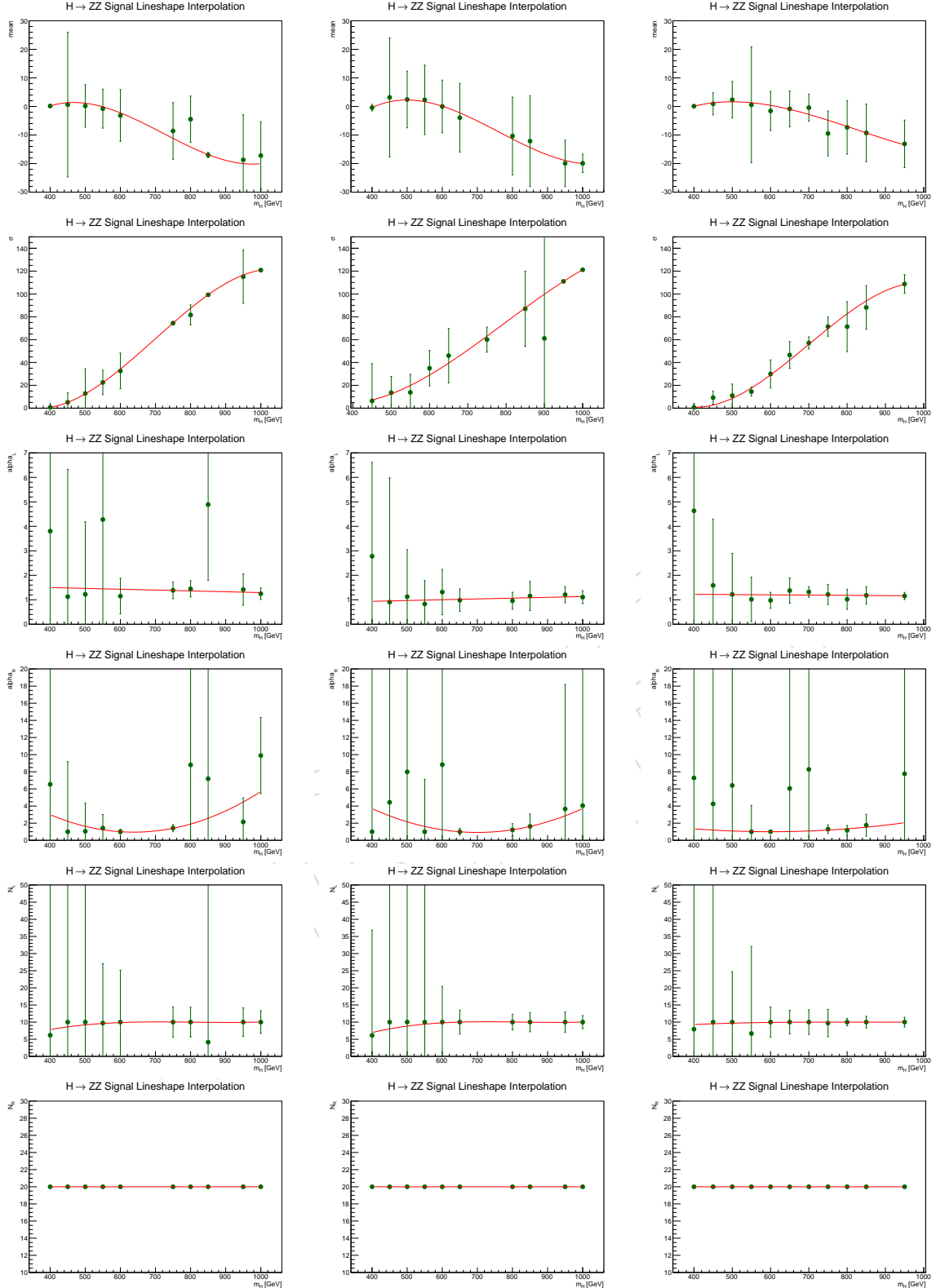


Figure 38: Linear and constant fits of the 4 parameters describing the signal $f(m_{4l}|m_H)$ pdf as a function of m_H . The pdf is modeled as a double crystal-ball function convoluted with the relativistic Breit-Wigner function described in the text. From the first row to the last one, the crystal-ball's mean, σ , α_1 , α_2 , n_1 and n_2 parameters are shown respectively for 4μ (left), $4e$ (center) and $2\mu 2e$ (right) events simulated for $\sqrt{s} = 8$ TeV.

7.3 Signal model uncertainties

Systematic errors on signal model can be factorized into (a) those affecting the overall event yield and (b) uncertainties affecting the shape of signal event distributions:

The uncertainties affecting the overall event yields are as follows:

- Theoretical total cross section uncertainties;
- Theoretical uncertainties on the $H \rightarrow ZZ$ branching fraction;
- Theoretical uncertainties on signal event acceptance within kinematic cuts on leptons;
- Instrumental uncertainties

The uncertainties affecting the shape of event distributions are as follows:

- Theoretical uncertainties on the distribution $pdf(m_{H^*} | m_H)$ (Eq. ??);
- Instrumental uncertainties on the detector response function $CB(m_{4\ell} | m_{H^*})$ (Eq. ??);
- Theoretical uncertainties on Kinematic Discriminant (KD) distribution $pdf(KD | m_H)$ to be introduced later in Sec. 10;
- Instrumental uncertainties on the KD distributions (these are currently assumed negligible).

The next sub-sections discuss all these systematic errors, except for uncertainties on KD distributions, which is discussed in Sec. 10.

7.3.1 Theoretical uncertainties on the signal model

Total signal cross section

Systematic errors on the signal total cross section for *each* production mechanism and for all Higgs boson masses are fully defined elsewhere [56]. They come from PDF+ α_s systematic errors and from theoretical uncertainties evaluated by varying QCD renormalization and factorization scales (μ_R and μ_F).

Per Ref. [57], the PDF+ α_s and QCD scale uncertainties are treated as uncorrelated. The 7 TeV and 8 TeV uncertainties are assumed to be 100% correlated.

Branching ratio BR($H \rightarrow 4l$)

The uncertainty on $BR(H \rightarrow 4l)$ is taken to be 2% [58] and assumed to be m_H -independent.

Signal acceptance

Depending on the Higgs boson mass, the lepton kinematic cuts restrict the signal acceptance to $\mathcal{A} \sim 0.6 - 0.9$ [52]. The acceptance uncertainties $\delta\mathcal{A}/\mathcal{A}$ are evaluated by using MCFM. For calculations, we used the $pp \rightarrow H \rightarrow ZZ \rightarrow ee\mu\mu$ process at 7 TeV with the following cuts: $m_{ee} > 12$, $m_{\mu\mu} > 12$, electrons' $p_T > 7$ and $|\eta| < 2.5$, and muons' $p_T > 5$ and $|\eta| < 2.4$. The minimal jet-lepton and lepton-lepton ΔR_{min} -distance were relaxed, i.e. set to zero. The cross sections are calculated inclusively in the number of jets found at NLO.

We assume that uncertainties on acceptance at 8 TeV are the same as at 7 TeV and are 100% correlated.

The sensitivity of the signal acceptance to the renormalization and factorization scales is evaluated by varying them by a factor of two up and down. The results are shown in Table 16. We find that the acceptance errors are very small (0.1-0.2%) and, therefore, can be neglected.

For estimation of the PDF+ α_s systematic errors, we use the PDF4LHC prescription [59]. The three PDF sets used are CT10 [60], MSTW08 [61], NNPDF [62]. The results is the envelope containing all variations for the three sets of PDFs. We assign a 2% mass-independent error to account for these uncertainties.

Per Ref. [?], the general recommendation is to treat the acceptance and total cross section uncertainties as uncorrelated. Past studies has shown a very little correlation for the low Higgs boson mass. For the high mass, the negative correlations seem to develop, which implies that by leaving these correlations out we make our results more conservative. For simplicity, we assign the exact same error to all production

Table 16: Signal acceptance \mathcal{A} for different QCD scales.

Higgs boson mass m_H (GeV)	120	200	400	500	600
Default \mathcal{A}_0 ($\mu_R = \mu_F = m_H/2$)	0.5421	0.7318	0.8120	0.8421	0.8637
\mathcal{A}_{up} ($\mu_R = \mu_F = m_H$)	0.5417	0.7317	0.8128	0.8427	0.8644
\mathcal{A}_{down} ($\mu_R = \mu_F = m_H/4$)	0.5430	0.7328	0.8119	0.8418	0.8632
$\delta\mathcal{A}/\mathcal{A} = \max \Delta\mathcal{A} /\mathcal{A}_0$	0.17%	0.14%	0.11%	0.07%	0.08%

¹²⁷⁴ mechanisms and assume that they are 100% correlated, which is also conservative.

¹²⁷⁵ **Theoretical uncertainties on the distribution** $pdf_1(m_{H^*}|m_H)$

¹²⁷⁶ These uncertainties were already described in Section 7.2.1.

DRAFT

7.3.2 Data-to-MC efficiency scale factors

Leptons in the signal $H \rightarrow ZZ \rightarrow 4\ell$ are prompt and their trigger and reconstruction/ID efficiencies as well as the impact parameter and isolation cut efficiencies can be readily evaluated directly from data by invoking the tag-and-probe (T&P) method applied to $Z \rightarrow \ell\ell$ events. The results of these measurements are reported in Sec. 4. In this section, we describe results of propagating the measured per-lepton efficiencies (and their errors). Two methods were used. They give comparable results.

Per-lepton Method

The observed data/Monte Carlo discrepancy in the lepton reconstruction and identification efficiencies measured with the data-driven techniques described in Section 4 is used to correct the Monte Carlo on an event-by-event basis. The uncertainties on this efficiency correction are propagated independently to obtain a systematic uncertainty on the final yields for signals and ZZ background.

In practice, the per-lepton data/MC ratio is used to weight individual events (to correct yields for data/MC differences). For each MC sample, five hundred toy MC experiments are ran. In each experiment, the data/MC correction are floated once with a gaussian hypothesis, where the gaussian mean is the central value of the data/MC ratio and the width the associated error. The total number of events is therefore calculated. The systematic uncertainty is taken as the RMS of the distribution of the total number of expected events in the five hundred toys.

The resulting systematics are reported in the Figures 39 and 40 for the 7 and 8 TeV analysis respectively.

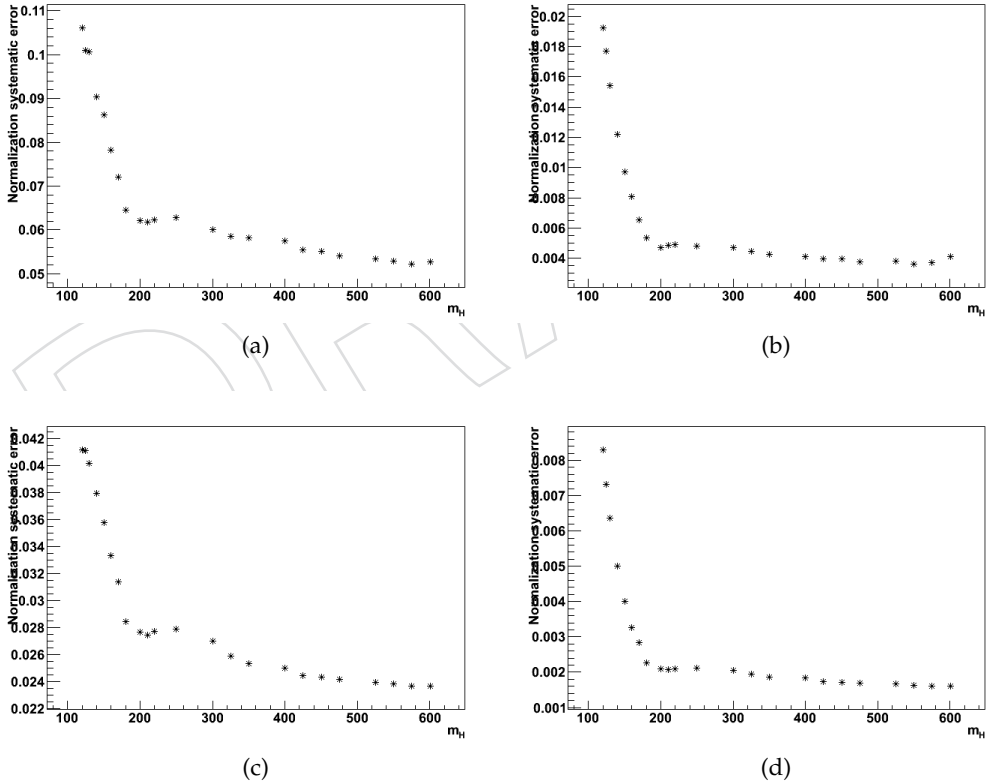


Figure 39: Instrumental Uncertainties related to data/MC differences in efficiencies in reconstruction, identification, isolation and $|SIP|$ as a function of m_H , for (a) 4e channel, (b) 4 μ channel (c) 2e2 μ channel (electron only uncertainties), (d) 2e2 μ channel (muon only uncertainties). Results are for 7 TeV data.

In addition, we had in quadrature a 1.5% uncertainty related to trigger. The errors related to the mo-

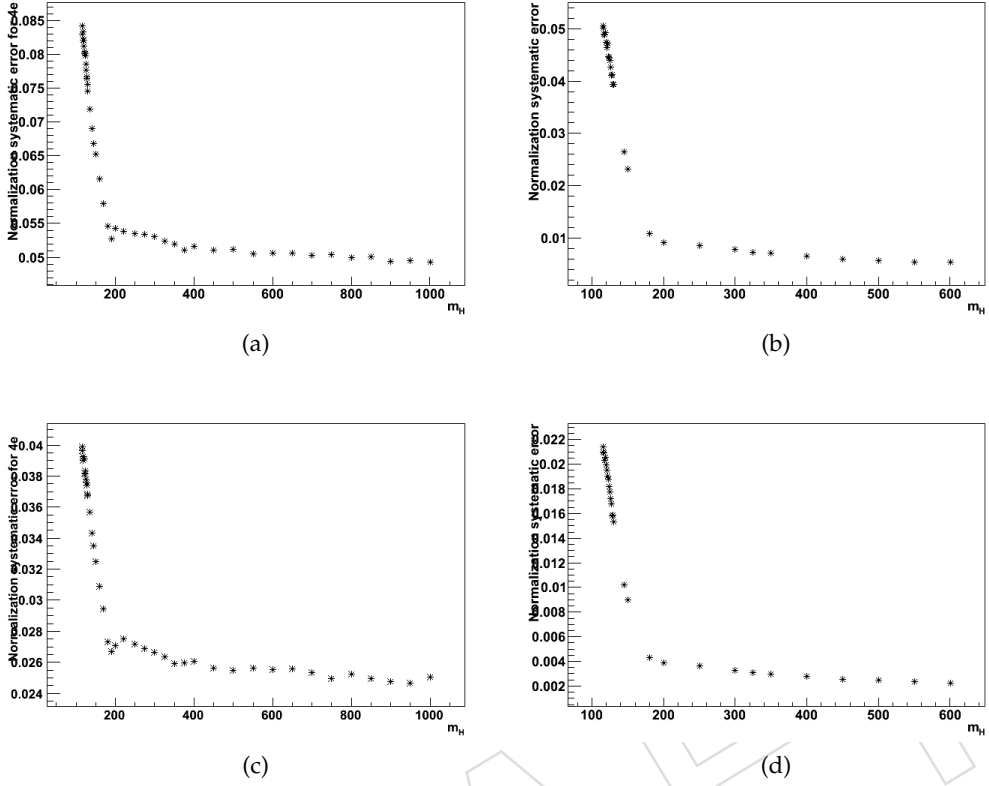


Figure 40: Instrumental Uncertainties related to data/MC differences in efficiencies in reconstruction, identification, isolation and $|SIP|$ as a function of m_H , for (a) 4e channel, (b) 4 μ channel (c) 2e2 μ channel (electron only uncertainties), (d) 2e2 μ channel (muon only uncertainties). Results are for 8 TeV data.

1296 momentum energy scale and resolution will be discussed later in this section.

1297 7.4 Four-lepton mass: scale and resolution

1298 The quality of the momentum measurement of both electrons and muons can substantially vary de-
 1299 pending on the leptons characteristics. For electrons, the resolution is dominated by the fluctuations of
 1300 the measured energy due to bremsstrahlung in the tracker material. For muons the resolution is mainly
 1301 dependant of the muon p_T and η .

1302 Therefore this entails that the 4ℓ mass resolution varies broadly, by as much as a factor of 2-3, as will be
 1303 shown in the next section. Therefore, mixing together events with well and poorly measured 4ℓ masses
 1304 dilutes the Higgs search sensitivity. In this section, we introduce an advanced analysis technique that
 1305 takes into account mass resolutions assessed on the event-by-event basis.

1306 The gain in sensitivity is not expected to be as much as in $H \rightarrow \gamma\gamma$ search, where events with better
 1307 $m_{\gamma\gamma}$ resolution have smaller backgrounds. In the case of the $H \rightarrow ZZ \rightarrow 4\ell$ analysis, the $m_{4\ell}$ observable
 1308 does not help in improving the signal-to-background discrimination. The whole gain comes solely from
 1309 the proper accounting for the signal mass resolutions for individual events.

1310 7.4.1 Scale and resolution via $Z \rightarrow 2\ell$ and J/ψ

1311 To validate the level of accuracy with which we know the absolute mass scale and resolution, we use
 1312 $Z \rightarrow \ell\ell$ and $J/\psi \rightarrow \ell\ell$ events.

1313 Electron scale and resolution from $Z \rightarrow \ell\ell$

1314 For electrons, $Z \rightarrow ee$ invariant mass are built in different categories in η and separating well and bad
 1315 measured electrons using the electron classification. This classification, used for the evaluation of the E-
 1316 p combined momentum, describes the amount of energy radiated by Bremsstrahlung and the quality of
 1317 reconstruction, therefore separating different momentum resolutions. Events are looked at in low and
 1318 high pile-up regimes. The distributions are fitted with a Breit-Wigner (fixed parameters) convoluted
 1319 with a Crystal Ball (free parameters). Fig 41 and 42 are showing the results obtained this way using
 1320 2012 data and comparing to MC expectations.

1321 Systematic uncertainties on electron energy scale can be extracted for these results. It is estimated as the
 1322 maximum deviation between data and MC of fitted $Z \rightarrow ee$ peak position in different categories of eta
 1323 and electron classes. Overall, data and MC agrees within 0.4%. Splitting by ECAL region, we reach 0.1%
 1324 for electron in the Barrel, and up to 0.4% for electrons in the ECAL Endcaps.

1325 We have also checked the dependency of the electron momentum scale with respect to pile-up. The
 1326 reconstructed $Z \rightarrow ee$ is built for different slices of number of vertices, in both data and MC, and are
 1327 fitted as described above. There are no significant variation of the Z peak with the number of vertices,
 1328 and MC is well following the data, as can be appreciated on the Figure 43.

1329 For the resolution, a similar strategy has been adopted, comparing the fitted σ_{CB} between data and MC.
 1330 The largest relative difference amounts to 22% which we take as systematics on the resolution for 2012
 1331 data.

1332 Linearity of Electron momentum scale

1333 The studies described above was mainly checking the scale for electrons with relatively high momenta.
 1334 We may account as a systematic a further possible non-linearity in the momentum estimation differen-
 1335 tially with respect the Monte Carlo when propagating the electron calibration estimated at the Z scale
 1336 to the scale typical of the electrons of an Higgs with mass $m_H \approx 125$ GeV.

1337 These further data – Monte Carlo discrepancies may be due to the material not perfect description in
 1338 front of the ECAL as well as the not perfect detector geometry description.

1339 To estimate this we perform fits to the $Z \rightarrow ee$ invariant mass distribution differentially in p_T and $|\eta|$ of
 1340 the probe electron, while the tag is integrated over all the possible phase space. In each fit the signal PDF
 1341 is described with a template built on Drell Yan Monte Carlo, and smoothed in the cases of low statistics.
 1342 Then the template fit is performed allowing one single scale parameter to float to match data and Monte

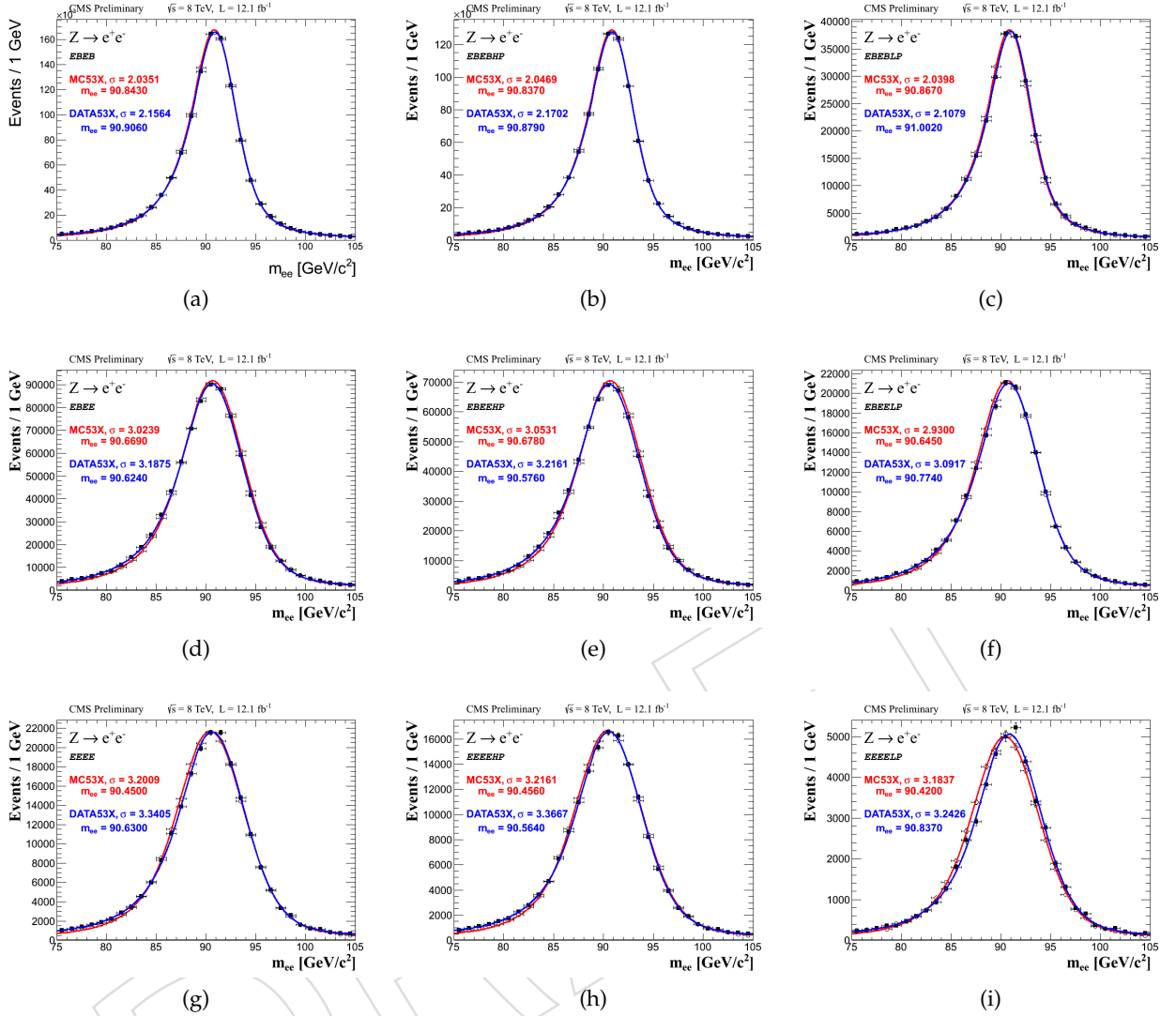


Figure 41: $Z \rightarrow e^+e^-$ events with both electrons in ECAL barrel (a) and for high (b) and low (c) pile-up regime, with one electron in ECAL Barrel, one in ECAL Endcap (d) and for high (e) and low (f) pile-up regime, with both electrons in ECAL endcaps (g) and for (i) pile-up and low (j) regime. Black points are 2012 data with a fit superimposed (blue line). Open square is MC with a fit superimposed (red line).

Carlo. The procedure is validated allowing also an extra smearing in the fit: with these template fits we get extra smearings that are compatible with the official ones reported above.

We show in Fig. 44 to Fig. 46 some examples of these fits for 8 TeV data. They are repeated also for the 7 TeV data/Monte Carlo.

In the statistic box of the fits the fitted extra scale parameter is shown.

We summarize this extra shifts as a function of p_T and $|\eta|$ in Fig. 47 for the 7 TeV data and in Fig. 48 for the 8 TeV data. They show that the extra shift is negligible around the point where the calibration was done, while there is an extra shift when going to lower p_T . The maximum drift is $\approx 0.4\%$ (0.4%) in the barrel and $\approx 0.9\%$ (0.4%) in the endcap for the 8 TeV data (7 TeV data). Conservatively, we take the value obtained in 8 TeV for the endcap data also for 7 TeV data (the difference being only in the endcap).

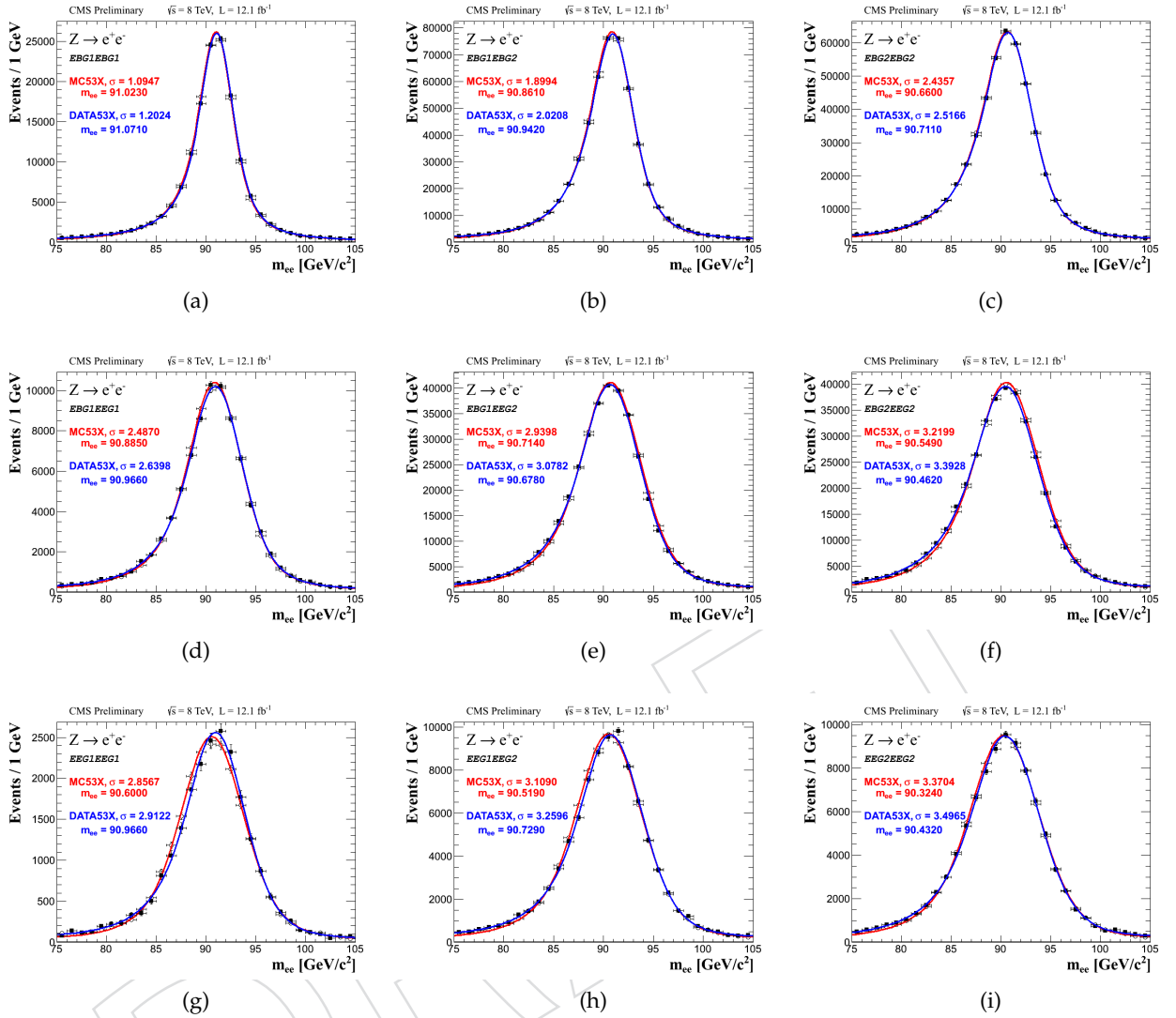


Figure 42: Z to electrons events categorized regarding the electrons classification with both non-showering electrons (golden or big-brem) (a) (d) (g), one non-showering, one showering (showering, bad-track or cracks) (b) (e) (h), both showering electrons (c), (f), (i). First row is for two electrons in ECAL barrel, second row is one electron in ECAL Barrel, the other in the Endcaps, third row is for both electrons in ECAL endcaps. Black points are 2012 data with a fit superimposed (blue line). Open square is MC with a fit superimposed (red line).

1353 We estimate the impact of this residual non linearity in data/Monte Carlo applying the expected shift
1354 to the electrons in a Monte Carlo sample of Higgs with $m_H = 125$ GeV, and recomputing the invariant
1355 mass. We then fit the mass distribution with a Double Crystal Ball function and we take the difference in
1356 the fitted mean between the nominal and the shifted distribution as event systematic due to this effect.

1357 The distributions for $2e2\mu$ and $4e$ are shown in Fig. 49 and Fig. 50 for the case of 7 TeV and 8 TeV,
1358 respectively.

1359 The systematics due to this effect applied are then the following ones:

- 1360 • 4e final state: extra 0.2% systematic
- 1361 • 2e2 μ final state: extra 0.1% systematic

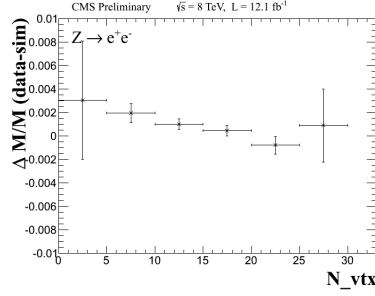


Figure 43: As a function of the number of vertices, differences between data and MC of the peak position, divided by the peak position in MC.

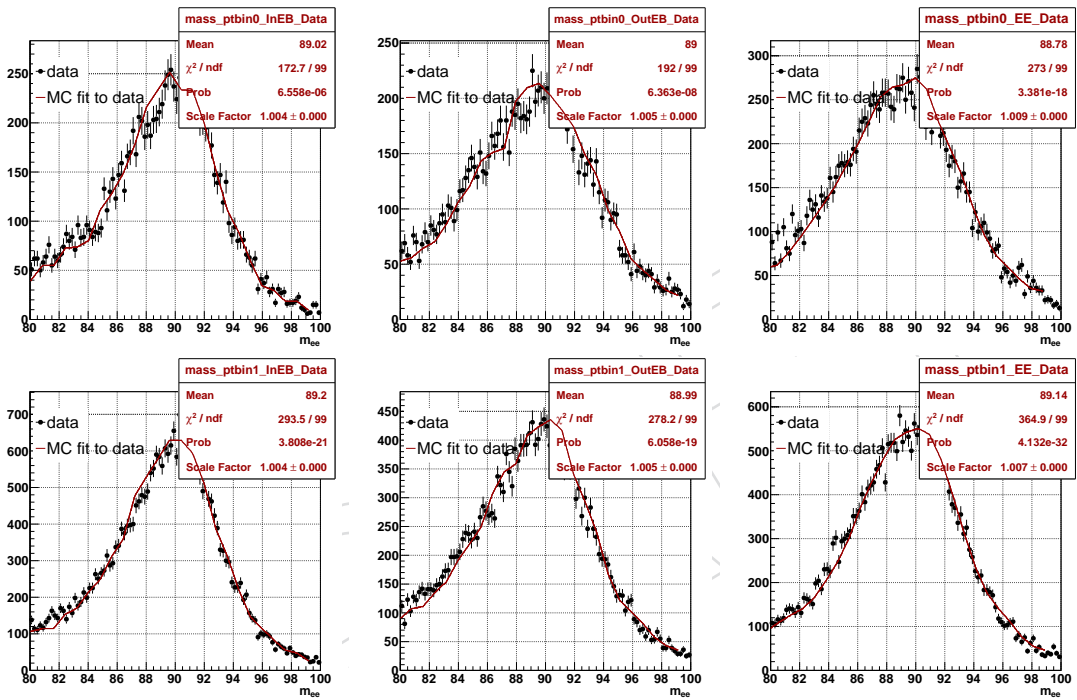


Figure 44: Template fits for the $Z \rightarrow ee$ for the probe $15 < p_T < 20$ GeV for $|\eta| < 1$ (left), $1 < |\eta| < 1.479$ (middle) and $|\eta| > 1.479$ (right) for 8 TeV data.

the effect on the invariant mass being better than the worst shift seen per electron because the core of the distribution is dominated, for kinematic and efficiency reasons, by electrons of moderate p_T in the barrel region where the scale is more precise.

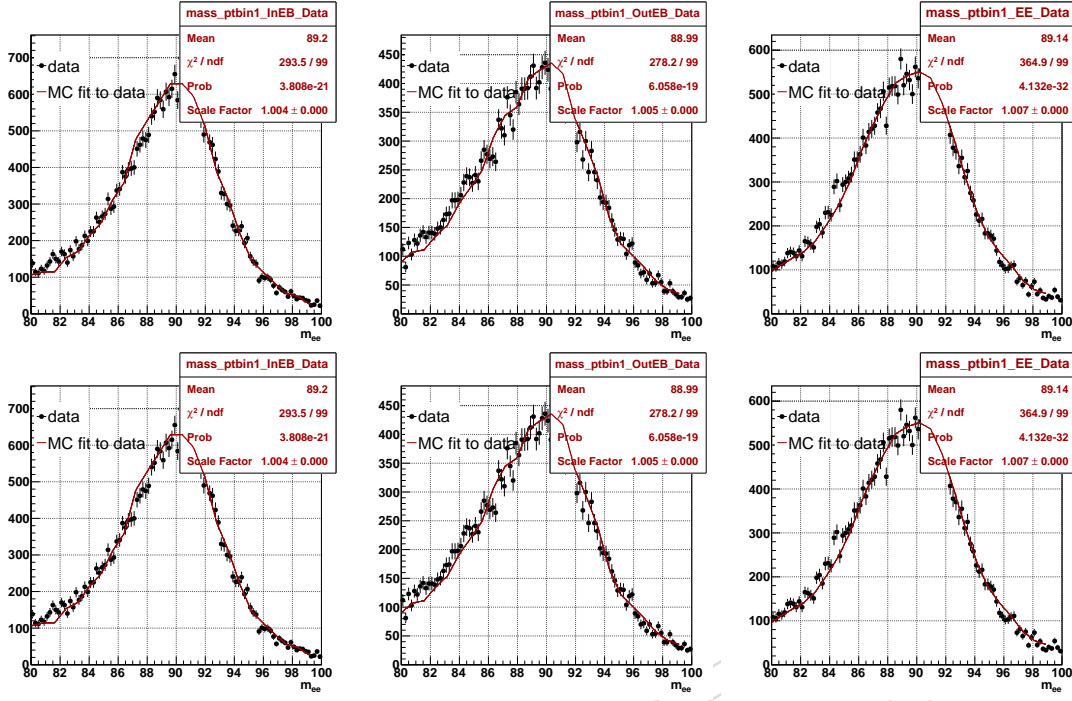


Figure 45: Template fits for the $Z \rightarrow ee$ for the probe $20 < p_T < 25$ GeV for $|\eta| < 1$ (left), $1 < |\eta| < 1.479$ (middle) and $|\eta| > 1.479$ (right) for 8 TeV data.

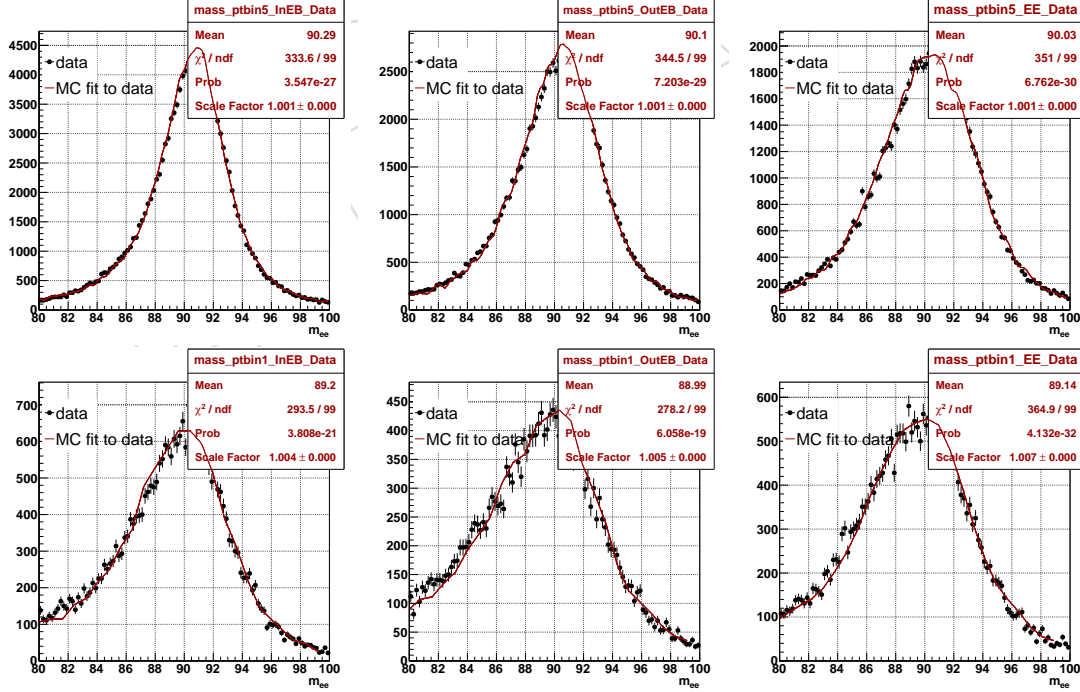


Figure 46: Template fits for the $Z \rightarrow ee$ for the probe $40 < p_T < 45$ GeV for $|\eta| < 1$ (left), $1 < |\eta| < 1.479$ (middle) and $|\eta| > 1.479$ (right) for 8 TeV data.

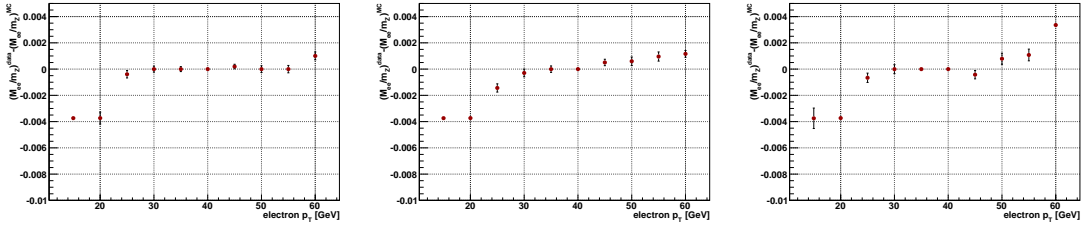


Figure 47: Extra data/Monte Carlo shifts as a function of electron p_T for $|\eta| < 1$ (left), $1 < |\eta| < 1.479$ (middle) and $|\eta| > 1.479$ (right) for 7 TeV data.

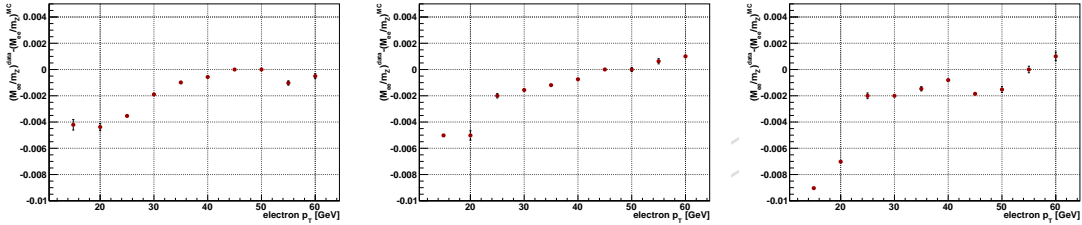


Figure 48: Extra data/Monte Carlo shifts as a function of electron p_T for $|\eta| < 1$ (left), $1 < |\eta| < 1.479$ (middle) and $|\eta| > 1.479$ (right) for 8 TeV data.

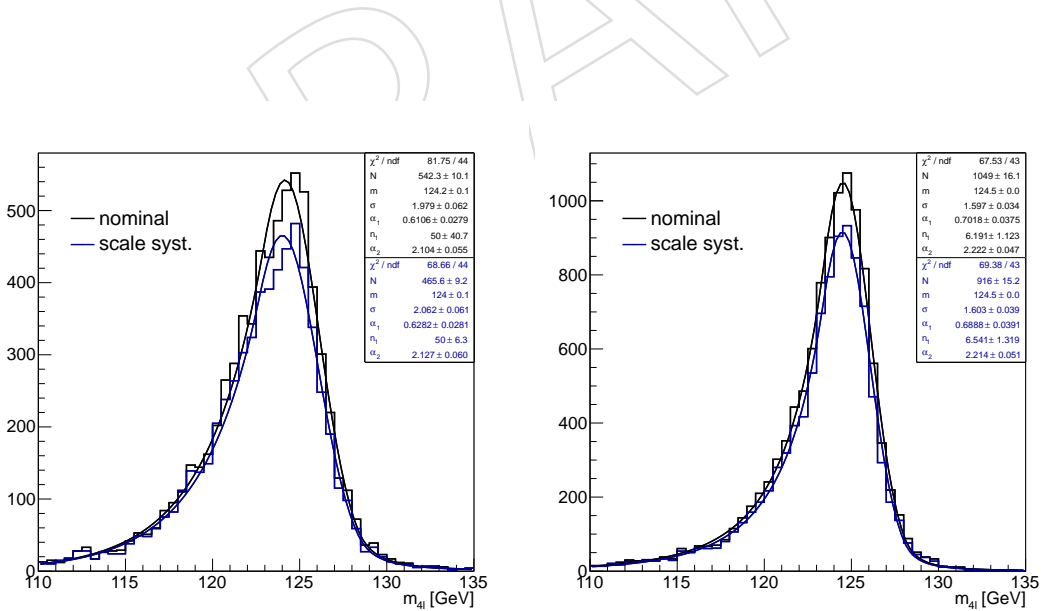


Figure 49: 4l invariant mass distribution with the nominal lepton momentum (black) and after the extra scale shifts are applied to the Monte Carlo (blue) with the double Crystal Ball fit superimposed, for the $4e$ (left) and $2e2\mu$ (right) final states in the case of 7 TeV data/Monte Carlo.

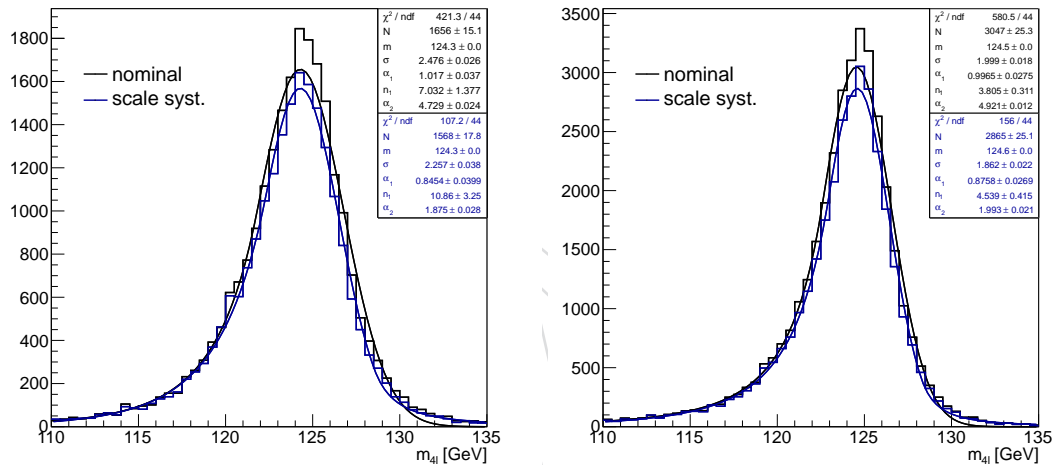


Figure 50: 4l invariant mass distribution with the nominal lepton momentum (black) and after the extra scale shifts are applied to the Monte Carlo (blue) with the double Crystal Ball fit superimposed, for the 4e (left) and 2e2 μ (right) final states in the case of 8 TeV data/Monte Carlo.

1365 **Muon Scale and resolution**

1366 The momentum scale and resolution after the calibration are validated in data using dimuons from J/ Ψ ,
 1367 Y and Z decays, to cover the full momentum range relevant for the H $\rightarrow 4\ell$ search. PF muons with
 1368 $p_T > 5$ GeV are considered, and for Z decays the PF isolation and SIP3D criteria used in the ZZ analysis
 1369 are also applied.

The events are separated in categories according to the average p_T and $|\eta|$ of the two muons, and the dimuon mass distributions in each category are fitted to extract the mass scale and resolution. As the signal lineshape for the H $\rightarrow 4\ell$ search is extracted from simulated events, only the relative difference between data and simulation in the momentum scale and resolution is relevant for the result, and therefore the results are presented in terms of the two quantities

$$\frac{\Delta M}{M} := \frac{M_{\text{data}} - M_{\text{sim.}}}{M_{\text{sim.}}}, \quad \frac{\Delta\sigma}{\sigma} := \frac{\sigma(M)_{\text{data}} - \sigma(M)_{\text{sim.}}}{\sigma(M)_{\text{sim.}}} . \quad (15)$$

1370 For J/ Ψ decays, the resonant signal is modelled with a Crystal Ball and the background with a third
 1371 order Bernstein polynomial; the mass scale and resolution are estimated from the mean and sigma of
 1372 the Crystal Ball. For Z decays, the parameterization used is a numerical convolution of a Breit-Wigner
 1373 and a Crystal Ball, and the background is neglected. For Y decays in data, the dimuon distribution is
 1374 modelled as the sum of three Crystal Balls corresponding to the 1S, 2S and 3S states, constraining the
 1375 mass separation between the three peaks to their nominal values from [47] and assuming a constant
 1376 $\sigma(M)/M$ for the three; the background is modelled as a fourth order Bernstein polynomial. For simu-
 1377 lated Y events, only the 1S state is used, modelled with a single Crystal Ball. Example fits to the dimuon
 1378 mass distribution in 2012 data and simulation are shown in Fig. 51 and ??.

1379 The results for the momentum scale and resolution are shown in Fig. 53 and 53, respectively. In 2011,
 1380 after the calibration the relative momentum scale is stable to within 0.1%, and the resolution within
 1381 about 10%. The calibration for 2012 data is still preliminary, and slightly less accurate at low momentum
 1382 than the 2011 one.

1383 Further validation can be done on the standard candle Z $\rightarrow 4\ell$ peak region, which is discussed in next
 1384 section.

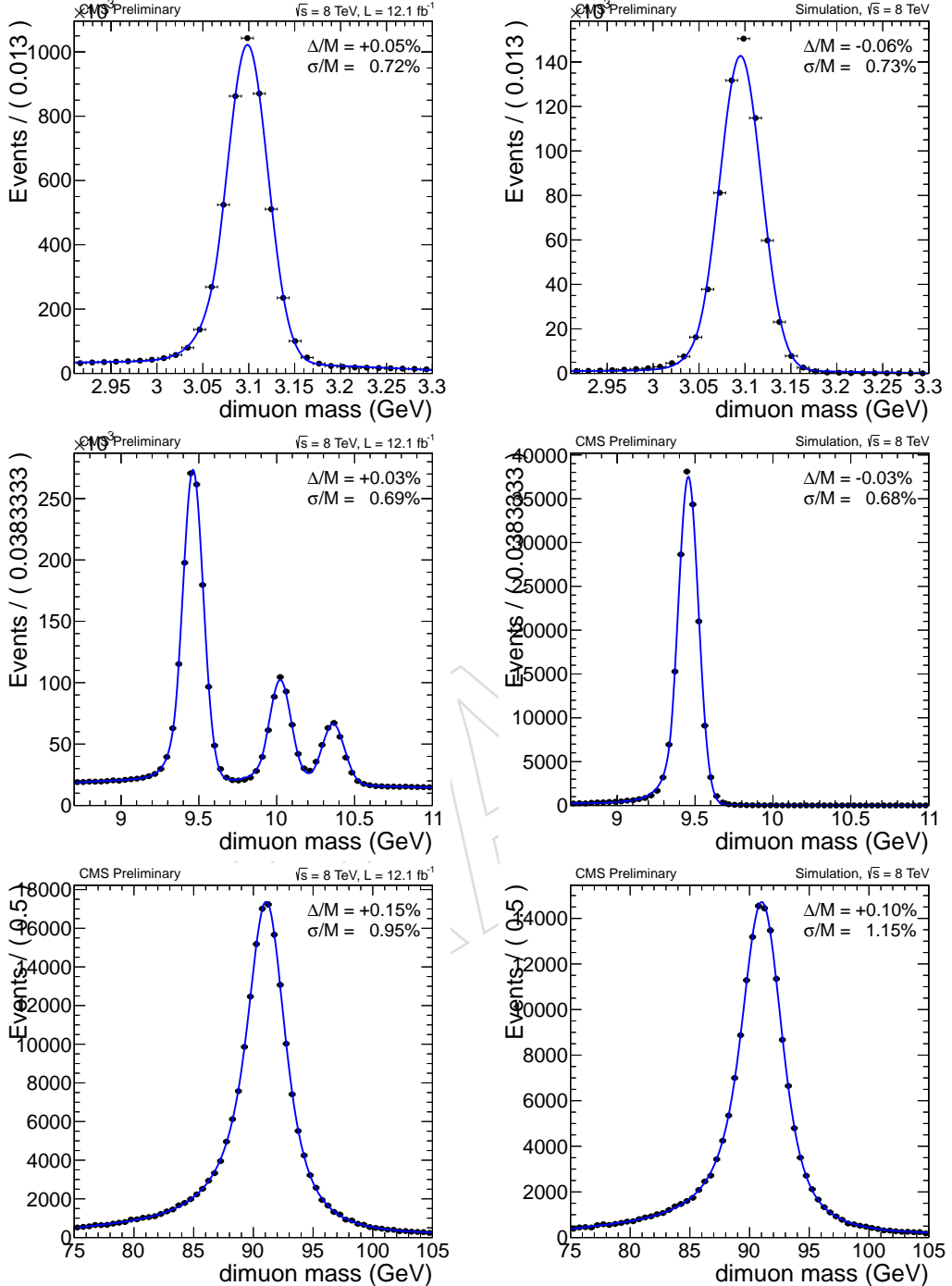


Figure 51: Example fits do the dimuon mass shapes in the central barrel, $|\eta| < 0.8$, in data (left) and simulation (right), for muons from J/ψ , Y and Z . The relative shift Δ/M with respect to the nominal mass of the resonance, and the relative width of the gaussian core of the resolution σ/M are given in each fit. For the Y simulation, only the $1S$ resonance is included.

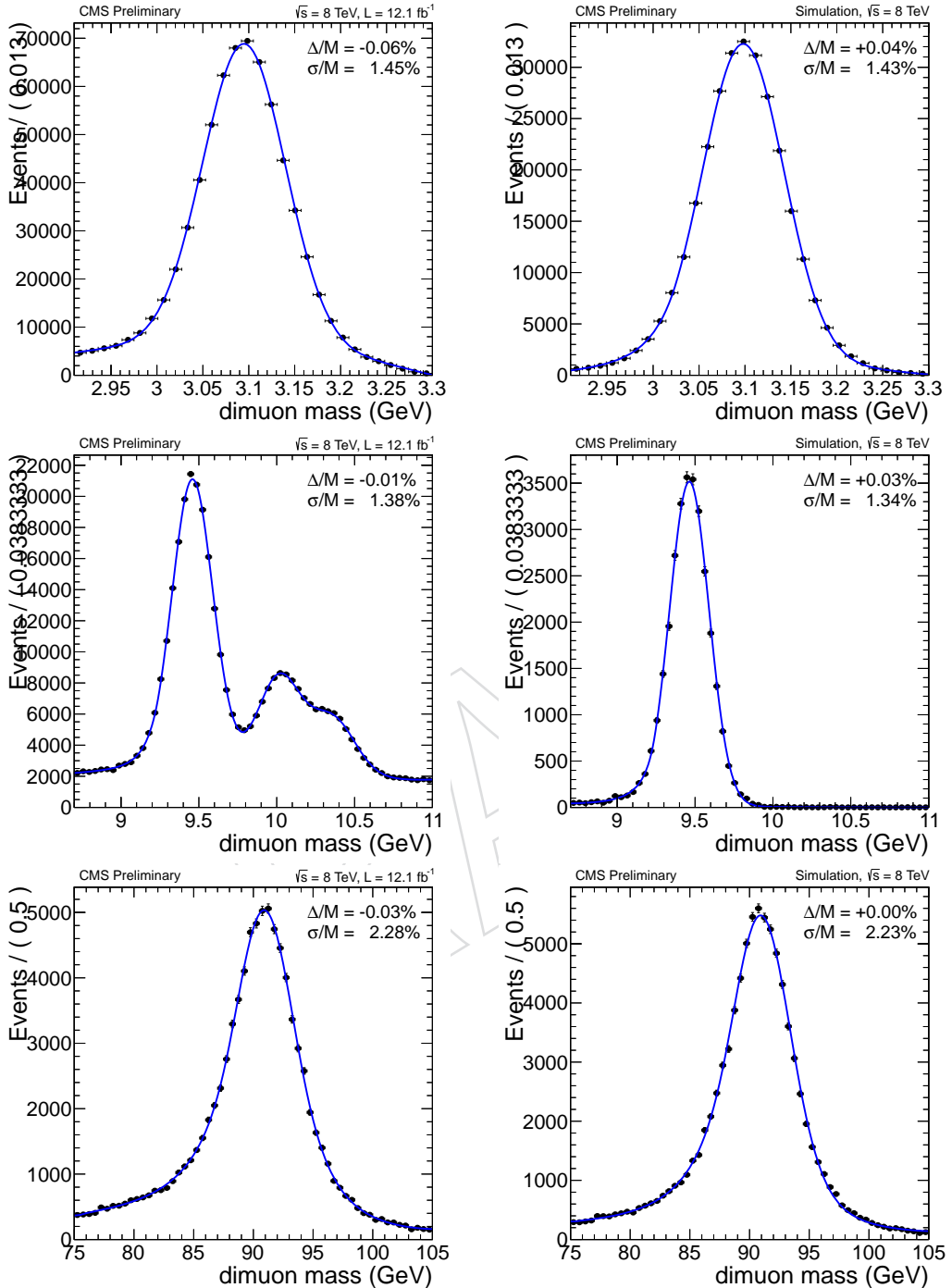


Figure 52: Example fits do the dimuon mass shapes in the central barrel, $|\eta| < 0.8$, in data (left) and simulation (right), for muons from J/ψ , Y and Z . The relative shift Δ/M with respect to the nominal mass of the resonance, and the relative width of the gaussian core of the resolution σ/M are given in each fit. For the Y simulation, only the $1S$ resonance is included.

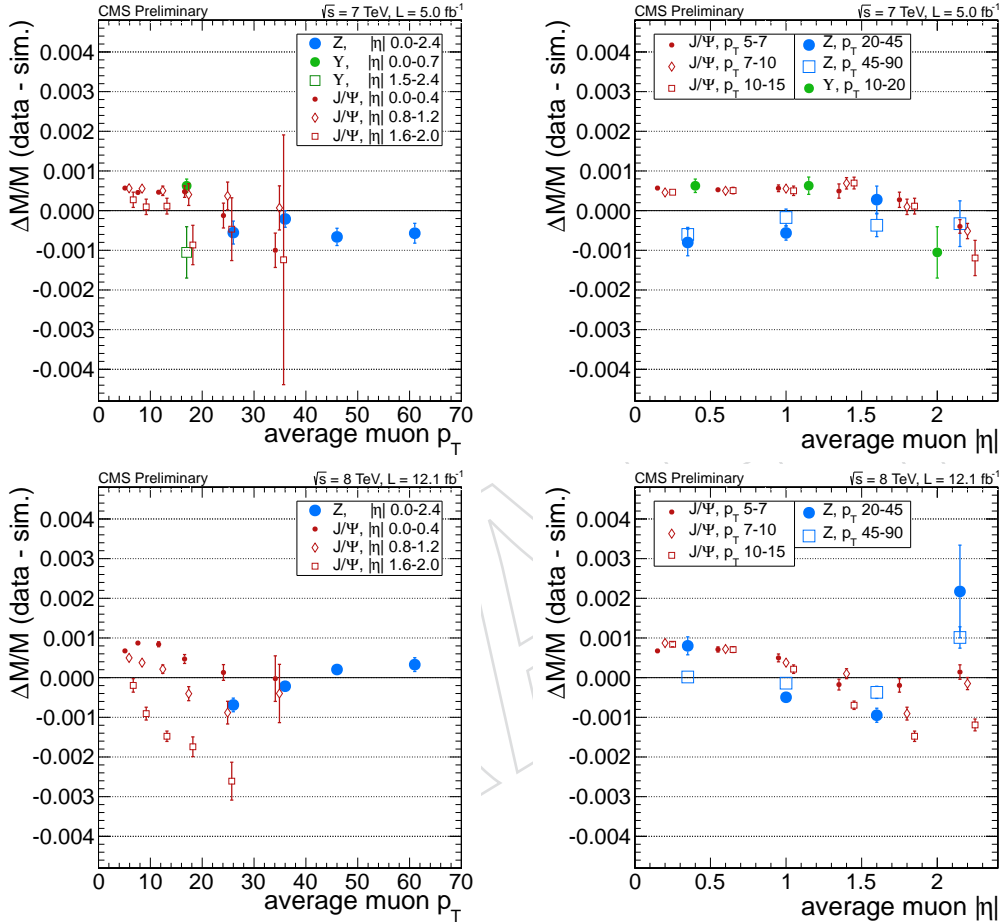


Figure 53: Relative difference between the dimuon mass scales in data and simulation extracted from J/Ψ , Y and Z decays, as function of the average muon p_T (left) and $|\eta|$ (right) for the 2011 data (top) and 2012 data (bottom). Markers for different p_T and $|\eta|$ bins are slightly displaced horizontally for legibility purposes. The uncertainties shown are statistical only.

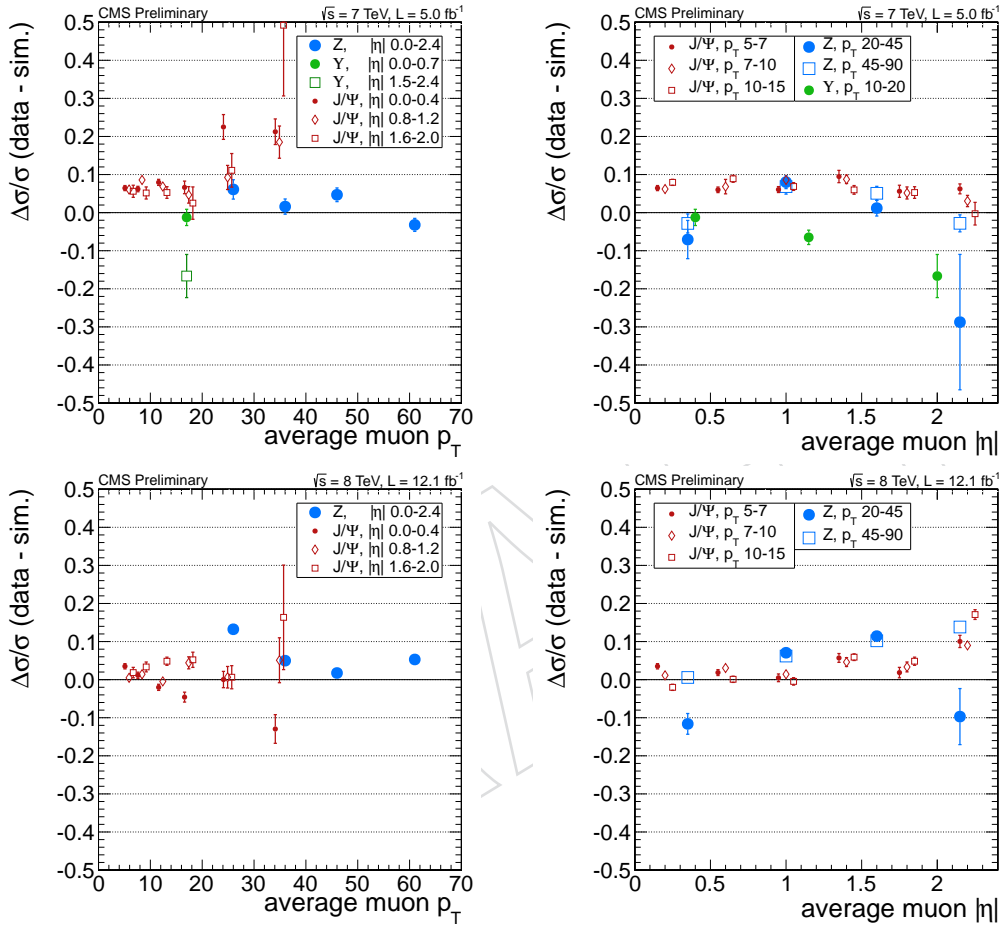


Figure 54: Relative difference between the dimuon mass resolutions in data and simulation extracted from J/Ψ , Y and Z decays, as function of the average muon p_T (left) and $|\eta|$ (right) for the 2011 data (top) and 2012 data (bottom). Markers for different p_T and $|\eta|$ bins are slightly displaced horizontally for legibility purposes. The uncertainties shown are statistical only.

7.4.2 Scale and resolution via $Z \rightarrow 4\ell$

The $Z \rightarrow 4\ell$ decays give a clean resonant peak in the four-lepton invariant mass distribution, which can be used as a standard candle in the context of the Higgs boson search in the $H \rightarrow ZZ \rightarrow 4\ell$ decay mode [63]. The number of events in the $Z \rightarrow 4\ell$ peak at $m_{4\ell} = m_Z$ is at least 5 times larger than the expected number of events for the SM Higgs boson with a mass near 125 GeV. Therefore, the $Z \rightarrow 4\ell$ peak can be used for a *direct* validation of our understanding of the four-lepton mass scale and the four-lepton mass resolution in the phase space just next to the Higgs boson four-lepton decays. To enhance the peak, the low end of the m_{Z2} -cut is relaxed from 12 to 4 GeV.

In the fit function, the background shape is taken from $pp \rightarrow ZZ \rightarrow 4\ell$ simulation, with the overall normalization floating in the fit. The signal shape is a convolution of the Breit-Wigner and Crystal Ball functions. The central value and width of the Breit-Wigner function are fixed at the Z boson mass m_Z and width Γ_Z [47]. The Crystal Ball parameters are free in the fit. One can split the events in the $Z \rightarrow 4\ell$ peak into those dominated by electron resolution ($Z \rightarrow 2e2\ell$) and those dominated by muon resolution ($Z \rightarrow 2\mu2\ell$), as is done with $Z \rightarrow 2\ell$ events, in order to better validate the scale and resolution for electrons and muons.

A fit of the MC with a Breit-Wigner function at GEN level is shown in fig. 55. In this fit, the mass of the Breit-Wigner is allowed to float. One can see there is an inherent shift in the Z mass from pdg value upwards on the order of 50 MeV. This could be due to the interference between s-channel and t-channel $qq \rightarrow ZZ \rightarrow 4\ell$, however it is covered by systematics used in the analysis.

Figure 58 shows the fit of the four-lepton mass distribution for the observed $Z \rightarrow 4\ell$ events in 7 TeV (left) and 8 TeV (right) data. One can see that the offset of the peak is 0.12 ± 0.42 GeV ($0.1 \pm 0.45\%$) for the 7 TeV data and 0.53 ± 0.35 GeV ($0.6 \pm 0.4\%$) for the 8 TeV data. The data can also be split into $Z \rightarrow 2e2\ell$ and $Z \rightarrow 2\mu2\ell$ events. These fits are shown fig. 57. Table 19 shows a summary of the scale and resolution parameters. These numbers can be used to validate the systematic errors of the four-lepton mass scale. With the current data, we can state that the average four-lepton mass scale does not show any significant bias with the 0.3% statistical uncertainty and we can measure the average four-lepton mass resolution with about 25% statistical uncertainty. The statistical error on the measured scale is now nearly comparable to the systematics used in the statistical analysis.

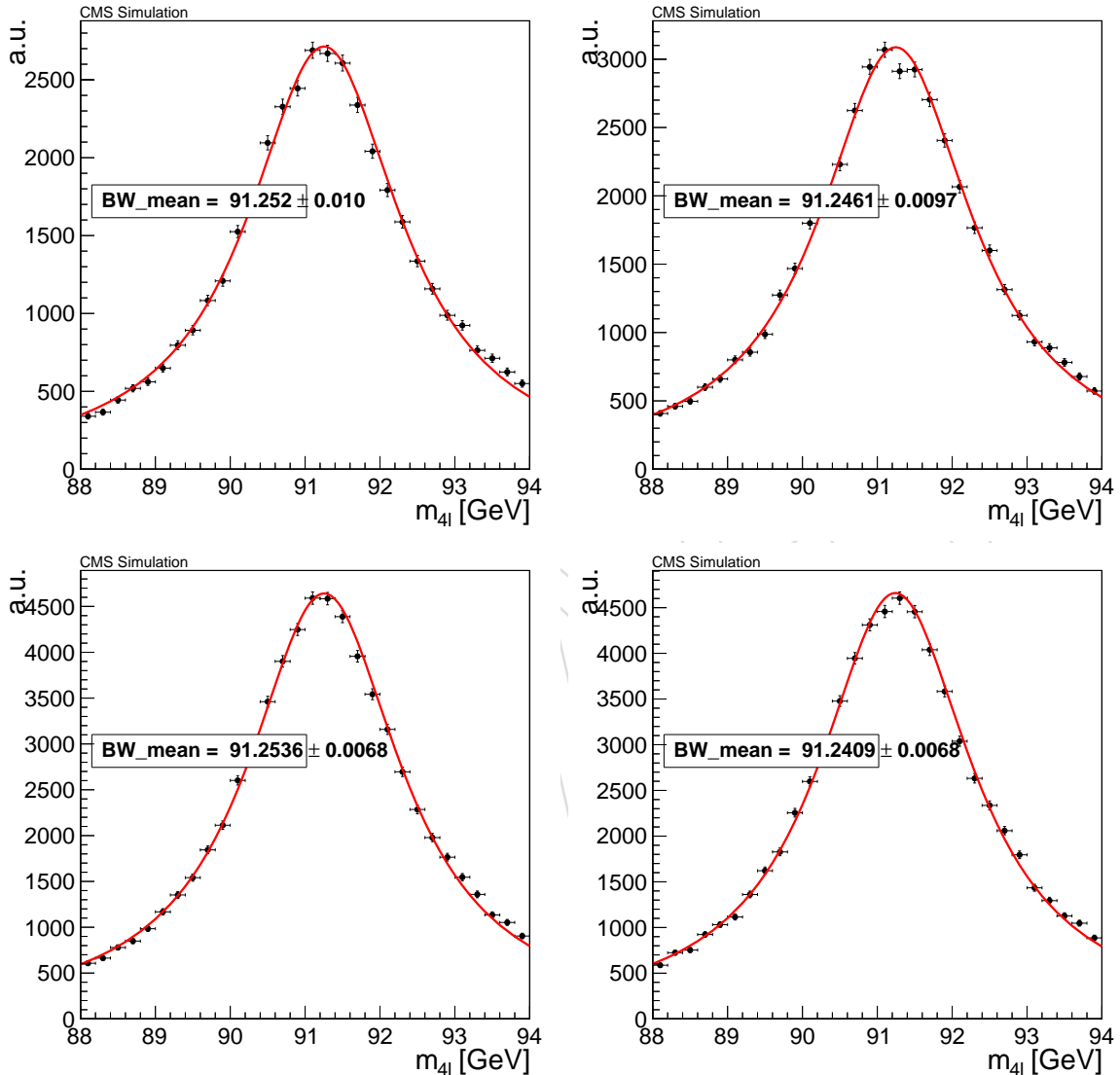


Figure 55: Four-lepton mass distribution in the 7 TeV (left) and 8 TeV (right) GEN MC for $Z \rightarrow 2e2\ell$ (top) and $Z \rightarrow 2\mu 2\ell$ (bottom) fitted with a Breit-Wigner with mass floating in the fit and width set to pdg value.

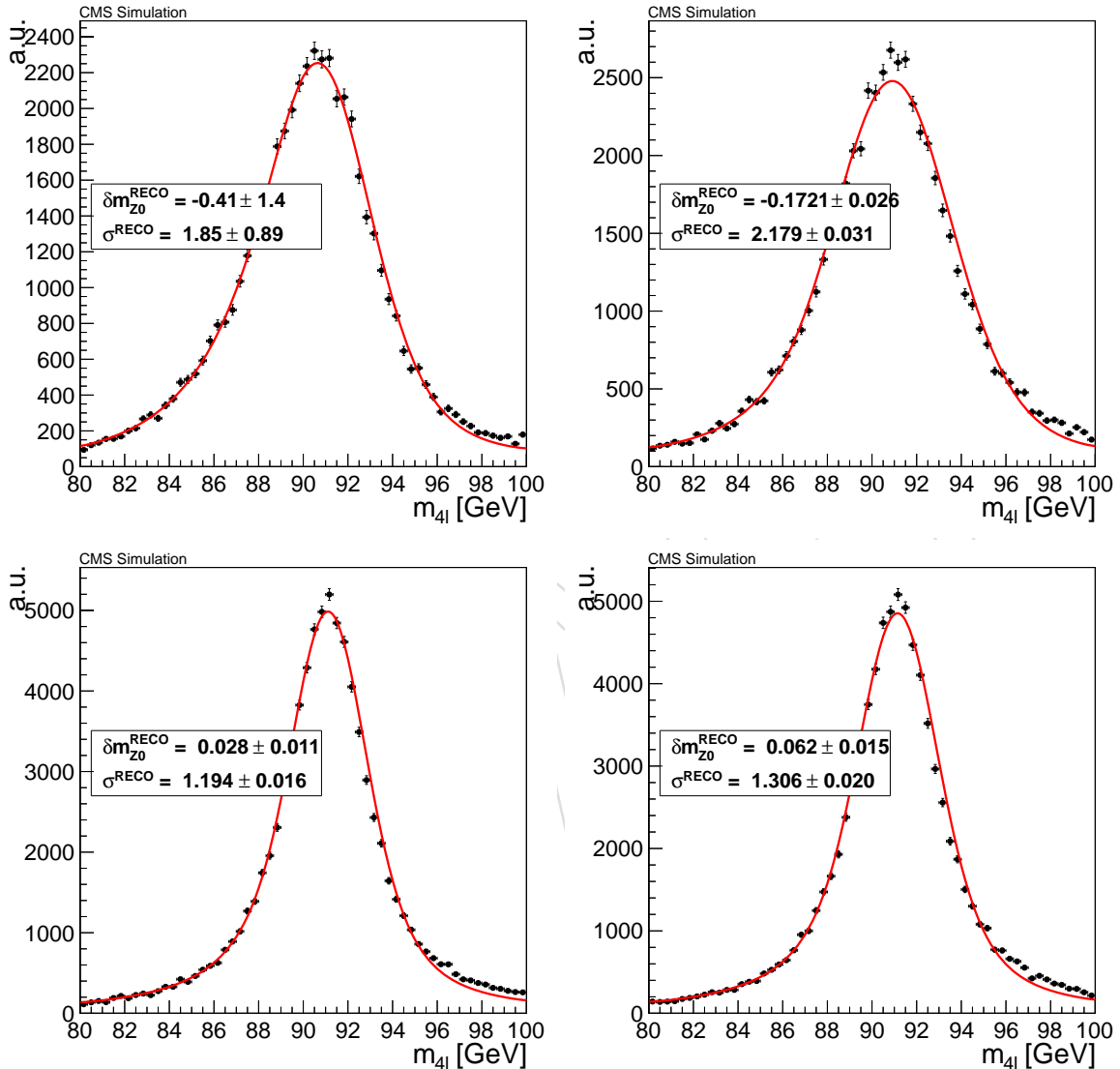


Figure 56: Four-lepton mass distribution in the 7 TeV MC (left) and 8 TeV RECO MC (right) for $Z \rightarrow 2e2\ell$ (top) and $Z \rightarrow 2\mu 2\ell$ (bottom) fitted with a Breit-Wigner convoluted with a Crystal Ball. The Breit-Wigner parameters are fixed to pdg values while the CB mean and sigma are allowed to float in the fit.

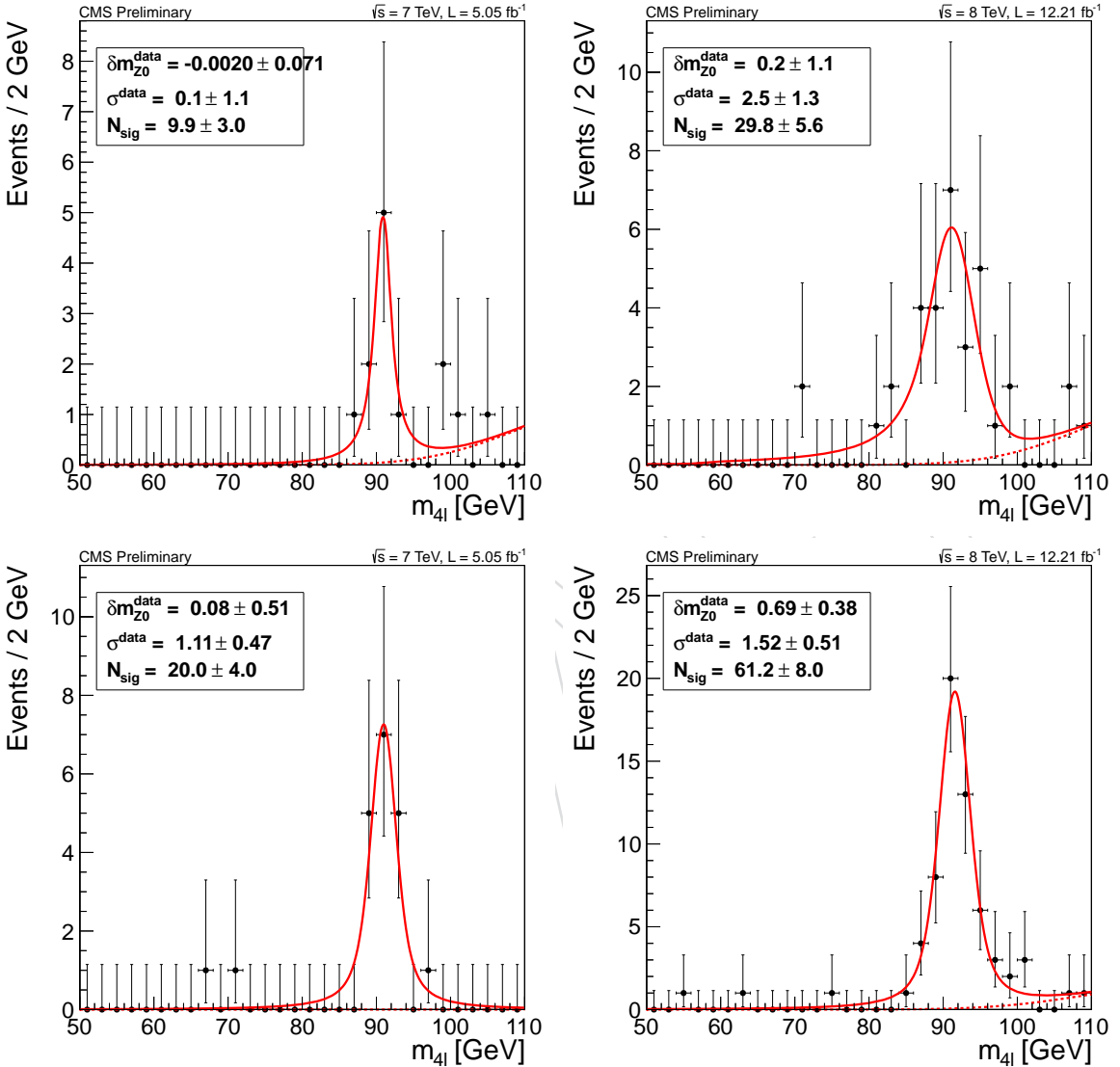


Figure 57: Four-lepton mass distribution in the 7 TeV data (left) and 8 TeV data (right). Data are shown with points. The top plots show $Z \rightarrow 2e2\ell$ while the bottom plots show $Z \rightarrow 2\mu 2\ell$ events. The solid line represents a simultaneous fit for the background and Z boson peak (see text for details).

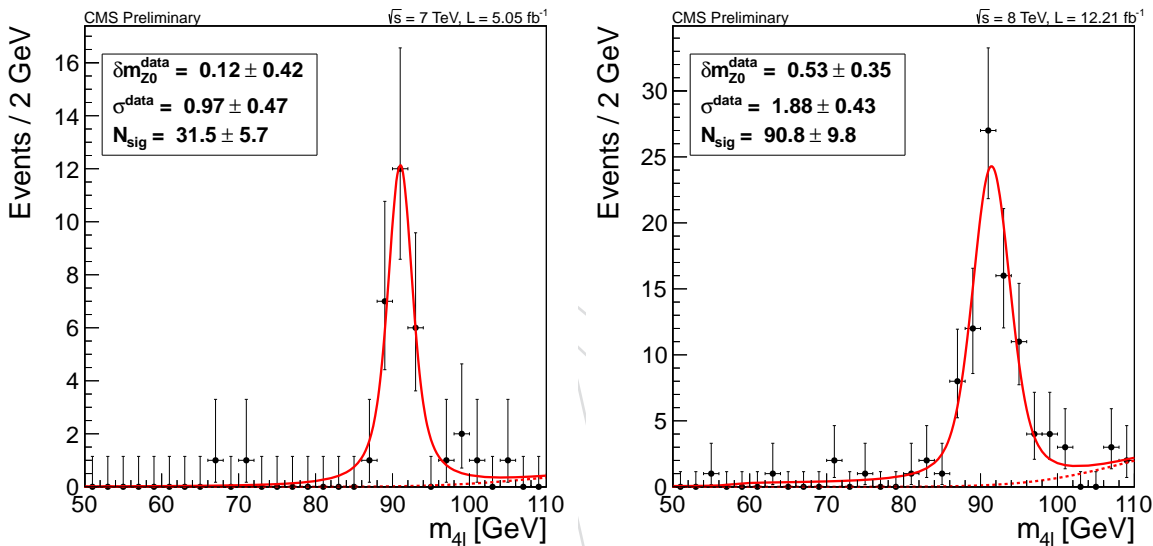


Figure 58: Four-lepton mass distribution in the 7 TeV data (left) and 8 TeV data (right). Data are shown with points. The three final states, $4e$, 4μ , and $2e2\mu$, are added together. The solid line represents a simultaneous fit for the background and Z boson peak (see text for details).

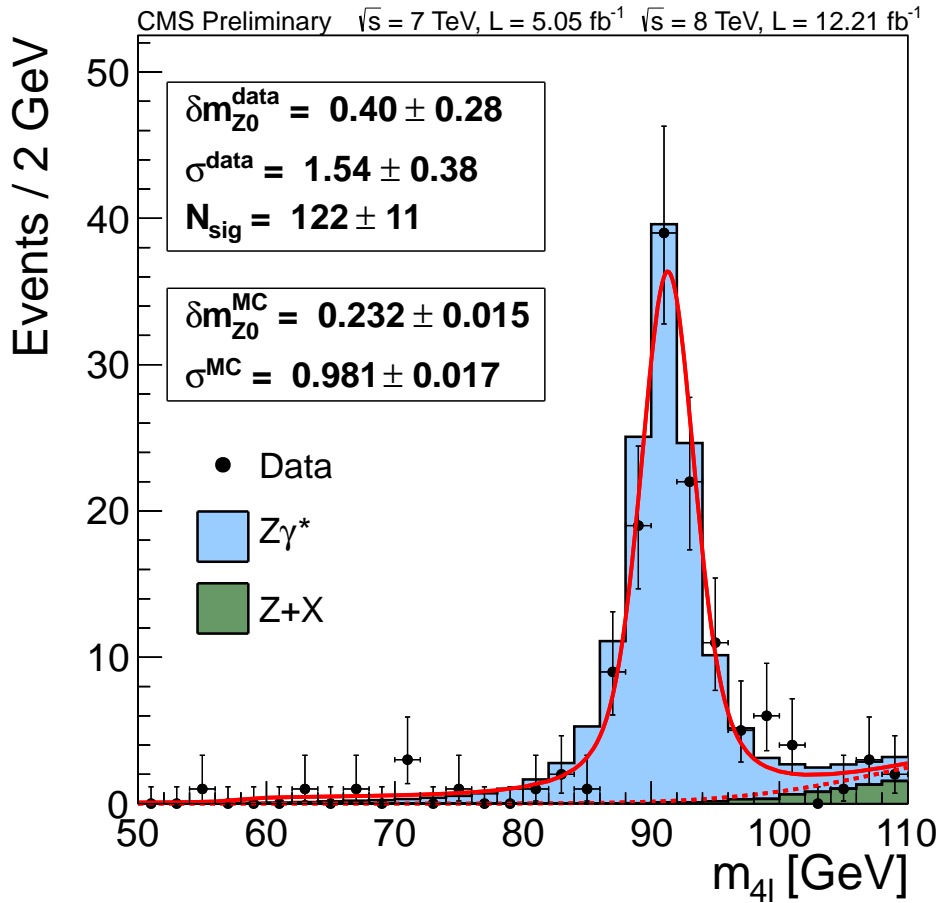


Figure 59: Four-lepton mass distribution in the 7 plus 8 TeV data. Data are shown with points. The three final states, $4e$, 4μ , and $2e2\mu$, are added together. The solid line represents a simultaneous fit for the background and Z boson peak (see text for details). MC is shown by the colored histogram. The number of observed events in the peak in data is 115, while the number of expected events from MC is 127.4.

Table 17: Fit results from GEN $Z \rightarrow 4\ell$ events in MC.

Final state channels	m_Z (GeV)	
	7 TeV	8 TeV
$2e2\ell$	91.252 ± 0.010	91.2461 ± 0.0097
$2\mu2\ell$	91.2536 ± 0.0068	91.2409 ± 0.0068

Table 18: Fit results from RECO $Z \rightarrow 4\ell$ events in MC.

Final state channels	δm (GeV)		σ (GeV)	
	7 TeV	8 TeV	7 TeV	8 TeV
$2e2\ell$	-0.41 ± 1.4	-0.1721 ± 0.026	1.85 ± 0.89	2.179 ± 0.031
$2\mu2\ell$	0.028 ± 0.011	0.062 ± 0.015	1.194 ± 0.016	1.306 ± 0.020

Table 19: Fit results from $Z \rightarrow 4\ell$ events in Data.

Final state channels	δm (GeV)		σ (GeV)	
	7 TeV	8 TeV	7 TeV	8 TeV
4ℓ	0.12 ± 0.42	0.53 ± 0.35	0.97 ± 0.47	1.88 ± 0.43
$2e2\ell$	-0.002 ± 0.071	0.2 ± 1.1	0.1 ± 1.1	2.5 ± 1.3
$2\mu2\ell$	0.08 ± 0.51	0.69 ± 0.38	1.11 ± 0.47	1.52 ± 0.51

7.4.3 4ℓ Event-by-Event Error: Error propagation

Event-by-event mass errors can be evaluated starting from the errors on the individual lepton momenta in different ways.

Individual lepton errors are computed on a per-event basis for muons using the full error matrix as obtained from the muon track fit, and for the ecalDriven electrons using the estimated momentum error as obtained from the combination of the ECAL and tracker measurement, neglecting the uncertainty on the track direction from the GSF fit. For non-ecalDriven electrons, we currently don't have an error (this should come at some point but not for HCP). Thus we adopted a simple parametrisation of the ECAL energy error and combine it with the tracker momentum error as it is done for the ECAL-driven electrons. For FSR photons, the PF parametrization is used.

In principle, one should apply all necessary calibration, correction and smearing on the lepton/photon momentum scale, etc. However, currently those are not applied yet because of time constraint.

In the following we describe two approaches for deriving mass errors. In the first approach the individual lepton momentum measurement errors are propagated to the 4ℓ mass error and to the Z1 and Z2 mass errors using an analytical error propagation including all correlations. In the alternative approach, the directional errors for muons are additionally neglected, and to propagate uncertainties of individual leptons to the uncertainty on the invariant mass, each δm corresponding to individual lepton momentum variation is calculated separately, and then the measured resolution on the invariant mass of the four leptons is taken as the quadrature sum of the four individual δm :

$$\begin{aligned} m_0 &= F(p_{T1}, \phi_1, \eta_1; p_{T2}, \phi_2, \eta_2; p_{T3}, \phi_3, \eta_3; p_{T4}, \phi_4, \eta_4) \\ \delta m_i &= F(\dots; p_{Ti} + \delta p_{Ti}, \phi_i, \eta_i; \dots) - m_0 \\ \delta m &= \sqrt{\delta m_1^2 + \delta m_2^2 + \delta m_3^2 + \delta m_4^2} \end{aligned}$$

Figure 60 shows the scatter distribution of mass errors from the two approaches on 125 GeV Higgs MC sample for $4e$, 4μ , $2e2\mu$, $4\mu + \gamma$ and $2e2\mu + \gamma$ final states separately, one can see that the two approaches give very similar results which nicely cross checks each other, the difference is less than 1%. Note that the uncertainty on the mass resolution is currently 20%.

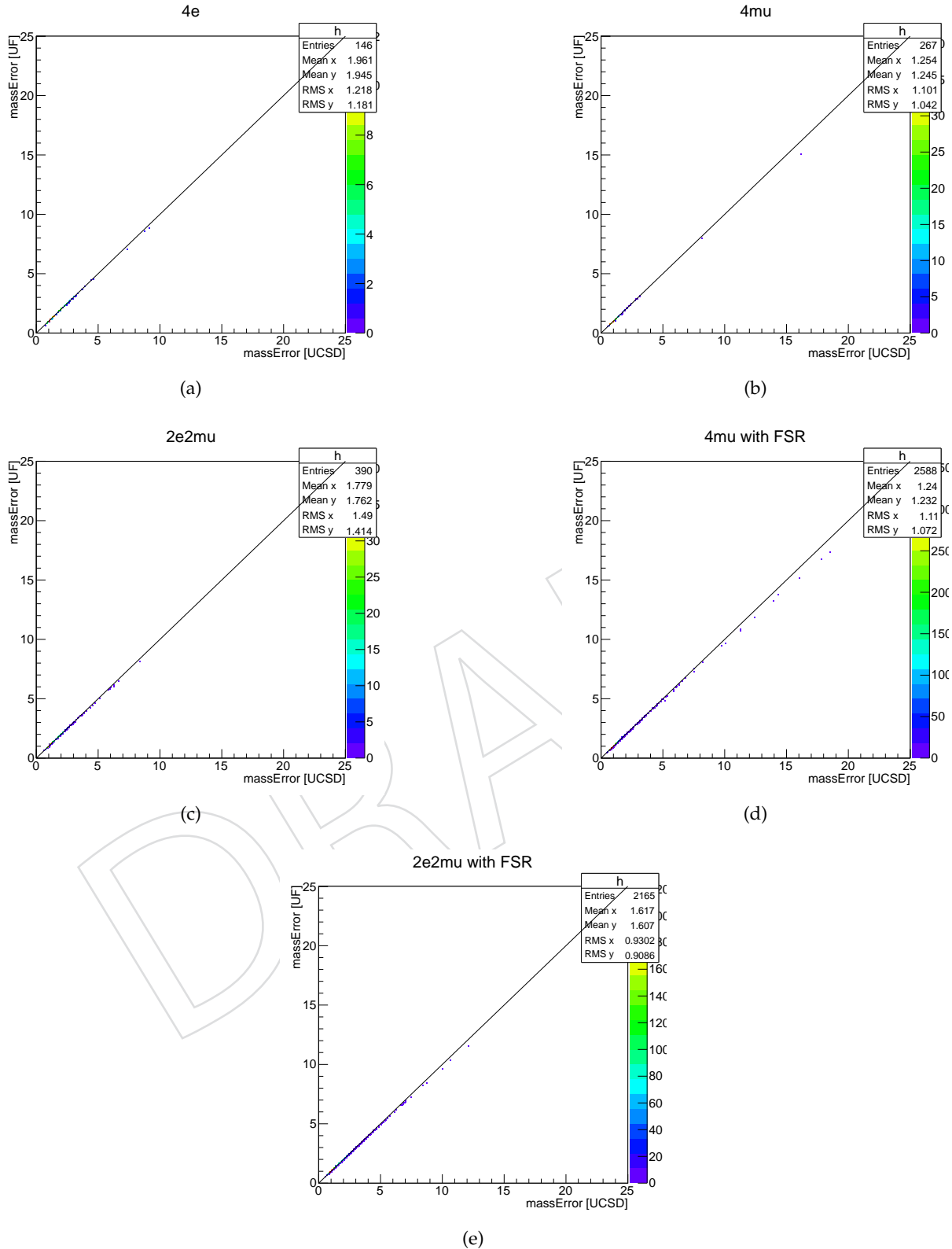


Figure 60: Comparison of four-lepton mass errors calculated from the two approaches on 125 GeV Higgs sample for 4e (top left), 4 μ (top right), 2e2 μ (middle left), 4 μ + γ (middle right) and 2e2 μ + γ (bottom).

7.4.4 Calibration of event-by-event errors

The event-by-event uncertainties on the lepton momenta obtained by the CMSSW reconstruction need to be calibrated before they can be used to describe the expected four-lepton mass spectrum.

7.4.4.1 Single-lepton calibration from MC In the case of muons, a first level of calibration is done at the per-level level on the basis of simulated events, to take into account the improvement in the resolution in the endcaps from the momentum scale calibration and for the smearing introduced in the simulation to bring the resolution closer to the one observed in data. This correction is derived in fine bins of p_T and η by requiring the RMS of the pull distribution of $1/p$ to be equal to one; the $1/p$ variable is used instead of p_T since its distribution is more Gaussian.

Results for this calibration on simulated muons are shown in Fig. 61, and range between about 0.7 and about 1.5. The correction factors are larger for higher p_T muons, since the resolution in the low momentum region is dominated by multiple scattering, fairly well modelled in the simulation, and unaffected by the calibration which is mainly aimed at correcting for weak modes in the tracker alignment.

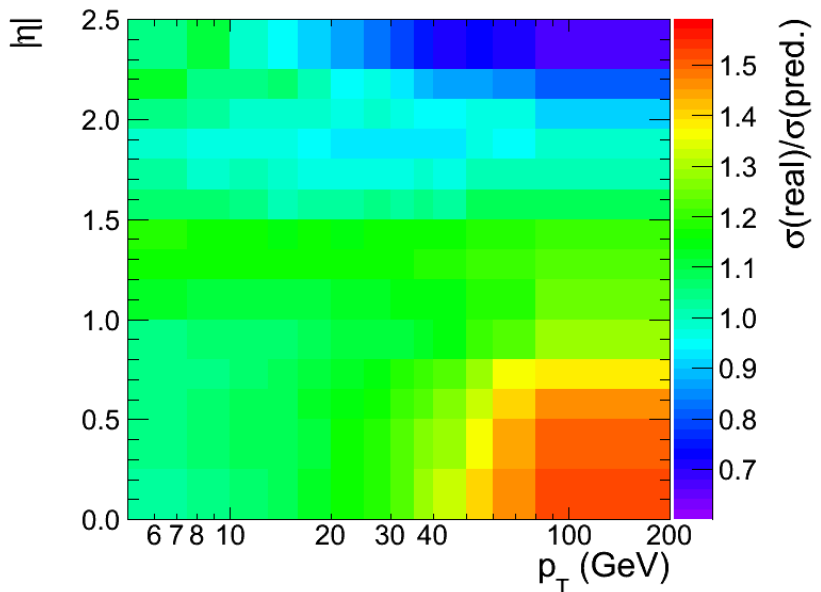


Figure 61: Correction factors for the per-muon momentum uncertainties derived from simulated events corresponding to the 2012 dataset.

For electrons, this level of calibration using simulated events is not needed, as the energy regression and calibration procedures result in estimated energy uncertainties that correctly describe the core of the energy resolution.

7.4.4.2 Corrections from Z and J/ Ψ events Studies on simulated signal events and on Z and J/ Ψ events in data show that a calibration of the Gaussian core of the per-lepton resolution is not sufficient to achieve a correct modelling of the invariant mass distribution from multiple leptons. Several factors contribute to this discrepancy: the contribution of the non-Gaussian tails at single-lepton level to the Gaussian core of the multi-lepton resolution, the unrecovered final state radiation, and the presence of non-uniform energy scale biases as function of the lepton kinematic and quality.

A calibration factor for the estimated per-lepton momentum resolutions is therefore determined from fits to the invariant mass distribution of reconstructed Z decays in data and simulation, in several regions of pseudorapidity. In the case of muons, separate correction factors for low p_T are determined from J/ Ψ events. These correction factors are in the 5 – 15% range for muons, and about twice that size for electrons, as expected given the larger non-Gaussian tails and the larger non-uniformity of the energy scale in the electron case.

muons, $p_T < 20$	2011 Data	2011 Sim.	2012 Data	2012 Sim.
$ \eta < 0.8$	1.00	1.06	1.03	1.08
$0.8 < \eta < 1.6$	0.98	1.07	1.01	1.08
$1.6 < \eta < 2.4$	0.96	1.07	0.99	1.06
muons, $p_T > 20$	2011 Data	2011 Sim.	2012 Data	2012 Sim.
$ \eta < 0.8$	1.09	1.16	1.03	1.07
$0.8 < \eta < 1.6$	1.16	1.03	1.07	1.05
$1.6 < \eta < 2.4$	0.95	0.99	1.09	1.03
electrons	2011 Data	2011 Sim.	2012 Data	2012 Sim.
$ \eta < 0.8$	1.25	1.27	1.30	1.27
$0.8 < \eta < 1.5$	1.16	1.11	1.24	1.22
$1.5 < \eta < 2.0$	1.30	1.30	1.22	1.17
$2.0 < \eta < 2.5$	1.16	1.24	1.14	1.13

Table 20: Correction factors for the per-lepton momentum uncertainties derived from Z and J/ Ψ events in data and simulations. For muons, these corrections are on top of the ones derived from pull distributions at the single lepton level given in Fig. 61. For electrons in 2012 data a slightly different binning in $|\eta|$ is used, [0.0, 1.0, 1.5, 1.9, 2.5], as it yields a more uniform correction factor within each bin.

7.4.5 MC based expectations

FIXME: update all the plots here with Regression + Rochester corrections for muons + full 8 TeV dataset. But methodoly will remain the same

The error evaluation is checked on MC performing pulls distributions. If the errors are correctly evaluated the pull should have a sigma of 1 in the gaussian case. In case of asymmetrical lepton momentum distributions, the RMS of the pull should be one with the errors defined as the RMS of the lepton momentum distributions. It has been demonstrated using toy MC experiments that if the errors are defined as the sigma of the gaussian part of the lepton momentum distribution, the sigma of the gaussian part of the pull should be 1, and if the errors are defined as the effective RMS it is the effective RMS of the pull distribution which should be one.

The Figure 62 shows the MC pull distributions for the 4e channel, for electron momentum and mass measurement. This shows that the individual pull width is different from the Higgs pull width. This effect is understood to be mostly induced by the asymmetry of the electron momentum distribution. When combining asymmetrical distributions from individual leptons to form the m4l distribution, one sees that a pull on individual lepton with an effective RMS at 1 propagates into a pull for the m4l distribution with an effective RMS greater than 1. This means the errors on m4l are underestimated. This has been studied using toy MC experiments, the Figure 63 shows the effective RMS of the m4l pull distributions and of the lepton momentum pull distributions vs asymmetry, defined as the mean-mode of the relative lepton momentum distribution from toy MC experiments.

The Figure 64 shows the MC pull distributions for the (a) 4e, (b) 4 μ and (c) 2e2 μ final states as a function of the m_{4l} reconstructed mass. In the case of electrons, where the momentum distributions show large asymmetries, the errors have been chosen as the effective RMS (effRMS). This choice implies that the effRMS of the pull for the case of electrons is rather shown, together with the σ for comparison.

As will be shown in the next sections, applying the corrections to the single lepton errors, the pulls of 4-lepton mass distributions will be close to one, demonstrating a good control of the event-by-event errors.

Figure 77 shows the MC-predicted $m_{4\ell}$ mass resolution versus reconstructed mass for and $H \rightarrow ZZ \rightarrow 4\ell$ Monte Carlo samples. The plots are obtained for the CMSSW 4.2 MC samples. The uncertainties on lepton p_T used in calculations of $m_{4\ell}$ uncertainties are taken from MC.

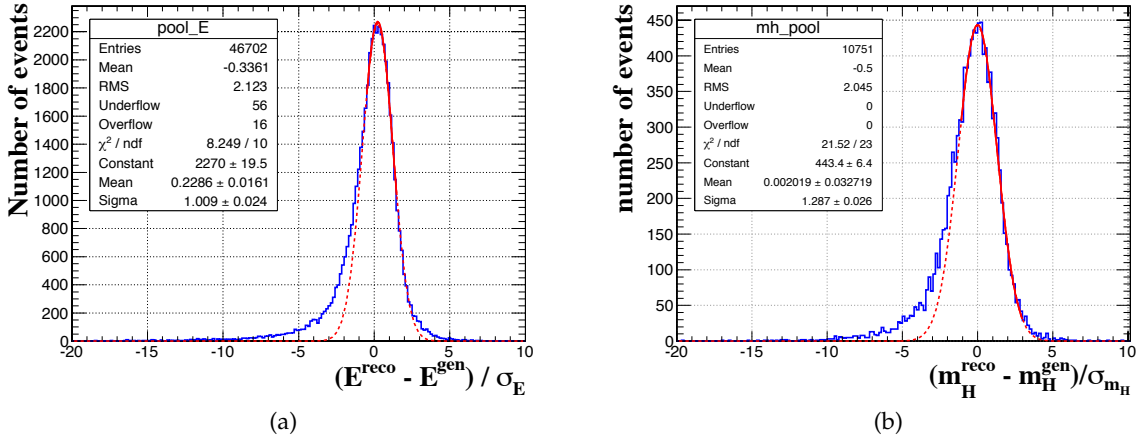


Figure 62: MC pull distributions for a Higgs mass of 120 GeV decaying in the $4e$ channel. (a) pull per electron (b) pull per Higgs event.

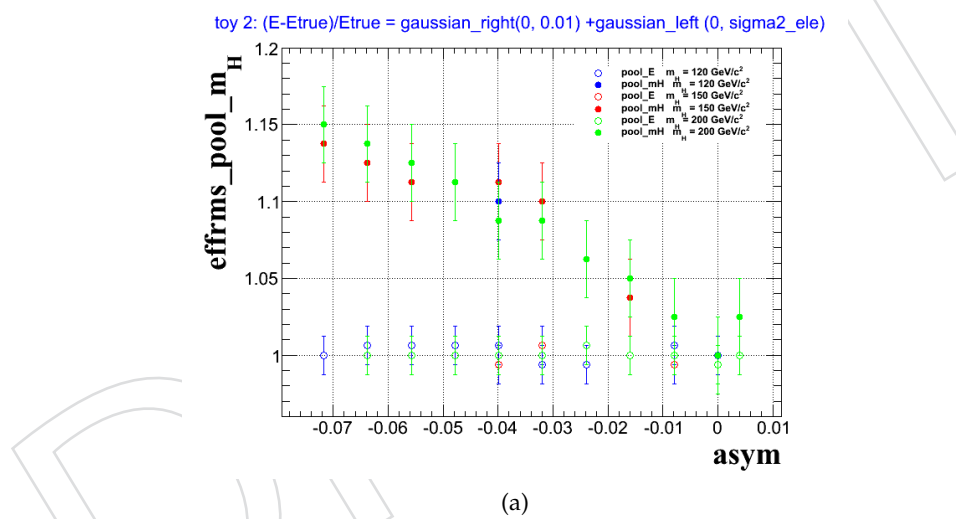


Figure 63: Effective RMS of the m_{4l} pull distributions (plain dots) and of the lepton momentum (open dots) pull distributions vs asymmetry for different m_H .

1493 7.4.6 Validation of errors

1494 7.4.7 Data-driven validation of per-event mass error

1495 To validate the level of accuracy with which we can predict the absolute mass scale and resolution,
 1496 we use $Z \rightarrow \ell\ell$ events. The Z events are classified into ten categories based on what mass resolution
 1497 we would predict. The corrections on per-lepton p_T error (1/p pull correction and residual lineshape
 1498 correction for muons and lineshape correction for electrons described in corrections from Z and J/Ψ
 1499 events) are propagator in to the dilepton mass error, and as a results, the predicted mass resolution. The
 1500 Z mass shape of these events in each category is fit with the convoluted Breit-Wigner (fixed parameters,
 1501 taken from PDG) and Crystal Ball (free parameters).

1502 The di-muon invariant mass spectrum with their fits are shown in figure 66 for data (left) and MC Z
 1503 sample (right). From top to bottom correspond to the four categories which are based on the relative pre-

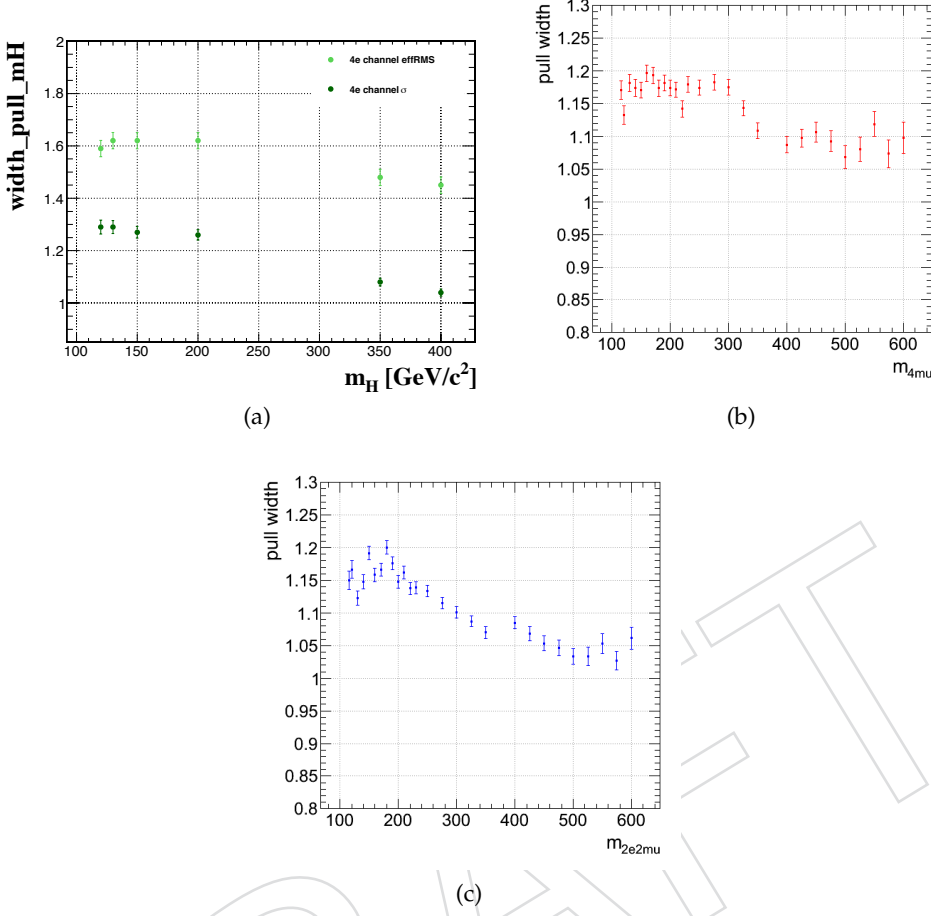


Figure 64: Widths of the MC pull distributions in function of the Higgs mass hypotheses for the (a) 4e, (b) 4 μ and (c) 2e2 μ final states.

1504 dicted mass resolution. Figure 67 shows the observed relative mass peak shift and relative instrumental
 1505 width (Crystal Ball parameters divided by the nominal Z mass) for the di-muon Z events. The dashed
 1506 lines represent the systematic errors we can assign to our ability to predict absolute muon momentum
 1507 scale ($\pm 0.3\%$) and muon momentum resolution ($\pm 20\%$, or, more accurately, $\kappa = 1.2$). (Currently, these
 1508 results are without correction on error estimations).

1509 The di-electron invariant mass spectrum with their fits are shown in figure 68 for data (left) and MC Z
 1510 sample (right). Figure 69 shows the observed relative mass peak shift and relative instrumental width
 1511 for the di-electron Z events. The dashed lines represent the systematic errors we can assign to our ability
 1512 to predict absolute electron momentum scale ($\pm 0.4\%$) and electron momentum resolution ($\pm 20\%$).

1513 We also categorize Zs according to leptons' pseudorapidity, i.e. Barrel-Barrel, Barrel-Endcap and Endcap-
 1514 Endcap. In each category, we then further divide them into sub categories according to the predicted
 1515 mass resolution. As can be seen in figure 70, the observed mass resolution are also within the quoted
 1516 systematics above. The mass scale shifts are shown in figure 71

1517 For $Z \rightarrow ee$, we also categorize them according to both electrons' classification. The best category
 1518 is made of two electrons both are in barrel and non-showering. The worst category is made of two
 1519 electrons both are in endcap and showering. The rest Z events form the medium category. In each
 1520 category, we then further divide them into sub categories according to the predicted mass resolution.
 1521 As can be seen in figure 72, the observed mass resolution are also within the quoted systematics above,
 1522 except the worst category.

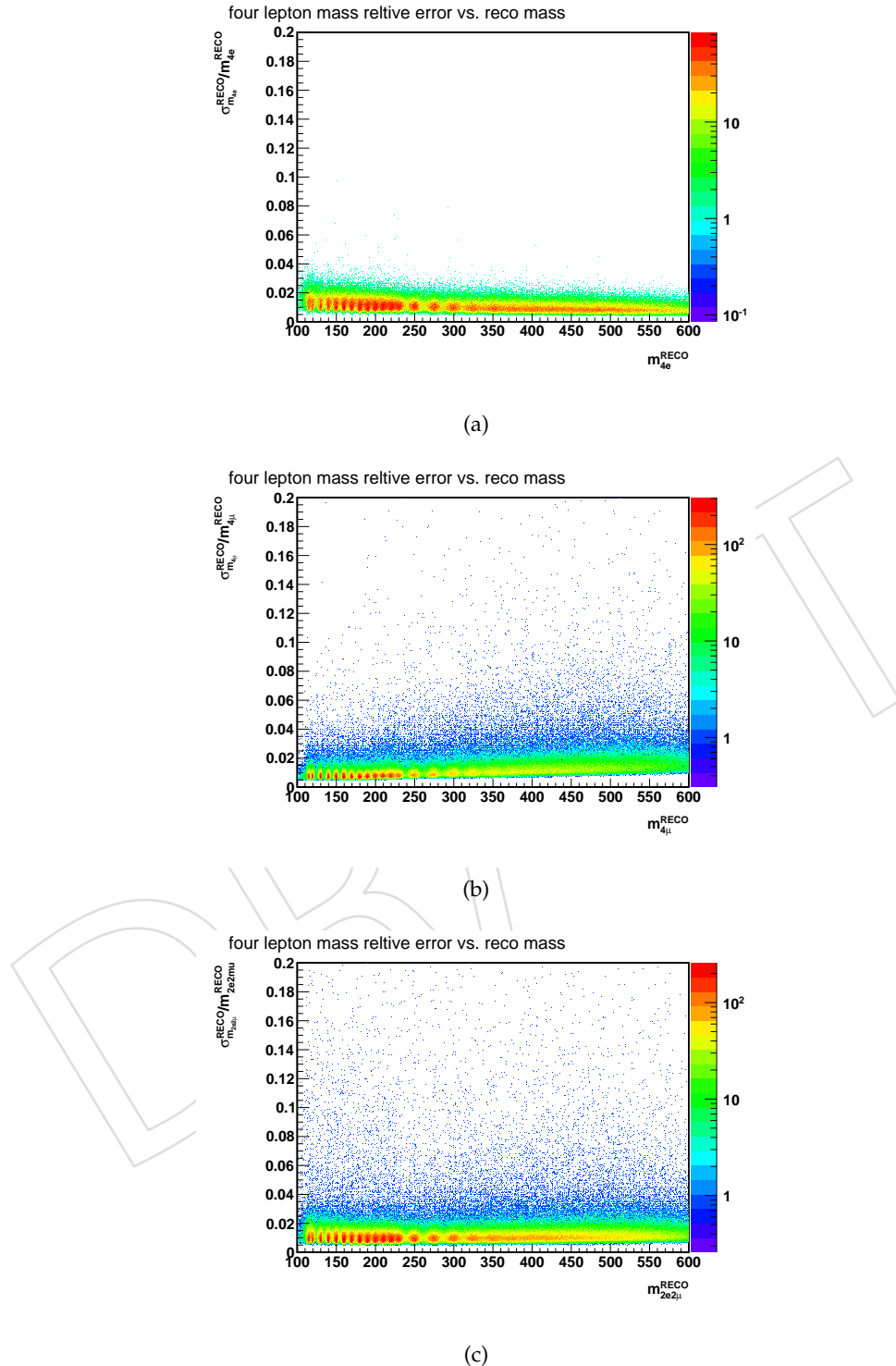


Figure 65: Expected Higgs boson mass resolutions versus Higgs candidates reconstructed mass. Three plots are for the three final states: $4e$ (a), 4μ (b) and $2e2\mu$ (c).

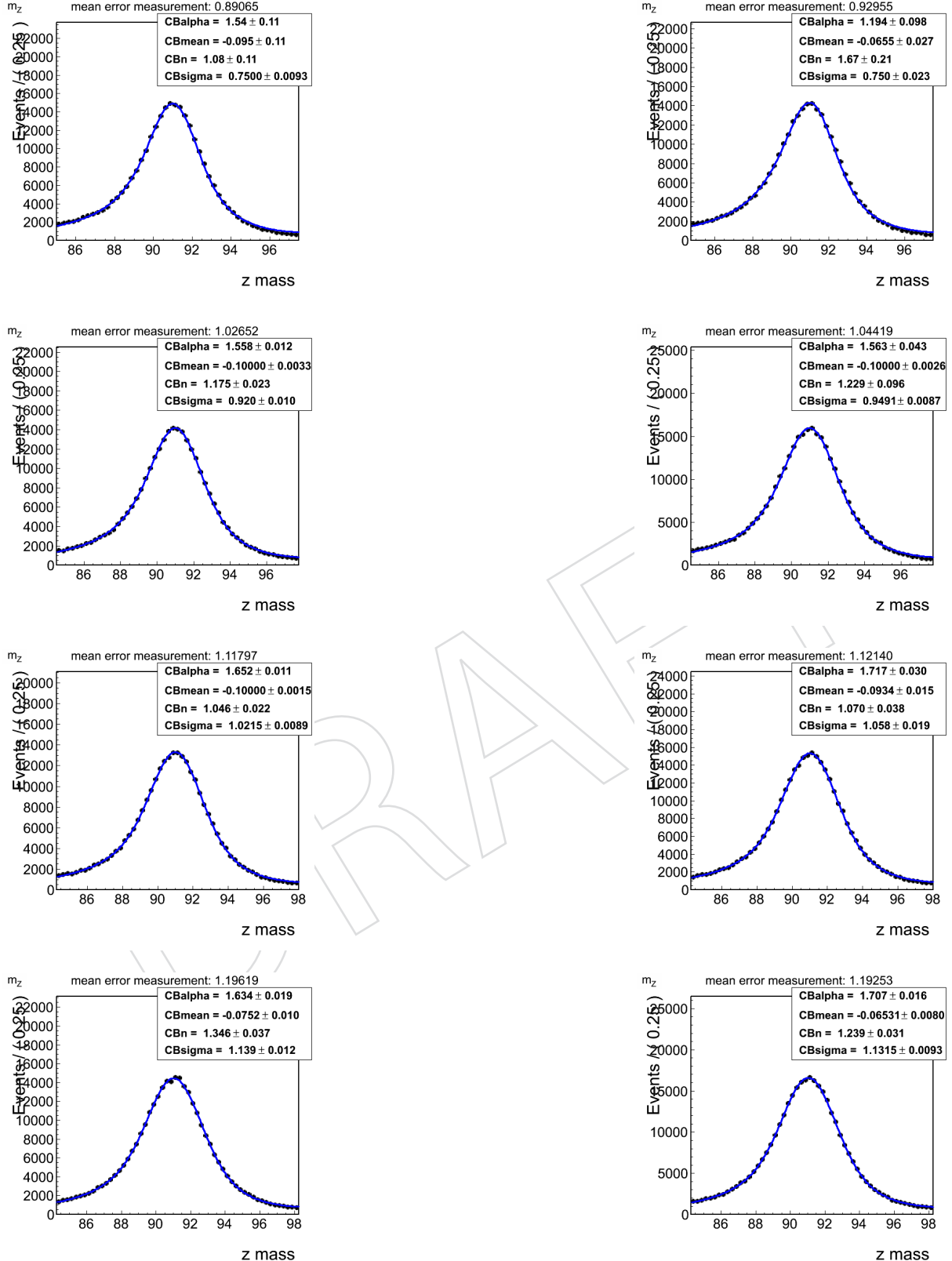


Figure 66: Di-muon invariant mass spectrum (points) and fits with convoluted function of Breit-Wigner and Crystal Ball for data (left) and MC (right) Z events. From top to bottom correspond to the four categories which are based on the predicted mass resolution.

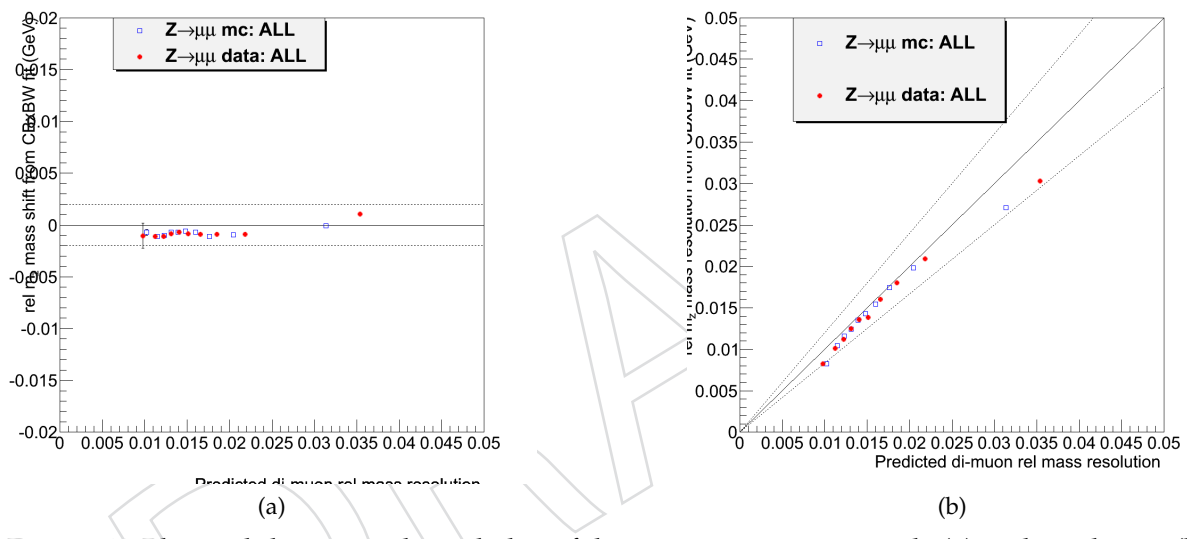


Figure 67: Plots validating our knowledge of the muon momentum scale (a) and resolution (b).

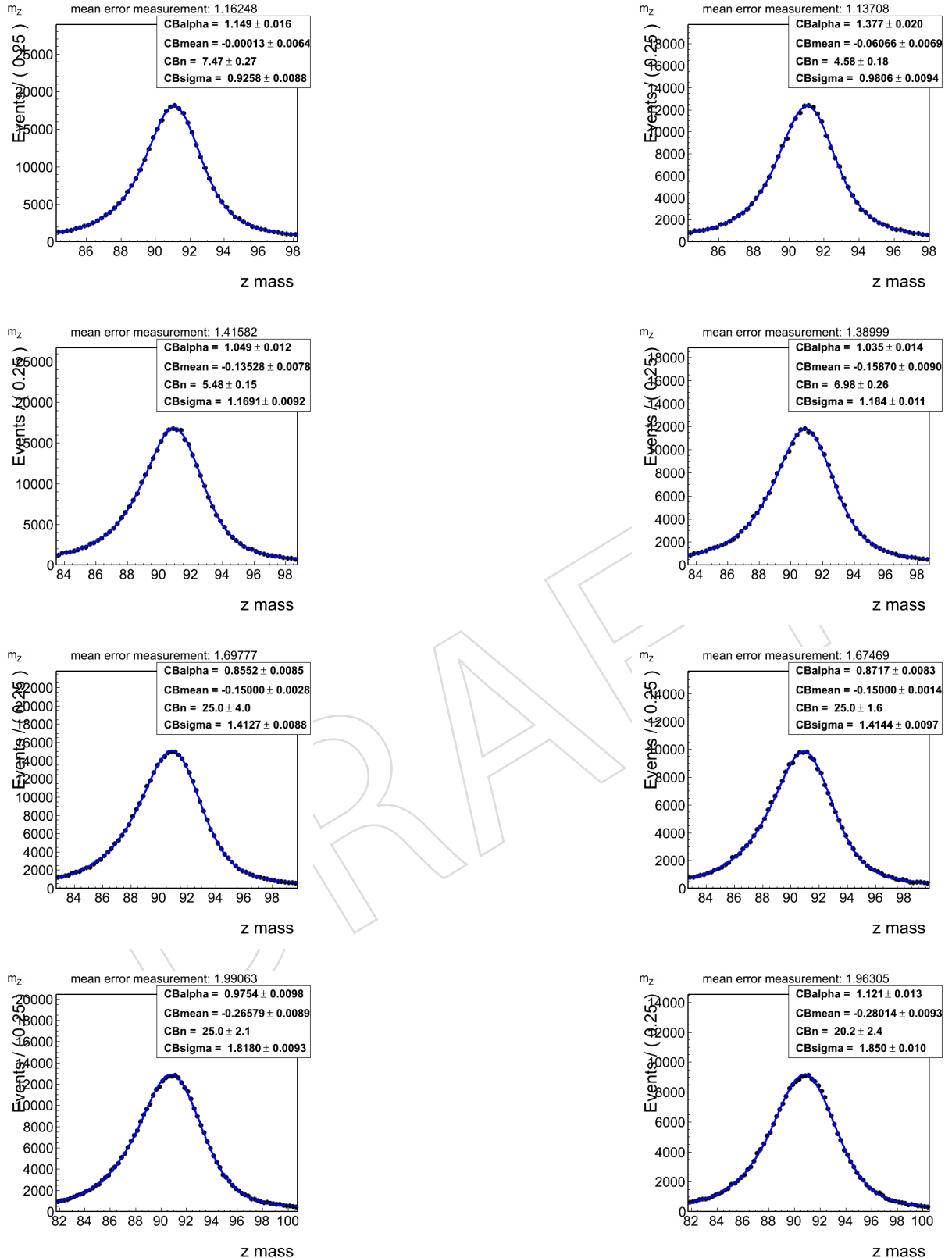


Figure 68: Di-electron invariant mass spectrum (points) and fits with convoluted function of Breit-Wigner and Crystal Ball for data (left) and MC (right) Z events. From top to bottom correspond to the four categories which are based on the predicted mass resolution.

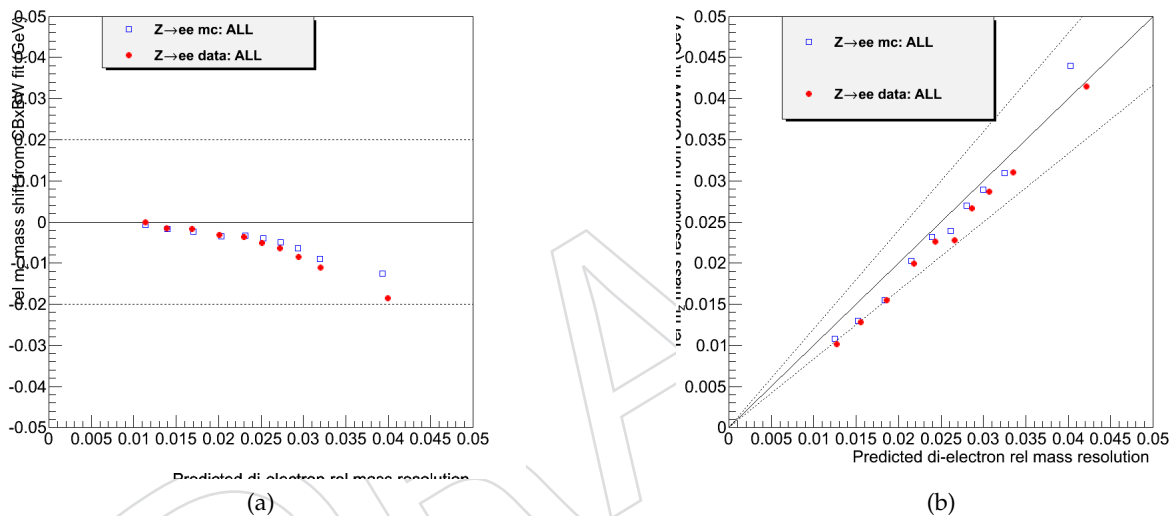


Figure 69: Plots validating our knowledge of the electron momentum scale (a) and resolution (b).

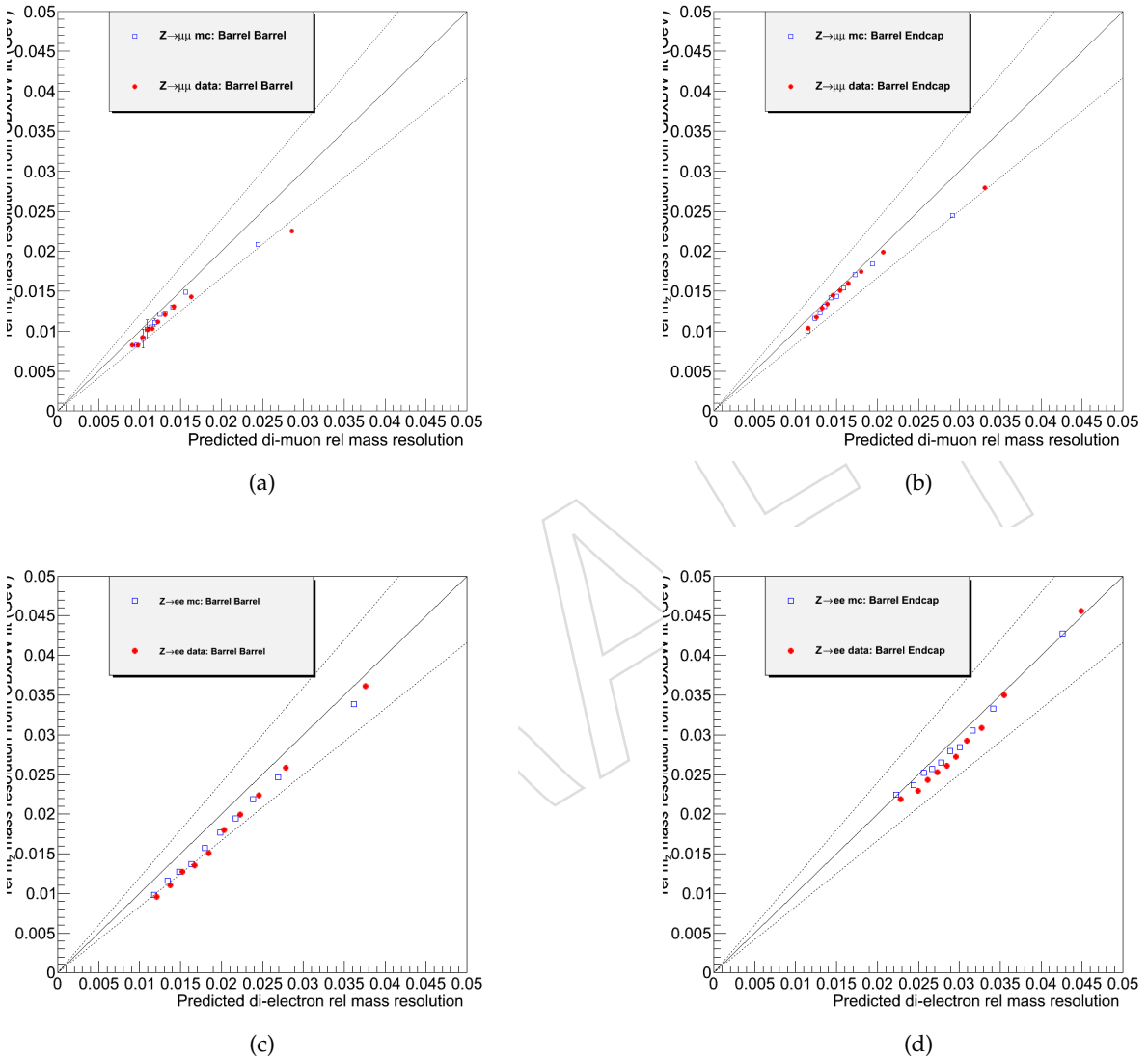


Figure 70: Plots validating our knowledge of the muon (top) and electron (bottom) momentum resolution for Barrel-Barrel (left) and Barrel-Endcap (right) categories.

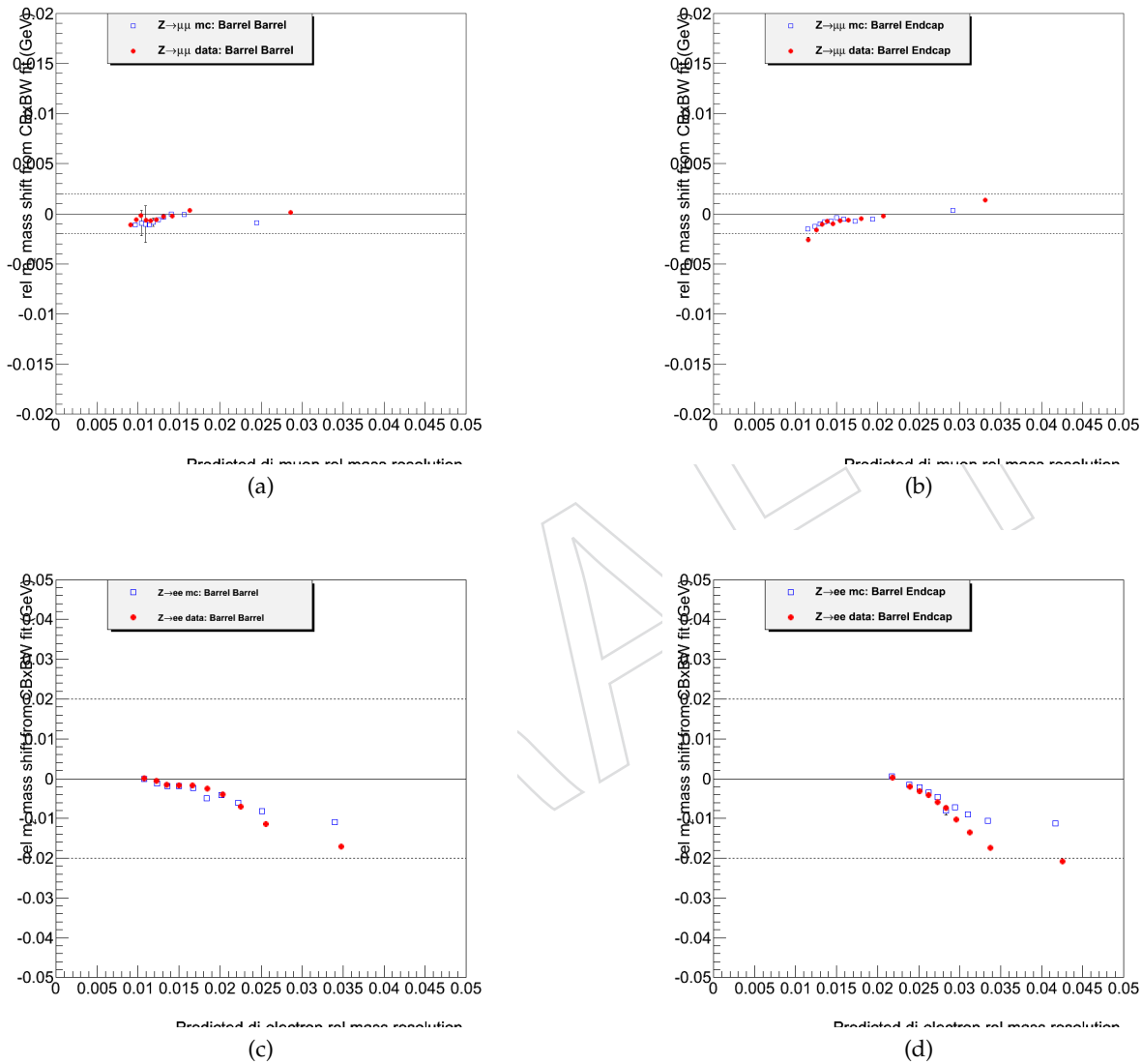


Figure 71: Plots validating our knowledge of the muon (top) and electron (bottom) mass scale shift for Barrel-Barrel (left) and Barrel-Endcap (right) categories.

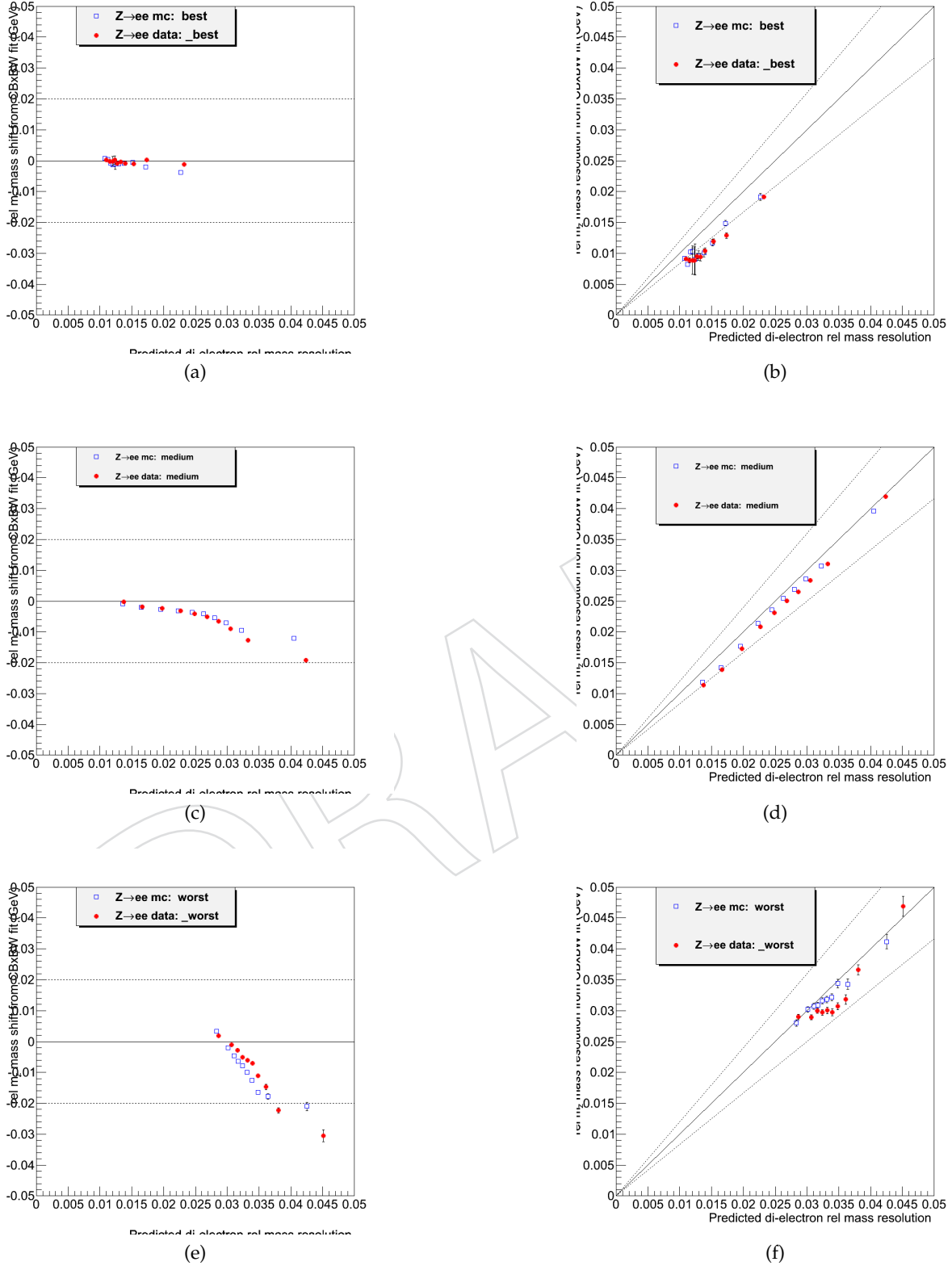


Figure 72: Plots validating our knowledge of the electron momentum resolution for best (top), medium (middle) and worst (bottom) categories. Left for mass scale shift and right for resolution.

7.4.8 Closure test on Higgs to four lepton events after p_T error correction

As seen in the previous section, the measured and predicted resolution have good agreement which are safely within the 20% uncertainty, validating the per-event error and correction factor for per-lepton p_T error. Then the question becomes whether the closure test becomes better including the per-lepton p_T error correction. In the following, we use the Higgs sample at 125GeV as an example to demonstrate the improved closure between predicted and measured resolution.

As shown in figure 73, the predicted and measured resolution have better agreement after the per-lepton p_T error correction.

7.4.9 Looking into the four-lepton control regions

The closure test on the Higgs MC samples indicate that the predicted resolution has good agreement with the measured resolution with 20% systematic uncertainty. Now the question becomes whether data and MC agree on the mass error distribution for four-lepton system. To answer this question, the error distributions in several control region are investigated.

1. $Z \rightarrow 4L$ control region As discussed in the $Z \rightarrow 4L$ section, the decays give a clean resonant peak in the four-lepton invariant mass distribution, which can be used as a standard candle in the context of the Higgs boson search in the four-lepton decay mode. The figure 74 shows the distribution of relative mass error distribution for data and MC in mass window [80-100GeV].
2. $ZZ \rightarrow 4L$ control region The four-lepton mass window is chosen to be [180-200GeV] as shown in figure 75, where the dominant events are expected to be di-boson decay.
3. $Z+X$ control region The relative mass error distribution in 2 Prompt + 2 Fail region is shown in figure 76 for mass window [110-130GeV]. The simulation and data have reasonable agreement.

7.4.10 MC based expectations of 4ℓ events

Figure 77 shows the MC-predicted $m_{4\ell}$ mass resolution versus reconstructed mass for $H \rightarrow ZZ \rightarrow 4\ell$ Monte Carlo samples. The plots are obtained for the CMSSW 4.2 MC samples.

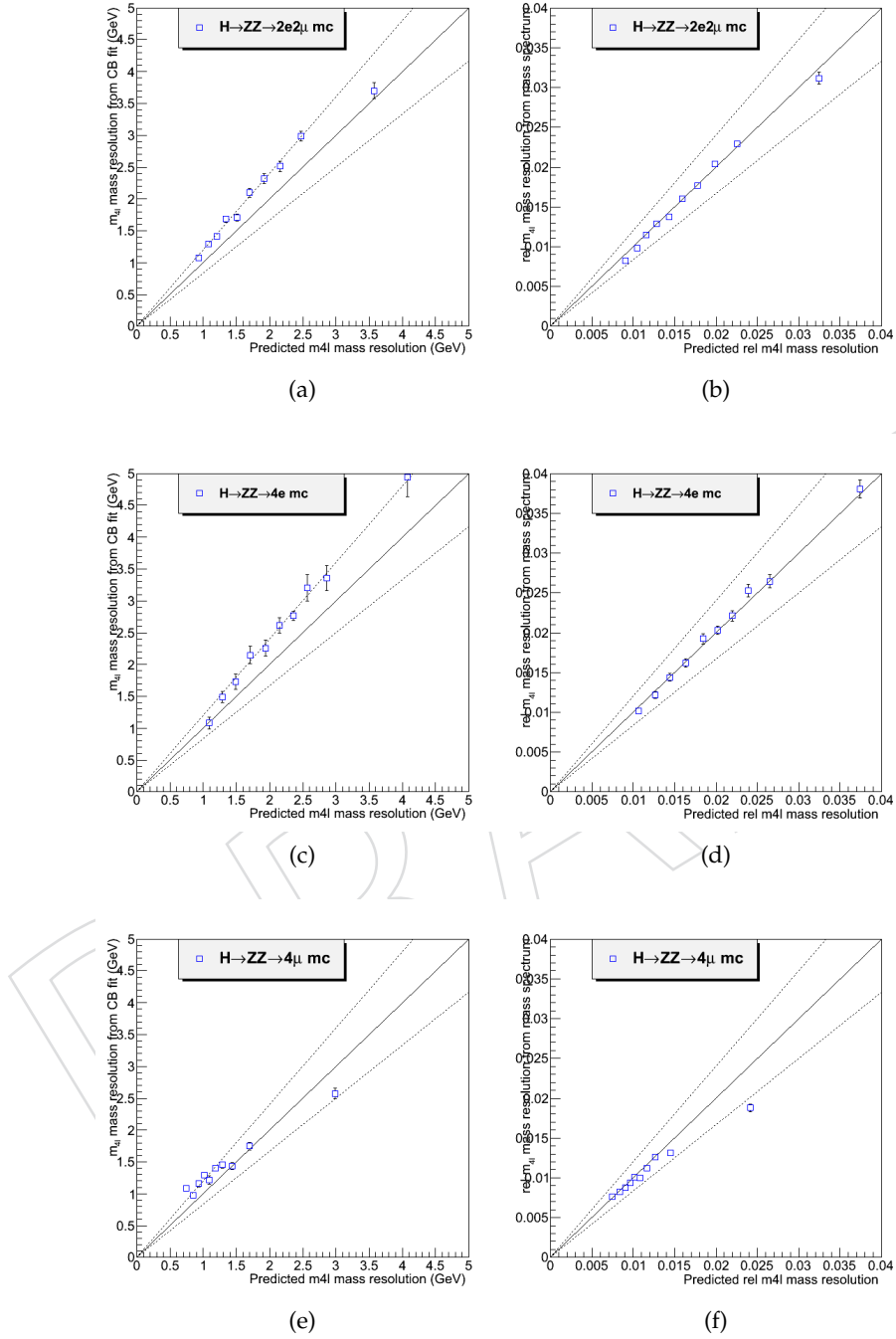


Figure 73: Left column: the correlation between measured and predicted resolution using mass error without any per-lepton pT error correction; right column: the correlation between measured and predicted resolution using mass error including per-lepton pT error correction for muons and electrons

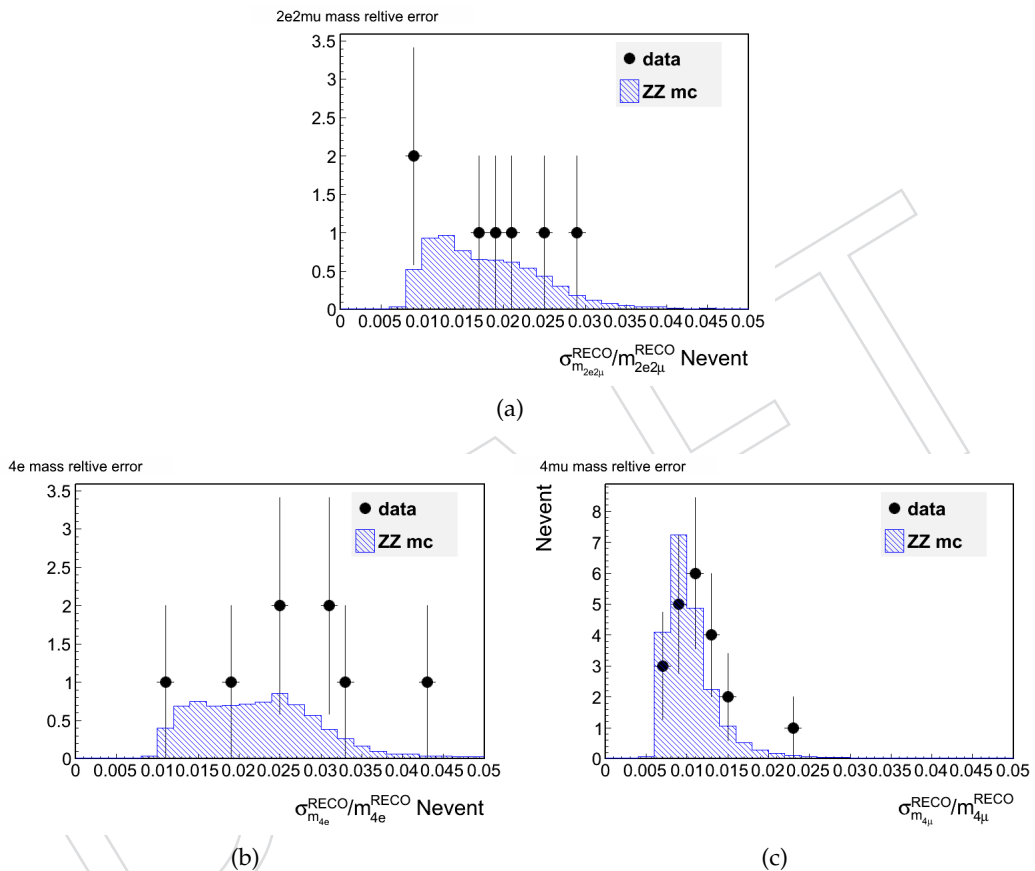


Figure 74: Relative mass error distribution for data and mc in $Z \rightarrow 4L$ region m_{4l} in [80-100GeV]: a) 2e2mu b) 4e c) 4mu

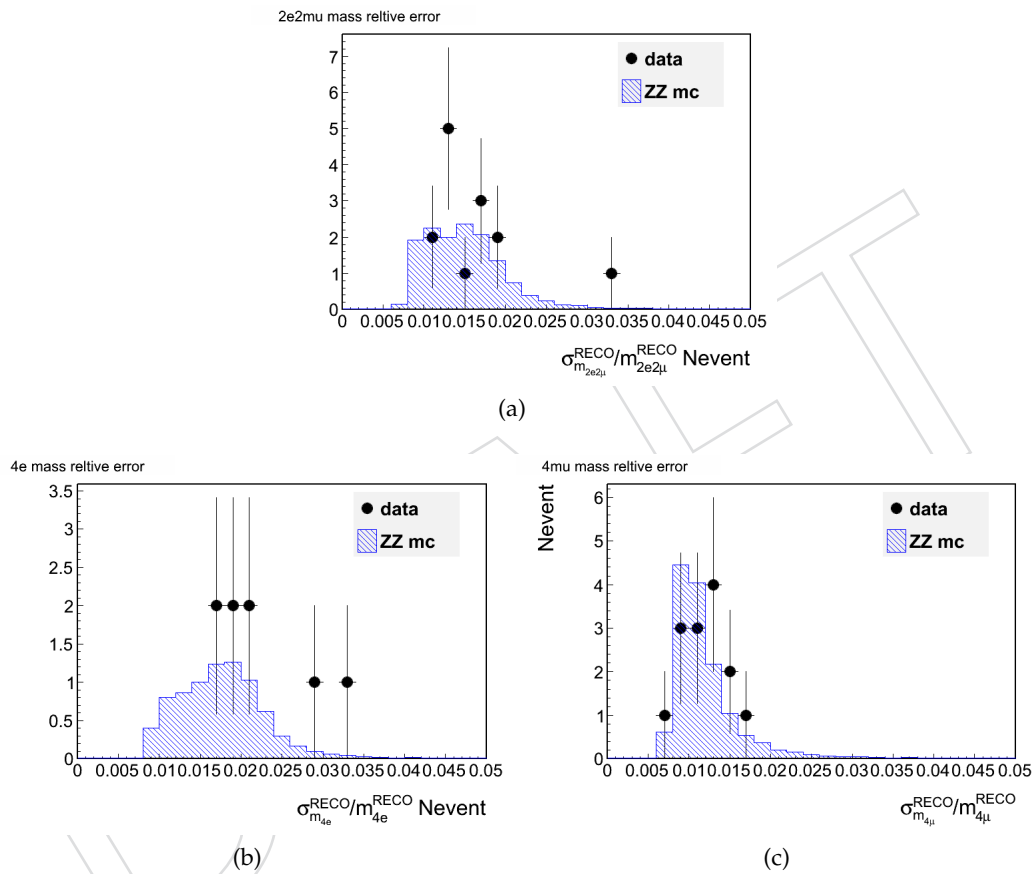


Figure 75: Relative mass error distribution for data and mc in $Z \rightarrow 4L$ region m_{4l} in [180-200GeV]: a) 2e2mu b) 4e c) 4mu

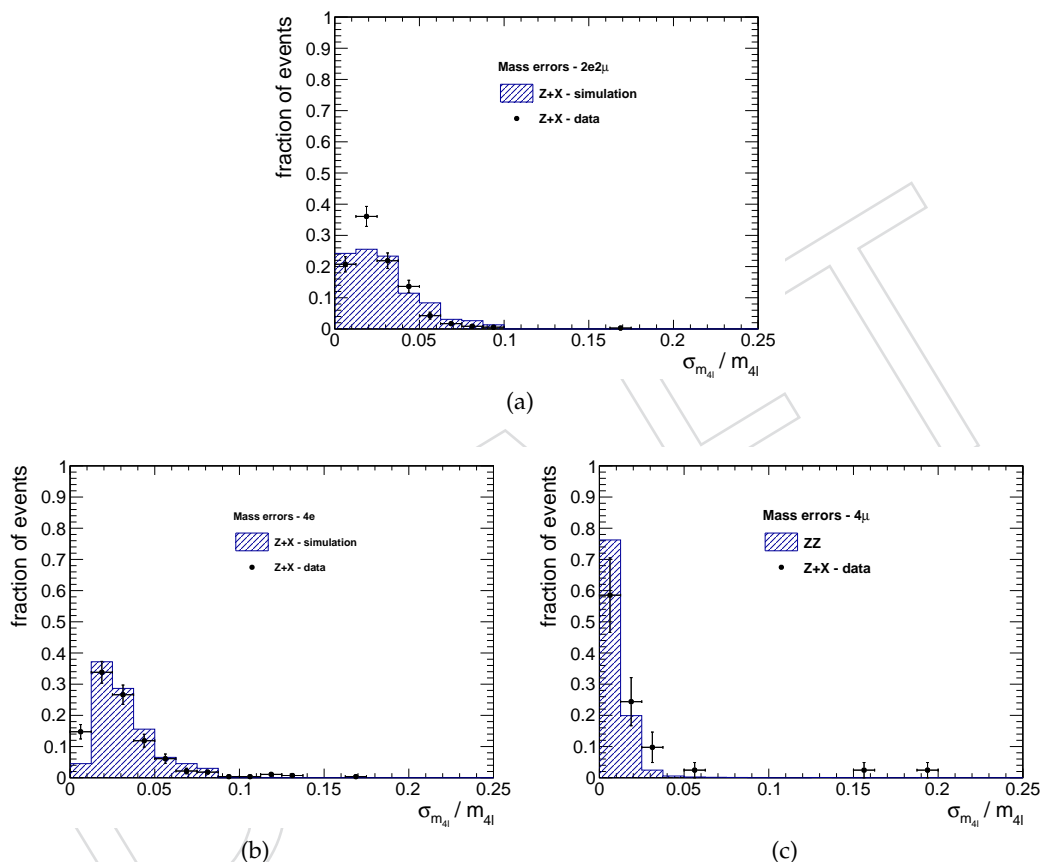


Figure 76: Relative mass error distribution for data and mc in $Z+X$ control region m_{4l} in [110-130GeV]: a) 2e2 μ b) 4e c) 4 μ

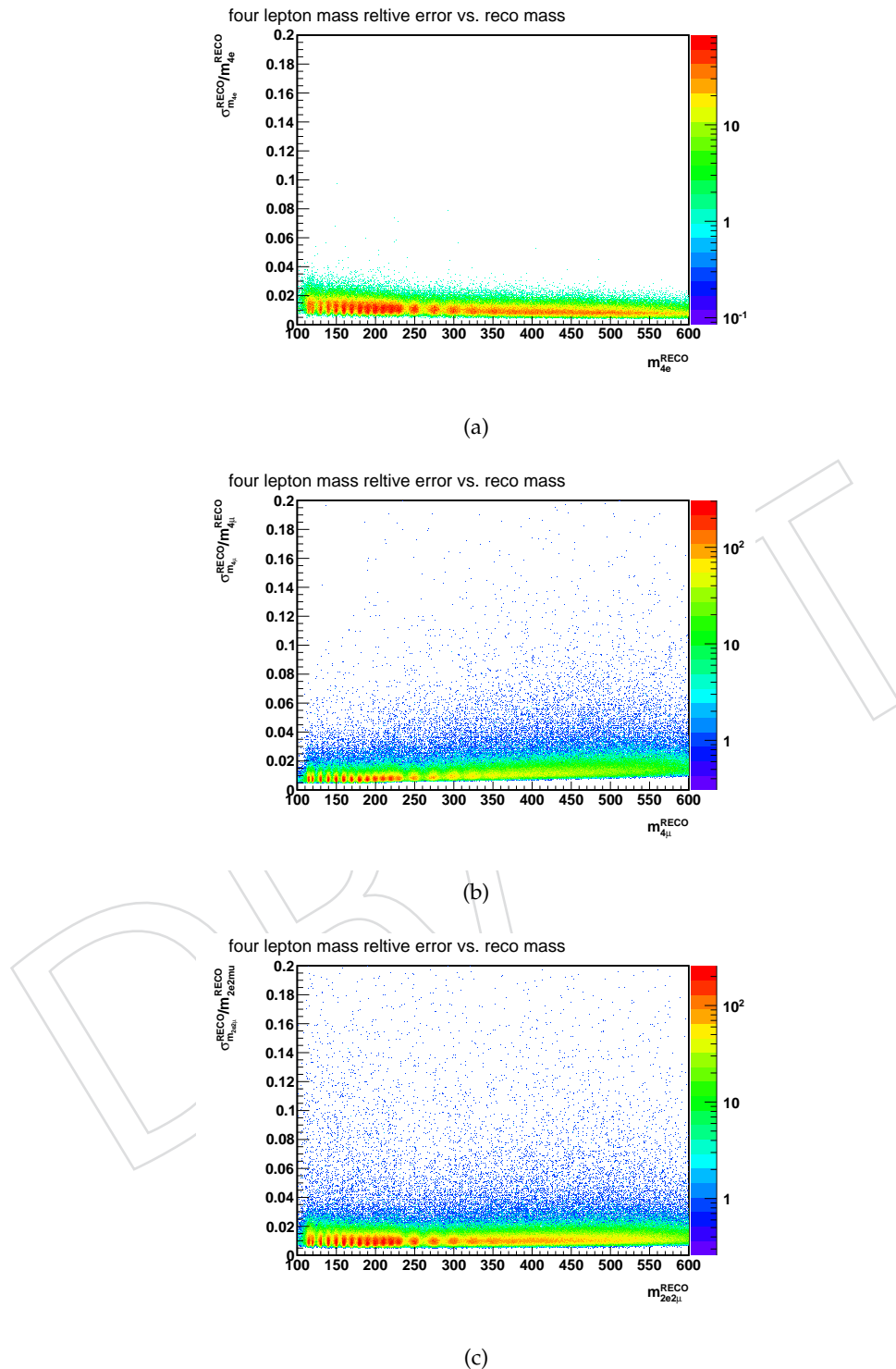


Figure 77: NEED UPDATE Expected Higgs boson mass resolutions versus Higgs candidates reconstructed mass. Three plots are for the three final states: $4e$ (a), 4μ (b) and $2e2\mu$ (c).

1547 7.4.11 Systematics

1548 Currently we assign 20% uncertainty on the mass resolution according to the data driven validation
1549 studies. Including electron regression energy correction and muon Rochester scale correction and so on
1550 will improve the systematics uncertainties. One need to be carefull not to overestimate the uncertainty
1551 as it may not be conservative. One should look at the data/MC residual differences and assign proper
1552 uncertainties.

1553 7.4.12 Results

1554 Figure 78 shows $m_{4\ell}$ mass resolutions for the observed $4e$, 4μ , and $2e2\mu$ events in the low mass region.
1555 Figure 79 shows the comparison of errors obtained in data with two approaches separately. Good agree-
1556 ment between two approaches can be seen.

DRAFT

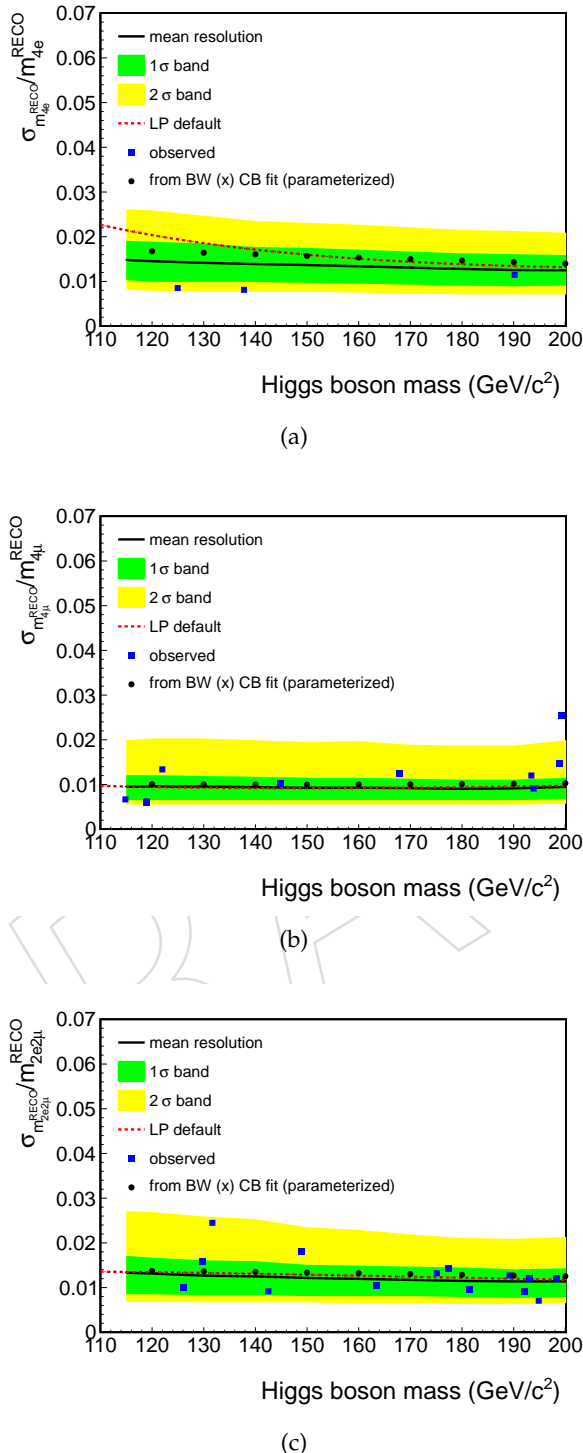
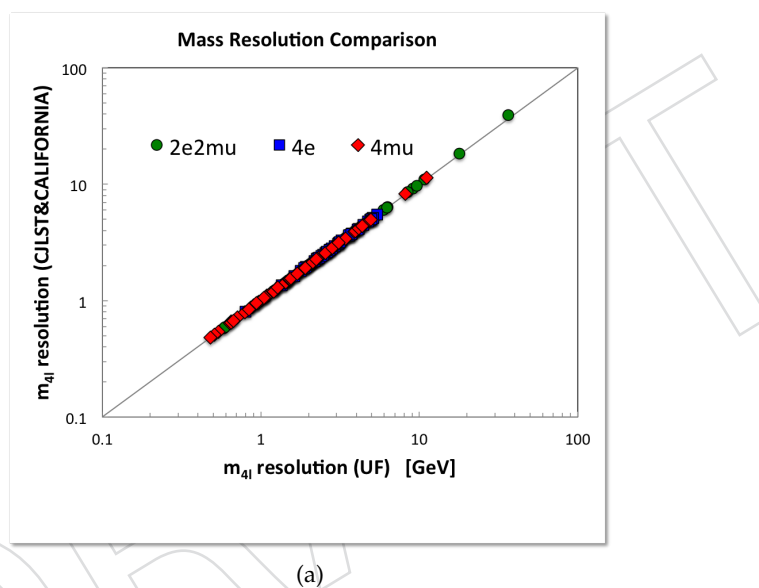


Figure 78: Zoom at the mass resolutions of the observed low mass events (squares). The green (yellow) band indicates the range expected to contain 68% (95%) of all events. The black solid line is the median resolution in MC. The dotted red line is the resolution used in AN-11-123. Three plots are for the three final states: 4e (a), 4μ (b) and 2e2μ (c).



(a)

Figure 79: Comparison of mass errors of observed data events between two independent approaches.

1557 8 Irreducible ZZ Background Model and uncertainties

1558 8.1 ZZ^(*) yields

The expected rate in any given mass range $[m_1, m_2]$ is obtained directly from the absolute rate predicted by the MC model simulation:

$$N_{\text{expect}}^{\text{ZZ}} [m_1, m_2] = \int_{m_1}^{m_2} \left(\frac{dN}{dm_{4\ell}} \right)_{\text{MC}} dm_{4\ell} \quad (16)$$

1559 When used for comparisons with data, the method is affected by the full systematics uncertainties on
 1560 the pp integrated luminosity and the theory errors as well as systematic errors on acceptance within
 1561 analysis cuts.

1562 8.2 ZZ^(*) Background Model

The $pp \rightarrow ZZ \rightarrow 4\ell$ backgrounds (NLO and $gg \rightarrow ZZ$) are modeled using the functional form very similar to that of the signal:

$$\text{ZZ@NLO} : \frac{dN}{dm_{4\ell}} = C(m_{4\ell}) \cdot N^{\text{MC}}(m_{4\ell}) \cdot F_{\text{ZZNLO}}(m_{4\ell}), \quad (17)$$

$$\text{gg} \rightarrow \text{ZZ} : \frac{dN}{dm_{4\ell}} = C(m_{4\ell}) \cdot N^{\text{MC}}(m_{4\ell}) \cdot F_{\text{gg2ZZ}}(m_{4\ell}). \quad (18)$$

1563 where the overall data-to-MC correction factors $C(m_{4\ell})$ are assumed to be the same as for the Higgs
 1564 events with $m_H = m_{4\ell}$. The validity of this assumption is addressed later in section on systematic
 1565 errors.

1566 The functions $F_{\text{ZZNLO}}(m_{4\ell})$ and $F_{\text{gg2ZZ}}(m_{4\ell})$ are parameterized separately for $4e$, 4μ , and $2e2\mu$ using the
 1567 simulated distributions as follows:

$$f_1(m, \vec{a}) = \left(0.5 + 0.5 \text{erf} \left(\frac{m - a_1}{a_2} \right) \right) \cdot \frac{a_4}{1 + e^{(m-a_1)/a_3}} \quad (19)$$

$$f_2(m, \vec{b}) = \left(0.5 + 0.5 \text{erf} \left(\frac{m - b_1}{b_2} \right) \right) \cdot \left(\frac{b_4}{1 + e^{(m-b_1)/b_3}} + \frac{b_6}{1 + e^{(m-b_1)/b_5}} \right) \quad (20)$$

$$f_3(m, \vec{c}) = \left(0.5 + 0.5 \text{erf} \left(\frac{m - c_1}{c_2} \right) \right) \cdot \frac{c_4}{1 + e^{(m-c_1)/c_3}} \quad (21)$$

$$F_{\text{ZZNLO}}(m, \vec{a}, \vec{b}, \vec{c}) = f_1 + f_2 + f_3 \quad (22)$$

$$F_{\text{gg2ZZ}}(m, \vec{a}, \vec{b}, \vec{c}) = f_1 + f_2 \quad (23)$$

1568 The ZZ background shape fits are shown in Fig. 80. We do not find any systematic uncertainties that
 1569 would distort the ZZ $\rightarrow 4\ell$ mass distributions in a substantial way over the mass range corresponding to
 1570 the Higgs boson width. Therefore, all uncertainties on the ZZ-background are included as uncertainties
 1571 in normalization, whose absolute scale may depend on the Higgs boson mass m_H being probed in the
 1572 search.

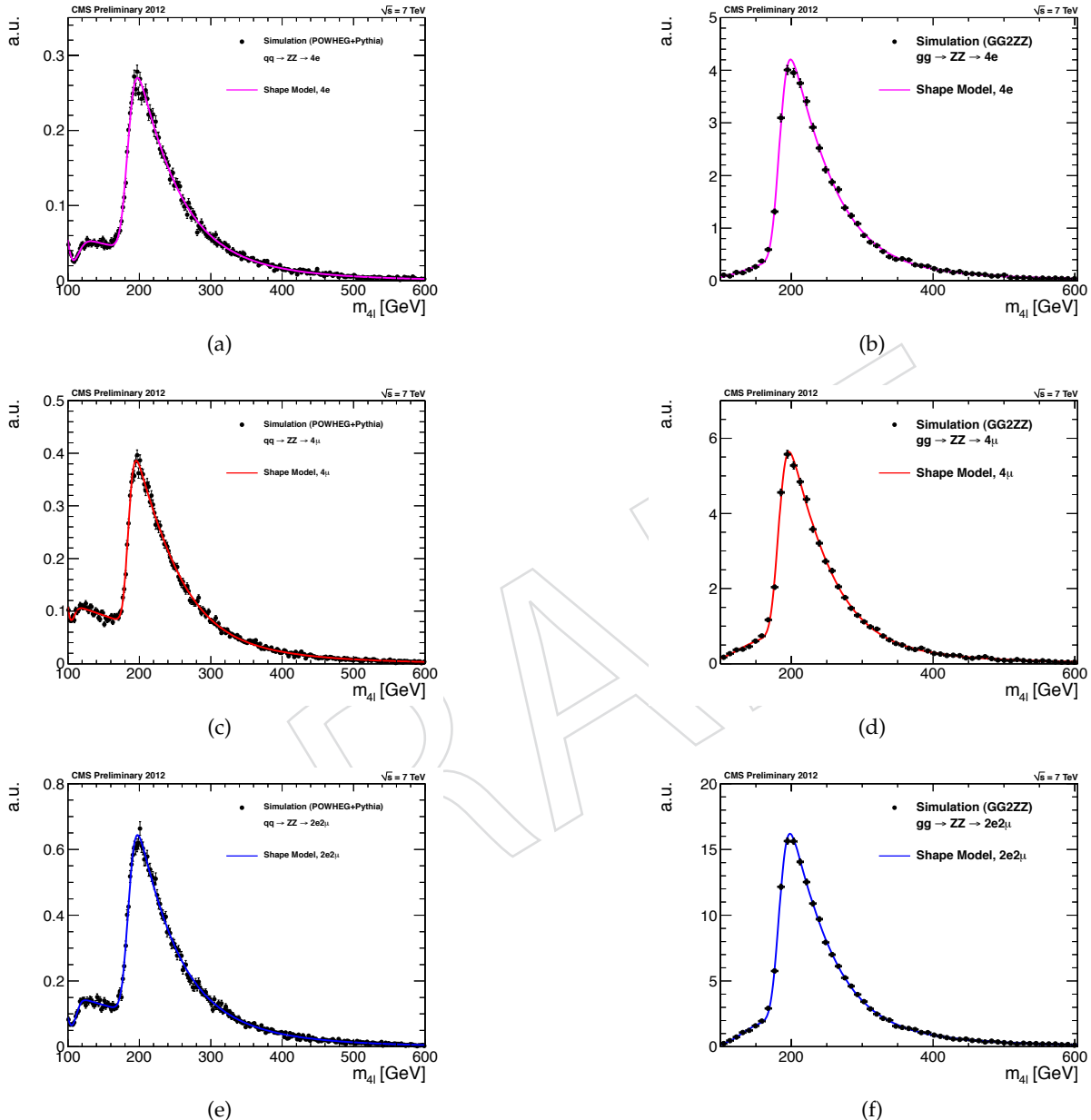


Figure 80: Probability density functions describing the NLO ZZ (left) and $gg \rightarrow ZZ$ (right) background shape for $4e$ (top), 4μ (middle), and $2e2\mu$ (bottom) final states. Center of mass energy is 7 TeV .

1573 **8.3 ZZ^(*) model uncertainties**

1574 **8.3.1 Theoretical uncertainties**

1575 **Event yield uncertainties as a function of $m_{4\ell}$**

1576 PDF+ α_s and QCD scale uncertainties for $pp \rightarrow ZZ \rightarrow 4\ell$ at NLO and $gg \rightarrow ZZ \rightarrow 4\ell$ are evaluated
 1577 using MCFM [64]. We use the $2e2\mu$ final state and the following fiducial cuts for leptons: $m_{ee} > 12$,
 1578 $m_{\mu\mu} > 12$, electrons' $p_T > 7$ and $|\eta| < 2.5$, and muons' $p_T > 5$ and $|\eta| < 2.4$. The minimal jet-lepton and
 1579 lepton-lepton ΔR_{min} -distance were relaxed, i.e. set to zero. The cross sections are calculated inclusively
 1580 in the number of jets found at NLO. The uncertainties are assessed both for 7 TeV and 8 TeV. Per Ref. [?]
 1581], the PDF+ α_s and QCD scale uncertainties are treated as uncorrelated. However, uncertainties between
 1582 7 TeV and 8 TeV are assumed 100% correlated.

1583 For estimation of the PDF+ α_s systematic errors, we use the PDF4LHC prescription [59]. The three
 1584 PDF sets used are CT10 [60], MSTW08 [61], NNPDF [62]. The obtained results are summarized in
 1585 Figs. 81. The four-lepton mass dependent PDF+ α_s systematic errors, for both 7 TeV and 8 TeV, can be
 1586 parametrized as follows:

$$\text{ZZ@NLO : } \kappa(m_{4\ell}) = 1 + 0.0035\sqrt{(m_{4\ell} - 30)} \quad (24)$$

$$gg \rightarrow \text{ZZ} : \kappa(m_{4\ell}) = 1 + 0.0066\sqrt{(m_{4\ell} - 10)} \quad (25)$$

1587 For estimation of QCD scale systematic errors, we calculate variations in the differential cross section
 1588 $d\sigma/dm_{4\ell}$ as we change the renormalization and factorization scales by a factor of two up and down from
 1589 their default setting $\mu_R = \mu_F = m_Z$. The obtained results are summarized in Fig. 82. The four-lepton
 1590 mass dependent QCD scale systematic errors, for both 7 TeV and 8 TeV, can be parametrized as follows:

$$\text{ZZ@NLO : } \kappa(m_{4\ell}) = 1.00 + 0.01\sqrt{(m_{4\ell} - 20)/13} \quad (26)$$

$$gg \rightarrow \text{ZZ} : \kappa(m_{4\ell}) = 1.04 + 0.10\sqrt{(m_{4\ell} + 40)/40} \quad (27)$$

1591 **Shape uncertainties**

1592 The shape uncertainties in $m_{4\ell}$ distribution imply the knowledge of correlations between possible event
 1593 yield variations at different $m_{4\ell}$ points. For simplicity, we assume 100% correlations between errors
 1594 across the entire $m_{4\ell}$ mass range.

1595 For a given test Higgs boson mass M_H , the signal is a localized peak in the $m_{4\ell}$ distribution. We do
 1596 not expect large variations in signal shape in the narrow regions under the Higgs boson peak, which is
 1597 confirmed by looking at the local shape changes due to QCD scale PDF variations. This holds true even
 1598 for the high mass Higgs boson.

1599 The knowledge of correlation of the background under the signal peak and far outside in sidebands is
 1600 relevant for the signal inference only if the sidebands have a sufficient statistical power to constrain the
 1601 prior-to-the-experiment uncertainties. This is not the case in this analysis with the current amount of
 1602 data. With $\mathcal{O}(70)$ observed $ZZ \rightarrow 4\ell$ events, the statistical error is about 12%, which is larger than the
 1603 current theoretical error of 5%.

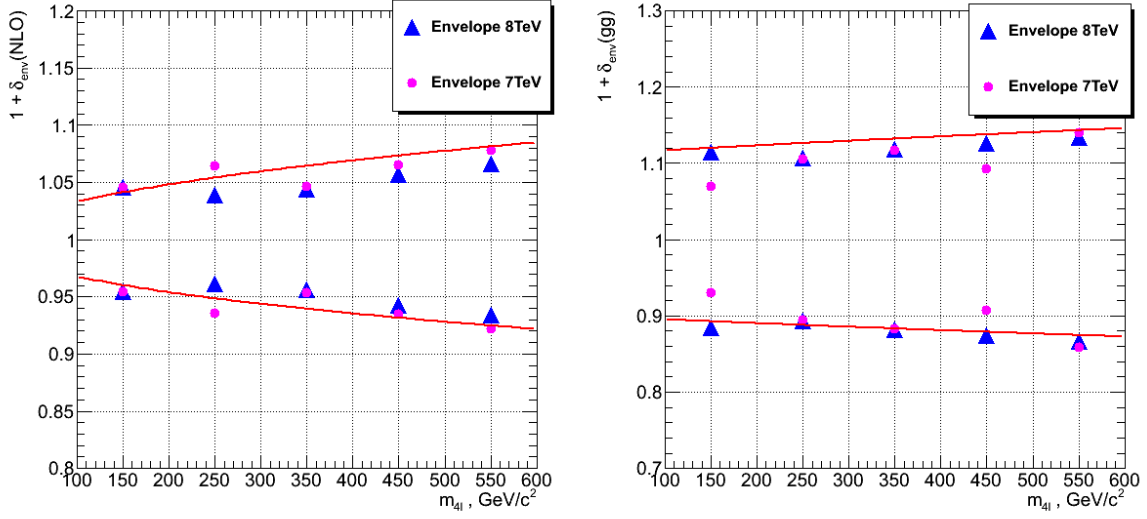


Figure 81: PDF+ α_s uncertainties for (left) $pp \rightarrow ZZ \rightarrow 4\ell$ at NLO and (right) $gg \rightarrow ZZ \rightarrow 4\ell$ processes. The points are evaluated uncertainties. The curves are the fit systematic error $\kappa(m_{4\ell})$ to be used in the statistical analysis. These errors are driven by two independent nuisance parameters pdf_qqbar for $pp \rightarrow ZZ \rightarrow 4\ell$ at NLO and pdf_gg for $gg \rightarrow ZZ \rightarrow 4\ell$.

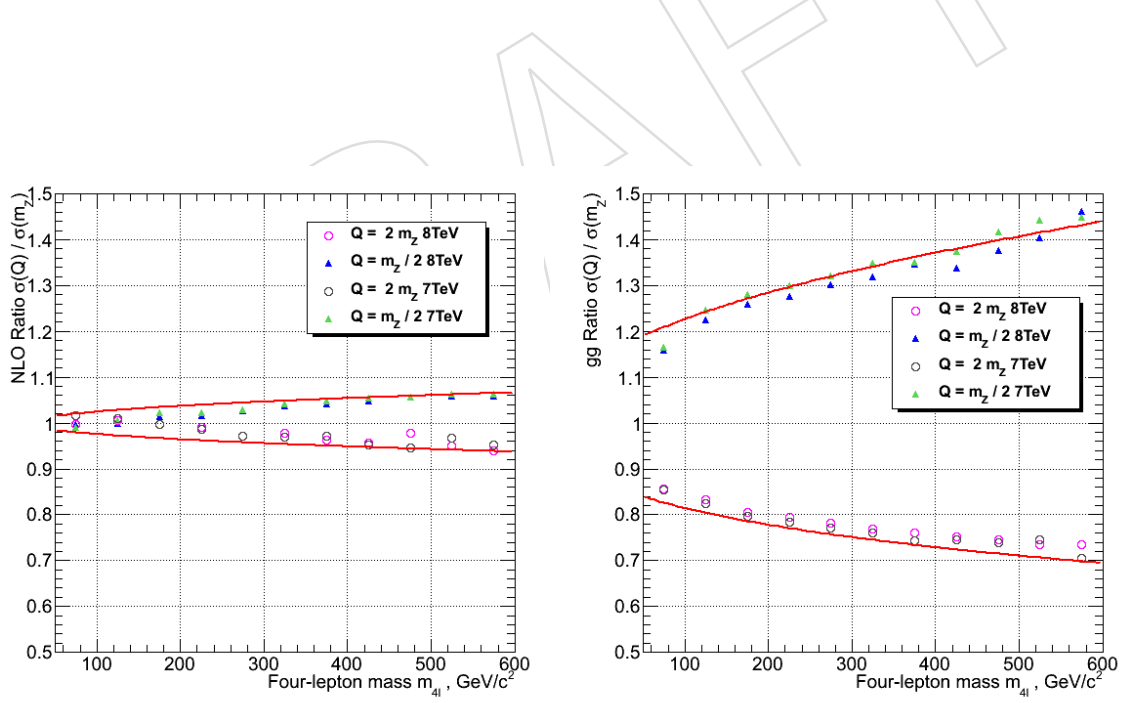


Figure 82: QCD scale uncertainties for (left) $pp \rightarrow ZZ \rightarrow 4\ell$ at NLO and (right) $gg \rightarrow ZZ \rightarrow 4\ell$ processes. The points are evaluated uncertainties. The curves are the fit systematic error $\kappa(m_{4\ell})$ to be used in the statistical analysis. These errors are driven by two independent nuisance parameters $QCDscale_VV$ for $pp \rightarrow ZZ \rightarrow 4\ell$ at NLO and $QCDscale_ggVV$ for $gg \rightarrow ZZ \rightarrow 4\ell$.

1604 **8.3.2 Instrumental uncertainties**

DRAFT

9 Reducible Background Model and Systematic Uncertainties

9.1 Reducible background prediction

The methods used to estimate reducible background is un-changed with respect to [20, 21]. The main strategy is repeated and updated results are shown.

The reducible backgrounds for the $H \rightarrow ZZ \rightarrow 4\ell$ analysis are processes which contain one or more non-prompt leptons in the four-lepton final state. The main sources of non-prompt leptons are non-isolated electrons and muons coming from decays of heavy-flavour mesons, mis-reconstructed jets (usually originating from light-flavour quarks) and electrons from γ conversions. In the further discussion, we will consider “fake lepton” any jet mis-reconstructed as a lepton and any lepton originating from a heavy meson decay. In a similar way, any electron originating from a photon conversion will be considered “fake electron”.

In the $H \rightarrow ZZ \rightarrow 4\ell$ analysis the rate of these backgrounds processes is estimated by measuring the probability for fake electrons f_e and fake muons f_μ which do pass predefined loose selection criteria to also pass the final selection criteria. These probabilities are applied in dedicated control samples in order to extract the background yield expected in the signal region. We will refer to these probabilities as fake ratios.

The loose lepton selection criteria are described in Section 6. In addition, the leptons should pass the $SIP_{3D} < 4$ criteria of the analysis. The cross-cleaning defined in 6 for electrons is applied.

9.1.1 Tight-to-loose ratios in Z+1L

In order to measure the lepton fake ratios f_e, f_μ , we select samples of $Z(\ell\ell) + e$ and $Z(\ell\ell) + \mu$ events that are expected to be completely dominated by final states which include a Z boson and a fake lepton. These events are required to have two same flavour, opposite charge leptons with $p_T > 20/10$ GeV passing the tight selection criteria, thus forming the Z candidate. In addition, there is exactly one lepton passing the loose selection criteria as defined above. This lepton is used as the probe lepton for the fake ratio measurement. The invariant mass of this lepton and the opposite sign lepton from the reconstructed Z candidate should satisfy $m_{2l} > 4$ GeV. Each event is required to have missing transverse energy $E_T^{\text{miss}} < 25$ GeV to suppress contamination due to prompt leptons from WZ and $t\bar{t}$ processes.

Two complementary approaches are considered while evaluating and applying the fake ratios. In one approach (used in Method A described below) the fake ratios are evaluated using a tight requirement of $|M_{inv}(\ell_1, \ell_2) - M_Z| < 10$ GeV to reduce the bias in the fake ratios from photon (asymmetric) conversions populating low $m_{\ell\ell}$. This approach allows measurement of the tight-to-loose ratios for the “true” fake leptons. In the second approach (used in Method AA described below) the tight-to-loose ratios are measured by using a relaxed invariant mass requirement of $40 \text{ GeV} < M_{inv}(\ell_1, \ell_2) < 120 \text{ GeV}$ which is consistent with the dilepton invariant mass requirement in the Higgs selection. This is done to have a background composition in the fake rate sample which is similar to the expected reducible background composition in the signal region.

The measured differential p_T distributions of the fake ratios using the tight Z mass requirement of $|M_{inv}(\ell_1, \ell_2) - M_Z| < 10$ GeV are shown in Figure 83. Figure 84 shows the fake ratios as a function of p_T on relaxing the Z mass requirement to $40 \text{ GeV} < M_{inv}(\ell_1, \ell_2) < 120 \text{ GeV}$. It can be observed that the fake ratios show dependance on the lepton p_T - in particular, the fake ratios increase in the region of high p_T . This effect is in part caused by the fact that the criteria used to suppress the WZ and $t\bar{t}$ processes are not efficient in this region of p_T .

The dependance of the fake ratios on the exact composition of background processes in a region of interest is one of the main sources of the systematic uncertainties of the method. The procedures to estimate these systematic effects in data and simulation will be discussed in the section 9.2.

As it can be appreciated on 84, the fake ratios are not showing significant difference between 2012 A+B (ICHEP) and 2012 C (post-ICHEP) data taking periods. The final estimation of reducible background in the 8 TeV analysis is therefore performed using fake ratios measured on the full 2012 A+B+C period.

1653 Moreover, it is to be noted that the muon fake ratios slightly increased with respect to the ICHEP analysis
 1654 (see Figures 85) due to the new the additional ghost cleaning using shared segments (see Section 3.2.3).

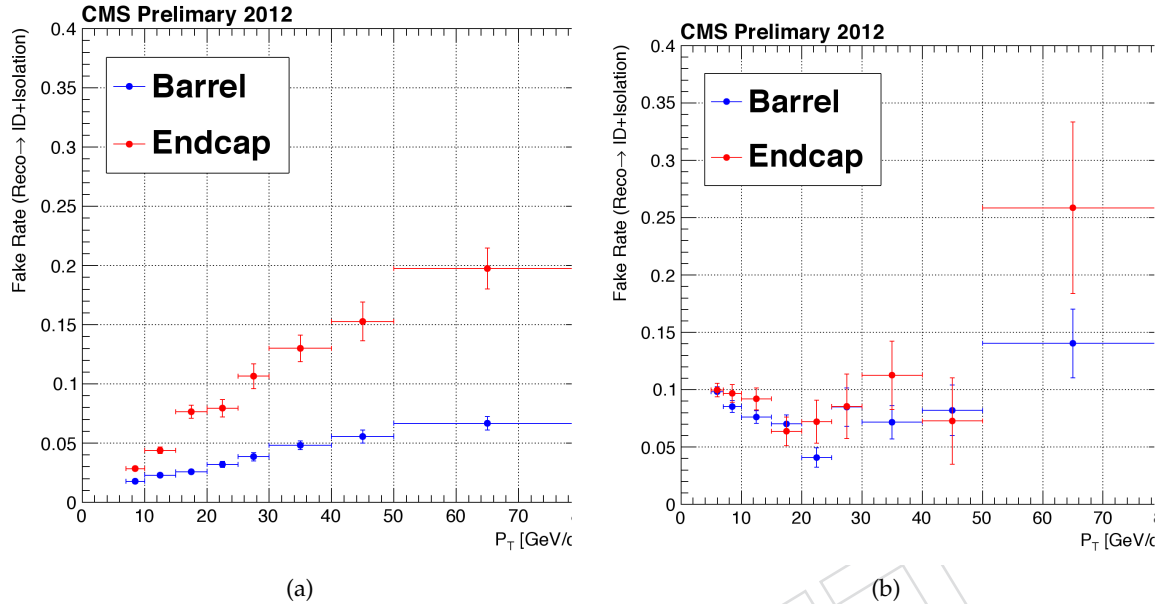


Figure 83: Fake rate measured for a probe lepton which satisfy loose selection, in the $Z(\ell\ell) + e$ (left) and $Z(\ell\ell) + \mu$ (right) samples as defined in the text. These fake ratios are used by Method A. The distributions correspond to the 8 TeV data for leptons in the Barrel (blue) and in the endcaps (red).

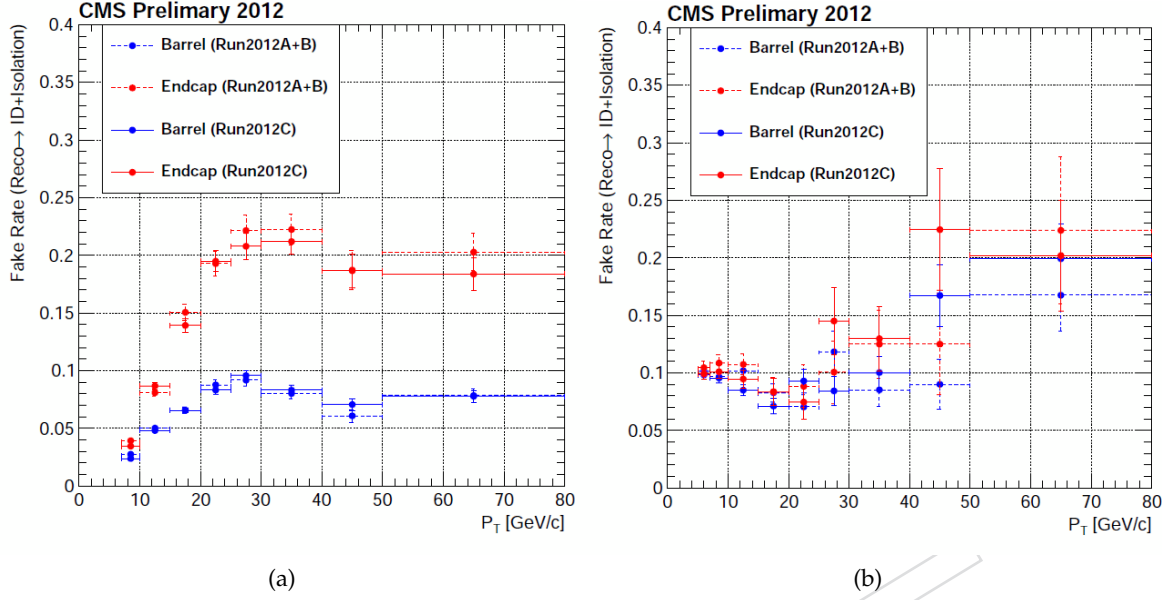


Figure 84: Fake rate measured for a probe lepton which satisfy loose selection, in the $Z(\ell\ell) + e$ (left) and $Z(\ell\ell) + \mu$ (right) samples as defined in the text. These fake ratios are used by Method A. The distributions correspond to the 8 TeV data for leptons in the Barrel (blue) and in the endcaps (red) and separated between 2012 AB (dashed line) and 2012 C (solid line) data taking periods.

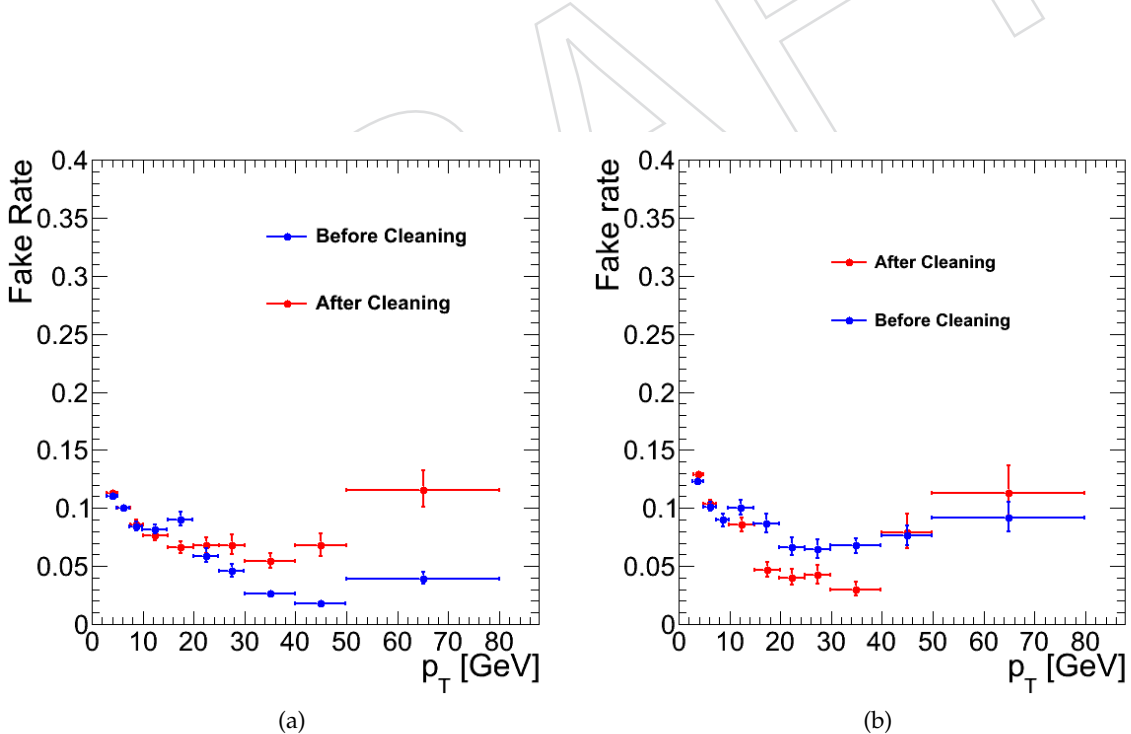


Figure 85: Fake rate measured for a probe muon which satisfy loose selection in the $Z(\ell\ell) + \mu$ (right) samples as defined in the text, before (blue) and after (red) the additional ghost muon cleaning using shared segments. Distributions are shown for the 8 TeV data for muons in the barrel (left) and in the endcaps (right).

1655 **9.1.2 Control regions and extrapolation**

1656 **9.1.2.1 Method A** Two control samples are obtained as subsets of four lepton events which pass
 1657 the “Higgs candidate” selection step, as described in previous sections. First control sample is obtained
 1658 by requiring two leptons not to pass the final identification and isolation criteria, but to pass the loose
 1659 lepton requirements as defined in Section 6. The other two leptons should pass the final selection criteria.
 1660 This sample is denoted as “2 Prompt + 2 Fail” (2P+2F) sample. It is expected to be populated with events
 1661 that intrinsically have only two prompt leptons (e.g. $DY, t\bar{t}$). Second control sample is obtained by
 1662 requiring one of the four leptons not to pass the final identification and isolation criteria, but to pass the
 1663 loose lepton requirements. The other three leptons should pass the final selection criteria. This control
 1664 sample is denoted as “3 Prompt + 1 Fail” (3P+1F) sample. It is expected to be populated with the type
 1665 of events that populate the 2P+2F region, as well as with the events that intrinsically have three prompt
 1666 leptons (e.g. $WZ, Z\gamma^{(*)}$).

1667 The control samples obtained in this way are expected to be enriched with the fake leptons and are used
 1668 to estimate the rate of the reducible background events in the signal region.

1669 The invariant mass distribution of events in the control region 2P+2F is shown for data in Figures 86 and
 1670 87. The distributions are shown for $4e$ (a), 4μ (b), $2e2\mu$ (c) and cumulative 4ℓ final states separately. The
 1671 shape of the observed mass distributions is fitted using the Landau function in a form $n_0 \text{Landau}(\mu, c)$,
 1672 normalized to the event yield. The fitting is performed for each of the $4e, 2e2\mu, 4\ell$ channels separately.
 1673 Due to the limited statistical accuracy in the 4μ final state, the fitting in this channel is performed with
 1674 the $2e2\mu$ shape and then normalized to the event yield. For the same reasons, the The results are shown
 1675 in Table 21.

Table 21: Mass shape fit parameters. Fitting of the invariant mass is performed in the control region with the $n_0 \text{Landau}(\mu, c)$ function. Due to the limited statistical accuracy, the fitting is performed for each of the $4e, 2e2\mu, 4\ell$ channels separately. In case of the 4μ final state, the fitting is performed with the $2e2\mu$ shape and normalized to the event yield. The parameters are shown for the fitting function normalized to unity.

Parameter	shift μ	scale c
$4e$, data, 7 TeV	140.3	17.9
$2e2\mu$, data, 7 TeV	132.8	16.2
$4e$, data, 8 TeV	143.0	17.1
$2e2\mu$, data, 8 TeV	141.1	16.7

1676 The invariant mass distribution of events in the control region 3P+1F is shown for data in Figure 88.
 1677 The distributions are again shown for $4e$ (a), 4μ (b), $2e2\mu$ (c) and cumulative 4ℓ final states separately.
 1678 The expected number of reducible background events in the 3P+1F region $N_{3\text{PIF}}^{\text{bkg}}$ can be computed from
 1679 the number of events observed in the 2P+2F control region $N_{2\text{P2F}}$ by weighting each of the events in
 1680 the region with the factor $(\frac{f_i}{1-f_i} + \frac{f_j}{1-f_j})$, where f_i and f_j correspond to the fake ratios of the two loose
 1681 leptons in the event:

$$N_{3\text{PIF}}^{\text{bkg}} = \sum \left(\frac{f_i}{1-f_i} + \frac{f_j}{1-f_j} \right) N_{2\text{P2F}} \quad (28)$$

1682 Figure 88 shows distribution of the expected number of reducible background events in this region
 1683 stacked on the distribution of irreducible backgrounds taken from simulation ($ZZ \rightarrow 4\ell$). The difference
 1684 in the distributions of the observed number of events and the expected contribution form the 2P+2P
 1685 region is an indication of the presence of processes with three prompt leptons in this region.

1686 The expected contribution of reducible background processes with two fake leptons in the signal region
 1687 can be computed from the number of events observed in the 2P+2F control region $N_{2\text{P2F}}$ by weighting
 1688 each of the events in that region with the factor $\frac{f_i}{1-f_i} \frac{f_j}{1-f_j}$, where f_i and f_j correspond to the fake ratios of
 1689 the two loose leptons. Similarly, the expected contribution of reducible background processes with one
 1690 fake leptons in the signal region can be computed from the difference between the number of observed

events in the 3P+1F control region $N_{3\text{P}1\text{F}}$ and the expected contribution from the 2P+2F region and ZZ processes in the signal region $N_{3\text{P}1\text{F}}^{\text{ZZ}} + N_{3\text{P}1\text{F}}^{\text{bkg}}$. The $N_{3\text{P}1\text{F}}^{\text{bkg}}$ is given by the equation 28 and $N_{3\text{P}1\text{F}}^{\text{ZZ}}$ is the contribution from ZZ which is taken from simulation. Therefore, the full expression for the prediction can be symbolically written as:

$$N_{\text{SR}}^{\text{bkg}} = \sum \frac{f_i}{(1-f_i)} (N_{3\text{P}1\text{F}} - N_{3\text{P}1\text{F}}^{\text{bkg}} - N_{3\text{P}1\text{F}}^{\text{ZZ}}) + \sum \frac{f_i}{(1-f_i)} \frac{f_j}{(1-f_j)} N_{2\text{P}2\text{F}} \quad (29)$$

The table 22 shows the expected number of events in the signal regions from the reducible background processes, both for the 7 TeV and 8 TeV data. Only statistical uncertainties are quoted in the table. Systematic uncertainties on these predictions and a procedure to estimate them from measurements in data will be discussed in the following chapters.

Table 22: The contribution of reducible background processes in the signal region predicted from measurements in data using the Method A. The quoted predictions correspond to the 7 TeV and the 8 TeV data.

baseline	4e	4μ	$2e2\mu$
7 TeV	$1.6 \pm 0.1_{\text{stat.}}$	$1.1 \pm 0.1_{\text{stat.}}$	$2.9 \pm 0.1_{\text{stat.}}$
8 TeV	$3.0 \pm 0.1_{\text{stat.}}$	$2.0 \pm 0.1_{\text{stat.}}$	$5.2 \pm 0.1_{\text{stat.}}$

DRAFT

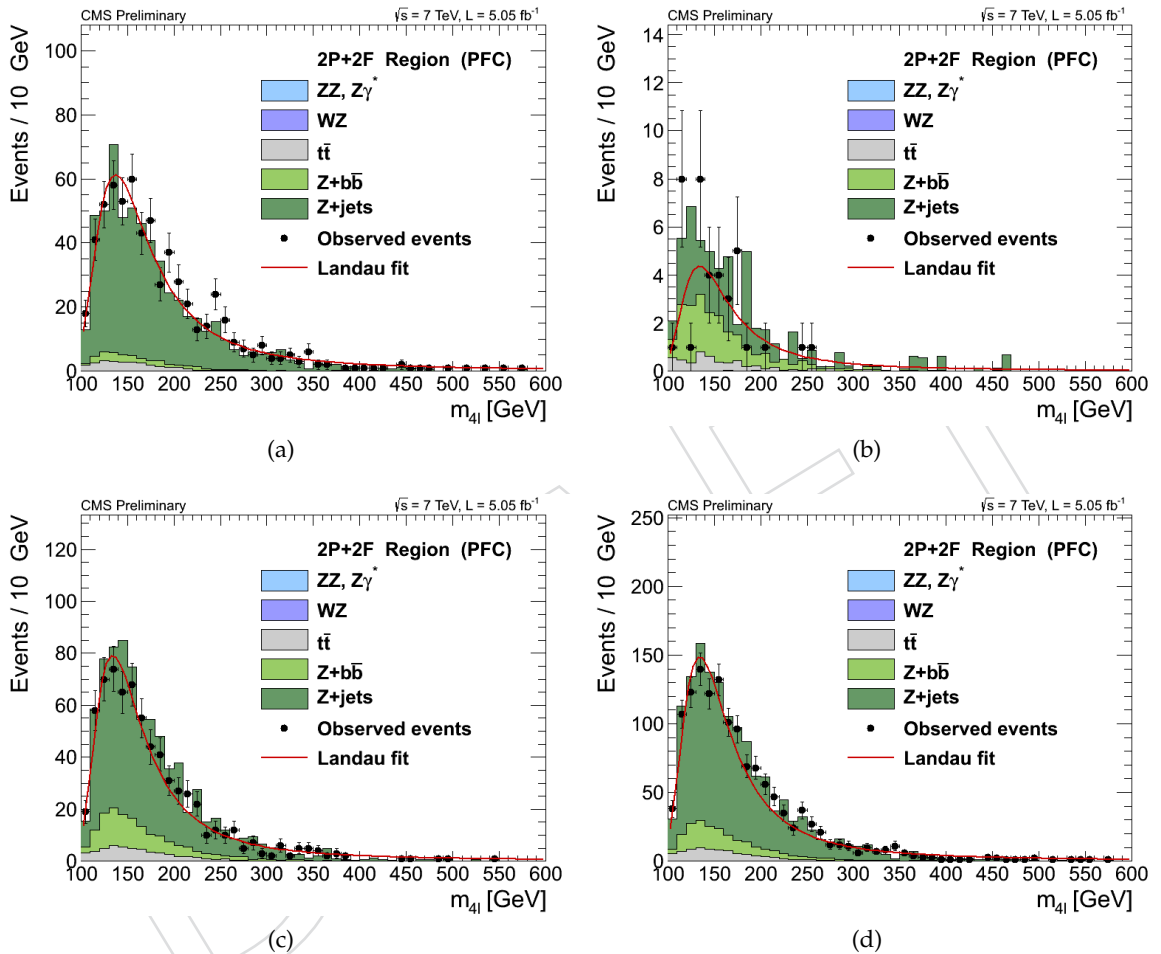


Figure 86: Invariant mass distribution of events in the control region 2P+2F for $4e$ (a), 4μ (b), $2e2\mu$ (c), and cumulative 4ℓ final states. The distributions are fitted with the Landau function. The distributions correspond to the 7 TeV data. **FIXME TO BE UPDATED**

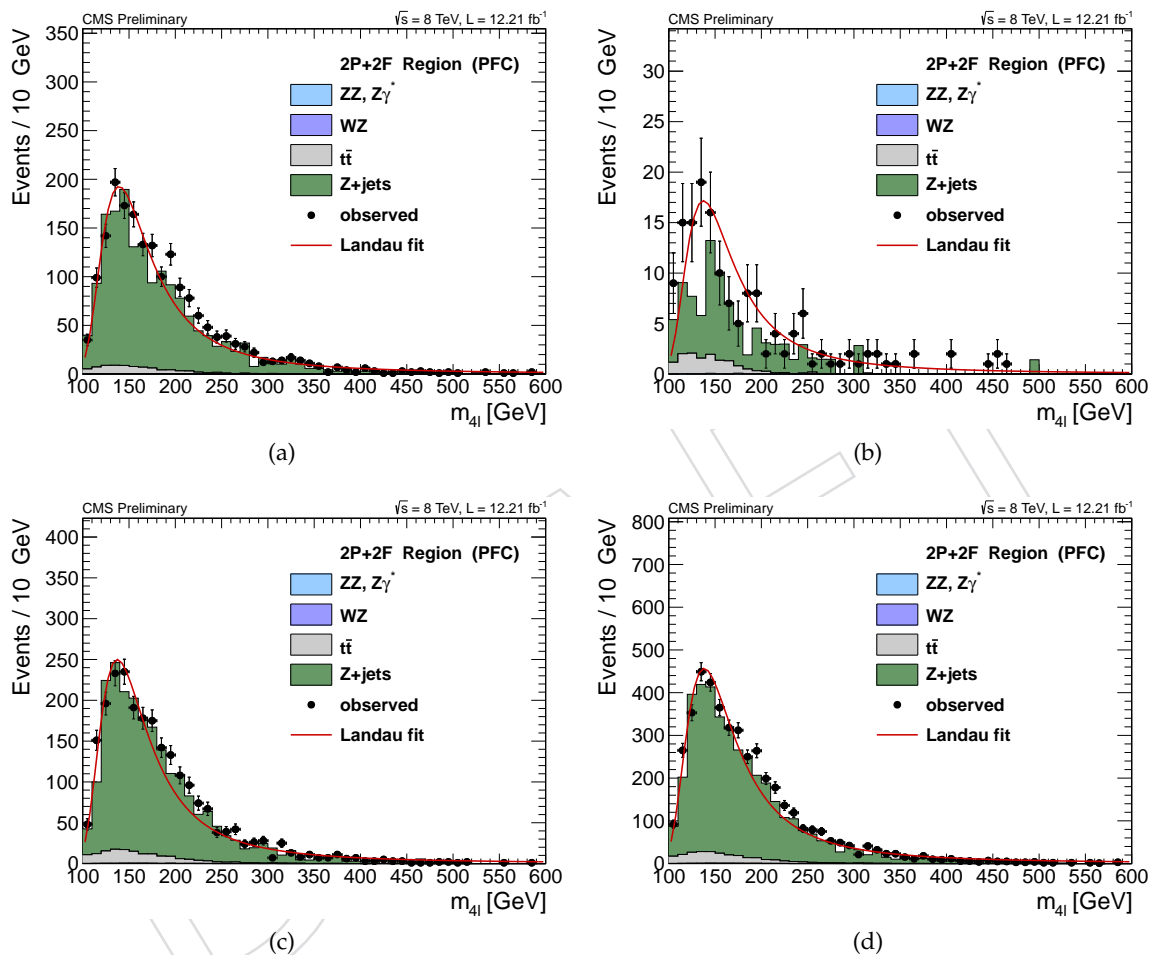


Figure 87: Invariant mass distribution of events in the control region 2P+2F for $4e$ (a), 4μ (b), $2e2\mu$ (c), and cumulative 4ℓ final states. The distributions are fitted with the Landau function. The distributions correspond to the 8 TeV data.

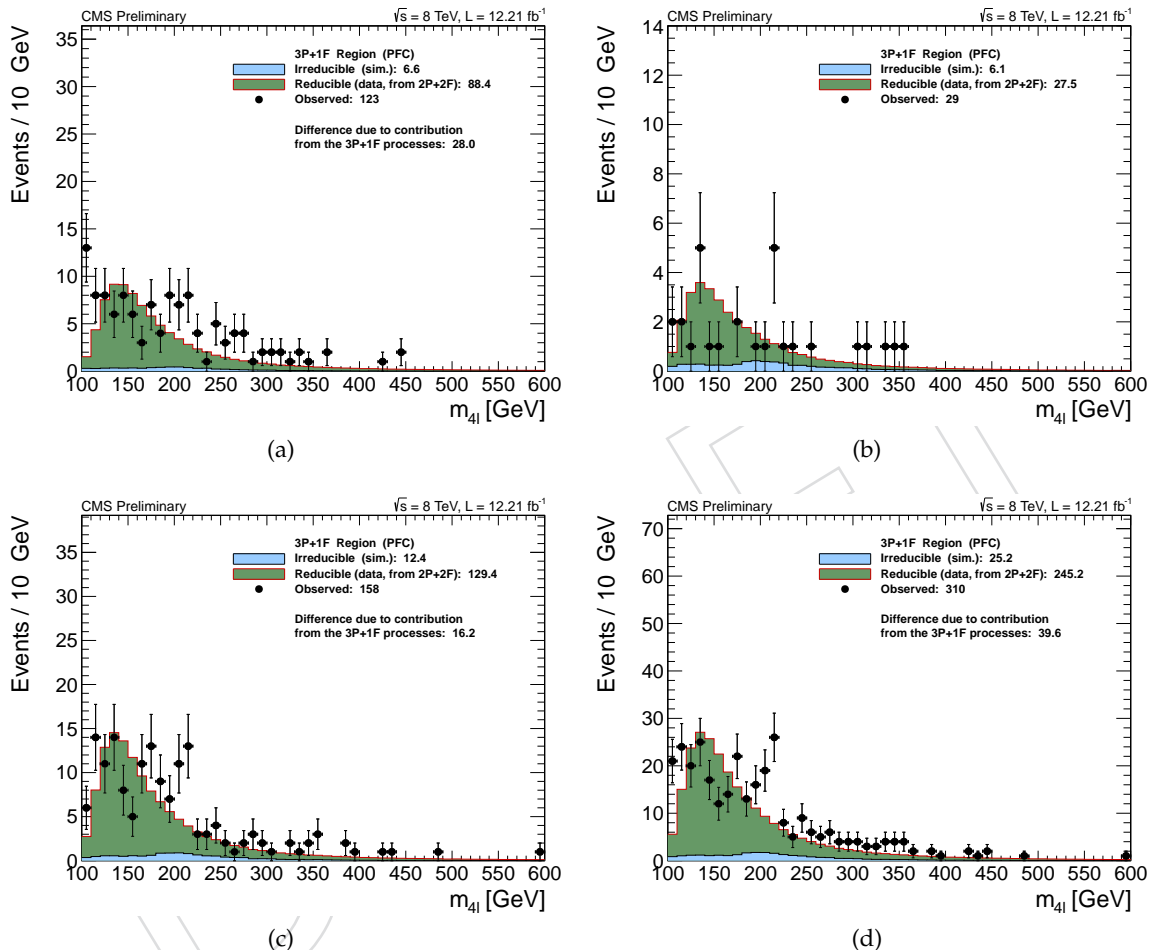


Figure 88: Invariant mass distribution of events in the control region 3P+1F for $4e$ (a), 4μ (b), $2e2\mu$ (c), and cumulative 4ℓ final states. The distribution of the estimated contribution from the reducible background events in this region is stacked on the distribution of irreducible backgrounds taken from simulation (e.g. $ZZ \rightarrow 4\ell$).

1699 **9.1.2.2 Method AA** The second method used to control the reducible background allows to have
 1700 an inclusive measurement of all the main reducible backgrounds at the same time.

1701 The control sample is obtained as subsets of the events that satisfy the first step of the selection (*First Z*
 1702 step, see section 6), requiring an additional pair of *loose leptons* of same sign (to avoid signal contamination)
 1703 and same flavour (SS-SF: $e^\pm e^\pm, \mu^\pm \mu^\pm$). The SS-SF leptons are requested to pass SIP_{3D} cut while no
 1704 identification or isolation requirements are imposed. The reconstructed invariant mass of the SS-SF lepto-
 1705 nts has to satisfy the baseline or the high-mass selections and the reconstructed four-lepton invariant
 1706 mass is required to satisfy $m_{4\ell} > 100$ GeV/ c^2 . From this set of events the inclusive number of reducible
 1707 background in the signal region is obtained taking into account the probability for the two additional
 1708 leptons to pass the isolation and identification analysis cuts obtained from a fake rate measurement.

1709 **Extraction to the signal region**

Starting from the control sample previously described, the final reducible background prediction in the signal region is given by the following expression:

$$N_{\text{expect}}^{Z+X} = N^{\text{DATA}} \times (\frac{\text{OS}}{\text{SS}})^{\text{MC}} \times \epsilon_1(p_T, \eta) \times \epsilon_2(p_T, \eta) \quad (30)$$

1710 where:

- 1711 • N^{DATA} is the number of events in the control region,
 1712 • $(\frac{\text{OS}}{\text{SS}})^{\text{MC}}$ is a correction factor between opposite sign and same sign control samples,
 1713 • $\epsilon_i(p_T, \eta)$ is the fake rate probability for each of additional pair of *loose leptons* ($i = 1, 2$) in
 1714 function of p_T and η .

DRAFT

1715 **SS vs OS**

1716 Figures 89 and 90 are showing the comparison between data and MC of samples selected with SS-SF
 1717 and OS-SF samples for all three channels for both 7 and 8 TeV data. A reasonable agreement is achieved
 1718 between data and MC for the 7 TeV. For 8 TeV, the lack of MC statistics prevents to draw any meaningful
 1719 conclusions. The differences in rates (taken from MC, with ZZ contribution subtracted) between OS and
 1720 SS samples are used to compute the correction factor in equation 30 for the final data-driven estimation.
 1721 They are estimated as 0.97(1.23, 1.01) for the $4e(4\mu, 2e2\mu)$ final states with 7 TeV samples. Due to lack of
 1722 statistics for the 8 TeV MonteCarlo samples, the same factors are applied to the 8 TeV analysis.

1723 **Cross checks**

1724 A full MC closure test was performed. Unfortunately, due to lack of statistics in MC samples after, only
 1725 the $2e2\mu$ channel was tested. Fake rate was computed and parameterized using MC samples, the same
 1726 way as in the DATA. Estimated reducible background extracted using formula 30 were compared to the
 1727 rates estimated applying the full selection on MC samples. The two methods agree fairly, given the large
 1728 statistical errors.

1729 **Results on DATA**

1730 With the 5.1 fb^{-1} of collected integrated luminosity at 7 TeV and 12.2 fb^{-1} of 8 TeV, the number of
 1731 events from $Z+X$ expected and the relative systematics and statistical errors in the signal region in a
 1732 mass range from $m_1 = 100 \text{ GeV}/c^2$ to $m_2 = 600 \text{ GeV}/c^2$ for the baseline, and high-mass selections are
 1733 listed in table 23 and 24. The statistical error quoted represents the number of events in the control
 1734 region, while the systematics one is extracting varying the fake rates by ± 1 sigma and inflated by 10%
 1735 according to the WZ underestimation.

Table 23: The number of events from $Z+X$ expected and the relative systematics and statistical errors in the signal region in a mass range from $m_1 = 100 \text{ GeV}/c^2$ to $m_2 = 600 \text{ GeV}/c^2$, for baseline analysis and for 7 TeV data.

	baseline (full range)
$N^{Z+X \rightarrow 4e}$	$2.2 \pm 0.1 \text{ (4\%)} \text{ (stat., 739 events)} \pm 1.1 \text{ (50\%)} \text{ (syst.)}$
$N^{Z+X \rightarrow 4\mu}$	$0.8 \pm 0.1 \text{ (12\%)} \text{ (stat., 63 events)} \pm 0.4 \text{ (50\%)} \text{ (syst.)}$
$N^{Z+X \rightarrow 2e2\mu}$	$3.0 \pm 0.1 \text{ (3\%)} \text{ (stat., 875 events)} \pm 1.5 \text{ (50\%)} \text{ (syst.)}$

Table 24: The number of events from $Z+X$ expected and the relative systematics and statistical errors in the signal region in a mass range from $m_1 = 100 \text{ GeV}/c^2$ to $m_2 = 600 \text{ GeV}/c^2$, for baseline and for 8 TeV data.

	baseline (full range)
$N^{Z+X \rightarrow 4e}$	$6.1 \pm 0.1 \text{ (2\%)} \text{ (stat., 2531 events)} \pm 3.1 \text{ (50\%)} \text{ (syst.)}$
$N^{Z+X \rightarrow 4\mu}$	$2.2 \pm 0.1 \text{ (6\%)} \text{ (stat., 223 events)} \pm 1.1 \text{ (50\%)} \text{ (syst.)}$
$N^{Z+X \rightarrow 2e2\mu}$	$8.9 \pm 0.2 \text{ (2\%)} \text{ (stat., 3215 events)} \pm 4.5 \text{ (50\%)} \text{ (syst.)}$

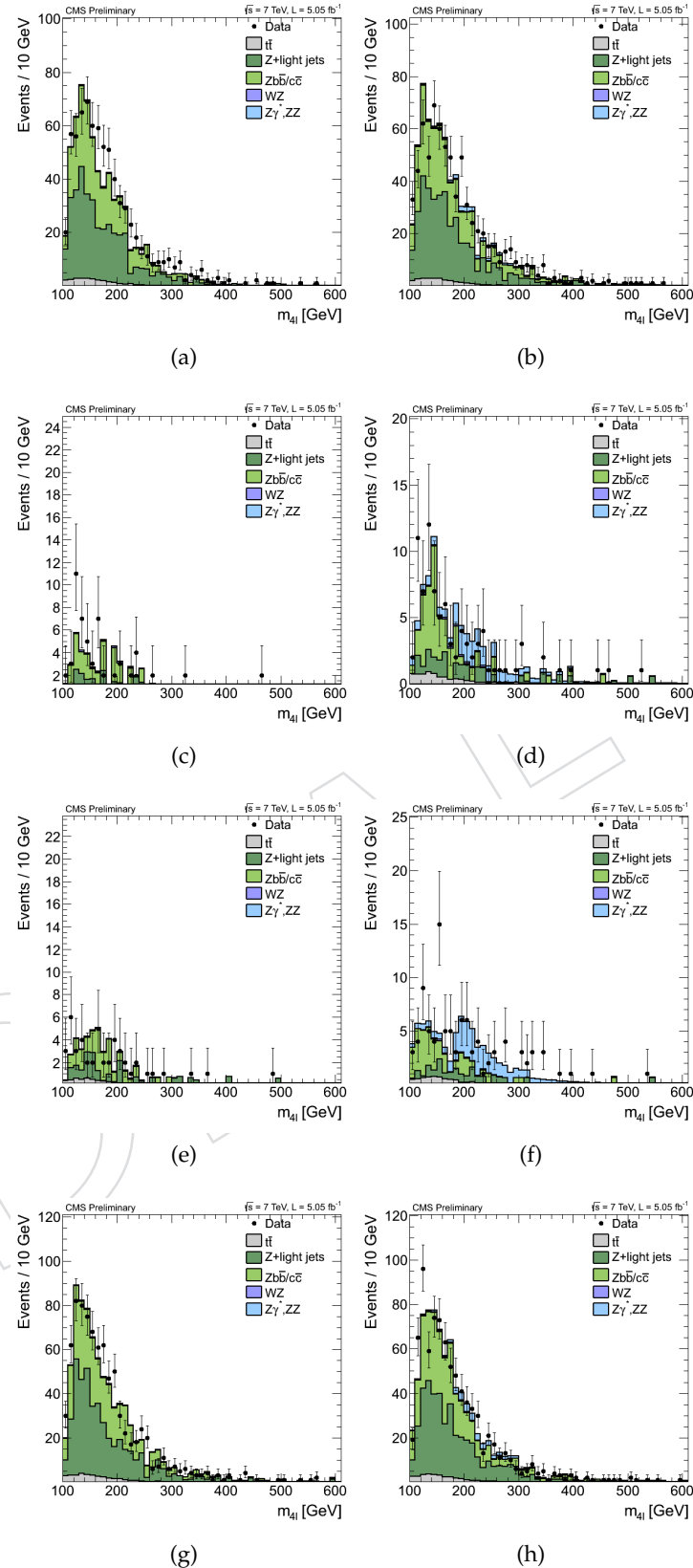


Figure 89: DATA-MC comparison of the SS-SF (on the left) and OS-SF (on the right) samples in the $Z+X$ background control samples. (a) and (b) $4e$, (c) and (d) 4μ , (e) and (f) $2e2\mu$, (g) and (h) $2\mu 2e$. The distributions correspond to 5.1 fb^{-1} of 7 TeV data.

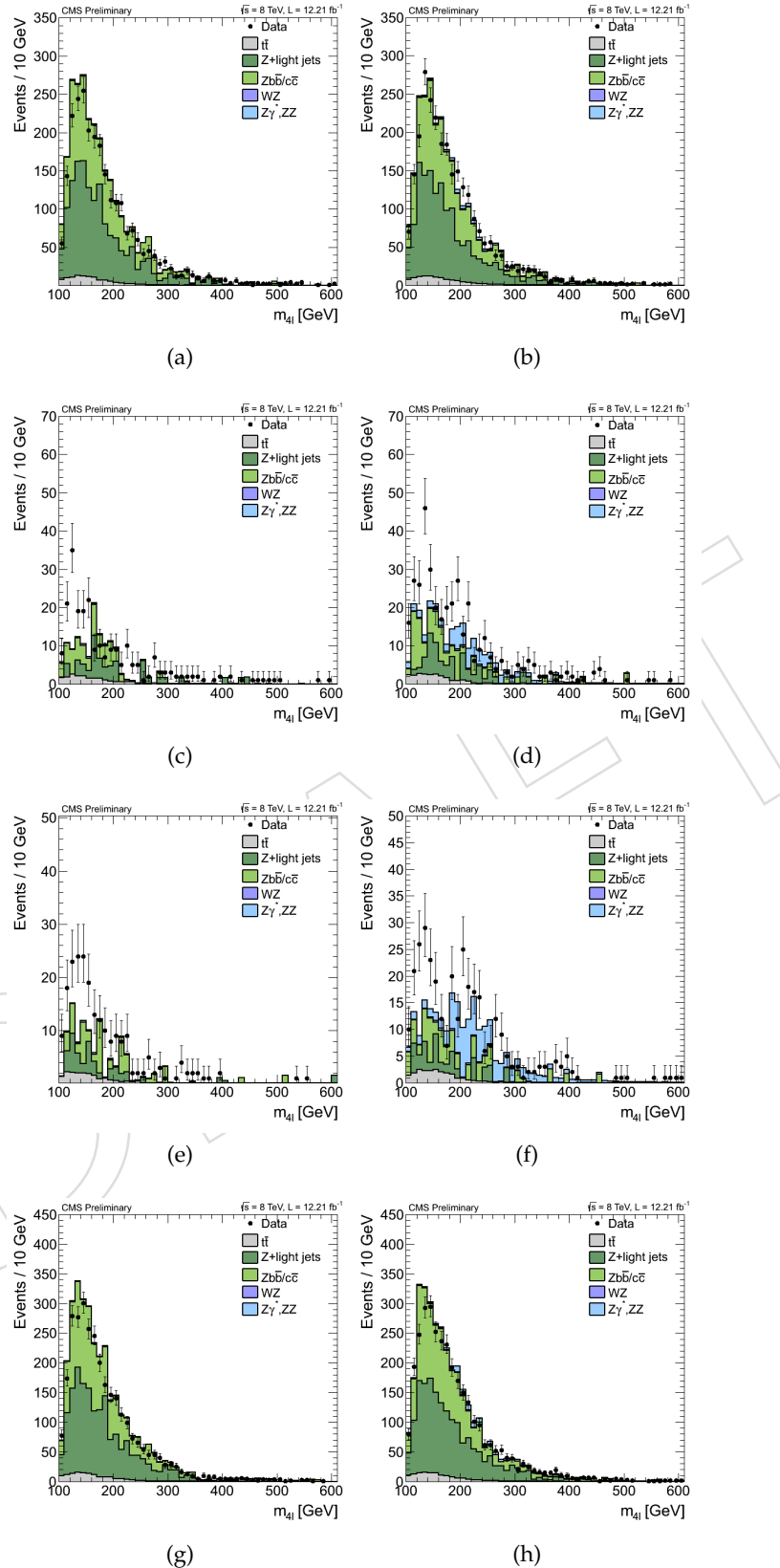


Figure 90: DATA-MC comparison of the SS-SF (on the left) and OS-SF (on the right) samples in the $Z+X$ background control samples. (a) and (b) $4e$, (c) and (d) 4μ . The distributions correspond to 12.2 fb^{-1} of 8 TeV data.

9.2 Reducible Backgrounds Uncertainties

One of the important aspects of the reducible background prediction method is the assessment of the statistical and systematic uncertainties. There are several sources of uncertainties:

- Statistical uncertainty due to the limited size of the samples in the control regions where we measure and where we apply the fake ratio method,
- Different compositions of reducible background processes ($DY, t\bar{t}, WZ, Z\gamma^{(*)}$) in the region where we measure and where we apply the fake ratio method,
- Choice of the functional form for the m_{4l} shape that is used to extrapolate from the full range of the invariant m_{4l} mass to the range of interest.

The systematic uncertainties will be estimated using two approaches:

- Estimate the systematic uncertainty for the prediction method using the MC closure test,
- Estimate directly the systematic uncertainty for the prediction method using the “orthogonal” 4l data samples with the “wrong combination of charge and flavour”.

9.2.1 Statistics in 4l Control Sample

The limited size of the samples in the control regions where we measure and where we apply the fake ratios is the source of the statistical uncertainties of the method. The dominating statistical uncertainty is driven by the number of events in the control region and is typically in the range of 5-10%.

9.2.2 Sensitivity of Fake Ratios to Background Composition

9.2.3 Closure Test (in Data and/or Simulation)

9.2.3.1 Closure test of method A with wrong combination leptons A way to validate the reducible backgrounds prediction method and to estimate its associated systematic uncertainty is to apply the same method in the subset of four-lepton events which satisfy the Higgs selection criteria but leptons have “wrong combination of charges and flavours” (WFC). These samples are expected to be free of the signal.

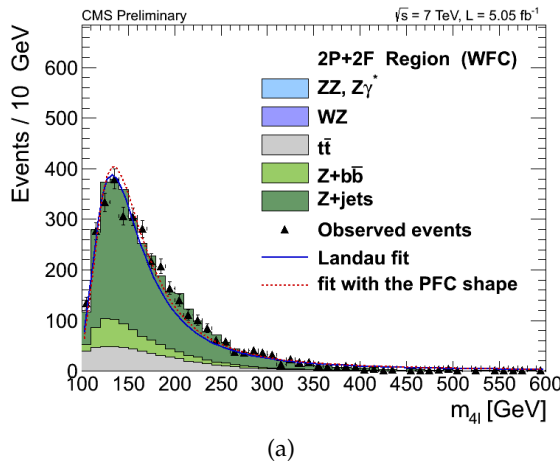
The distribution of four-lepton invariant mass for data events in the WFC 2P+2F control region is shown in Figure 91. The distribution is shown for the cumulative 4ℓ final state. The shape of the observed mass distribution is fitted using the Landau function convoluted with the 4th order polynomial, as in the case of selection with “proper combination of lepton charges and flavours” (PFC) defined in the previous section.

The distribution of four-lepton invariant mass for the 4ℓ final state events in the WFC Signal region is shown for 7TeV data in Figure 92 (left). The figure also shows distribution of the expected number of reducible background events in this region stacked on the distribution of irreducible backgrounds taken from simulation ($ZZ \rightarrow 4\ell$). The expected number of reducible background events is computed by the method A outlined above.

A reasonably good agreement between the predicted and the observed number of events in the WFC 3P+1F control region (Figure 92) is a validation of the method by measurements performed in data. The difference between the predicted and the observed number of events in the WFC Signal region can be used as a direct measure of the uncertainty of the method. Taking into account low statistical accuracy, the uncertainty is estimated to be less than 50%. The estimation of the uncertainty is dominated by the limited statistics (30% statistical uncertainty) and is expected to improve with the increase of the integrated luminosity.

9.2.3.2 Closure test of method AA with Z + opposite flavor leptons A closely related closure test has been performed for method AA, using samples of Z plus two opposite flavor leptons (e, μ).

A “signal” sample is selected using the selection and kinematic cuts of the baseline Higgs phase space



(a)

Figure 91: Invariant mass distribution of events in the WFC 2P+2F control region for $4e$ (a), 4μ (b), $2e2\mu$ (c), and cumulative 4ℓ final states. The distributions are fitted with the Landau function convoluted with the 4^{th} order polynomial (see text for details). The fit with the shape used in the PFC 2P+2F control region is overlaid on top. The difference between the two shapes can be used as a measure of the uncertainty on the shape of the fitting function.

defined in section 6, the only difference being that $e^\pm \mu^\mp$ pairs are used, instead of $l^\pm l^\mp$ pairs, to make the “ Z_2 ” candidate. The “signal” sample is expected to be dominated by events where the “ Z_2 ” candidate is made from two fake leptons. This reducible background component is obtained by applying method AA to a control sample of Z_1 plus two loose leptons of same sign and opposite flavor ($Z_1 + e^\pm \mu^\mp$). For simplicity, the OS to SS correction factor is taken to be the same as for the main analysis.

21 events are observed in the 2012 $Z_1 + e\mu$ “signal” sample (10 events where $Z_1 \rightarrow \mu\mu$ and 11 events where $Z_1 \rightarrow ee$). The corresponding four-lepton invariant mass distribution is shown in Fig. 93. The reducible background component obtained from method AA is shown as the green histogram. The predicted yield amounts to 13.7 ± 2.1 events, where the error combines the (subleading) uncertainty due to the statistics of the control sample (3063 events) and the uncertainty due to the fake rate fractions. Events with one or two genuine e or μ leptons also contribute to the “signal” sample and this contribution is estimated from Monte-Carlo samples. The contribution of ZZ events (where one Z decays to ee or $\mu\mu$, and the other Z decays into $\tau\tau$ followed by $\tau \rightarrow e\nu\nu$ and $\tau \rightarrow \mu\nu\nu$) amounts to 4.7 ± 0.15 events. An additional source of $Z + e\mu$ events comes from the production of a Z boson in association with a $t\bar{t}$ pair, where both top quarks decay semi-leptonically leading to two isolated leptons. This amounts to 1.75 ± 1.15 events. WZ events with an additional fake lepton contribute 0.9 ± 0.1 event. Finally, a small but visible contribution from Higgs bosons is expected, dominated by ZH production with $H \rightarrow \tau\tau$ followed by leptonic decays of both taus. For a Higgs mass of 125 GeV it amounts to ~ 0.3 event. The total expected background of 21.4 events compares well with the number of observed events. Despite the limited statistics, this allows the predictions of the AA method to be validated within 35 – 40%.

Comparisons between the observations and the predictions have also been made separately for $Z_1 \rightarrow ee$ and $Z_1 \rightarrow \mu\mu$, and for the distribution of the transverse momentum of the e and μ that make the “ Z_2 ”, showing an acceptable level of agreement within the small statistics.

9.2.4 Choice of Functional Form for M4L Shape

The functional form for the m_{4l} shape that is used to extrapolate from the full range of the invariant m_{4l} mass to the range of interest is also one source of the systematic uncertainty. In order to estimate this uncertainty we have looked at the differences between the shapes of predicted background distributions for all three channels. The envelope of differences between these shapes of distributions is used as a measure of the uncertainty of the shape. The uncertainty is estimated to be up to 10 - 15%. Since the difference of the shapes slowly varies with m_{4l} , it is taken as a constant term and is practically absorbed in the much larger uncertainty on the predicted yield of backgrounds (see previous chapter). The shapes

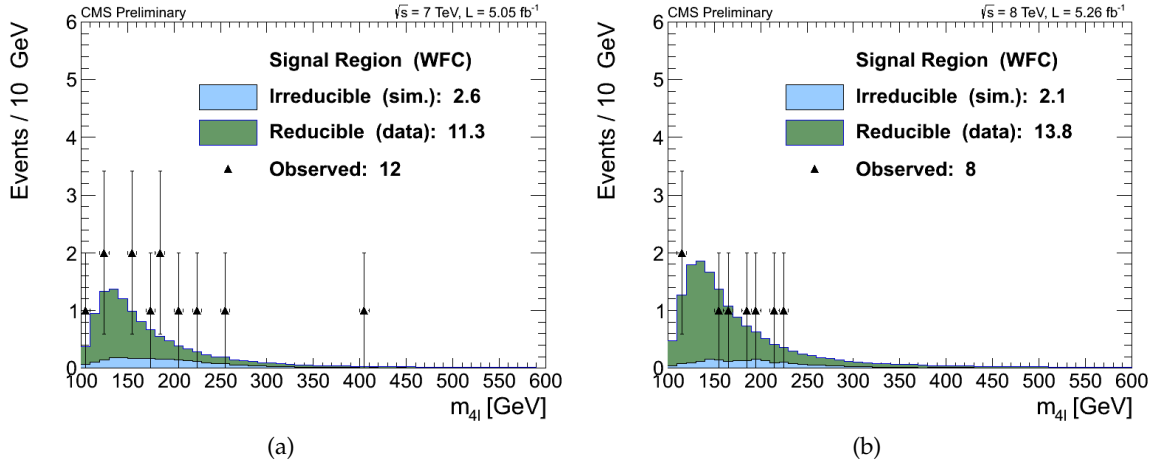


Figure 92: Results of the prediction method applied in the 4l data sample with the “wrong combination of charge and flavour” (as defined in the text above). Figures show the “closure” test in the signal region for the 7 TeV data (left) and 8 TeV data (right). The difference between the predicted and the observed number of events in the WFC Signal region is used as a measure of the uncertainty of the prediction method A. **FIXME TO BE UPDATED**

1812 of predicted background m_{4l} distributions for $4e$ and 4μ channels are shown in Figure 94.

1813 9.3 Summary

1814 Two methods for the prediction of the contribution of reducible background processes in the signal
 1815 region are presented with associated uncertainties in the previous two section. The Table 25 below
 1816 shows the summary of the results of both methods. As the final estimate of this contribution, we take
 1817 the mean value of the results of the two methods, while as the uncertainty of the result we quote the one
 1818 that covers the uncertainties of both methods (using the symmetric log-normal distribution). Figure 95
 1819 is a visual representation of the predictions of individual methods and the combined results.

Table 25: The summary of the results of two methods for the prediction of the contribution of reducible background processes in the signal region. The arithmetic mean value of the results of the two methods is taken as the final estimate of this contribution, while the uncertainty of the result is the one that covers the uncertainties of both methods. The table shows symmetric individual uncertainties for two methods, while in the combination and statistical analysis these are treated with the (a)symmetric log-normal distribution. The quoted predictions correspond to the 5.1 fb^{-1} of 7 TeV data and the 12.2 fb^{-1} of 8 TeV data.

	7 TeV	$4e$	4μ	$2e2\mu$
Method A		1.6	1.1	2.9
Method AA		2.2	0.8	3.0
Combined central value	1.9	1.0	3.0	
Combined κ_{\min}	0.4	0.4	0.5	
Combined κ_{\max}	2.3	2.5	2.0	
	8 TeV	$4e$	4μ	$2e2\mu$
Method A		3	2.0	5.2
Method AA		6.1	2.2	8.9
Combined central value	4.5	2.1	7.1	
Combined κ_{\min}	0.3	0.5	0.4	
Combined κ_{\max}	2.7	2.1	2.6	

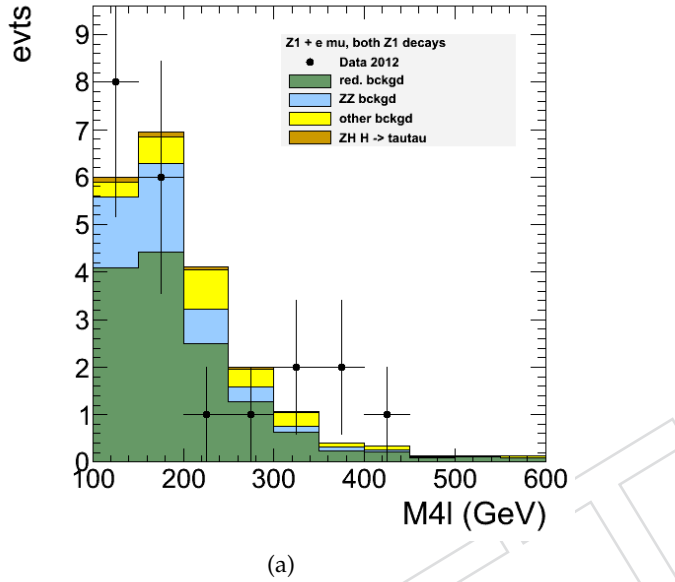


Figure 93: Invariant four-lepton mass distribution of $Z + e\mu$ events for 2012 data (dots), compared to the expectation from Z plus two fake leptons as predicted by method AA (green histogram), from ZZ events (blue histogram), from WZ and $t\bar{t}Z$ production (yellow histogram), and from Higgs production (orange histogram).

Table 26: The summary of the parameters of the predicted shape of reducible background processes in the signal region for 7 TeV (upper part) and 8 TeV of data (lower part). The estimated uncertainty on the shape is found to be below 10-15% and is included in the uncertainties quoted above (as discussed in the text).

	7 TeV	n_0	m	c
4e	–	148.0	20.6	
2e2mu	–	143.1	19.9	
4mu	–	133.8	15.4	
	8 TeV	n_0	m	c
4e	–	148.9	20.2	
2e2mu	–	146.4	19.6	
4mu	–	140.3	21.7	

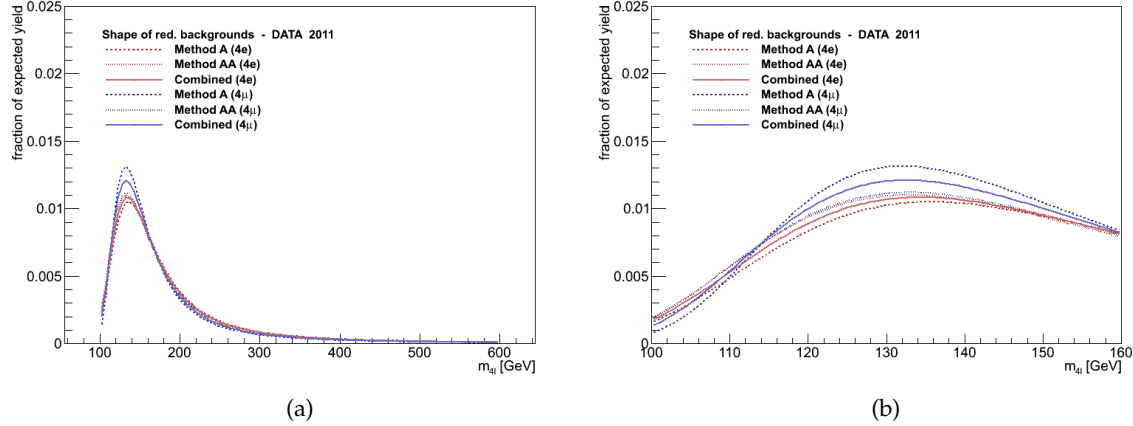


Figure 94: The shapes of predicted background m_{4l} distributions for $4e$ and 4μ channels. The envelope of differences between the shapes of distributions can be used as a measure of the uncertainty of the shape. The uncertainty is estimated to be in the range 10 - 15% and is absorbed in the much larger uncertainty on the predicted yield of backgrounds. **FIXME TO BE UPDATED**

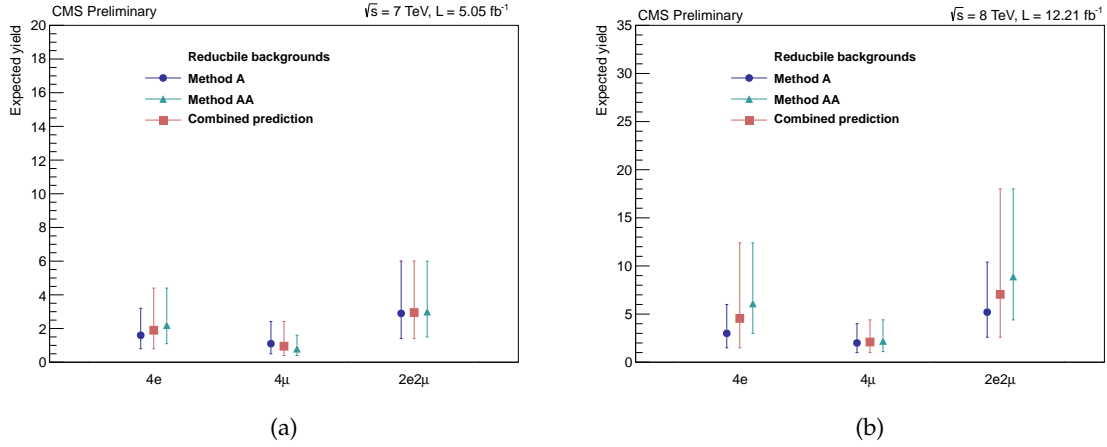


Figure 95: The visual representation of the predictions of individual methods and the combined results of two methods. The final estimate is taken as the geometrical mean of the two extreme values allowed by the two methods. The uncertainty of the result is the one that covers the uncertainties of both methods (symmetric log-normal distribution).

10 Kinematic Discriminant (MELA)

10.1 Introduction of the methodology

1822 Kinematics of the Higgs decay to ZZ final state has been extensively studied in the literature in appli-
 1823 cation to the studies of the Higgs boson or new exotic boson properties, see for example Refs. [65–76].
 1824 Only recently a complete set of angular observables was introduced in Ref. [74] and it was suggested
 1825 that it may also help in background rejection. This approach was recently introduced in the analysis of
 1826 the decay $H \rightarrow ZZ \rightarrow 2\ell 2q$ [77] on CMS and we adopt a similar methodology in $H \rightarrow ZZ \rightarrow 4\ell$. In this
 1827 approach, the signal-to-background probability is created using analytical or empirical multi-dimension
 1828 likelihood for an event to be signal or background. Signal and background analytical parameterizations
 1829 are taken from Refs. [74] and [76], respectively. In the following, we introduce the methodology in more
 1830 detail with the analytical MELA approach (Matrix Element Likelihood Approach). As cross-checks,
 1831 kinematics has also been studied with Boosted Decision Trees, Bayesian Neural Networks, and numeri-
 1832 cal Matrix Element, as discussed in Appendixes.

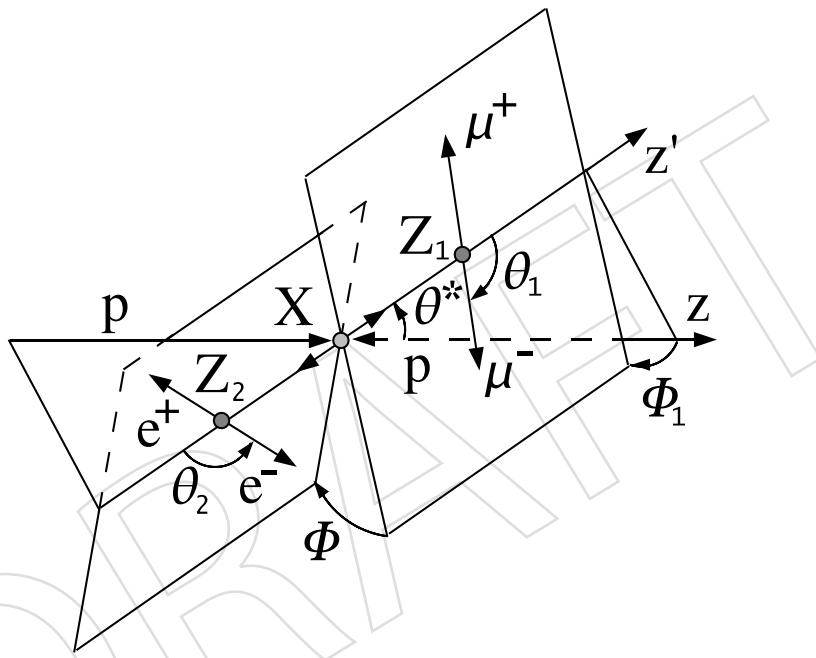


Figure 96: Left: Illustration of a particle X production and decay $ab \rightarrow X \rightarrow Z_1 Z_2 \rightarrow 4\ell$ with the two production angles θ^* and Φ_1 shown in the X rest frame and three decay angles θ_1 , θ_2 , and Φ shown in the P_i rest frames [74].

1833 In Fig. 96 we illustrate the angular distribution in the production and decay chain $ab \rightarrow X \rightarrow ZZ \rightarrow 4\ell$.
 1834 The angular distribution can be expressed as a function of three helicity angles θ_1 , θ_2 , and Φ , and two
 1835 production angles θ^* and Φ_1 . The full kinematics in the production and decay of an X resonance $ab \rightarrow$
 1836 $X \rightarrow Z_1 Z_2 \rightarrow 4\ell$ can be described with the help of the following 12 observables (reflecting all degrees of
 1837 freedom with four lepton momenta):

- 1838 • three resonance masses (including the off-shell cases): $m_{4\ell}$, m_1 , m_2 ;
- 1839 • five production and decay angles defined in Fig. 96 as $\vec{\Omega} = \{\theta^*, \Phi_1, \theta_1, \theta_2, \Phi\}$;
- 1840 • longitudinal boost of the resonance, expressed as rapidity Y ;
- 1841 • transverse momentum of the resonance p_T and its azimuthal angle;
- 1842 • one arbitrary azimuthal angle Φ^* reflecting the overall orientation of the system.

1843 The 2011 baseline analysis of the $H \rightarrow ZZ \rightarrow 4\ell$ channel employed cuts on the two $Z^{(*)}$ invariant

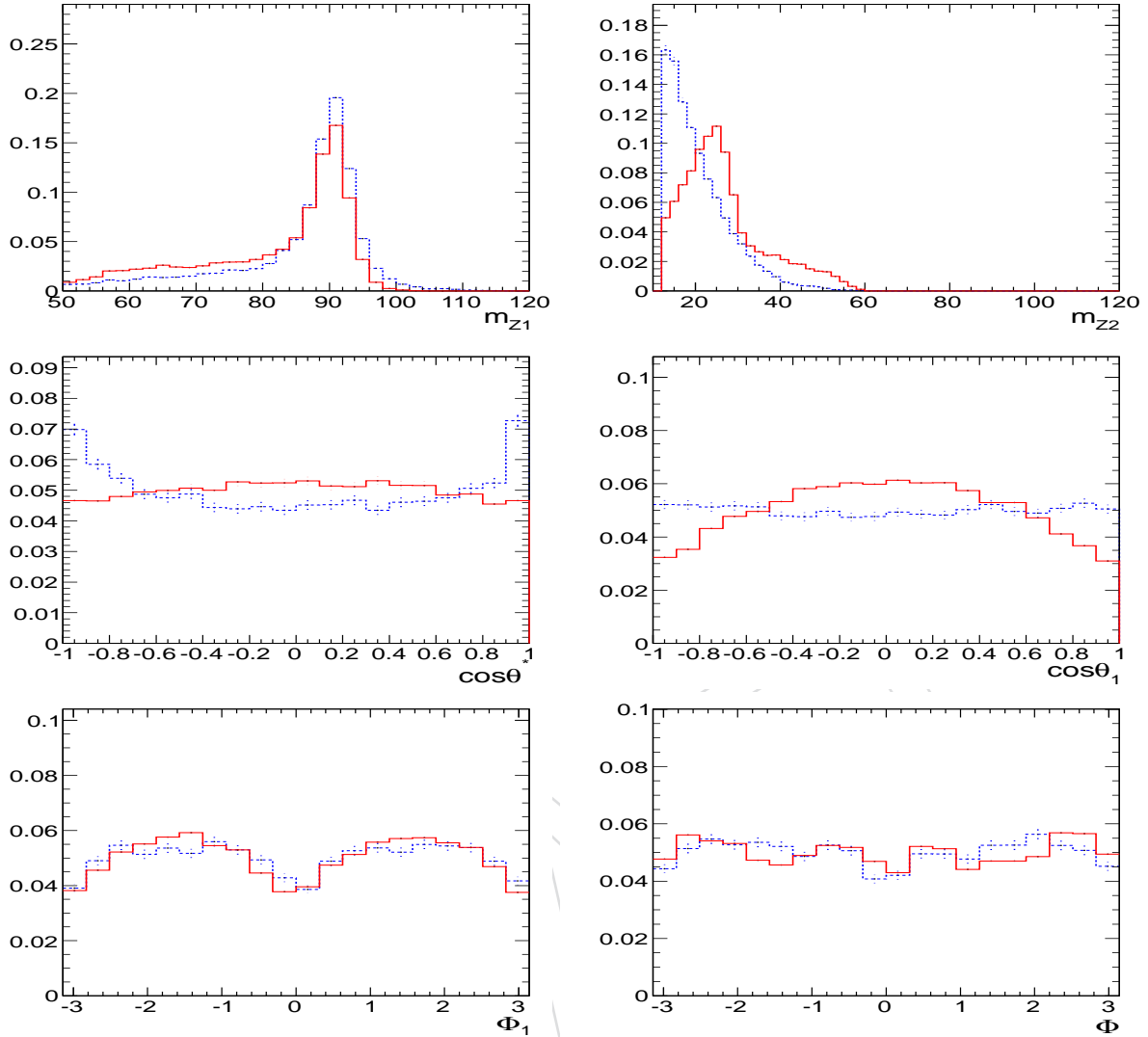


Figure 97: Distribution of Higgs signal events with $m_H = 120$ GeV (solid red) and background ZZ events (dashed blue) in the range $100 < m_{4\ell} < 135$ GeV. Top-left: m_1 ; top-right: m_2 ; middle-left: $\cos\theta^*$; middle-right: $\cos\theta_{1,2}$ (both angles have the same distribution); bottom-left: Φ_1 ; bottom-right: Φ .

masses m_1 and m_2 with the shape-based fit of the $m_{4\ell}$ distribution. In the current approach, we expand information used and construct a kinematic discriminant KD from the seven mass and angular observables $KD = F\{m_1, m_2, \theta^*, \Phi_1, \theta_1, \theta_2, \Phi\}$ and perform a 2D shape fit with the two observables ($m_{4\ell}, KD$). In Figs. 97 and 98 we show separation power between signal and background for each individual observable. The KD discriminant combines this power in a single observable using full correlation of all input observables in the most optimal way. In this approach we remove from consideration those observables which depend on QCD kinematics, such as Y , p_T , and its azimuthal angle, and keep only observables coming from well-understood electro-weak Quantum Mechanics of the processes of either Higgs or continuum ZZ production. In particular, these seven observables are independent from the Higgs production mechanism, as long as we consider the SM Higgs boson. The same seven observables are also the key input to measuring the new boson properties, such as spin and CP quantum numbers, should a new boson be discovered.

It has been noted that Y and p_T distributions are different for processes dominated by gluon fusion

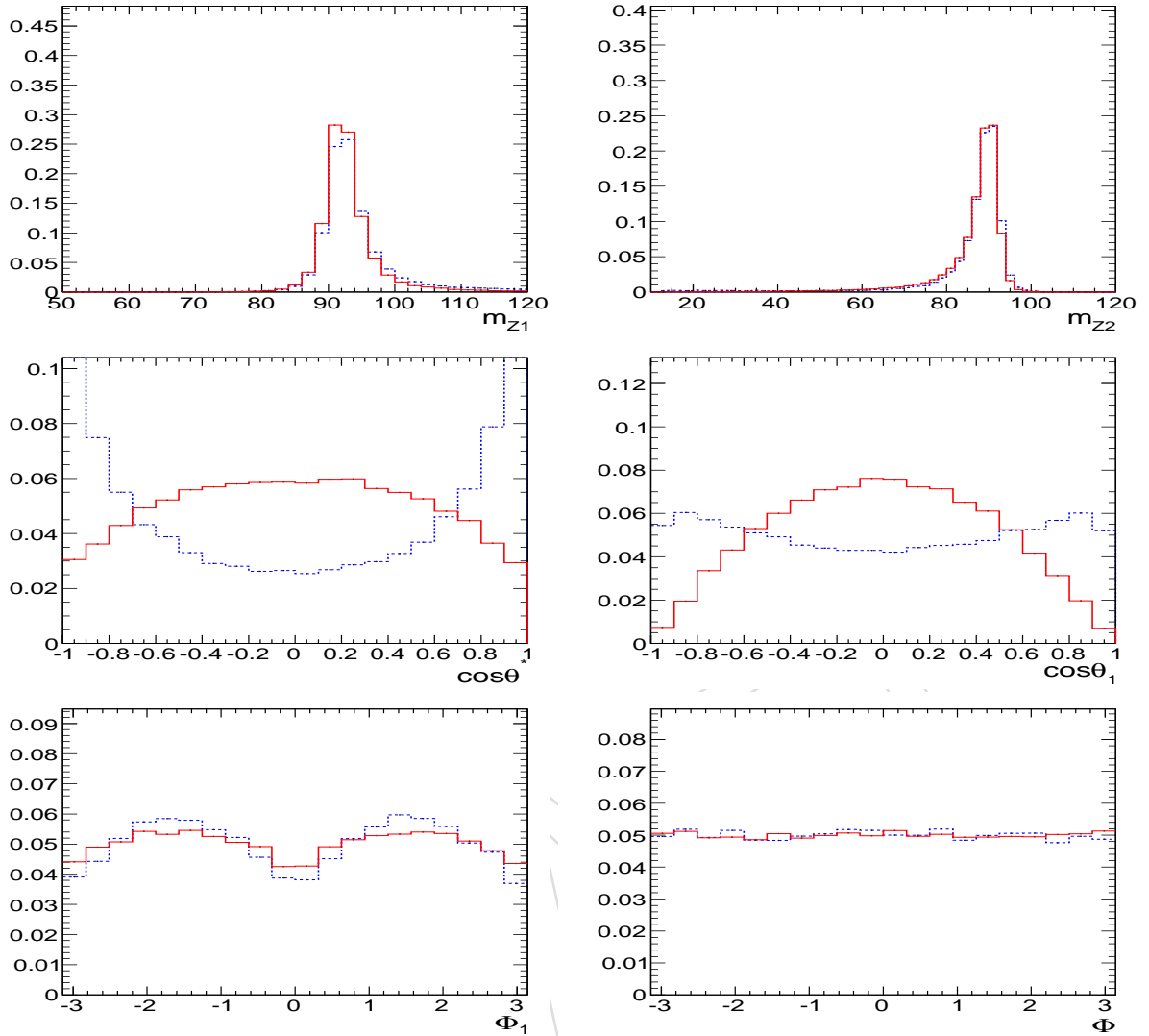


Figure 98: Distribution of Higgs signal events with $m_H = 400$ GeV (solid red) and background ZZ events (dashed blue) in the range $300 < m_{4\ell} < 500$ GeV. Top-left: m_1 ; top-right: m_2 ; middle-left: $\cos \theta^*$; middle-right: $\cos \theta_{1,2}$ (both angles have the same distribution); bottom-left: Φ_1 ; bottom-right: Φ .

(signal) and $q\bar{q}$ production (background), due to larger longitudinal boost of the $q\bar{q}$ system and larger Initial State Radiation (QCD ISR) in gluon fusion. However, these observables are fully driven by QCD effects and require further validation. Therefore, they are not used in the current analysis.

10.2 Construction of the MELA discriminant

Construction of the kinematic discriminant, KD, in the MELA approach (Matrix Element Likelihood Approach) relies on probability for an event with a set of observables $(m_{4\ell}, m_1, m_2, \vec{\Omega})$ to come either from signal or background

$$\mathcal{P}_{\text{sig}}(m_1, m_2, \vec{\Omega} | m_{4\ell}) \quad (31)$$

$$\mathcal{P}_{\text{bkg}}(m_1, m_2, \vec{\Omega} | m_{4\ell}) \quad (32)$$

1864 where probabilities are normalized with respect to the seven observables while treating $m_{4\ell}$ as a con-
 1865 ditional parameter. These probabilities are calculated analytically and are quoted in Ref. [74] for signal
 1866 and in Ref. [76] for continuum ZZ background. Then the discriminant is constructed as follows

$$\text{KD} = \frac{\mathcal{P}_{\text{sig}}}{\mathcal{P}_{\text{sig}} + \mathcal{P}_{\text{bkg}}} = \left[1 + \frac{\mathcal{P}_{\text{bkg}}(m_1, m_2, \vec{\Omega} | m_{4\ell})}{\mathcal{P}_{\text{sig}}(m_1, m_2, \vec{\Omega} | m_{4\ell})} \right]^{-1} \quad (33)$$

1867 There are several considerations in the above construction. This discriminant is continuously distributed
 1868 between 0 and 1, with signal being closer to 1 and background closer to 0. The signal probability is pa-
 1869 rameterized as a function of $m_{4\ell}$ instead of m_H . This allows continuous selection of the data-sample
 1870 independent of the m_H hypothesis. Both signal and background probabilities are normalized for any
 1871 given value of $m_{4\ell}$, which removes unnecessary correlation of KD with $m_{4\ell}$ and makes further fit imple-
 1872 mentation more robust. Parameterization is performed for ideal distributions, not including the detector
 1873 effects, and therefore does not require any training. This is still an optimal approach because detector ac-
 1874 ceptance effects are identical for signal and background and would cancel in the ratio in Eq. (33). From
 1875 statistical considerations the above construction of the KD is the most optimal given the input under
 1876 consideration. The input to the KD construction can be carefully controlled, certain observables can be
 1877 integrated out or included depending on the level of confidence in the input.

1878 The ideal probability density functions for signal and irreducible background can both be calculated
 1879 from first principles. For signal, we use the analytical distributions derived in [78]. The projections
 1880 of this probability density function are shown on top of SM Higgs events, generated at leading order
 1881 through gluon-gluon fusion, in figure 101. The background probability density function was calculated
 1882 in [76]. Although [76] only includes diagrams where the intermediate state is a pair of Z bosons, recent
 1883 progress has been made to include $Z\gamma^* \rightarrow 4\ell$ and $Z \rightarrow 4\ell$ diagrams and extend the validity to lower
 1884 values of $m_{4\ell}$ where these process are dominant. Projections of the irreducible background probability
 1885 density function are shown in figure 100 on top of leading order madgraph MC events.

1886 For background below threshold, it is also possible to substitute the analytical parameterization with the
 1887 correlated template distribution illustrated in Fig. 99. This simplified parameterization was used in the
 1888 past for events below the $2m_Z$ kinematic threshold while the analytic PDF mentioned above was used
 1889 above threshold, fixing both Z masses to 91.2 GeV. The current strategy is to use the state-of-the-art ZZ
 1890 parameterization and the same 8 inputs for all values of $m_{4\ell}$. The gain from these improvements is
 1891 shown by the ROC curves in figure 102.

1892 The background template distribution in Fig. 99 includes the most important correlations of five angles
 1893 and two masses m_1 and m_2 as a function of $m_{4\ell}$ as well as of the two masses m_1 and m_2 with respect to
 1894 each other. For example, for a given value of $m_{4\ell}$ there is a kinematic constraint $(m_1 + m_2) \leq m_{4\ell}$. We
 1895 also use the convention $m_1 > m_2$ without any loss of information, which explains the triangular shape
 1896 in Fig. 99.

1897 The resulting MELA KD distributions for signal and background are shown in Fig. 103 in three dif-
 1898 ferent mass ranges. Good agreement is found between data and background MC. Overall, significant
 1899 separation between signal and background is evident from the MELA KD distributions.

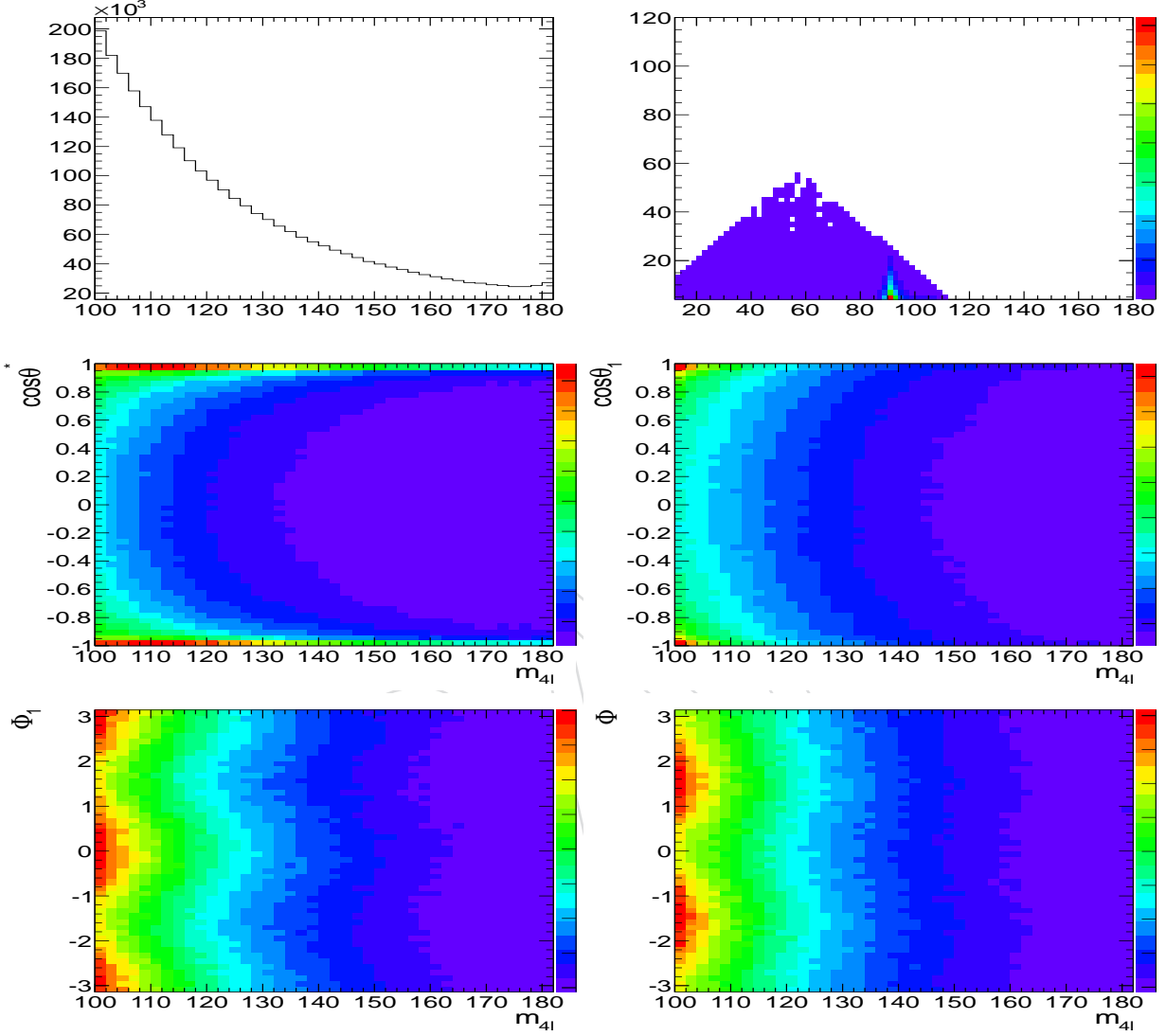


Figure 99: Parameterization of continuum ZZ background probability distribution \mathcal{P}_{bkg} using generator-level POWHEG events in the mass range [100,180] GeV. Top-left: m_{4l} distribution. Top-right: m_2 vs m_1 distribution in a narrow slice of m_{4l} around 125 GeV. Middle-left: $\cos\theta^*$ vs m_{4l} distribution. Middle-right: $\cos\theta_{1,2}$ vs m_{4l} distribution. Bottom-left: Φ_1 vs m_{4l} distribution. Bottom-right: Φ vs m_{4l} distribution.

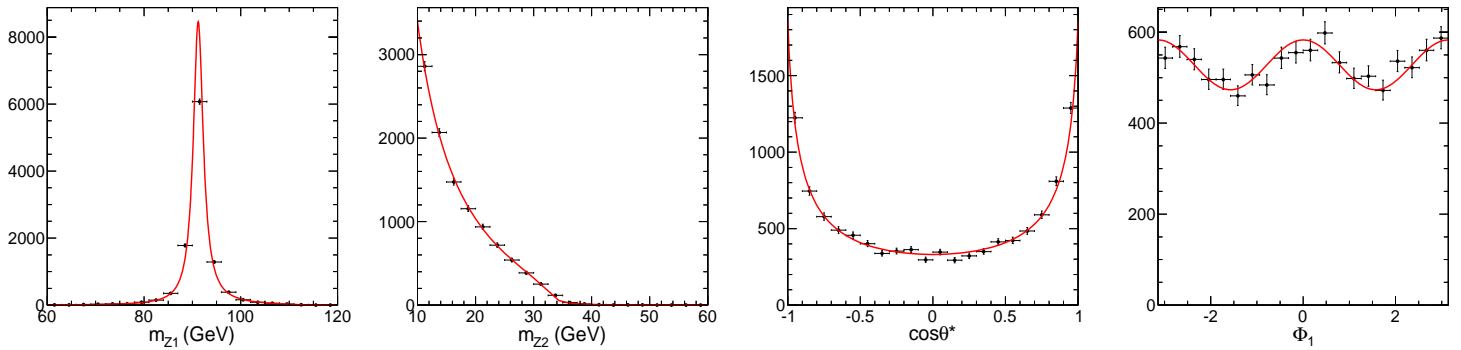


Figure 100: Projections of ZZ continuum PDF. Data is leading order ideal Madgraph MC events which includes both $ZZ \rightarrow 4\ell$ and $Z\gamma^* \rightarrow 4\ell$ processes.

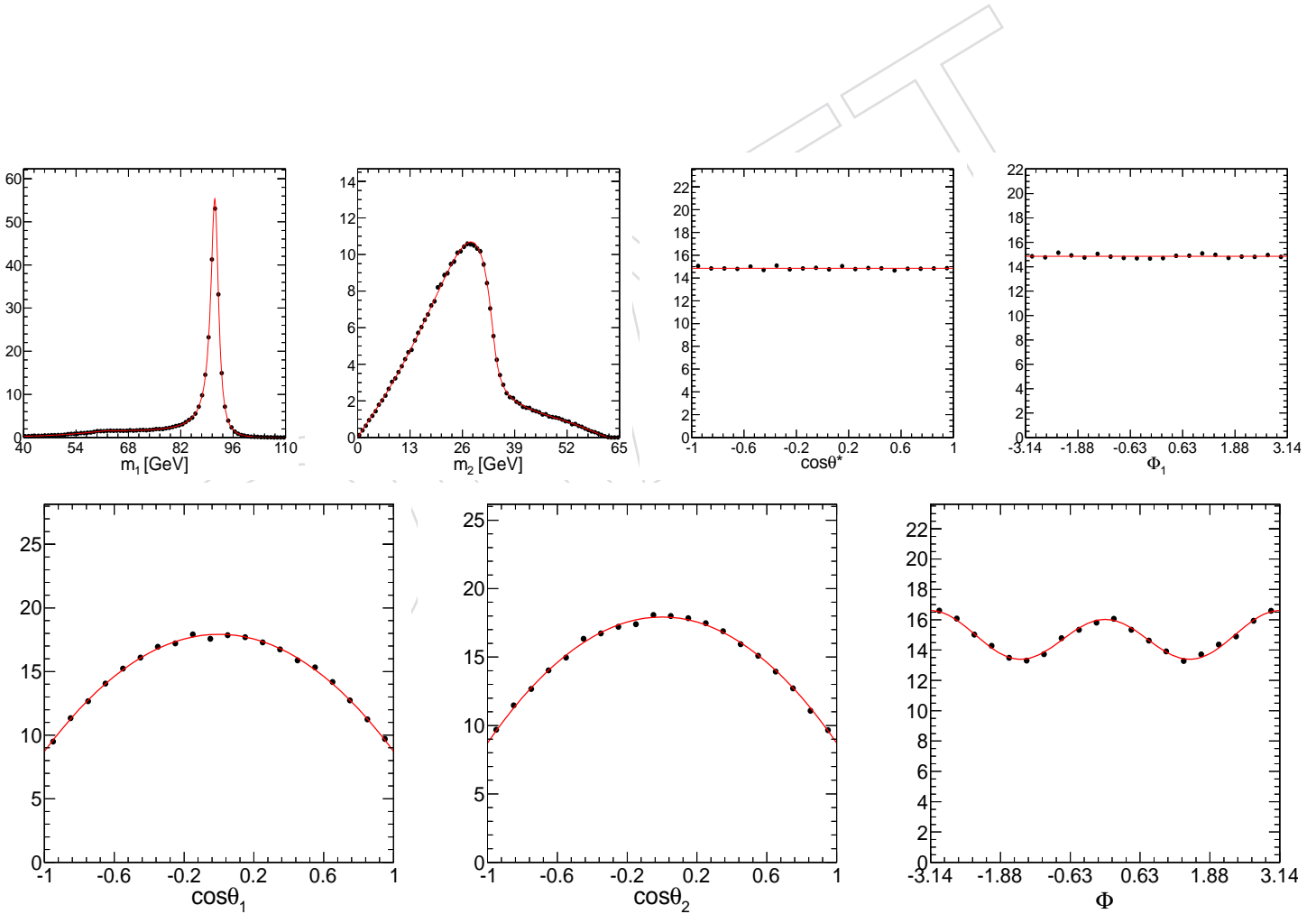


Figure 101: Projections of SM Higgs PDF. Data is leading order ideal JHUGen MC events.

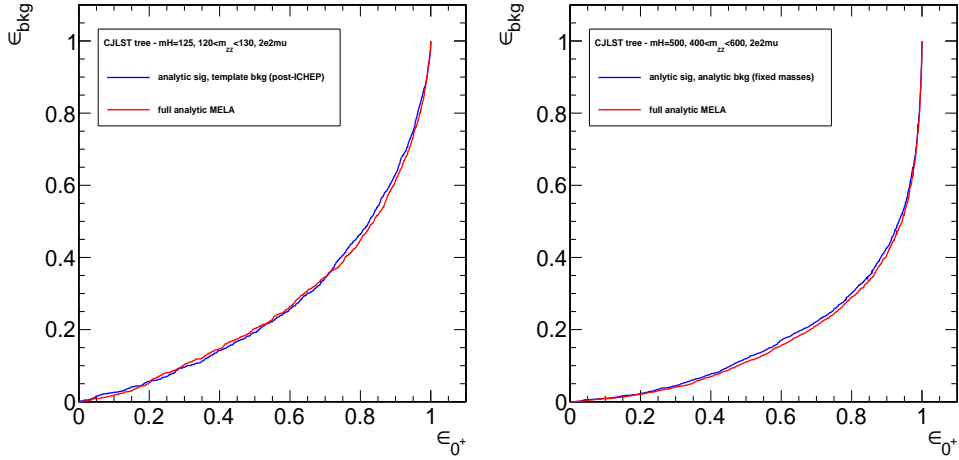


Figure 102: ROC curves using discriminant from ICHEP, with template background at low mass and fixed $m_{1,2}$ at high mass, versus new discriminant with full analytic parameterization for a 125 GeV signal (left) and 500 GeV signal (right).

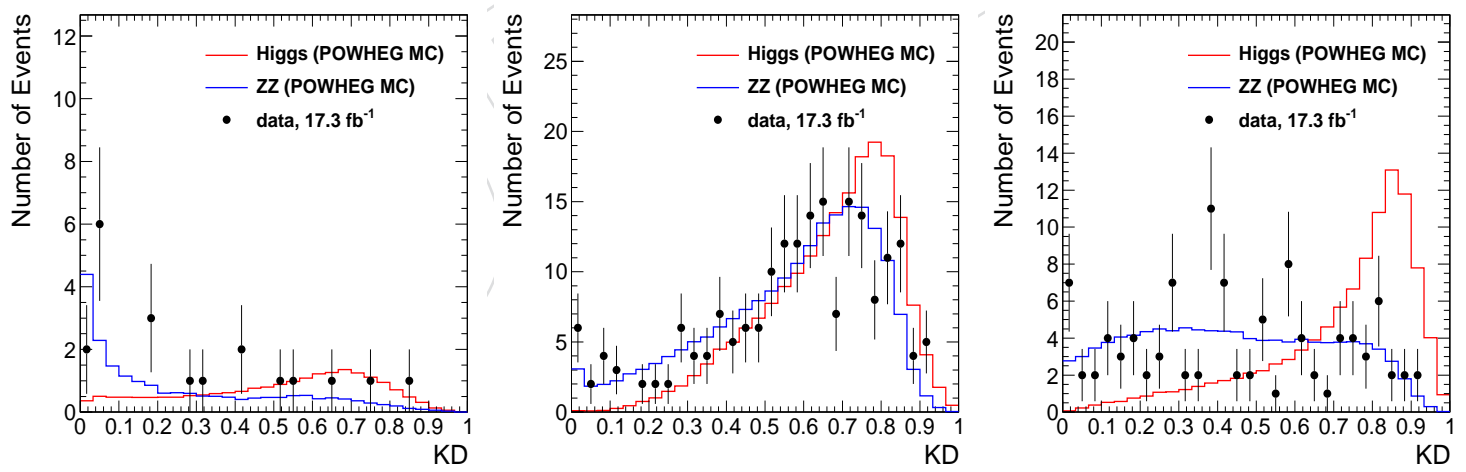


Figure 103: The KD distributions for signal and background in three mass ranges: $140 < m_{4\ell} < 160$ GeV (top), $200 < m_{4\ell} < 300$ GeV (middle), and $250 < m_{4\ell} < 450$ GeV (bottom). The signal (red solid histogram) is shown for $m_H = 150, 250$, and 350 GeV, respectively. The ZZ continuum background is shown as blue solid histogram. The top plot also shows $Z + X$ background estimated from data control region.

1900 10.2.1 Changes since ICHEP

1901 As stated above, for ICHEP the ZZ background below threshold was described by a template. In this
 1902 old version of MELA package, the users where inputting the wrong angle as Φ_1 . Anyway this angle
 1903 provides little separation, therefore this made MELA just slightly sub-optimal. In implementing the
 1904 phenomenological formula in the CMS code also a typo was introduced in the relative complex phase
 1905 of the three amplitudes A_{00}, A_{++}, A_{--} for the Higgs boson. This is another small improvement with
 1906 respect to the old MELA package. None of the above affected the validity of results, everything was
 1907 done consistently between data and MC.

1908 Putting aside this small fixes, the main improvement since ICHEP is due to the usage of the new available
 1909 analytical PDF to describe the ZZ background below threshold, including also the $Z\gamma^*$ contribution.
 1910 We moved to this new PDF coherently in the whole the $M(ZZ)$ spectrum, therefore we use now
 1911 also the 2 Z masses, on top of the 5 angles defined in Fig. 96, as input to the MELA calculation for all
 1912 $M(ZZ)$ values. Because of this improvement, the MELA shape changed coherently in signal and back-
 1913 ground as shown in Fig. 104. As a consequence, the comparison of the MELA values event-by-event
 1914 between different MELA version does not bring any information. In order to judge the changes the sig-
 1915 nals and background shapes have to be compared simultaneously in the ROC curve, as shown in Fig. 102.
 1916 Also a comparison between the MELA version with template and the new fully analytic implementation
 1917 has been performed on the p-values and the upper limit: with the new version the improvement in the
 p-value at 126 GeV is 1% and at high Higgs mass the improvement in the upper limit is 5%.

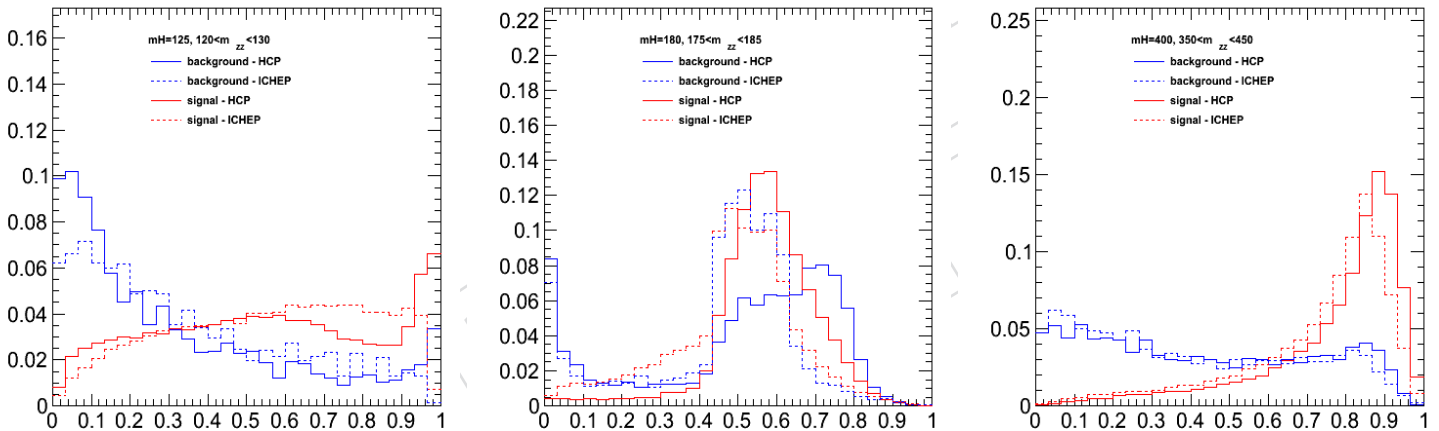


Figure 104: Comparison of MELA shapes using the ICHEP version and the new optimized version of the package. From left to right, the plots refer to an Higgs mass of 125 GeV, 180 GeV and 400 GeV.

1918
 1919 Additional improvements in signal over background separation has been observed by introducing pro-
 1920 duction variables (Higgs rapidity and transverse momentum) in the kinematic discriminant. On the
 1921 other hand, the transverse momentum distribution is a powerful discriminator for the properties mea-
 1922 surement (eg, to isolate the Vector Boson Fusion contribution, as described in Sec. A). Therefore, it is
 1923 optimal to keep the transverse momentum as a separate variable entering the analysis without com-
 1924 bining it with the kinematic discriminant, otherwise information about VBF production will be lost.
 1925 Moreover the control of the systematics on the production mechanism in the whole $m_{4\ell}$ spectrum is dif-
 1926 ficult to achieve and requires special care. For example, the effect of the Heavy Quark approximation in
 1927 the POWHEG MC samples used in this analysis is expected to largely overestimate the high tail of the
 1928 Higgs p_T distribution, especially for large Higgs masses, as shown in [79].

1929 10.3 Parameterization of the MELA discriminant

1930 While the MELA parameterization is performed using the ideal distributions in Eq. (33), the resulting
 1931 observable KD is a certain number for each event candidate. This observable is parameterized using
 1932 MC samples (with full CMS simulation and with data-to-MC corrections applied) for the Quantum
 1933 Mechanical processes that we model well, such as signal and ZZ background, and using data control
 1934 samples for instrumental and reducible background, such as $Z + X$. It is important to note that we use
 1935 only invariant masses and angles in the sequential process with ZZ system production and decay, which
 1936 is under good control from basic Quantum Mechanics and electroweak couplings, no QCD effects are
 1937 included. The KD observable is no more complex than the di-lepton invariant mass for example, and it
 1938 is even more reliable than p_T of the objects, which in turn depend on QCD effects in production.

1939 The KD distributions are somewhat affected by interference of identical leptons in the final states $ZZ \rightarrow$
 1940 $e^+e^-e^+e^-$ and $\mu^+\mu^-\mu^+\mu^-$, but not in $2e2\mu$. First of all, this effect is only relevant at low masses, be-
 1941 low the ZZ threshold, where at least one of the Z bosons is off-shell and therefore the phase-space for
 1942 interference increases. The background simulation of continuum ZZ background already includes inter-
 1943 ference effects and this is taken into account when KD distributions are parameterized for background.
 1944 The signal POWHEG+Pythia simulation of $H \rightarrow ZZ$ signal does not include such interference effect and
 1945 we use Prophecy event generator to calculate the difference. This is shown in Fig. 105, where this effect
 1946 is visible only at the low mass and essentially disappears at around $m_H = 160$ GeV. We perform a linear
 1947 fit of the ratio and apply mass-dependent re-scaling algorithm to MC simulation when KD distribution
 1948 is parameterized for signal. This mass-dependence is shown in Fig. 106.

1949 The KD distributions depend on the value of the $m_{4\ell}$, due to kinematics dependence on the mass. There-
 1950 fore, any further analysis of the data which includes KD must also include its full correlation with $m_{4\ell}$.
 1951 Below $2m_Z$ threshold, the dominant background is $q\bar{q} \rightarrow ZZ$ with a secondary contribution of $Z + X$
 1952 background. Above $2m_Z$ threshold, the dominant background is also $q\bar{q} \rightarrow ZZ$ with a secondary contribu-
 1953 tion of $gg \rightarrow ZZ$ background. For the signal, $q\bar{q} \rightarrow ZZ$ and $gg \rightarrow ZZ$ background, the ideal angular
 1954 and mass distributions come from basic quantum mechanics given the EWK couplings and are modeled
 1955 well by MC (apart from interference effect in signal, as corrected and discussed above).

1956 Detector effects may alter the KD distribution due to mis-modeling of lepton efficiency and resolutions.
 1957 Our estimates showed that those have very small effects on KD distributions because, as opposed to $m_{4\ell}$,
 1958 there is no distinct peak and smearing of broad distribution is a small effect. In Fig. 107, we show an
 1959 example of the shape variation due to extreme variation of MC efficiency by changing the Tag-and-Probe
 1960 corrections from those obtained from data to flat ones (typically this variation is larger than the errors).
 1961 In Fig. 108, we show an example of the shape variation due to extreme variation of MC resolution in
 1962 the $H \rightarrow ZZ \rightarrow 4e$ channel. Therefore, we ignore such detector effects in systematic uncertainties for the
 1963 KD, they are significantly smaller than statistical effects in the data to be analyzed.

1964 In Fig. 109 we show comparison of the KD distributions in several slices of $m_{4\ell}$ below threshold for
 1965 data control sample for $Z + X$ background, MC control sample for $Z + X$ background, for MC POWHEG
 1966 simulation of $q\bar{q} \rightarrow ZZ$ background. Two important conclusions could drawn. First, there is a good
 1967 agreement between the $Z + X$ background parameterization in data and MC, which gives us confidence
 1968 in the $Z + X$ background estimation. Second, data-driven $Z + X$ background distributions and contin-
 1969 num $q\bar{q} \rightarrow ZZ$ distribution are in good agreement. Therefore, a joint background parameterization can
 1970 be used, with any potential difference observed in these plots treated as systematic uncertainty. In order
 1971 to include systematics in the analysis, we create alternative KD distributions according to the linear fit
 1972 slope and its error by re-scaling the distributions according to that slope (with error on the slope added),
 1973 as shown in Fig. 109. It is also observed that the shape of the KD changes somewhat as a function of
 1974 $m_{4\ell}$, but its main feature remains, background peaks towards zero while signal peaks towards one.

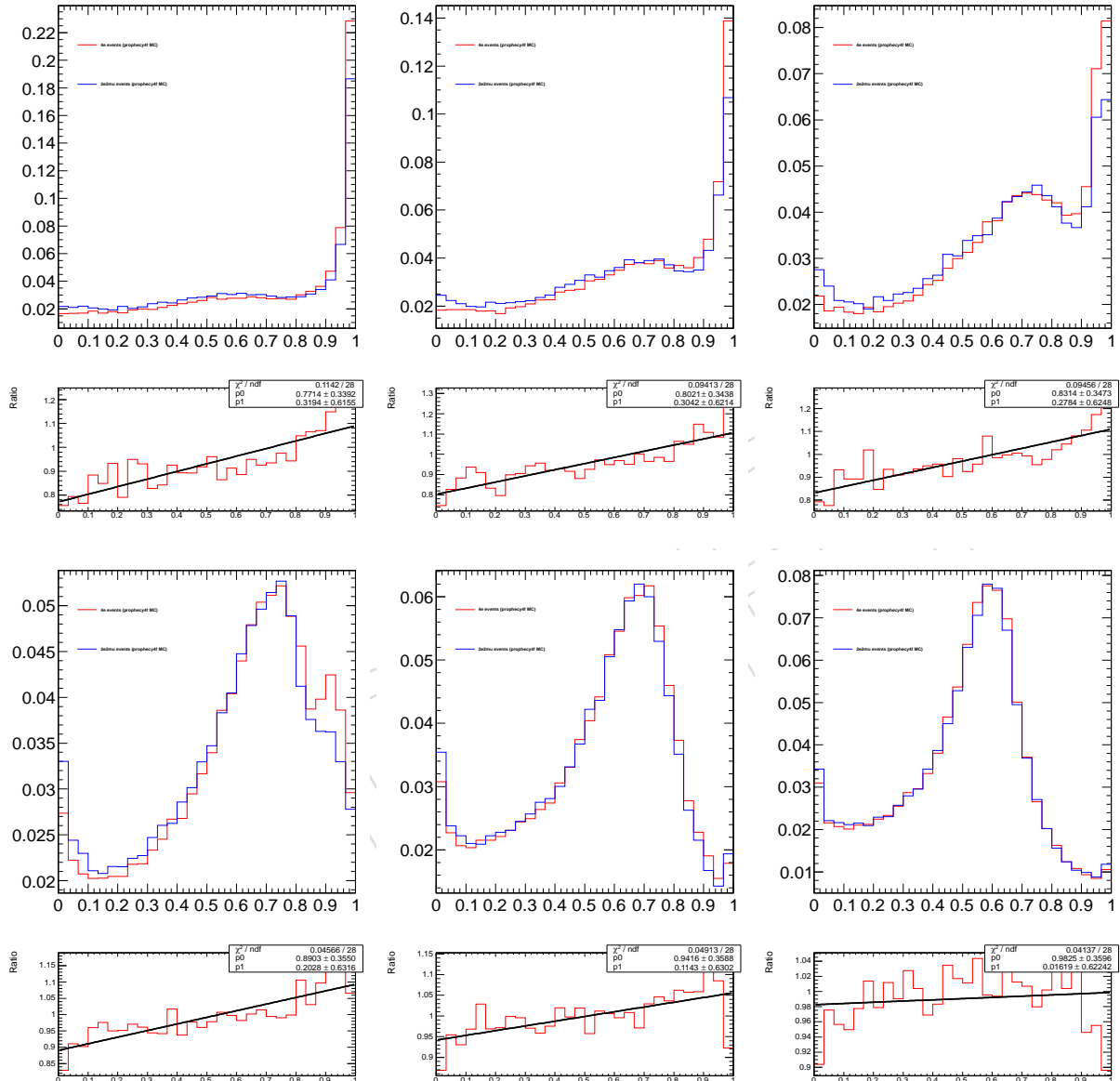


Figure 105: Distribution of signal MELA KD with and without interference effects and the ratio. Several m_H hypotheses are shown, top row: 120, 125, 130 GeV, bottom row: 140, 150, 160 GeV.

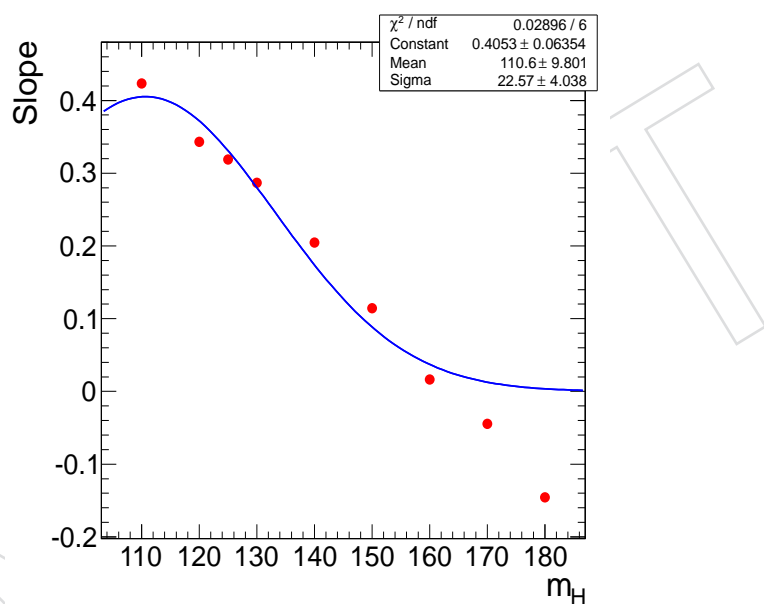


Figure 106: Slope of the correction to interference effect shown in Fig. 105 as a function of m_H .

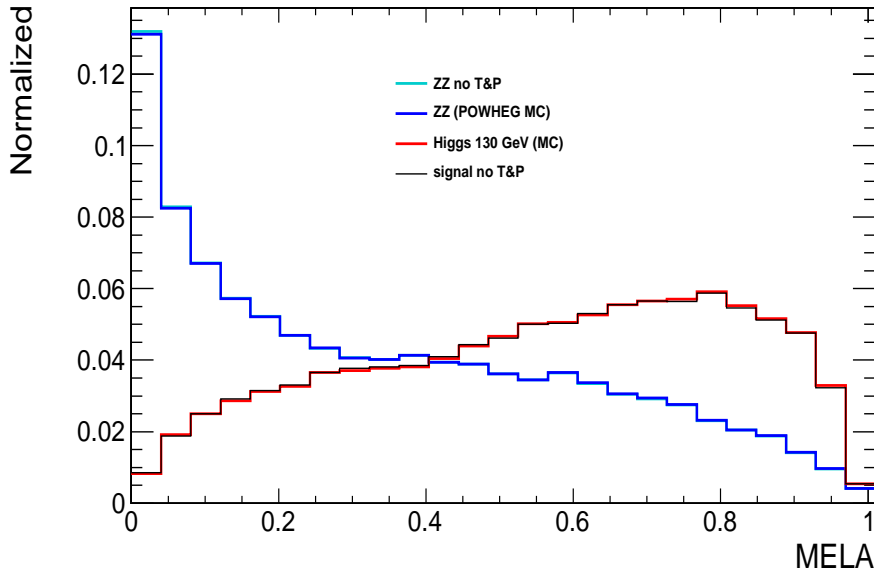


Figure 107: Distribution of the MELA KD for ZZ background and 130 GeV Higgs signal in MC, for events below $2m_Z$ threshold (background peaks towards 0 and signal peaks towards 1). For both signal and background two very close distributions are shown: with and without the Tag-and-Probe corrections for data-MC differences.

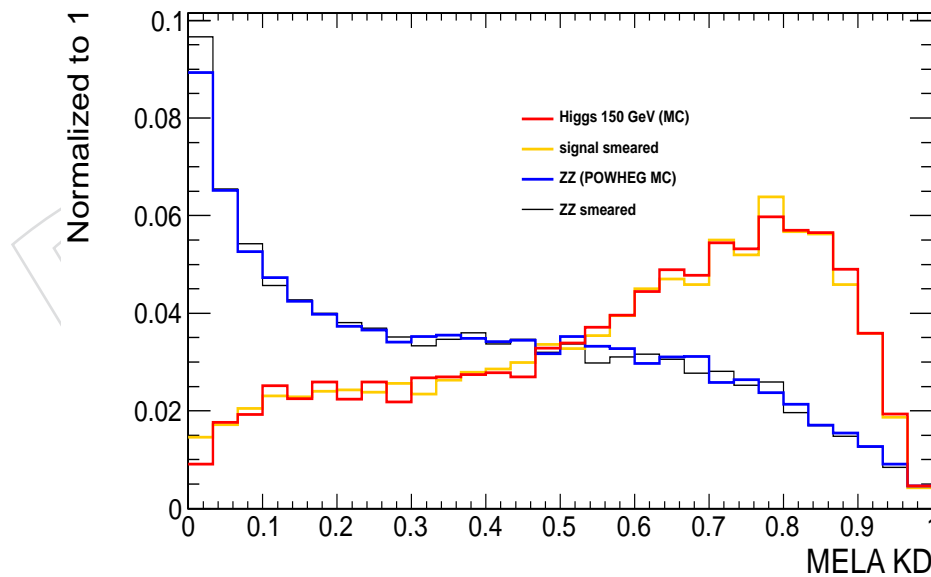


Figure 108: Distribution of the MELA KD for ZZ background and 150 GeV Higgs signal in MC, for events below $2m_Z$ threshold (background peaks towards 0 and signal peaks towards 1). For both signal and background two very close distributions are shown: with and without smearing of electron energy resolution, which is equal to uncertainty on this resolution. Only $H \rightarrow ZZ \rightarrow 4e$ channel is considered here, to show the largest effect.

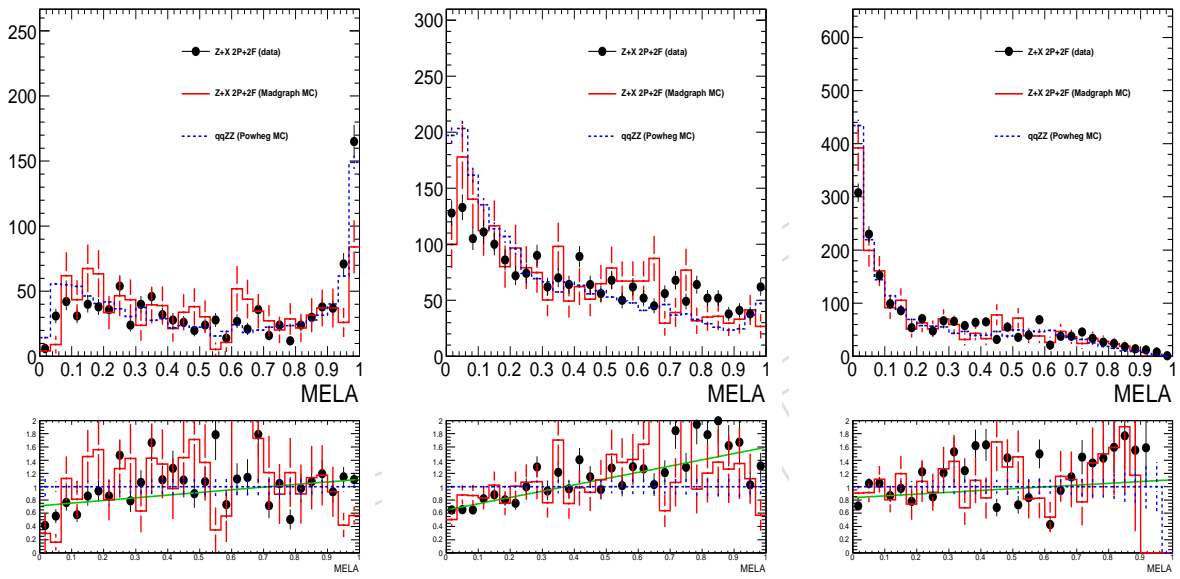


Figure 109: Parameterization of background MELA KD in several $m_{4\ell}$ ranges (in GeV). Left: [100,120]; middle: [120,140]; right: [140,160]. Points show data control sample for $Z + X$ background, red solid histogram shows MC control sample for $Z + X$ background, blue dashed histogram shows MC POWHEG simulation of ZZ background. Bottom plots show the ratio between the $Z + X$ background and ZZ background distributions.

1975 11 Summary of Selection and Systematic Uncertainties

1976 In this Section we summarize the input to the statistical analysis discussed in Section 12, expected and
 1977 observed yields, their uncertainties, and distributions of events in most critical observables. Discussion
 1978 of the shape models is presented elsewhere.

1979 11.1 Event yields and errors

1980 The number of candidates observed in 2011 and 2012 data, as well as the estimated background in the
 1981 signal region, are reported in Tables 29 and 28 for the baseline selection.

Table 27: The number of event candidates observed in 2011 data for 5.1 fb^{-1} , compared to the mean expected background and signal rates for each final state for $100 < m_{4\ell} < 1000 \text{ GeV}$. For the Z +X background, the estimations are based on data.

Channel	4e	4μ	2e2 μ
ZZ background	15.06 ± 1.71	22.58 ± 2.23	35.66 ± 3.64
Z+ X	$1.88^{+2.45}_{-1.13}$	$0.99^{+1.49}_{-0.6}$	$2.97^{+2.97}_{-1.49}$
All background expected	$16.94^{+2.99}_{-2.05}$	$23.58^{+2.68}_{-2.31}$	$38.63^{+4.7}_{-3.93}$
$m_H = 125 \text{ GeV}$	0.65 ± 0.1	1.2 ± 0.13	1.54 ± 0.18
$m_H = 126 \text{ GeV}$	0.72 ± 0.11	1.3 ± 0.14	1.71 ± 0.2
$m_H = 200 \text{ GeV}$	4.12 ± 0.48	5.86 ± 0.59	9.84 ± 1.02
$m_H = 350 \text{ GeV}$	2.34 ± 0.28	3.21 ± 0.34	5.59 ± 0.61
$m_H = 500 \text{ GeV}$	0.81 ± 0.1	1.08 ± 0.12	1.89 ± 0.21
Observed	14	20	43

Table 28: The number of event candidates observed in 2012 data 12.2 fb^{-1} , compared to the mean expected background and signal rates for each final state for $100 < m_{4\ell} < 1000 \text{ GeV}$. For the Z +X background, the estimations are based on data.

Channel	4e	4μ	2e2 μ
ZZ background	40.2 ± 4.7	60.14 ± 6.66	98.35 ± 10.71
Z+ X	$4.46^{+7.58}_{-3.12}$	$2.08^{+2.29}_{-1.04}$	$7.04^{+11.26}_{-4.22}$
All background expected	$44.66^{+8.92}_{-5.64}$	$62.22^{+7.04}_{-6.74}$	$105.39^{+15.54}_{-11.51}$
$m_H = 125 \text{ GeV}$	1.8 ± 0.25	3.47 ± 0.41	4.52 ± 0.54
$m_H = 126 \text{ GeV}$	1.99 ± 0.28	3.79 ± 0.44	4.99 ± 0.6
$m_H = 200 \text{ GeV}$	12.68 ± 1.52	17.82 ± 2.02	30.4 ± 3.38
$m_H = 350 \text{ GeV}$	7.66 ± 0.94	10.27 ± 1.19	18.2 ± 2.07
$m_H = 500 \text{ GeV}$	2.8 ± 0.35	3.68 ± 0.43	6.51 ± 0.75
Observed	45	75	119

1982 11.2 Distributions of events

1983 The reconstructed four-lepton invariant mass distribution is shown in Figure 110 for the full dataset,
 1984 where different mass ranges, including the mass below 100 GeV (not used for analysis). These distribu-
 1985 tions are also shown in Figs. 111 and 112 but splitted by channel, and for 7 and 8 TeV data separately.

1986 The reconstructed di-lepton invariant mass and MELA KD distributions are shown in Figure 113.

1987 The SM background distributions are obtained combining the rate normalization from from data-driven
 1988 methods and knowledge on shapes taken from the MC samples.

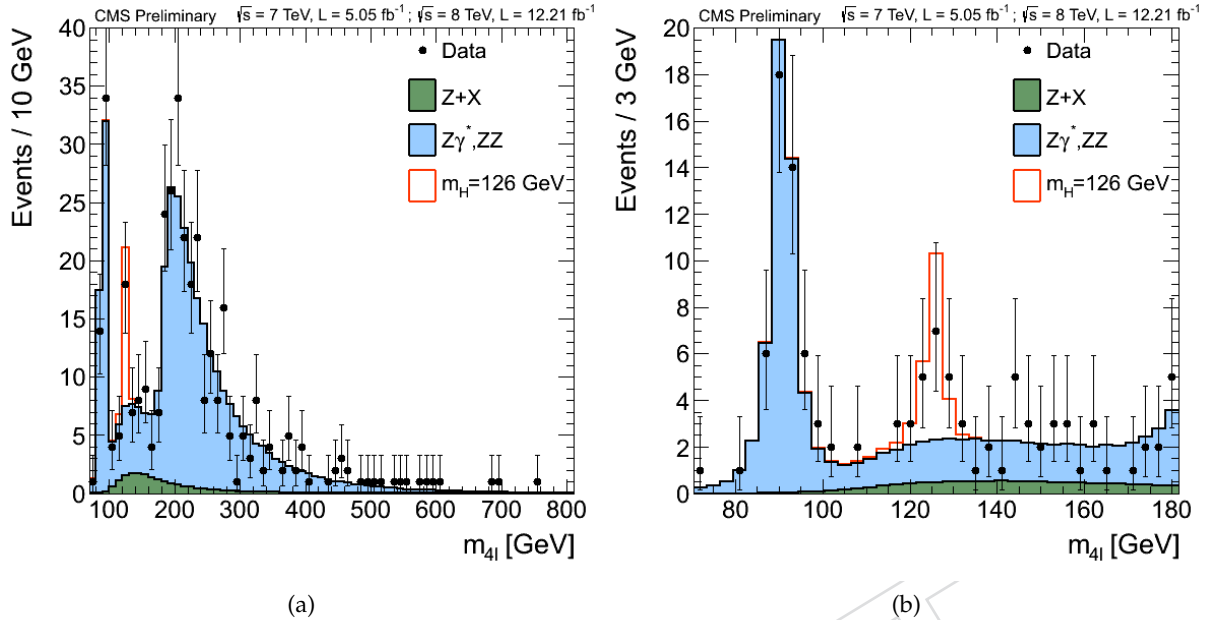


Figure 110: Distribution of the four-lepton reconstructed mass. Region $m_{4l} < 100 \text{ GeV}$ is shown but not used in analysis. The sample correspond to an integrated luminosity of $\mathcal{L} = 5.1 \text{ fb}^{-1}$ of 2011 data and $\mathcal{L} = 12.2 \text{ fb}^{-1}$ of 2012 data.

1989 The correlation between the four-lepton reconstructed mass and KD, or the reconstructed mass of the
1990 second or first lepton pair are shown in Figs. 114.

Table 29: The number of event candidates observed, compared to the mean expected background and signal rates for each final state. For the $Z + X$ background, the estimations are based on data. The results are given integrated over the full mass measurement range for the Higgs boson search from 100 to 1000 GeV and for 2011 and 2012 data combined.

Channel	4e	4μ	$2e2\mu$
ZZbackground	55.26 ± 6.4	82.73 ± 8.89	134.0 ± 14.35
$Z + X$	$6.34^{+10.03}_{-4.25}$	$3.07^{+3.78}_{-1.64}$	$10.02^{+14.24}_{-5.71}$
All background expected	$61.61^{+11.91}_{-7.69}$	$85.8^{+9.73}_{-9.05}$	$144.02^{+20.24}_{-15.44}$
$m_H = 125 \text{ GeV}$	2.46 ± 0.35	4.67 ± 0.53	6.07 ± 0.72
$m_H = 126 \text{ GeV}$	2.71 ± 0.39	5.09 ± 0.58	6.7 ± 0.8
$m_H = 200 \text{ GeV}$	16.81 ± 2.01	23.68 ± 2.61	40.25 ± 4.4
$m_H = 350 \text{ GeV}$	10.0 ± 1.22	13.47 ± 1.52	23.8 ± 2.68
$m_H = 500 \text{ GeV}$	3.6 ± 0.45	4.76 ± 0.55	8.4 ± 0.97
Observed	59	95	162

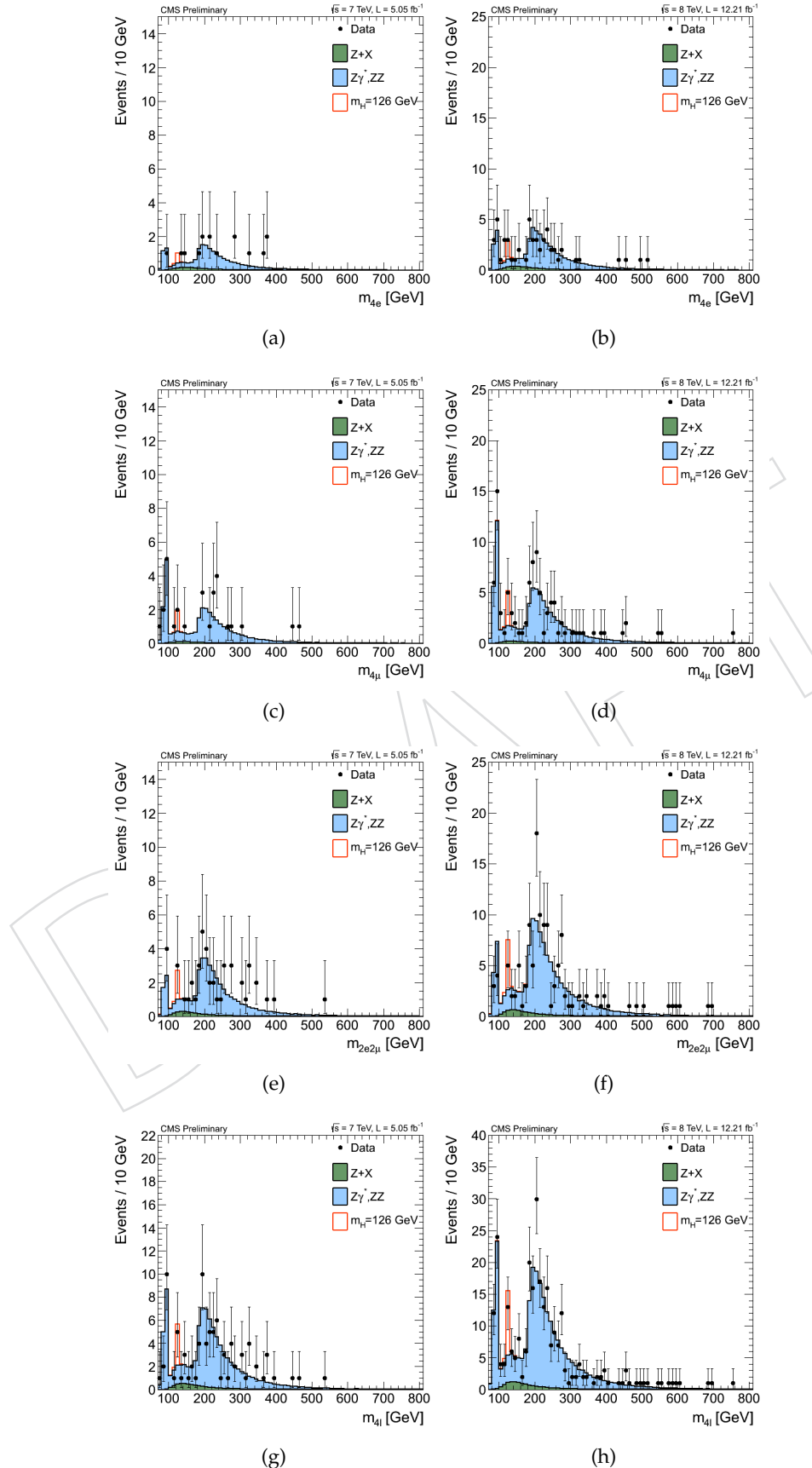


Figure 111: Distribution of the four-lepton reconstructed mass in several sub-channels: $4e$ (top), 4μ (middle top), $2e2\mu$ (middle bottom), for all channels combined (bottom) and for 7 TeV (left) and 8 TeV (right).

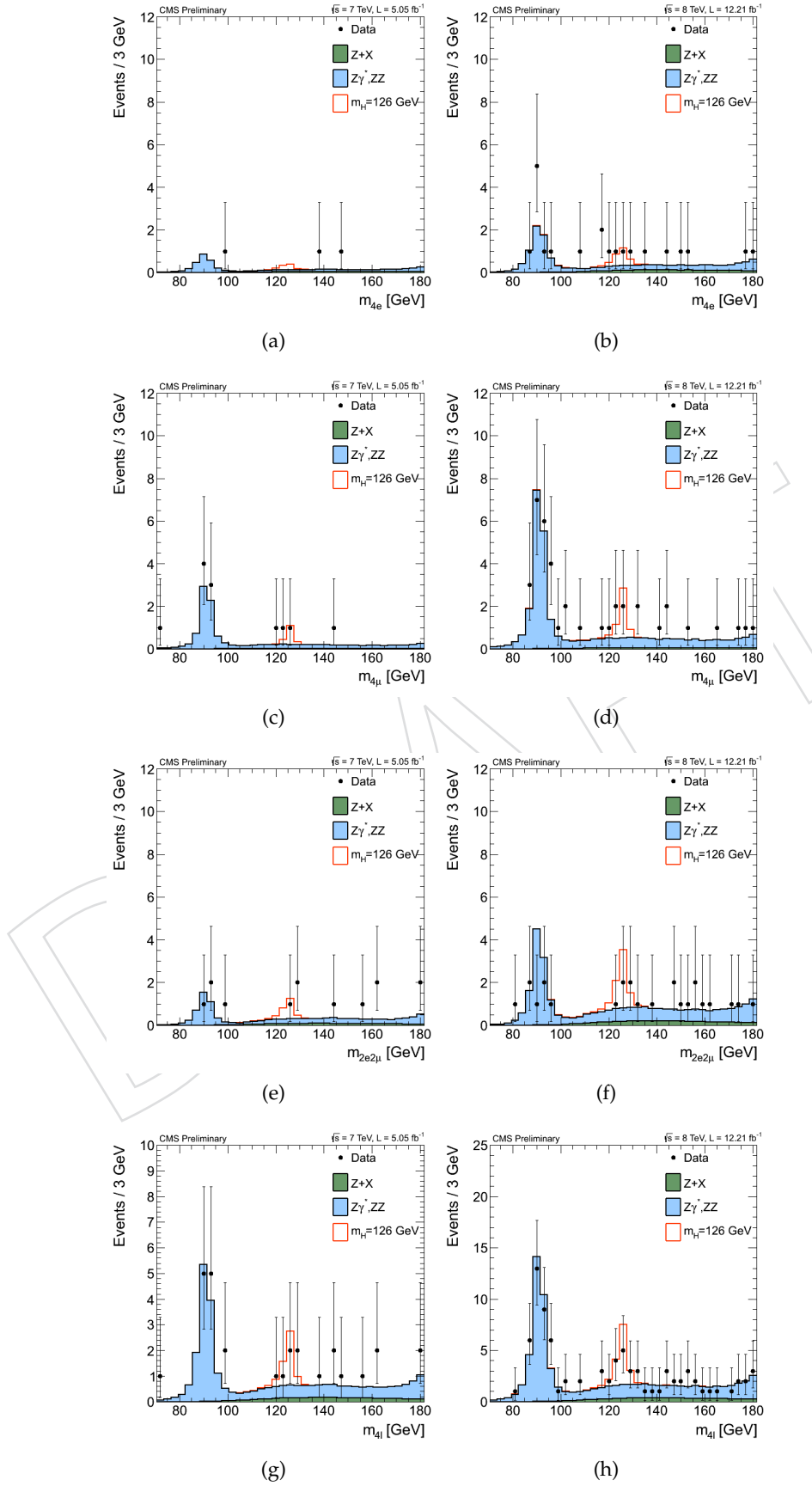


Figure 112: Distribution of the four-lepton reconstructed mass in the low-mass range in several sub-channels: $4e$ (top), 4μ (middle top), $2e2\mu$ (middle bottom), for all channels combined (bottom) and for 7 TeV (left) and 8 TeV (right).

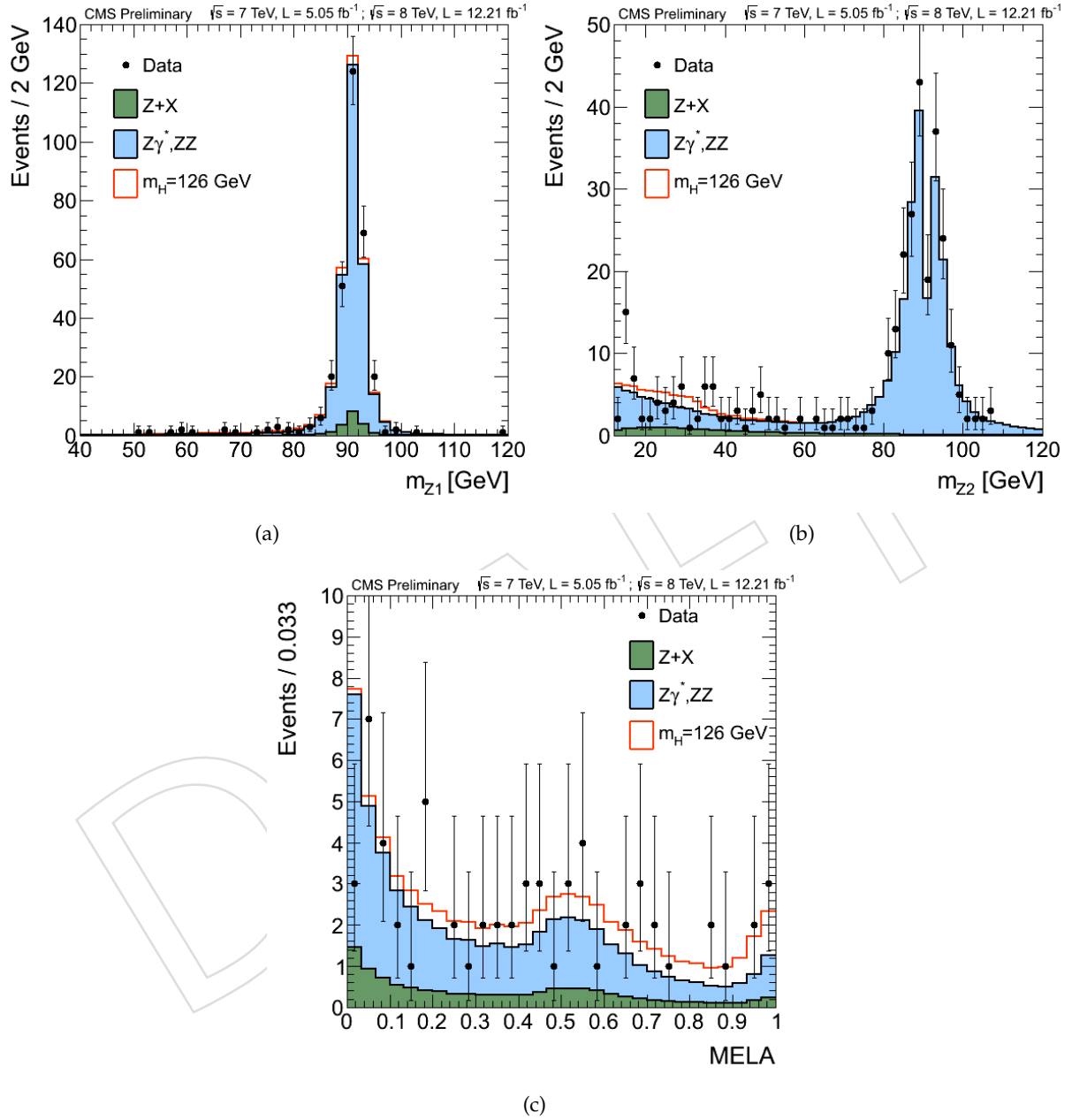


Figure 113: Distribution of Z_1 (top left) and Z_2 (top right) invariant mass, MELA KD in the mass range (100-180 GeV/c^2) on the bottom. The samples correspond to an integrated luminosity of $\mathcal{L} = 5.1 \text{ fb}^{-1}$ for the 7 TeV data, and 12.2 fb^{-1} for the 8 TeV data.

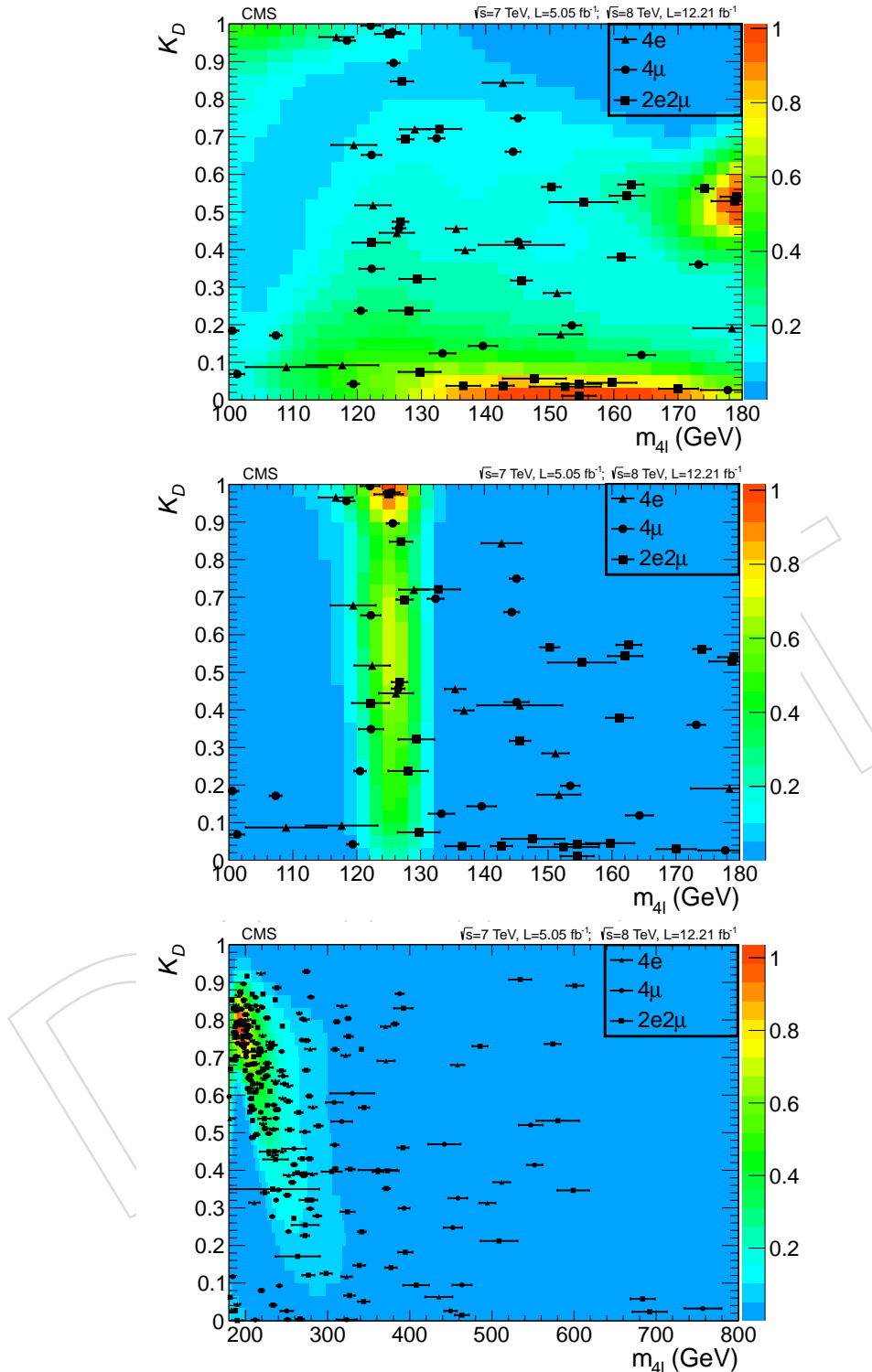


Figure 114: Distribution of the MELA KD versus the four-lepton reconstructed mass $m_{4\ell}$ for 2011 and 2012 data combined. Circles are 4μ events, triangles $4e$ events and squares $2e2\mu$ events. Event-by-event errors is attached to each event. Top plot: low-mass range with contours for background expectation. Middle plot: low-mass range with contours for signal expectation with $m_H = 126$ GeV. Bottom plot: high-mass range with contours for background expectation.

1991 11.3 Anatomy of the signal

1992 The reconstructed four-lepton invariant mass distribution is shown in Figure 115 for the full dataset
 1993 in the low mass range, before and after a cut at 0.5 on the Kinematic Discriminant³. It can be nicely
 1994 appreciated that the background is diminished by a large factor while the signal peak remains.

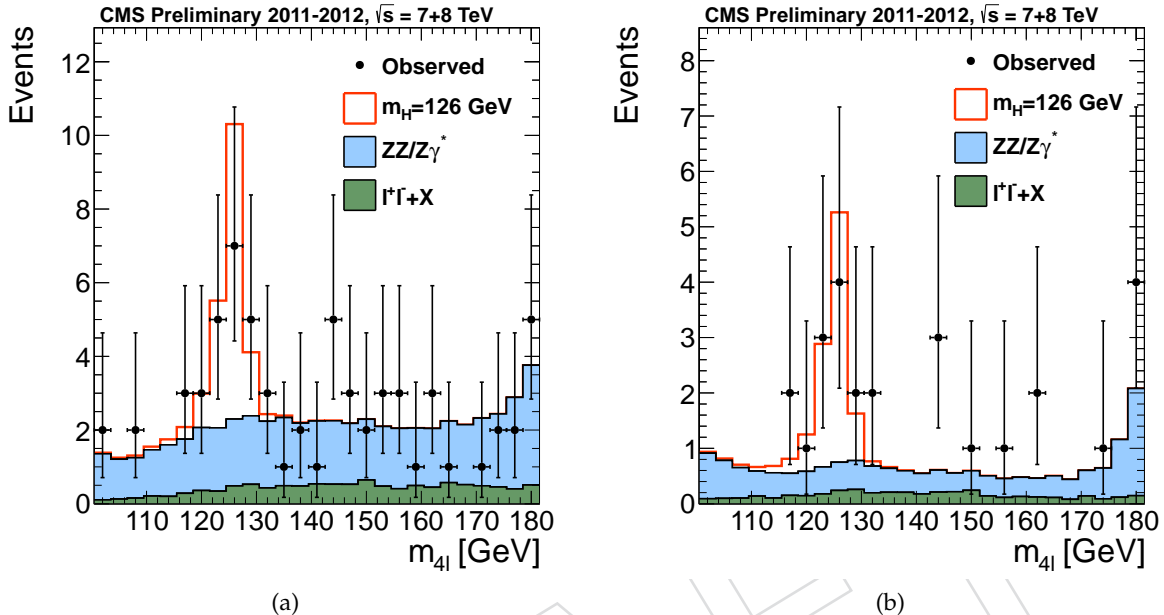


Figure 115: Distribution of the four-lepton reconstructed mass before (left) and after (right) a cut on the Kinematic Discriminant (≥ 0.5). The sample correspond to an integrated luminosity of $\mathcal{L} = 5.1 \text{ fb}^{-1}$ of 2011 data and $\mathcal{L} = 12.2 \text{ fb}^{-1}$ of 2012 data.

1995 Distributions of the main observables of the analysis are also shown on Figure 116 for the events located
 1996 in three bins around the peak of the observed signal, namely between 121.5 and 130.5 GeV.

1997 The correlation between the four-lepton reconstructed mass and the reconstructed mass of the second
 1998 or first lepton pair are shown in Figs. 117.

³this cut keeps about 60% of the signal while keeping only 30% the background

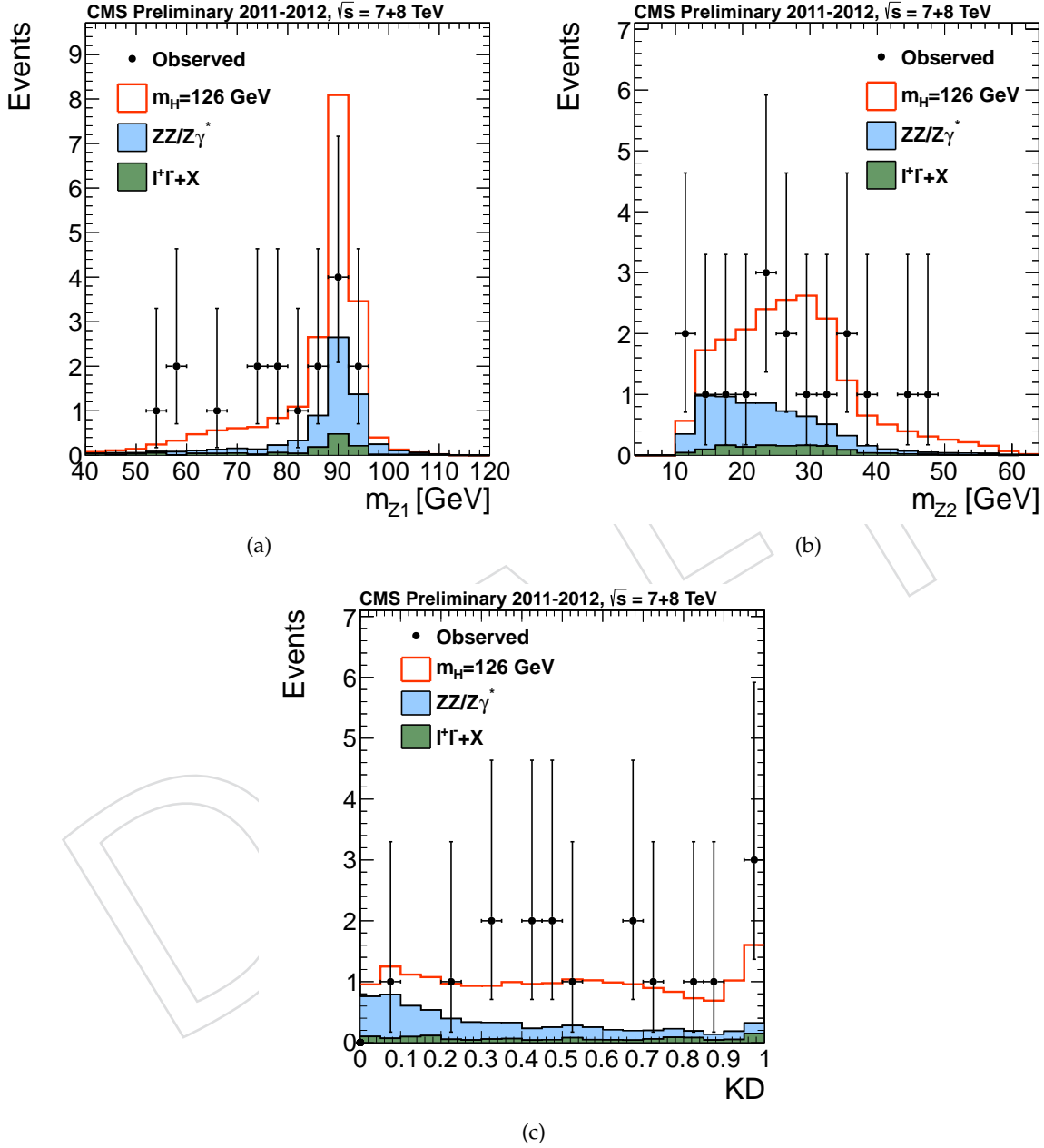


Figure 116: Distribution of Z_1 (top left) and Z_2 (top right) invariant mass, MELA KD in the mass range ($121.5-130.5 \text{ GeV}/c^2$) on the bottom. The samples correspond to an integrated luminosity of $\mathcal{L} = 5.1 \text{ fb}^{-1}$ for the 7 TeV data, and 12.2 fb^{-1} for the 8 TeV data.

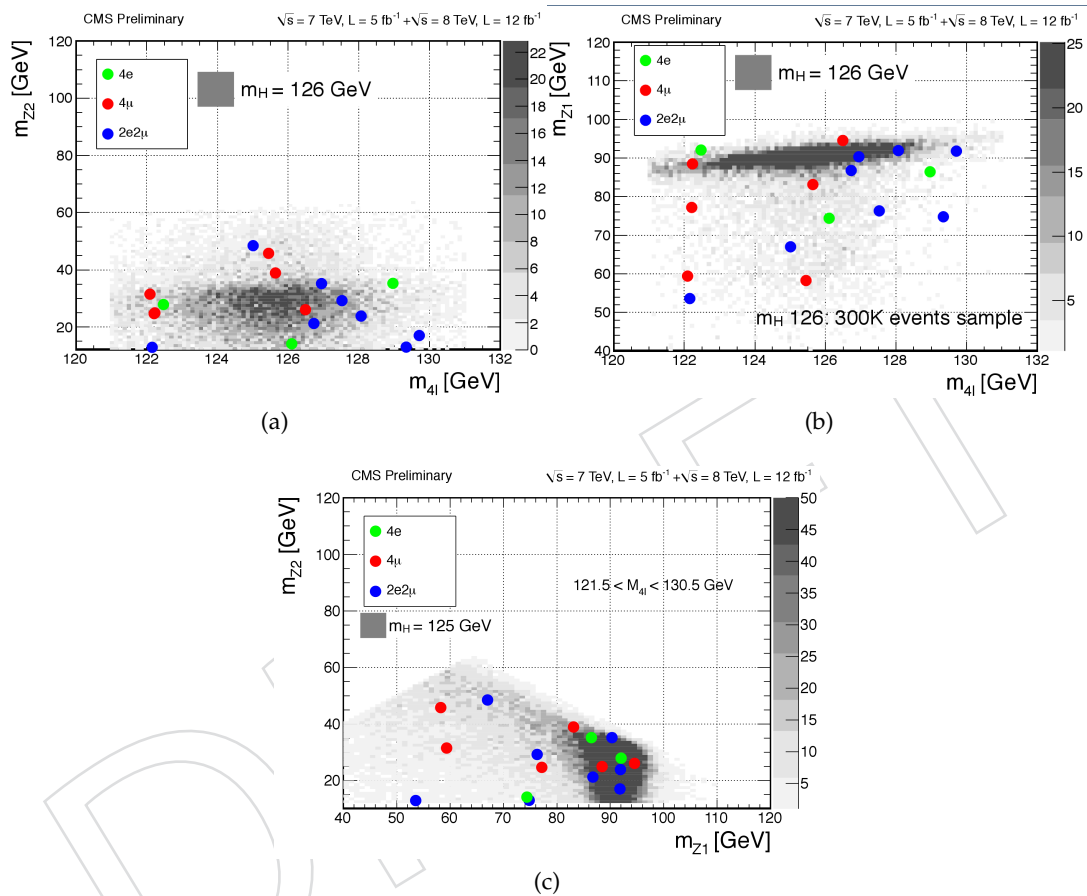


Figure 117: Distribution of the reconstructed mass of the second lepton pair (M_{Z2} , top left) or the reconstructed mass of the first lepton pair (M_{Z1} , top right) versus the four-lepton reconstructed mass (M_{4l}) for the $4e$ (green circle), 4μ (green circle) and $2e2\mu$ (blue circle) final states. M_{Z2} vs M_{Z1} is also shown (bottom). Shaded histograms represent the expectations for a signal with $m_H=126$ GeV. The sample correspond to an integrated luminosity of $\mathcal{L} = 5.1 \text{ fb}^{-1}$ of 2011 data and $\mathcal{L} = 12.2 \text{ fb}^{-1}$ of 2012 data.

¹⁹⁹⁹ **11.4 FSR performances**

²⁰⁰⁰ The FSR recovery algorithm affects 21 events selected in 2011 and 2012 data. The properties of the
²⁰⁰¹ selected events are included in table ??.

$m_{4\ell}$	$m_{4\ell+\gamma}$	$p_T(\gamma)$	$\min\Delta R(\ell, \gamma)$	Z affected
191.62836	196.46037	4.0201878	0.0725129	Z_1
154.14547	212.37142	48.498153	0.0127985	Z_1
217.21096	241.26227	20.150938	0.0274190	Z_1
90.727626	99.944570	7.3589038	0	Z_1
262.60244	269.67286	4.2291932	0.0412425	Z_2
243.34988	245.90804	2.8282477	5.960e-08	Z_1
108.21291	120.53121	9.9008379	0.0250456	Z_1
174.49852	218.61174	20.671079	0.0193634	Z_1
183.16119	188.12688	4.8733825	0.0479542	Z_2
169.48703	200.71623	10.757437	0.0444185	Z_1
113.37769	122.16128	4.4912734	0.0538658	Z_2
316.42562	344.25120	10.521068	0.0263784	Z_2
199.63793	201.79604	2.2494859	0.0674357	Z_2
204.73402	222.47363	14.906189	0.163262	Z_2
355.04828	371.52907	11.308774	0.1308002	Z_1
219.62179	230.65086	8.6164255	0.0362535	Z_2
446.23279	458.12644	10.874712	0.3644125	Z_1
204.52711	233.39366	19.946832	0.4769297	Z_1
56.283663	90.093741	25.018220	0.0484993	Z_1
258.65478	268.70371	9.7407245	0.2752697	Z_2
115.17896	126.49631	7.6711731	0.3087299	Z_1

Table 30: Properties of the events with identified FSR photons in the processed dataset

²⁰⁰² The observed FSR rate is 5.8 ± 1.4 % consistent with the expectation. In eight of the FSR events, Z_2
²⁰⁰³ is affected and this happens mainly at high four-lepton mass where Z_2 is on-shell except one events
²⁰⁰⁴ aT 122.5 GeV. The presence of FSR in Z_2 at low mass denotes that the event is more compatible with
²⁰⁰⁵ background where the FSR rate is muich higher.

²⁰⁰⁶ Figure 118 shows the correlation of the four lepton mass before and after FSR recovery for the two
²⁰⁰⁷ affected final states.

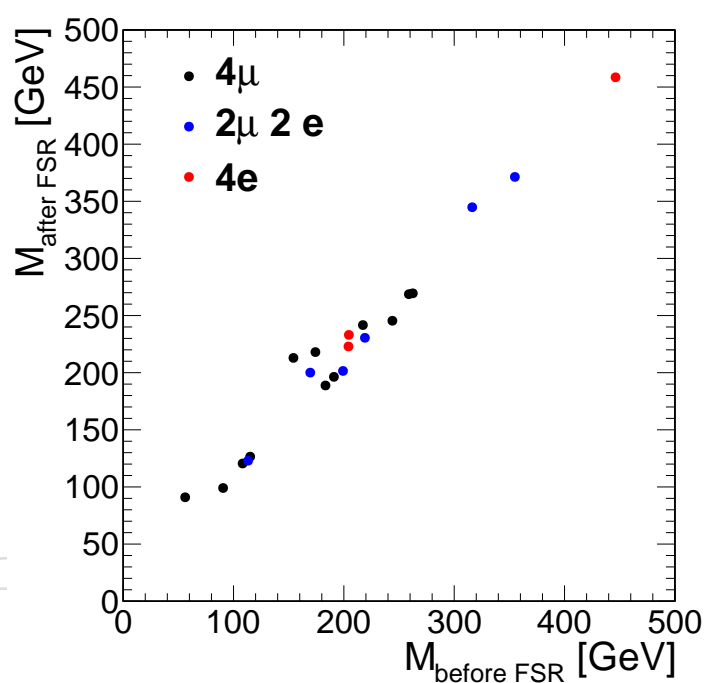


Figure 118: Invariant mass of the final selected events before and after FSR recovery

2008 11.5 Summary of systematic uncertainties

2009 **FIXME to update some parts ... but we don't expect major changes. Hence we put the same tables**
2010 and numbers as for ICHEP as we are finalizing updates (new tag and probe, energy scale/smearing,
2011 ...)

2012 The summary of systematic uncertainties for the analysis parts on 2011 and 2012 collected data is pro-
2013 vided in the Tab. 31, 32, 33, 34. All systematic uncertainties are correlated between 7 and 8 TeV samples
2014 except uncertainty on luminosity. Log-normal uncertainty on Z+jets normalization is correlated between
2015 7 and 8 TeV samples, but it is correlated between different final states (i.e. it is correlated for 4e 7 TeV
2016 and 4e 8 TeV, but it is not correlated for example for 4e and 4mu). Uncertainties affecting muons and
2017 electrons are correlated to any other channel that contains those objects and are given combined and per
2018 event. Uncertainties on MELA template shapes are introduced through alternative shapes which are
2019 representing 1 sigma errors.

Table 31: Simulated samples for 7 TeV: Summary of the magnitude of theoretical and phenomenological systematic uncertainties in percent for $H \rightarrow ZZ \rightarrow 4\ell$ and $ZZ \rightarrow 4\ell$. Errors are common to all 4ℓ channels. Last three lines are parametric uncertainties on the shape of the HZZ4L signal Crystal Ball (mean, sigma and tail parameter).

Source of uncertainties	Error for different processes					ZZ	ggZZ
	ggH	VBF	WH	ZH	ttH		
gg partonic luminosity	7.5-10				0-10		10
$qq/q\bar{q}$ partonic luminosity		2.2-4.7	0-4.5	0-5.0			5
QCD scale uncert. for $gg \rightarrow H$	8.7-10						
QCD scale uncert. for VBF qqH		0-1.5					
QCD scale uncert. for VH			0-0.75	0-1.3			
QCD scale uncert. for ttH					0-8.3		
4ℓ -acceptance for $gg \rightarrow H$	negl.	negl.	negl.	negl.	negl.		
Uncertainty on $BR(H \rightarrow 4\ell)$	2	2	2	2	2		
QCD scale uncert. for $ZZ(\text{NLO})$						2.6-6.7	
QCD scale uncert. for $gg \rightarrow ZZ$							24-44
CB mean, parametric			0.4				
CB sigma, parametric			20				
CB tail parameter, parametric			5.0				

Table 32: Simulated samples for 8 TeV: Summary of the magnitude of theoretical and phenomenological systematic uncertainties in percent for $H \rightarrow ZZ \rightarrow 4\ell$ and $ZZ \rightarrow 4\ell$. Errors are common to all 4ℓ channels. Last three lines are parametric uncertainties on the shape of the HZZ4L signal Crystal Ball (related to scale and resolution uncertainties mean, sigma, and tail parameter).

Source of uncertainties	Error for different processes						
	ggH	VBF	WH	ZH	ttH	ZZ	ggZZ
gg partonic luminosity	7.2-9.2				0-9.8		10
$q\bar{q}/q\bar{q}$ partonic luminosity		1.2-1.8	0-4.5	0-5.0			5
QCD scale uncert. for $gg \rightarrow H$	5.5-7.9						
QCD scale uncert. for VBF $q\bar{q}H$		0.1-0.2					
QCD scale uncert. for VH			0-0.6	0-1.5			
QCD scale uncert. for ttH					0-8.8		
4ℓ -acceptance for $gg \rightarrow H$	negl.	negl.	negl.	negl.	negl.		
Uncertainty on $BR(H \rightarrow 4\ell)$	2	2	2	2	2		
QCD scale uncert. for $ZZ(\text{NLO})$						2.6-6.7	
QCD scale uncert. for $gg \rightarrow ZZ$							24-44
CB mean, parametric			0.4				
CB sigma, parametric			20				
CB tail parameter, parametric			5.0				

Table 33: 7 and 8 TeV samples: Summary of the magnitude of instrumental systematic uncertainties in percent for $H \rightarrow ZZ \rightarrow 4\ell$ and $ZZ \rightarrow 4\ell$. The instrumental systematic uncertainties for all five Higgs boson production mechanisms are assumed to be same, similarly on $ZZ \rightarrow 4\ell$ (NLO) and $gg \rightarrow ZZ \rightarrow 4\ell$.

Source of uncertainties	Error for different processes					
	$H \rightarrow ZZ \rightarrow 4\ell$		$ZZ/ggZZ \rightarrow 4\ell$			
	4e	4 μ	2e2 μ	4e	4 μ	2e2 μ
Luminosity				2.2 (5 for 8 TeV)		
Trigger				1.5%		
electron reco/ID/isolation (4e)				6.2-11		
muon reco/ID/isolation (4mu)				1.9		

Table 34: 7 and 8 TeV samples: Summary of the magnitude of systematic uncertainties (asymmetric) in percent for the reducible 4ℓ backgrounds (for 8 TeV in parenthesis). There are several uncertainties (as described earlier in the paper). Below we give the combined uncertainty.

4e	4 μ	2e2 μ
-40..+90 (-30..+90)	-	-
-	-40..+60 (-40..+80)	-
-	-	-50..+60 (-30..+100)

2020 12 Statistical Analysis

2021 12.1 Methodology using 2D distributions ($m_{4\ell}$, KD)

2022 The ($m_{4\ell}$, KD) unbinned distributions of the selected events are split into six categories based on three
 2023 final states (4μ , $4e$, $2\mu 2e$) and two running periods (7 and 8 TeV). These events are examined for 183
 2024 hypothetical Higgs boson masses m_H in a range between 110 GeV and 600 GeV, where the mass steps
 2025 are optimized to account for the expected width, Γ , and resolution for measurement of m_H [80]. For
 2026 each mass hypothesis, we perform a simultaneous likelihood fit of the six two-dimensional ($m_{4\ell}$, KD)
 2027 distributions using the statistical approaches discussed in Ref. [80]. As a cross-check, we have also stud-
 2028 ied one-dimensional $m_{4\ell}$ distributions and found consistent, but systematically higher median expected
 2029 limits. We adopt the modified frequentist construction CL_s [80–82] as the primary method for reporting
 2030 limits. As a complementary method to the frequentist paradigm, we use the Bayesian approach [83] and
 2031 find consistent results.

2032 The probability distribution of $\mathcal{P}^{1D}(m_{4\ell})$ for the background is parameterized with empirical functions
 2033 using MC simulation for ZZ background and data control regions for Z + X background. The recon-
 2034 structed signal $m_{4\ell}$ distributions are described with a relativistic Breit-Wigner parametrization convo-
 2035 luted with a two-sided Crystal-Ball function [84]. The correlated two-dimensional ($m_{4\ell}$, KD) distribu-
 2036 tion is described by the two-dimensional probability distribution $\mathcal{P}(m_{4\ell}, \text{KD})$ for signal and background
 2037 as follows

$$\mathcal{P}_{\text{sig}}(m_{4\ell}, \text{KD}) = \mathcal{P}_{\text{sig}}^{1D}(m_{4\ell}) \times \mathcal{T}_{\text{sig}}(m_{4\ell}, \text{KD}) \quad (34)$$

$$\mathcal{P}_{\text{bkg}}(m_{4\ell}, \text{KD}) = \mathcal{P}_{\text{bkg}}^{1D}(m_{4\ell}) \times \mathcal{T}_{\text{bkg}}(m_{4\ell}, \text{KD}) \quad (35)$$

2038 where $\mathcal{P}_{\text{sig}}^{1D}(m_{4\ell})$ and $\mathcal{P}_{\text{bkg}}^{1D}(m_{4\ell})$ are the analytical 1D distributions used in 1D fits. The 2D distributions
 2039 $\mathcal{T}_{\text{sig}}(m_{4\ell}, \text{KD})$ and $\mathcal{T}_{\text{bkg}}(m_{4\ell}, \text{KD})$ are templates, or 2D histograms, which are normalized in the KD di-
 2040 rectation at any given value of $m_{4\ell}$. This ensures that projections of the 2D functions in Eqs. (34) and (35)
 2041 on $m_{4\ell}$ are identical to analytical $\mathcal{P}_{\text{sig}}^{1D}(m_{4\ell})$ and $\mathcal{P}_{\text{bkg}}^{1D}(m_{4\ell})$ distributions. The templates are created from
 2042 simulated samples and are shown in Fig. 119 and 120 for low and high mass ranges, respectively.

2043 At the low mass, different electron and muon p_T thresholds and efficiencies affect kinematics. Therefore,
 2044 KD distributions may be different between $4e$, 4μ , and $2e2\mu$ channels. We keep templates different at
 2045 low mass. However, at high mass low p_T thresholds do not affect kinematics (angles only) much and
 2046 we have a joint template distributions for the three channels. We also combine 7 TeV and 8 TeV samples,
 2047 since kinematics is the same in both cases. Still, due to limited statistics in the background MC samples
 2048 available, population of events in the bins of templates may be limited, or even zero, at high mass (in the
 2049 tail of the $m_{4\ell}$ distribution). We apply a smoothing procedure such that when the number of simulated
 2050 events entering the bin is low, the bin value is averaged over the range of 3×3 bins for $m_{4\ell} < 180$ GeV,
 2051 5×5 for $180 < m_{4\ell} < 300$ GeV (with the exception of KD near zero), 7×7 for $m_{4\ell} > 300$ GeV. There is
 2052 an overall protection that no template bin should have zero probability.

2053 As it was shown earlier, both $q\bar{q} \rightarrow ZZ$ and Z + X background can be described by the same tem-
 2054 plates and any small potential difference is covered by systematics, which is taken to be 100% correlated
 2055 between different channels and LHC run periods.

2056 12.2 Limits

2057 In Fig. 121 we show expected limits obtained with a fit of the ($m_{4\ell}$, KD) distribution.

2058 12.3 Significance of excesses

2059 In Fig. 122 we show the significance of the local fluctuation with respect to the Standard Model expecta-
 2060 tion. The comparison between 1D and 2D fits is shown in Fig. 123.

2061 12.4 Cross section/signal strength

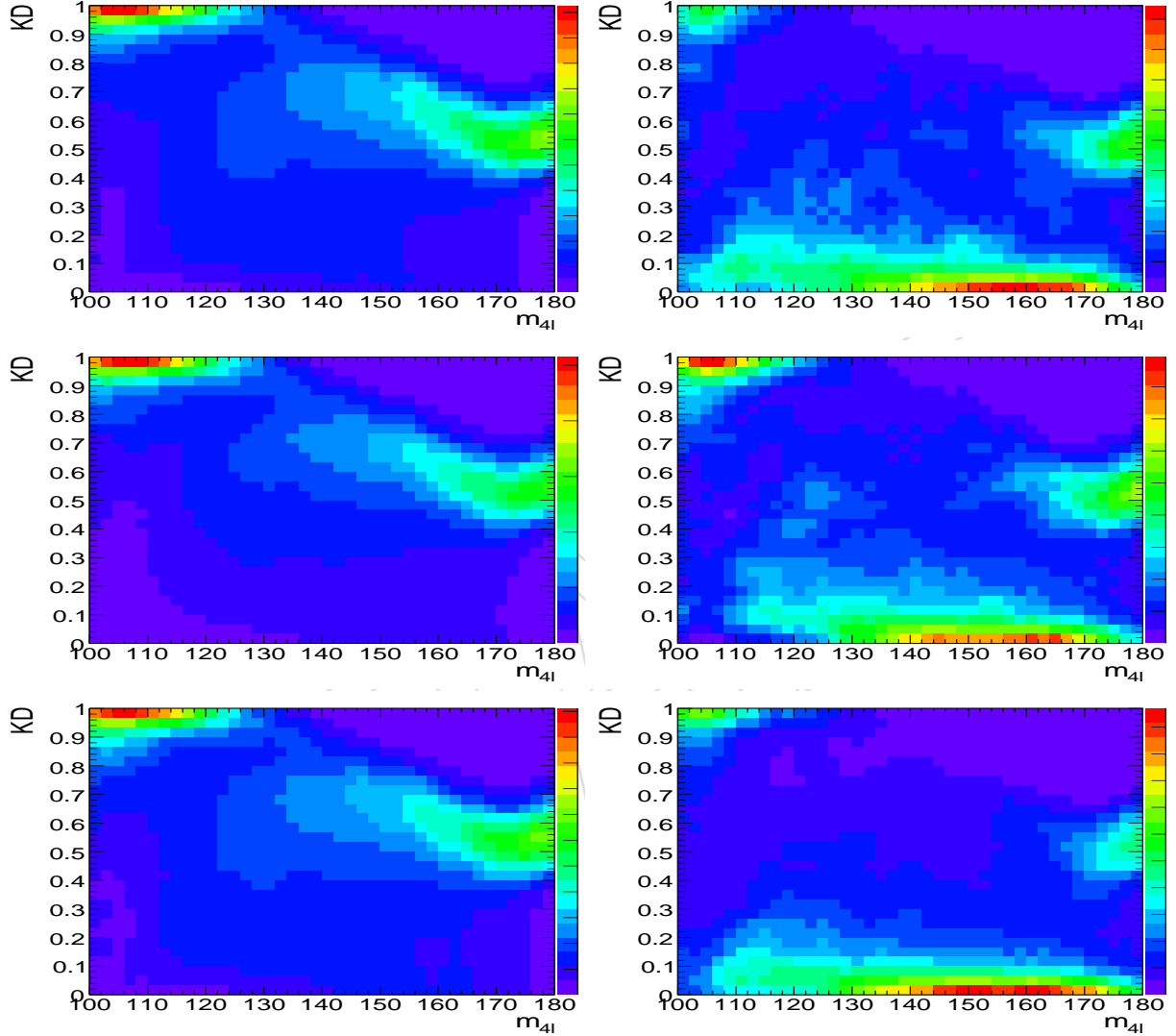


Figure 119: Parameterization signal and $q\bar{q} \rightarrow ZZ$ background template distributions $\mathcal{T}_{\text{sig}}(m_{4\ell}, \text{KD})$ (left) and $\mathcal{T}_{\text{bkg}}(m_{4\ell}, \text{KD})$ (right) from Eqs. (34) and (35) in three channels: $2e2\mu$ (top), $4e$ (middle), and 4μ (bottom).

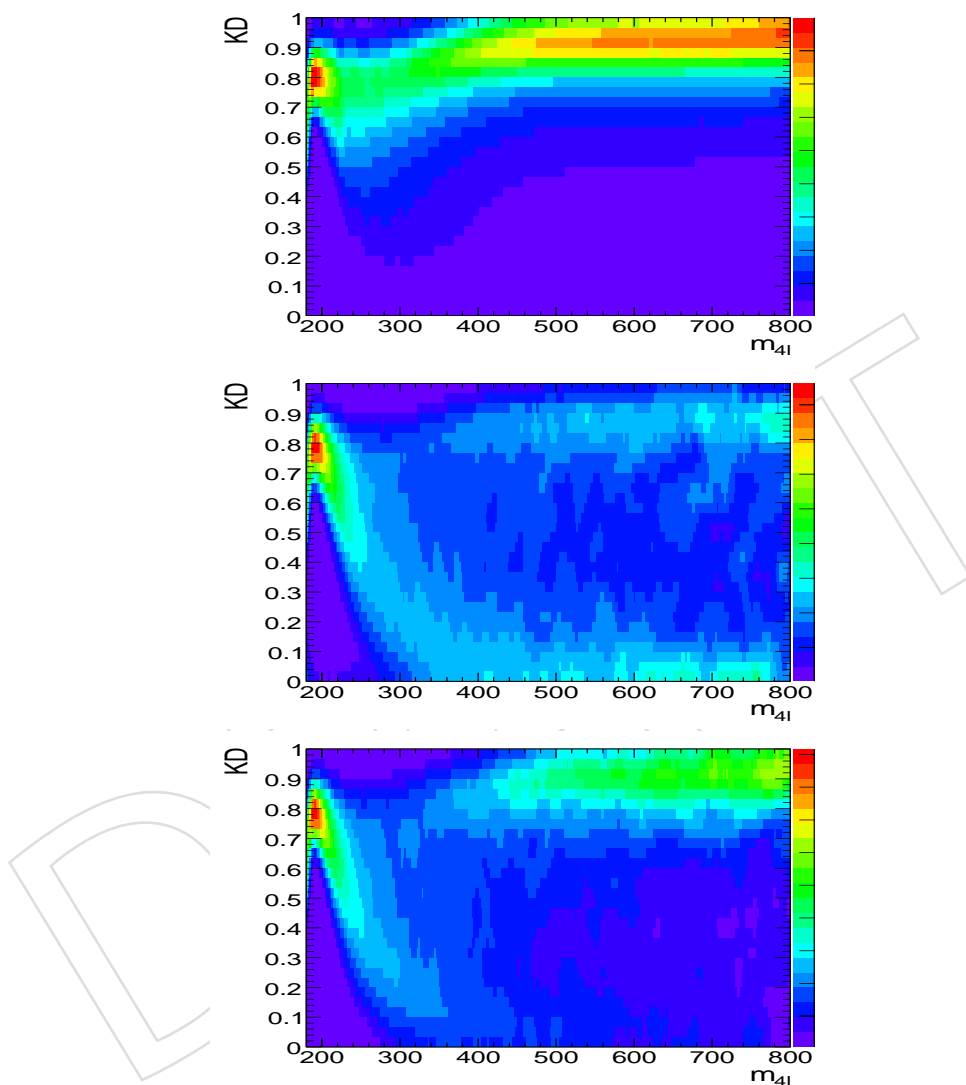


Figure 120: Parameterization of template distributions $\mathcal{T}(m_{4\ell}, \text{KD})$ for signal (top), $q\bar{q} \rightarrow ZZ$ background (middle), and $gg \rightarrow ZZ$ background (bottom).

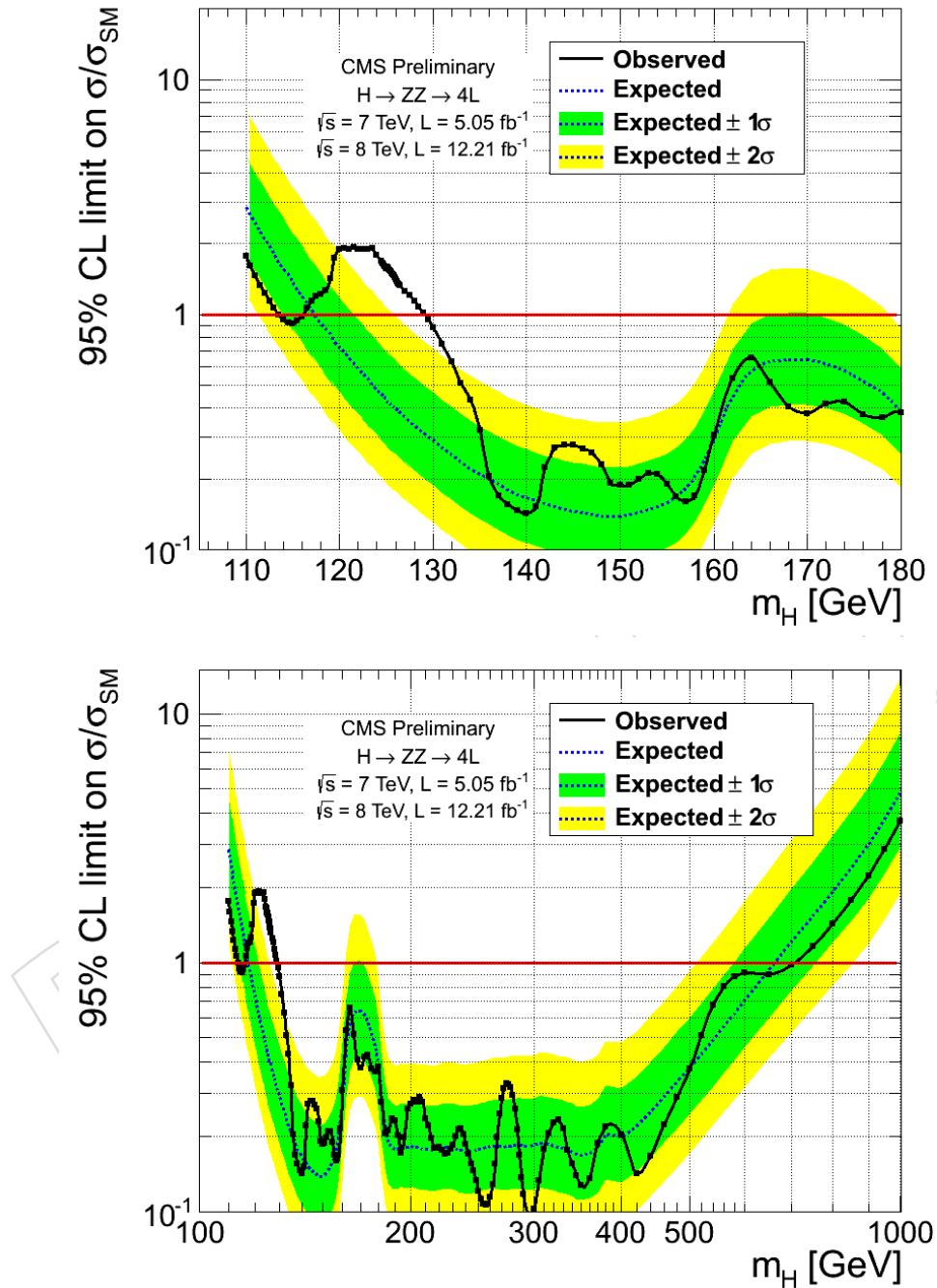


Figure 121: Observed and expected 95% CL upper limit on the ratio of the production cross section to the SM expectation with the 2D fit. 2011 and 2012 data-samples are used. The 68% and 95% ranges of expectation for the background-only model are also shown with green and yellow bands, respectively. Top plot: lower mass range only, bottom plot: full mass range.

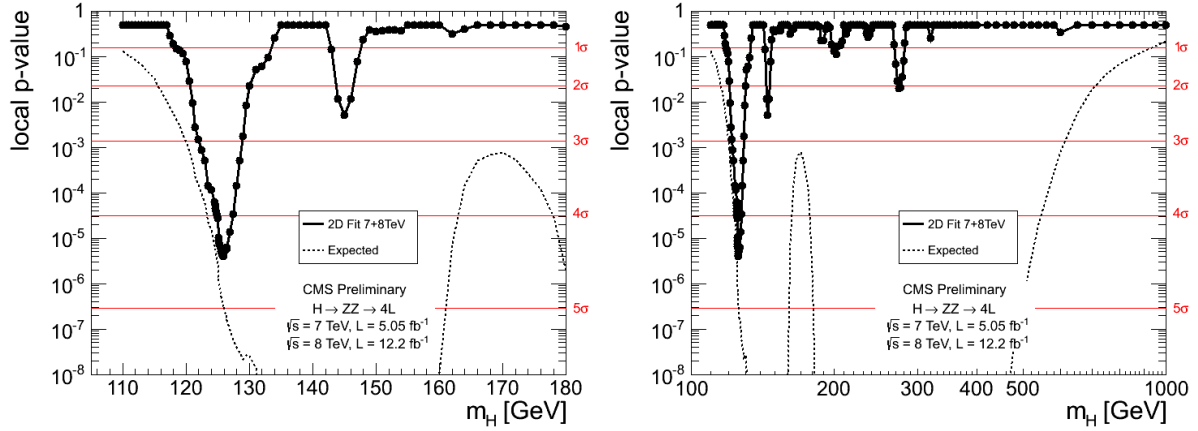


Figure 122: Significance of the local fluctuations with respect to the standard model expectation as a function of the Higgs boson mass for an integrated luminosity of 5.1 fb^{-1} at 7 TeV and 12.2 fb^{-1} at 8 TeV in the low mass range ($110\text{-}180 \text{ GeV}/c^2$) on the left and in the mass range ($110\text{-}1000 \text{ GeV}/c^2$) on the right. Dashed line shows mean expected significance of the SM Higgs signal for a given mass hypothesis.

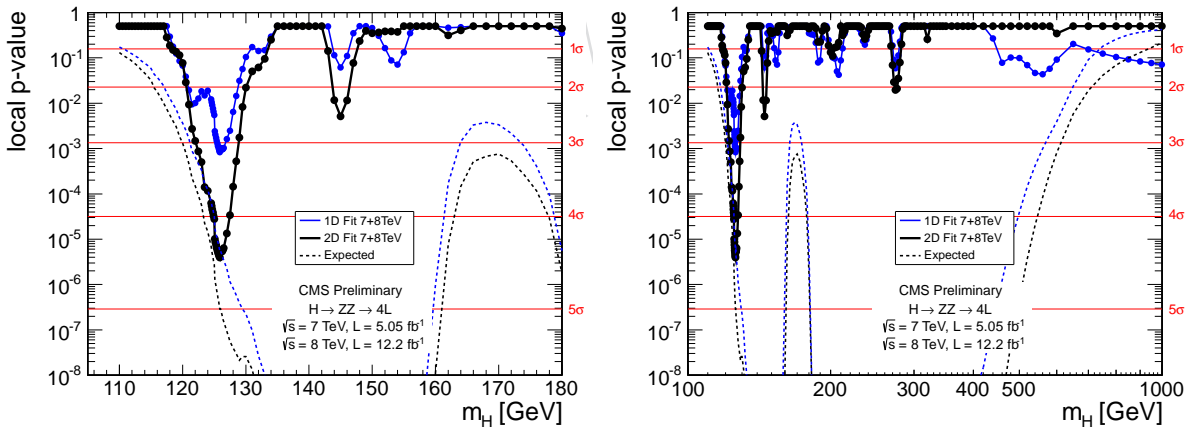


Figure 123: Significance of the local fluctuations with respect to the standard model expectation as a function of the Higgs boson mass for an integrated luminosity of 5.1 fb^{-1} at 7 TeV and 12.2 fb^{-1} at 8 TeV with a 1D (blue) and 2D (black) analysis, in the mass range ($110\text{-}180 \text{ GeV}/c^2$) on the left and in the mass range ($110\text{-}1000 \text{ GeV}/c^2$) on the right. Dashed line shows mean expected significance of the SM Higgs signal for a given mass hypothesis.

12.5 Statistical analysis with per-event mass error as observable

The quality of the momentum measurement of both electrons and muons can substantially vary depending on the leptons characteristics. Therefore this entails that the 4ℓ mass resolution varies broadly, by as much as a factor of 2-3. Therefore, mixing together events with well and poorly measured 4ℓ masses dilutes the Higgs search sensitivity. In this section, we introduce an advanced analysis technique that takes into account mass resolutions assessed on the event-by-event basis. The gain in the *expected Higgs boson mass measurement* is 7%. Also, with event-by-event errors, we will be able to make the *most accurate estimate of the error* on the boson mass, given the actual data we have at hand.

12.5.1 Modeling of mass error distributions

The mass error validation are documented in the dedicated per-event mass error section. We then take mass error distributions of signal and ZZ from MC, and Z+jets from data control region. For ZZ and signal 4mu channel, the shapes are fitted with a pdf composed by Landau and LogNormal. In signal 4mu events, the relative mass error distributions stay the same across the whole mass window. For ZZ and signal 4e and 2e2mu channels, the shapes are fitted with a pdf composed by Landau and Gaussian. Figure 124 shows as example for 125 GeV Higgs sample and ZZ background sample in the mass range from 120 to 130 GeV.

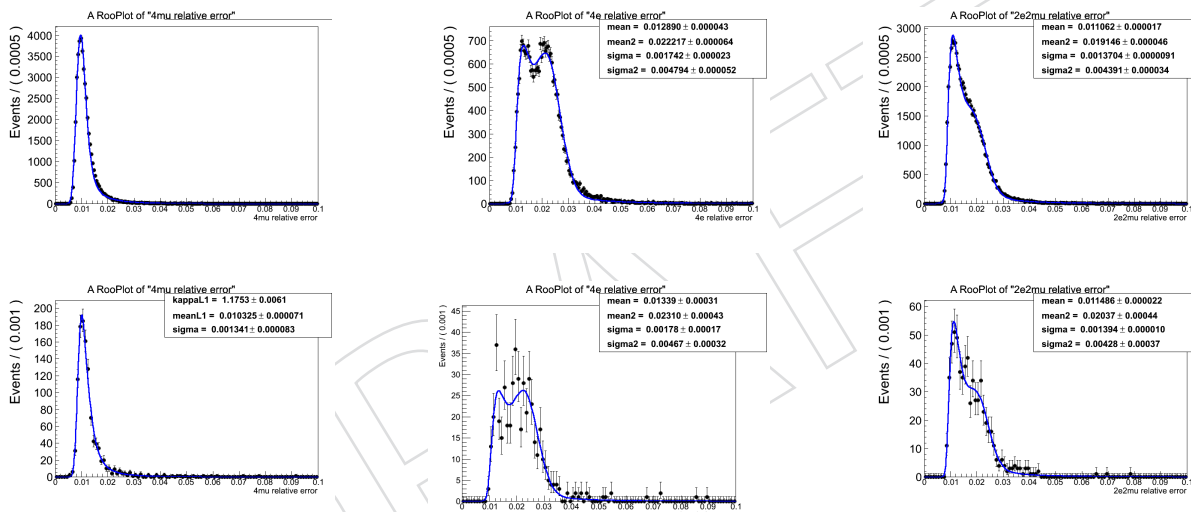


Figure 124: 4-lepton mass error distributions (points) and fits for signal (top) and ZZ (bottom) MC samples. 4mu (left) channel is using a pdf of Landau and Lognormal, 4e(middle) and 2e2mu(right) are fitted with a pdf also composed by

We then parameterize fitted parameters as a function of Higgs mass, shown in figure 125 to 130, for signal and ZZ background separately.

For reducible backgrounds, we use control region with relaxed cuts to gain statistics, compare the mass error distribution of the events in control region with ZZ background in MC also Z+Jets MC samples. Since Z+Jets 4mu distribution is very close to ZZ 4mu, we take ZZ 4mu fits for Z+jets 4mu, simply because reducible 4mu backgrounds are also dominated by real muons. While in electron case, the contribution are mostly from real fakes, which have much worse resolutions. The Z+Jets 4e and 2e2mu distributions are fitted with a pdf composed by Landau and Gaussian, shown in figure 131. They are within a mass window from 120 to 130.

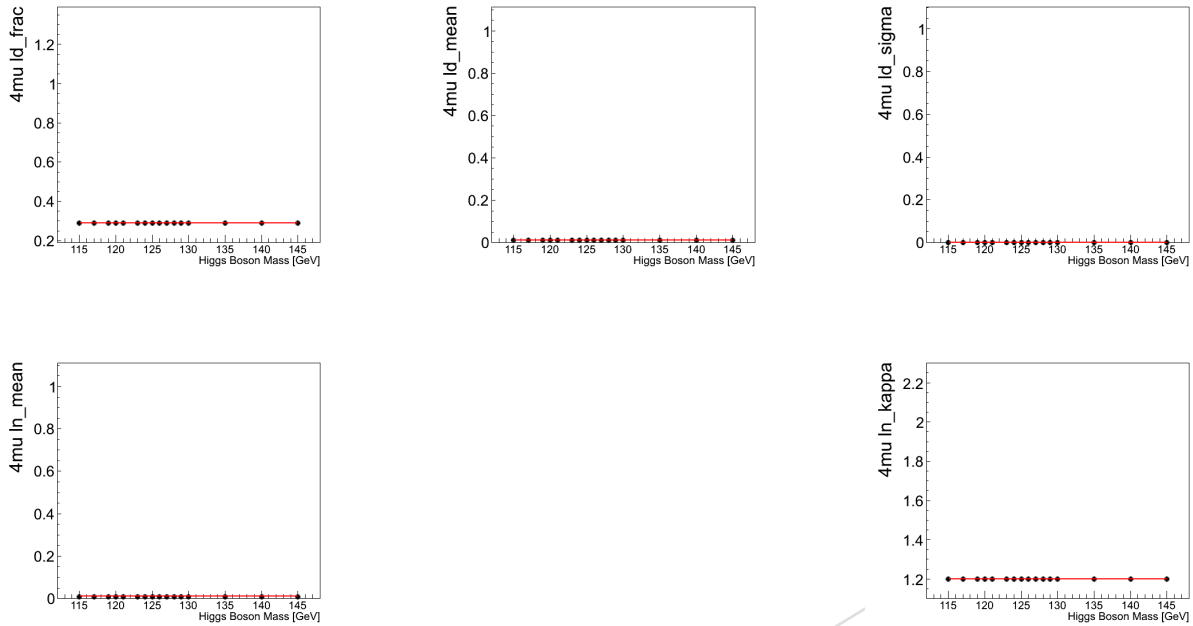


Figure 125: Smoothed parameterization of the fits on 4mu mass error distributions for signal. From top left to bottom right: fraction of Landau component, Landau mean, Landau sigma, LogNormal mean, LogNormal kappa.

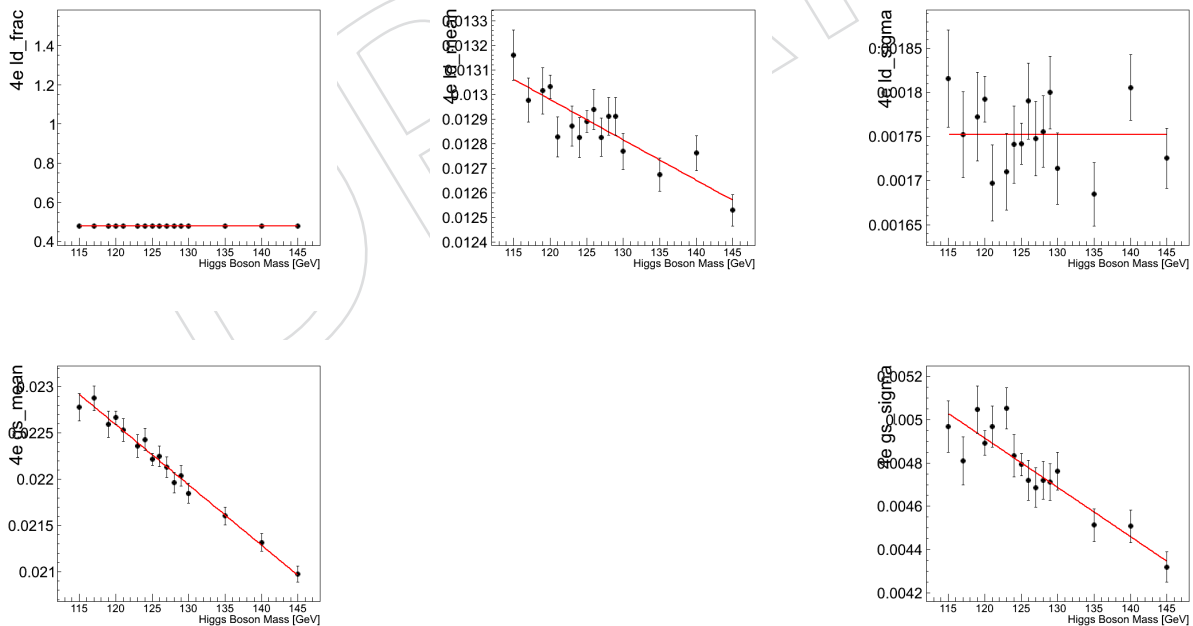


Figure 126: Smoothed parameterization of the fits on 4e relative mass error distributions for signal. From top left to bottom right: fraction of Landau component, Landau mean, Landau sigma, Gaussian mean, Gaussian sigma.

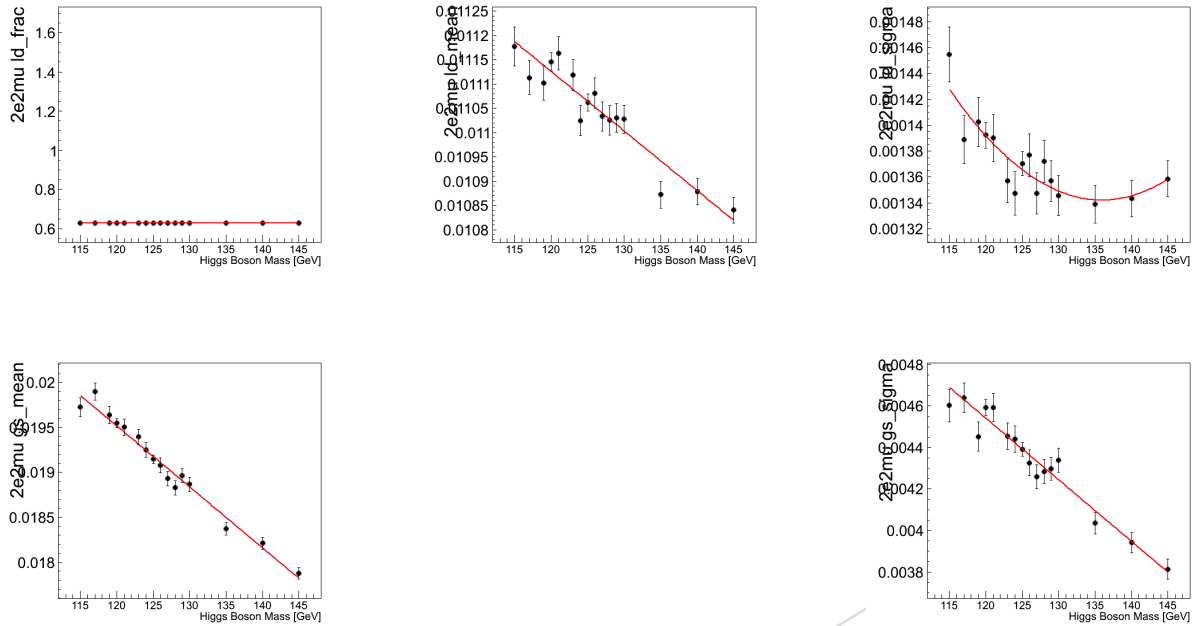


Figure 127: Smoothed parameterization of the fits on 2e2mu relative mass error distributions for signal. From top left to bottom right: fraction of Landau component, Landau mean, Landau sigma, Gaussian mean, Gaussian sigma.

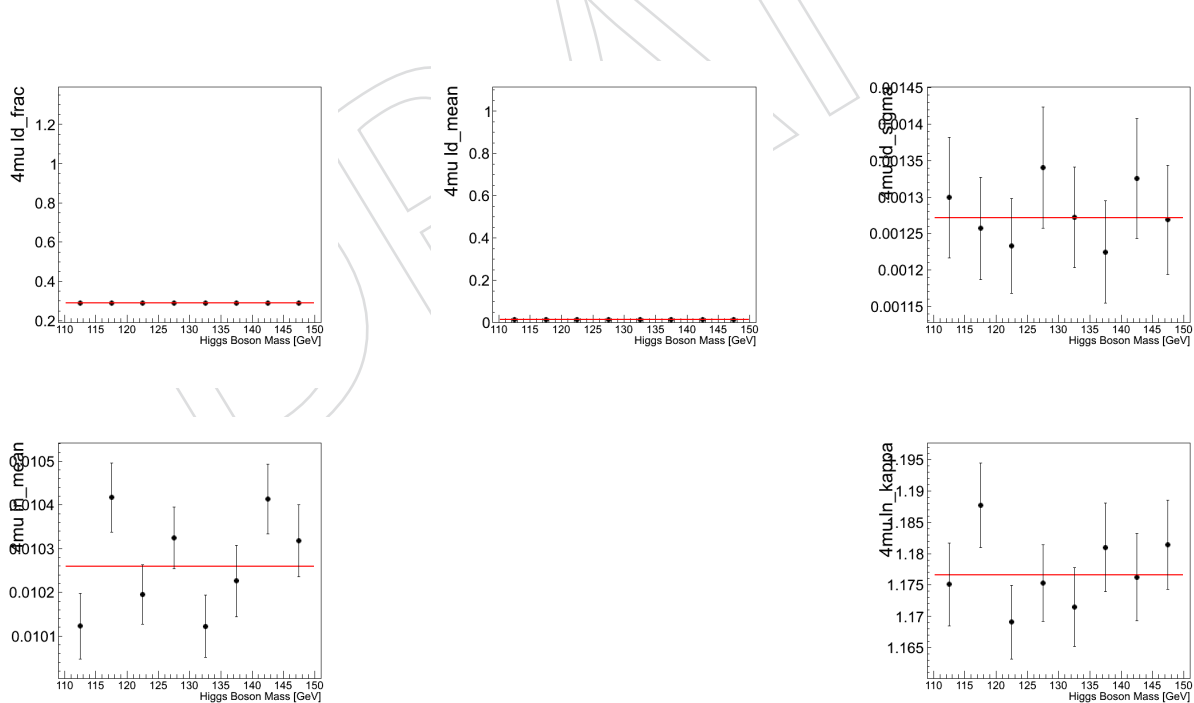


Figure 128: Smoothed parameterization of the fits on 4mu mass error distributions for ZZ. From top left to bottom right: fraction of Landau component, Landau mean, Landau sigma, LogNormal mean, LogNormal kappa.

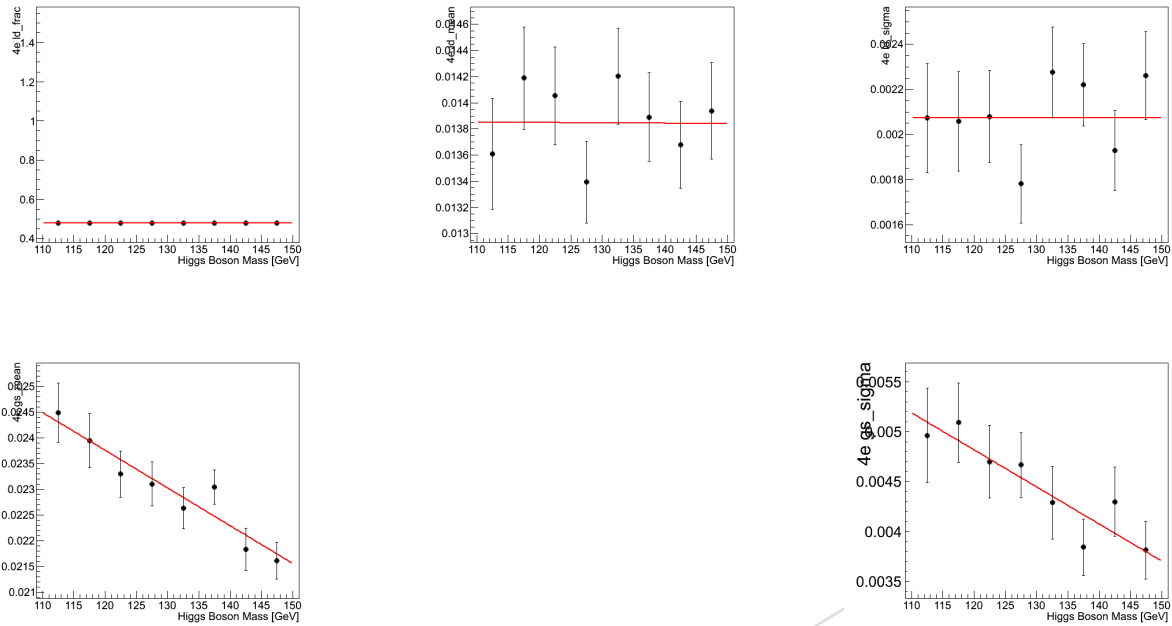


Figure 129: Smoothed parameterization of the fits on 4e relative mass error distributions for ZZ. From top left to bottom right: fraction of Landau component, Landau mean, Landau sigma, Gaussian mean, Gaussian sigma.

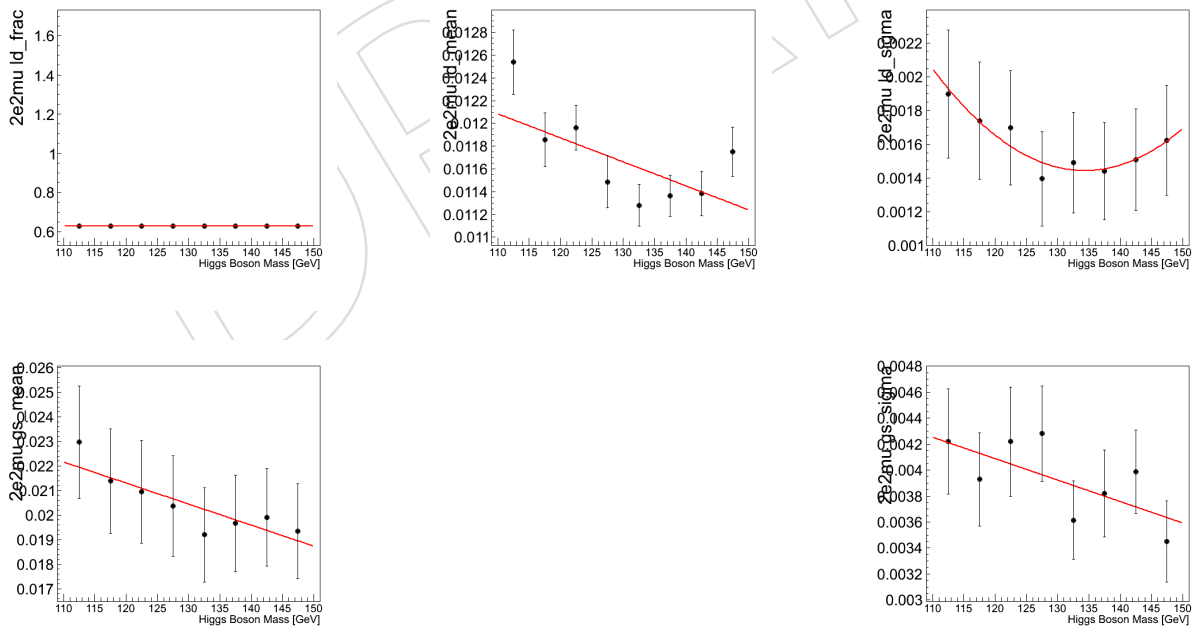


Figure 130: Smoothed parameterization of the fits on 2e2mu relative mass error distributions for ZZ. From top left to bottom right: fraction of Landau component, Landau mean, Landau sigma, Gaussian mean, Gaussian sigma.

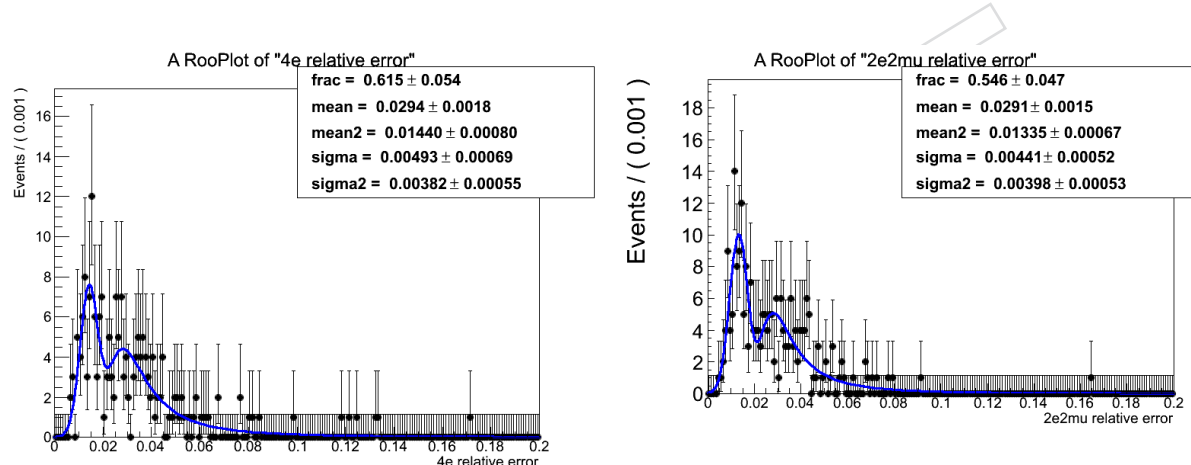


Figure 131: Relative mass error distribution from data control region for ZJets 4e (left) and 2e2mu (right), with fits by Landau+Gaussian.

2087 12.5.2 Statistical methodology and validation

2088 We construct 2D conditional PDF for mass error versus mass, i.e.

$$\mathcal{P}_{\text{sig}}(m_{4\ell}, EBE) = \mathcal{P}_{\text{sig}}^{\text{1D}}(m_{4\ell}) \times \mathcal{P}_{\text{sig}}(EBE|m_{4\ell}) \quad (36)$$

$$\mathcal{P}_{\text{bkg}}(m_{4\ell}, EBE) = \mathcal{P}_{\text{bkg}}^{\text{1D}}(m_{4\ell}) \times \mathcal{P}_{\text{bkg}}(EBE|m_{4\ell}) \quad (37)$$

2089 For signal, sigma of CB function is replaced with mass error for each event.

2090 To take the KD observable, we construct 3D pdf as follows,

$$\mathcal{P}_{\text{sig}}(m_{4\ell}, EBE, KD) = \mathcal{P}_{\text{sig}}^{\text{1D}}(m_{4\ell}) \times \mathcal{P}_{\text{sig}}(EBE|m_{4\ell}) \times \mathcal{P}_{\text{sig}}(KD|m_{4\ell}) \quad (38)$$

$$\mathcal{P}_{\text{bkg}}(m_{4\ell}, EBE, KD) = \mathcal{P}_{\text{bkg}}^{\text{1D}}(m_{4\ell}) \times \mathcal{P}_{\text{bkg}}(EBE|m_{4\ell}) \times \mathcal{P}_{\text{bkg}}(KD|m_{4\ell}) \quad (39)$$

2091 The 3D construction is based on the assumption that there is no correlation between mass error and
 2092 KD which is ok after looking at the distributions of mass error versus KD. Figure 132 shows that there
 2093 is negligible correlation between mass error and Kinematic Discriminant by calculating the correlation
 2094 factor (very small) in signal and ZZ background samples separately.

2095 We further perform a study with fully simulated Monte Carlo samples to check whether there is any
 2096 potential bias due to unaccounted correlation which are naturally built in those samples.

2097 We take 8 TeV MC 125 GeV ggH and ZZ samples, and concentrate on the mass window [105 – 140] GeV
 2098 defined in the data cards for 125 GeV mass hypothesis. The expected signal and background yields are
 2099 rescaled to 20 fb-1 from ICHEP 8 TeV data cards. Uncertainties stay unchanged. Note that we assume
 2100 20% uncertainty on the event-by-event errors. In each toy, number of events are tossed from Poissonians
 2101 of above expectation, randomly picked from the MC samples. To avoid any possible bias, we don't reuse
 2102 any MC event, so totally it amounts only 323 toys.

2103 Figure 133 shows mass residual (left) and pull (right) distribution for 3D statistical analysis. The mean of
 2104 residuals is used to quantify potential bias in the mass measurement. The mass pull is defined as (fitted
 2105 mass - 125 GeV) / (fitted mass uncertainty) in each toy. The width of pulls characterizes how accurately
 2106 we assign the error on the mass measurement. One can see that the mean of residuals is around 0, which
 2107 means *there is no bias*. One can see that the width of pulls is around 1, which means *the error of the mass
 2108 measurement is correctly calculated*.

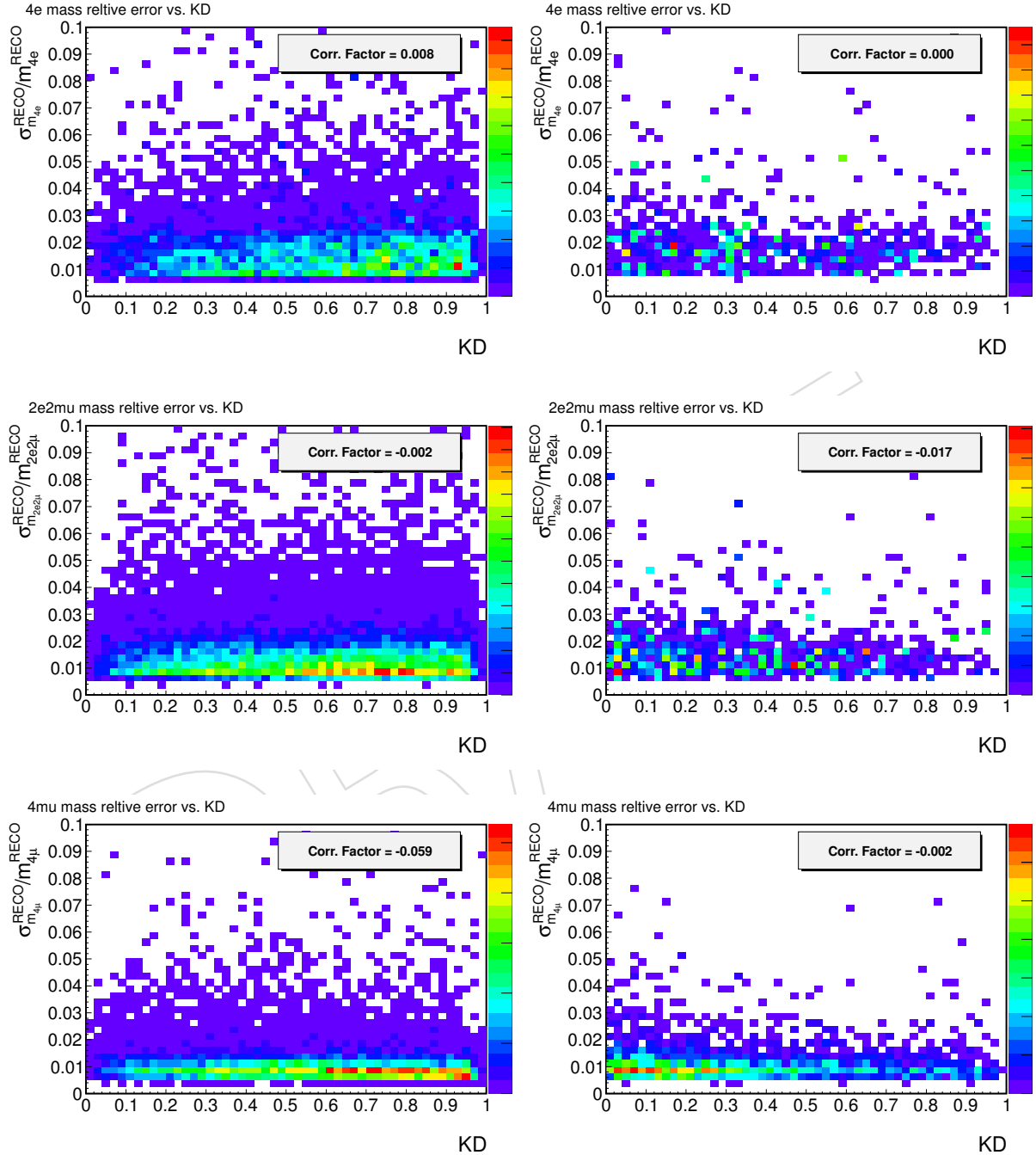


Figure 132: 4-lepton mass error versus KD distributions (points) for 125 GeV Higgs signal (left) and ZZ (right) MC samples. The correlation factors are displayed on the figures as well.

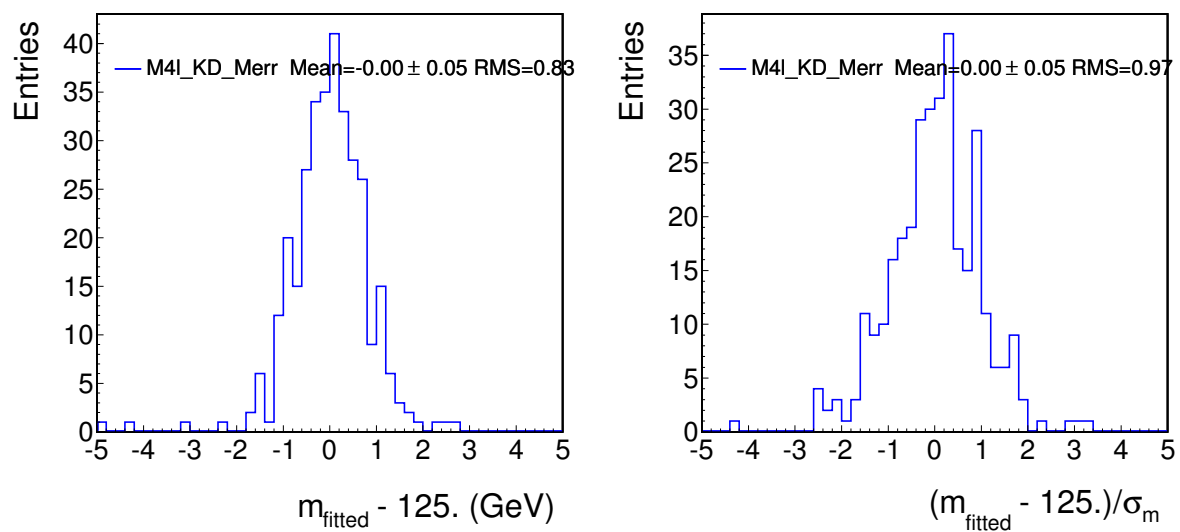


Figure 133: Mass residual (left) and pull (right) distribution with Monte Carlo samples.

2109 **12.5.3 Expected improved performance**

2110 The gain in sensitivity is not expected to be as much as in $H \rightarrow \gamma\gamma$ search, where events with better
2111 $m_{\gamma\gamma}$ resolution have smaller backgrounds. In the case of the $H \rightarrow ZZ \rightarrow 4\ell$ analysis, the $m_{4\ell}$ observable
2112 does not help in improving the signal-to-background discrimination. The whole gain comes solely from
2113 the proper accounting for the signal mass resolutions for individual events.

2114 To asses the improvement, we construct 4 sets of data cards

- 2115 • 1D: M4l
- 2116 • 2D: M4l vs. KD
- 2117 • 2D: M4l vs. Merr
- 2118 • 3D: M4l vs. KD vs. Merr

2119 and start from ICHEP 8 TeV inputs with lumi being rescaled to 20 fb-1.

2120 Then, we generate 20K toys from the 3D data cards with MH=125 GeV and SM signal strength. Statical
2121 analysis are performed on these toys and for 4 sets data cards separately.

2122 The fitted mass and its uncertainty of each toy are shown in the figure 134. One can expect on average the
2123 uncertainty of mass measurement is improved by 7%. Figure 134 (bottom) shows the scatter distribution
2124 of two measured mass errors from 2D (M4l vs. KD) and 3D fittings, where one can see that the measured
2125 mass errors are often smaller (more accurate) with 3D fitting.

2126 The significance distributions of the 4 sets of data cards based on the above toys are shown in the
2127 figure 135 (left). Including per-event mass error, the expected significance can be improved by 3% .
2128 Figure 135 (right) shows the best fitted signal strength, on which there is no improvement as RMS is
2129 basically the same for all four methods of fitting.

2130 **12.5.4 Results**

2131 With HCP data set, we perform the likelihood scan in the mass versus signal strength space shown
2132 in figure 136. Both results with and without per-event mass error are shown. Solid ellipses are 68% CL
2133 contours, for ndof=2 and $\Delta NLL=2.3$. Without per-event mass error, $MH=126.2^{+1.01}_{-1.09}$ GeV, while with per-
2134 event mass error, it gives $MH=126.2^{+0.87}_{-0.98}$ GeV. Including per-event mass error gives 10% improvement
2135 with current data we have.

2136 With 1D likelihood scan over mass, i.e. profiling signal strength, the results with/without per-event
2137 mass error are shown in figure 137. With per-event mass error, the best estimate of Higgs mass is
2138 $126.2^{+0.58}_{-0.63}$ GeV, which is 6% more precise than the one without per-event mass error ($126.2^{+0.65}_{-0.68}$) GeV.

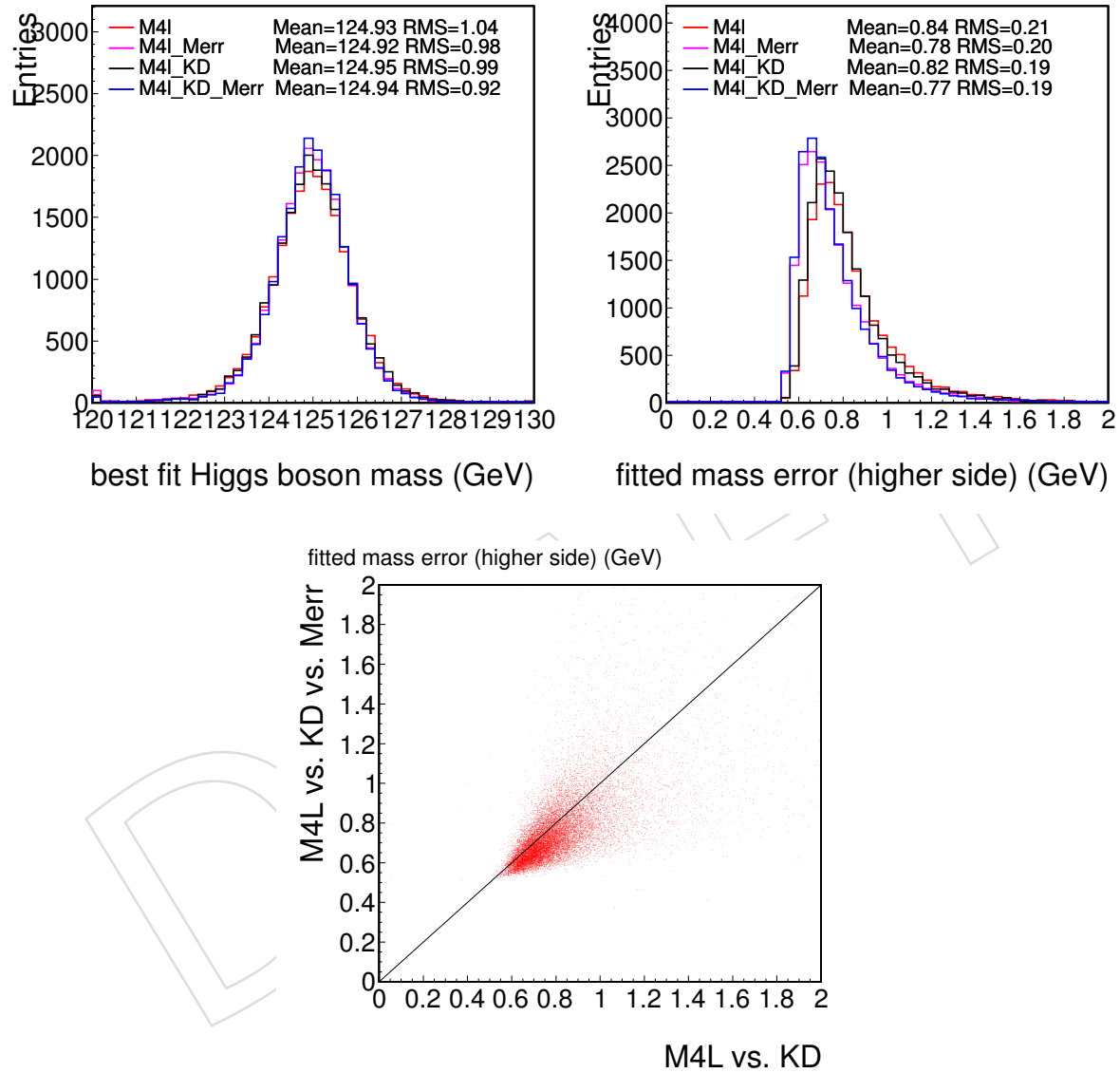


Figure 134: Expected distribution of fitted mass (top left) and its uncertainty (top right) from 4 sets of data cards for 20 fb-1 8 TeV data. In bottom, it's the scatter distribution of two measured mass errors from 2D (M4l vs. KD) and 3D fittings.

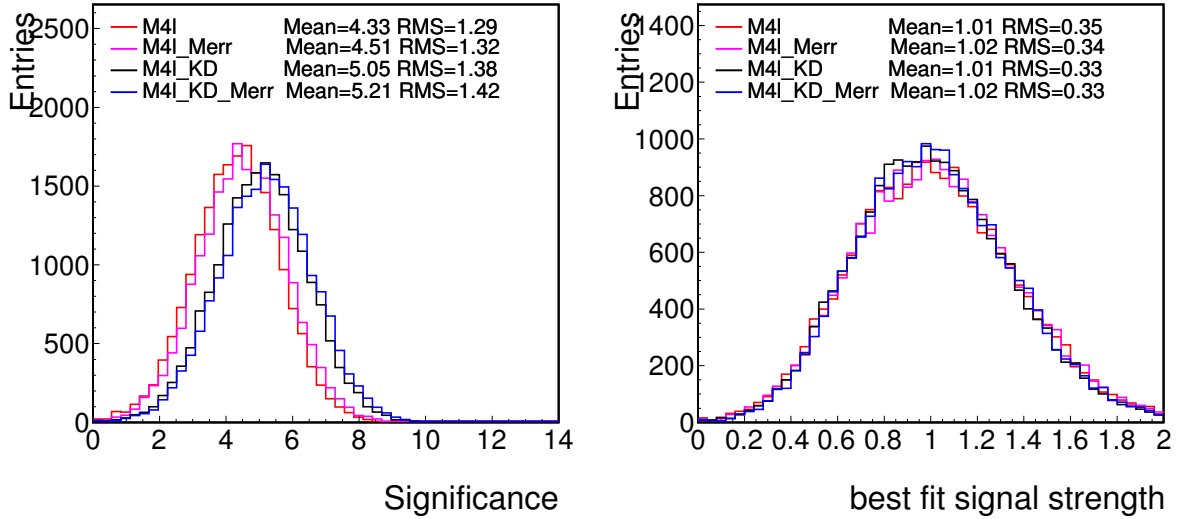


Figure 135: Expected significances (left) and muhat (right) from 4 sets of data cards for 20 fb⁻¹ 8 TeV data.

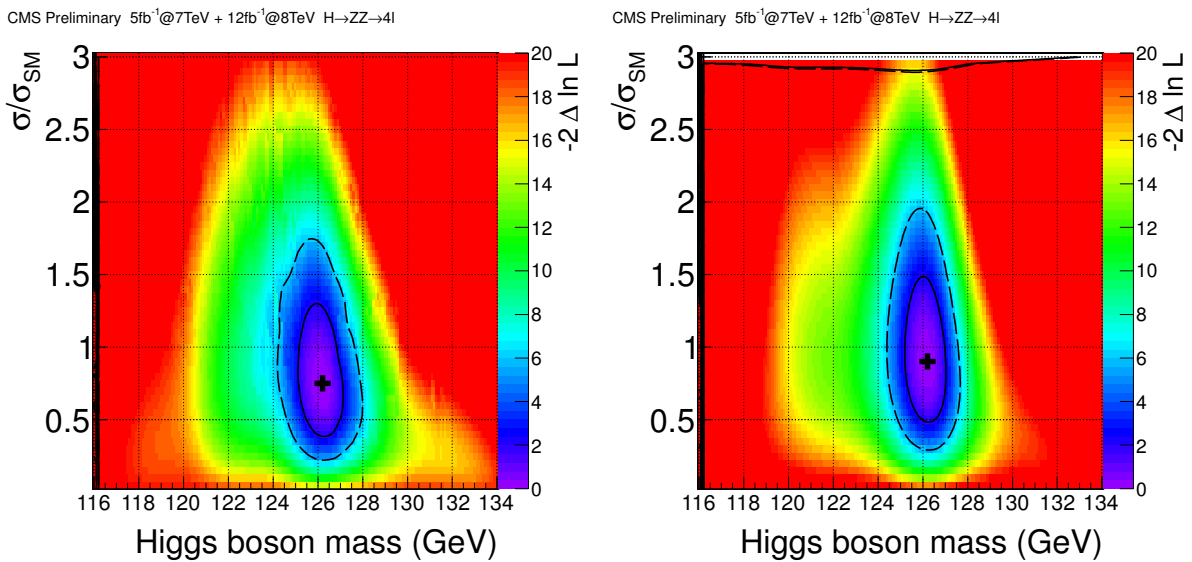


Figure 136: Temperature plots for likelihood scan of mass versus signal strength, for 2D (left) analysis and 3D analysis (right).

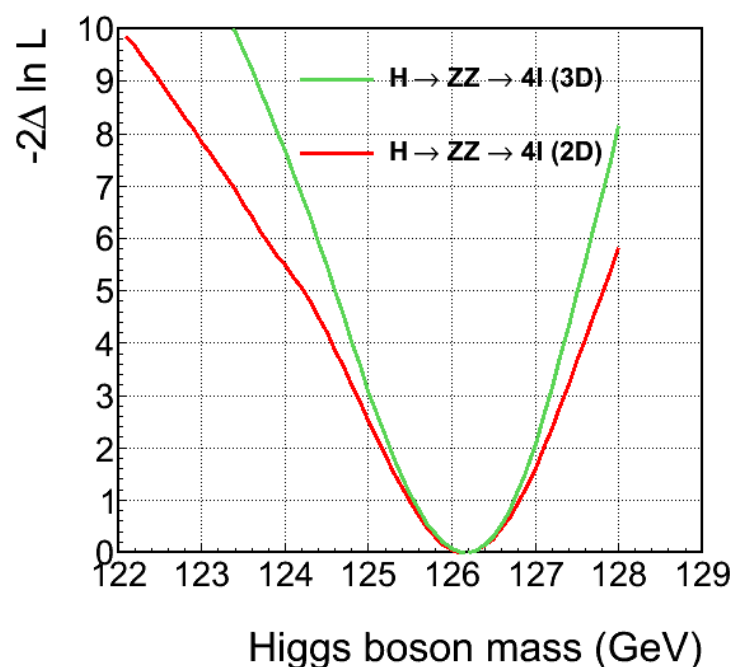


Figure 137: 1D likelihood scan as a function of mass, for 2D (left) analysis and 3D analysis (right).

2139 12.6 Approach to Higgs Boson Spin and Parity Measurements

2140 Given the new resonance observed at the LHC, it will be crucial to determine the spin and quantum
 2141 numbers of the new particle and its couplings to Standard Model fields as accurately as possible. The
 2142 full-case study has been presented in Ref. [74, 78] and CMS internal study in Ref. [85]. Here we adopt
 2143 a simplified version of that approach following the MELA methodology in Section 10, where instead
 2144 of signal-to-background probability ratio we construct probability ratio for two signal hypotheses. The
 2145 discriminant for signal hypothesis testing is constructed as follows

$$\mathcal{D}_{J^P} = \frac{\mathcal{P}_{\text{SM}}}{\mathcal{P}_{\text{SM}} + \mathcal{P}_{J^P}} = \left[1 + \frac{\mathcal{P}_{J^P}(m_1, m_2, \vec{\Omega}|m_{4\ell})}{\mathcal{P}_{\text{SM}}(m_1, m_2, \vec{\Omega}|m_{4\ell})} \right]^{-1}, \quad (40)$$

2146 where $\vec{\Omega}$ are five angles describing kinematics of production and decay of a boson in its frame, \mathcal{P}_{SM} is the
 2147 probability distribution for the SM Higgs boson hypothesis, and \mathcal{P}_{J^P} is the probability for an alternative
 2148 model, which are calculated analytically and are quoted in Ref. [74].

We consider two spin-parity models, one is the pure pseudo-scalar state $J^P = 0^-$ and the other is the spin-two state with the minimal graviton-like coupling to the bosons with $J^P = 2^+$. The most general decay amplitude for a spin-zero boson can be defined as

$$A = v^{-1} \epsilon_1^{*\mu} \epsilon_2^{*\nu} \left(a_1 g_{\mu\nu} m_H^2 + a_2 q_\mu q_\nu + a_3 \epsilon_{\mu\nu\alpha\beta} q_1^\alpha q_2^\beta \right) = A_1 + A_2 + A_3, \quad (41)$$

2149 where ϵ_i are the Z boson polarization vectors, q_i are their momenta, and $q = q_1 + q_2$. The SM Higgs
 2150 boson decay is dominated by the A_1 amplitude, while the $J^P = 0^-$ state decay is expected to be dom-
 2151 inated by the A_3 amplitude. The \mathcal{D}_{0^-} discriminant is therefore optimal for discrimination between
 2152 the $|A_1|^2$ and $|A_3|^2$ amplitude contributions, while we find their potential interference to have negli-
 2153 gible effect on the discriminant distribution or the overall yield of events. We define the parameter
 2154 $f_{a3} = |A_3|^2 / (|A_1|^2 + |A_3|^2)$, where we neglect the $|A_2|^2$ contribution. This parameter allows us to pro-
 2155 vide consistency tests of the $f_{a3} = 0$ and $f_{a3} = 1$ scenarios, as well as consider contribution of both
 2156 amplitudes in the decay. However, we would like to stress that f_{a3} is not a parameter which defines the
 2157 mixture of parity-even and parity-odd states. The latter would require model-dependent interpretation
 2158 of the f_{a3} measurement. In the SM, f_{a3} is expected to be essentially zero.

2159 Here we illustrate the power of the above approach with the example of a narrow resonance at 125 GeV
 2160 with two hypotheses scalar ($J^P = 0^+$) and pseudo-scalar ($J^P = 0^-$) Higgs. The alternative hypotheses
 2161 of a resonance are produced with the generator from Ref. [74] (JHU generator). Similarly to discussion
 2162 in Section 10, the seven observables $\{m_1, m_2, \vec{\Omega}\}$ appear different for resonances with different quantum
 2163 numbers, as shown in Fig. 138 and Fig. 139 with samples generated according to the $J^P = 0^+$ and
 2164 $J^P = 0^-$ hypotheses.

2165 Distributions of the discriminant \mathcal{D}_{0^-} for scalar-to-pseudoscalar separation (“*pseudoMELA*”) are shown
 2166 in the left-hand side of Fig. 140. These distributions are shown for values of the reconstructed mass
 2167 in the range $[120 - 130]$ GeV and for signal and background. In the right-hand side of the same fig-
 2168 ure, we also show distributions of the discriminant \mathcal{D}_{2^+} optimized for separation of $J^P = 0^+$ and 2^+
 2169 (minimal couplings) hypotheses (“*graviMELA*”). In Fig. 141 we show the distribution of the angles after
 2170 the reconstruction, acceptance and full analysis selection for pseudoscalar, graviton, scalar signal, and
 2171 background, in the region $120 < m_{4\ell} < 130$ GeV.

2172 In order to achieve the best separation power, one has to separate the events coming the SM background
 2173 from the signal ones. Ideally, in order to achieve this the fit should include all three observables with
 2174 KD as well, but for simplicity we omit it here. In order to perform such a 3D statistical analysis in the
 2175 future, larger amounts of simulated events for both the signal and the background will be needed.

2176 A statistically equivalent approach has been taken which allows a more simple 2D analysis. With this
 2177 approach, the statistical analysis remains similar to the nominal analysis, except that instead of the kine-
 2178 matic discriminant for signal-to-background separation, we use the above kinematic discriminant \mathcal{D}_{J^P}
 2179 for separation between the two signal hypotheses. The second observable combines the $m_{4\ell}$ probability

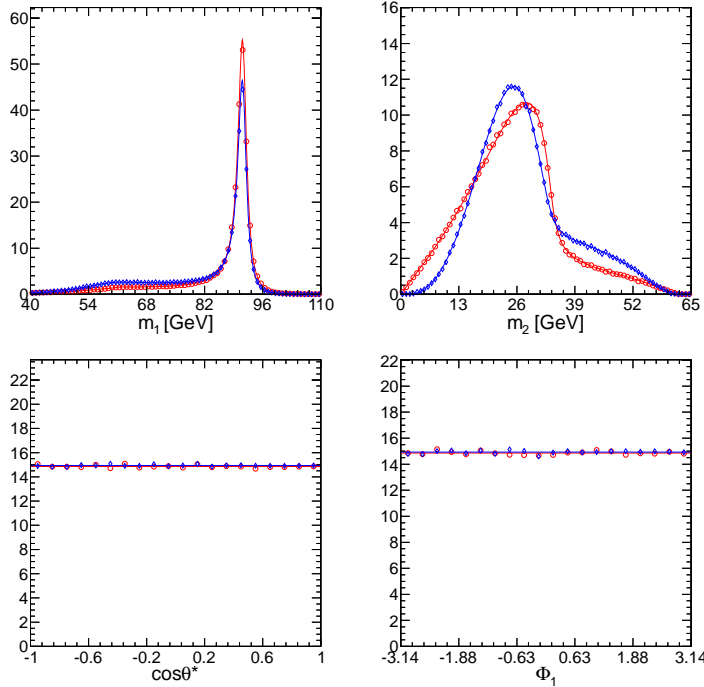


Figure 138: Distribution of the observables m_1 , m_2 (top row), $\cos\theta^*$, and Φ_1 (bottom row), generated for $m_X = 125$ GeV with leading order JHU generator events and projections of the ideal angular distributions. Two resonance hypotheses are shown: $J^P = 0^+$ (red) and 0^- (blue).

2180 together with the kinematic probability of the angular and mass distribution as used in the KD calcu-
 2181 lation, $SMD = \mathcal{P}_{sig}/(\mathcal{P}_{sig} + \mathcal{P}_{bkg})$, where probabilities \mathcal{P} also include the $m_{4\ell}$ parameterizations. The
 2182 analysis of the SMD discriminant is statistically equivalent to the 2D analysis of the $m_{4\ell}$ and KD dis-
 2183 tributions. The spin-parity hypothesis analysis is a 2D analysis of the $(\mathcal{D}_{bkg}, \mathcal{D}_{J^P})$ distributions where
 2184 correlations of observables are included in the probability parameterizations. We denote the observable
 2185 by SMD in the following (and informally called *superMELA*). Such a variable is defined as

$$SMD = \frac{\mathcal{P}_{sig}}{\mathcal{P}_{sig} + \mathcal{P}_{bkg}} = \left[1 + \frac{\mathcal{P}_{bkg}(m_1, m_2, \vec{\Omega} | m_{4\ell}) \times \mathcal{P}_{bkg}(m_{4\ell})}{\mathcal{P}_{sig}(m_1, m_2, \vec{\Omega} | m_{4\ell}) \times \mathcal{P}_{sig}(m_{4\ell})} \right]^{-1}. \quad (42)$$

2186 The distribution of SMD is shown in Fig. 142 for two signal hypotheses of mass 125 GeV and the irre-
 2187ducible background. The corresponding ROC curve for these two samples after all selections and in an
 2188 invariant mass window of $105 < m_{4\ell} < 140$ GeV is shown in the right plot of figure 143. The gain in
 2189 sensitivity of this variable is considerable which is to be expected since $m_{4\ell}$ is the single most powerful
 2190 discriminant for background.

2191 12.6.1 Illustration of the data

2192 In Fig. 144 distributions of SMD (superMELA, top), \mathcal{D}_{0^-} (pseudoMELA, left), and \mathcal{D}_{2^+} (graviMELA,
 2193 right) are shown. There is a clear excess of signal visible near $SMD=1$. The signal-enhanced plot of \mathcal{D}_{0^-}
 2194 shows some preference for the SM-like distribution of events. The \mathcal{D}_{2^+} distribution provided relatively
 2195 weak separation between the two hypotheses with the present statistics.

2196 12.6.2 Implementation of the statistical analysis and results

2197 The technical implementation of the statistical analysis is done in the framework of the RooStats-based
 2198 CMS Higgs combination tools. We build the (SMD, pseudoMELA) 2D template distribution, instead

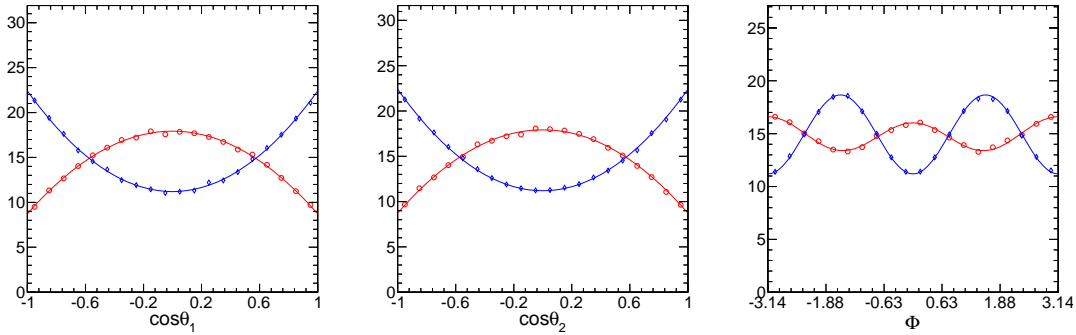


Figure 139: Distribution of the observables $\cos \theta_1$, $\cos \theta_2$, and Φ generated for $m_X = 125$ GeV with leading order JHU generator events and projections of the ideal angular distributions. Two resonance hypotheses are shown: $J^P = 0^+$ (red) and 0^- (blue).

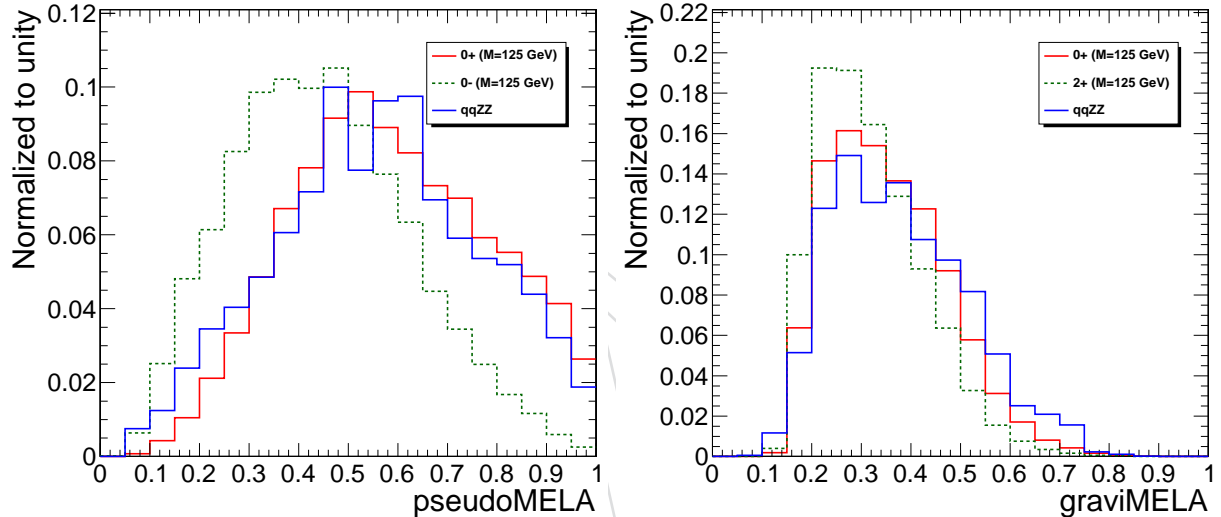


Figure 140: Distributions of the \mathcal{D}_{0^-} (pseudoMELA) discriminant (for scalar-to-pseudoscalar separation, left) and \mathcal{D}_{2^+} (graviMELA) discriminant (for scalar-to-spin-two separation, right). The distributions are shown for mass around 125 GeV and for signal (0^+ red, 0^- green, 2^+ KK graviton magenta) and background (blue). All MC distributions are shown for the full CMSSW simulation, except for KK graviton model which is shown with fast track parameter smearing and acceptance effects (CMSSW samples are pending).

2199 of the 2D (MELA, $m_{4\ell}$) as in the baseline analysis. In calculating SMD, one must choose a value of
 2200 m_H for the parametrizations of P_{sig} in Eq.42. This value was chosen to be 125 GeV for the following
 2201 studies. In the future, this value could be modified in agreement with the other analyses carried out in
 2202 the Higgs group of CMS. Fig. 145 shows the templates using as input for the calculation the SM qqZZ
 2203 background, a SM Higgs with $m_H = 125$ GeV and a PS Higgs with $m_H = 125$ GeV, for the three decay
 2204 channels separately.

2205 We construct the parameter $2 \ln(\mathcal{L}_1 / \mathcal{L}_2)$ with the likelihood \mathcal{L} evaluated for the two models. The signal
 2206 strength in the fit was left free to float as nuisance parameter. All systematic uncertainties included in
 2207 the nominal analysis are incorporated in the hypothesis separation analysis as well. The uncertainty on
 2208 the mass distribution of the signal coming from the scale and resolution of the leptons is included by
 2209 creating alternative templates scaling and smearing the value of $m_{4\ell}$ in input to the SMD calculation.

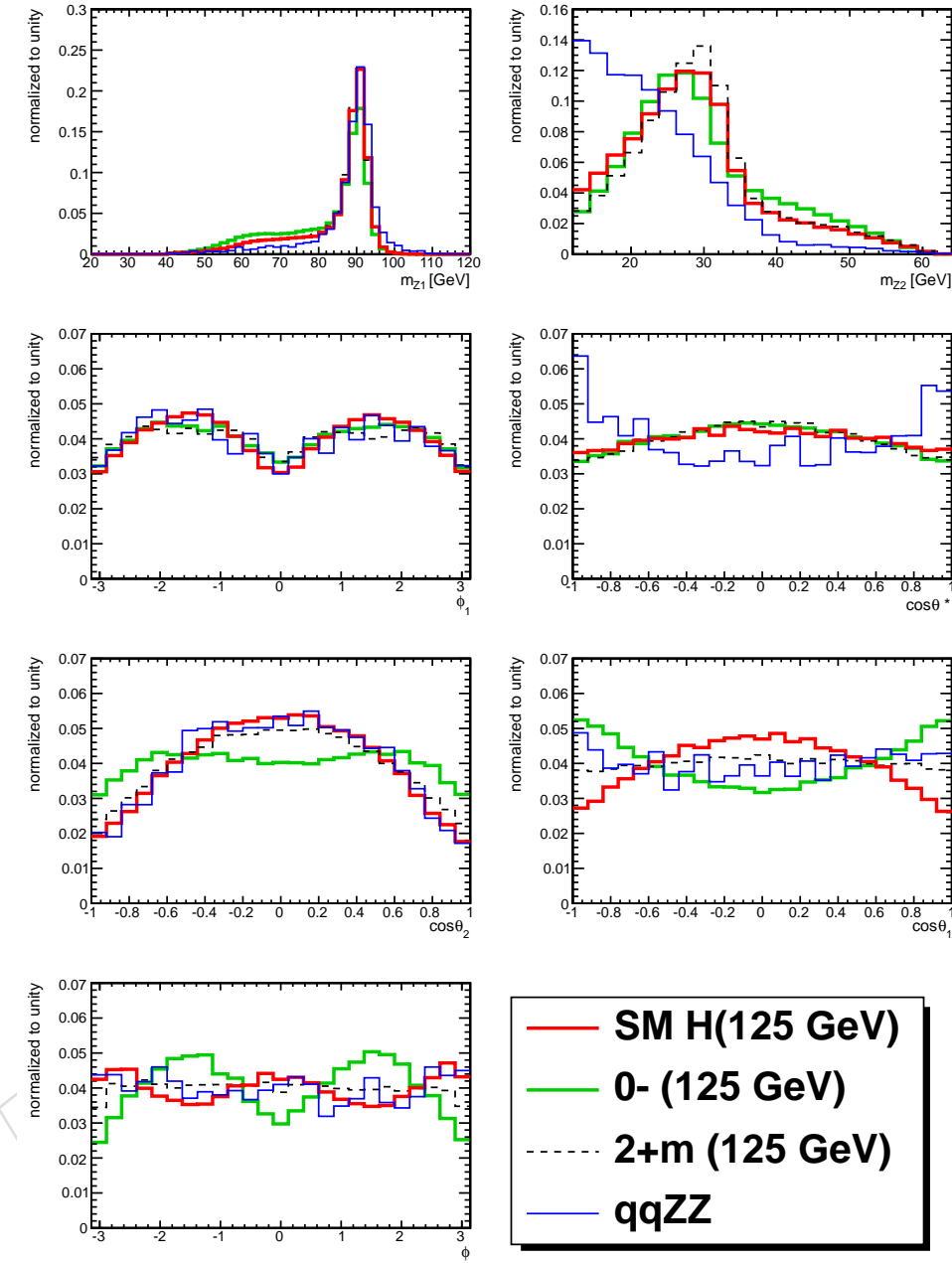


Figure 141: Distribution of angles and dilepton masses in the region $120 < m_{4\ell} < 130$ for different spin hypothesis (pseudoscalar and minimal-couplings graviton) compared with SM signal and qqZZ background.

Examples of these alternative templates are presented in Fig.146. A morphing between the nominal and alternative templates takes this into account when calculating the likelihoods during the statistical analysis. In a similar fashion, an uncertainty on the shape of the template for the Z+X background is applied. The template for the Z+X is obtained from data in the Z+X control region. In a way similar to the baseline analysis, the shape of the qqZZ template is used as shape systematic. This covers conservatively uncertainties on the shape of both SMD and \mathcal{D}_{0^-} (pseudoMELA) for the Z+X background, uncertainties that could be due both to differences between control and signal region and to limited statistics in the control region. For example the shapes of \mathcal{D}_{0^-} (pseudoMELA) and SMD for Z + X background could

2218 be well modeled by the $q\bar{q} \rightarrow ZZ$, as shown in Fig. 147.

2219 At this moment CMSSW simulation samples for signal do not include interference of identical leptons
 2220 in the final state ($4e$ and 4μ) and the alternative spin-parity signal simulation is available at 125 GeV and
 2221 not 126 GeV. To account for both effects, we apply re-weighting of the (SMD, D_{0-}) templates obtained
 2222 from fullsim CMSSW simulation using the ratio of expectation from generator-based simulation with
 2223 interference at 126 GeV. These correction factors and expected change in the distributions are shown in
 2224 Fig. 148. Results remain stable with such a correction to the spin-zero samples.

2225 MC studies indicate that with a luminosity of $5.05 fb^{-1}$ at 7 TeV and $12.21 fb^{-1}$ at 8 TeV and for a boson
 2226 with mass $m_H = 126$ GeV the expected signal significance is 4.6σ and the average hypothesis separation
 2227 significance is 1.93σ . In any particular experiment separation from either 0^+ or 0^- hypothesis may vary
 2228 depending on statistical distribution of events. The expected signal separation tossing toy experiments
 2229 for each signal hypothesis along with observation in data are shown in Fig. 149. The distribution of
 2230 $q = -2\ln(\mathcal{L}_{0-}/\mathcal{L}_{SM})$ is shown with generated samples of background and signal of two types (SM
 2231 0^+ and 0^-) for $m_H = 126$ GeV. Here the likelihoods \mathcal{L} are calculated with the signal rates allowed to
 2232 float independently for each signal type and the nuisance parameters are treated as independent. The
 2233 expected distributions are generated with signal cross-section equal to that of the SM, which is consistent
 2234 with observation. The observed value of q indicates that the hypothesis of $J^P = 0^-$ quantum numbers
 2235 is inconsistent with observation within 2.4 standard deviations, while the SM assignment is consistent
 2236 within 0.5 standard deviations. Using the CL_S criterion, the probability for $J^P = 0^-$ hypothesis is 2.4%.

2237 As discussed above, one can also use D_{0-} (pseudoMELA) to determine the parameter f_{a3} . To measure
 2238 the value of f_{a3} , one can approximate the (SMD, D_{0-}) probability density function by taking a mixture
 2239 of the probability density functions generated for the 0^+ and 0^- states, ignoring the interference terms.
 2240 This approximation is justified in Fig. 150 where the approximated distribution of D_{0-} (dashed purple
 2241 line) and distribution from a fully simulated mixed parity state (green) are shown. Likelihood scans
 2242 in 2 dimensions can then be used to constrain f_{a3} . The result is shown in Fig. 151 and corresponds to
 2243 $f_{a3} = 0.00^{+0.31}_{-0.00}$.

2244 The separation between the two cases 0^+ and 2^+ (minimal couplings) is weaker because the distribu-
 2245 tions of the specific D_{2+} for the different 2^+ and 0^+ hypotheses are similar, as shown in Fig. 140. MC
 2246 studies indicate that with a luminosity of $5.05 fb^{-1}$ at 7 TeV and $12.21 fb^{-1}$ at 8 TeV and for a boson
 2247 with mass $m_H = 126$ GeV the hypothesis separation significance is 1.2σ . The expected signal separation
 2248 tossing toy experiments for each signal hypothesis along with observation in data are shown in Fig. 153.
 2249 With the current statistics both the spin hypotheses $J = 0^+$ and $J = 2$ (minimal couplings) are consis-
 2250 tent with the observation, respectively inside 0.4 and 0.8 standard deviations. We note that the spin-2
 2251 hypothesis test been obtained with the full simulation for the mass $m_H = 126$ GeV and with lepton in-
 2252 terference included in the simulation of the $4e$ and 4μ channels, therefore no additional re-weighting of
 2253 MC samples was needed.

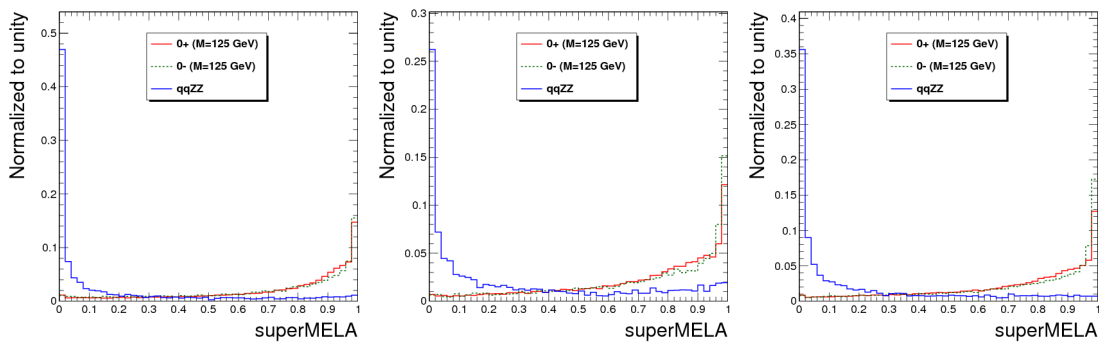


Figure 142: Distribution of SMD for 125 GeV SM Higgs and irreducible background events in the range $105 < m_{4l} < 140$ GeV, broken down by channel (left: 4μ , center: $4e$, right: $2e2\mu$).

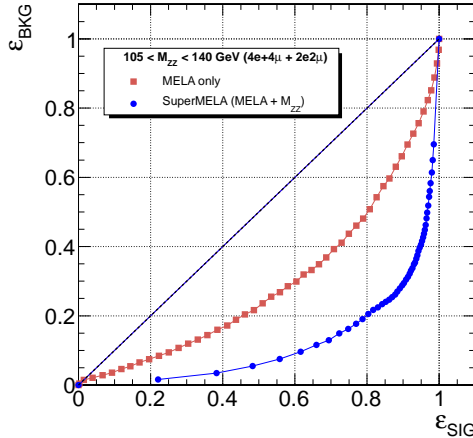


Figure 143: ROC curve using MELA (red square markers) or SMD (blue dots)

2254 12.6.3 Cross-check analysis with cut on KD

2255 An alternative and less powerful way to perform statistical analysis for the spin-parity hypotheses sep-
 2256 aration consists in fitting the 2D distribution $(\mathcal{D}_{J^P}, m_{4\ell})$ with a cut on $KD > 0.5$ to enhance signal over
 2257 background. This approach is sub-optimal as it exploits only partial KD information for separating
 2258 the signal from the SM background. The results for this approach are shown in Fig. 154. With this
 2259 approach, the parity hypotheses $J = 0^+$ and $J = 0^-$ (minimal couplings) are consistent with the obser-
 2260 vation, respectively inside 0.1 and 1.7 standard deviations, with the expected separation of 1.8 standard
 2261 deviations. The spin hypotheses $J = 0^+$ and $J = 2^+$ are consistent with the observation, respectively
 2262 inside 0.7 and 0.1 standard deviations, with the expected separation of 0.8 standard deviations.

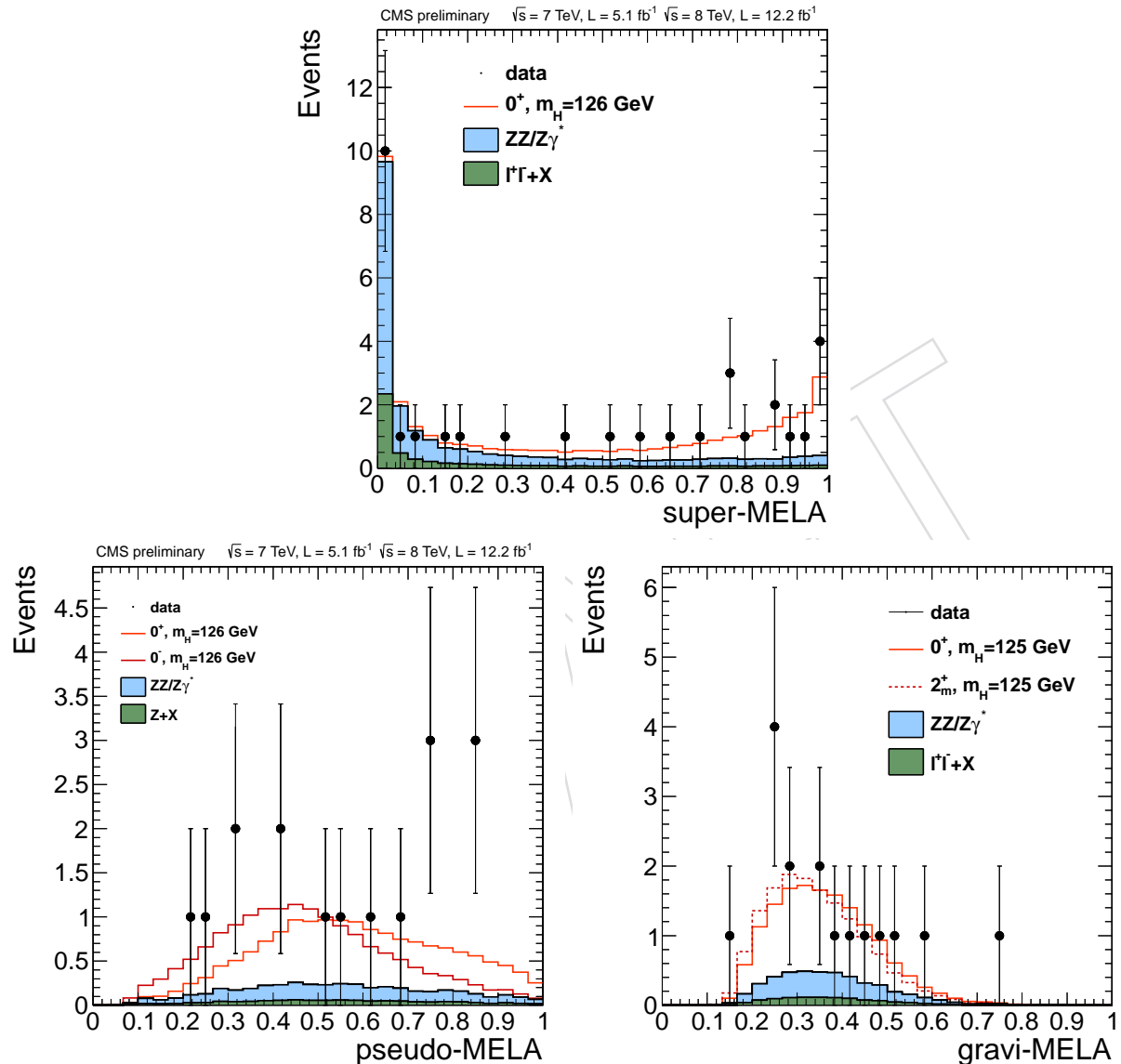


Figure 144: Distributions of SMD (superMELA, top), \mathcal{D}_{0^-} (pseudoMELA, left), and \mathcal{D}_{2^+} (graviMELA, right) for data, expected signal for two hypotheses and expected background. A cut $SMD > 0.5$ is applied when \mathcal{D}_{0^-} and \mathcal{D}_{2^+} are shown, to suppress background.

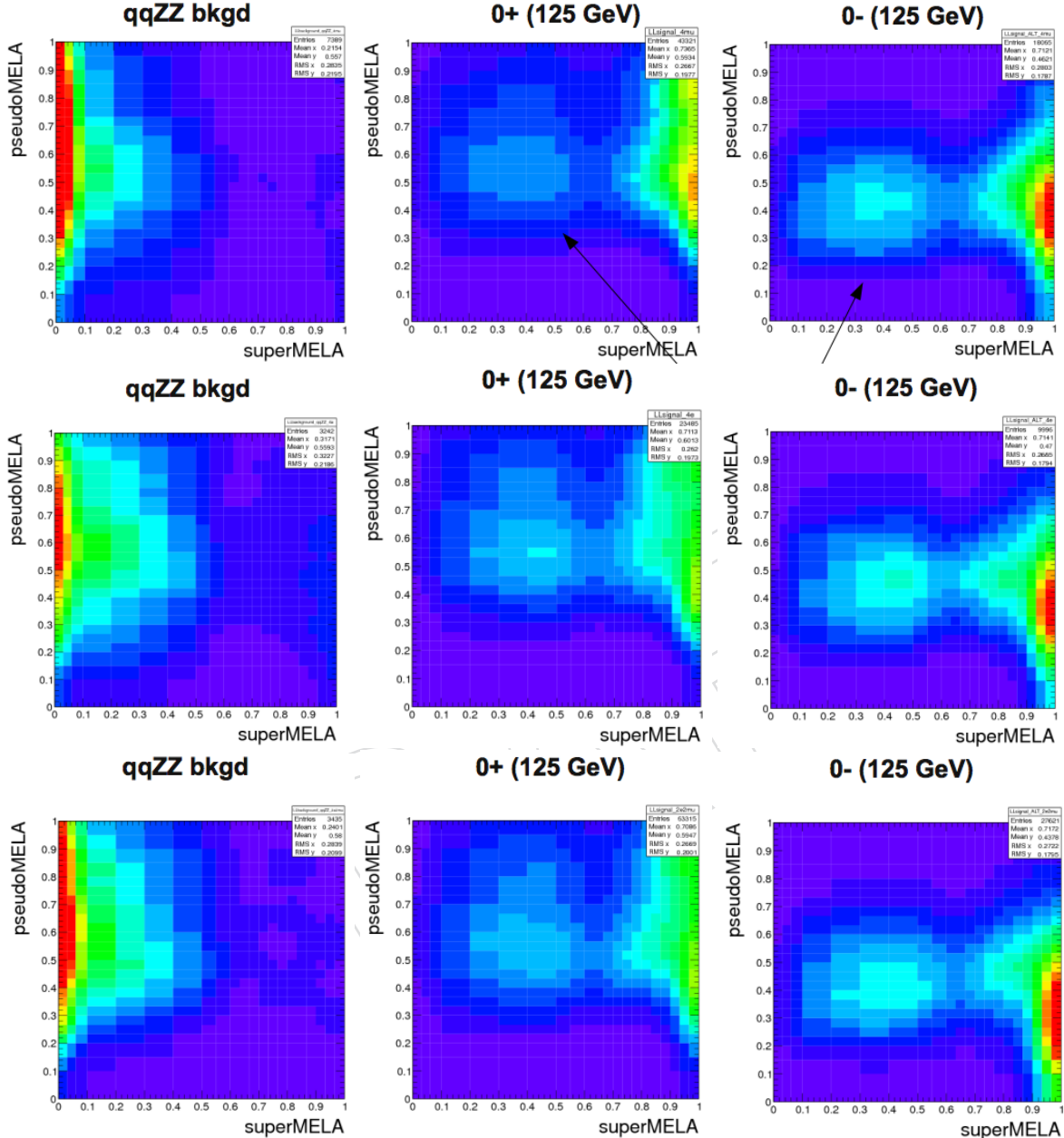


Figure 145: Bi-dimensional templates (SMD, pseudoMELA) used for the spin and CP property measurement. The templates are presented separately for the 4 μ (top row), 4e (middle row) and 2e2 μ (bottom row), respectively. In each row, the left-hand side plot shows the template for the simulation of the SM qqZZ background, while the central plot refers to the SM Higgs ($m_H = 125$ GeV) and the right-hand side plot to a PS Higgs ($m_H = 125$ GeV). All templates are produced from 8 TeV MC with a cut $105 < m_{4\ell} < 140$ GeV.

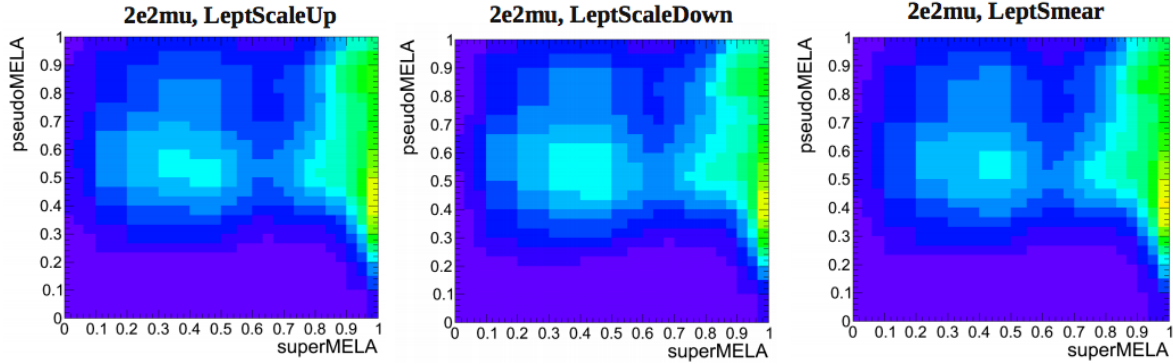


Figure 146: Alternative (SMD, \mathcal{D}_{0-}) 2D templates used as shape systematics for the signal in the $2e2\mu$ channel. Left: lepton scale shifted up by one sigma; Center: lepton scale shifted down by one sigma; Right: lepton energy smeared up by resolution. All templates are shown with a cut $105 < m_{4\ell} < 140 \text{ GeV}$.

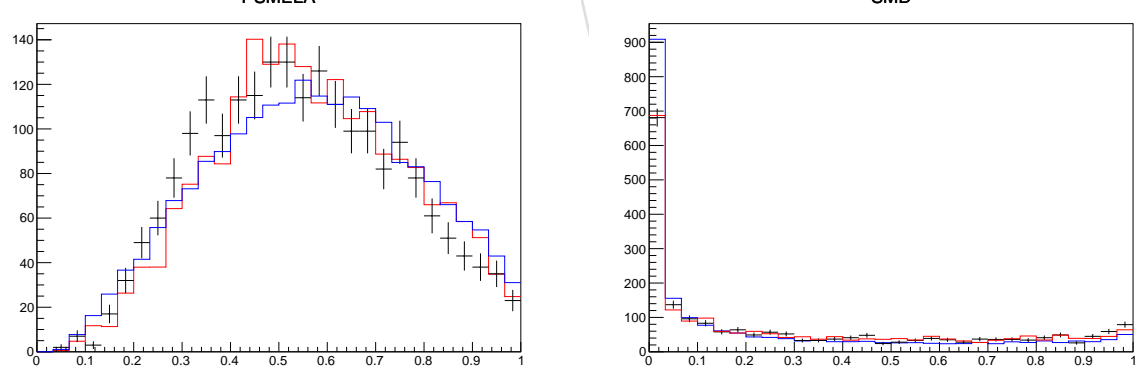


Figure 147: Distribution of \mathcal{D}_{0-} (left) and SMD (right) for $Z + X$ background in the control sample for data (black points), MC (red histogram) and for $q\bar{q} \rightarrow ZZ$ MC (blue solid histogram). The plot is presented for the mass range $105 < m_{4\ell} < 140 \text{ GeV}$.

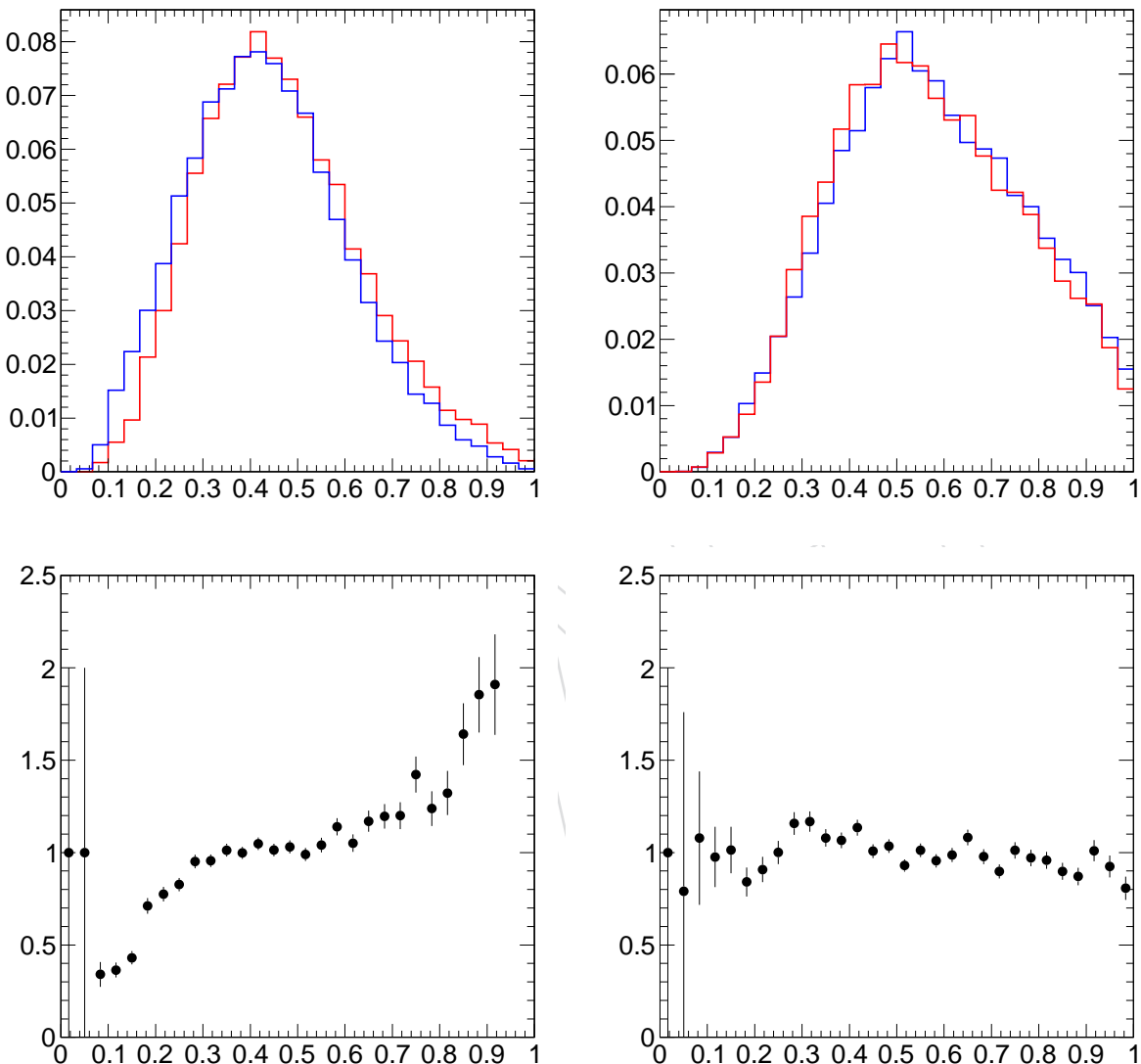


Figure 148: Top: Distribution of \mathcal{D}_{0^-} for 0^- (left) and 0^+ (right) samples before (blue) and after (red) effects of interference and mass change from 125 to 126 GeV are included. Bottom: re-weighting correction to the 0^- (left) and 0^+ (right) distributions of \mathcal{D}_{0^-} , in the 4μ channel.

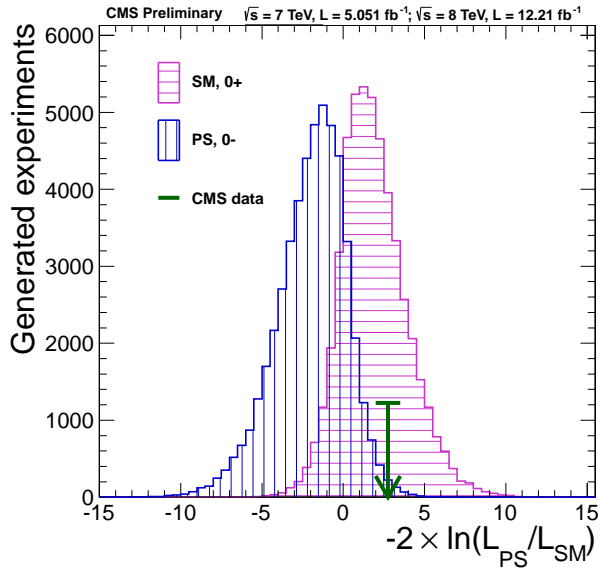


Figure 149: Distribution of $-2\ln(\mathcal{L}_1/\mathcal{L}_2)$ of toy experiments tossed according to a 0^+ signal hypothesis (magenta, horizontal hatching) and 0^- signal hypothesis (blue, vertical hatching) for $m_H = 126 \text{ GeV}$. The yields used in the generation of the pseudo-experiments are those expected with 5.05 fb^{-1} at 7 TeV and 12.21 fb^{-1} at 8 TeV of data. The arrow indicates observed value in data.

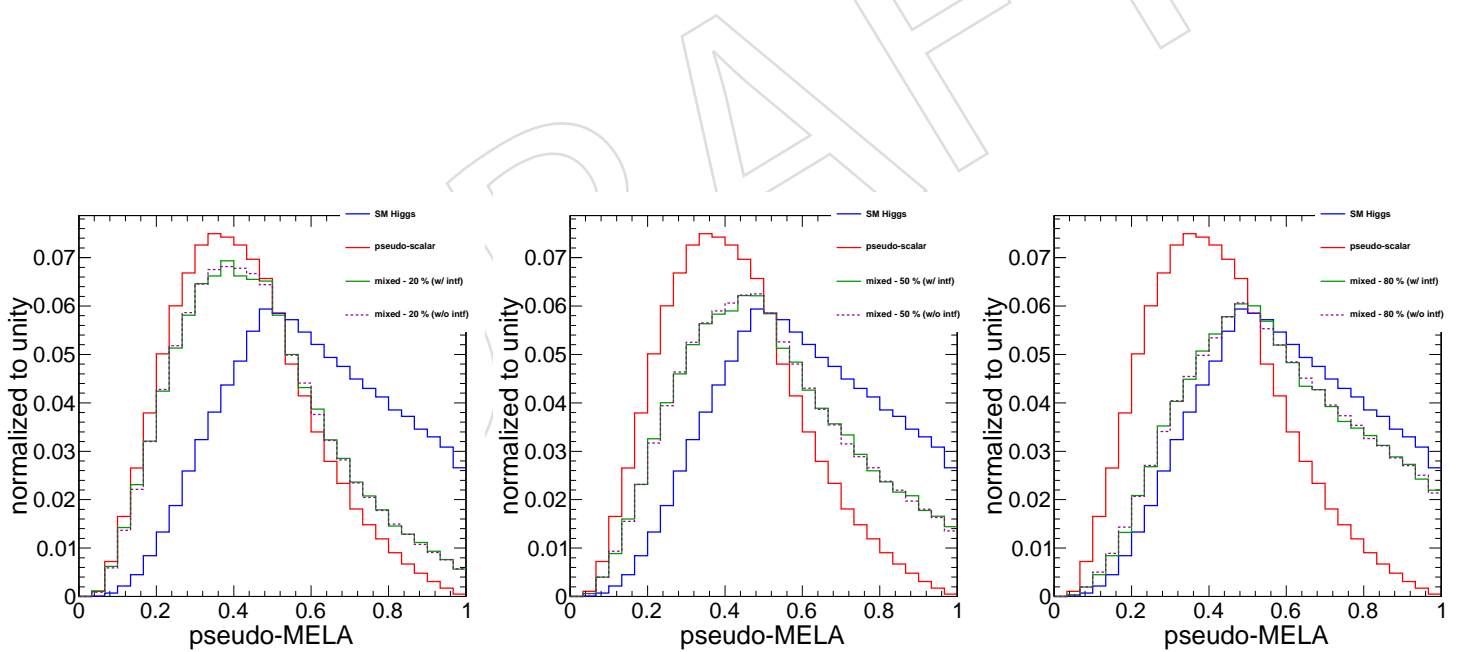


Figure 150: Distribution of \mathcal{D}_{0-} (pseudoMELA) for several choice models, SM Higgs ($f_{a3} = 0$) in blue, $f_{a3} = 1$ in red. In green and dashed purple are two different model for different fractions of f_{a3} generated, green is the fully simulated model while dashed purple shows an approximation in which the interference of the two amplitudes is neglected. The different plots show variable f_{a3} . The left is $f_{a3} = 0.8$, the middle is $f_{a3} = 0.5$, and the right is $f_{a3} = 0.2$.

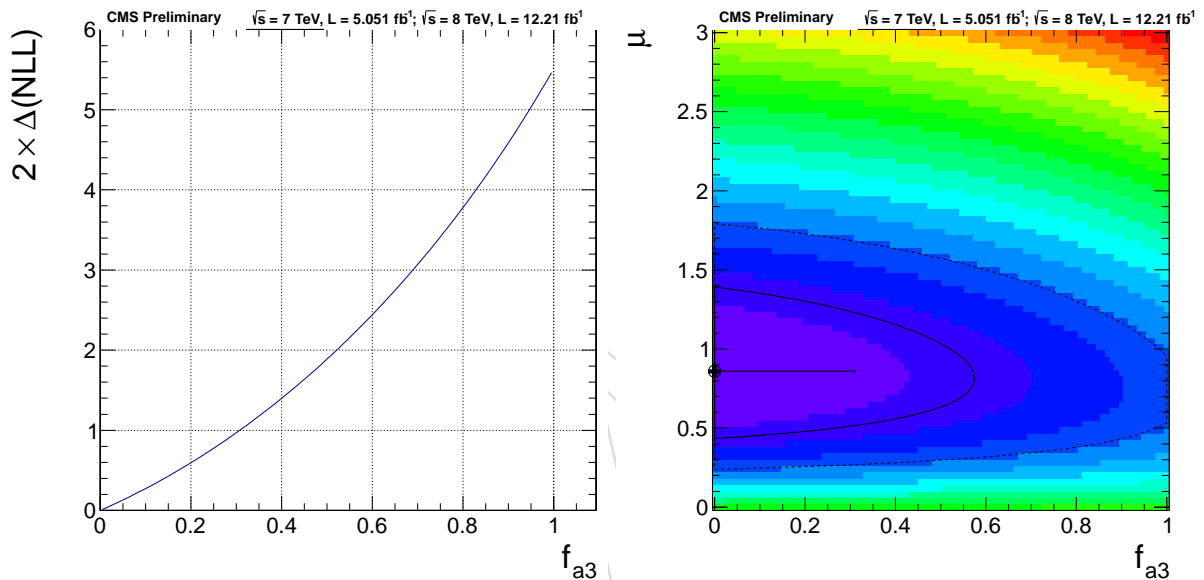


Figure 151: Distribution of $-2 \ln \mathcal{L}$ as a function of amplitude fraction f_{a3} (1D left) and with signal strength μ (2D right). The central point shows the minimum value of $-2 \ln \mathcal{L}$, the solid and dashed contours show 68% and 95% CL contours in two dimensions. The cross indicates the one-dimensional 68% CL intervals.

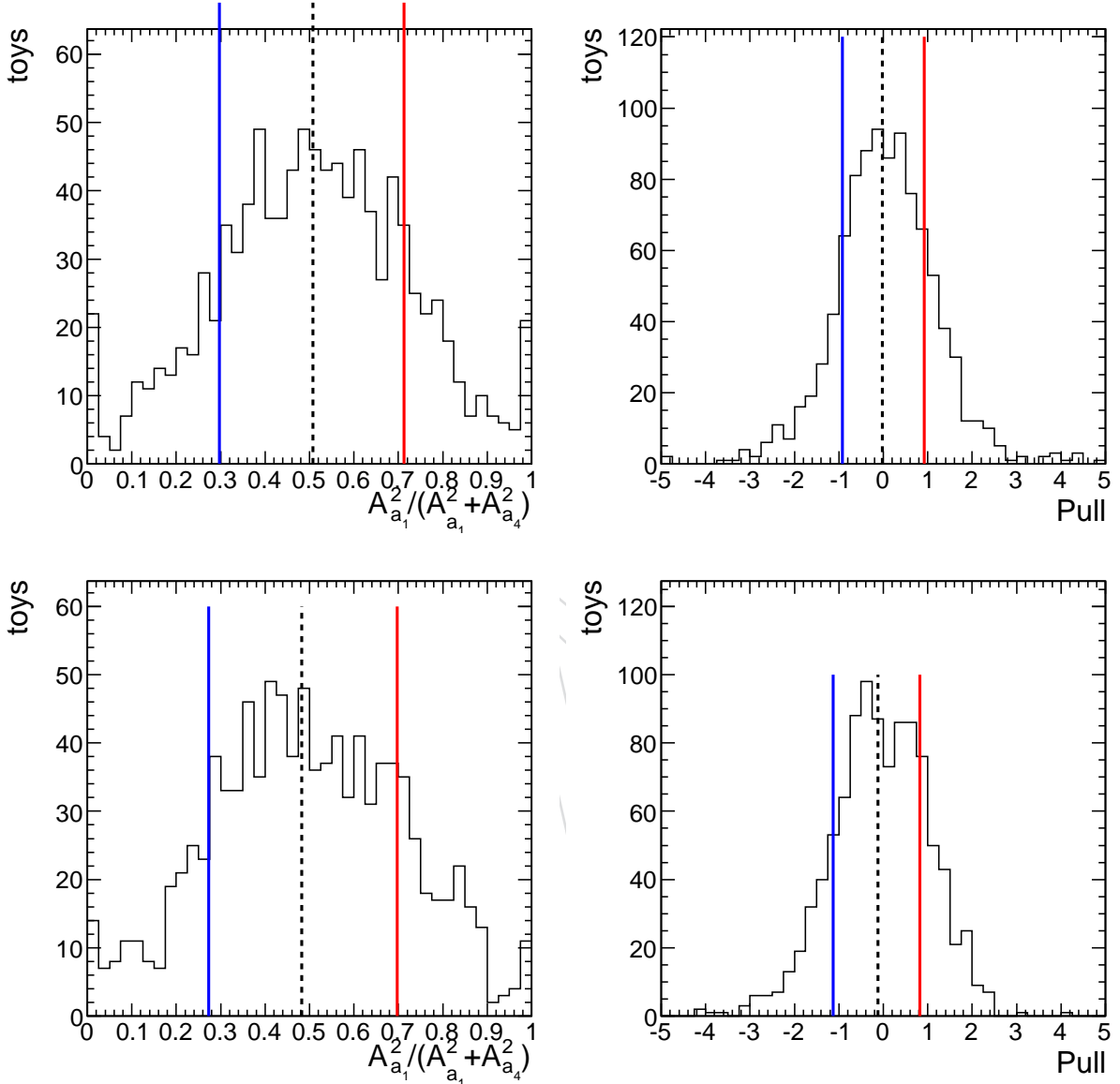


Figure 152: Toy study fitting f_{a3} with the generated value of 0.5. Distributions in the left column show the best fit value of f_{a3} while the right column shows the pull distribution of f_{a3} . The top row used the full analytic expression leave only one parameter float while the bottom row relied on a 2D template of $m_{4\ell}$ and the discriminant \mathcal{D}_{0^-} .

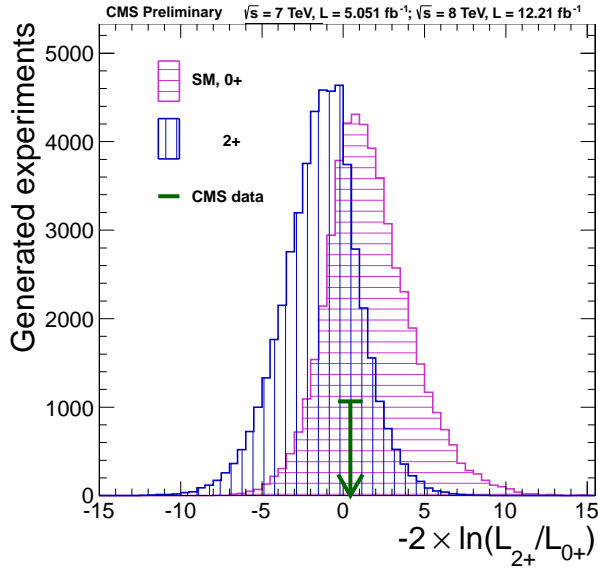


Figure 153: Distribution of $-2\ln(\mathcal{L}_1/\mathcal{L}_2)$ of toy experiments tossed according to a 0^+ signal hypothesis (magenta, horizontal hatching) and 2_{min}^+ signal hypothesis (blue, vertical hatching) for $m_H = 126 \text{ GeV}$. The yields used in the generation of the pseudo-experiments are those expected with 5.05 fb^{-1} at 7 TeV and 12.21 fb^{-1} at 8 TeV of data. The arrow indicates observed value in data.

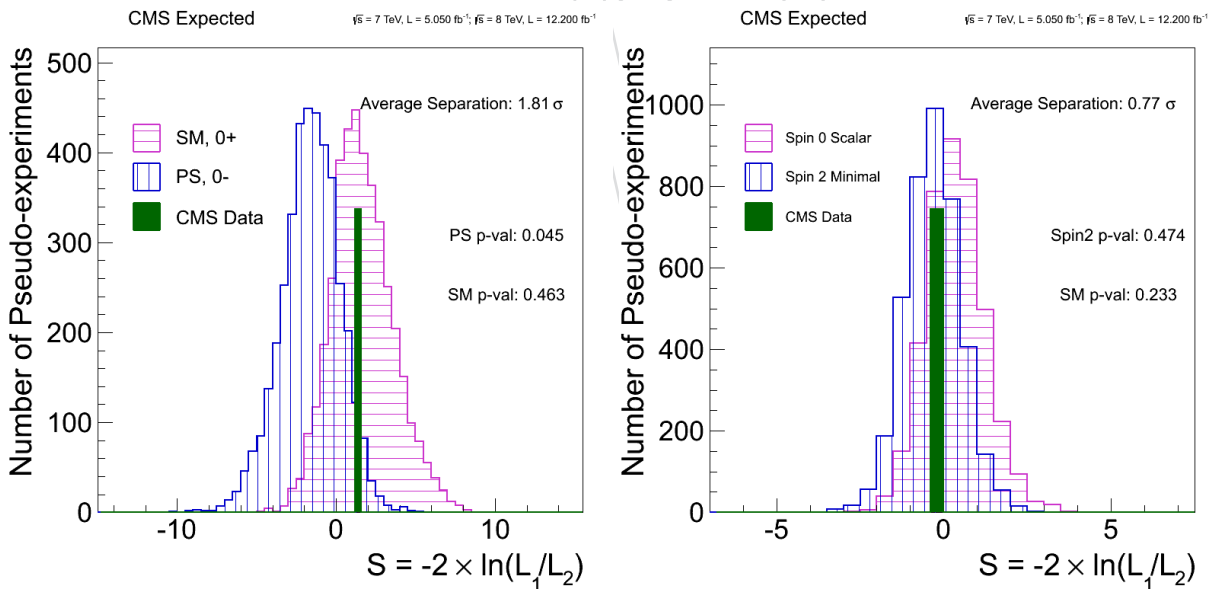


Figure 154: Results of the spin-parity analysis with sub-optimal statistical analysis: distribution of $-2\ln(\mathcal{L}_1/\mathcal{L}_2)$ of toy experiments tossed according to a 0^+ signal hypothesis (magenta, horizontal hatching) and 0^- (left) or 2_{min}^+ (right) signal hypothesis (blue, vertical hatching) for $m_H = 125 \text{ GeV}$. The yields used in the generation of the pseudo-experiments are those expected with 5.05 fb^{-1} at 7 TeV and 12.21 fb^{-1} at 8 TeV of data. The arrows indicates observed values in data.

2263 13 Summary and Conclusions

2264 In summary, a study of the standard model Higgs boson has been presented in the four-lepton decay
 2265 modes, $H \rightarrow 4\ell$ and $H \rightarrow 2\ell 2\tau$. The mass distributions are measured with four-lepton invariant
 2266 masses $m_{4\ell}$ or $m_{2\ell 2\tau} > 100$ GeV using 5.1 fb^{-1} at $\sqrt{s} = 7$ TeV and 12.2 fb^{-1} at $\sqrt{s} = 8$ TeV. The mea-
 2267 surements are interpreted using for each event the information from the measured four-lepton mass,
 2268 the mass uncertainty, and a kinematic discriminant. Upper limits at 95% confidence level exclude the
 2269 SM-like Higgs boson in the ranges 113–116 GeV and 129–720 GeV while the expected exclusion range
 2270 is 118–670 GeV. The new boson recently discovered by the ATLAS and CMS experiments is observed
 2271 in the 4ℓ channel, with a local significance of 4.5 standard deviations above the expected background.
 2272 The signal strength μ , relative to the expectation for the standard model Higgs boson, is measured to
 2273 be $\mu = 0.80^{+0.35}_{-0.28}$ at 126 GeV. A measurement of its mass gives $126.2 \pm 0.6 \text{ (stat)} \pm 0.2 \text{ (syst)}$ GeV. The
 2274 hypothesis 0^+ of the standard model for the spin $J = 0$ and parity $P = +1$ quantum numbers is found
 2275 to be consistent with the observation. The data disfavor the pseudoscalar hypothesis 0^- with a CL_s
 2276 value of 2.4%. The fraction of a CP-violating contribution to the decay amplitude, expressed through
 2277 the fraction f_{a3} of the corresponding decay rate, is measured to be $f_{a3} = 0.00^{+0.31}_{-0.00}$, and thus consistent
 2278 with SM expectation.

2279 References

- [1] S. L. Glashow, “Partial Symmetries of Weak Interactions”, *Nucl. Phys.* **22** (1961) 579–588, doi:[10.1016/0029-5582\(61\)90469-2](https://doi.org/10.1016/0029-5582(61)90469-2).
- [2] S. Weinberg, “A Model of Leptons”, *Phys. Rev. Lett.* **19** (1967) 1264–1266, doi:[10.1103/PhysRevLett.19.1264](https://doi.org/10.1103/PhysRevLett.19.1264).
- [3] A. Salam, “Elementary Particle Physics”, *N. Svartholm ed., Almqvist and Wiksell, Stockholm* (1968).
- [4] F. Englert and R. Brout, “Broken Symmetry and the Mass of Gauge Vector Mesons”, *Phys. Rev. Lett.* **13** (1964) 321–322, doi:[10.1103/PhysRevLett.13.321](https://doi.org/10.1103/PhysRevLett.13.321).
- [5] P. W. Higgs, “Broken symmetries, massless particles and gauge fields”, *Phys. Lett.* **12** (1964) 132–133, doi:[10.1016/0031-9163\(64\)91136-9](https://doi.org/10.1016/0031-9163(64)91136-9).
- [6] P. W. Higgs, “Broken Symmetries and the Masses of Gauge Bosons”, *Phys. Rev. Lett.* **13** (1964) 508–509, doi:[10.1103/PhysRevLett.13.508](https://doi.org/10.1103/PhysRevLett.13.508).
- [7] G. Guralnik, C. Hagen, and T. Kibble, “Global Conservation Laws and Massless Particles”, *Phys. Rev. Lett.* **13** (1964) 585–587, doi:[10.1103/PhysRevLett.13.585](https://doi.org/10.1103/PhysRevLett.13.585).
- [8] P. W. Higgs, “Spontaneous Symmetry Breakdown without Massless Bosons”, *Phys. Rev.* **145** (1966) 1156–1163, doi:[10.1103/PhysRev.145.1156](https://doi.org/10.1103/PhysRev.145.1156).
- [9] T. Kibble, “Symmetry breaking in nonAbelian gauge theories”, *Phys. Rev.* **155** (1967) 1554–1561, doi:[10.1103/PhysRev.155.1554](https://doi.org/10.1103/PhysRev.155.1554).
- [10] ATLAS Collaboration, “Search for the Standard Model Higgs boson in the decay channel $H \rightarrow ZZ(*) \rightarrow 4l$ with 4.8 fb^{-1} of pp collision data at $\sqrt{s} = 7$ TeV with ATLAS”, *Phys. Lett.* **B710** (2012) 383–402, arXiv:[1202.1415](https://arxiv.org/abs/1202.1415).
- [11] CMS Collaboration, “Search for the standard model Higgs boson in the decay channel H to ZZ to 4 leptons in pp collisions at $\sqrt{s} = 7$ TeV”, arXiv:[1202.1997](https://arxiv.org/abs/1202.1997).
- [12] ATLAS Collaboration, “Combined search for the Standard Model Higgs boson using up to 4.9 fb^{-1} of pp collision data at $\sqrt{s} = 7$ TeV with the ATLAS detector at the LHC”, *Phys. Lett.* **B710** (2012) 49–66, arXiv:[1202.1408](https://arxiv.org/abs/1202.1408).
- [13] CMS Collaboration, “Combined results of searches for the standard model Higgs boson in pp collisions at $\sqrt{s} = 7$ TeV”, *Phys. Lett.* **B710** (2012) 26–48, arXiv:[1202.1488](https://arxiv.org/abs/1202.1488).

- [14] LEP Working Group for Higgs boson searches, ALEPH Collaboration, DELPHI Collaboration, L3 Collaboration, OPAL Collaboration, “Search for the standard model Higgs boson at LEP”, *Phys.Lett.* **B565** (2003) 61–75, doi:10.1016/S0370-2693(03)00614-2, arXiv:hep-ex/0306033.
- [15] CDF and D0 Collaborations, “Combination of Tevatron Searches for the Standard Model Higgs Boson in the W^+W^- Decay Mode”, *Phys. Rev. Lett.* **104** (2010) 061802, doi:10.1103/PhysRevLett.104.061802. a more recent, unpublished, limit is given in preprint arXiv:1103.3233.
- [16] ALEPH, CDF, D0, DELPHI, L3, OPAL, SLD Collaborations, the LEP Electroweak Working Group, the Tevatron Electroweak Working Group, and the SLD Electroweak and Heavy Flavour Groups, “Precision Electroweak Measurements and Constraints on the Standard Model”, technical report, (2010).
- [17] ALEPH, CDF, D0, DELPHI, L3, OPAL, SLD Collaborations, the LEP Electroweak Working Group, the Tevatron Electroweak Working Group, and the SLD Electroweak and Heavy Flavour Groups, “Precision electroweak measurements on the Z resonance”, *Phys. Rept.* **427** (2006) 257, doi:10.1016/j.physrep.2005.12.006, arXiv:hep-ex/0509008.
- [18] CMS Collaboration, “Search for the standard model Higgs boson in the H to ZZ to ll tau tau decay channel in pp collisions at $\sqrt{s}=7$ TeV”, *JHEP* **1203** (2012) 081, arXiv:1202.3617.
- [19] CMS Collaboration, “The CMS experiment at the CERN LHC”, *JINST* **3** (2008) S08004, doi:10.1088/1748-0221/3/08/S08004.
- [20] N. Amapane et al., “Search for the standard model Higgs boson in the decya channel $H \rightarrow ZZ \rightarrow 4\ell$ in pp collisions”, *CMS AN* **2012/141** (2012).
- [21] CMS Collaboration, “Observation of a new boson at a mass of 125 GeV with the CMS experiment at the LHC”, *Phys.Lett.* **B716** (2012) 30–61, doi:10.1016/j.physletb.2012.08.021, arXiv:1207.7235.
- [22] Marlow, D, “talk at the CMS GWM”, <https://indico.cern.ch/getFile.py/access?contribId=2&resId=0&materialId=slides&confId=123724> (2011).
- [23] Pierini, M., “talk at the Joint PVT/PO Meeting”, <https://twiki.cern.ch/twiki/bin/viewauth/CMS/PdwgMain> (2011).
- [24] LHC Higgs Cross Section Working Group, “Handbook of LHC Higgs Cross Sections: 1. Inclusive Observables”, CERN Report CERN-2011-002, (2011).
- [25] T. Sjöstrand, S. Mrenna, and P. Z. Skands, “PYTHIA 6.4 Physics and Manual”, *JHEP* **05** (2006) 026, doi:10.1088/1126-6708/2006/05/026, arXiv:hep-ph/0603175.
- [26] J. Alwall et al., “MadGraph/MadEvent v4: The New Web Generation”, *JHEP* **09** (2007) 028, doi:10.1088/1126-6708/2007/09/028, arXiv:0706.2334.
- [27] S. Frixione, P. Nason, and C. Oleari, “Matching NLO QCD computations with Parton Shower simulations: the POWHEG method”, *JHEP* **11** (2007) 070, doi:10.1088/1126-6708/2007/11/070, arXiv:0709.2092.
- [28] T. Binoth, N. Kauer, and P. Mertsch, “Gluon-induced QCD corrections to $pp \rightarrow ZZ \rightarrow \ell\bar{\ell}\ell'\bar{\ell}'$ ”, in *Proceedings of the XVI Int. Workshop on Deep-Inelastic Scattering and Related Topics (DIS'07)*. 2008. arXiv:0807.0024. doi:10.3360/dis.2008.142.
- [29] S. Baffioni et al., “Electron Reconstruction in CMS”, *CMS Note* **2006/040** (2006).
- [30] S. Baffioni et al., “Electron Reconstruction in CMS”, *CMS Analysis Note* **2009/164** (2009).
- [31] CMS Collaboration, “Electron reconstruction and identification at $\sqrt{s} = 7$ TeV”, *CMS Physics Analysis Summary CMS-PAS-EGM-10-004* (2010).
- [32] CMS Collaboration, “Electron commissioning results at at $\sqrt{s} = 7$ TeV”, *CMS Detector Performance Summaries* **2011/003** (2011).

- 2355 [33] S. Baffioni et al., "Electron Charge Determination Commissioning from 7 TeV Data", *CMS AN*
2356 **2010/468** (2010).
- 2357 [34] H $\rightarrow\gamma\gamma$ Working Group, "Updated measurements of the new Higgs-like boson at 125 GeV in the
2358 two photon decay channel", (31 October, 2012). CMS AN-12-374.
- 2359 [35] "Egamma electron energy scale twiki page".
- 2360 [36] A. Benaglia et al., "Search for a Standard Model Higgs boson decaying into two photons in 2012
2361 data", *CMS AN* **2012/160** (2012).
- 2362 [37] Y. Chen et al., "Electron Energy Reconstruction Using a Multivariate Regression", *CMS AN*
2363 **2012/327** (2012).
- 2364 [38] e/g POG, "Electron Selection Criteria in 2012", *CMS AN* **2012/201** (2012).
- 2365 [39] CMS Collaboration, "MUO-10-004: Performance of CMS muon reconstruction in pp collision
2366 events at $\sqrt{s} = 7$ TeV", technical report, (2010). In preparation to *JINST*.
- 2367 [40] CMS Collaboration, "Measurement of tracking efficiency", *CMS Physics Analysis Summary*
2368 **CMS-PAS-TRK-10-002** (2010).
- 2369 [41] A. Bodek and J. Han, "Improved Rochester Misalignment and Muon Scale Corrections Extracted
2370 for 2011A, 2011B CMS Data", *CMS AN* **2012/298** (2012).
- 2371 [42] CMS Collaboration, "Commissioning of the particle-flow event reconstruction with leptons from
2372 J/Psi and W decays at 7 TeV", *CMS Physics Analysis Summary* **CMS-PAS-PFT-10-003** (2010).
- 2373 [43] M. Cacciari and G. P. Salam, "Pileup subtraction using jet areas", *Phys. Lett.* **B659** (2008) 119–126,
2374 doi:10.1016/j.physletb.2007.09.077, arXiv:0707.1378.
- 2375 [44] M. Cacciari, G. P. Salam, and G. Soyez, "The Catchment Area of Jets", *JHEP* **04** (2008) 005,
2376 doi:10.1088/1126-6708/2008/04/005, arXiv:0802.1188.
- 2377 [45] G. Daskalakis et al., "Measuring Electron Efficiencies at CMS with Early Data", *CMS Analysis*
2378 **Note** **2007/019** (2007).
- 2379 [46] S. Baffioni et al., "Electron Efficiency Measurement from 7 TeV Data", *CMS AN* **2010/471** (2010).
- 2380 [47] K. Nakamura et al. (Particle Data Group), "The Review of Particle Physics", *J. Phys. G* **37** (2010)
2381 075021.
- 2382 [48] CMS, "Electron VBF Selection", <https://twiki.cern.ch/twiki/bin/viewauth/CMS/VbtfEleID2011> (2011).
- 2383 [49] CMS, "Electron reconstruction efficiency measurement for 2011",
2384 <https://twiki.cern.ch/twiki/bin/view/CMS/EgCommissioningAndPhysicsDeliverables> (2011).
- 2385 [50] G. Petrucciani, "Measurement of the tracking efficiency for muons using the tag and probe
2386 method", *CMS AN* **2011/149** (2011).
- 2387 [51] CMS Collaboration, "TRK-10-001: Description and Performance of the CMS Track and Primary
2388 Vertex Reconstruction", (2011). In preparation.
- 2389 [52] P. Avery, M. Chen, A. Drozdetskiy, A. Korytov, G. Mitselmakher, M. Snowball, "A complete model
2390 of the four-lepton invariant mass distributions for $H \rightarrow ZZ \rightarrow 4\ell$ and $ZZ \rightarrow 4\ell$ events", (29 May,
2391 2011). CMS AN-11-202.
- 2392 [53] S. Goria, G. Passarino, and D. Rosco, "The Higgs Boson Lineshape", *Nucl.Phys.* **B864** (2012)
2393 530–579, doi:10.1016/j.nuclphysb.2012.07.006, arXiv:1112.5517.
- 2394 [54] "LHC Higgs Cross Section Working Group web page".
- 2395 [55] G. Passarino, "Higgs Interference Effects in $gg \rightarrow$ and their Uncertainty", *JHEP* **1208** (2012) 146,
2396 doi:10.1007/JHEP08(2012)146, arXiv:1206.3824.
- 2397 [56] LHC Higgs Cross Section Working Group et al., "Handbook of LHC Higgs cross sections: 1.
2398 Inclusive observables", CERN-2011-002 (CERN, Geneva, 2011, All the numbers can be obtained at
2399 <https://twiki.cern.ch/twiki/bin/view/LHCPhysics/CrossSections>) arXiv:1101.0593.

- [57] ATLAS and CMS Collaborations Collaboration, "LHC Higgs Combination Working Group report", *ATL-PHYS-PUB-2011-11, CMS NOTE-2011/005* (2011).
- [58] "Higgs Branching ratio errors".
- [59] S. Alekhin et al., "The PDF4LHC working group interim report", [arXiv:hep-ph/1101.0536](#).
- [60] H. L. Lai, M. Guzzi, J. Huston, Z. Li, P. M. Nadolsky, J. Pumplin and C. P. Yuan, "New parton distributions for collider physics", *Phys.Rev. D* (2010), no. 82, 074024.
- [61] A. D. Martin, W. J. Stirling, R. S. Thorne and G. Watt, "Parton distributions for the LHC", *Eur. Phys. J. C* (2009), no. 63, 189.
- [62] R. D. Ball, L. Del Debbio, S. Forte, A. Guffanti, J. I. Latorre, J. Rojo and M. Ubiali, "A first unbiased global NLO determination of parton distributions and their uncertainties", *Nucl. Phys. B* (2010), no. 838, 136.
- [63] "Observation of Z to 4l production in pp collisions at 7 TeV".
- [64] C. W. John Campbell, Keith Ellis, "MCFM - Monte Carlo for FeMtobarn processes", (2011).
- [65] A. Soni and R. Xu, "Probing CP violation via Higgs decays to four leptons", *Phys.Rev. D48* (1993) 5259–5263, doi:[10.1103/PhysRevD.48.5259](https://doi.org/10.1103/PhysRevD.48.5259), [arXiv:hep-ph/9301225](#).
- [66] V. D. Barger et al., "Higgs bosons: Intermediate mass range at e+ e- colliders", *Phys.Rev. D49* (1994) 79–90, doi:[10.1103/PhysRevD.49.79](https://doi.org/10.1103/PhysRevD.49.79), [arXiv:hep-ph/9306270](#).
- [67] S. Choi et al., "Identifying the Higgs spin and parity in decays to Z pairs", *Phys.Lett. B553* (2003) 61–71, doi:[10.1016/S0370-2693\(02\)03191-X](https://doi.org/10.1016/S0370-2693(02)03191-X), [arXiv:hep-ph/0210077](#).
- [68] B. Allanach et al., "Exploring small extra dimensions at the large hadron collider", *JHEP 0212* (2002) 039, [arXiv:hep-ph/0211205](#).
- [69] C. Buszello et al., "Prospective analysis of spin- and CP-sensitive variables in $H \rightarrow ZZ \rightarrow l(1)^+l(1)^-l(2)^+l(2)^-$ at the LHC", *Eur.Phys.J. C32* (2004) 209–219, doi:[10.1140/epjc/s2003-01392-0](https://doi.org/10.1140/epjc/s2003-01392-0), [arXiv:hep-ph/0212396](#).
- [70] R. M. Godbole, . Miller, D.J., and M. M. Muhlleitner, "Aspects of CP violation in the H ZZ coupling at the LHC", *JHEP 0712* (2007) 031, doi:[10.1088/1126-6708/2007/12/031](https://doi.org/10.1088/1126-6708/2007/12/031), [arXiv:0708.0458](#).
- [71] W.-Y. Keung, I. Low, and J. Shu, "Landau-Yang Theorem and Decays of a Z' Boson into Two Z Bosons", *Phys.Rev.Lett. 101* (2008) 091802, doi:[10.1103/PhysRevLett.101.091802](https://doi.org/10.1103/PhysRevLett.101.091802), [arXiv:0806.2864](#).
- [72] O. Antipin and A. Soni, "Towards establishing the spin of warped gravitons", *JHEP 0810* (2008) 018, doi:[10.1088/1126-6708/2008/10/018](https://doi.org/10.1088/1126-6708/2008/10/018), [arXiv:0806.3427](#).
- [73] K. Hagiwara, Q. Li, and K. Mawatari, "Jet angular correlation in vector-boson fusion processes at hadron colliders", *JHEP 0907* (2009) 101, doi:[10.1088/1126-6708/2009/07/101](https://doi.org/10.1088/1126-6708/2009/07/101), [arXiv:0905.4314](#).
- [74] Y. Gao et al., "Spin determination of single-produced resonances at hadron colliders", *Phys.Rev. D81* (2010) 075022, doi:[10.1103/PhysRevD.81.075022](https://doi.org/10.1103/PhysRevD.81.075022), [arXiv:1001.3396](#).
- [75] A. De Rujula et al., "Higgs look-alikes at the LHC", *Phys.Rev. D82* (2010) 013003, doi:[10.1103/PhysRevD.82.013003](https://doi.org/10.1103/PhysRevD.82.013003), [arXiv:1001.5300](#).
- [76] J. S. Gainer et al., "Improving the sensitivity of Higgs boson searches in the golden channel", *JHEP 1111* (2011) 027, doi:[10.1007/JHEP11\(2011\)027](https://doi.org/10.1007/JHEP11(2011)027), [arXiv:1108.2274](#).
- [77] CMS Collaboration, "Search for a Higgs boson in the decay channel H to ZZ(*) to q qbar l-l+ in pp collisions at sqrt(s) = 7 TeV", *JHEP 1204* (2012) 036, [arXiv:1202.1416](#).
- [78] S. Bolognesi et al., "On the spin and parity of a single-produced resonance at the LHC", *Submitted to Phys.Rev.*

- 2445 [79] E. Bagnaschi et al., “Higgs production via gluon fusion in the POWHEG approach in the SM and
2446 in the MSSM”, *JHEP* **1202** (2012) 088, doi:10.1007/JHEP02(2012)088, arXiv:1111.2854.
- 2447 [80] ATLAS and CMS Collaborations, LHC Higgs Combination Group, “Procedure for the LHC Higgs
2448 boson search combination in Summer 2011”, ATL-PHYS-PUB/CMS NOTE 2011-11, 2011/005,
2449 (2011).
- 2450 [81] T. Junk, “Confidence level computation for combining searches with small statistics”, *Nucl.
2451 Instrum. Meth. A* **434** (1999) 435, doi:10.1016/S0168-9002(99)00498-2,
2452 arXiv:hep-ex/9902006.
- 2453 [82] A. Read, “Modified frequentist analysis of search results (the CL_s method)”, Technical Report
2454 CERN-OPEN-2000-005, CERN, (2000).
- 2455 [83] Particle Data Group, “Review of particle physics”, *J. Phys. G* **37** (2010) 075021,
2456 doi:10.1088/0954-3899/37/7A/075021.
- 2457 [84] M. Oreglia, “A study of the reactions $\psi\prime \rightarrow \gamma\gamma\psi$ ”. PhD thesis, Stanford
2458 University, 1980. SLAC-0236.
- 2459 [85] A. Bonato et al., “Angular Analysis of Resonances $pp \rightarrow X \rightarrow ZZ$ ”, *CMS Analysis Note* **2010-351**.
- 2460 [86] CMS Collaboration, “Measurement of the Λ_b cross section and the $\bar{\Lambda}_b$ to Λ_b ratio with $J/\psi\Lambda$
2461 decays in pp collisions at $\sqrt{s} = 7$ TeV”, *Phys.Lett.* **B714** (2012) 136,
2462 doi:10.1016/j.physletb.2012.05.063.
- 2463 [87] D. De Florian et al., “Higgs boson production at the LHC: transverse momentum resummation
2464 effects in the $H \rightarrow \gamma\gamma$, $H \rightarrow WW \rightarrow \ell\nu\ell\nu$ and $H \rightarrow ZZ \rightarrow 4\ell$ decay modes”,
2465 arXiv:1203.6321v1.
- 2466 [88] T. Melia et al., “ ZZ , $W^\pm Z$ and W^+W^- production, including γ/Z interference, singly resonant
2467 contributions and interference for identical leptons”, *JHEP* **1111** (2011) 078.
- 2468 [89] CMS Collaboration, “Measurement of the Rapidity and Transverse Momentum Distributions of Z
2469 Bosons in pp Collisions at $\sqrt{s}=7$ TeV”, *Phys.Rev.* **D85** (2012) 032002,
2470 doi:10.1103/PhysRevD.85.032002, arXiv:1110.4973.

2471 A Appendix #1 Approach to VBF/VH Production Mechanism Mea- 2472 surement

2473 For the SM Higgs, the production mechanism contributing mostly to the total cross section is gluon-
 2474 gluon fusion ("gg", $\simeq 88\%$). A smaller fraction of the cross section comes from qq-initiated vector boson
 2475 fusion ("VBF", $\simeq 7\%$), while even smaller contributions are due to associated Higgs production with a
 2476 W, Z ("VH"), or $t\bar{t}$ pair ("ttH"). Separating the gg/ttH and VBF/VH contribution is particularly relevant
 2477 for Higgs coupling measurement, as in the first case the coupling to the fermions of the virtual loop is
 2478 involved, while in the other only Higgs-to-vector-boson couplings are present.

2479 Experimentally, two features are mostly distinctive of VBF/VH w.r.t. gg-produced events. First, in
 2480 VBF production the two jets resulting from the recoil of the two virtual vector bosons are sometimes
 2481 detectable in the experiment acceptance. Second, the distribution of the Higgs transverse momentum is
 2482 expected to be much harder in the VBF/VH case, as shown in Fig. 155 top.

2483 This second method has the advantage of being independent on the forward jet cuts, but systematics
 2484 from theoretical p_T distributions of signal and background must be carefully taken into account. It must
 2485 be noted that, while the jet tagging method is meant to select only the VBF process, the $p_{T,4\ell}$ method
 2486 cannot distinguish between VBF and the less abundant VH process: Figure 155 (bottom) shows the
 2487 similarity of the two spectra.

2488 Our approach is therefore structured as follows. We consider two categories of selected events in this
 2489 signal region:

- 2490 • (a) events with a pair of tagged jets and
- 2491 • (b) all other events.

2492 The default 2D fit used to determine the signal strength ($f(m_{4\ell}, \text{KD}) \sim P(m_{4\ell}) \cdot P(\text{KD}|m_{4\ell})$) is extended
 2493 with a third dimension:

- 2494 • for events of type (a) this is the normalized distribution of a linear Fisher discriminant (VD)
 which combine the invariant mass of the 2 leading jets and their $\Delta\eta$ (M_{jj} , $\Delta\eta_{jj}$),
- 2496 • while for events of type (b) this is $p_{T,4\ell}/m_{4\ell}$.

2497 It has to be noted that both of these probabilities could be introduced with a simple product, or as
 2498 conditional to KD or $m_{4\ell}$, taking into account possible correlations with either variable distribution. The
 2499 Fisher discriminant has a small correlation with mass in the qqH signal, while no correlation is expected
 2500 nor observed with the angular KD in any of the processes. Therefore the model is built as following.

- 2501 • In the dijet tagged category the model is defined as $f(m_{4\ell}, \text{KD}, \text{VD}) \sim P(m_{4\ell}) \cdot P(\text{KD}|m_{4\ell}) \cdot$
 $P(\text{VD}|m_{4\ell})$. The p_T of the ZZ system is highly correlated with the mass of the system, we
 consider instead $p_{T,4\ell}/m_{4\ell}$ which has a smaller correlation with mass.
- 2504 • For the untagged events the model is built as $f(m_{4\ell}, \text{KD}, p_{T,4\ell}/m_{4\ell}) \sim P(m_{4\ell}) \cdot P(\text{KD}|m_{4\ell}) \cdot$
 $P(p_{T,4\ell}/m_{4\ell}|m_{4\ell})$, so no correlation between $p_{T,4\ell}/m_{4\ell}$ and KD is included. This assumption
 has been tested with toys at low mass and a bias of less than 1% has been found on the
 extracted p-value and on the value of the couplings.

2508 Given the proper description of the correlation with mass, the model is going to be extended to the full
 2509 mass range from 100 GeV to 1 TeV. The fit to the VBF and gg production rates are done in the region
 2510 106-141 GeV for an Higgs of 126 GeV mass and all the results presented in Sec. A.6 are evaluated in the
 2511 mass region 110-140 GeV.

2512 Analytical or template descriptions are determined from simulated events (or control region in case of
 2513 Z+X background) separately for the following 8 sources, which contribute to the events in the signal
 2514 region:

- 2515 • Signal: gg, VBF, WH, ZH, $t\bar{t}$ H
- 2516 • Background: $q\bar{q} \rightarrow ZZ, Z+X, gg \rightarrow ZZ$

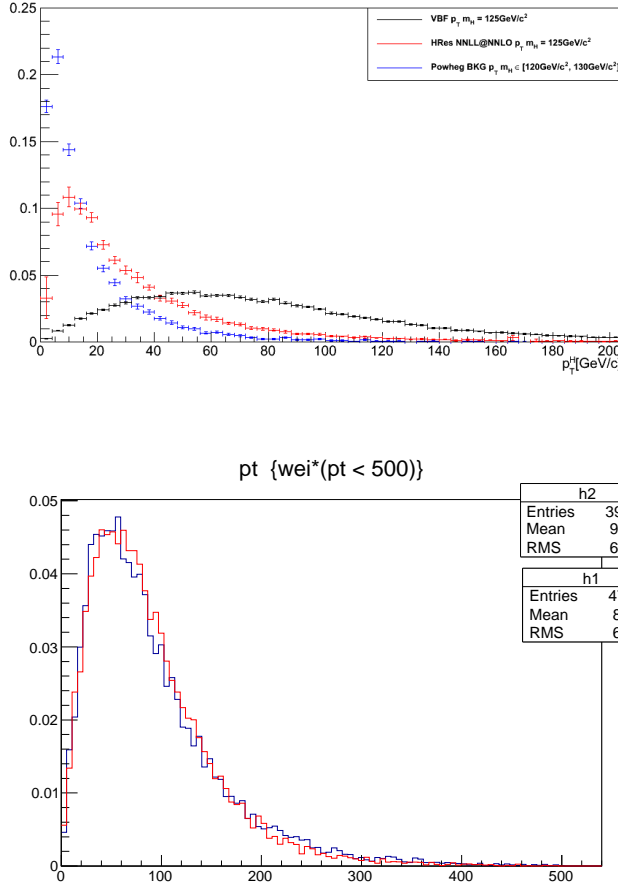


Figure 155: Top: $p_{T,4\ell}$ distribution at generator level for $gg \rightarrow H$ and VBF signal at 126 GeV and ZZ background MC in the region [120, 130] GeV, at a center-of-mass energy of 8 TeV (colors in legend). Bottom: $p_{T,4\ell}$ distribution at generator level for VBF MC (blue) and a weighted mixture of WH, ZH and $t\bar{t} H$ MC (red).

2517 A.1 Selection of tagged VBF events

2518 The forward di-jet signature can be detected in very large fraction of the VBF events. Due to the very
 2519 small VBF cross section and branching fraction to four leptons the jet tagging requirements need to be
 2520 as loose as possible. The main challenge for the measurement of the VBF fraction is not the background
 2521 but the contamination of gluon fusion.

2522 The jets are required to have a transverse momentum above 30 GeV and be constrained within a pseudo-
 2523 rapidity range of $\eta < 4.7$. All the default jet energy corrections are applied (L1FastJet, L2Absolute,
 2524 L3Relative and residual for data). To reject instrumental noise the loose jet ID suggested by the JetMET
 2525 POG is applied. The main source of fake VBF jets comes from PU where a dijet signature in a PU vertex
 2526 fakes a signal event in the primary vertex. This contribution is reduced by requiring a PU jet ID using a
 2527 multivariate approach. The working point is the loose MVA working point.

2528 About 50% of the VBF events have two jets in the final state while in the case of the gluon fusion this is
 2529 valid for 8% of the events. For events with two jets the main observables that discriminate signal and
 2530 gluon fusion/background are the $\Delta\eta$ between the two jets and the invariant mass of the two jet system
 2531 M_{jj} . Figure 156 shows the distribution of the VBF discrimination variables demonstrating the separation
 2532 power and also data vs simulation comparison for the control region defined by $140 < M_{4\ell} < 300 \text{ GeV}$

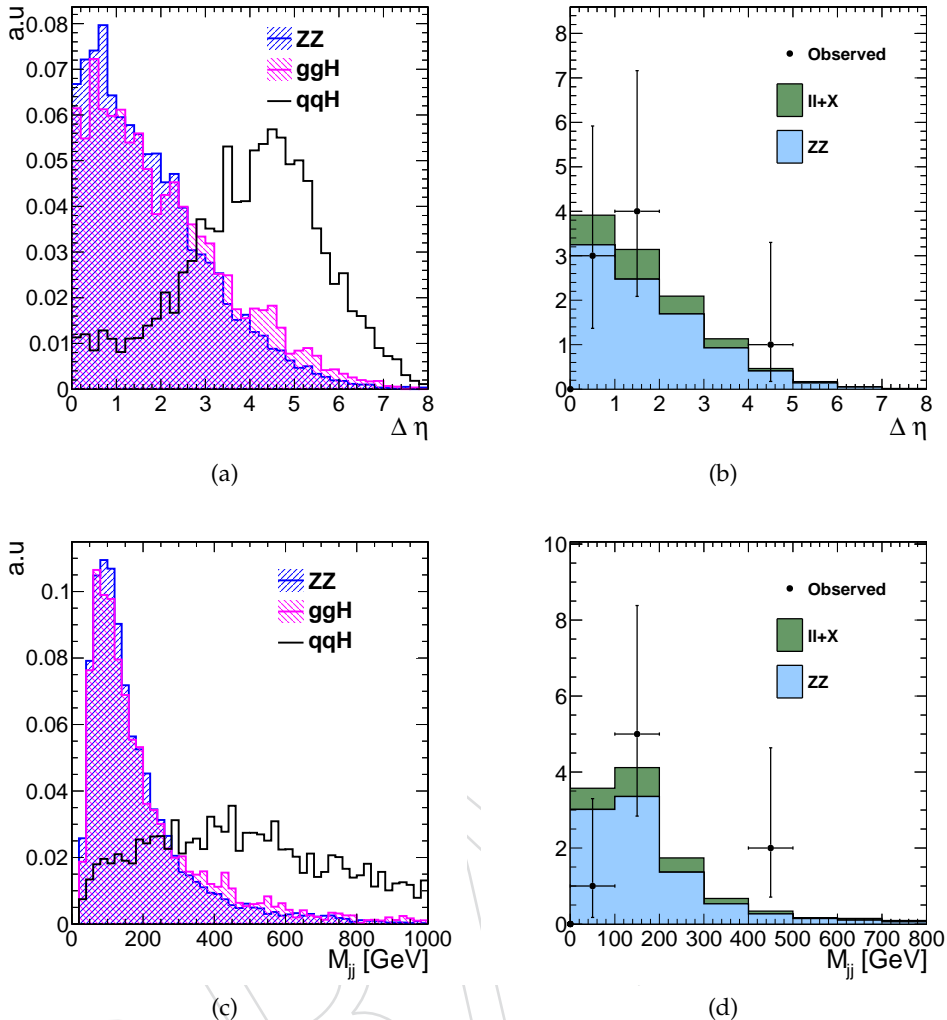


Figure 156: VBF discrimination variables vs gluon fusion and ZZ background (left) and comparison between data and simulation in the control region of $140 < M_{4l} < 300$ GeV for $5+12 fb^{-1}$ (right).

being dominated by ZZ background. The statistics corresponding to di-jet events is limited, however it seems that there is good agreement in the distributions.

To maximize the performance of the analysis, the VBF tagged category is defined as events with two jets or more. Instead of cutting on VBF variables it is preferred to perform a fit extracting the VBF yield. To minimize the number of dimensions in this fit the variables are combined into a linear Fisher discriminant given by:

$$VD = 9.407 \cdot 10^{-2} \times \Delta\eta + 4.1581 \cdot 10^{-4} \times M_{jj} [\text{GeV}] \quad (43)$$

Figure 157 shows the comparison of VBF and gluon fusion for the Fisher discriminant and the data vs simulation comparison in the control region.

For each of the 8 components described above we compute templates from MC (or control region in case of Z+X background) . Given the available statistics, proper smoothing/fitting is applied in order to avoid large statistical fluctuations and empty template regions. The template for ggH and qqH contribution is filled with event coming from all the samples with different masses and a simple smoothing algorithm is applied. In Fig. 158- 159, the templates for ggH and qqH are shown, as well as 1D Fisher

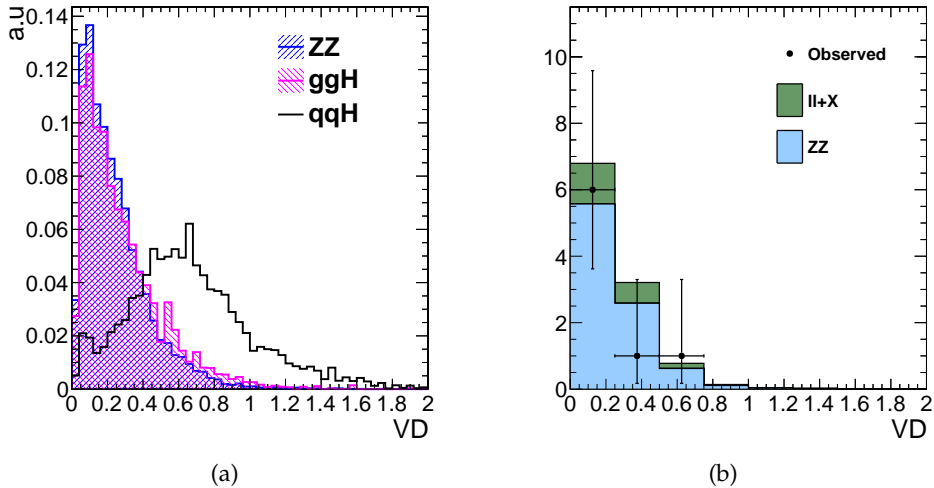


Figure 157: Linear Fisher Discriminant combining VBF discrimination variables. Comparsion of signal vs background (left) and data vs simulation in the control region for $5+12\text{ fb}^{-1}$ (right).

2542 projections for different mass ranges. Projections before and after the smoothing are also reported to
2543 show that no bias is introduced by the smoothing procedure.

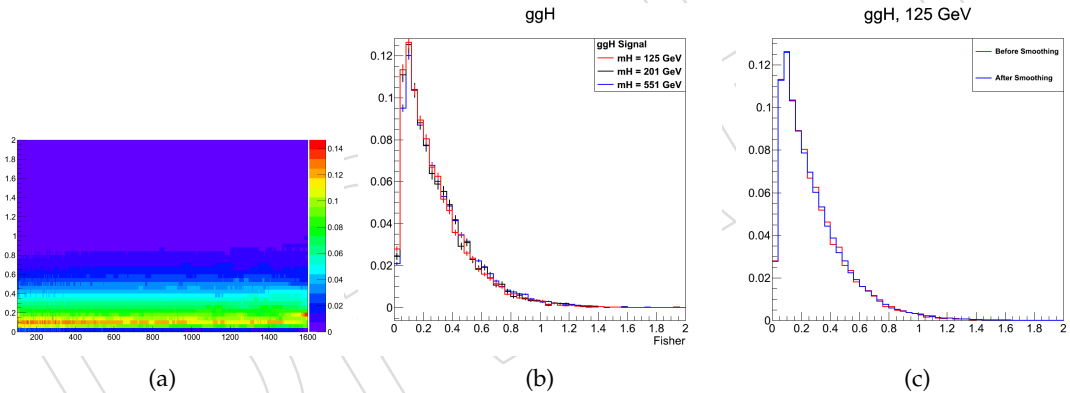


Figure 158: Dijet category in ggH process: Fisher vs m_{4l} template (left), Fisher projection for few mass samples (center: red 125 GeV, blue 200 GeV, blue 550 GeV), comparison of Fisher projection before and after smoothing procedure

2544 While in case of VBF the 2 jets are clearly correlated with the Higgs production and therefore there
2545 is a correlation between the Fisher and the Higgs mass, almost no dependence of Fisher over mass is
2546 observed in the ggH process. Similarly, for all the other signal and background processes no sizable
2547 dependence is expected and no dependence is observed. For the WH and qqZZ cases since enough
2548 MC statistics is available, the template use the same Fisher shape uniformly below $2m_Z$ threshold and
2549 another shape uniformly above threshold, as can be seen in Fig. 160-161. For the ZH signal as well for
2550 the ggZZ background the same Fisher shape, obtained from all the available MC samples, is repeated
2551 uniformly for all the m_{4l} values in the template, as can be seen in Fig. 162-163. In all these processes, the
2552 smoothing procedure is applied, moreover a simple exponential extrapolation is performed in order to
2553 fill the tail of the Fisher distribution. Huge variations of this tiny extrapolated tail has been considered
2554 with no effect on the final results.

2555 The samples with lower available statistics corresponds to ttH (from MC) and Z+4jets (from data CR).
2556 This two contributions are indeed expected to be very small. The Fisher distribution for total available

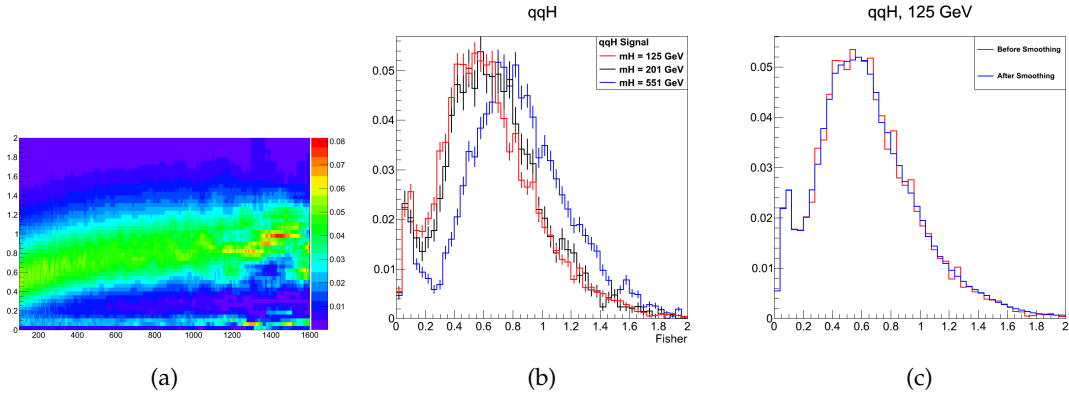


Figure 159: Dijet category in qqH process: Fisher vs m4l template (left), Fisher projection for few mass samples (center: red 125 GeV, blue 200 GeV, blue 550 GeV), comparison of Fisher projection before and after smoothing procedure

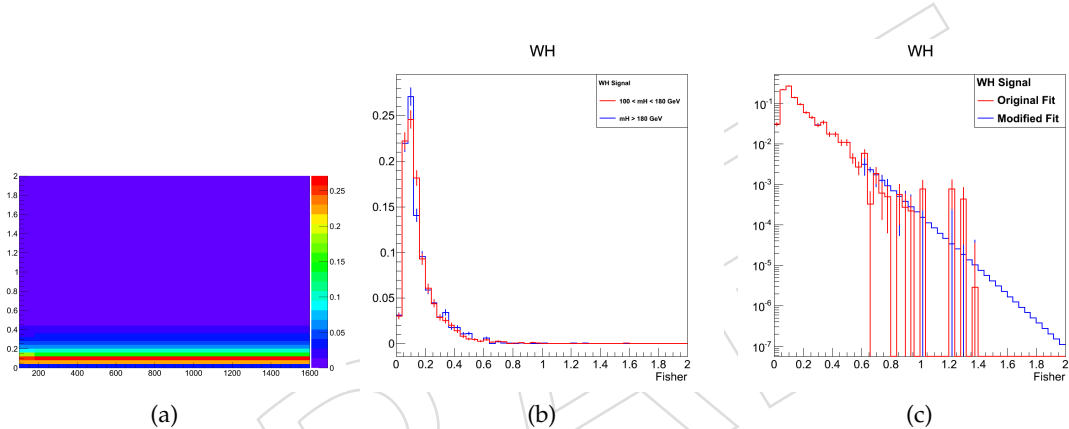


Figure 160: Dijet category in WH process: Fisher vs m4l template (left), Fisher projection below and above $2m_Z$ threshold (center: red 100-180 GeV, blue > 180 GeV), fit to extrapolate the Fisher in the whole phase space (right)

2557 MC statistics is fitted and the shape is used uniformly for all the masses in the template. The results are
2558 shown in Fig. 164-165

2559 In order to calculate the signal and background rates in the dijet and in the untagged category, we
2560 consider the inclusive efficiencies (same as in the inclusive analysis for HCP) and we extract from MC
2561 the ratios of dijet events to total events. This allows us to isolate the leptonic processes in the inclusive
2562 efficiencies from any tagging effects. Plots for the relevant ratios can be seen in Fig. 166- 167. In addition,
2563 crosschecks were done to compare the m4l signal shapes fitted by the dijet and nondijet tagged samples.
2564 As shown in Fig. 168, the shapes are consistent between both samples, so the inclusive fit was used.

The reducible background is estimated by factorizing the VBF selection from the fake rate. The overall yield in the VBF tagged category for the reducible background is given by:

$$N_{Z+X}^{\text{tagged}} = N_{Z+X}^{\text{inclusive}} \times f_{2j}, \quad (44)$$

2565 where $N_{Z+X}^{\text{inclusive}}$ is the number of inclusive reducible background events as selected in the baseline anal-
2566 ysis and f_{2j} is the probability of a 2 jet presence in an enriched background control region that has been
2567 selected to be the $Z + SS$ pair region. The value of f_{2j} is of the order of 1%.

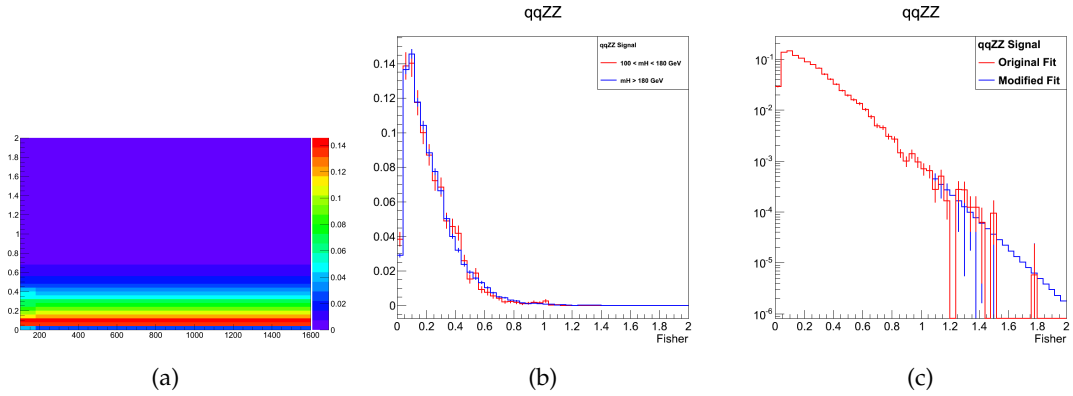


Figure 161: Dijet category in qqZZ process: Fisher vs m_{4l} template (left), Fisher projection below and above $2m_Z$ threshold (center: red $100-180 \text{ GeV}$, blue $>180 \text{ GeV}$), fit to extrapolate the Fisher in the whole phase space (right)

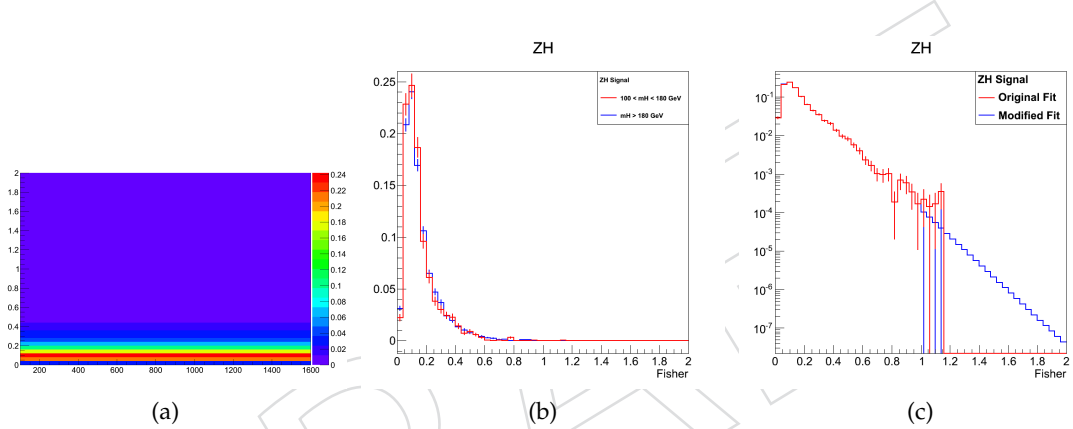


Figure 162: Dijet category in ZH process: Fisher vs m_{4l} template (left), Fisher projection below and above $2m_Z$ threshold (center: red $100-180 \text{ GeV}$, blue $>180 \text{ GeV}$), fit to extrapolate the Fisher in the whole phase space (right)

2568 A.2 Systematic sources on the VBF tag

- 2569 The requirement of 2 jets in the tagged category has implications in the knowledge of the signal and
2570 background contribution in this category.
- 2571 The uncertainty on the VBF normalization and ggH pollution into the dijet category, is, respectively, 10%
2572 and 30%, following the recommendations of the Higgs Cross Section Working Group (HXSWG). The
2573 Fisher shape uncertainty in ggH and VBF needs to be properly computed comparing different Monte
2574 Carlo, this is under study in the HXSWG as well. A similar approach can be considered to compute the
2575 normalization and shape systematics of the ZZ background in the dijet category.
- 2576 The largest experimental systematics on the Fisher shape is due to the Jet Energy Scale (JES). The JES has
2577 been changed by $\pm 1\sigma$ following the prescription of the JETMET group. As expected, there is no effect
2578 on the $\Delta\eta(jj)$ variable, while the effect on the $M(jj)$ and Fisher distributions can be seen in Fig. 169 and
2579 it is included as systematics.

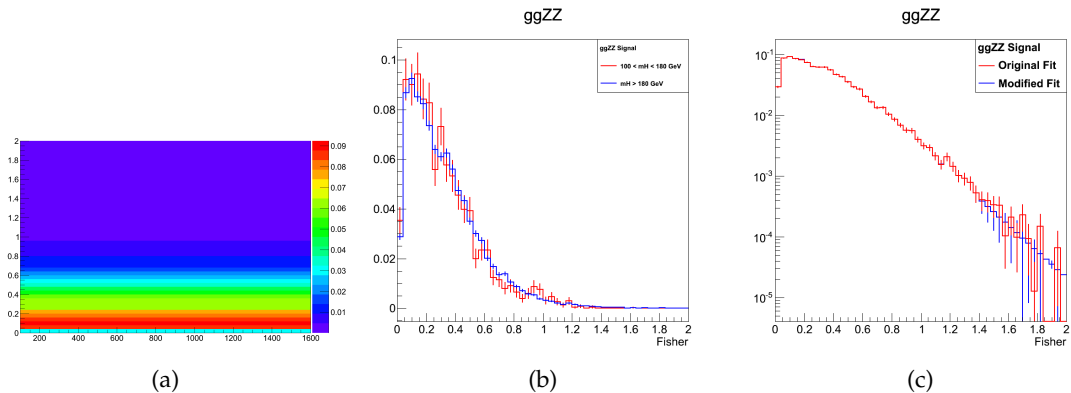


Figure 163: Dijet category in ggZZ process: Fisher vs m_{4l} template (left), Fisher projection below and above $2m_Z$ threshold (center: red $100-180$ GeV, blue >180 GeV), fit to extrapolate the Fisher in the whole phase space (right)

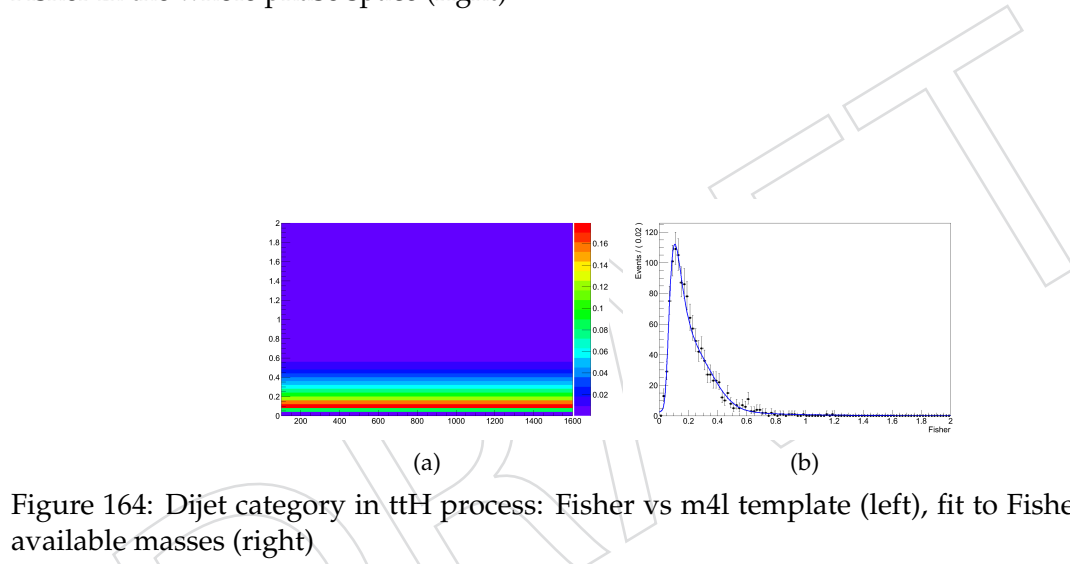


Figure 164: Dijet category in ttH process: Fisher vs m_{4l} template (left), fit to Fisher for all the available masses (right)

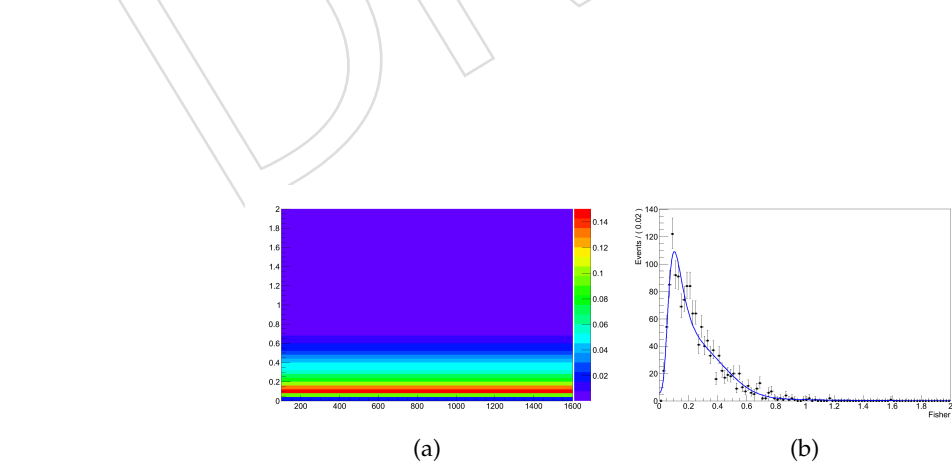


Figure 165: Dijet category in Z+X process: Fisher vs m_{4l} template (left), fit to Fisher from control regions (right)

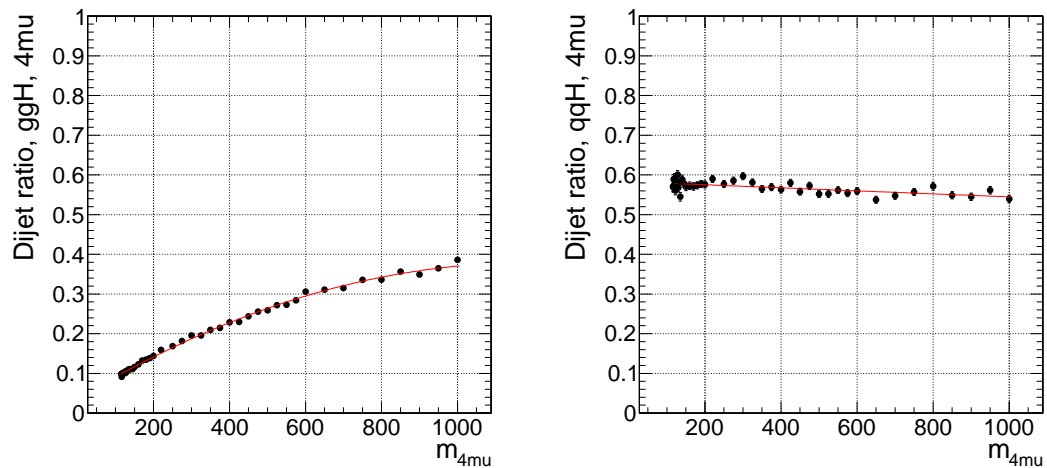


Figure 166: Ratio of dijet tagged to total events at 8 TeV for 4mu final state as functions of $m_{4\ell}$ for ggH (left) and qqH (right)

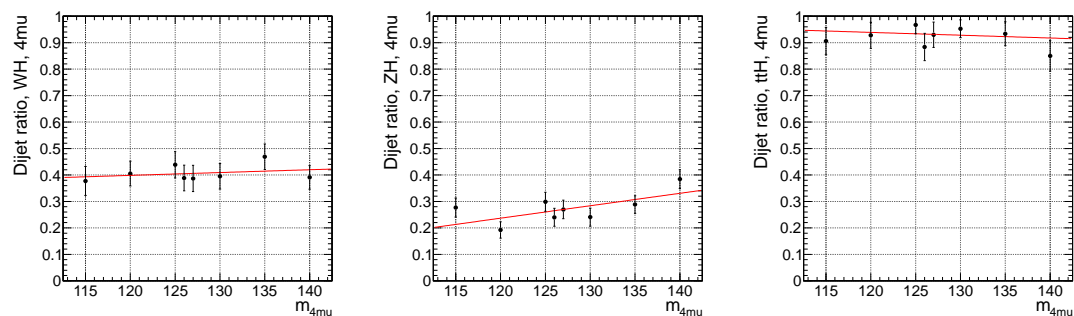


Figure 167: Ratio of dijet tagged to total events at 8 TeV for 4mu final state as functions of $m_{4\ell}$ for WH (left) and ZH (center) and ttH (right)

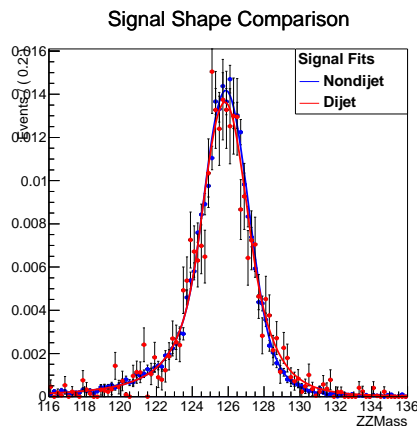


Figure 168: Comparison of MZZ shape in MC and corresponding fits for the Dijet and Non-dijet tagged events for a 126 GeV ggH sample

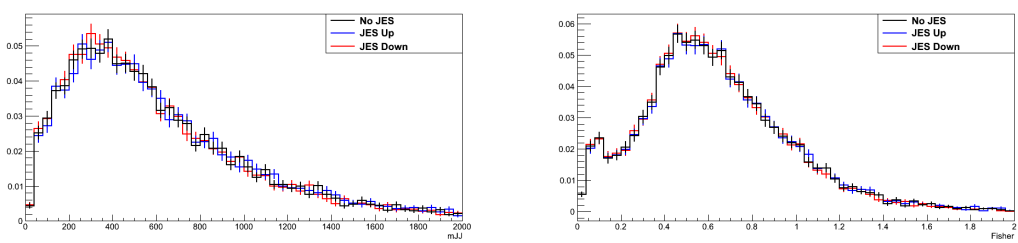


Figure 169: Jet Energy Scale systematics in $M(jj)$ (left) and Fisher (right) distributions

2580 A.3 $p_{\text{T},4\ell}/m_{4\ell}$ description for untagged VBF events - 126 GeV

Distributions of $p_{\text{T},4\ell}/m_{4\ell}$ after selection are obtained from MC events. Spectra are fitted with a Tsallis function (used to model FONLL results for heavy-flavors, see e.g. [86]):

$$\mathcal{T}(x = p_{\text{T},4\ell}/m_{4\ell}) \propto x^{n_1} e^{-bx} \left(1 + \frac{\sqrt{x^2 + m^2} - m}{n_2 T}\right)^{-n_2} \quad (45)$$

2581 summed to an exponential function, in order to smooth effect coming from large and/or negative
2582 weights.

2583 For VBF Higgs and ZZ non-resonant production the description provided by the default MC (POWHEG)
2584 is considered as default.

2585 For reducible background the $p_{\text{T},4\ell}/m_{4\ell}$ distribution is obtained from the application of fake rates to
2586 control regions as explained in Sec. 9.1.2.

2587 For gg production the default (POWHEG) description is known to be suboptimal with respect to the
2588 new implementation in the `HRes` 1.0 generator [87] that includes fixed-order NNLO effects but also
2589 (most importantly) performs a resummation of the logarithmic terms (large at low p_{T}) at the NNL order.
2590 Reconstructed $p_{\text{T},4\ell}$ spectra are therefore reweighted based on the value of the generated $p_{\text{T},4\ell}$ value.
2591 `HRes` spectra are obtained from running the generator with default parameters. A second reweighting
2592 is applied considering finite top-quark mass effects, which are not included in the `HRes` calculation,
2593 leading to not-so-reliable p_{T} spectra for $p_{\text{T},4\ell} \geq m_t$. With POWHEG we determine the spectrum difference
2594 between using this approximation and the full calculation using finite quark masses, and apply it
2595 to NNLO spectrum.

2596 The result of fits to the 8 components considered here is shown in Fig. 170 and Fig. 171 for a Higgs of
2597 mass 126 GeV at 8 TeV; Fig. 172 shows corresponding fits to the gg and ZZ non-resonant components, to
2598 show the small difference between the two c.o.m. energies. $t\bar{t}$ H component is missing because basically
2599 all events have a signature with two or more jets: for those we assign $p_{\text{T},4\ell}/m_{4\ell}$ shape equal to the VBF
2600 category and a normalization uncertainty of 100%.

2601 To have a qualitative estimate of the discrimination power of this variable ROC curves are obtained
2602 from the signal MC distributions of $p_{\text{T},4\ell}$, by simply applying a lower cut on this variable. They are
2603 shown in Fig. 173. It is remarkable to notice that the use of $p_{\text{T},4\ell}/m_{4\ell}$ compensates the relatively low
2604 VBF efficiency of the tagging technique (left) and is not degraded when applied only to the not-tagged
2605 category (right).

2606 Analytical distributions of $p_{\text{T},4\ell}/m_{4\ell}$ are used to build 2D templates vs. the $m_{4\ell}$ variable, exactly like the
2607 Fisher discriminant case. In a restricted region around 126 GeV, the choice of the $p_{\text{T},4\ell}/m_{4\ell}$ variable re-
2608 sults in no correlation with $m_{4\ell}$, for all samples within statistical uncertainties. This is shown in Fig. 174.
2609 Templates are therefore made of a constant function over the narrow $m_{4\ell}$ range.

2610 A.4 $p_{\text{T},4\ell}/m_{4\ell}$ description for untagged VBF events - full mass range

2611 For the full mass range, the non-correlation assumption is not valid anymore. The 2D templates are
2612 therefore built in the following way:

- 2613 • $p_{\text{T},4\ell}/m_{4\ell}$ distributions are fitted for some (8-12) benchmark mass points, spanning from low
2614 to high masses (Fig. 175 shows an example for $q\bar{q} \rightarrow ZZ$), varying the smallest possible num-
2615 ber of Tsallis parameter that still allows to obtain good fit χ^2 's.
- 2616 • Tsallis parameters obtained from these fits are at their time fitted as a function of $m_{4\ell}$, using
2617 simple polynomials. Non-derivativity of the fitting functions is allowed at the point $m_{4\ell}=$
2618 $2m_Z$, to consider the different kinematics present in the process where both Z's become real
2619 (Fig. 176 shows an example for $q\bar{q} \rightarrow ZZ$).
- 2620 • 2D templates are built varying the fitted Tsallis parameters from the above step over the full
2621 mass range (Fig. 177 shows an example for $q\bar{q} \rightarrow ZZ$).

2622 **A.5 Systematic sources on $p_{T,4\ell}/m_{4\ell}$ description**

2623 In addition to the limited size of the MC templates, the following systematic uncertainties are considered
 2624 on $p_{T,4\ell}$ shapes. For each source new sets of Tsallis parameters are provided per each source.

2625 For $gg \rightarrow H$ signal we include:

- 2626 • **Uncertainty on the resummation scale.** HRes is re-run using three different values of the re-
 2627 summation scale, and results are compared between the default value ($\mu_Q = m_H/2$) and two
 2628 alternative ones ($\mu_Q = m_H$ and $\mu_Q = m_H/4$). Other scales in the calculation (factorization,
 2629 renormalization) are varied fractionally by the same amount, following the recipe in [87]. The
 2630 result is shown in Fig. 178, left.
- 2631 • **Uncertainty on the infinite top-mass approximation.** HRes applies strictly the infinite top-
 2632 mass approximation. With POWHEG we verified the spectrum difference between using
 2633 this approximation and the full calculation using finite quark masses, and this is used as a
 2634 conservative systematic uncertainty. The result is shown in Fig. 178, right.

2635 In VBF H signal the shape uncertainty at high $p_{T,4\ell}$ does not suffer from resummation effects at NLO,
 2636 due to the low amount of QCG radiation, so we can use the standard theoretical uncertainties used in
 2637 these calculations:

- 2638 • **PDF variations.** We consider the spectrum difference at generator level between the sets of
 2639 PDFs: CT10 (default), NNPDF2.1 and MSTW2008. This is applied as weight to the selected
 2640 samples and the systematics is estimated from the maximum difference in the resulting spec-
 2641 tra, as shown in Fig. 179, left.
- 2642 • **Renormalization and factorization scale variations.** We consider the spectrum difference at
 2643 generator level between the sets of renormalization and factorization scale suggested in [88].
 2644 This is applied as weight to the selected samples and the systematics is estimated from the
 2645 maximum difference in the resulting spectra, as shown in Fig. 179, right.

2646 VH signal shapes are not easily available at NLO with present MC generators. Therefore we rely on LO
 2647 spectra by Pythia and, due to the similarity of the spectrum with the VBF case (Figure 155 bottom), we
 2648 also apply the same uncertainties.

2649 For background we include:

- 2650 • **Statistical uncertainty on amount of reducible background.** The shape of $Z+X$ background
 2651 is determined from control regions and the uncertainty on the fit of the $p_{T,4\ell}/m_{4\ell}$ shape due
 2652 to the limited statistics is considered as systematics
- 2653 • **Shape of ZZ at high p_T .** The procedure is identical to the one used in VBF signal for PDF and
 2654 scale variations (Bin migration effect: 0.8-1.8%).
- 2655 • **Shape of ZZ at low p_T .** For this complete calculation of resummation effects are not available.
 2656 Therefore we use control samples in data from single-Z production [89]. The spectra for these
 2657 data samples are shown in Fig. 180 and compared to POWHEG MC. The data/MC difference
 2658 is fit with a linear function and this difference is used to reweight the POWHEG spectrum to
 2659 obtain a systematic uncertainty. In order to confirm this effect at a mass larger than the Z , the
 2660 effect is found to be of the same shape at higher ZZ mass, in the non-blinded region [140, 300]
 2661 GeV.

2662 In addition, a common systematics to all samples comes from the fact that not for all $p_{T,4\ell}/m_{4\ell}$ is totally
 2663 uncorrelated with KD: a small correlation is present in some (Fig. 181). Since the 3D fit model used
 2664 assumes factorization between KD and $p_{T,4\ell}/m_{4\ell}, m_{4\ell}$ probabilities, an additional systematics is con-
 2665 sidered making fits only to evens in the extreme KD regions ($KD < 0.2$ and $KD > 0.8$) and using the
 2666 alternative PDFs found as “up” and “down” systematic variations.

2667 **A.5.1 Vector boson cross section fit: method**

For the measurement of the VBF fraction the signal model is redefined by replacing the signal strength by two parameters of interest:

$$L_s = \mu_F(\mathcal{L}(ggH) + \mathcal{L}(ttH)) + \mu_V(\mathcal{L}(qqH) + \mathcal{L}(VH)) \quad (46)$$

Instead of the cross sections themselves, scale factors μ_V, μ_F are applied defining the deviations of the cross sections from the SM values. The new model has two parameters of interest corresponding to μ_F, μ_V . To extract the two parameters, the events are split into the tag and non-tagged category. In the non tagged category a 3D model is used utilizing the mass ($m_{4\ell}$), the kinematic discriminant and the momentum p_T of the four-lepton system. The model is defined as following:

$$\mathcal{L}_{\text{untagged}} = \mathcal{L}(m_{4\ell}) \times \mathcal{L}(K_D|m_{4\ell}) \times \mathcal{L}(p_T/m_{4\ell}|m_{4\ell}) \quad (47)$$

2668 This model neglects correlations between the transverse momentum and the kinematic discriminant.
 2669 Since a small correlation is visible, the difference is assigned as a systematic on the transverse momentum over mass shape.
 2670

In the tagged category a 3D model is used exploiting the ($m_{4\ell}$), the kinematic discriminant and the Fisher discriminant.

$$\mathcal{L}_{\text{tagged}} = \mathcal{L}(m_{4\ell}) \times \mathcal{L}(K_D|m_{4\ell}) \times \mathcal{L}(V_D|m_{4\ell}) \quad (48)$$

2671 The two categories are fitted simultaneously. The systematics uncertainties are introduced as nuisance
 2672 parameters while shape morphing is implemented for systematics affecting the shapes.

2673 **A.6 Results**

2674 The number of expected and observed dijet and not-dijet events is shown in Tab. 36.

	$N_{\text{jets}} < 2$ ($5+12fb^{-1}$)	$N_{\text{jets}} > 1$ ($5+12fb^{-1}$)	$N_{\text{jets}} < 2$ ($5+20fb^{-1}$)	$N_{\text{jets}} > 1$ ($5+20fb^{-1}$)
ggH	11.30	1.38	16.68	2.03
qqH	0.43	0.60	0.63	0.88
WH	0.27	0.17	0.39	0.26
ZH	0.19	0.06	0.28	0.09
ttH	0.00	0.08	0.01	0.12
qqZZ	17.02	0.57	24.86	0.85
ggZZ	0.31	0.02	0.45	0.03
Z+X	5.19	0.05	7.54	0.08

Table 35: Number of expected events with $5 fb^{-1}$ at 7 TeV and $12(20) fb^{-1}$ at 8 TeV in the two categories: dijet tagged and untagged events in the mass range $106 < m_{4\ell} < 141$ GeV.

2675 **A.6.1 P-value scan with the HCP dataset.**

2676 The full analysis has been performed and the results shown in Fig. 182 has been obtained. The expected
 2677 (observed) significance of the signal at 126 GeV is 5.9 (4.9) σ in the fit with VBF approach, and 5.0 (4.5)
 2678 σ without the VBF approach. The in observed data no golden VBF events with two jets are observed,
 2679 which leads to less than average expected increase in observed p-value. Nonetheless, significance of
 2680 observed signal is increased due to additional information in the fit, such as p_T of the Higgs boson
 2681 candidate. In Fig. 183 projections on the observables for the tagged and untagged events are shown.

2682 **A.6.2 Vector boson cross section results**

2683 A 2D likelihood scan is performed on the model assuming the HCP dataset luminosity. A preliminary
 2684 result showing a fast likelihood scan (without profiling the nuisances) and utilizing a PseudoAsimov

	7TeV Untagged	7TeV Tagged	8TeV Untagged	8TeV Tagged
ggH:	2.897264	0.3685498	8.42143	1.000691
qqH:	0.1196839	0.1425773	0.320932	0.4457455
ttH:	0.000699938	0.01755223	0.003967388	0.0581785
WH:	0.0759964	0.04476066	0.1990172	0.1325907
ZH:	0.0539274	0.01270992	0.1386818	0.04922273
observation	7	0	23	2
qqZZ:	4.7513	0.1186	12.2825	0.1186
ggZZ:	0.0784	0.0052	0.1896	0.0052
ZX:	1.5054	0.0131	3.6811	0.0131

Table 36: Number of expected and observed events for 5 fb^{-1} at 7 TeV and $12(20) \text{ fb}^{-1}$ at 8 TeV separately in the two categories: dijet tagged and untagged events in the mass range $106 < m_{4\ell} < 141 \text{ GeV}$.

2685 dataset of 200 events is shown in Fig. 184. The new VBF/VH discrimination capabilities provide large
 2686 constraint in the 2D space. If the fermion induced production is profiled out the expected measured
 2687 vector boson to fermion fraction is expected to be 0.12 ± 0.24 .

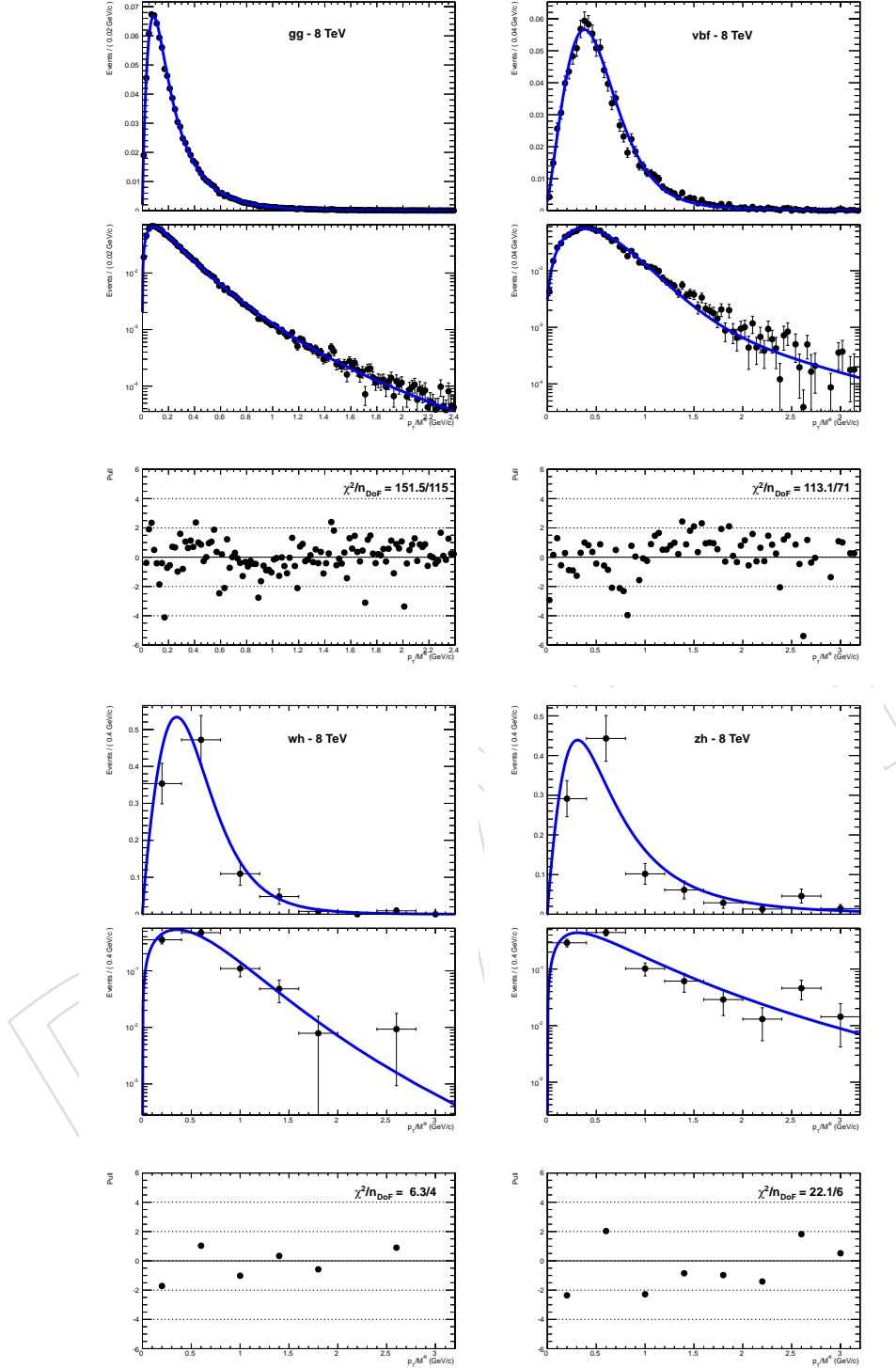


Figure 170: Fit to the $p_{T,4\ell} / m_{4\ell}$ distribution after selection for $gg \rightarrow H$ signal at 126 GeV (left top), VBF (right top), WH (left bottom), and ZH (right bottom) signals at the same mass at a center-of-mass energy of 8 TeV. The functions used are Tsallis plus exponential (see text) for all signals. The upper panels show fit results, in linear and log scales, while the lower panel is the fit pull ($(\text{data}-\text{PDF})/\sigma_{\text{data}}$).

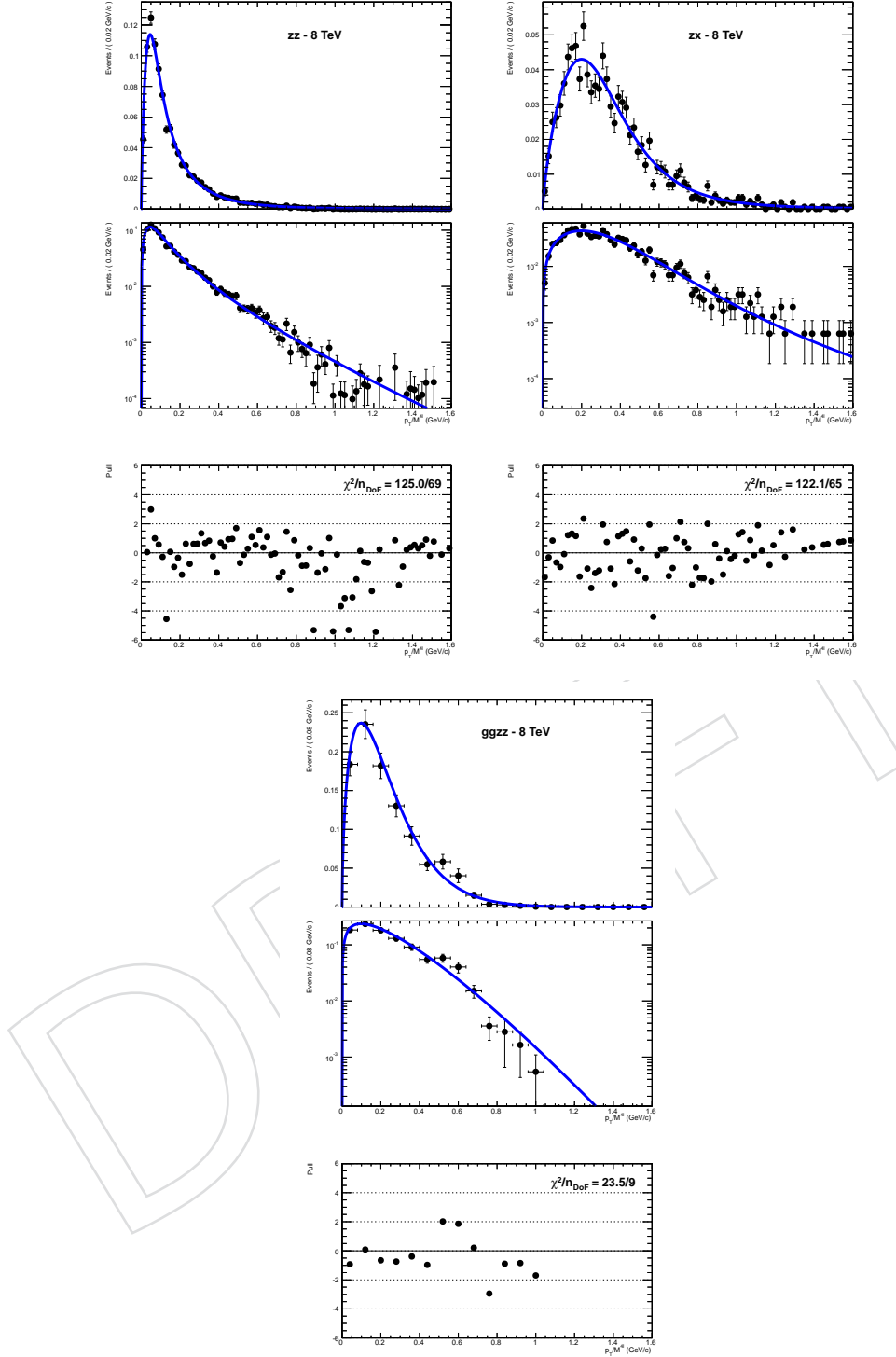


Figure 171: Fit to the $p_{T,4\ell}/m_{4\ell}$ distribution after selection for $q\bar{q} \rightarrow ZZ$ background MC in the region [106, 141] GeV (left top) and reducible background extrapolated in the region [106, 141] GeV (right top), and $gg \rightarrow ZZ$ background MC in the region [106, 141] GeV (bottom) at a center-of-mass energy of 8 TeV. The functions used are Tsallis plus exponential (see text) for all and a simple Tsallis for ZZ background. The upper panels show fit results, in linear and log scales, while the lower panel is the fit pull ((data-PDF)/ σ_{data}).

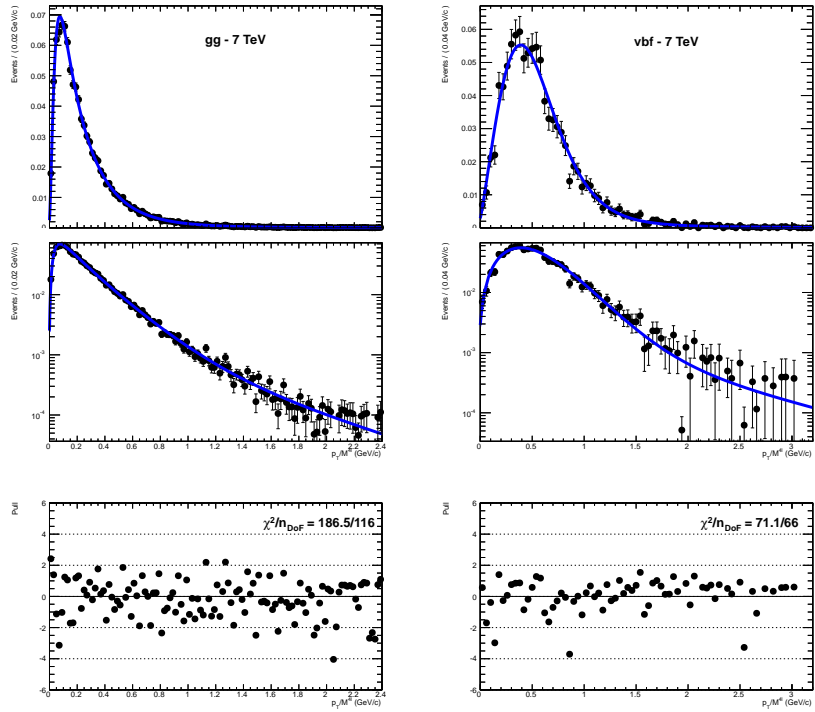


Figure 172: Fit to the $p_{T,4\ell}/m_{4\ell}$ distribution after selection for $gg \rightarrow H$ signal at 126 GeV (left) and VBF signal (right) at a center-of-mass energy of 7 TeV. Conventions are the same as Fig. 170.

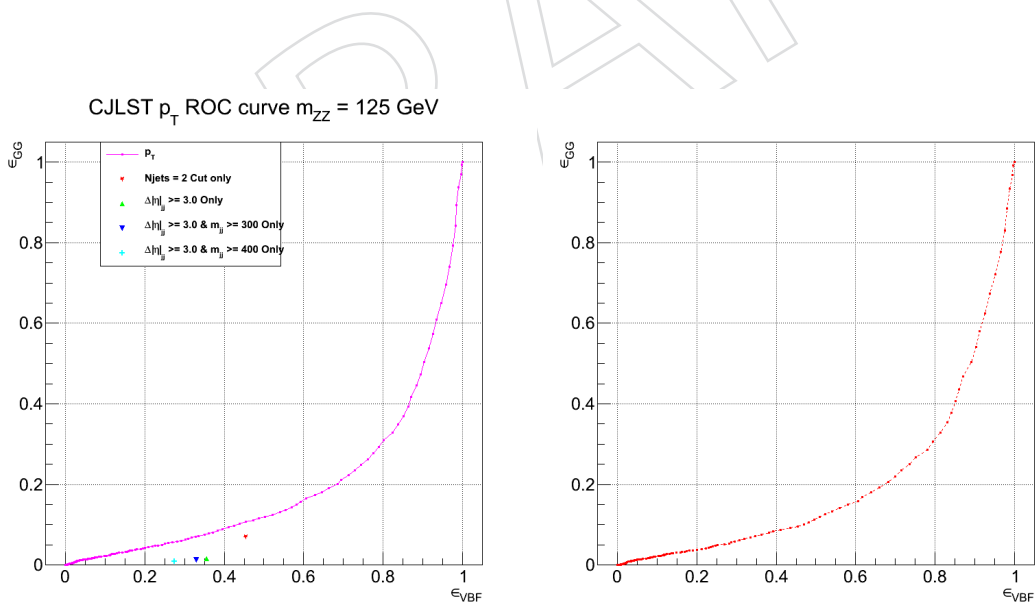


Figure 173: $gg \rightarrow H$ vs. VBF signal efficiency (ROC curve) for a lower cut on $p_{T,4\ell}$, at 126 GeV. In the left figure, working points for some baseline tagging selections (explained in Section A.1) are compared to the $p_{T,4\ell}$ discrimination power. In the right figure, the curve is shown only for events failing tagging selections.

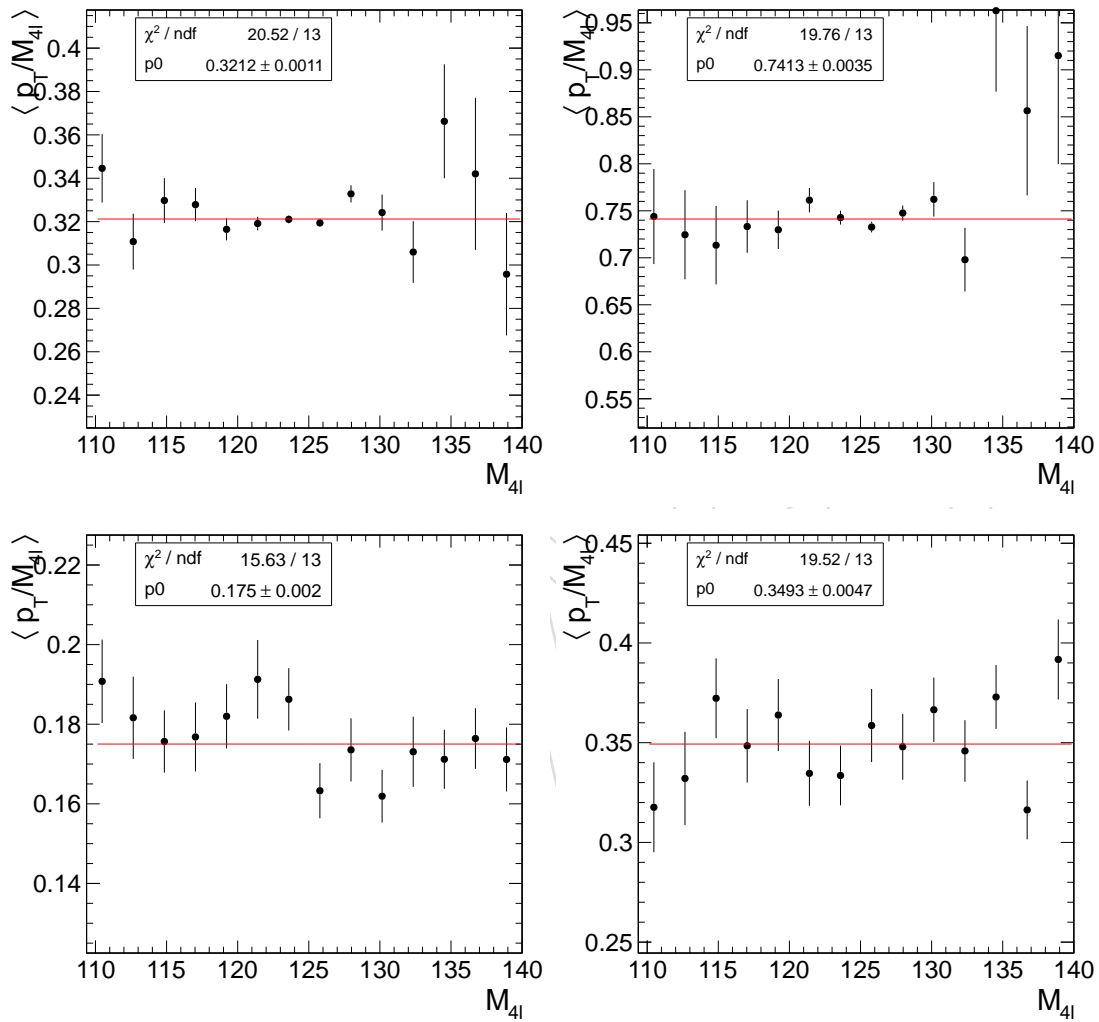


Figure 174: Profile plots of $p_{T,4\ell}/m_{4\ell}$ vs. $m_{4\ell}$, showing absence of correlation between the two variables. Shown are the main contributions to the 4ℓ yield in data: gg (top left), VBF (top right), $q\bar{q} \rightarrow ZZ$ (bottom left) and $Z+X$ (bottom right).

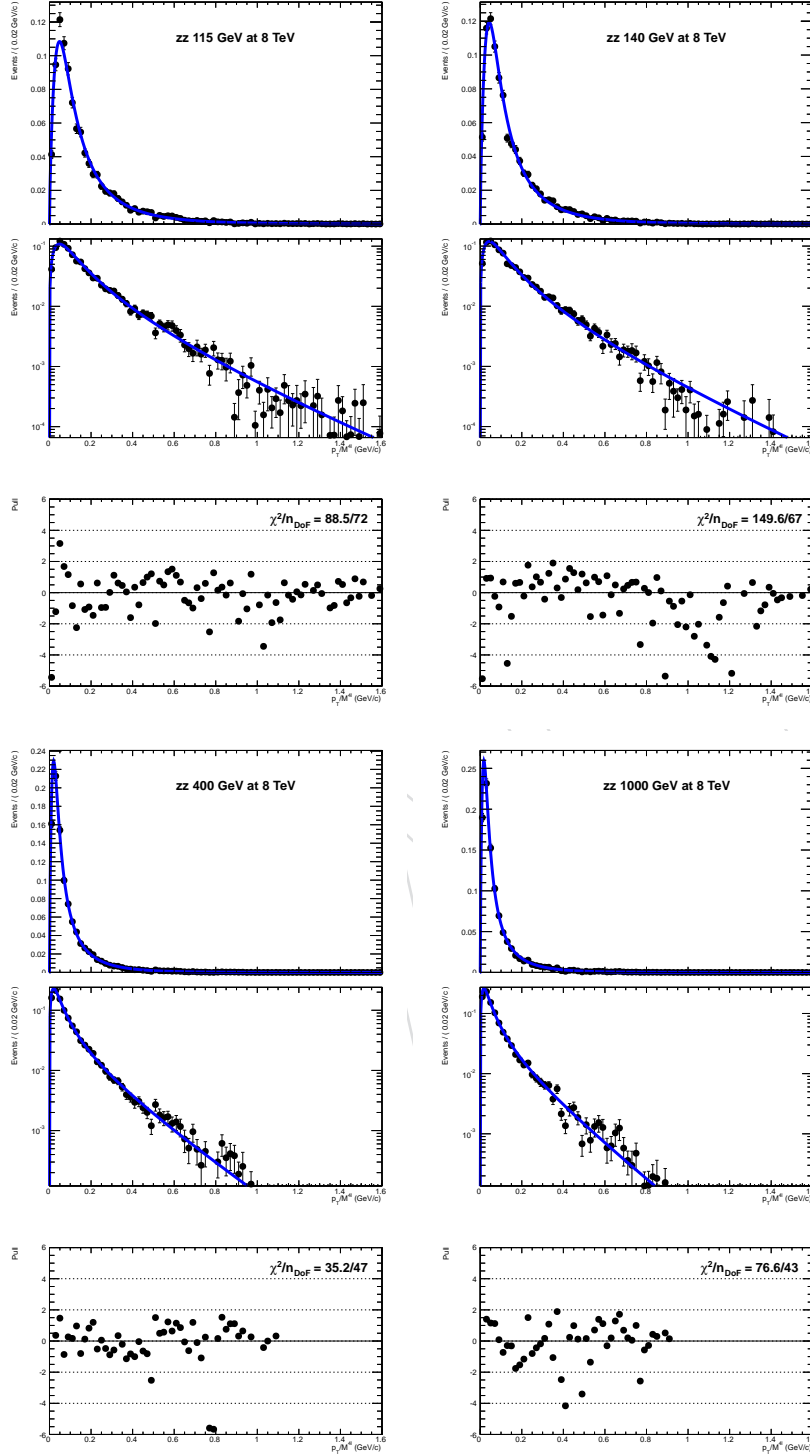


Figure 175: Fit to the $p_{T,4\ell}/m_{4\ell}$ distribution after selection for $q\bar{q} \rightarrow ZZ$ in a mass window around 115 GeV (top left), 140 GeV (top right), 400 GeV (bottom left) and 1 TeV (bottom right) at a center-of-mass energy of 8 TeV. The functions used are Tsallis plus exponential (see text) for all signals. The upper panels show fit results, in linear and log scales, while the lower panel is the fit pull ((data-PDF)/ σ_{data}).

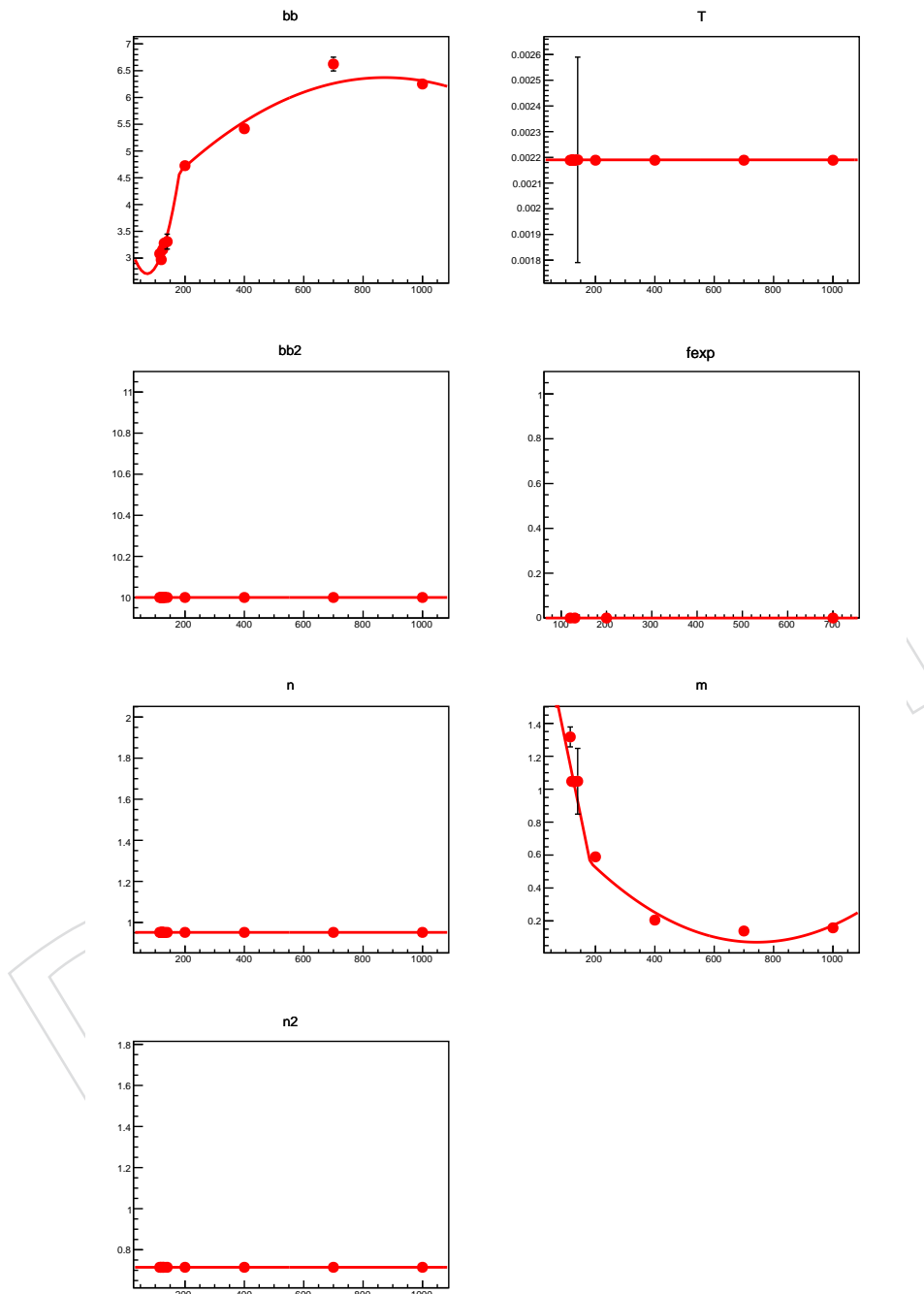


Figure 176: Split-polynomial fits of Tsallis parameters for $q\bar{q} \rightarrow ZZ$ at a center-of-mass energy of 8 TeV. Flat lines correspond to parameters that do not vary from mass point to mass point. The splitting point corresponds to $m_{4\ell} = 2m_Z$.

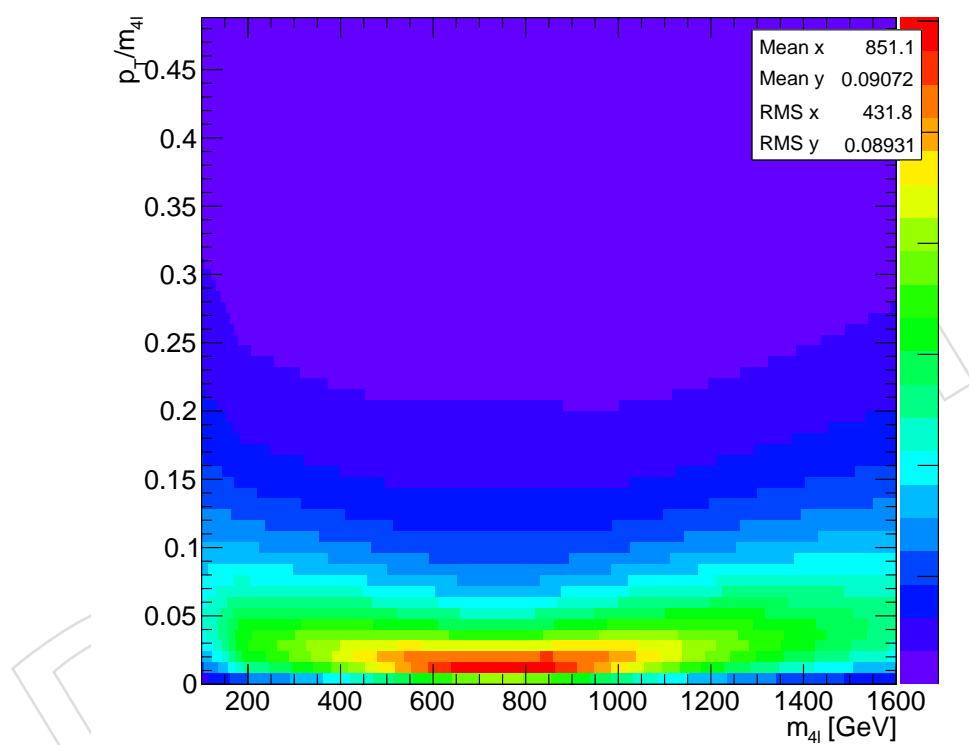


Figure 177: 2D template in the full mass range for $q\bar{q} \rightarrow ZZ$ at a center-of-mass energy of 8 TeV.

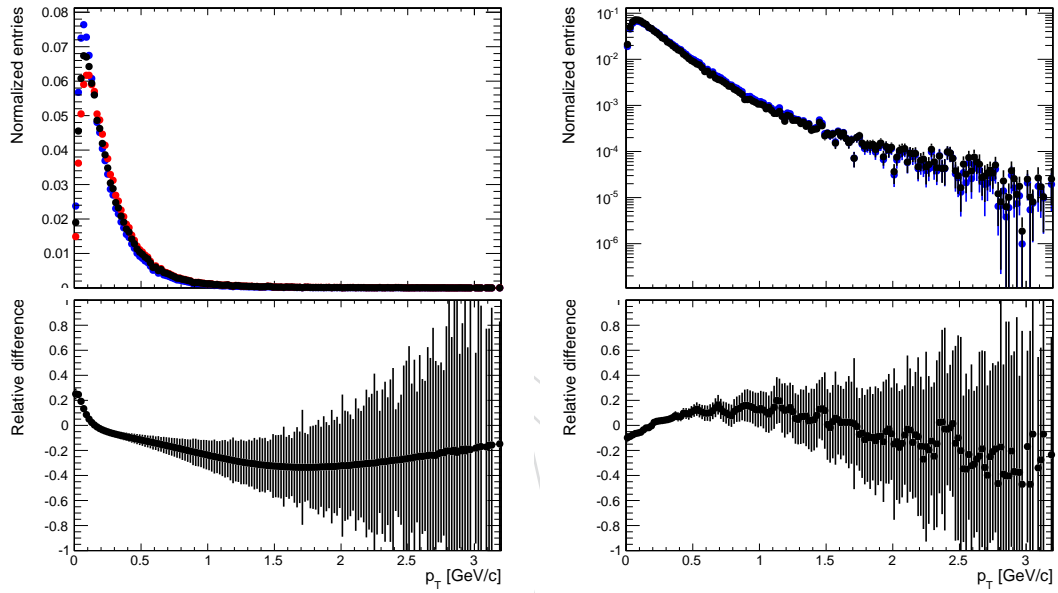


Figure 178: Left: Comparison of the $p_{T,4\ell}$ spectra for $gg \rightarrow H$ signal with H_{Res} reweighting and different resummation scales: $\mu_Q = m_H/2$, i.e. the default (black), $\mu_Q = m_H$ (red) and $\mu_Q = m_H/4$ (blue). The relative difference between the black and red histograms is shown in the lower panel. Right: Comparison of the $p_{T,4\ell}$ spectra for $gg \rightarrow H$ signal with POWHEG implementing finite heavy-quark mass corrections (black), and not implementing them (blue). The relative difference is shown in the lower panel.

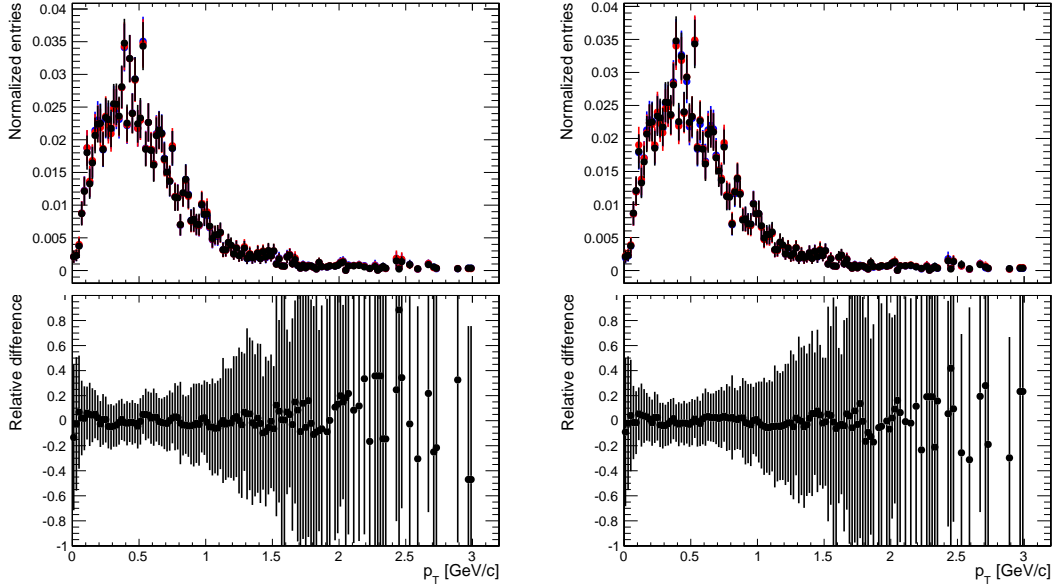


Figure 179: Left: Comparison of the $p_{T,4\ell}$ spectra for VBF H signal with CT10 PDFs, i.e. the default (black), NNPDF (red) and MSTW (blue). The maximum difference per bin between the black and blue/red histograms, is shown in the lower panel. Right: Comparison of the $p_{T,4\ell}$ spectra for VBF H signal with default factorization and renormalization scales ($\mu_F = \mu_H = \mu$) (black), $\mu_F = \mu_H = \mu/2$ (red) and $\mu_F = \mu_H = 2\mu$ (blue). The maximum difference per bin between the black, the blue/red histograms, and 4 other cases (see [88]) is shown in the lower panel.

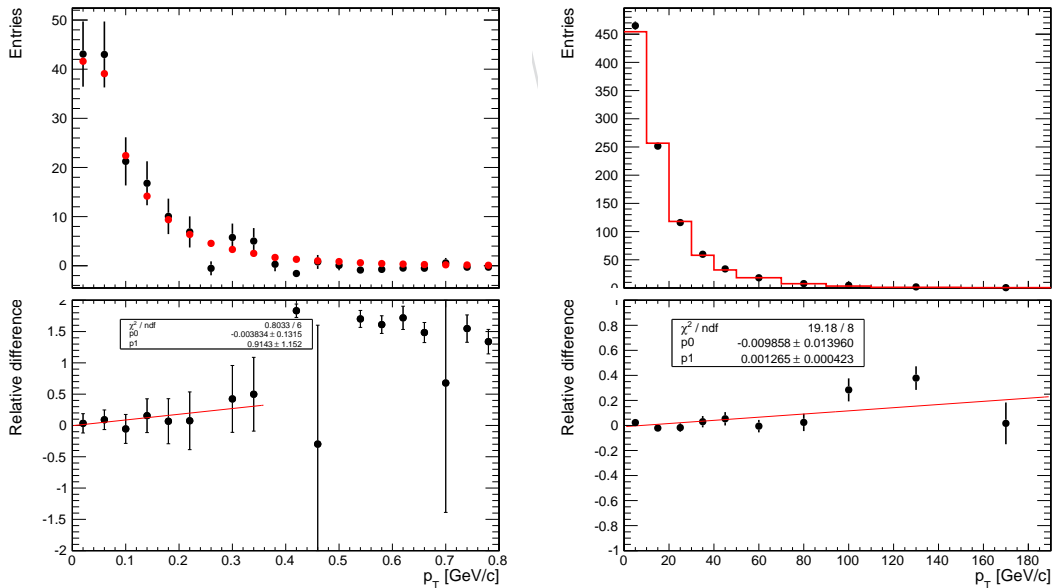


Figure 180: Data to POWHEG comparison for data in the non-blinded region of this analysis (left) and the Z-production analysis at 7 TeV (right) [89]. The lower panels show the relative data/MC discrepancy, with the linear fit described in the text.

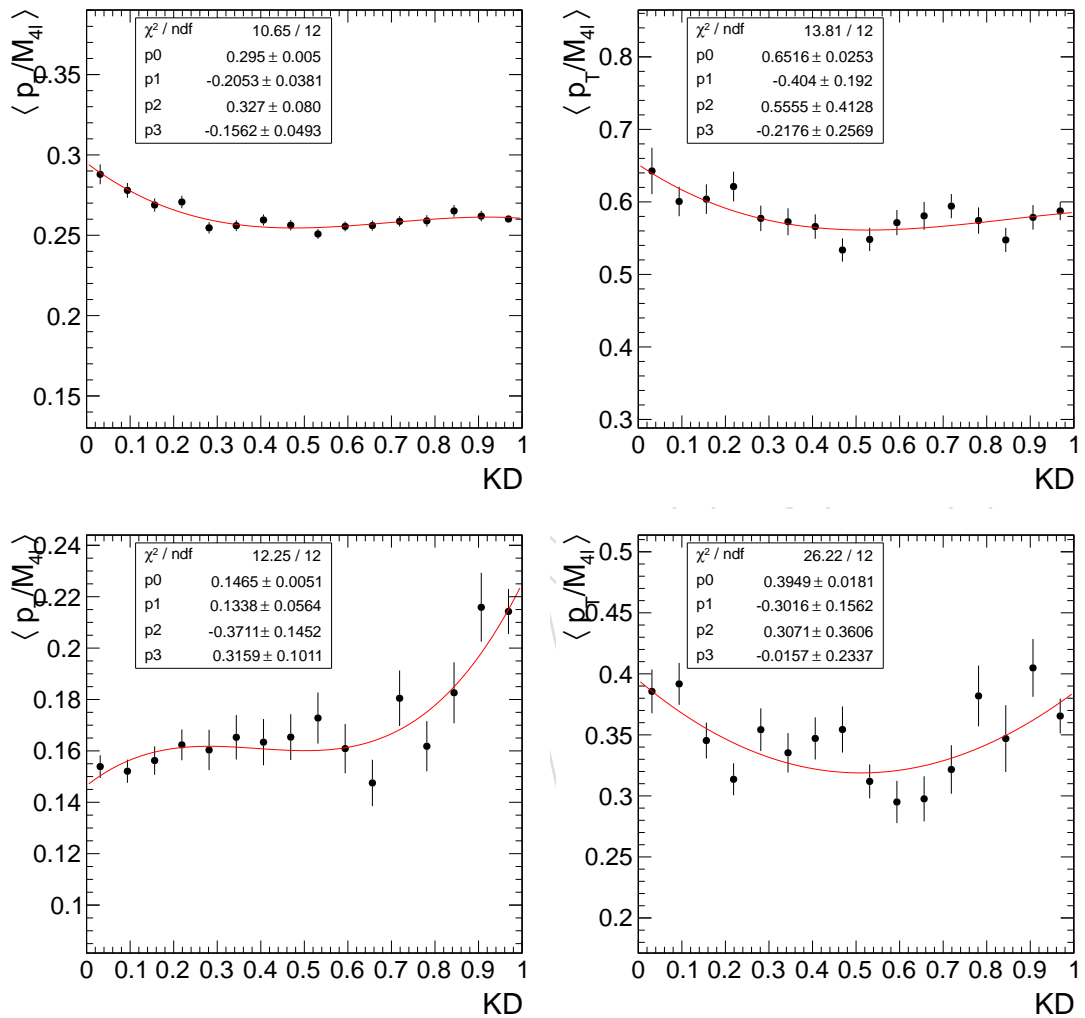


Figure 181: Profile plots of $p_{T,4\ell}/m_{4\ell}$ vs. KD, showing small correlations between the two variables in some samples. Shown are the main contributions to the 4ℓ yield in data: gg (top left), VBF (top right), $q\bar{q} \rightarrow ZZ$ (bottom left) and Z+X (bottom right).

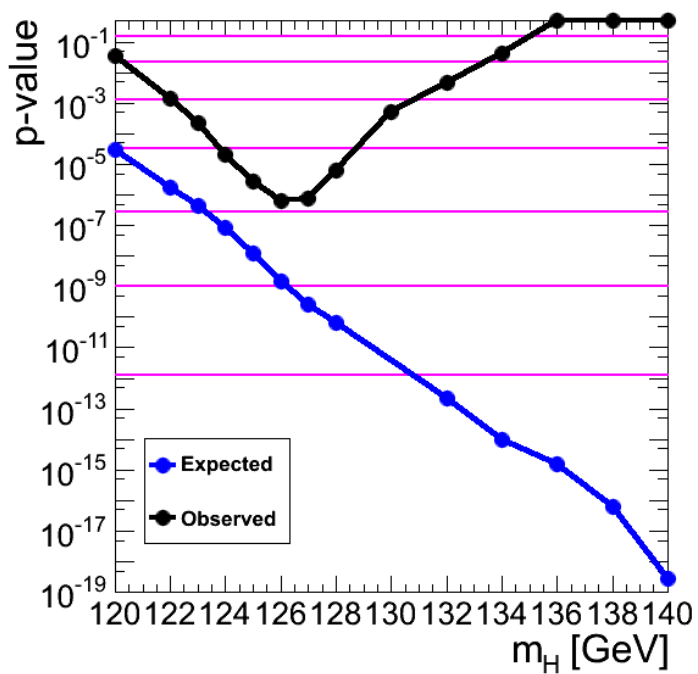


Figure 182: The scan of p-values as a function of mass using the VBF approach with the HCP dataset.

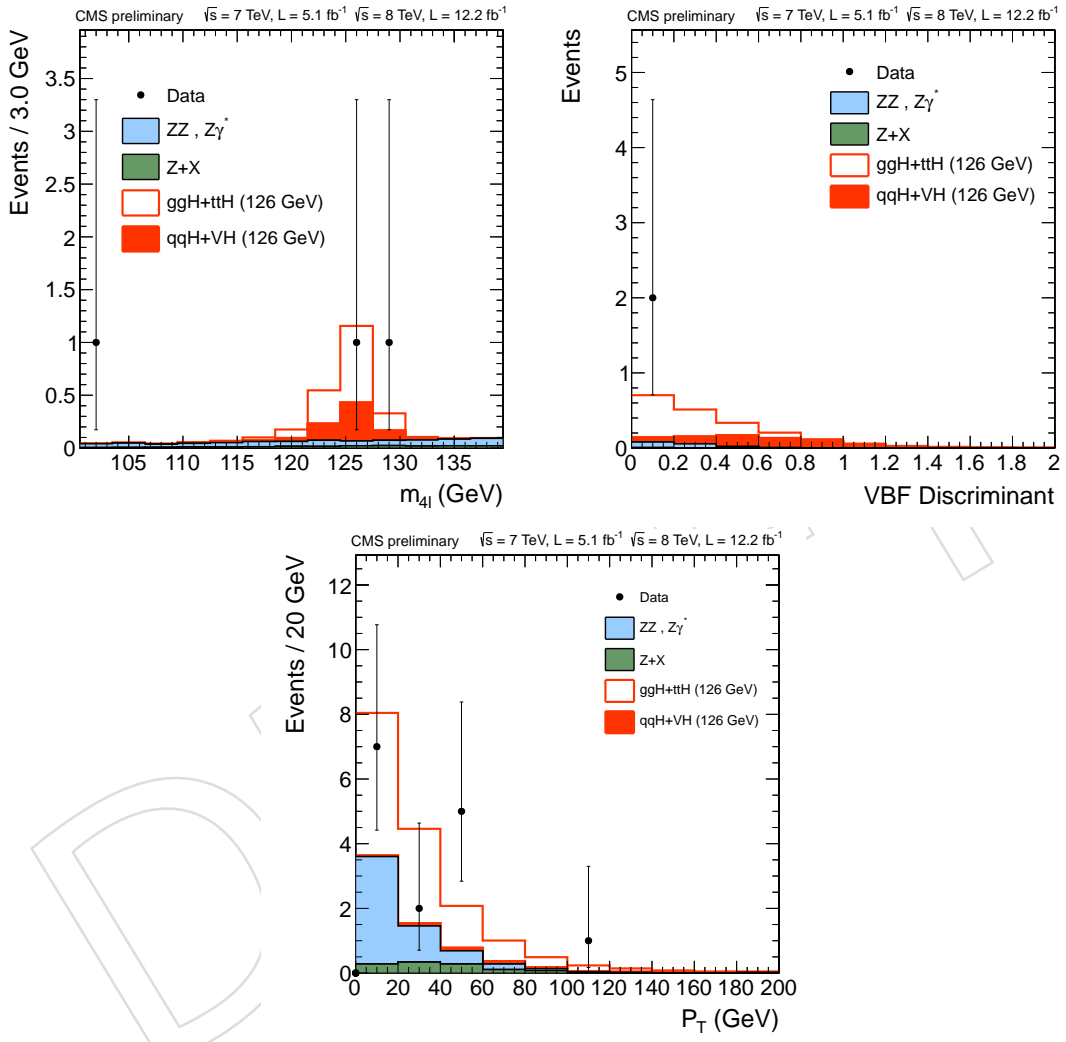


Figure 183: Distribution of $m_{4\ell}$ (top-left) and Fisher (top-right) in the tagged category, and p_T in the untagged category (bottom). The mass range $121.5 < m_{4\ell} < 130.5$ GeV is used for the Fisher and p_T plots.

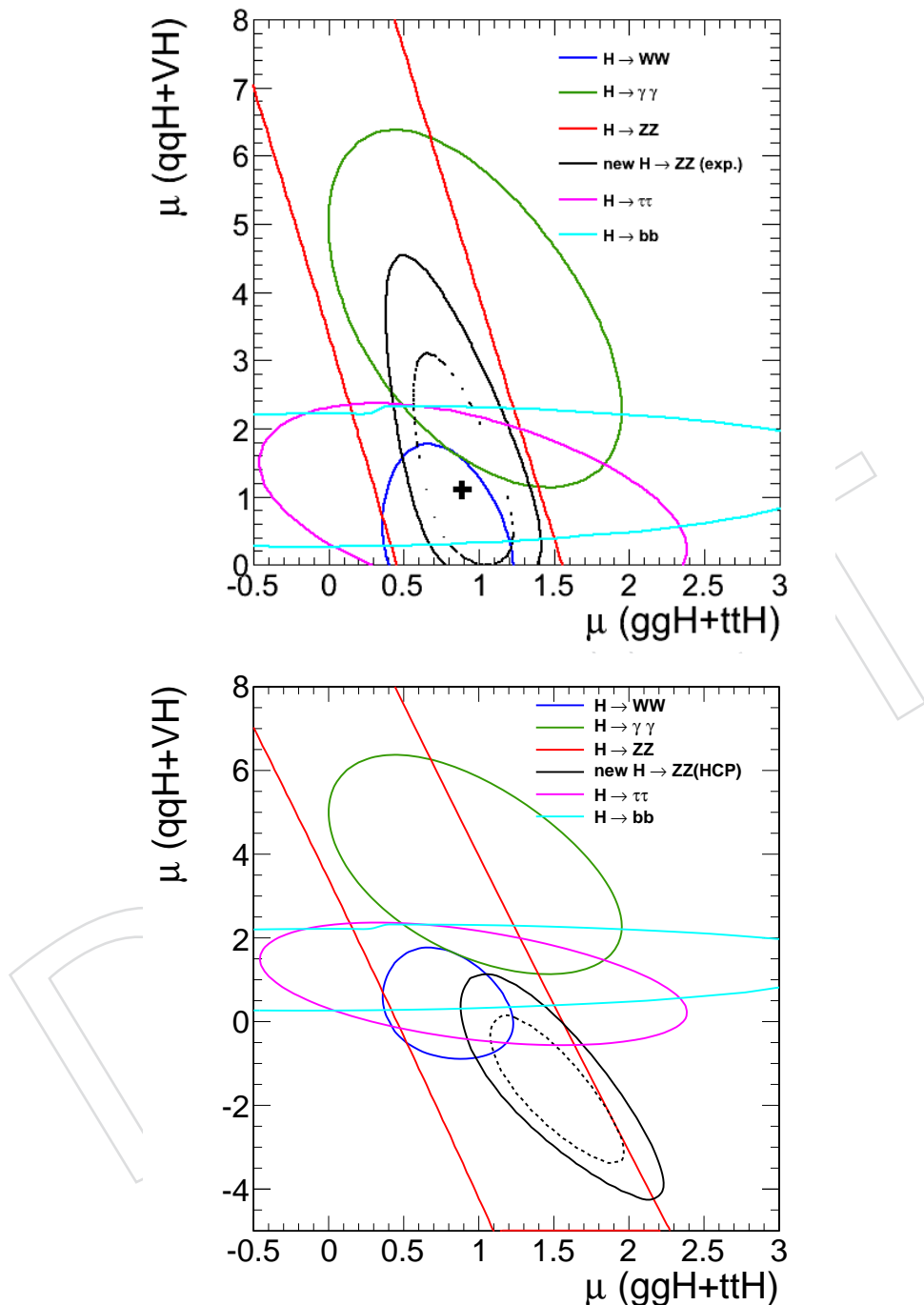


Figure 184: Likelihood scan of disentangling the production mechanisms. Observed results for channels other than ZZ are shown with HCP dataset. The ZZ result is shown as expected (top) and observed (bottom). The 68% CL contours are shown for a 2D parameter estimation (solid line) and the standard error ellipse (dashed line).

2688 B Appendix #2 Control of lepton efficiencies from data, tables

DRAFT

2689 **C Appendix #3 Control of lepton efficiencies from data, tables**

DRAFT

2690 D Appendix #4 Analysis using MEKD Kinematic Discriminant

2691 D.1 Matrix Element Kinematic Discriminant (MEKD)

2692 In this chapter we describe how the measurements in the HZZ4l analysis can be performed using the
 2693 matrix element kinematic discriminant (MEKD) which is extracted using standard and publicly avail-
 2694 able HEP tools. These include tools needed to generate model files from an arbitrary Lagrangian, such
 2695 as FeynRules [?] and LanHEP [?], as well as tools to calculate the matrix elements using these model
 2696 files, such as MadGraph [?], CalcHEP [?], and CompHEP [?]. One of the advantages of this approach is
 2697 that, taken together, these tools allow for relatively automatic implementation of new models and au-
 2698 tomatic generation of matrix elements [?]. In addition, these tools are standard, public, well tested and
 2699 commonly used in the community of HEP phenomenologists. The basics of this method is described in
 2700 details here [?], while the code to calculate leading order MEKD based on MadGraph libraries is publicly
 2701 available here [?].

2702 In general, when constructing a log-likelihood ratio to compare the hypothesis that there is some signal
 2703 (s) and some background (b) present to the hypothesis that only background is present, one finds that
 2704 the dependence on event-by-event information is through the quantity:

$$2705 D(\theta_s; \theta_b; x_i) = \frac{P_s(\theta_s; x_i)}{P_b(\theta_b; x_i)} \quad (49)$$

2706 In particle physics, the probabilities P_s and P_b can be related to the differential cross section of a signal
 2707 or background process with respect to the variables considered, normalized by the appropriate total
 2708 cross-section. It has been shown [?] that up to an overall normalization (which includes the ratio of total
 2709 signal and background cross sections, as well as potential differences in color or symmetry factors) this
 discriminant D is:

$$2710 D(\theta_s; \theta_b; x_i) \sim \frac{\sum_j f_{s_j, q_1}^p(x_1) f_{s_j, q_2}^p(x_2) |\mathcal{M}_{s_j}(p_i)|^2}{\sum_k f_{s_k, q_1}^p(x_1) f_{s_k, q_2}^p(x_2) |\mathcal{M}_{s_k}(p_i)|^2} \quad (50)$$

2711 where $f_{s_j, q_1}^p(x_1)$ and $f_{s_j, q_2}^p(x_2)$ are the relevant parton distribution functions, and $|\mathcal{M}_{s_k}(p_i)|^2$ is the squared
 2712 matrix element for the signal (background) process labelled j (k). The problem that the Higgs boson mass
 2713 M_H is a priori unknown is overcome by setting $M_H = M_{4l}$. In what follows, we consider the following
 quantity for the calculation of the discriminant and we name it MEKD:

$$2714 MEKD(p_i; m_{4l}) \equiv \ln \left(\frac{f_g^p(x_1) f_g^p(x_2) |\mathcal{M}_{sig}(p_i; m_{4l})|^2}{\sum_q [f_q^p(x_1) f_{\bar{q}}^p(x_2) |\mathcal{M}_{bkg}(p_i; m_{4l})|^2 + (q \leftrightarrow \bar{q})]} \right) \quad (51)$$

2715 There are at least three publicly available HEP event generators that can be used to produce these kine-
 2716 matic discriminants (KDs): MadGraph, CalcHEP and MCFM. In addition, there is a similar tool MELA
 2717 used within the CMS collaboration. In Table 37 we compare the functionality of different matrix ele-
 2718 ment KD calculators. The table demonstrates that different tools have different advantages and disad-
 2719 vantages. Nevertheless, it is interesting to note that MadGraph, CalcHEP and MCFM calculate matrix
 2720 element for $2 \rightarrow 4$ process and offer a possibility of using the available information about the initial state
 2721 (to this end, one must weigh the usual matrix element by the parton distribution functions). In addition,
 2722 the MCFM has an advantage over the other tools as it is already a NLO tool, but the tools are also about
 2723 to implement the NLO (e.g. nloMELA)

2724 Figures 185 shows ROC curves from MadGraph, CalcHEP and MCFM KDs produced at GEN-level
 2725 using the LO MadGraph MC sample. The ROC curves from different KD calculators present important
 2726 benchmark for the method itself. The level of agreement between CalcHEP and Madgraph is excellent.
 2727 In case of the MCFM agreement is excellent for the $2e2\mu$ final state, and approximate for the 4μ and $4e$
 2728 final states due to the missing interference terms [?]. The results presented in this chapter are obtained
 using the discriminant calculated by the MEKD code based on MadGraph.

Table 37: Approximations used in MadGraph-based MEKD, CalcHEP-based MEKD, MCFM-based MEKD, and AnalyticMELA KD.

Code feature/approximation	MadGraph	MEKD CalcHEP	MCFM	MELA
Input variables	four \vec{p}' 's	four \vec{p}' 's	four \vec{p}' 's	2 masses, 5 angles
Matrix element for	2 → 4	2 → 4	2 → 4	1 → 4
Permutations/interference in $2e2\mu$	yes	yes	no	no
Initial state pdf	yes	yes	yes	no

2729 Figures 186 shows ROC curves from MadGraph-based MEKD and MELA KD produced using the
 2730 RECO-level NLO Powheg MC samples. It can be observed that disagreement is larger in case of the
 2731 same-flavour final state. This can be contributed to the missing interference terms in MELA KD.

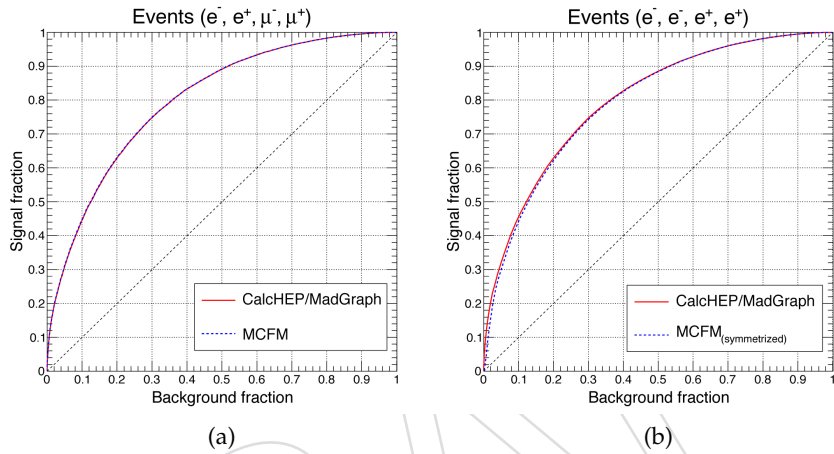


Figure 185: ROC curves obtained at GEN-level from LO MadGraph MC samples for $2e2\mu$ events (left) and $4e$ events (right) in mass window 120-130 GeV. Plots shows comparison between the MadGraph/CalcHEP-based MEKD and MCFM-based MEKD. Signal sample corresponds to $m_H = 125$ GeV.

2732 In addition, we investigate if information on initial states would of any benefit to the signal and back-
 2733 ground separation. In Figure 187 we compare the ROC curves obtained from the KD which is calculated
 2734 with and without PDF information. It can be seen that, in the absence of acceptance cuts, the difference
 2735 between the two ROC curves is quite significant. However, after the acceptance cuts are applied, the
 2736 curves become quite similar and the advantage of using 'KD calculated with PDF information can be
 2737 quantified as being at the percent level [?].

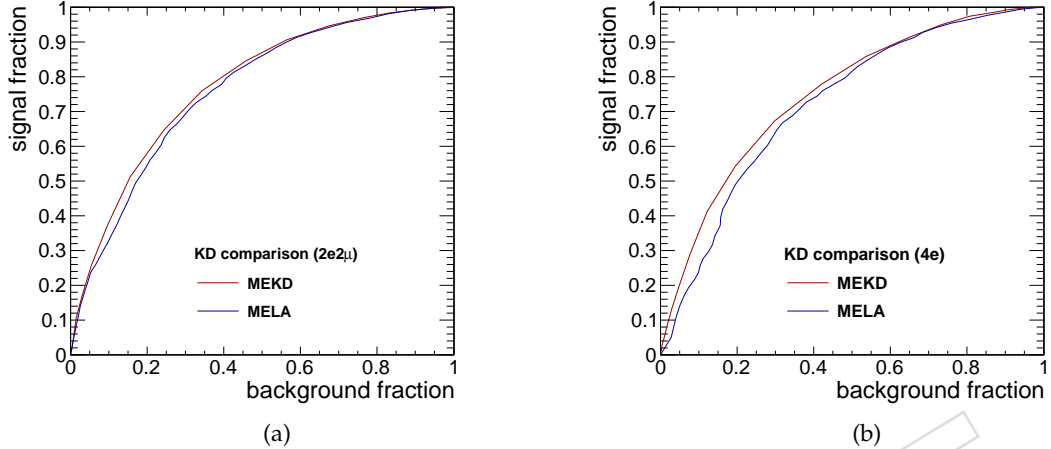


Figure 186: ROC curves obtained at RECO-level from NLO Powheg MC samples for $2e2\mu$ events (left) and $4e$ events (right) in mass window 120-130 GeV. Plots shows comparison between the MadGraph-based MEKD and MELA KD. Signal sample corresponds to $m_H = 125$ GeV.

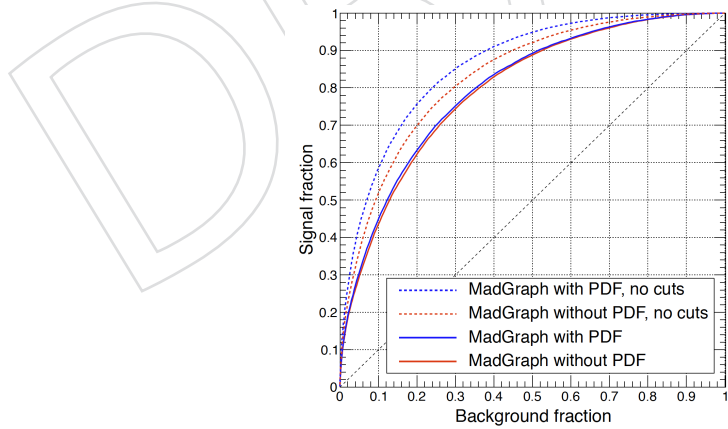


Figure 187: Gains in signal-vs-background separation due to including PDFs (or, equivalently, event rapidity) information. The dashed lines are for events with no p_T and η cuts; solid lines are in the reduced phase space after applying p_T and η cuts. The curves are obtained with gen-level leptons using the MadGraph MC sample.

2738 We also investigate the impact of non-perfect reconstruction on the performance of the MEKD variable.
 2739 Figure 188 (left) shows the effect of instrumental inefficiency, momentum mis-measurements, and FSR
 2740 on the signal-vs-background separation for 4ℓ events. The four ROC curves shown are obtained
 2741 using MEKD code and Powheg MC samples and they correspond to:

- 2742 1. STAT=3 gen-level leptons after gen-level cuts,
 2743 2. STAT=3 gen-level leptons after reco-level cuts (loss and smearing of the phase space due to reco
 2744 inefficiency),
 2745 3. STAT=3 gen-level leptons after reco-level cuts with pT's smeared by 2% (toy momentum smear-
 2746 ing),
 2747 4. reco-level leptons after reco-level cuts (FSR + real momentum smearing),

2748 Figure 188 (right) shows ROC curves for $4e$, $2e2\mu$, and 4μ events, separately. These plots highlight the
 2749 role of instrumental inefficiency, momentum mis-measurements, and FSR on the discrimination power
 2750 of MEKD (and any other KD variable). (TO BE UPDATED)



Figure 188: (Left) The effect of instrumental inefficiency, momentum mis-measurements, and FSR on the signal-vs-background separation for 4ℓ events. (Right) ROC curves for $4e$, $2e2\mu$, and 4μ events at RECO level. All curves are obtained with Powheg MC sample.

2751 **D.2 Kinematic Discriminant distributions and parameterization**

2752 In this section we analyze KD_{MEKD} distributions, obtain their parameterizations, and assess various
 2753 sources of systematic errors. All distributions shown are at the reconstruction level after all analysis
 2754 selections applied, unless stated otherwise.

2755 **D.2.1 KD_{MEKD} for signal and ZZ background**

2756 Characteristic 2D-distributions of MEKD in the low $m_{4\ell}$ mass range [80,140] GeV are shown for signal
 2757 and ZZ-background ($m_{4\ell}$, KD) in Figs. 189, 190. One can see that...

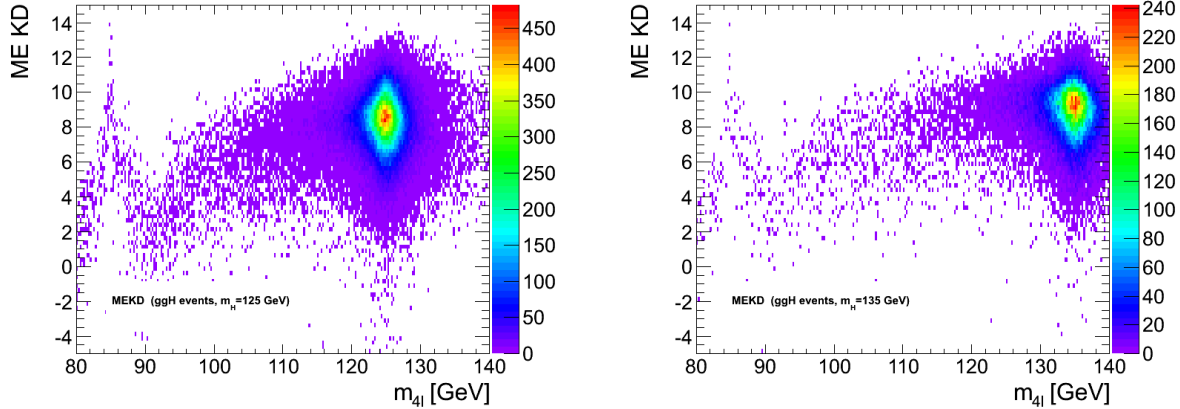


Figure 189: 2D distributions ($m_{4\ell}$, KD) for a Higgs boson with mass 125 GeV (left) and 135 GeV (right) in the [80;140] GeV range

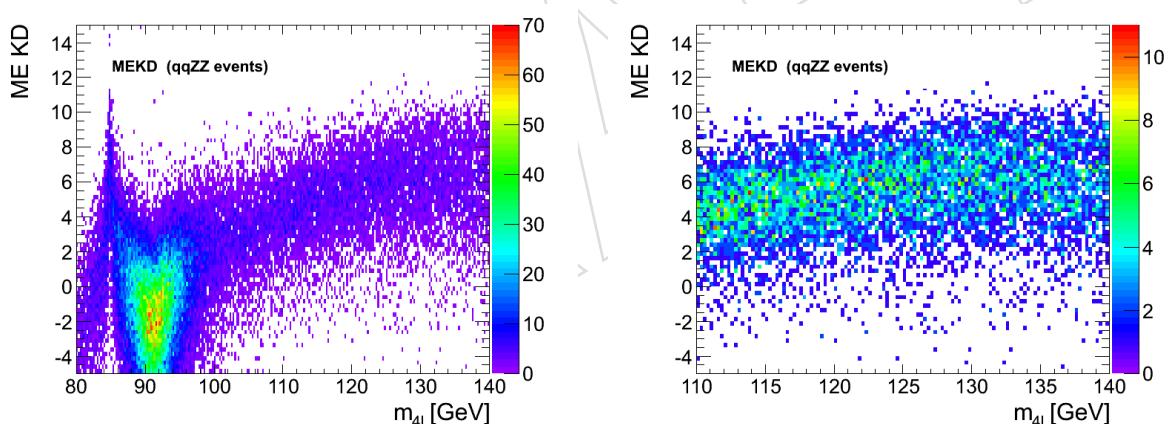


Figure 190: 2D distributions ($m_{4\ell}$, KD) for ZZ background in the [80;140] GeV range with $Z \rightarrow 4\ell$ peak present (left) and suppressed (right)

2758 Examples of signal and ZZ-background ($m_{4\ell}$, KD) 2D-distributions in the full mass range [100,800] GeV
 2759 are shown in Fig. 191. One can see that...

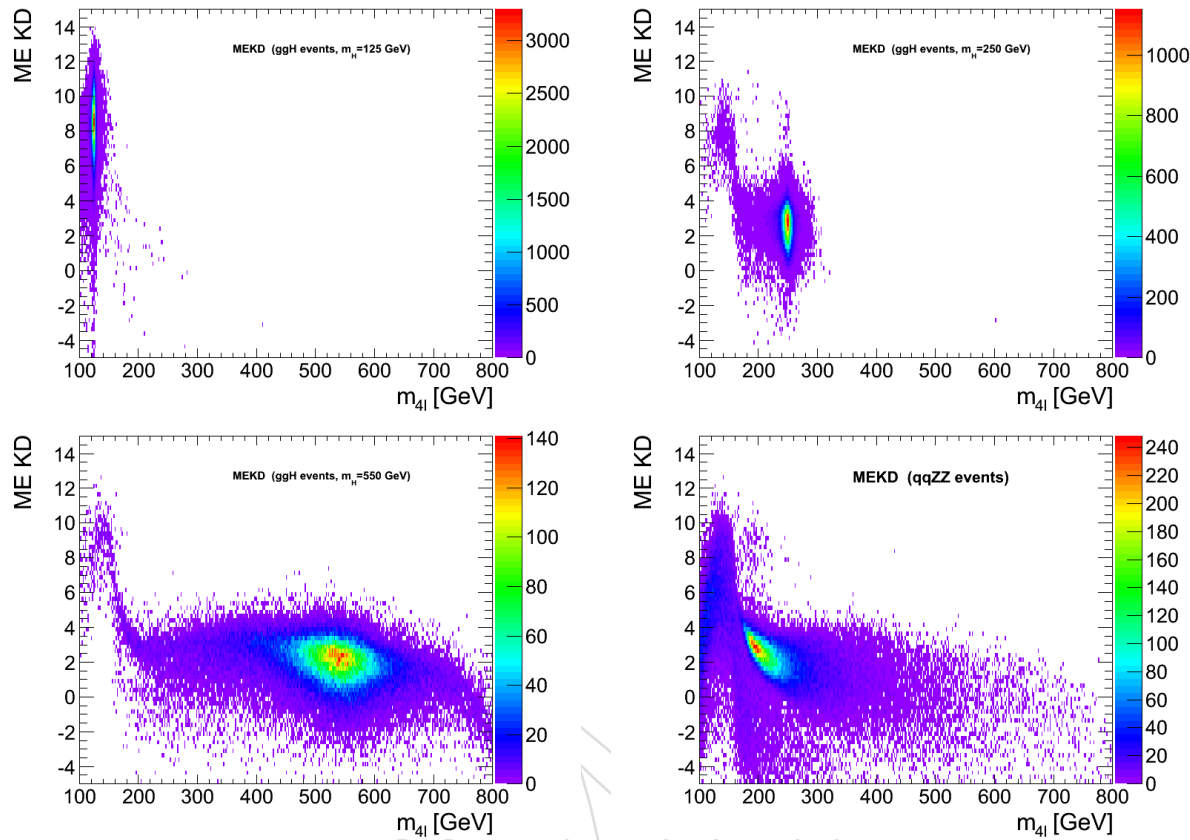


Figure 191: 2D distributions ($m_{4\ell}$, KD) for a Higgs boson with mass XXX, XXX, XXX GeV and ZZ background in the [100;800] GeV range

In order to parameterise the 2D distributions of KD for signal and background we split these distributions into a range of m_{4l} 1D-slices. Figures ?? shows examples of 1D-slices of KD_{MEKD} for 4μ events for both signal and ZZ background. The 1-D distributions of KD obtained in individual slices are fit with the double Gaussian function:

$$f_{KD}(a_0, a1, a2, a3, a4) = a_2 \frac{1}{\sqrt{2\pi a_1^2}} e^{-\frac{(x-a_0)^2}{2a_1^2}} + (1 - a_2) \frac{1}{\sqrt{2\pi a_4^2}} e^{-\frac{(x-a_3)^2}{2a_4^2}} \quad (52)$$

where the 5 parameters are 2 pairs of gaussian mean and sigma ($a_0, a1$) and ($a_3, a4$), while $a2$ is the so called "mixing" parameter between two gaussians. Fitted distributions and results of the fit for 4μ events are shown with solid and dashed line in the figure above, respectively. The distributions and fitting results are equivalent for the other two final states. The dependance of these parameters on m_{4l} is smoothed out by performing further fitting using empirical function of m_{4l} :

$$a_i(m_{4l}) = p_{i,0} + p_{i,1}\sqrt{m_{4l}} + p_{i,2}m_{4l} \quad (53)$$

As an illustration, the fitting results are shown for signal in Figure 193. Fitting results of the similar quality are obtained in case of background. (TO BE UPDATED)

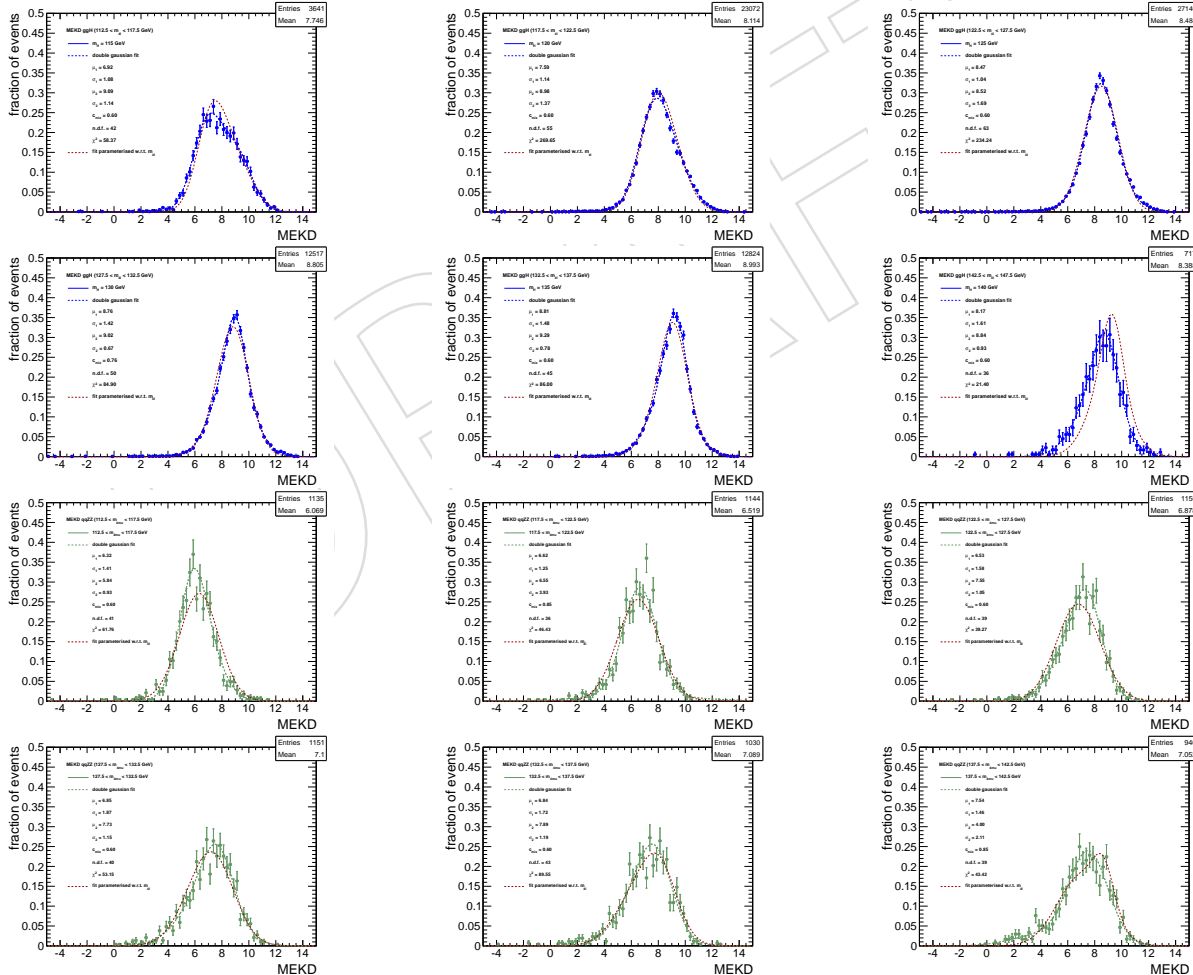


Figure 192: 1D-slices of KD_{MEKD} for signal and background for 4μ . Points are distribution from MC. Lines are fits specific to the shown slice.

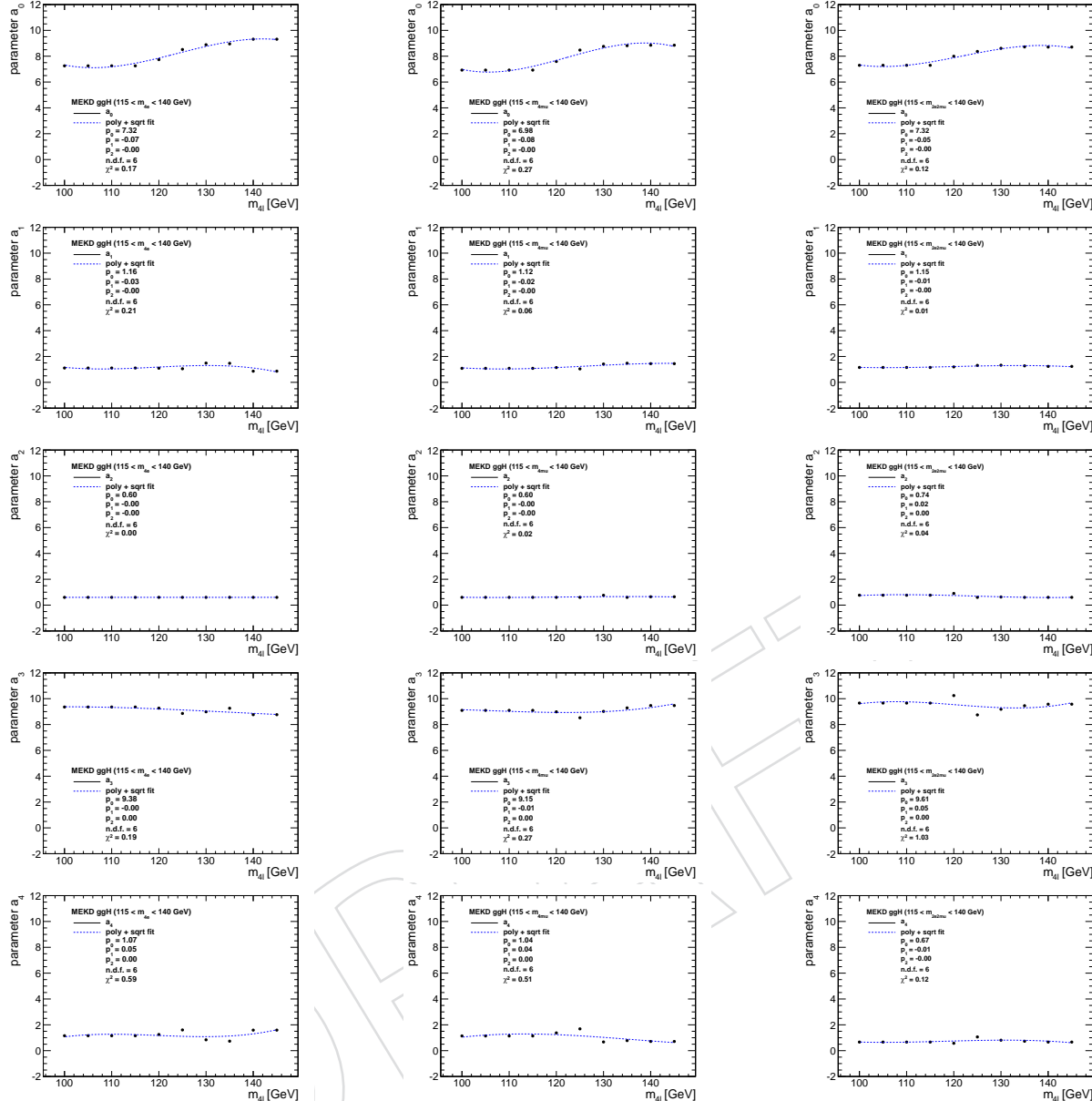


Figure 193: Five parameters of the function describing KD distributions for signal in all mass slices for 4e (left), 4μ (center), and 2e2μ (right). The solid lines show interpolation used for a smooth interpolation between tested mass points (slices), as described in text above.

2771 D.2.2 Systematic errors on KD_{MEKD} for signal and ZZ background

2772 The main source of the theoretical uncertainty for the MEKD is the uncertainty on the PDFs. We evaluate this effect by varying the choice of the PDFs and observing its effect on the. The expected effect is
2773 negligible. (TO BE UPDATED)

2775

2776 The instrumental effects are assessed following the procedure outlined in section XX above and evaluating the effects of instrumental inefficiency, momentum mis-measurements, and FSR on the the signal-
2777 vs-background separation for 4ℓ events (Figure 188 (left)). (TO BE UPDATED)

2779

2780 **D.2.3 KD_{MEKD} for reducible background**

2781 In order to understand the KD distribution for the reducible backgrounds, we look into the Z+X control
2782 regions in data. Due to the low statistics, we compare KD distribution obtained in data in the com-
2783 bined 4ℓ final state (not $4e/4\mu/2e2\mu$ separately) with the KD distribution in ZZ MC. For the reason of
2784 low statistics, we perform this comparison in small number of slices of $m_{4\ell}$. In case the differences be-
2785 tween reducible and ZZ backgrounds are not very large, we should be able to use the ZZ KD-shapes
2786 for reducible background with additional systematic uncertainty that would cover the observed differ-
2787 ences. We address the question of correlations of the shape systematics between $4e/4\mu/2e2\mu$ -channels
2788 by looking into two extremes of 0% and 100% correlations. (TO BE UPDATED)

D.3 Results and comparison with MELA

2789 In this chapter we perform the set of measurements using the MEKD described in previous section
2790 and the available statistical machinery. We produce the results for limits, p-values, cross-section, mass
2791 measurement, as well as J^{CP} determination. We compare these results with the MELA results presented
2792 in chapter XX. All the relevant non-KD specific aspects of the analysis are already covered in the chapters
2793 of the main body of this AN. (TO BE UPDATED)



2794 E Appendix #5 Matrix Element with Vector Algebra Method for 2795 $H \rightarrow ZZ \rightarrow 4\ell$ Studies

2796 In this section we describe the matrix element (ME) with vector algebra method based kinematic dis-
 2797 criminant. This method evaluates the event probability densities based on the differential cross-section
 2798 calculation. The technique is mathematically equivalent to analytical parameterization based on an-
 2799 gular and mass distributions, except for normalization of probabilities, which is absent in the case of
 2800 cross-section calculation but can be effectively accounted for with an ad hoc correction factor. This
 2801 method is based on vector algebra implemented in the event generators and for this reason could be
 2802 faster to implement when the process is ready in the generator application, in particular for background
 2803 processes. For example both $q\bar{q} \rightarrow ZZ$ and $gg \rightarrow ZZ$ background processes are implemented in the
 2804 MCFM program [64] library and could be adapted for the purpose of this approach. For the signal, the
 2805 JHUGen [74, 78] calculation is provided for any arbitrary couplings of any spin-0, 1, or 2 resonance and
 2806 is therefore adopted for the signal parameterization. MCFM provides matrix element only for the SM
 2807 Higgs signal, therefore JHUGen signal parameterization allows us to have the most general approach for
 2808 any signal hypothesis testing. Both analytical parameterization developed within CMS and the vector
 2809 algebra in JHUGen were shown to provide nearly identical results [78]. Both analytical parameterization
 2810 of the matrix element and the vector algebra implementation discussed below have been implemented
 2811 in the MELA package.

For a given process, the differential cross-section is described as [47]:

$$d\sigma = \frac{(2\pi)^4 |M|^2}{4\sqrt{(q_1 q_2)^2 - m_{q_1}^2 m_{q_2}^2}} d\Phi_n(q_1 + q_2; p_1, \dots, p_n), \quad (54)$$

2812 where $|M|$ is the Lorentz invariant matrix element; q_1, q_2 and m_{q_1}, m_{q_2} are the four momenta and masses
 2813 of the incident particles (in our case quarks or gluons), p_i is the four momentum of the i -th outgoing
 2814 particle, and $d\Phi_n$ is the n -body phase space given by:

$$d\Phi_n(q_1 + q_2; p_1, \dots, p_n) = \delta^4(q_1 + q_2 - \sum_{i=1}^n p_i) \prod_{i=1}^n \frac{d^3 p_i}{(2\pi)^3 2E_i}. \quad (55)$$

2815 where the sum runs over the n outgoing particles produced in the collision.

In the case of the $H \rightarrow ZZ \rightarrow 4\ell$ search, at the rest frame of the Higgs boson, the final states is fully described by a minimal sets of kinematic observables including 5 angles ($\cos \theta^*, \Phi_1, \cos \theta_1, \cos \theta_2, \Phi$) and 3 invariant masses ($m_1, m_2, m_{4\ell}$). Therefore we can calculate the four-momenta of all the incident and out-going particles based on these 8 observables. The four-momenta of all these particles are then taken as input to calculate the invariant matrix element $|M|^2$ for both the signal $H \rightarrow ZZ \rightarrow 4\ell$ and $q\bar{q} \rightarrow ZZ \rightarrow 4\ell$ processes. The event based $|M|^2$ calculation is done numerically through either MCFM [64] or JHUGen [74, 78]. We then construct a single kinematic discriminant based as below (va stands for vector algebra):

$$K_D(va) = \frac{|M|_{\text{sig}}^2}{|M|_{\text{sig}}^2 + C \cdot |M|_{\text{bkg}}^2}. \quad (56)$$

2816 E.1 ME evaluated with MCFM

2817 Figure 194 shows the $K_D(va)$ distributions comparing signal $gg \rightarrow H(125) \rightarrow ZZ \rightarrow 2e2\mu$ and $q\bar{q} \rightarrow ZZ \rightarrow 2e2\mu$ in two different four-lepton mass ranges. This discriminant is equivalent to the analytical-
 2818 parameterization of the K_D . We compare the performance of $K_D(va)$ with other approaches by evaluat-
 2819 ing the signal and background selection efficiency curves (ROC curves). We compare the ROC curves
 2820 of two independent implementations of the vector algebra ME methods using the same generator-level
 2821 events we find identical performance shown in Figure 195. In Fig. 196 we compare the ROC curves
 2822 using $K_D(va)$ with K_D with analytical PDF and similar performance.
 2823

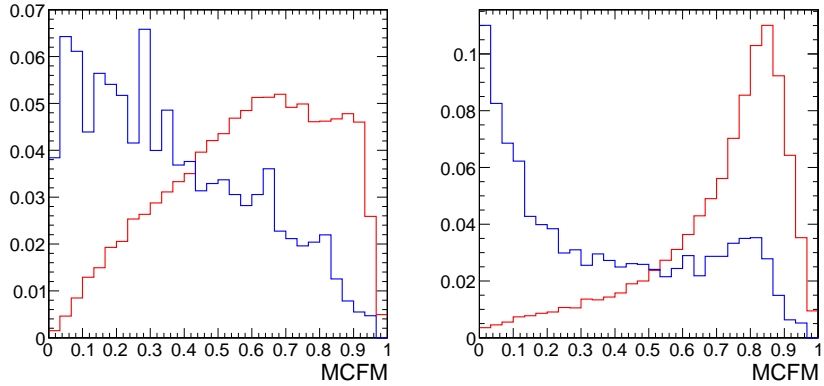


Figure 194: The $k_D(\text{va})$ distribution comparing the signal $H \rightarrow ZZ \rightarrow 4\ell$ and background $q\bar{q} \rightarrow ZZ \rightarrow 4\ell$ processes with both low (left) and high (right) four-lepton masses. The low mass range corresponds to [120-130] GeV with the signal chosen with a Higgs mass of 125 GeV, while the high mass range corresponds to [400-600] GeV with the signal chosen with a Higgs mass of 500 GeV. The distributions are normalized to unity to view the shape differences.

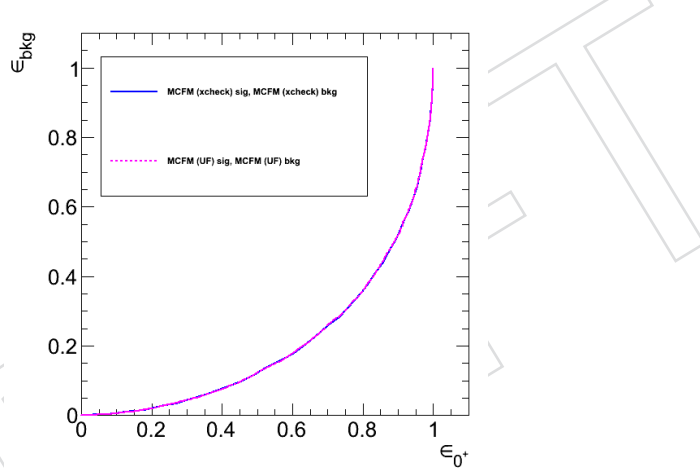


Figure 195: The ROC curves comparing two implementations $k_D(\text{va})$. The magenta dashed line is evaluated based on the MEKD implementation while the solid blue line is based on the MCFM/JHUGen implementation. The signal and background samples used in this comparison are the LO MadGraph events.

2824 E.2 ME evaluated with JHUGen for signal hypothesis separations

2825 To validate the JHUGen $|M|^2$ calculation, we compare the output with the one calculated in MCFM using
 2826 the same SM Higgs events. As shown in Fig. 197, we found the two methods give consistent outputs on
 2827 event by event base.

2828 We then include the $|M|^2$ calculation for the other signal hypotheses. The $|M|^2$ calculated for two sig-
 2829 nificant hypotheses are used to construct the hypothesis separation discriminants “pseudo-ME” similar to
 2830 pseudo-MELA (for separation of SM 0^+ and 0^-) and “gravi-ME” similar to gravi-MELA (for separation
 2831 of SM 0^+ and $2^+ + m$ with minimal couplings). Any other spin-parity discriminant is constructed in a
 2832 similar manner without any limitation.

2833 Figure 198 shows the pseudo-ME distributions for 0^+ and 0^- signals and ZZ background in different
 2834 lepton final states. Comparing the ROC curves for separating the 0^+ and 0^- signals we find identical
 2835 performance between pseudo-MELA and pseudo-ME discriminants in all lepton final states, as shown
 2836 in Fig. 199. ROC curves comparing the performance of gravi-ME and gravi-MELA are shown in Fig. 200.
 2837 There is good agreement of the two completely independent methods, one using analytical parameteri-

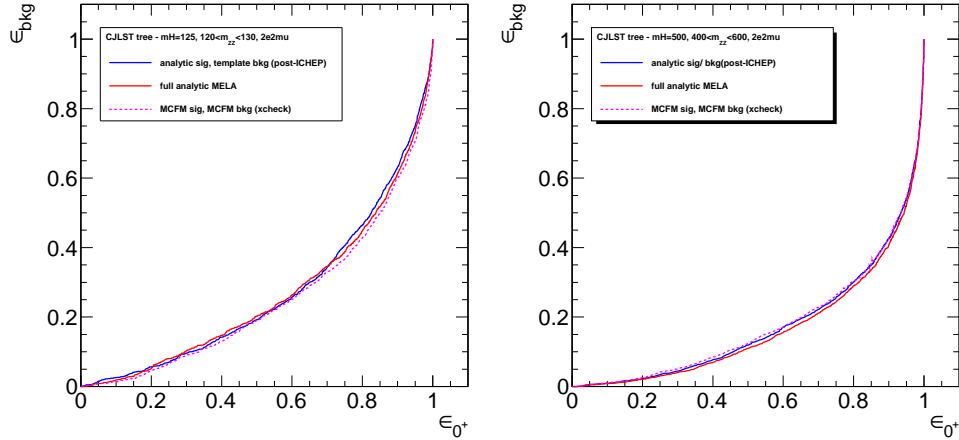


Figure 196: The ROC curves comparing the $k_D(\text{va})$ discriminant with other approaches evaluated for both low and high four-lepton masses.

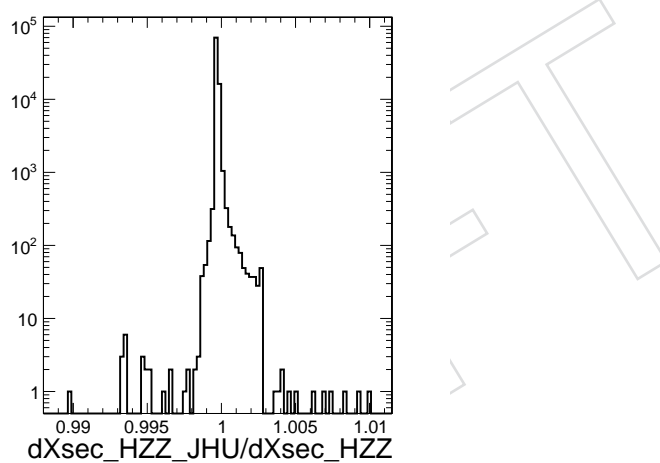


Figure 197: $|M|^2$ evaluated in JHUGen relative to the one from MCFM for $gg \rightarrow H(125) \rightarrow 4\ell$ process.

2838 zation of angular and mass distributions, and the other using vector algebra from event generator matrix
2839 elements.

2840 The statistical analysis remains similar to the nominal analysis, except that instead of the kinematic
2841 discriminant hypothesis separation pseudo-MELA or gravi-MELA, we use pseudo-ME or gravi-ME
2842 observables. The spin-parity hypothesis analysis is a 2D analysis of the (superMELA, pseudoME) or
2843 (superMELA, graviME) distributions where correlations of observables are included in the probability
2844 parameterizations. Figure 201 shows distribution of $q = -2\ln(\mathcal{L}_{J^P}/\mathcal{L}_{\text{SM}})$ with generated samples of
2845 background and signal of two types (SM 0^+ and J^P) for $m_H = 125$ GeV. Here the likelihoods \mathcal{L} are
2846 calculated with the signal rates allowed to float independently for each signal type and the nuisance pa-
2847 rameters are treated as independent. The expected distributions are generated with signal cross-section
2848 equal to that of the SM, which is consistent with observation. The expected separation is 1.97σ and 1.02σ
2849 for 0^- and 2^+ hypotheses, in excellent agreement with expectations using analytical MELA parameter-
2850 ization. Effects of the lepton interference are discussed in more detail below.

2851 E.3 Correction for lepton interference and parameterization of KD templates

2852 All the MC samples generated for Higgs boson $H \rightarrow ZZ \rightarrow 4\ell$ decays through summer 2012 did not in-
2853 clude modeling of interference between the identical leptons in the final state. This effect is relevant only

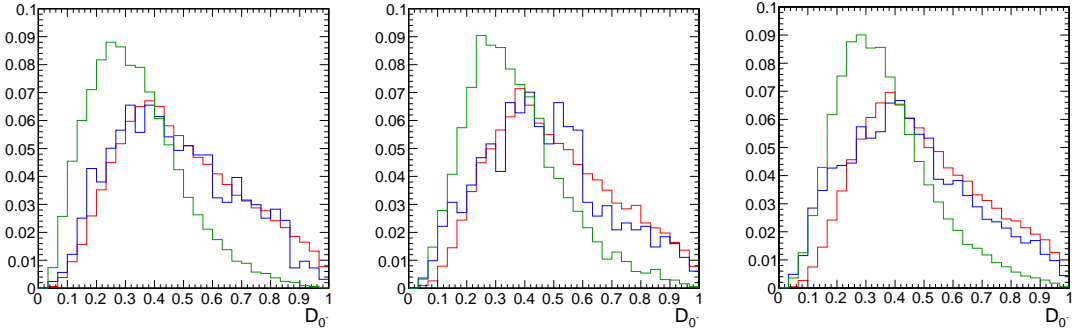


Figure 198: Pseudo-ME discriminant for separating 0^+ and 0^- hypothesis, comparing the two signal hypotheses and ZZ background in the $2e2\mu$ (left), $4e$ (middle) and 4μ final states. MC events after full selection with $m_{4\ell}$ in the mass range of [120-130] GeV are used. Distributions are normalized to unity to for shape comparison.

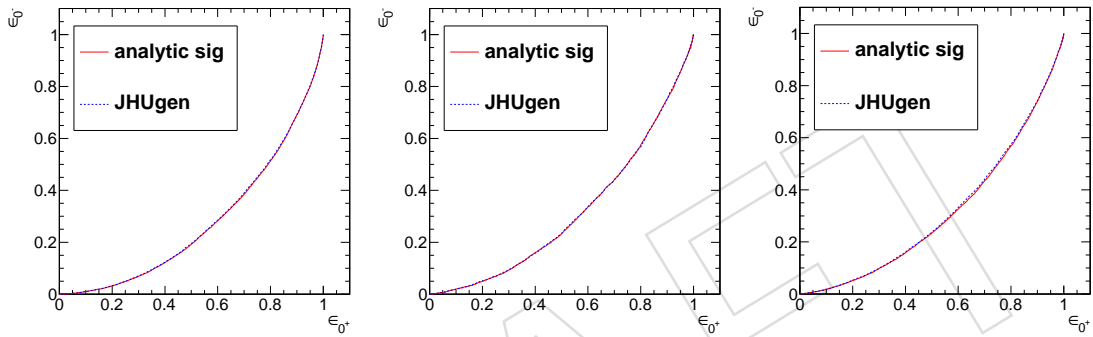


Figure 199: ROC curves comparing the performance of pseudo-ME and pseudo-MELA in $2e2\mu$ (left), $4e$ (middle) and 4μ (right) final states. In these comparisons we use the same MC events after full selection with $m_{4\ell}$ in the range of [120-130] GeV.

for the $4e$ and 4μ final state, that is 50% of events under study, and the size of the effect for spin-zero signal (either signal-to-background separation or signal-to-signal separation) is found to be of the order of few percent (see following sections). Nonetheless, it is important to correct the MC samples to model the effect of lepton interference. At the time of ICHEP-2012 or HCP-2012 conferences, a re-weighting procedure documented in Section 12 was applied based on the value of the kinematic discriminant. While this procedure was sufficient, it was not ideal since it was tuned to a particular method of calculating the discriminant. In parallel with the HCP-2012 update, documented in this note, a new procedure based on the full matrix element with JHUGen was introduced. The JHUGen package allows both generation of unweighted events for CMSSW simulation and calculation of the matrix element for kinematic discriminant calculation. We adopt the latter functionality for re-weighting of events according to the formula weight = $|M(4\mu)|^2 / |M(2e2\mu)|^2$. The results of this procedure are shown with fullsim CMSSW samples, both POWHEG+Pythia and JHUGen, see Fig. 202. The sample generated without interference but after the re-weighting correction is consistent with the sample generated with interference, leading to a successful closure test.

Following the same procedure as outline in Section 12, the 2D conditional templates $T(m_{4\ell}, KD)$ are created, with proper accounting for lepton interference in both MC samples and the matrix element calculation, as discussed above. These templates are shown in Fig. E.3. A special care is taken to properly normalize the probabilities of the signal and background in the KD calculation in such a manner that at each value of $m_{4\ell}$ the value of $KD=0.5$ corresponds to equal probability for signal to be above 0.5 and background to be below 0.5. This leads to a smooth population of signal and background densities across the 2D templates. The proper accounting for lepton interference is shown in Fig. 204 where small improvement in signal-to-background separation is visible in the $4e$ and 4μ channels.

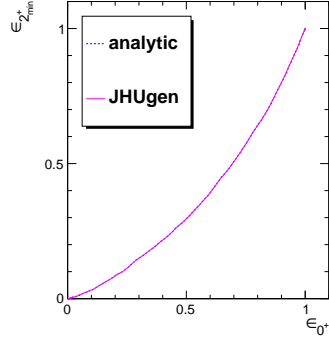


Figure 200: ROC curves comparing the performance of gravi-ME and gravi-MELA.

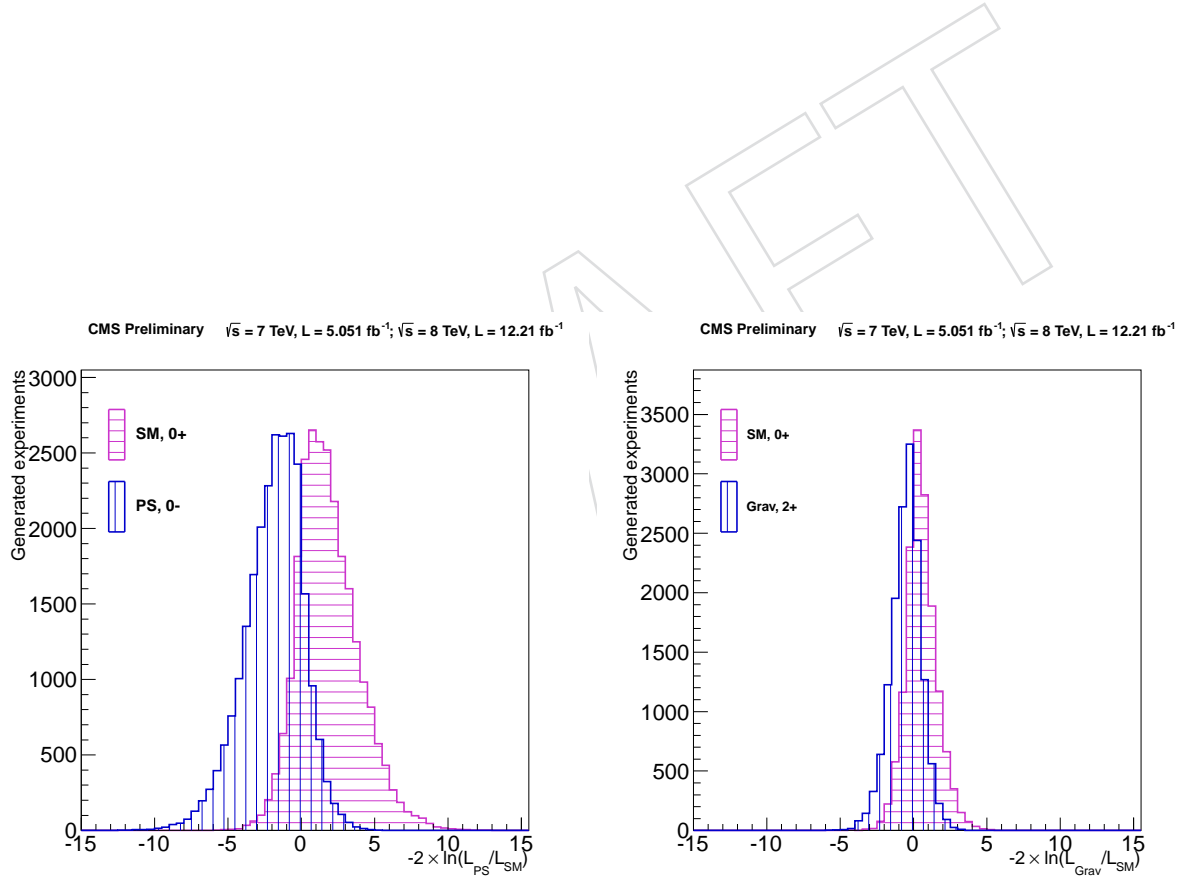


Figure 201: Distribution of $q = -2 \ln(\mathcal{L}_{0^+} / \mathcal{L}_{\text{SM}})$ (left) and $q = -2 \ln(\mathcal{L}_{2^+} / \mathcal{L}_{\text{SM}})$ (right) for two signal types (0^+ horizontally hatched histogram, alternative J^P vertically hatched histogram) for $m_H = 125 \text{ GeV}$ shown with a large number of generated experiments. The arrows indicate the observed value.

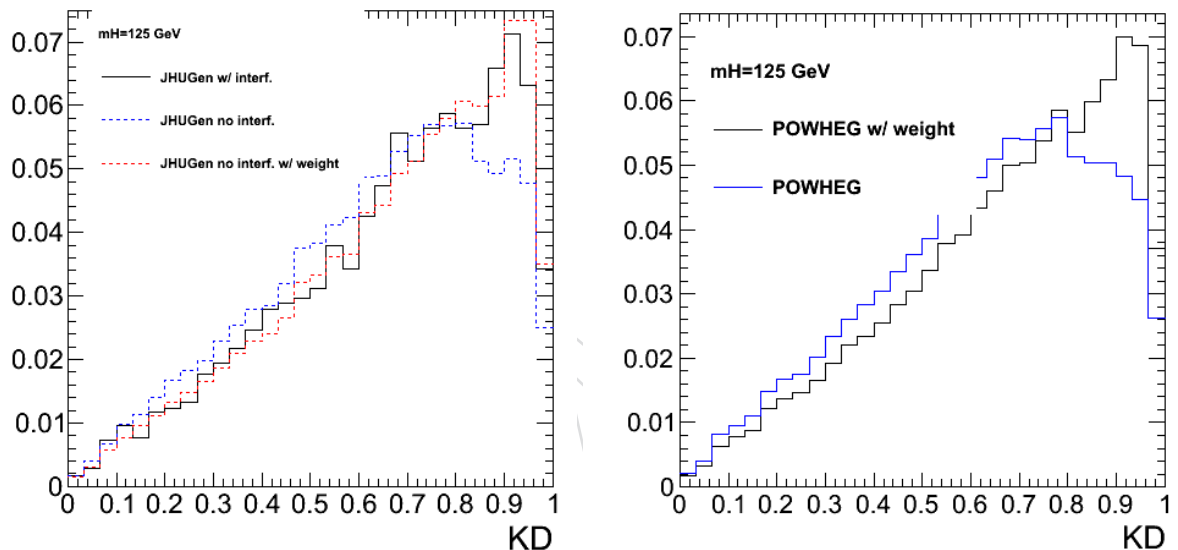


Figure 202: Distribution of the MELA K_D with vector algebra implementation in the $H \rightarrow ZZ \rightarrow 4\mu$ channel for $m_H = 125$ GeV. Left: JHUGen fullsim samples generated with lepton interference (solid black), without lepton interference (dashed blue), and without lepton interference but with re-weighting discussed in text (dashed red). Right: POWHEG+Pythia fullsim sample generated without lepton interference (solid blue), and after re-weighting discussed in text (solid black).

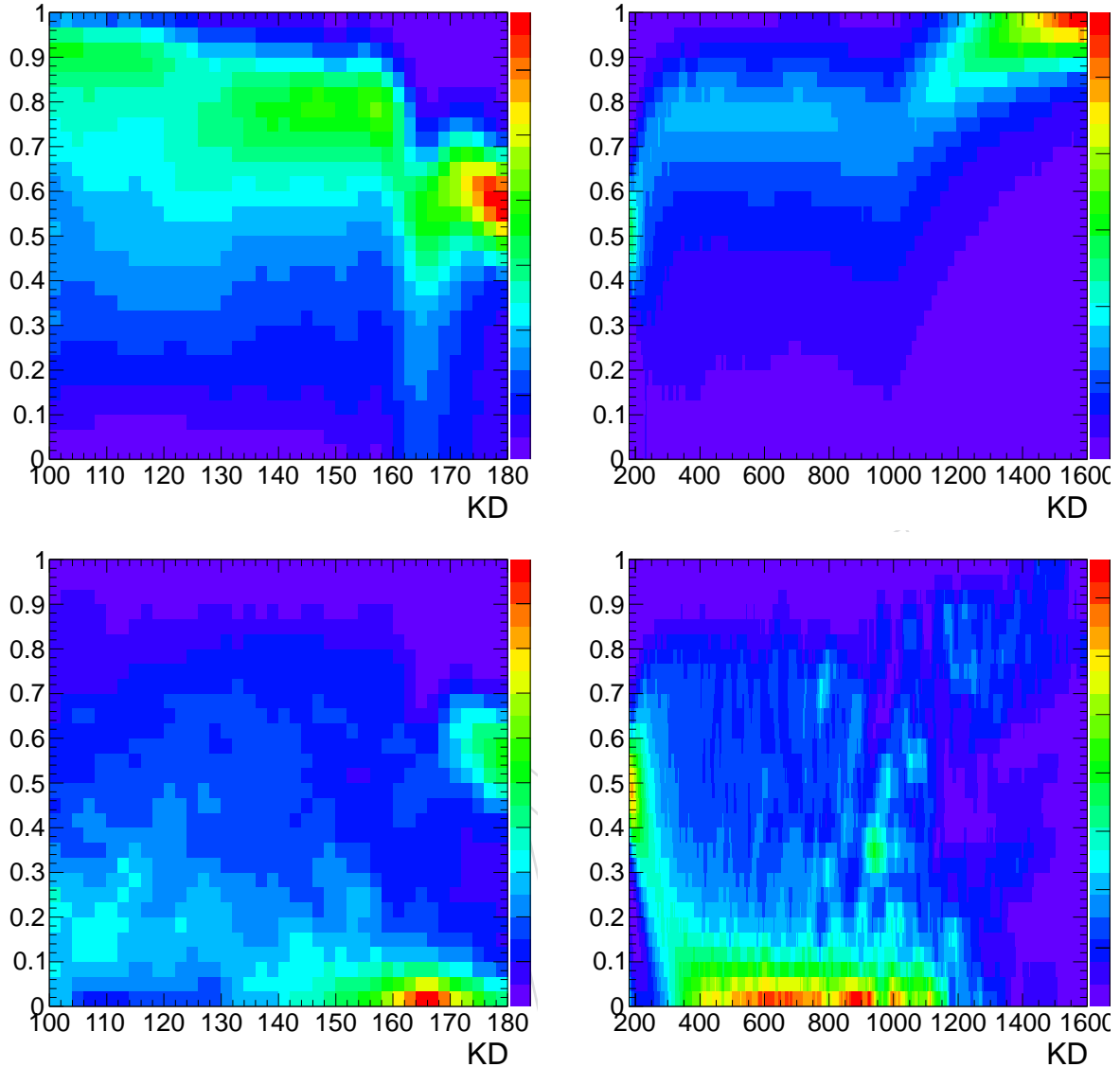


Figure 203: Conditional templates $T(m_{4\ell}, KD)$ for the $H \rightarrow ZZ \rightarrow 2e2\mu$ channel for signal (top) and $q\bar{q} \rightarrow ZZ$ background (bottom) in the zoomed (left) and the full (right) mass ranges.

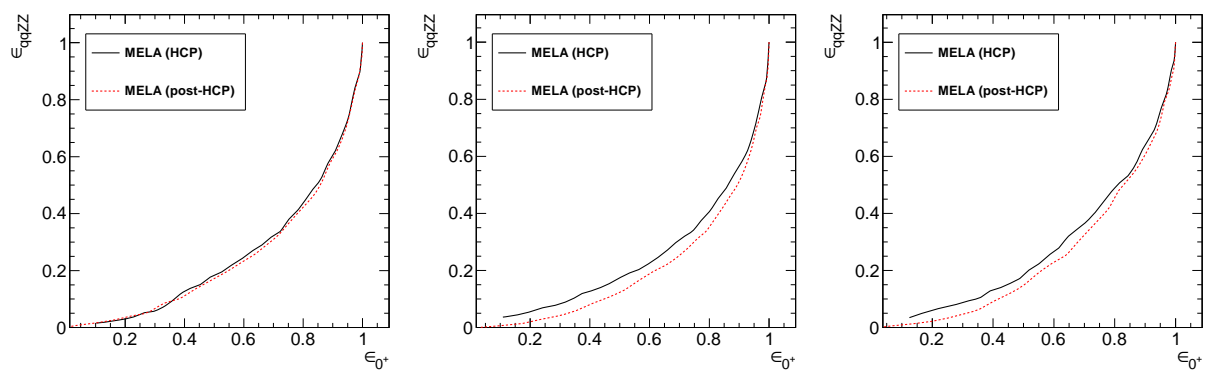


Figure 204: The ROC curves comparing the MELA KD with (post-HCP) and without (HCP) including lepton interference.

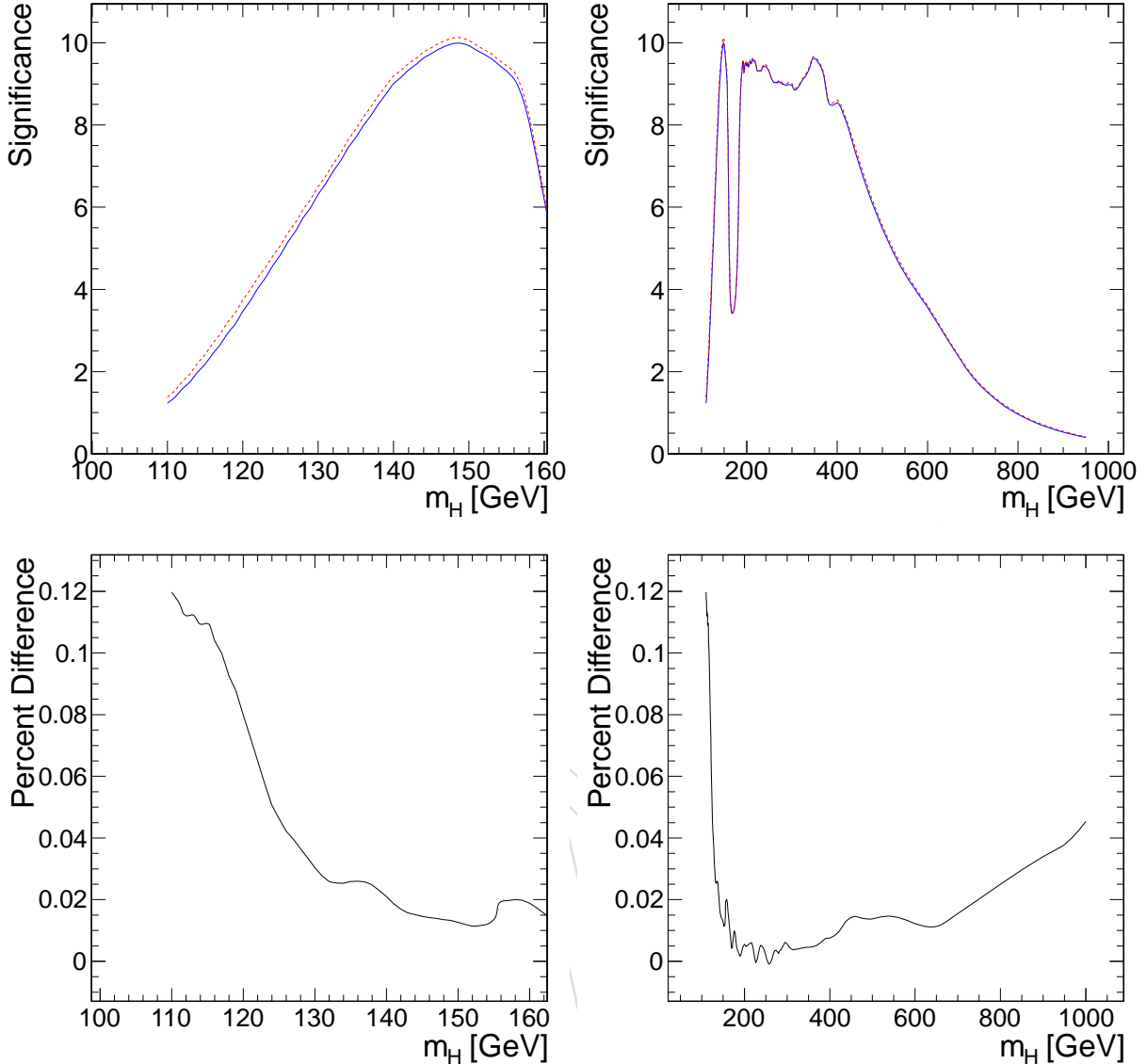


Figure 205: Comparison of the expected significance using the MELA KD with (post-HCP) and without (HCP) including lepton interference. Top: expected significance for a SM Higgs boson observation using HCP dataset ($5+12 \text{ fb}^{-1}$). Bottom: fractional improvement in expected significance. The zoomed (left) and the full (right) mass ranges are shown.

2876 E.4 Performance with the KD

2877 With the KD parameterization discussed in the previous sub-section and keeping the rest of the analysis
 2878 unchanged with respect to analysis approved for the HCP-2012 conference, we have performed the
 2879 fit for the SM Higgs boson observation using HCP dataset ($5+12 \text{ fb}^{-1}$). Expected results are shown in
 2880 Fig. 205. The effect of lepton interference on expected significance is a few percent around $m_H = 125 \text{ GeV}$
 2881 and above.

2882 E.5 Spin-parity analysis

2883 With the spin-parity KD parameterization discussed in the previous sub-sections (that is calculation of
 2884 pseudo-MELA and gravi-MELA using the vector algebra approach) and keeping the rest of the analysis
 2885 unchanged with respect to analysis approved for the HCP-2012 conference (such as calculation of the
 2886 super-MELA variable for signal-to-background separation), we have performed the fits for the SM Higgs

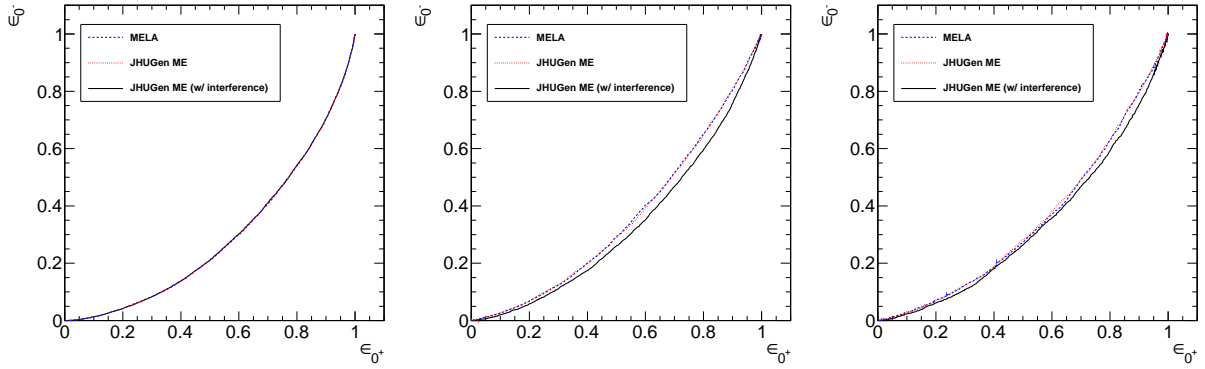


Figure 206: The ROC curves comparing the pseudo-MELA KD with (post-HCP) and without (HCP) including lepton interference.

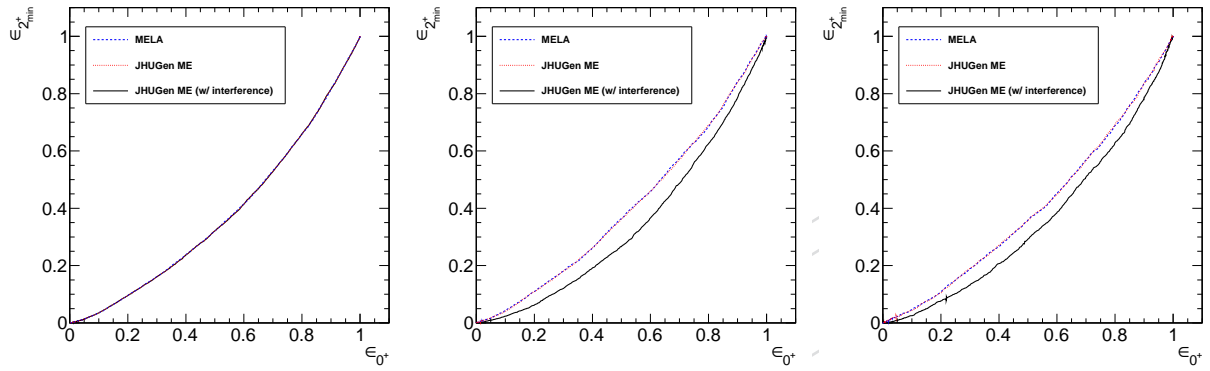


Figure 207: The ROC curves comparing the gravi-MELA KD with (post-HCP) and without (HCP) including lepton interference.

boson spin-parity properties using HCP dataset ($5+12 \text{ fb}^{-1}$). The comparison of pseudo-MELA and gravi-MELA variables with and without including lepton interference in the discriminant calculation (but always including lepton interference in the MC samples) is shown in Figs. 206 and 207. The effect of interference in the spin-zero case is small, while it is bigger in the spin-two case. Repeating the rest of the analysis in exactly the same manner as for HCP, only exchanging the pseudo-MELA and gravi-MELA observables using the vector algebra approach both with and without including interference, we obtain results shown in Table 38 and Fig. 208. There is a 2.6% difference in expected separation for the spin-0 case and 12.3% in the spin-2 case.

Table 38: Expected separation of the SM Higgs boson model 0^+ and an alternative J^P model (0^- or 2^+) for $m_H = 126 \text{ GeV}$ obtained with a large number of generated experiments.

	no interference in ME	with interference in ME
$0^+ \text{ vs } 0^-$	1.91σ	1.96σ
$0^+ \text{ vs } 2^+$	1.22σ	1.37σ

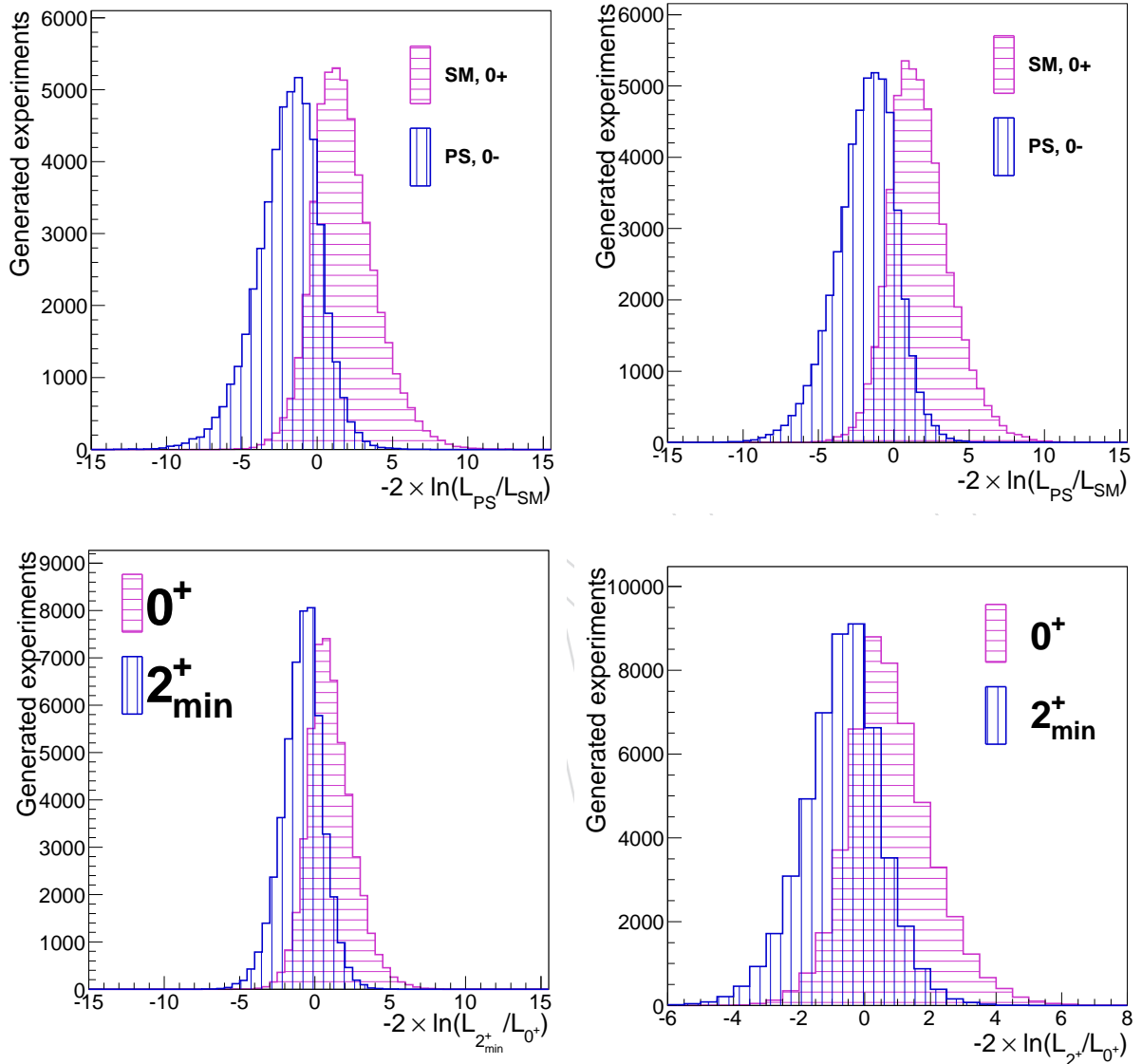


Figure 208: Distribution of $q = -2\ln(\mathcal{L}_{0-}/\mathcal{L}_{SM})$ (top) and $q = -2\ln(\mathcal{L}_{2+}/\mathcal{L}_{SM})$ (bottom) for two signal types (0^+ horizontally hatched histogram, alternative J^P vertically hatched histogram) for $m_H = 126$ GeV shown with a large number of generated experiments. Left: including lepton interference in the KD, Right: without including lepton interference in the KD parameterization.